



## **EERC Final Report**

Prepared for  
The Petroleum Institute  
Abu Dhabi, UAE

Prepared by  
Prof. Nariman Farvardin, Provost  
Principal Investigator and EERC Project Director

Prof. Avram Bar-Cohen, Chair  
EERC Project Deputy Director

Dr. Azar Nazeri  
EERC Research Manager

A.J. Clark School of Engineering  
University of Maryland, College Park, MD 20742, USA

December 30, 2008



## **EERC Key Contributors**

### **University of Maryland – College Park, MD, USA**

Sami Ainane  
Shapour Azarm  
Balakumar Balachandran  
Avram Bar-Cohen  
John Cable  
Serguei Dessiatoun  
Nariman Farvardin  
Ashwani K. Gupta  
Ali Haghani  
Yunho Hwang  
Greg Jackson  
PK Kannan  
Ken Kiger  
Mohammad Modarres  
Reinhard Radermacher  
Amir Riaz

### **Petroleum Institute – Abu Dhabi, UAE**

Ali Almansoori  
Ahmed Abdala  
Youssef Abdel-Magid  
Tareq Al Ameri  
Saleh Al Hashimi  
Valerie Eveloy  
Afshin Goharzadeh  
Mansour Karkoub  
Rocky Kubo  
Michael Ohadi  
Peter Rodgers  
Mohamed Sassi  
Abdenmour Seibi

# Table of Contents

<b>List of EERC Key Contributors</b>	<b>2</b>
<b>Table of Contents</b>	<b>3</b>
<b>Executive Summary</b>	<b>5</b>
<b>1. Introduction</b>	<b>7</b>
<b>2. Overview of EERC Achievements</b>	<b>8</b>
A. Research	
B. Education and Knowledge Transfer	
C. International Visibility	
D. Meeting ADNOC's Needs	
<b>3. Educational Projects</b>	<b>21</b>
<b>Fundamentals of Engineering Education</b>	<b>22</b>
S. Ainane (UMD), P. Rodgers (PI)	
<b>Development and Delivery of Course Material for Engineering Project Management Courses</b>	<b>24</b>
A. Haghani (UMD), J. Cable (UMD)	
<b>4. Research Projects</b>	<b>25</b>
<b>4.1. Energy Recovery and Conversion</b>	
<b>Force-Fed Cooling of Photovoltaic Arrays for High Efficiency Solar Energy Systems</b>	<b>26</b>
S. Dessiatoun (UMD), A. Shooshtari (UMD), M. Ohadi (PI)	
<b>Sulfur Recovery from Gas Stream using Flameless and Flame Combustion Reactor</b>	<b>52</b>
A.K. Gupta (UMD), M. Sassi (PI)	
<b>Solid Oxide Fuel Cells for CO<sub>2</sub> Capture and Enhanced Oil Recovery</b>	<b>84</b>
G. Jackson (UMD), V. Eveloy (PI), A. Almansoori (PI)	
<b>Fundamental Immiscible Porous Media Studies for Improved Reservoir Models</b>	<b>96</b>
K. Kiger (UMD), A. Riaz (UMD), A. Shooshtari (UMD)	
<b>Solar Cooling</b>	<b>99</b>
R. Radermacher (UMD), Y. Hwang (UMD) R. Kubo (PI), P. Rodgers (PI)	

<b>Waste Heat Utilization in the Petroleum Industry</b>	<b>121</b>
R. Radermacher (UMD), Yunho Hwang (UMD), S. Al Hashimi (PI), P. Rodgers (PI)	
<b>4.2. Energy Efficient Transport Processes</b>	<b>133</b>
<b>Thermally Enhanced Polymer Heat Exchanger for Seawater Applications</b>	<b>134</b>
A. Bar-Cohen (UMD), P. Rodgers (PI), A. Abdala (PI)	
<b>Study of Condensing Flows in a Micro-scale Channel with a Micro-element Array and Visual Techniques</b>	<b>153</b>
S. Dessiatoun (UMD), A. Shooshtari (UMD), M. Ohadi (UMD), A. Goharzadeh (PI)	
<b>An EHD-Enhanced Gas/Liquid Separator</b>	<b>183</b>
S. Dessiatoun (UMD), A. Shooshtari (UMD), M. Ohadi (PI), A. Goharzadeh (PI)	
<b>4.3. Energy System Management</b>	<b>205</b>
<b>Robust Optimization of Petrochemical Systems</b>	<b>206</b>
S. Azarm (UMD), S. Al Hashimi (PI), A. Alimansoori (PI)	
<b>Dynamics and Control of Drill Strings on Fixed and Floating Platforms</b>	<b>231</b>
B. Balachandran (UMD), M. Karkoub (PI), Y. Abdelmagid (PI)	
<b>Developing Corporate Dashboards for Multi-Unit Firms: An Agent-Based Approach</b>	<b>270</b>
P. K. Kannan (UMD), A. Almansoori (PI)	
<b>Development of a Probabilistic Model for Degradation Effects of Corrosion-Fatigue-Cracking in Oil and Gas Pipelines</b>	<b>281</b>
M. Modarres (UMD), A. Seibi (PI)	
 <b>Appendices</b>	
<b>Appendix A: Program for Second EERC Workshop</b>	<b>303</b>
<b>Appendix B: List of Attendees for Second EERC Workshop</b>	<b>305</b>

## Executive Summary

This document is the final report on Phase I of the Energy Education and Research Collaboration (EERC) between the Petroleum Institute (PI) and the University of Maryland (UMD). The primary goals of EERC are to bring a world-class education in engineering and applied sciences to the citizens of the UAE and to foster culture of pioneering and applied research especially in the field of energy.

The EERC Phase I program started in October of 2006 for a period of 2 years. It involved an initial stage where a small team of faculty and administrators from both institutions focused on identifying and exploring areas of mutual benefit to both PI and UMD. Working closely together, the PI and UMD representatives studied and analyzed the needs of both institutions, selected specific research and educational programs, and identified and planned milestones for the successful execution of the EERC mission.

On the research front, Phase I started with 10 projects in diverse energy-related topics, such as Solid-Oxide Fuel Cells, Waste-Heat Utilization in the Petroleum Industry, and Polymer Heat-Exchangers for Seawater Applications. After the first EERC Workshop in January 2008, and at the request of PI administration, UMD consolidated the 10 projects into three cohesive research thrusts: *Energy Recovery and Conversion*, *Energy Efficient Transport Processes*, and *Energy System Management*. The purpose of this consolidation was to enhance coordination and collaboration between PI and UMD faculty, to aid in identifying research areas of joint interest, and to enable a smooth transition to the longer term collaborative programs. All research projects successfully achieved their stated objectives, as reported in seven technical quarterly reports issued during the past two years and in the extensive summaries provided in the present report. The scientific results were also disseminated via more than 40 publications and presentations at archival journals and international conferences.

On the educational front, EERC secured an agreement by the Maryland Board of Professional Engineers to offer the Fundamentals of Engineering (FE) Exam to PI at Abu Dhabi, as a possible academic assessment metric at PI, an important step in introducing professional engineering (PE) licensing for ADNOC, and a first step towards ABET accreditation of PI. As part of this activity EERC developed review course materials to prepare PI faculty and students for the exam. EERC also developed and delivered several courses in Engineering Project Management to PI and GASCO and performed a feasibility study of establishing a graduate program in Engineering Project Management at PI.

Knowledge transfer and human resource development has been the core objective of the educational component of EERC. This is manifested by the continued assignment of Dr. Michael Ohadi as the Provost and acting President at PI, and by support in administrative affairs by Dr. Bar-Cohen and UMD Provost Dr. Farvardin, who serves on the PI's Institutional Advisory Board. Other activities included more than thirty-five visits by the faculty, administrators, and students of the two institutions, two research review workshops at PI, delivery of several graduate and undergraduate engineering courses, a sabbatical stay of a UMD faculty at PI, and the education of four ADNOC scholars at UMD, three of whom are expected to graduate and join PI as new faculty in 2009.

These activities have measurably impacted both education and research and have provided the foundation for a culture of excellence in both areas, and have given great international visibility to the PI. International and outside recognition of this collaboration far exceeded expectations, with than forty five publications in international archival journals and conference proceedings, and two jointly organized "Energy 2030" conferences, an international forum dedicated to addressing

energy resources and technologies in 2030. Moreover, to increase PI's international visibility of PI, UMD President Dr. C.D. Mote gave the 2008 commencement speech at PI. In addition, several UMD faculty attended two PI commencements in 2007 and 2008.

EERC's activities were designed to be highly relevant to the needs the oil and gas industry in general, and to ADNOC in particular. The most significant development in this area, besides offering short courses to ADNOC engineers and executives and visiting ADNOC facilities, was to hire a research faculty at UMD to conduct research in reservoir modeling, which is of great interest to ADNOC and its subsidiaries. This research will be conducted in close collaboration with Stanford University and PI.

Phase I concluded with the submission of a proposed long-term collaboration plan for future phases of EERC, based on the continuation and expansion of the successfully implemented EERC projects, as well as the addition of new activities of mutual interest to PI and UMD.

# 1. Introduction

To provide world-class education to the citizens of the United Arab Emirates in engineering and the applied sciences, the Petroleum Institute (PI) of Abu Dhabi, UAE, has entered into a long-term collaborative effort with the University of Maryland (UMD) to enhance its own undergraduate, graduate studies/research, and continuing education practices. The PI was founded by Emiri decree in 2001 under the direction of H.H. Sheikh Khalifa bin Zayed Al-Nahyanand. It is sponsored by a consortium of Abu Dhabi National Oil Company (ADNOC) and its international partners (Shell, BP, Total, and Japan Oil Development Company).

ADNOC and other member companies and industrial partners have significant interests in the areas of petroleum gas and oil fuel exploration, petroleum fuel refining, safety, reliability and environmental issues, and advanced design tools for enhanced recovery and processing. Therefore, the student training at the PI must encompass critical elements in all of these fields, incorporating cutting-edge research and technology innovations. As has been demonstrated over the past two years, UMD is in a strong position to lend its expertise in these fields in active collaboration with the PI.

The PI and UMD recognize the many potential benefits for both institutions that could result specifically from collaborative educational and research activities in the field of Energy Sciences and Engineering. The Energy Education and Research Collaboration (EERC) was therefore created within the A.J. Clark School of Engineering at the University of Maryland to provide the administrative structure and academic oversight for these collaborative efforts.

Phase I collaboration between PI and UMD has focused on identifying near-term and long-term goals and on deploying and implementing best practices in both research and education. In the Phase I program, a small team of faculty and administrative staff from both institutions dedicated a significant part of their time to identifying and exploring areas of mutual benefit to both PI and UMD. These activities have measurably impacted both education and research and have provided the foundation for a culture of excellence in both areas. UMD and PI faculty and researchers have jointly reported to PI on their progress in the various areas of this collaboration on a quarterly basis via video conferences and quarterly reports. Seven such quarterly reports were completed and submitted to PI, and ten video conferences were conducted during the last two years.

This Final Report is the culmination of all the activities and progress achieved and reported in the past two years. The overall educational achievements of the collaboration are summarized in the first section of the report, in Sections 2 and 3, while the accomplishments of individual research projects are reported in Section 4.

## 2. Overview of EERC Achievements

The following provides an overview of the achievements of the various Phase I EERC activities. Part A provides highlights of the research efforts, with more detailed summaries provided in Section 4. Part B describes the efforts and outcome of educational activities; Part C is a summary of the achievements in the international arena; and Part D explains the steps the EERC took to address ADNOC's needs.

### A. Research

On the research front, Phase I began with 10 projects in diverse energy related topics. Three projects were added later with seed funding. After the first EERC Workshop in January 2008, and at the request of PI administration, UMD consolidated the projects into three cohesive research thrusts: *Energy Recovery and Conversion*, *Energy Efficient Transport Processes*, and *Energy System Management*. The purpose of this consolidation was to enhance coordination and collaboration between PI and UMD faculty, to aid in identifying research areas of joint interest, and to enable a smooth transition to the longer term collaborative programs. All research projects successfully achieved their stated objectives, as reported in seven technical quarterly reports issued during the past two years, and in the extensive summaries provided in the present report. The scientific results were also disseminated via more than 40 publications and presentations at archival journals and international conferences.

#### ***Projects***

##### **1. Energy Recovery and Conversion**

- Force-Fed Cooling of Photovoltaic Arrays for High Efficiency Solar Energy Systems
- Sulfur Recovery from Gas Stream using Flameless and Flame Combustion Reactors
- Solid Oxide Fuel Cells for CO<sub>2</sub> Capture and Enhanced Oil Recovery
- Fundamental Immiscible Porous Media Studies for Improved Reservoir Models
- Solar Cooling
- Waste Heat Utilization in the Petroleum Industry

##### **2. Energy Efficient Transport Processes**

- Thermally Enhanced Polymer Heat Exchanger for Seawater Applications
- Study of Condensing Flows in a Micro-Scale Channel with a Micro-Element Array and Visual Techniques
- An EHD-Enhanced Gas/Liquid Separator

### 3. Energy System Management

- Robust Optimization of Petrochemical Systems
- Dynamics and Control of Drill Strings on Fixed and Floating Platforms
- Developing Corporate Dashboards for Multi-Unit Firms: An Agent-Based Approach
- Development of a Probabilistic Model for Degradation Effects of Corrosion-Fatigue Cracking in Oil and Gas Pipelines

### **Publications**

1. Li, G., M. Li, S. Azarm, S. Al Hashimi, T. Al Ameri, and N. Al Qasas, "Improving Multi-Objective Genetic Algorithms with Adaptive Design of Experiments and Online Metamodeling," *Structural and Multidisciplinary Optimization*, Vol. 37, No. 5, pp. 447-461, DOI: 10.1007/s00158-008-0251-6 (2009).
2. Li, M., Azarm, S., Williams, N., Al Hashimi, S., Almansoori, A., and Al Qasas, N., "Integrated Multi-Objective Robust Optimization and Sensitivity Analysis with Irreducible and Reducible Interval Uncertainty," *Engineering Optimization*, 2008 (submitted).
3. Hu, W. Li, M., Azarm, S., Al Hashimi, S., Almansoori, A., and Al Qasas, N., "An Efficient Single-level Robust Approach for Multi-objective Optimization with Interval," 2008 (working paper, under preparation).
4. W. Hu, N. Al-Qasas, M. Li, S. Al Hashimi, and S. Azarm, "Multi-Objective Robust Optimization of Energy Systems," Poster and Abstract, Energy 2030, Abu Dhabi, UAE, Nov 4-5, 2008.
5. Bar-Cohen, A., Rodgers, P., and Cevallos, J., 2008, "Application of Thermally Conductive Thermoplastics to Seawater-Cooled Liquid-Liquid Heat Exchangers," Proceedings 5th European Thermal-Sciences Conference, Eindhoven, Netherlands, paper HEX\_10
6. Bar-Cohen, A., Rodgers, P., and Cevallos, J., 2008, "Application of Thermally-Enhanced Thermoplastics to Seawater-Cooled Liquid-Liquid Heat Exchangers," Proceedings 2nd International Energy 2030 Conference, Abu Dhabi, United Arab Emirates, pp. 354-364.
7. Luckow, P., Bar-Cohen, A., Rodgers, P., and Cevallos, J., 2008, "Energy Efficient Polymers for Gas-Liquid Heat Exchangers," Proceedings ASME 2nd International Conference on Energy Sustainability, Jacksonville, FL.
8. Luckow, P., Bar-Cohen, A., Rodgers, P., and Cevallos, J., 2008, "Energy Efficient Polymers for Gas-Liquid Heat Exchangers," Proceedings 2nd International Energy 2030 Conference, Abu Dhabi, United Arab Emirates, Poster Presentation, pp. 138-141 (abstract).
9. Bar-Cohen, A., Gupta, S.K., Rodgers, P., Cevallos, J., and Adi, M., "Mold Filling Metamodel for Polymer Composite Heat Exchangers," Proceedings 2nd International Energy 2030 Conference, Abu Dhabi, United Arab Emirates, Poster Presentation, pp. 319-321 (abstract) In Preparation
10. A. Bar-Cohen, Luckow, P., Rodgers, P., 2009, "Minimum Mass Polymer Seawater Heat Exchangers for LNG Applications," International Symposium on Convective Heat and Mass

Transfer in Sustainable Energy. Yasmine Hammamet, Tunisia.

11. Bar-Cohen, A., Cevallos, J.G., Bergles, A., Gupta, S.K., Rodgers, P., Polymer Heat Exchangers: Past, Present, Future Prospects.
12. Cevallos, J.G., Gupta S.K., Bar-Cohen, A., Mold Filling Metamodel for Polymer Composite Heat Exchangers (tentative title).
13. A. Riaz & H. Tchelepi, "Stability of two-phase vertical flow in EOR applications," Poster at Energy 2030 Conference in Abu Dhabi.
14. K. Kiger and C.-H. Pan, "Turbulent dynamics of particle-laden pipeline flow," Poster at Energy 2030 Conference in Abu Dhabi.
15. Maxey, C., Jackson, G.S., Reihani, S.-A.S., DeCaluwe, S.C., Patel, S., Veeraragavan, A., and Cadou, C.P., "Integration of Catalytic Combustion and Heat Recovery with Meso-Scale Solid Oxide Fuel Cell System," ASME Paper # IMECE-2008-67040, presented at IMECE-2008, Boston, MA, November 2008.
16. DeCaluwe, S.C., Zhu, H., Kee, R.J., and Jackson, G.S., "Importance of anode microstructure in modeling solid oxide fuel cells." *Journal Of The Electrochemical Society*, Vol. 155(6): 2008. pp. B538-B546.
17. Jawlik, P. "Effects of Ceria Addition on Ni-YSZ Anodes in Solid Oxide Fuel Cells Operating on Hydrogen and Syngas Fuel Feeds," M.S. Thesis, University of Maryland, College Park, MD, December 2008.
18. Jawlik, P., Patel, S., and Jackson, G.S. "Ni/CeO<sub>2</sub>/YSZ anodes for direct butane feeds in SOFC's" (in preparation).
19. Patel, S., DeCaluwe, S., and Jackson, G.S. "Detailed modeling performance of SOFC's on syngas operation" (in preparation).
20. C.-M. Liao, B. Balachandran, M. Karkoub, and Y. Abdel-Magid, "*Drill String Dynamics*," Twelfth Conference on Nonlinear Vibrations, Dynamics, and Multibody Systems, Blacksburg, VA, USA, June 1-5, 2008.
21. C.-M. Liao, B. Balachandran, M. Karkoub, and Y. Abdel-Magid, "*Reduced-Order Models of Drill String Dynamics*," Second International Energy 2030 Conference, Abu-Dhabi, UAE, Nov. 2008.
22. M. Karkoub, Y. Abdel-Magid, and B. Balachandran "Drill String Torsional Vibration Suppression Using GA Optimized Controllers," Canadian Journal of Petroleum Technology, submitted for publication, 2008.
23. C.-M. Liao, B. Balachandran, M. Karkoub, and Y. Abdel-Magid, "*Drill-String Vibrations: Reduced-Order Models and Experimental Results*," *ASME Journal of Vibration and Acoustics*, in preparation for submission.
24. M. Chooka, M. Modarres, A. Seibi, "Development of a Probabilistic Model for Mechanistic Evaluation of Reliability of Oil Pipelines Subject to Corrosion-Fatigue Cracking," ASME DAC 2008.
25. M. Chooka, M. Modarres, A. Seibi, "Development of a Probabilistic Model for Mechanistic Evaluation of Reliability of Oil Pipelines Subject to Corrosion-Fatigue Cracking," Probabilistic Safety Assessment & Analysis (PSA) 200, Knoxville, Tennessee in the period 7-11 Sep 2008.

26. M. Modarres, and M. Chooka, Poster presentation at PHM-International Conference on Prognostics and Health Management (affiliated with the IEEE Reliability Society), Denver, CO October 2008.
27. M. Chooka, M. Modarres, A. Seibi, Poster presentation at the Second International Energy 2030 Conference held in Abu Dhabi, UAE, from 4-5 November 2008.
28. Hwang, Y., Radermacher, R., Al Alili, A., Kubo, I., 2008, "Review of Solar Cooling Technologies," *HVAC&R Research*, Volume 14, Number 3, pp. 507-528.
29. Al-Alili, A., Hwang, Y., Radermacher, R., Kubo, I. and P. Rodgers, 2008, "High Efficiency Solar Cooling Technique," *Energy 2030*, Abu Dhabi, UAE.
30. Kalinowski P., Hwang Y., Radermacher R., Al Hashimi S., Rodgers P., "Waste Heat Powered Absorption Refrigeration System In The LNG Recovery Process," International Sorption Heat Pump Conference 2008, 23-26 September, 2008, Seoul, Korea.
31. Mortazavi, A., Hwang, Y., Radermacher, R., S. Al-Hashimi, and P. Rodgers, *Performance Enhancement of APCI LNG Plant*, Energy 2030 conference November, 2008.
32. Mortazavi, A., Hwang, Y., Radermacher, R., S. Al-Hashimi, and P. Rodgers, *Enhancement of LNG Propane Cycle through Waste Heat Powered Absorption Cooling*, Energy 2030 conference November, 2008.
33. C. Somers, A. Mortazavi, Y. Hwang, R. Radermacher, S. Al-Hashimi, and P. Rodgers, *Modeling Absorption Chillers in ASPEN*, Energy 2030 conference November, 2008.
34. Selim, H., Gupta, A. K. and Sassi, M., Variation of Optimum Claus Reactor Temperature with Acid Gas Composition, IECEC Conference, Cleveland, OH, July 28-30, 2008, Paper No. AIAA-2008-5797.
35. Selim, H., Gupta, A. K. and Sassi, M., Reduced Mechanism for Hydrogen Sulfide Oxidation, 47<sup>th</sup> AIAA Aerospace Sciences Conference, Orlando, FL, January 5-8, 2009, Paper No. AIAA-2009-1392.
36. Gupta and M. Sassi, "Simulations of Claus Furnace," Invited Keynote International Workshop on Advances in Combustion Science and Technology, India, Jan 2008.
37. Sassi, M., Ben Rejab, S., and Gupta, A. K., "CFD Simulation of Combustion," 5<sup>th</sup> Mediterranean Combustion Symposium (MCS-5), Monastir, Tunisia, September, 2007.
38. Mohamed Sassi and Ashwani K. Gupta, "Sulfur Recovery from Acid," accepted, American Journal of Environmental Sciences.
39. E. Al-Hajri, S. Dessiatoun, A. Shooshtari, M. Ohadi and A. Goharzadeh, "Performance Characterization of Two Selected Refrigerants in a Flat-Plate Micro-Tube Condenser," Second International Energy 2030 Conference, Abu-Dhabi, UAE, Nov. 2008.
40. S. Chowdhury, E. AL-Hajri, S. Dessiatoun, A. Shooshtari, M. Ohadi and A. Goharzadeh, "An Experimental Study of Condensation Heat Transfer and Pressure Drop in a Single High Aspect Ratio Micro-channel for Refrigerant R134a", 4th International Conference on Nanochannels, Microchannels and Minichannels, ASME, June 19-21, 2006, Limerick, Ireland.

41. S. Dessiatoun, S. Chowdhury, E. Al-Hajri, E. Cetegen, M. Ohadi and A. Goharzadeh, "Studies on Condensation of Refrigerants in a High Aspect Ratio Minichannel and in a Novel Micro-groove Surface Heat Exchanger-Development of Micro-condensers in Compact two Phase Cooling Systems", Proceedings of the Fifth International Conference on Nanochannels, Microchannels and Minichannels ASME ICNMM2007, June 18-20, 2007, Puebla, Mexico.
42. E. Al-Hajri, S. Dessiatoun, A. Shooshtari, M. Ohadi and A. Goharzadeh, "Performance Characterization of Two Selected Refrigerants in a Flat-Plate Micro-Tube Condenser", (Pending to be published in ASHRAE HCAV&R Journal).
43. S. Dessiatoun, S. Chowdhury, E. Al-Hajri, E. Cetegen, M. Ohadi and A. Goharzadeh, "Studies on Condensation of Refrigerants in a High Aspect Ratio Minichannel and in a Novel Micro-groove Surface Heat Exchanger-Development of Micro-condensers in Compact two Phase Cooling Systems", Submitted to the International Journal of Heat Transfer, 2008.
44. Elnaz Kermani S. Dessiatoun, A. Shooshtari, and M. Ohadi, "Experimental Investigation of Heat Transfer Performance of a Manifold Microchannel Heat Sink for Cooling of Concentrated Solar Cells" to be presented in 59th Electronic Components and Technology Conference (ECTC) to be held in San Diego, California, USA on May 26-May 29, 2009.
45. M. Alshehhi, S. Dessiatoun, A. Shooshtari, M. Ohadi and A. Goharzadeh, "Electrohydrodynamic (EHD)-Enhanced Separation of Fine Liquid Droplets from Gas Flows - Application to Refrigeration and Petro-chemical Processes", Second International Energy 2030 Conference, Abu-Dhabi, UAE, Nov. 2008.
46. M. Alshehhi, S. Dessiatoun, A. Shooshtari, M. Ohadi and A. Goharzadeh "Parametric Performance Analysis of an Electrostatic Wire-Cylinder Aerosol Separator in Laminar Flow Using a Numerical Modeling Approach", to be submitted to HVAC & R Journal
47. M. Alshehhi, S. Dessiatoun, A. Shooshtari, and M. Ohadi, "Electrohydrodynamic Enhanced Separation of Immiscible Oil Droplets from an Air Flow", to be published in International Journal of Refrigeration

## **B. Education and Knowledge Transfer**

Knowledge transfer is at the heart of the educational arm of the EERC. The knowledge transfer between the two institutions is manifested by the following activities:

- Dr. Michael Ohadi's continued assignment as the Provost and acting President at PI.
- Continued direct support of Dr. Michael Ohadi by Provost Farvardin and Dr. Bar-Cohen in administrative affairs.
- Professor Mikhael Anisimov's sabbatical for one year at PI.
- Internship of five PI summer students at UMD in the summer of 2008.
- Internship of four UMD graduate students conducting research at PI in the last two years.
- Delivery of four project management courses to ADNOC managers at PI.
- Delivery of three engineering courses (distance-taught), and one administrative skills workshop to PI in the last two years.
- Education of four UMD ADNOC Scholars, three of whom are expected to finish their Ph.D.'s in 2008/2009 and join the PI faculty.
- Delivery of the Future Faculty Program (FFP) to four UAE nationals (one Ph.D. and three Ph.D. candidates) in the summer of 2008. The pilot FFP workshop, dedicated to training

- and educating future PI faculty, lasted six weeks and included a teaching practicum and a series of seminars on teaching and research.
- Graduation of two EERC students —one Masters and one Ph.D. Meanwhile, ten other M.S. and Ph.D. students at both institutions are pursuing their education through the support of the EERC, with most nearing completion of their degree in spring semester 2009.
  - Preparation of PI's students and faculty for the FE exams and making preparations to facilitate the delivery of the exam to PI. Due to UMD's persistent efforts, the Maryland Board of Professional Engineers has agreed to sponsor the FE exam in Abu Dhabi.

### ***EERC Workshops at PI***

#### **First EERC Workshop, January 4-5, 2008, Abu Dhabi**

The first annual Workshop of the Energy Education and Research Collaboration (EERC) between the University of Maryland and the Petroleum Institute (PI) was conducted in Abu Dhabi, United Arab Emirates on January 4-5, 2008 in the presence of University of Maryland President Dr. C.D. Mote, Jr., and His Excellency Dr. Yousef Omeir bin Yousef Al Omeir, Chairman of the Board of the Petroleum Institute and CEO of Abu Dhabi National Oil Company. The workshop reviewed the accomplishments of the EERC's first year and identified ways to secure the path and achieve the promise of this broad education and research collaboration.

President Mote and nine University of Maryland faculty participated in the workshop. Among the Maryland attendees were Chair and Distinguished University Professor of Mechanical Engineering Dr. Avram Bar-Cohen, Civil and Environmental Engineering Chair Dr. Ali Haghani, Senior Associate Dean of the Robert H. Smith School of Business Dr. G. Anandalingam, EERC Research Manager Dr. Azar Nazeri, and Professors Shapour Azarm, A.K. Gupta, Greg Jackson, Mohammad Modarres, and Reinhard Radermacher, all of the Mechanical Engineering Department. Workshop attendees representing the Petroleum Institute included Chief Academic Officer and Acting Executive Director Mike Ohadi, along with Professors Ali Almansoori, Ahmed Abdala, Neveen Al Qasas, Tareq Al Ameri, Mohamed Sassi, Saleh Al-Hashimi, Isoroku Kubo, Abdennour Seibi, Mansour Karkoub, Youssef Abdel Magid, Valerie Evely, Afshin Goharzadeh, and Peter Rodgers.

The first day of the workshop featured Maryland and PI joint faculty presentations reviewing each of the thirteen EERC educational and research projects. Dr. Bar-Cohen highlighted collaboration achievements - including ten joint journal and conference publications completed in the first year, more than twenty faculty visits between PI & Maryland, and the education and advisement of more than twenty Ph.D. and M. S. students sponsored under the agreement.

The second day of the workshop focused on the development of a shared future vision for the EERC, including educational programs, extracurricular student activities, infrastructure development, and research in the science and technology of energy systems. Presentations by President Mote, and Dr. Bin Yousef, and Dr. Ohadi set the stage for very fruitful discussions. Particular attention was devoted to the articulation of two proposed research thrusts: Models and Experiments in Fuel Processing and Energy Conversion and Models, Methods, and Tools in Health Prognostics/Maintenance and Decision Support Systems.

At the end of the workshop Dr. Bin Yousef expressed his pleasure with the initial EERC accomplishments and his optimism for the future of the collaboration, and emphasized the need for UMD and PI faculty to work as one team.

After the January 2008 workshop (discussed below), UM complied with PI's request to consolidate the existing 10 projects into smaller, more cohesive research areas. The result of this effort was the aggregation of the projects into three research thrust areas: Efficient Energy Recovery and Conversion, Energy Transport Processes, and Energy System Management. The

objectives of these research groups are to provide more coherency and closer collaboration between PI and UM faculty, to aid in identifying research areas of joint interest, and to enable a smooth transition to the next phase of the collaboration.

### **Second EERC Workshop, November 2-3, 2008, Abu Dhabi**

The Second EERC Workshop was convened on Nov 2-3, 2008 in Abu Dhabi, UAE, as the first phase of this collaboration was coming to an end. The objectives were to review the progress of the last two years, define the scope of the next phase, and provide an opportunity to network and embark on new research areas and expand the existing ones. The workshop was a successful event, well-attended by UMD and PI faculty, representatives of the ADNOC Operating Companies (OpCo's) and many PI students. The workshop program is described in Appendix A and a list of the attendees is attached as Appendix B.

The first day of the Workshop began with Prof. Ohadi, PI Provost (on assignment from UMD), welcoming the participants and outlining the aims of the workshop. Prof. Bar-Cohen followed with an overview of the past and the future of the EERC, which was followed by presentations on the four proposed thrust areas for the next phase of the EERC collaboration: "Energy Recovery and Conversion" by Prof. A. Gupta, "Energy Efficient Transport Processes" by Prof. R. Radermacher, "Energy Systems Management" by Prof. S. Azarm, and "Education and Transfer of Best Practices" by Dr. A. Nazeri. In addition, Dr. Amir Riaz from UMD and Dr. Hamad Karki, a new PI faculty, presented two new emerging topics of research under EERC collaboration, Reservoir Modeling and Robotics.

All the presentations were followed by substantive discussions with active participation of the PI faculty, OpCo representatives, and PI's Director of Research Dr. Karl Bertussen. Most partnered projects, some of the emerging topics, and all of the educational activities were subjects of great interest throughout the workshop. Enhanced Oil Recovery (EOR) was viewed as a very important area of research and will be the basis for a separate MURI proposal involving Stanford, Maryland and Louisiana. Sulfur Recovery, Engineering and Business Decision Making, Dynamics and Control of Drill Strings in Horizontal Reservoirs, Waste-heat Utilization, Fiber Optics, Sensor Systems, and Nanoparticle Catalysis for Petroleum Processes and Measurement for Online Monitoring were the topics that attracted the greatest interest in the discussions ensuing the presentations of the thrust areas along with general support for all the partnered projects.

On the second day of the workshop, breakout sessions were held on each thrust area with participation of current PI collaborators and several new PI faculty eager to join the EERC.

- Prof. Azarm and PK Kannan met with the following faculty on the Energy System Management research thrust: Naveen Al Qasas, Abdellatif Bouchakha, Peter Voulgaris, A. Seibi, Albert Wijeweera, Saleh Al Hashimi, and Ali Almansoori.
- Prof. Radermacher held a meeting with Dr. Lana Chaar and Lisa Lamont, both from the Electrical Engineering department at PI, on a new research topic, "Development of Ocean Based Renewable Energy Resources."
- Prof. Ashwani, met with several PI faculty, namely Dr. Ahmed Al Shoabi, Dr. Mohammed Sassi and Dr. Lyes Khezzar
- Prof. Bar-Cohen and Dr. Nazeri met with several members of the PI administrative body and faculty, namely PI's Head of Graduate Council, Dr. Abdurrahim ElKeib, and the Director of the Arzanah (women's) campus, Dr. Nadia AlHasani.
- Dr. Nazeri had two meetings with several women faculty—Dr. Lana Chaar, Dr. Lisa lamont, Dr. Sandra Vega, Dr. Mirella Elkadi, and Dr. Ghada Bassioni. All women faculty were excited about the prospect of a Women In Engineering (WIE) program at

PI. These discussions led to concrete ideas that would dovetail into some of the successful programs underway at University of Maryland's WIE.

- Dr. Nazeri met with Dr. Karki, and Ebrahim El Hajri on the robotics activity and how research and students activities in this area can synergistically complement each other.

Before the end of the second day, PI had arranged for UMD faculty to meet with over 25 PI seniors with GPA's of 3.4 or higher on pursuing graduate programs at PI or overseas.

In the wrap-up discussion at the end of the workshop, with key PI faculty, Dr. Nanadakumar, Dr. Al Hasani, Dr. Berteussen and Mike Ohadi, UMD was repeatedly complemented on a well-organized and well-attended workshop. Reference was also made to re-structuring the EERC proposal into 4 primary categories: **Partnered Research**, which are the current tasks in three thrust areas, **Mentored Research** to support UMD faculty who will serve as mentors and research collaborators for new PI faculty, the **Industrially-Relevant Research** to develop foundation technologies, together with PI faculty, for addressing urgent needs in ADNOC OpCo's and **Enhanced Engineering Education Grants** to transfer and help implement "best practices" in undergraduate and graduate engineering education at PI.

From the workshop sessions, as well as the informal conversations during the breaks and lunch, it became clear that the PI leadership puts great emphasis on broadly-defined "capacity building" – attracting and retaining outstanding faculty, mentoring returning Emirati PhD's, enhancing the careers of women faculty, strengthening the research and educational skills of the faculty, attracting and retaining more and better students, successfully transitioning to a Sharia-compatible co-educational campus, and enhancing PI's ability to meet the research needs of ADNOC's OpCo's. Thus, proposed future EERC thrusts and tasks will be evaluated in terms of their contribution to one or more of these elements of "capacity building."

### **UMD Visits To PI**

- Amir Shoostari, 1 month working visit to PI, May 2007
- Mohamed Alshehhi visited P.I., GASCO and ADGAS from May 3-9 2008
- Mohamed Alshehhi visited P.I., GASCO and ADGAS from Dec 8 -13 2007
- Serguei Dessiatoun visited P.I., GASCO and ADGAS from May 3-9 2008
- Serguei Dessiatoun visited P.I., GASCO and ADGAS from Dec 8 -13 2007
- A. K. Gupta: EERC and Energy 2030 conference (Nov 1-5, 2008)
- A. K. Gupta: Jan 08 (commencement + 1sr EEERC workshop).
- A. K. Gupta: June 2006 to attend the first PI commencement
- A. K. Gupta: July 25-28, 2006:
  - R. Radermacher:
    - a. With Mike Ohadi visiting German Universities
    - b. June 16-20, 2006, Commencement
    - c. October 28-11/03, 2006 Energy 2030
    - d. October 20-23, 2007 Research Collaboration
    - e. January 03-06, 2008 Collaboration Workshop
    - f. November 01-04, 2008 Energy 2030
- Juan Cevallos visited the Petroleum Institute in Abu Dhabi in the summer of 2007, to work alongside Prof. Peter Rodgers to prepare his first publication, and to meet with ADGAS officials regarding their heat exchanger needs.
- B. Balachandran visited PI and NDC from February 19 to February 24, 2006
- Patrick Luckow visited the Petroleum Institute during the summer of 2008 to work on two of his publications.
- P. K. Kannan visited Petroleum Institute on November 1-3, 2008

- Mohamed Chookah visited Ruwais & Abu Dhabi Refineries of Takreer to collect data in Oct 2007.
- M. Chookah participated in the first Energy Education and Research Collaboration (EERC) Workshop held at the PI in Abu Dhabi from 4-5 January, 2008.
- Dr. Modarres participated in the first EERC Workshop from 4-5 January, 2008.
- Jawlik, P. to PI for Energy 2030, November 2006
- Jackson, G. to PI for program review, March 2007.
- Jackson, G. to PI for 1<sup>st</sup> EERC workshop, January 2008.
- Jackson G. to PI for 2<sup>nd</sup> EERC workshop, January 2008.
- S. Azarm visited PI three times: in Nov 2007, January 2008, and Nov 2008.

### ***PI Visits to UMD***

- H.E. Yousef Omaid Bin Yousef, visited UMD March 2006, August 2008
- Afshin Goharzadeh, 2 weeks working visit to University of Maryland, July 2007.
- Professors Al Hasimi and Al Mansoori visited UMD and met with Dr. Azarm
- Nandakumar, K. to UMD for program review, September 2008.
- Dr. Ali Al-Mansoori was hosted by Dr. Modarres to explore new project regimes of common interest.
- Dr. Seibi was hosted in Nov 2007 to attend M. Chookah's PhD thesis proposal and discuss the project's different aspects
- Dr. Seibi visited UMD in Sept 2008 to discuss the latest progress in the project and finalize the testing equipment shipment destination to UMD.
- Mahmoud Adi, a senior undergraduate at The Petroleum Institute, conducted the Moldflow simulations as part of a two-level factorial design experiment during his 2008 summer internship at UMD and will return for a 1-month internship in January 2009
- Professor M. Karkoub visited UMD from Oct. 31 to Nov. 2, 2008.
- A. Al Mansoori to UMD for program review, August 2007.

### ***Graduate Research Assistants (GRA)***

The following table lists the GRA's working on the EERC projects.

**Table: 1** List of GRAs participating on EERC projects

<b>Student</b>	<b>UM Professor</b>	<b>PI Professor</b>	<b>Degree</b>	<b>Funding Source</b>
Mohamed Chooka	Modarres	Seibi (TCM)	Ph.D.	ADNOC
Mohamed Alshehhi	Dessiatoun	Ohadi, Goharzadeh,	Ph.D.	ADNOC
Ebrahim Al-Hajri	Dessiatoun	Ohadi, Goharzadeh	Ph.D.	ADNOC
Elnaz Kermani	Dessiatoun	Ohadi,	M.S. (graduted)	EERC
Genzi Li	Azarm	Al Hashimi, Al Ameri	Ph.D. (graduated 8/2007)	EERC
Wei Wei Hu	Azarm	Al Hashimi, Almansoori	Ph.D.	EERC
Hatem Selim	Gupta	Sassi	Ph.D.	EERC
Juan Cevallos	Bar-Cohen	Rodgers, Abdala	M.S.	EERC
Chien-Min Liao	Balachandran	Karkoub (TCM)*, Abdelmagid	Ph.D.	EERC

Ali Alalili	Radermacher	Al Hashimi, Rodgers,	Ph.D.	ADNOC
Amir Mortazavi Chris Somers Paul Kalinowski	Radermacher	Al Hashemi. Rodgers	M.S. M.S. M.S. (graduated 9/2007)	EERC EERC Mannheim
Paul Jawlik	Jackson	Eveloy (TCM), Almansoori (TCM)*	M.S.	EERC
Siddharth Patel	jackson	Eveloy Almansoori	M.S.	EERC

### ***Internship of PI Summer Students at UMD, Summer 2008***

From the beginning, the Petroleum Institute's purpose has been to build future leaders in a leading industry at an institution well-recognized for its high standards. The management at the PI and the Abu Dhabi National Oil Company has supported this mission by providing not only a world class education, but also by giving the students a chance to build new experiences, especially in conducting research. This vision was implemented by building strong collaborations with world-ranked universities in engineering, with the greatest of these collaborations coming with the University of Maryland.

Five of the best PI students were chosen from the electrical, chemical, mechanical and petroleum departments to participate in a six-to-eight week research program conducted at the mechanical engineering department at UMD. These students were chosen based on their academic performance and extra curricular activities. UMD was glad to accept these students and provide the help needed to give these students the best research experience they could have in advanced engineering. The students participating in this activity are listed as follows:

- Amro Salah El Hag, Chemical engineering  
Supervising professor: Dr. Serguei Dessiatoun
- Bakeer Khaled Bakeer, Mechanical engineering  
Supervising professor: Dr. Greg Jackson
- Mahmoud Mohamed Adi, Mechanical engineering  
Supervising professors: Dr. A.K. Gupta and Dr. Avram Bar-Cohen
- Mohmed Saeed Al Hebsi, Petroleum Engineering  
Supervising professor: Dr. Amir Shoostari
- Mohamed Tamer Nader Chaklab, Electrical engineering  
Supervising professor: Dr. Miao Yu

## Participants in the PI summer research program at UMD



### ***Future Faculty Program (FFP)***

This program prepares ADNOC Scholars for their future academic positions at PI. The participants will be ADNOC Scholars who are close to completion of their Ph.D.'s at UMD or other institutions in the US or elsewhere. This program is modeled after a successful and competitive program at UMD introduced in 2007 to increase the number of Clark School Ph.D. graduates who obtain academic positions—in particular, faculty positions in prestigious engineering schools—and to improve the preparation of students for academic careers so that they can better succeed once they obtain such a position.

The FFP consists of a sequence of training seminars, a teaching practicum and a leadership component. Participants will attend seminars that train the students in some of the skills required for a successful academic career. Among the topics to be covered are giving effective oral presentations writing technical papers and reports, creating course content, and managing a class. In the Teaching Practicum each participant will be teamed with a senior faculty member and provided with the opportunity to co-teach a course. The Scholars are expected to be involved in all the aspects of the course; they will help develop the syllabus, teach some of the lectures, write and grade exams, and evaluate the students. Participants will also take a groundbreaking

executive leadership and innovation workshop, based on the current certificate program taught by two world-class professional schools, the R. Smith School of Business and MTECH of the Clark School of Engineering.

A pilot version of this program was offered to three ADNOC Scholars who are about to finish their PhD's at UMD and start their academic careers at PI next year, E. Al Hajri, M. Al Shehhi, M. Chooka, and one junior PI faculty Dr. H. Karki, during summer 2008 at UMD.

## **B. International Visibility**

UM President Dr. C.D. Mote was the commencement speaker at PI's graduation ceremony, and several UM faculty attended two PI commencements in 2007 and 2008. Meanwhile, Provost Nariman Farvardin serves on the PI's Institutional Advisory Board.

### ***Energy 2030 Conference***

UM & PI jointly organized two International Energy 2030 Conferences, an international forum dedicated to addressing energy resources and technologies in 2030. The second one was held on 4-5 November, 2008. The primary objective of the Energy 2030 Conference is to share views and information useful to the strategic planning of research and development in the oil and gas and broader energy areas, including energy availability and usage, transport, and environmental issues. The technical program comprised invited keynote talks by high-profile experts and scholars from around the world. The program topical areas included "Oil scenarios: from peak oil to plenty of oil," "Future of natural gas as a bridge and beyond," "Nuclear energy as an alternative," "Solar and wind energy, Hydrogen, methanol and ethanol as fuels," research and development needs in the oil and gas industries, and much more.

**Conference Chair** □ Prof. Michael Ohadi The Petroleum Institute □

**Conference Co-Chairs** Prof. Ashwani Gupta, University of Maryland  
Prof. Peter Rodgers, The Petroleum Institute

**Organizing Committee** □ Prof. Valérie Eveloy, The Petroleum Institute  
Prof. Saleh Al Hashimi, The Petroleum Institute  
Prof. Hamad Karki, The Petroleum Institute  
Dr. Didarul Islam, The Petroleum Institute  
Mr. David Drake, DMG World Media, UAE □  
Mr. Michael Giblin, The Petroleum Institute  
Ms. Eileen Michael, Re-ex Publishing, UAE □  
Ms. Jennifer Moore, DMG World Media, UAE  
Mr. Jamie Newbery, DMG World Media, UAE □  
Mr. Ashok Pillai, DMG World Media, UAE. □ □

**International Scientific Committee** □

Prof. Avram Bar-Cohen, University of Maryland  
Prof. Klaus Hein, University of Stuttgart, Germany □  
Prof. Reinhold Lang, University of Leoben, Austria □  
Prof. Reinhard Radermacher, University of Maryland □

## **C. Addressing ADNOC's Needs**

- Dr. Amir Riaz, a research professor from Stanford, was hired by UM to conduct research in reservoir modeling, which is of great interest to ADNOC. This research will be conducted in close collaboration with Stanford University and PI.
- A project management short course was delivered to GASCO in 2007 and was attended by more than 20 of its engineers and executives.

- EERC Ph.D. students and ADNOC Scholars and their advisor, Dr. S. Dessiatoun, visited ADNOC facilities last spring to learn directly about oil and gas fields and how to address the engineering problems related to these fields through their research.

A few other significant activities have been initiated and pursued at UM during the current phase of collaboration, such as helping PI in its search for new PI faculty and recruiting UM/PI joint graduate students. These activities will be pursued in the next phase of the collaboration.

### **3. Educational Projects**

# Fundamentals of Engineering (FE) Examination

UMD Investigators: Dr. Sami Ainane

PI Investigator: Dr. Peter Rodgers

Start Date: June 2006

FINAL REPORT

## 1. Abstract

The National Council of Examiners for Engineering and Surveying (NCEES), which is the official body that administers the FE exam, has detailed statistics on the results for examinees who undertake the FE exam and have attended EAC/ABET-accredited college/university engineering programs.

Apart from the FE exam process serving as a possible academic assessment metric at PI, ADNOC wishes to explore the possibility of introducing professional engineering (PE) licensing within its operations. The starting point for such a licensing process is the passing of the FE exam.

It was the goal of this project, therefore, to bring the NCEES FE Exam to the PI and to prepare PI students for the exam.

## 2. Objectives

- Design a review course to prepare PI students for the Fundamentals of Engineering Examination (FE Exam).
- Prepare and grade “practice” FE Exam for PI students.
- Use the practice FE Exam results to identify engineering program strengths/weaknesses.
- Determine whether an official NCEES FE Exam can be undertaken at the PI.

## 3. Approach

Tutorial sessions were developed to prepare PI students for undertaking trial FE exam, which covers the following topics:

- Mathematics, probability and statistics
- Statics, dynamics, strength of materials and materials science
- Thermodynamics and fluid mechanics
- Electrical circuits and computers
- Engineering economics
- Chemistry
- Ethics and business practices

This material was reviewed in 43 hours of tutorials, given in three-hour sessions. The revision materials were primarily supplied by UMD, supplemented by PI faculty input.

## 4. Results

Through efforts of the University of Maryland, the Maryland Board of Professional Engineers - has agreed to deliver the FE exam to Abu Dhabi, as PI will start the ABET accreditation process. The board members voted, unanimously, to sponsor the exam in Abu Dhabi provided the following conditions are met:

1. A third party will deliver and guarantee the integrity of the exam be identified.

2. The PI will receive the non-domestic accreditation by ABET.

Dr. Sami Ainane developed review course materials to prepare PI students for the exam. He also visited the PI in November 2007 to conduct review sessions. The PI administered practice exams, which were graded by Dr. Ainane, who sent the results to the PI.

## **5. Recommendations for Future Work**

- S. Ainane will develop new mock FE exams and conduct review sessions at the PI until the FE exam is offered in Abu Dhabi.
- Criterion 3, Program Outcomes, of the ABET 2008 Criteria for Accrediting Engineering Programs specifies that there must be an assessment and evaluation process that periodically documents and demonstrates the degree to which the program outcomes are attained. FE mock exams could be used as a direct assessment tool for programs outcomes at the PI.

## **6. Conclusion**

In continuation of the current efforts to bring the Fundamentals of Engineering exam to PI, UM will continue to design, review and prepare mock FE exams to prepare the students and faculty at PI. These exams will expand to include mechanical, chemical, electrical, and petroleum engineering. UM will continue to prepare PI faculty and students for FE exams by:

- Designing review courses for students
- Preparing and grading “practice” exams for PI students
- Using the practice exams to identify strengths and/weaknesses of engineering programs and students
- Planning a program to address in a timely manner the weaknesses of the programs and student difficulties.

## **6. References**

An overview of the FE exam process can be obtained at <http://www.ncees.org>, which is the official website for The National Council of Examiners for Engineering and Surveying (NCEES), which administers the FE exam.

# Development and Delivery of Course Material for Engineering Project Management Courses

UMD Investigators: Ali Haghani & John Cable

GRA's: None

PI Investigator(s): None

Start Date: October 2006

FINAL REPORT

## 1. Abstract/Objectives

Developed and delivered course materials for an Engineering Project Management program at PI, developed and delivered a short course for GASCO, and perform a feasibility study of establishing a graduate program at in Engineering Project Management at PI.

## 2. Justification and Background

PI's need to develop a graduate program in Engineering Project Management..

## 3. Approach

The material for all of these courses was derived from the course material for the engineering project management courses at the University of Maryland, supplemented by additional material developed by the CEE faculty as needed.

## 4. Two Year Plan

- Develop and deliver a one-week short course in project management for GASCO: January 2007 – delivered in Abu Dhabi in January.
- Develop and deliver materials for a semester-long course in project management: September 2007 – hand delivered in Abu Dhabi in January 2007 (7 months early)
- Develop and deliver course materials for design and construction contract law course. – delivered slides only for ENCE 421 in January with the rest due in September 2007. Delivered balance of materials in June 2007. (3 months early)
- Develop and deliver materials for two additional semester-long courses in project management at PI: The third and fourth courses were requested 7/15/07 and will be delivered in early 2008. They were promised for Spring 2008.

## 5. Summary of Results

- UMD delivered all the course materials to PI
- UMD/PM delivered a draft survey to PI 24 July 2007.
- A project management short course was delivered to GASCO in 2007 and was attended by more than 20 of its engineers and executives.
- UMD delivered two additional undergraduate courses from the Project Management Program the last week of March 2008: ENCE 422 Project Cost Accounting & Economics + ENCE423 Project Planning, Scheduling & Control.

## **4. Research Projects**

### ***4.1. Energy Recovery and Conversion Projects***

**Force-Fed Cooling of Photovoltaic Arrays for High-Efficiency  
Solar Energy Conversion Systems**

UMD Investigators: Dr. S. Dessiatoun, Dr. A. Shoostari

GRA's: E. Kermani,

PI Investigator(s): Dr. M. Ohadi, Dr. I. Kubo

Start Date: October 2006

**FINAL REPORT**

## 1. Abstract/Objectives

The proposed project created, based on a survey of available literature, a database on the available cooling techniques for high heat flux solar concentrator arrays necessary for efficient conversion of solar energy to electric power. The typical cooling load necessary for optimum radiation concentration and optimum photovoltaic conversion efficiency was identified, and a novel force-fed cooling technique that has been developed at UMD was applied to contain this cooling load. An experimental prototype and associated setup was designed and fabricated to verify the feasibility of this concept and the capacity for cooling by this technique. Based on these experimental results, the radiation concentration levels acceptable to this cooling capacity were redefined. The type of fluid and its flow rate, the temperature of the surface where solar radiation is incident, and the uniformity of temperature on this active area were the main issues that were addressed in this project. The scalability of this technique for uniform cooling of industry-scale extended area panels will be a guiding parameter for the design and development of the heat exchanger prototype. Cooling system enabling the operation of the concentrated PV array at of 1000 sun is a goal of this project.

## 2. Approach

### UM-side participation

1. Conduct extensive literature survey on PV radiation concentrators. Summarize available cooling technologies for these arrays with notes on their cost, size and other scalability issues.
2. Evaluate cooling loads, taking into account recent advances in radiation concentration technologies and conversion efficiencies.
3. Develop a force-fed heat exchanger prototype capable of rejection of this expected heat flux. Explore the possibility of MEMS fabrication techniques for creating micro-grooves integrated with solar panels. Also identify possible fluid choices and pumps to meet the demand.
4. Conduct experimental study on force-fed-based single- phase processes to determine cooling capacity.
5. Based on outcome of experiments, design, fabricate, and test a complete PV converter and cooler package in the field.
6. Make recommendations for a radiation concentration that is commensurate with this thermal management technique.

### PI-side participation

1. Provide information and symbiotic assistance to the UM team regarding current concentrator designs, available cooling techniques and expected heat loads.
2. Prepare a solar concentrator to be packaged with UM-made heat exchanger for final testing.
3. Corroborate UM testing of the concentrator and cooling element in UAE desert conditions

4. Provide contributions to the preparation of final project report and recommendations.

### 3. Results

#### *Literature review*

Solar energy is one of the most valuable sources of energy with the potential to produce a significant portion of the world's energy usage. Solar thermal and photovoltaic (PV) systems are the major solar energy technologies. While photovoltaic cells just utilize a small fraction of solar radiation from 15% for commercial usage to 40% for research lab cells to produce electricity [1], concentrating systems can focus sunlight onto solar cell for higher rate of conversion to electricity and lower costs. The size of an actual PV cell can be significantly reduced and high grade heat energy can be used for heating or cooling, increasing total energy efficiency to 80 or 90%. The concentrated PV system has the potential to be the most efficient and least expensive of all PV technologies [1]. At high concentrations, the PV cell cost becomes just a small part of the total system cost; therefore, the PV cell can be easily upgraded with technology advances of cell degradation.

Despite the fact that maximum solar flux concentrations can reach 84000 experimentally [2], there are limited studies on the development of medium- to high-concentration collectors due to challenging issues concerning the design and performance of the PV concentrating systems. One of the most important challenges in high concentration PV collectors is designing a system to achieve high flux of solar radiation with uniform flux distribution. High and non-uniform heat flux due to concentrated solar radiation affects the temperature distribution of the solar cell, resulting in the change of solar cell parameters, mainly its conversion efficiency [3]. It is well known that the efficiency of PV cells decreases dramatically with an increase in cell temperature, thus justifying the need for effective cooling of concentrating systems. The solar cell cooling method becomes a limiting factor in the development of highly concentrated modules. One of the proposed ways to cool the concentrated PV modules is using the hybrid systems to recover part of the waste heat and use it for other practical applications. This system maintains high electrical efficiency, and excess heat can be harnessed by combining both the thermal and photovoltaic system in a hybrid PV/thermal system so that the combined efficiency increases.

It is well known that by increasing the solar cell temperature, the efficiency decreases [4, 5 and 6]. The main reason for this decrease is the drop in open circuit voltage and fill factor. The most dominant reason for reduction in solar cells efficiency is the drop in open circuit voltage; the resulting efficiency drop is in order of 0.35% /°C. [3] Meneses-Rodriguez et al. [7] has studied the PV solar cell performance at high temperature theoretically. They confirmed that open-circuit voltage and fill factor decrease with temperature and concluded that the main reason for decrease in efficiency is a decrease in open circuit voltage and fill factor. They also studied the effect of light flux concentration on cell parameters for temperatures of 300 K and concluded that the increase in short circuit current with concentration level is much steeper than the increase in open-circuit voltage. Efficiency also increases with concentration level. They also concluded that for effective performance, proper combination of solar concentration and temperature must be chosen.

Markvart [6] suggested a logarithmic relationship for efficiency of cells under concentration based on short-circuit current and open-circuit voltage as following:

$$\eta(X) = \frac{V_{oc}(X)I_{sc}(X)FF}{G(X)} = \eta(1)\left[1 + \frac{kT}{qV_{oc}(1)} \ln(X)\right]$$

Where q is the magnitude of electron charge given as  $1.602 \times 10^{-19} \text{ C}$ , T is the temperature, and k is the Boltzmann constant  $1.38 \times 10^{-23} \text{ J/K}$ , and  $\eta(1)$ ,  $V_{oc}(1)$  are the efficiency and open-circuit voltage of solar cell without concentration. Based on this equation, solar cell efficiency graph

versus concentration can be plotted in Figure 1 for assumed input parameters of,  $V_{oc}=0.6$  V,  $I_{sc}=0.05$  A, and  $KT/q=0.026$  V.

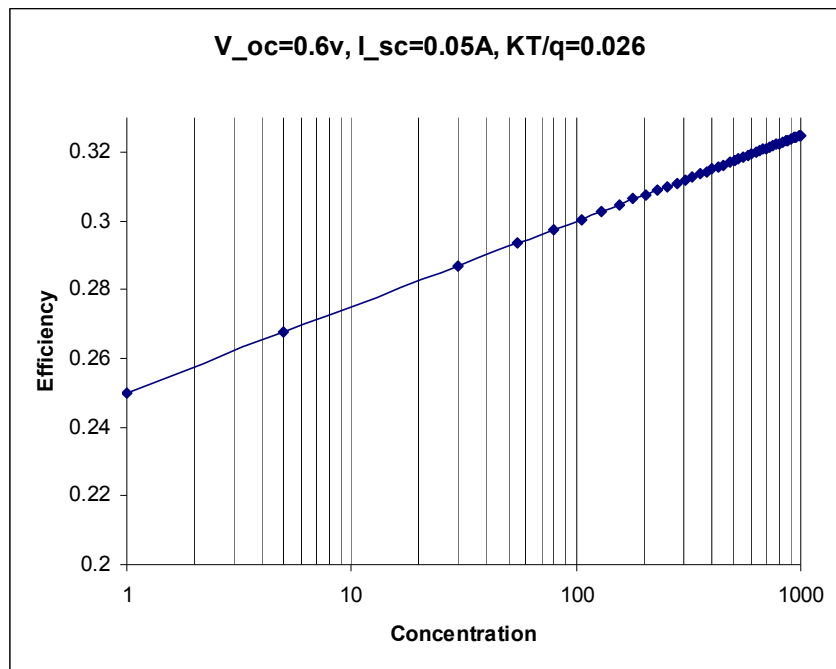


**Figure 1. Solar cell efficiency versus concentration for a single cell based on numerical calculation.**

However, it should be mentioned that efficiency will not increase infinitely. In fact, after a certain concentration (which depends on cell parameters such as temperature, short circuit current, and series resistance), the theoretical prediction does not hold anymore, and a decline in the efficiency is expected. This behavior is due to power losses, mainly through series resistance. From this figure it can be concluded that increasing the concentration up to the optimum point can result in higher efficiency. However, higher concentrations require more effective cooling of PV cells to prevent any negative impact of high temperature. At 1000 sun concentration the cooling system should be able to remove  $70 \text{ W/cm}^2$  of heat from PV array of such efficiency.

### **Design of the heat sink**

The most efficient cooling system for such heat flux from silicon PV array would be a microchannel heat sink. Microchannels are compact and structurally sound, and can dissipate very high heat flux with low superheat. First introduced by Tuckerman and Pease [8], they found wide application in electronics cooling and other cooling systems. However, microchannels have very high pressure drop and are not suitable for large array cooling.

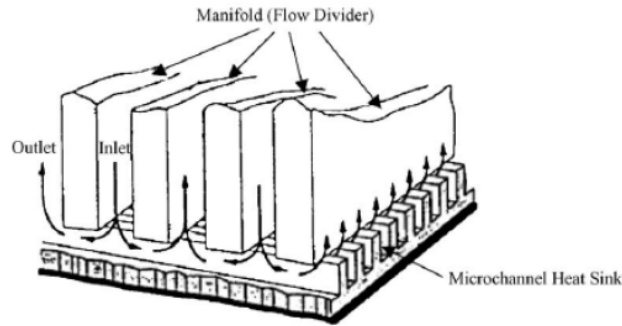


**Figure 2. Schematic of manifold heat sink adopted from [9]**

Copeland et al. [10] have been developing a manifold microchannel heat sink that combines high heat transfer and structural rigidity of microchannels with very low pressure drop. In this concept a microgrooved surface is transferred to a waste network of very short microchannels connected in parallel (Figure 2). One of the first studies in manifold microchannel has been done by Harpole et al. [11] in 1991. This concept seems like the most suitable for the large PV array cooling and was explored in this project.

### **Simulation of microchannel cooling**

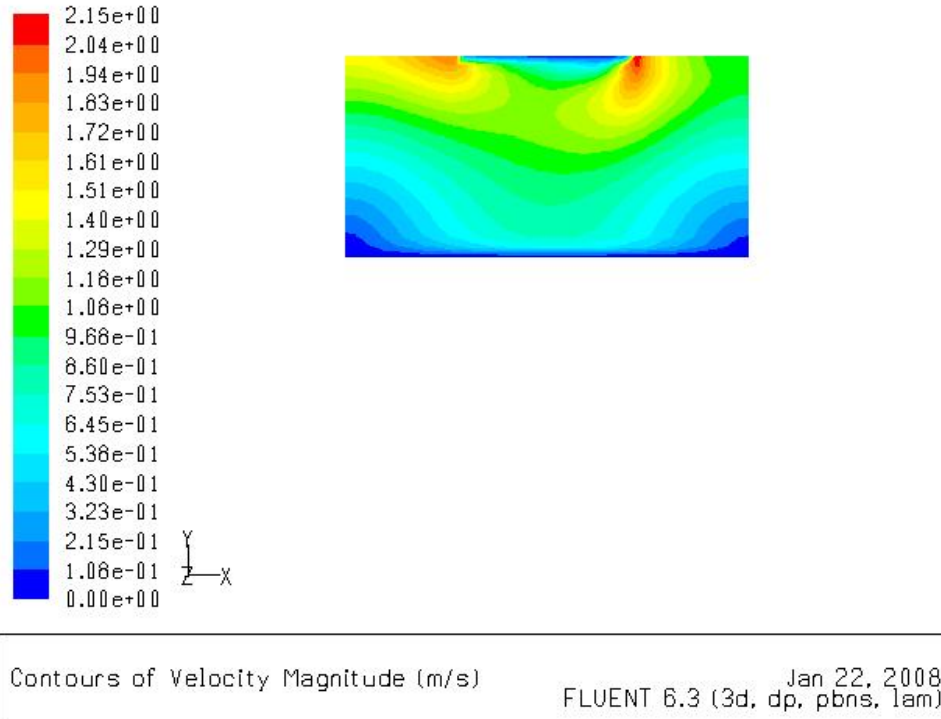
Modeling of different designs of manifolds and microchannels in FLUENT was conducted to study the effect of various geometrical parameters and to identify the optimum design. A parametric study on the number of manifolds per centimeter, the number of channels per centimeter, the channel aspect ratio, fin thickness, channel wall thickness, and inlet and outlet dimension was performed. Other parameters, such as inlet and outlet flow temperature, heat transfer coefficient, volumetric flow rate, and pumping power, were calculated. It was found that by increasing the number of manifolds per centimeter we could reach a much more uniform temperature on the cell surface, which is one of the main concerns in designing cooling techniques for solar cells under high concentration. The results from different designs with the same initial values were compared against each other in terms of channel base temperature, required pumping power of the system, and coefficient of performance. A number of designs were selected for fabrication and were evaluated experimentally.

In this part of the investigation, the main focus was on optimization of the microchannel structure operating in a single-phase mode. One quarter of the microchannel structure element and manifold was modeled as a 3D computational domain in Fluent® CFD solver to reduce the computation time. A constant heat flux of  $100 \text{ W/cm}^2$  was imposed as the boundary condition. Water at 300 K inlet temperature was used as the working fluid. The microchannel fabricated out of silicon with 250 channel/cm and a channel aspect ratio of 10.0 and another microchannel with 62 channel/cm and a channel aspect ratio of 2.5 were modeled as a base for the study. In both designs the number of manifolds per centimeter was equal to 25 but for two different designs, in which inlet equaled outlet and where inlet equaled twice the outlet. The major evaluating parameters were the base temperature and the required pumping power to maintain such heat removal.

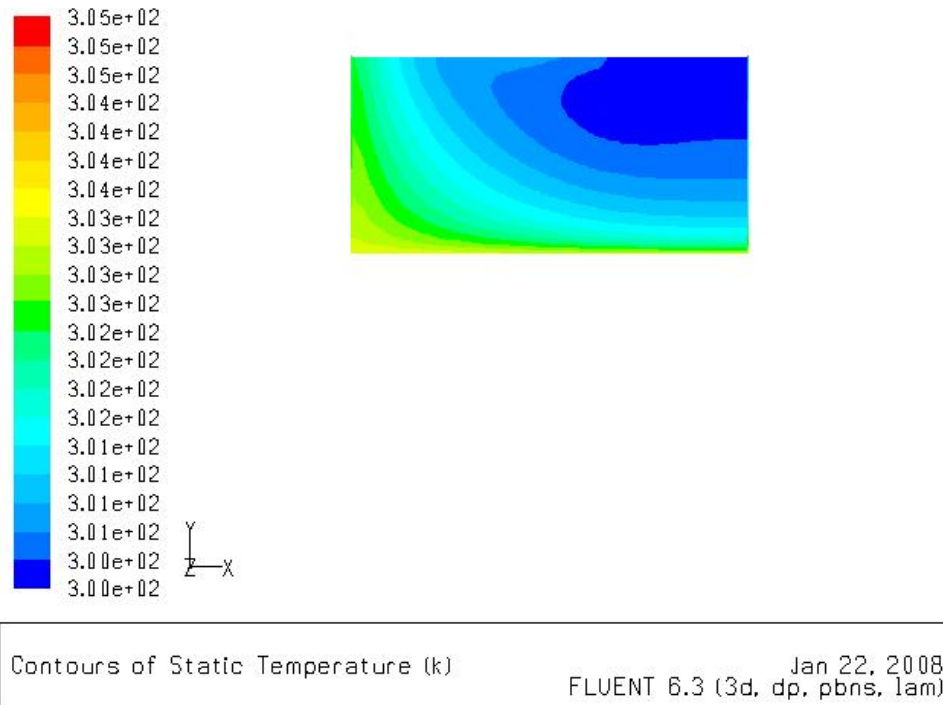
The geometry of the microchannel surface used in the simulation was similar to the surfaces fabricated. The  $20 \mu\text{m}$  channel width and  $200 \mu\text{m}$  channel depth in the two first cases and  $80 \mu\text{m}$  channel width and  $200 \mu\text{m}$  channel depth in last two cases were simulated in this model. In this simulation the fin thickness was equal to channel thickness.

Figure 3 presents the numerical results of the flow velocities in the computational domain for the channel with width of  $20 \mu\text{m}$  and where inlet flow distributor equaled the outlet (inlet and outlet wall thickness were  $240 \mu\text{m}$  and the disruptor wall thickness was  $160 \mu\text{m}$ ). The maximum coolant

velocity in this jet was 2.15 m/s. As it seems from Figure 4, fluid in the areas with low velocity heated up. The average base temperature was 305 K. The required pumping power to cool the plate of  $100 \text{ W/cm}^2$  was 1.75 W. The nominal area heat transfer coefficient was calculated by dividing the heat flux through the base area by the temperature difference between the average base surface temperature and the average of inlet and outlet fluid temperatures. The calculated nominal area heat transfer coefficient for the first geometry was  $239808 \text{ W/m}^2\text{K}$ .



**Figure 3. Velocity distribution in the fluid domain for the first design with channel width of  $20 \mu\text{m}$  and equal inlet and outlet.**



**Figure 4. Temperature distribution in fluid domain for first design with channel width of 20  $\mu\text{m}$  and equal inlet and outlet.**

In this study, numerical modeling of the microchannel with flow distributor was developed for single-phase operating conditions. Testing of several configurations was performed to optimize the structure and operating conditions. Water was used as a working fluid and silicon was the microchannel material.

Table 1 summarizes the results of the current computational analysis. In all of the configurations the number of manifolds per centimeter was 25. In the first and third designs the inlet and outlet were equal to 240  $\mu\text{m}$ , but in the second and fourth designs the inlet was twice the outlet, for which the manifold wall was thickened. Moreover, the first and second designs were for channels with an aspect ratio of 10; the third and fourth designs were for channels with an aspect ratio of 2.5. From a comparison of the first and second design we concluded that for designs where the inlet is greater than the outlet, maximum flow velocity increased and pressure loss in the manifold decreased so the pumping power decreased too. However the nominal heat transfer coefficient decreased and the base temperature increased. For high aspect ratio channels with a high number of channels per centimeter, it seems that although having the inlet bigger than outlet decreases the heat transfer coefficient, decreases in pumping power are more effective, and the increase in base temperature is not significant.

Configurations 3 and 4 were developed for the purpose of reducing aspect ratio while keeping the heat transfer parameters at the desired level. The geometry of the manifold used in those iterations is similar to that in the first and second designs, but the aspect ratio was reduced to 2.5, resulting in a reduction of the number of channels per centimeter from 250 to 62. As a result, it can be concluded that for lower aspect ratios, if the inlet is greater than outlet, base temperature increases drastically and heat transfer coefficient decreases. Although required pumping power decreases, it is better to have the inlet equal the outlet in this design.

The changes in geometry of the microgrooved surface and the feed channel explored in this study indicate uniform and higher heat transfer occurs for higher numbers of channels per centimeter, and that inlets bigger than outlets can decrease required pumping power.

**Table 1. Effect of change in computational element geometry on heat transfer and required pumping power at constant heat flux of 100 W/cm<sup>2</sup>**

Parameters		1	2	3	4
Inputs	Channel depth, (μm)	200	200	200	200
	Channel width, (μm)	20	20	80	80
	Inlet width, (μm)	240	240	240	240
	Outlet width, (μm)	240	120	240	120
	Inlet pressure, (kPa)	10	10	10	10
Results	Base Temperature (K)	305	305.46	306.7	307.75
	Heat transfer coefficient, (W/m <sup>2</sup> K)	239808	229621	163934	145348
	Maximum flow velocity (m/s)	2.15	2.24	3.84	4.06
	Pumping power (W)	1.75	1.23	3.89	2.37

### Mask layout and silicon wafer selection

The majority of University of Maryland micro-fabricating equipment is based on 4" silicon wafer size; therefore, this size was selected for the project. A 500 μm thick wafer, commonly used for PV cell production, was selected for fabrication of the microchannels. As thick silicon wafers are not readily available, a 1000 μm thick wafer was selected, which allows a fabrication manifold etching almost to the maximum limit of the Deep Reactive Ion Etching (DRIE) process and still reasonably inexpensive. Four Mylar mask layouts for the microchannels, manifold, heater, and holes were designed and ordered for microfabrication processes. Layout of the masks is shown in Figures 5 to 8.

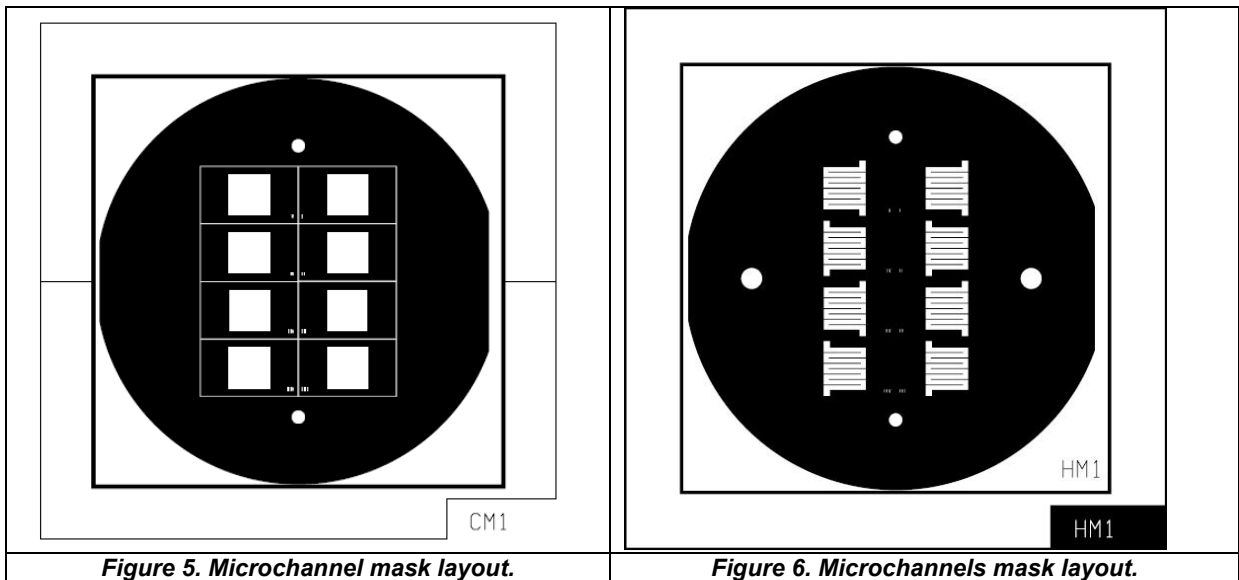


**Figure 5. Microchannel mask layout.**

**Figure 6. Microchannels mask layout.**

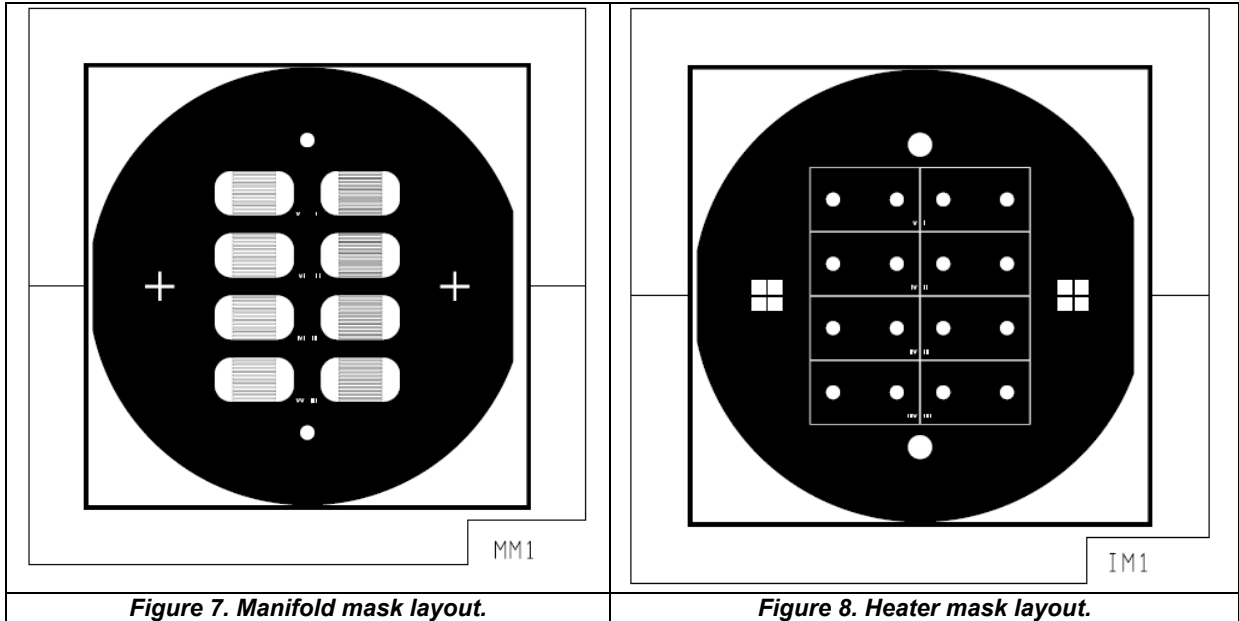


**Figure 7. Manifold mask layout.**

**Figure 8. Heater mask layout.**

### **Microfabrication**

- Microfabrication of channel
- Microfabrication of manifold
- Microfabrication of inlet and outlet holes
- Microfabrication of heater

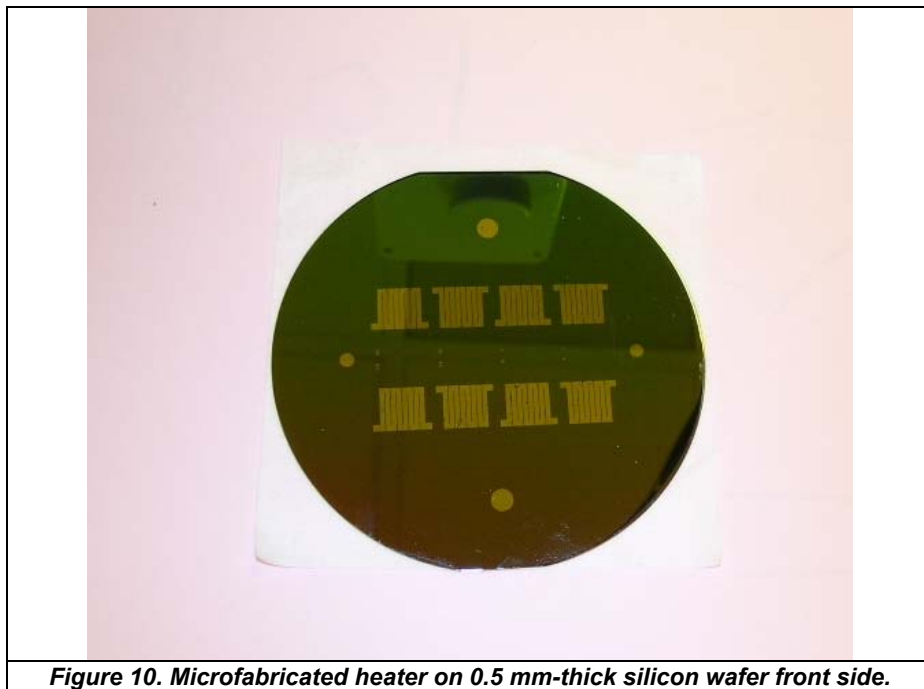
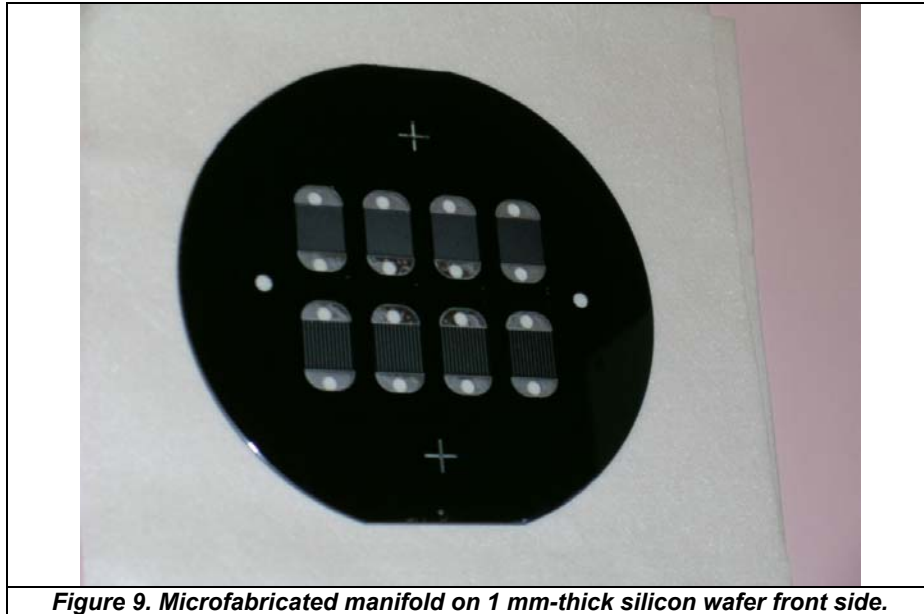
Microfabrication, which consists of technologies to fabricate micrometer-sized components, was needed for the microchannels of this project. We have completed the fabrication manifold, inlet and outlet holes, microchannels, and heater. All steps of a typical microfabrication process have been taken, namely of photolithography, UV exposure, and resist development, wet etching, deep reactive ion etching, and cleaning.

In first step the fabrication on 1 mm-thick silicon wafer for the manifold and inlet holes was produced such that the first inlet and outlet holes were fabricated and then the manifolds on the backside of the wafer were fabricated. Etching of parallel microchannels can be achieved with a chemical etching method such as wet etching or dry etching. In this work the Deep Reactive Ion Etching (DRIE) technique was used for both microchannels and manifolds. A standard Bosch process was implemented using an inductively coupled plasma (ICP) etcher in which RF-induced plasma accelerates the free ions, causing chemical reaction and bombardment of the surfaces to be etched. The Bosch process includes three steps which are repeated throughout the etching cycles. The first step is isotropic etching of the exposed area in the silicon wafer using SF<sub>6</sub>. A fluorinated polymer is subsequently deposited on both the trench sidewalls and bottom walls using C<sub>4</sub>F<sub>8</sub>. In the third step, SF<sub>6</sub> is used to etch the polymer anisotropically as it etches the bottom faster than the sidewalls. In the subsequent step, the sidewall is effectively protected by the polymer so that silicon etching occurs only at the bottom of the trench. In this work on the manifold wafer the DRIE was done for nearly 10 hours to achieve 500 μm manifold depth and 500 μm inlet and outlet holes.

The second step was the fabrication of the microchannel and heater. For this process, first the heater was fabricated out of platinum in a serpentine shape with the lift-off process on the front

side of a 500  $\mu\text{m}$  -thick silicon wafer. The microchannels were then fabricated on the back side of the wafer. In this design the deep reactive ion etching took about 5 hours for the microchannels.

Figure 9 shows the fabricated manifolds; Figure 10 and 11, the heater and microchannels.



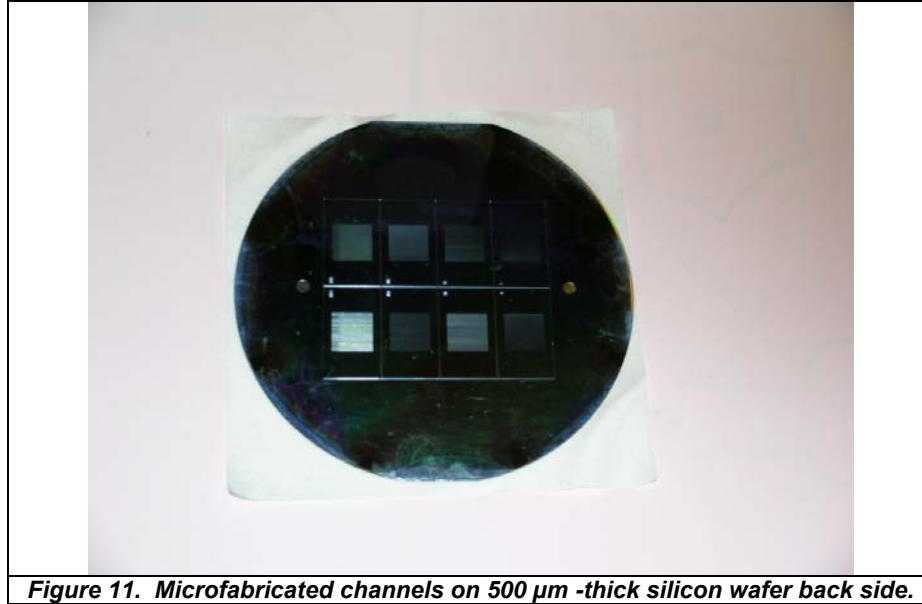
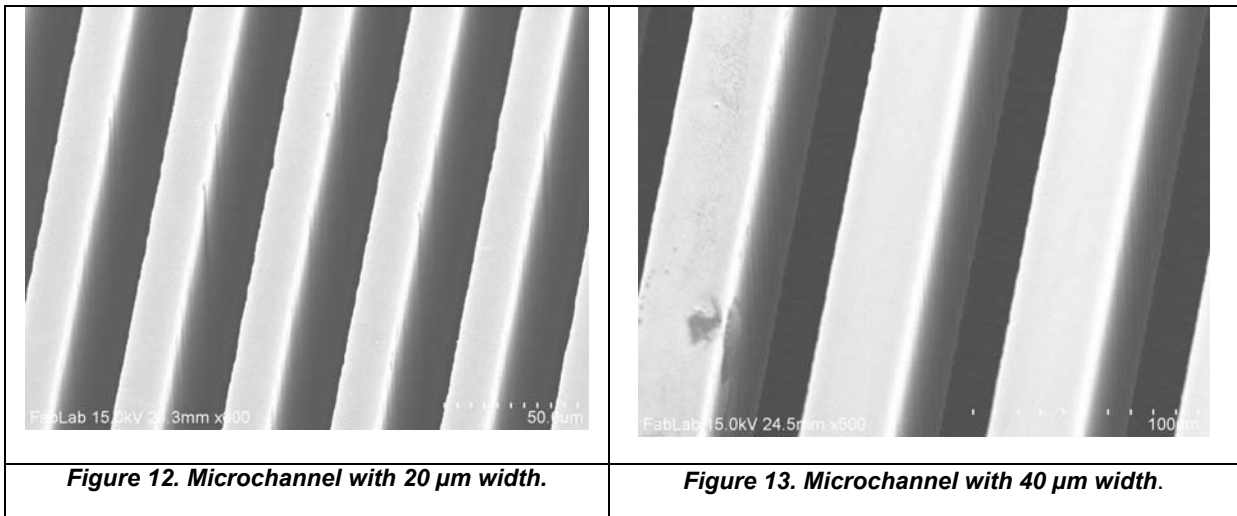


**Figure 11. Microfabricated channels on 500  $\mu\text{m}$  -thick silicon wafer back side.**

### **Scan electron microscopy**

A scan electron microscope (SEM) forms a three-dimensional image on a cathode-ray tube by moving a beam of focused electrons across an object and reading both the electrons scattered by the object and the secondary electrons produced by it. The main goal of SEM photography was to inspect the sidewalls for microdefects as well as the roughness of the bottom surfaces. The microchannel wafer was etched with the deep reactive ion etching method. This technique was intended to produce vertical side walls without taper and inclination. As can be seen in Figures 12, and 13, the verticality of the walls was properly achieved, and no significant inclination is visible. Moreover, the bottom surfaces of the channels are relatively smooth.



Figures 14 and 15 show the SEM photographs of the manifold. As can be seen, some micro-needles were created on the bottom face of the manifold wafer. These needles are likely due to the high etching depth (500  $\mu\text{m}$ ). The needles are more concentrated in the corner regions. In order to remove them, the sample was immersed in an ultrasonic bath, causing the needles to detach by vibration and improve the surface smoothness.

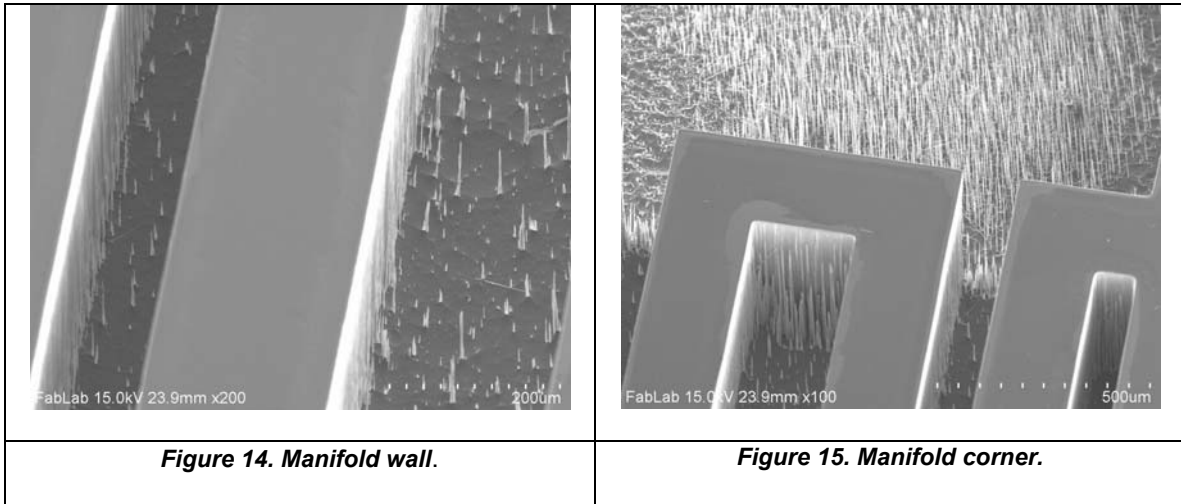


**Figure 14. Manifold wall.**

**Figure 15. Manifold corner.**

Two heat sinks have been completely packaged and tested under different input power levels. The geometrical dimensions of the microchannel in the two heat sinks tested are presented in Table 2.

**Table 2. Geometrical dimensions**

Channel depth, ( $\mu\text{m}$ )	200	200
Channel width, ( $\mu\text{m}$ )	20	40
Fin width, ( $\mu\text{m}$ )	20	40
Channel length, ( $\mu\text{m}$ )	400	400
Hydraulic diameter, ( $\mu\text{m}$ )	36	67
Number of channel per cm	250	125

The geometrical dimensions of the flow distributor for the two heat sinks are presented in Table 3.

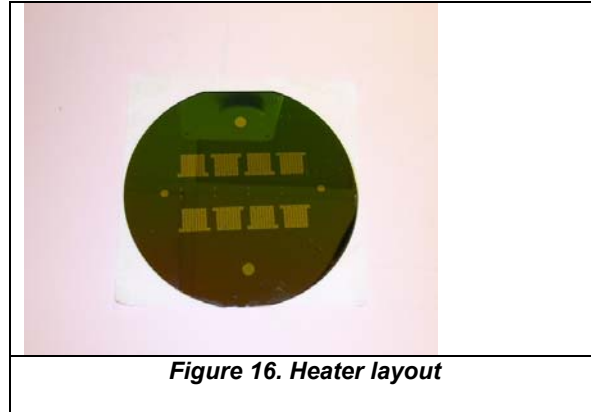
**Table 3. Geometrical dimensions of the manifold**

Inlet width, ( $\mu\text{m}$ )	120
outlet width, ( $\mu\text{m}$ )	240
Manifold height, ( $\mu\text{m}$ )	500
Manifold wall thickness, ( $\mu\text{m}$ )	220
Number of outlet flow	13
Number of inlet flow	13

### **Microfabrication of heaters**

Microfabrication of two different designs of heaters was carried out in the University of Maryland's microfabrication lab. The first generation of the heater was designed to provide an electrical resistance of about 100 ohms. The heater, in a serpentine shape, consisted of 100 A chromium

as an adhesion layer between the silicon oxide and platinum, and 1000 Å platinum acting as the main resistive element. A set of first-generation microfabricated heaters is shown in Figure 16. However, after microfabrication, a measurement of ohmic resistivity of heater resulted in values in the range of 400 Ω. In order to limit the material cost and provide a more cost-effective solution for the heater, a second heater design was developed in which chromium was chosen as the main resistance since its resistivity is close to platinum's. A thin layer of gold provided protection against any possible corrosion and oxidation of the chromium. Furthermore, in the second design the thickness of chromium was increased to 3000 Å to reduce the resistance, while the thickness of the gold layer was 300 Å. The resistances of the second heater design were measured and were found to be between 140 and 170 ohm, matching the design requirements.



### **Wafer bonding**

For this task the objective was to provide a eutectic bond between the manifold and microchannel wafers. To do so, a stack of number of metal layers was deposited on both sides of the microchannel and manifold wafer using an e-Beam evaporator. These layers were designed to serve as bonding layers for the AgSn eutectic bonds. The composition of the metal layers was as following: 100 Å chromium, 10000 Å silver, 2000 Å tin, and 500 Å gold. The chromium served as an adhesion layer between the metal layers and the silicon oxide and the gold layer acted as a corrosion and oxidation barrier. The first bonding trial with the whole wafers in a non-vacuumed oven at 350°C was not successful due to the oxidation of the tin. The next trial was performed on small pieces of experimental wafers in two different furnaces at 600°C and 800°C. After separating the wafers, the metal layer was not strong enough, and the temperature was very high. In the sample bonded at 600°C is shown, which after separating showed some gaps in the metal, which could be due to the lack of a vacuum environment in the furnace.

In another trial the thickness of metal stack was changed: the silver thickness was increased to 2 μm, and the tin was increased to 2 μm. This trial was carried out in a furnace at 600°C but without nitrogen and oxygen to reduce the existence of any air gaps between the metal layers. Moreover, in this trial samples were cut using a wafer cutting saw across the cutting line provided for this purpose before bonding. In Figure 17 the samples with the metal stack before bonding are shown. In Figure 18 an X-ray image of the device is presented. This image was used to inspect the existence of voids and quality of the bonded sample.

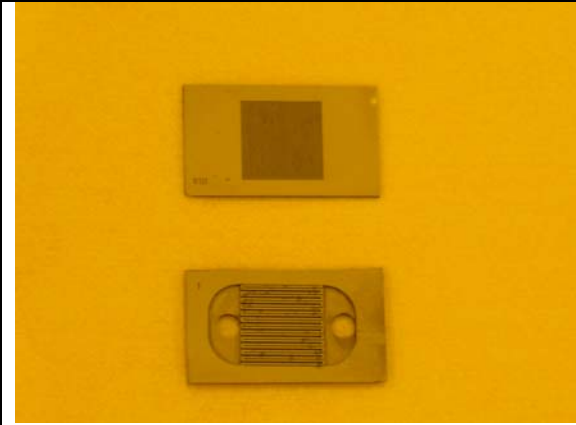


**Figure 17. Sample with metal stack before bonding.**

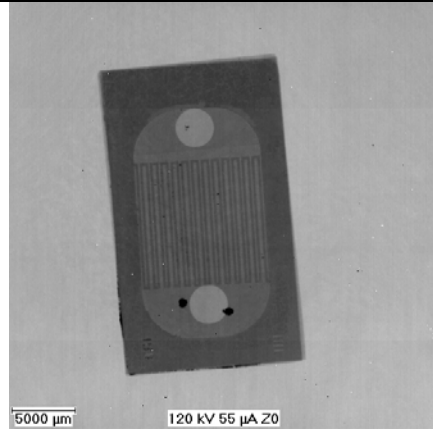


**Figure 18. X-ray image of bonded sample.**

### **Packaging**

A packaging technique was designed to secure and protect the sample. In this technique a box-shape package was produced from G10 with a place for the sample to rest, two holes for incoming and outgoing flows, and electrical connections for wire bonding pads. G10 laminate grades were produced by inserting continuous glass woven fabric impregnated with an epoxy resin binder while forming the sheet under high pressure. This material is used extensively in the electronics industry because its water absorption is extremely minimal and the G10 line of materials is not electrically conductive. It also exhibits superior mechanical and dimensional stability with a low coefficient of thermal expansion.

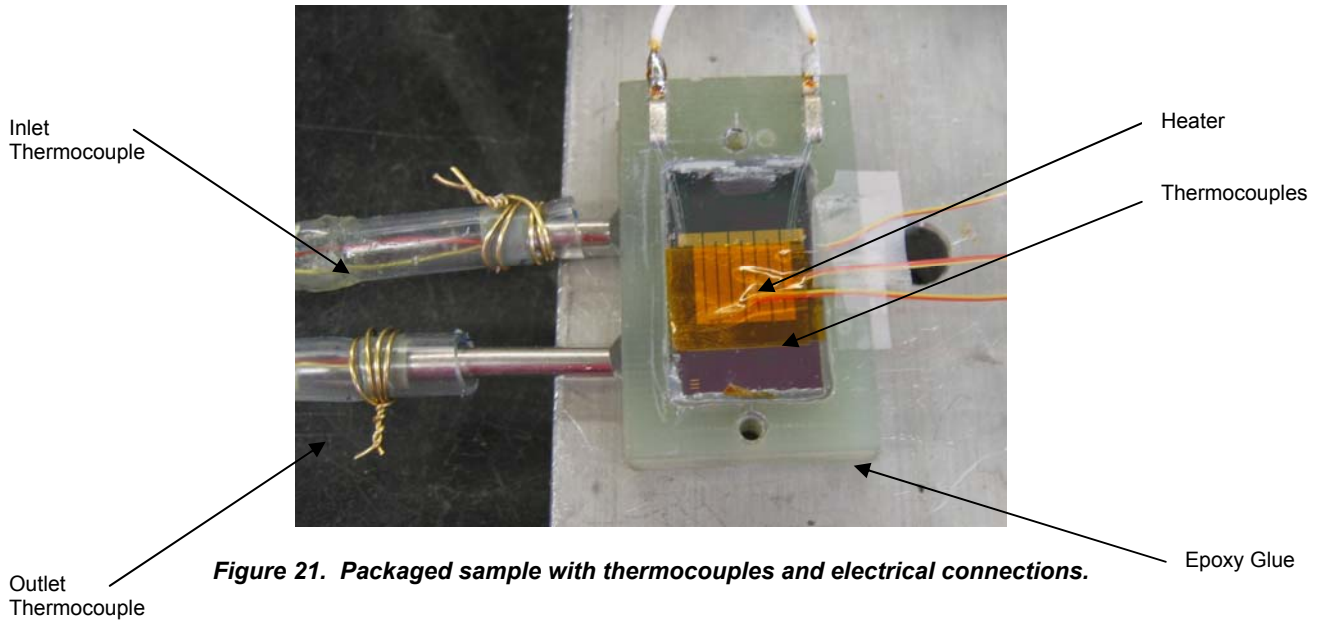


**Figure 19. G10 package base.**



**Figure 20. Complete PV cell package.**

Epoxy glue was used around the perimeter of the sample to fix it in the packaging test section, and two springs were used to keep the sample in place. Two thin rubber sheets used under and above the sample provide a smooth contact between the sample and the G10 package. The samples were then ready for wirebonding. Two pipes connected to inlet and outlet holes for refrigerant to pass through the sample. Three K-type thermocouples were used to find the temperature on the heater surface, at the inlet, and at the outlet. Figure 21 shows the packaged sample.



**Experimental setup**

The test section consists of the packaged sample with three K-type surface thermocouples: one thermocouple each at the inlet and outlet, and one thermocouple to find the zero temperature. The inlet was connected to a reservoir of distilled water and the outlet was connected to another reservoir to find the flow rate. Flow rate was measured by the division of weight of water by specific time. A nitrogen tank was connected to U type pressure gage device to measure the pressure applied to the system.

A programmable DC power supply (Sorenson, Inc., model #DLM150-4) provided power to the heater. The power supply was controlled by a data acquisition system (BenchLink Data Logger System) programmed on a personal computer through a general programming interface bus DAS card. Data was acquired through six thermocouples, a programmable power supply and BenchLink Data Logger System. The experimental setup diagram is shown in Figure 22. A close view of the test section is shown on the Figure 23.

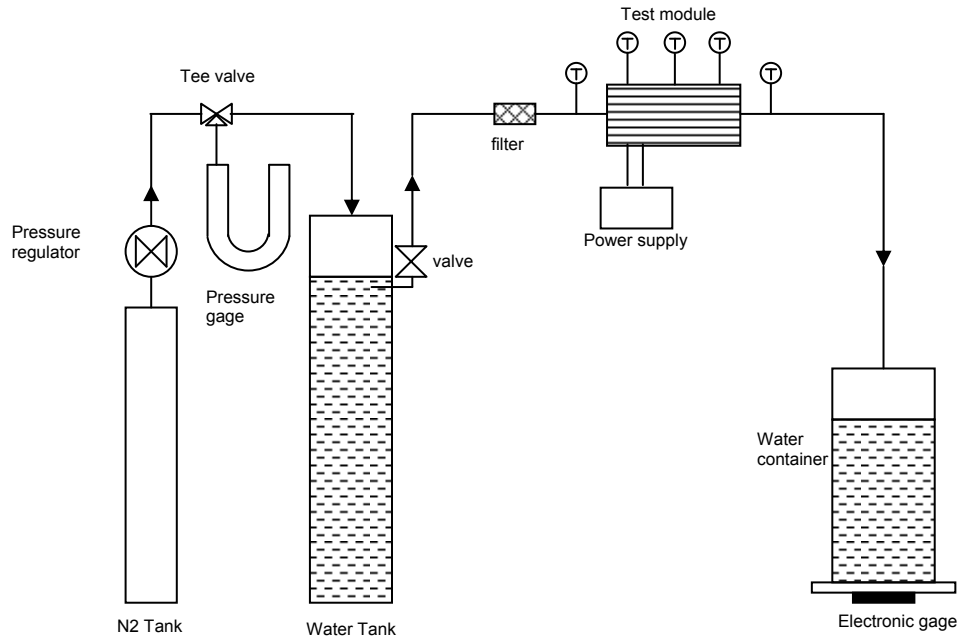


**Figure 22. Experimental setup.**

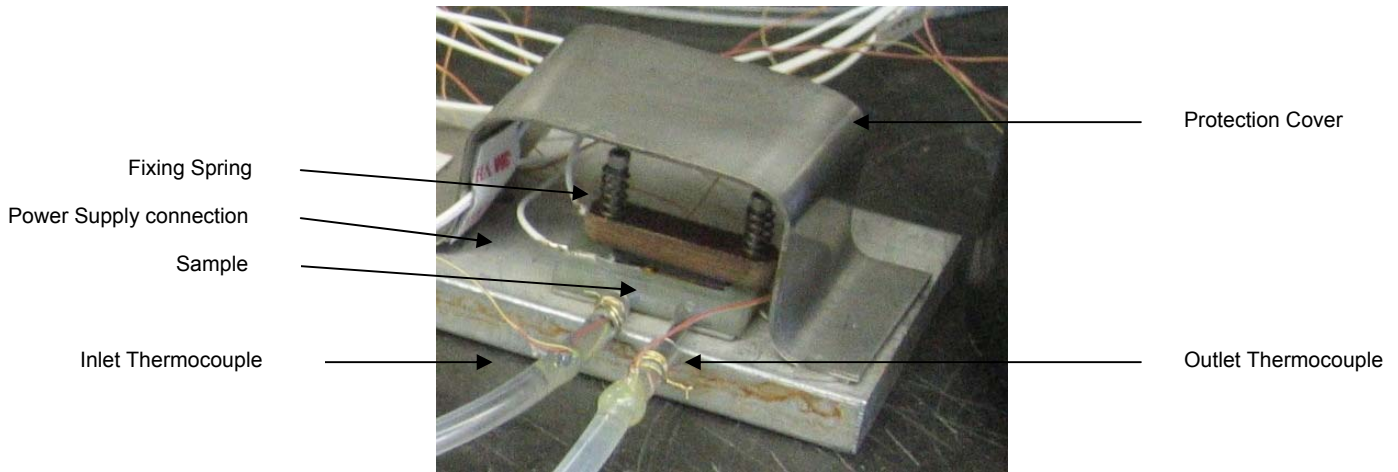


**Figure 23. Experimental sample.**

**Experimental procedure and test results**

The first step in running the experiment was to calibrate the thermocouples. All six K-type thermocouples were calibrated with the RTD thermocouple in a chiller with a temperature range

between 10 °C and 50 °C. The next step was to calibrate the heater resistance at different temperatures. For that, heated distilled water was run through the system, and with real time data acquisition card surface temperatures, inlet and outlet temperature and resistance were measured. Two calibration curves were plotted: the first, heater resistance versus average inlet and outlet water temperature, and the second, resistance versus average surface temperature. In the experiments voltage and current were measured, from which the heater resistance was calculated.

In the experiments the DC power supply was started at about 8 W and was increased every 10 W to about 58 W. At each power level, tests at six different pressure drops were performed. All the data from thermocouples and supplied power were recorded with the BenchLink Data Logger System and were exported to Microsoft Excel.

We tested two heat sinks in an open-loop test setup with water under different input power levels. Thermal parameters and pressure drop were measured.

A typical test run started with a degassing process. The trapped air was removed from the loop by running the system continuously for about 30 minutes. In the current experiments, the overall flow rate ranged from 0.3 gr/s to 1.3 gr/s. For each flow rate, the power input was increased from zero to the maximum output that the wire bond could tolerate. For each test run, the temperature and pressure drop were closely monitored. After about 5 minutes, steady-state condition was identified and data was sampled continuously for about one minute. Using the calibration curve, all temperatures were calibrated. After each test flow measurement was performed by collecting and weighing the DI water for certain amount of time, the power dissipation was determined from the product of the voltage and current measured at the heater.

It should be mentioned that actual heat input may be less than the measured value due to losses to the environment. Power input measured agreed within 5% of the heat transferred to the water.

Here the experimental results of the first heat sink with hydraulic diameter of 67 μm and second heat sink with hydraulic diameter of 36 μm are presented.

### Heat sink with hydraulic diameter of 67 μm

The heat transfer coefficient obtained at each flow rate is presented in Figure 23. The overall heat transfer coefficient  $h$  is calculated by

$$h = \frac{Q}{A\Delta T_m} = \frac{C_p \dot{m}(T_{out} - T_{in})}{A[T_w - 0.5(T_{in} - T_{out})]}$$

Heat transfer area  $A$  is defined as the total projected area. The heating power  $Q$  received by water is calculated by the energy conservation equation from the inlet and outlet working fluid temperature assuming negligible heat losses to the surroundings.  $\Delta T_m$  is the mean temperature difference between the channel walls and the working fluid.  $T_w$ , the average heater temperature, was determined by the three thermocouples placed on the heater.  $T_{in}$  and  $T_{out}$  are the inlet and outlet bulk temperatures of the working fluid. The mean temperature of the water  $0.5(T_{in} + T_{out})$  is used to characterize the physical properties of the working fluid, including thermal conductivity  $K$ , density  $\rho$ , and specific heat  $C_p$ .

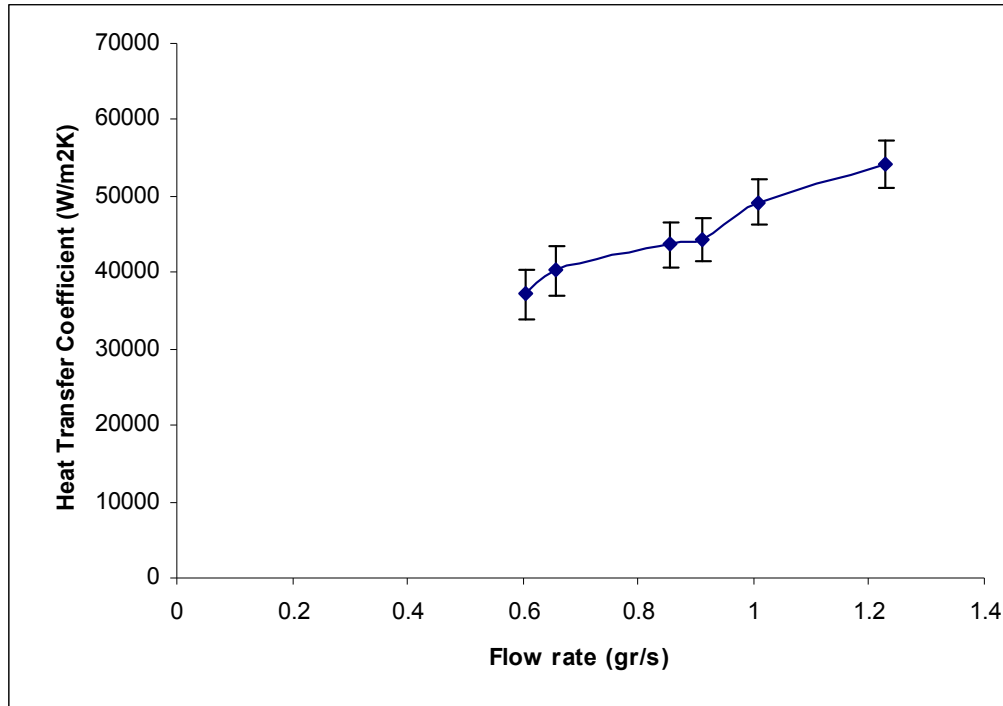


**Figure 24. Variation of heat transfer coefficient versus flow rate.**

As seen in Figure 24, the heat transfer coefficient increases as the water flow rate increases, and the variation seems linear. At its peak, the heat transfer coefficient is 57528 W/m<sup>2</sup>K. The uncertainty in heat transfer coefficient for all test points averaged 7% with a maximum uncertainty of 8.9%.

The temperature difference in the water between the inlet and outlet versus input power at different flow rates is plotted in Figure 25. The maximum power applied to this sample was 58 W, and water inlet temperature was 24 °C. As predicted, at each input power when the flow rate was low, temperature difference was high. Also, by increasing input power at constant flow rate, the water temperature difference increases. The maximum water temperature difference occurred at 58 W and 0.693 gr/s flow rate and was 20.3 °C.

The variation of average surface temperature versus input power at different flow rates is presented in Figure 26. Here it is seen that surface temperature increases linearly with an increase in power; however, it decreases with an increase in flow rate due to higher heat transfer coefficient. The maximum surface temperature was 48.2 °C, attained at 58 W and 0.66 gr/s flow rate.

The results of the pressure drop versus flow rate in this heat sink are presented in Figure 27. The flow rate between 0.6 gr/s and 1.2 gr/s and pressure drop between 5.84 kPa and 19.88 kPa was obtained for this case. The error in the pressure drop measurement is negligible, and the accuracy of the flow rate calculation is 0.05 gr/s.

By combining Figure 25 and Figure 26 one can conclude that this heat sink can provide water at minimum temperature of 75 °C, and keep the average surface temperature below 110 °C for the solar cell application.

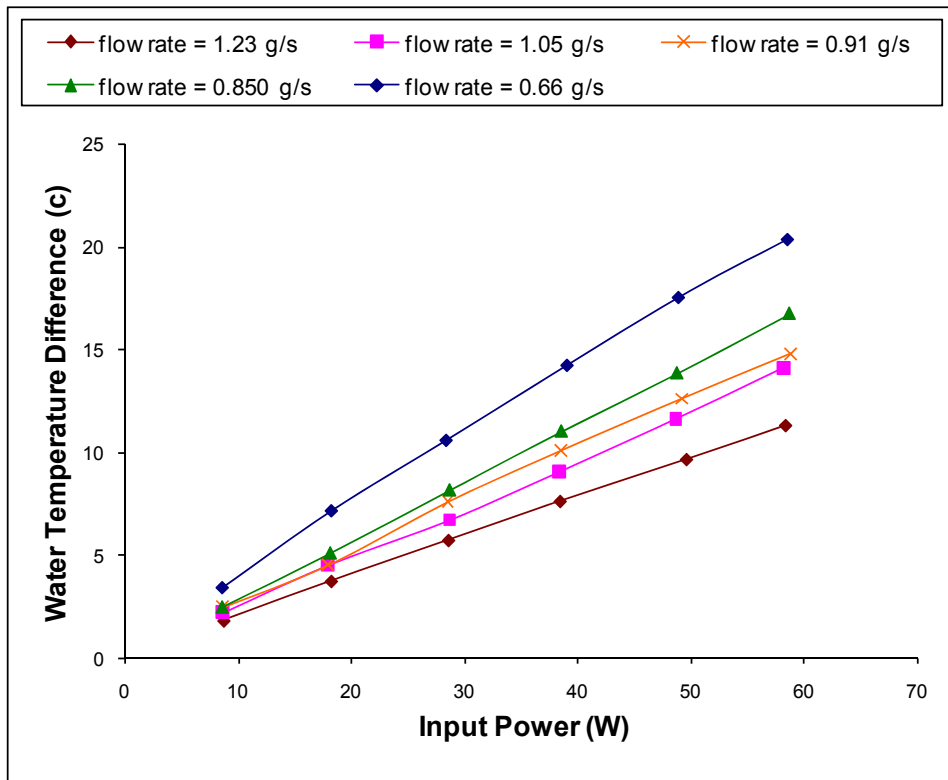


Figure 25. Variation of water temperature versus input power.

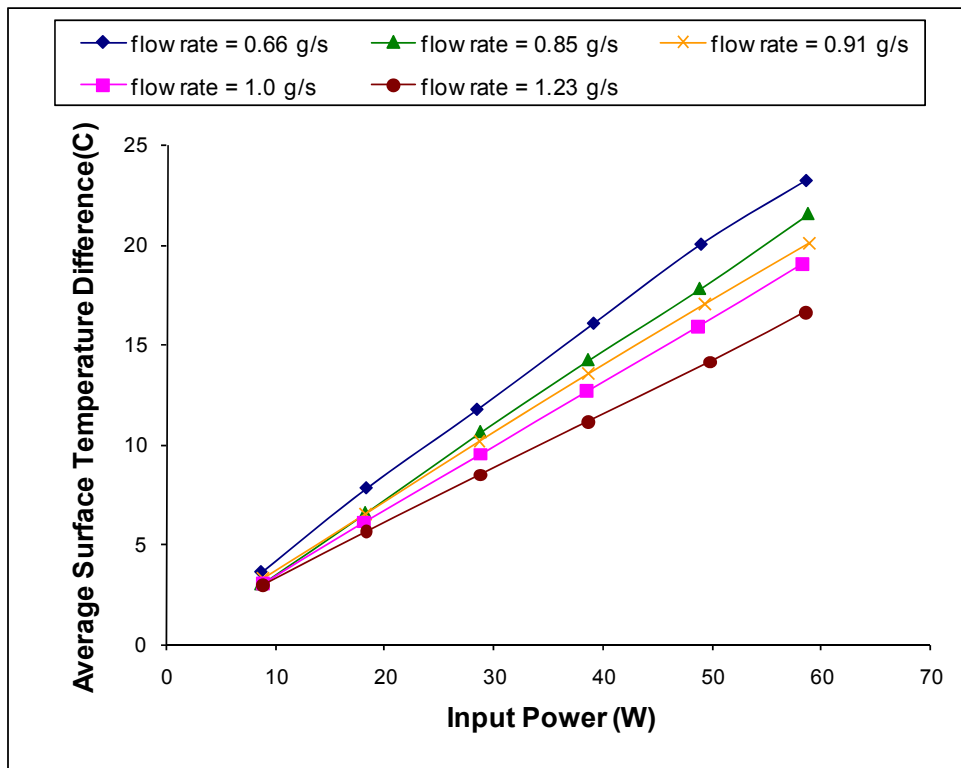


Figure 26. Variation of heater surface temperature versus input power.

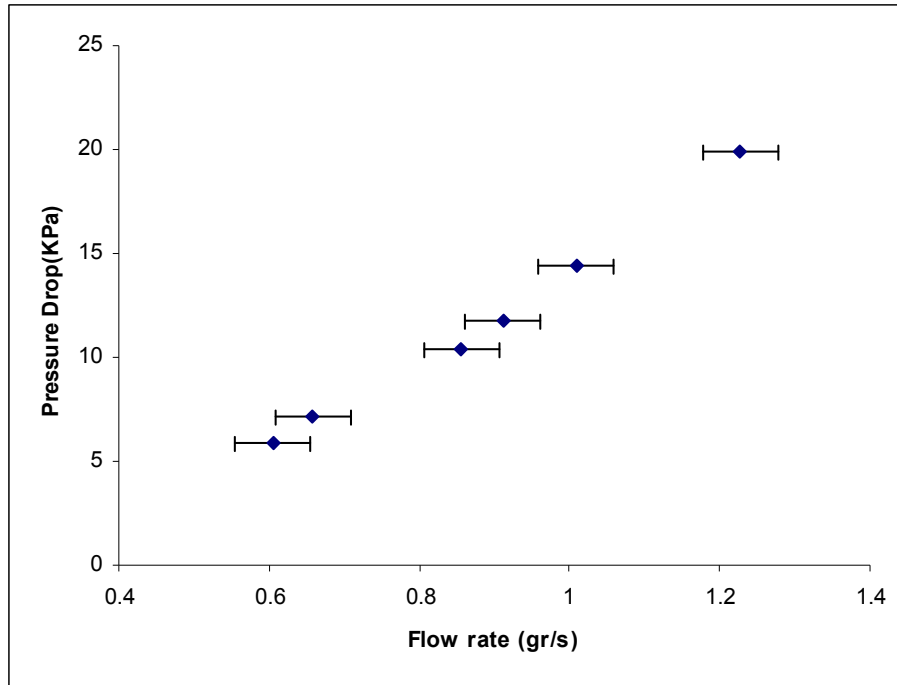


Figure 27. Variation of pressure drop versus flow rate.

**Heat sink with hydraulic diameter of 36  $\mu\text{m}$**

In Figure 28 the pressure drop versus flow rate for the heat sink with  $D_h = 36 \mu\text{m}$ . The flow rates for this sample varied between 0.3 gr/s and 1.1 gr/s. Pressure drop was obtained between 3.66 kPa and 22.67 kPa. Even for lower flow rates than for heat sink with  $D_h=67, \mu\text{m}$  pressure drop was higher.

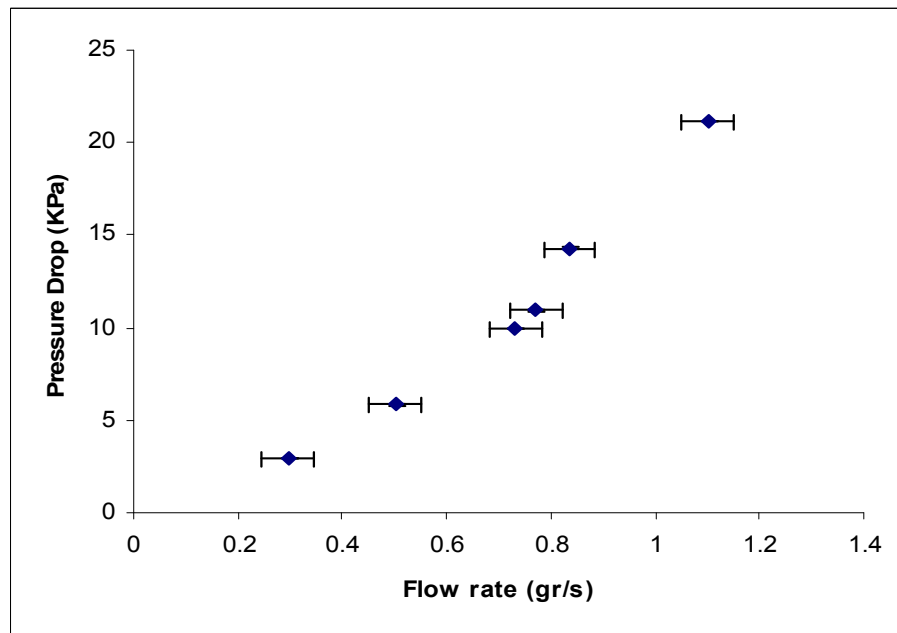


Figure 28. Variation of pressure drop versus flow rate.

The heat transfer coefficient versus flow rate for this sample is presented in Figure 29. Similar to the heat sink with  $D_h=67\ \mu\text{m}$ , the heat transfer coefficient increased with flow rate linearly, however it is on average 30% higher. The uncertainty in heat transfer coefficient for all test points averaged 8.5% with a maximum uncertainty of 17%.

As for the first sample, the temperature difference in water versus input power at different flow rate is plotted in Figure 30. The power increment in this sample was the same as the first, but the maximum power was increased to about 75 W and the inlet water temperature was 26 °C. The same trends were obtained for this sample, although in this case, at very low flow rate the temperature difference in water sharply increased to about 34 °C.

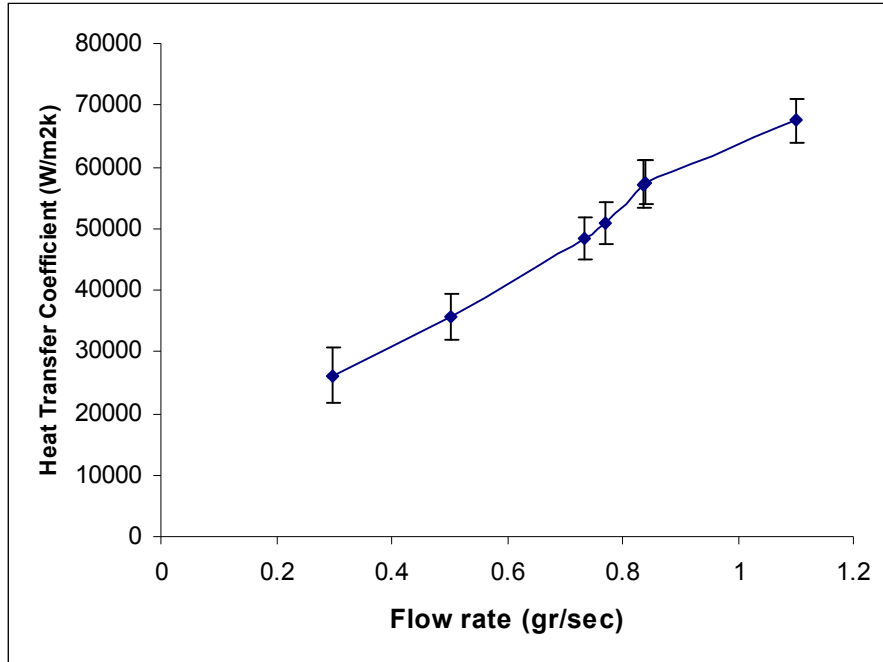


Figure 29. Variation of heat transfer coefficient versus flow rate for heat sink  $D_h=36\mu\text{m}$ .

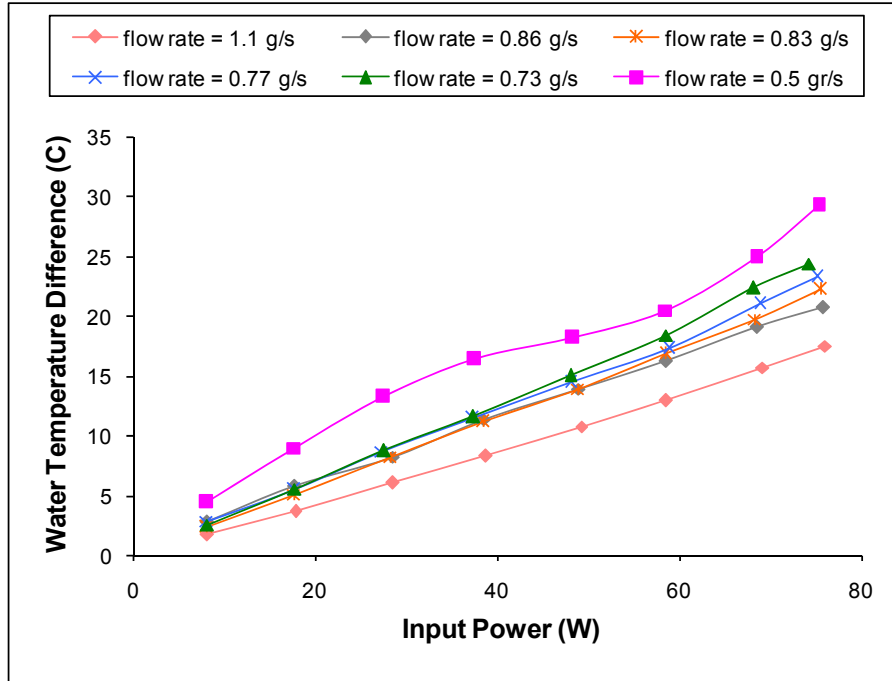


Figure 30. Variation of water temperature versus input power.

Figure 31 illustrates the average surface temperature versus input power at different flow rates. As demonstrated in the previous graph, the trend in this test and in sample one are the same except for a very low flow rate, at which surface temperature increased sharply with heat load.

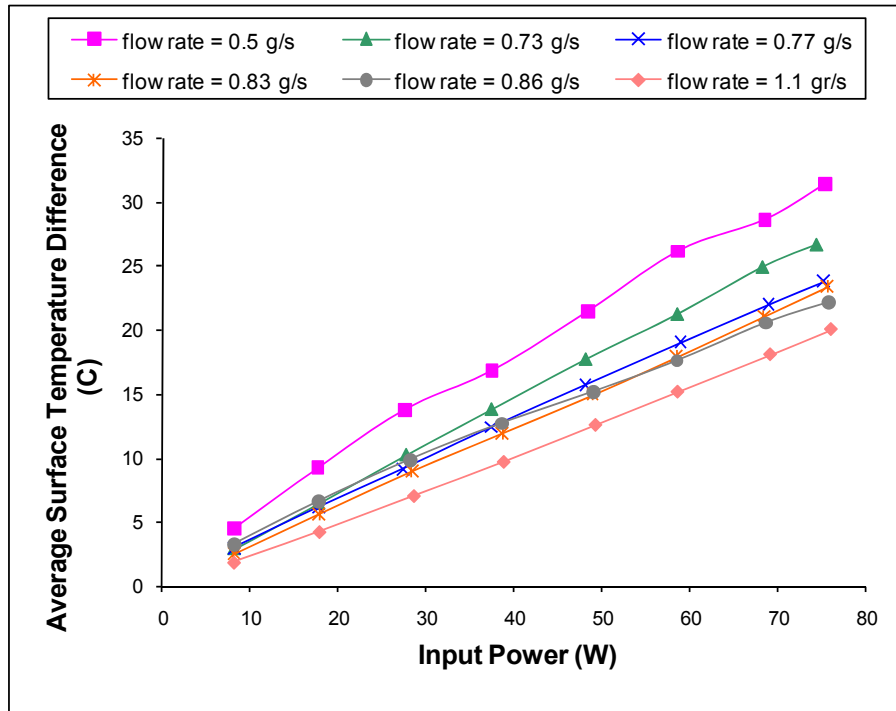


Figure 31. Variation of heater surface temperature versus input power.

These two graphs show that this heat sink can also provide hot water at minimum temperature of 70 °C and keep the average surface temperature below 110 °C for solar cell application up to heat flux of 75 W/cm<sup>2</sup>, which corresponds to the heat flux anticipated in PV cell of moderate efficiency operating at 1000 sun concentration.

### Comparison of the heat transfer performance of the heat sinks

We compared the Nusselt number versus Reynolds number for the two test samples. The overall Nusselt number for the de-ionized water flowing through the sample is defined as

$$Nu = \frac{hD_h}{K}$$

The mean temperature of the water is used to characterize physical properties of the de-ionized

water, and the hydraulic diameter is defined as  $\frac{4A}{P}$ . Figure 32 shows the effect of Reynolds number on the average Nusselt number. As the Reynolds number increases, a higher Nusselt number is obtained and overall agreement between these two samples is achieved.

These results were compared against the available literature, for which a study by Jiang et al. [12] was selected. Their research demonstrated that the average Nusselt number decreases from 12.9 to 3.0 with an increase in  $X^+$  (where  $X^+$  is defined as  $L/(RePrDh)$ ). They observed a two-flow regime in Nu. For the  $X^+$  relationship for  $X^+ < 0.05$ , the average Nusselt number decreases sharply with increasing  $X^+$ , whereas for  $X^+ > 0.05$  the average Nusselt number decreases very slowly with

increasing  $X^+$ . They concluded that different heat transfer regimes are due to flow regimes and the thermal entry effect and thus proposed a  $Nu$  and  $X^+$  correlation as:

$$Nu = 0.52 \left( \frac{Re Pr D_h}{L} \right)^{0.62}$$

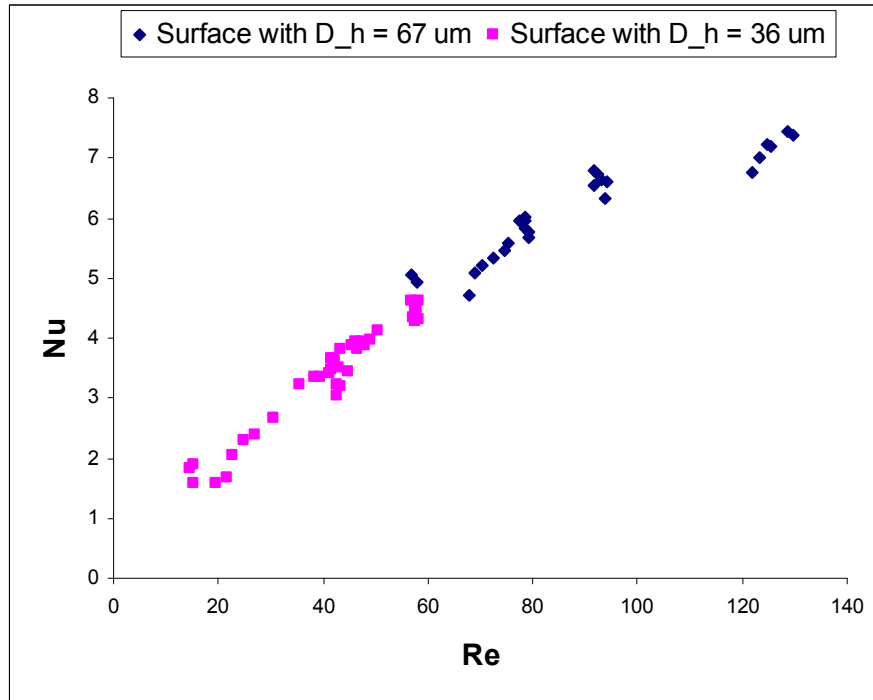


Figure 32. Variation of Nusselt number versus Reynolds number for first and second heat sinks.

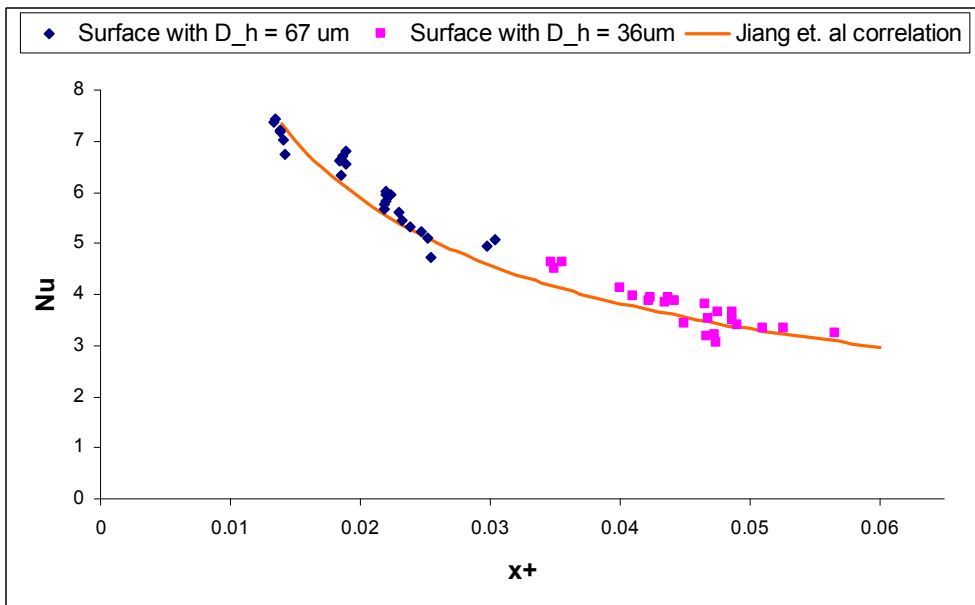
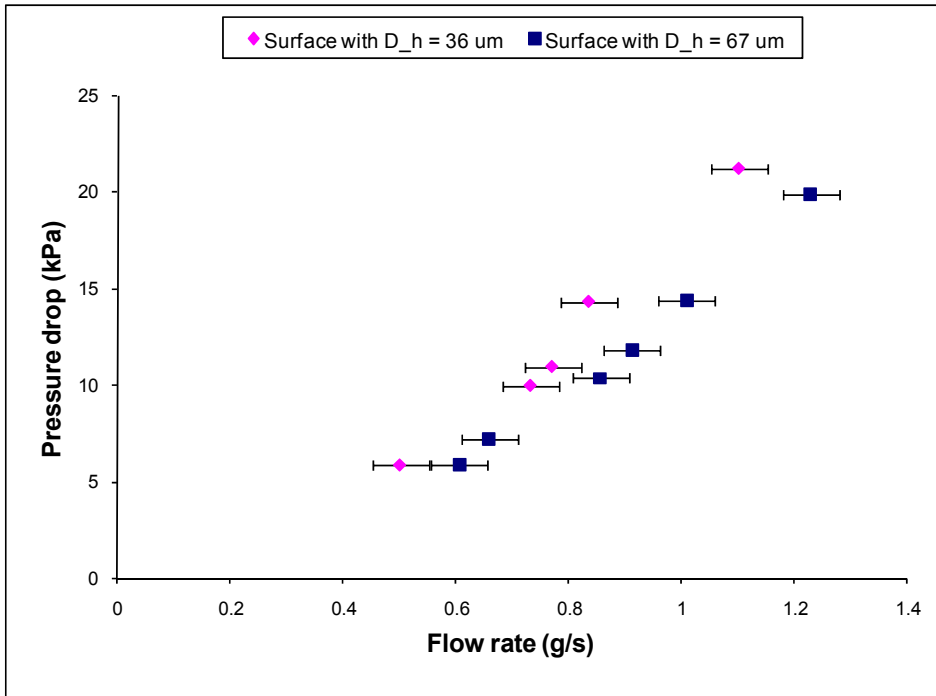


Figure 33. Variation of Nusselt versus  $X^+$  for two heat sinks.

This trend is also observed in the results of this research. As presented in Figure 33, the average Nusselt number versus  $X^+$  demonstrates a decreasing trend up to  $X^+ = 0.05$ , which proves that the flow in microchannels is in the developing regime. As predicted, the manifold helps to promote redeveloping flow in each channel, which enhances the heat transfer capability. The experimental results demonstrate reasonable agreement with the Jiang et al. correlation.

### Comparison of the pressure drop of the heat sinks

A comparison between heat sinks pressure drop versus flow rate is presented in Figure 34. Although it is expected that in the heat sink with  $D_h=36 \mu\text{m}$  it is expected to be at least twice higher compare to heat sink with  $D_h=67 \mu\text{m}$ , the pressure drop difference for this heat sinks is in fact not significant. This suggested that microchannels themselves just partially contribute to the heat sink pressure drop.



**Figure 34: Comparison of pressure drop between first and second sample.**

To calculate the pressure drop in the microchannel the following correlation by Jiang et al. for friction factor in rectangular microchannel is used. The friction factor is correlated with Re for laminar flow condition with Reynolds number smaller than 600.

$$f = 1639 / \text{Re}^{1.48}$$

Pressure drop in the microchannels is calculated with following equation:

$$\Delta p = f \frac{L}{D_h} \times \frac{V^2}{2} \times \rho$$

where  $\Delta p$  is pressure drop across the microchannel,  $\rho$  is the water density in terms of the mean value of the inlet and outlet temperature,  $D_h$  and L are the hydraulic diameter and the length of microchannel, V is the average velocity of water and  $f$  is the friction factor.

Microchannel pressure drop is calculated for two test cases and subtracted from the overall pressure drop to find the manifold pressure drop as presented in Figures 35 and 36.

Total pressure drop consists of two terms, microchannel pressure drop and manifold pressure drop. As expected since both samples have manifold with same geometrical dimension to distribute the flow into the microchannels, pressure drop in their manifold has same value and as predicted this is the dominant term in the total pressure drop. In the heat sink with  $D_h=36\ \mu\text{m}$  the contribution of microchannel pressure drop in total pressure drop on average is just 35%, as it shown on Figure 36. It is even lower for the heat sink with  $D_h=67\ \mu\text{m}$  On average this pressure drop is just 13% of the total pressure drop (Figure 35). The pressure drop of the manifold fabricated with the most advance microfabrication technique DRIE was the dominant even in the  $1\ \text{cm}^2$  heat sink. Therefore the total PV cell should be subdivided on even smaller than  $1\ \text{cm}^2$  segments or other techniques should be used for the fabrication of the manifold.

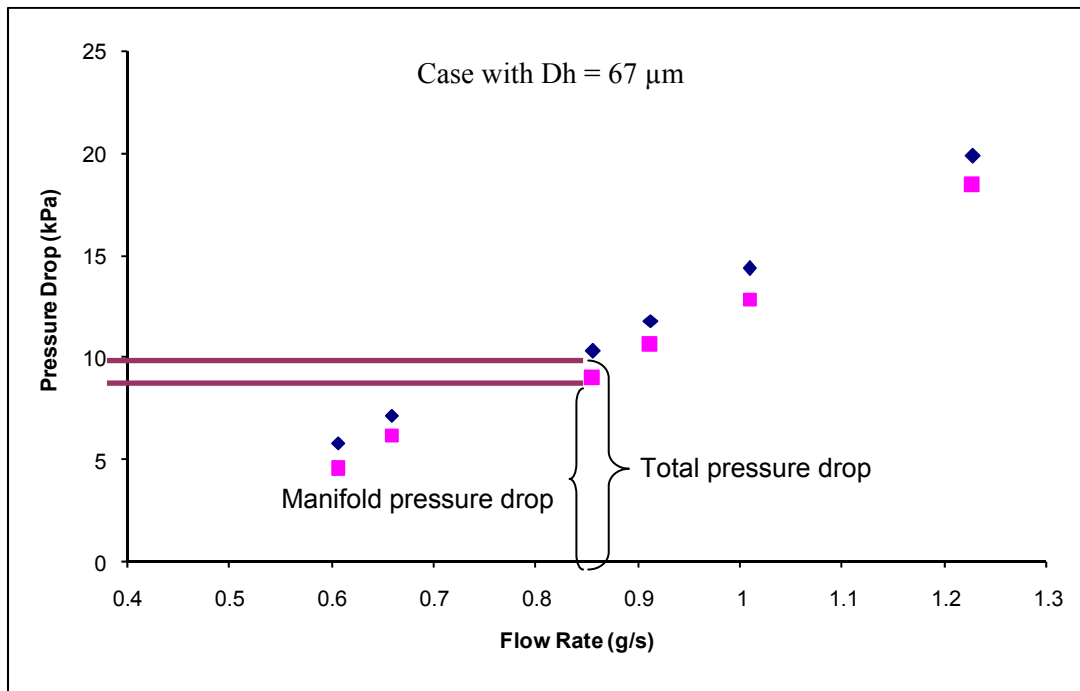
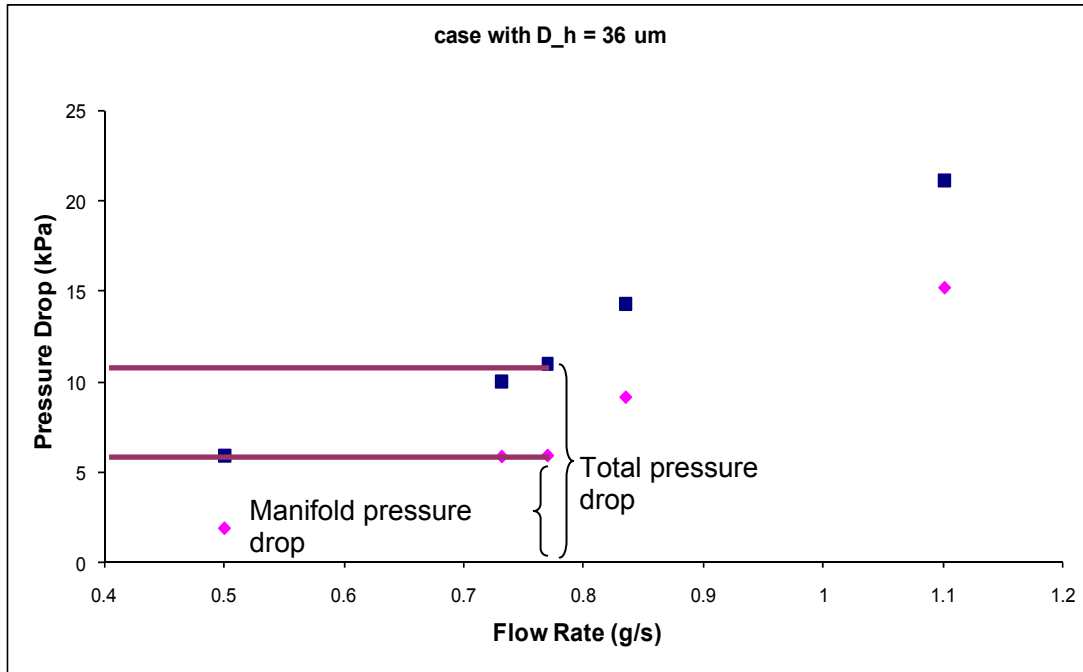


Figure 35: Total and manifold pressure drop for sample with hydraulic diameter of  $67\ \mu\text{m}$ .



**Figure 36: Total and manifold pressure drop for sample with hydraulic diameter of 36  $\mu\text{m}$ .**

## 5. Conclusion

Solar energy is one of the most valuable sources of energy and it has the potential to produce significant portion of the world's energy usage. The concentrating of solar energy decreases the cost PV cell, increases its efficiency, introduces the possibility to easily up-grating the PV cell and produce high grade heat for the secondary use. The total efficiency of the system can be increased to 80-90% in combination with system cost reduction.

Microfabricated on the back of solar cell microchannel manifold heat sink enables operation of the concentrated PV cell at 1000 sun concentration and produce high grade heat for the secondary use such as heating, hot water or cooling.

The pressure drop in the microfabricated silicon flow distributing manifold, fabricated by the most advanced etching technique dominates total system pressure drop even for 1  $\text{cm}^2$  PV cell. The PV array should be fragmented for the segments smaller than 1  $\text{cm}^2$  or some other technology should be used for manifold fabrication.

## 6. Recommendations for Future Work

The fragmentation of the PV array cooling system on smaller segments using multilayer silicon manifold or alternative manifold fabrication technologies should be explored.

The manifold microchannel heat sink should be fabricated on the top of actual PV cell and tested on the system level.

## 7. References

- [1] R. M. Swanson, "The promise of concentrators" *Prog. Photovolt. Res. Appl.*, 8 (2000) 93-111.
- [2] D. Cooke, P. Gleckman, H. Krebs, J. O'Gallagher, D. Saige, R. Winston, "Sunlight brighter than sun", *J. Nature*, 346 (1990) 802.

- [3] J. S. Coventry, "Performance of a concentrating photovoltaic/ thermal solar collector", *J. Solar Energy*, 78 (2005) 221-222.
- [4] A. Williams, "The Handbook of Photovoltaic Application", The Fairmont Press Inc., 1986.
- [5] A. Fahrenbruch, R. Bube, "Fundamentals of solar cells", Academic Press, New York, 1983.
- [6] T. Markvart, "Solar electricity", 2nd ed. Wiley, New York, 2000.
- [7] D. Meneses-Rodriguez, P. P. Horley, J. Gonzalez-Hernandez, Y. V. Vorobiev, P. N. Gorley, "Photovoltaic solar cells performance at elevated temperatures", *J. Solar Energy*, 78 (2005) 243-250.
- [8] D. B. Tuckerman, R. F. W. Pease, "High performance heat sink for VLSI", *IEEE Electron. Device Lett.* EDL2 (1982) 126-129.
- [9] P. X. Jiang, M. H. fan, G. S. Si, Z. P. Ren, "Thermal-Hydraulic performance of small scale micro-channel and porous-media heat-exchangers", *International Journal of Heat and Mass Transfer* 44 (2001) 1039-1051
- [10] D. Copeland, M. Behnia, W. Nakayama, "Manifold microchannel heat sink: Isothermal analysis", *IEEE Transaction on Component, Packaging, and Manufacturing Technology-Part A*, Vol. 20 No. 2 (1997) 96-102.
- [11] G. M. Harpole, J. E. Eninger, "Micro-channel heat exchanger optimization", Seventh IEEE Semi-Therm Symposium
- [12] P. X. Jiang, M. H. fan, G. S. Si, Z. P. Ren, "Thermal-Hydraulic performance of small scale micro-channel and porous-media heat-exchangers", *International Journal of Heat and Mass Transfer* 44 (2001) 1039-1051.

## **8. Publications**

"Experimental Investigation of Heat Transfer Performance of a Manifold Microchannel Heat Sink for Cooling of Concentrated Solar Cells" to be presented in 59th Electronic Components and Technology Conference (ECTC) to be held in San Diego, California, USA on May 26-May 29, 2009.

## **8. Visits**

- Amir Shoostari, 1 month working visit to PI, May 2007
- Serguei Dessiatoun visit to PI, Dec 8 -13 2007
- Serguei Dessiatoun visit to PI, May 3 -9 2008

## **9. GRA (names, degrees, graduation)**

Elnaz Kermani, Master of Science in Mechanical Engineering, graduated on December 2008

# Sulfur Recovery from Gas Stream using Flameless and Flame Combustion Reactor

UMD Investigators: Prof. Ashwani K. Gupta

GRA: Hatem Selim

PI Investigator(s): Dr. Mohamed Sassi

Student: Sami Ben Rejeb

Start Date: October 2006

FINAL REPORT

## 1. Objective/Abstract

The main objective is to obtain fundamental information on the thermal process for sulfur recovery from sour gas by conventional flame combustion and flameless combustion using numerical and experimental studies. The ultimate goal is to determine optimal operating conditions for enhanced sulfur conversion and recovery in the thermal process. An innovative flameless combustion process is examined for enhanced thermal stage sulfur recovery. Simulations from this advanced thermal conversion process is examined along with some preliminary examination of the data with experimental studies. The results are compared with the currently used flame combustion process for the Claus furnace sulfur recovery. We explore the operating conditions and develop reduced kinetic mechanism for sulfur chemistry under both flame and flameless modes of reactor operation in the process of enhanced sulfur recovery.

Specific objectives will be to provide:

- A comprehensive literature review of the existing flame combustion process for sulfur removal with special reference to sulfur chemistry
- Near isothermal reactor conditions that assist in the enhanced sulfur recovery process. In normal flame mode this mode is difficult to achieve. However flameless combustion provides new paths for enhanced sulfur recovery
- Detailed and reduced sulfur chemistry, and CFD simulation of flame and flameless combustion in the furnace
- Design of flameless combustion furnace for experimental verification of numerical results
- Measurements and characterization of the flameless combustion furnace using high temperature air combustion principles
- Experimental facility development
- Sample experimental results with different sulfur content gas streams in CO<sub>2</sub> or nitrogen gas using both flame and flameless combustion modes of furnace operation
- Determination of the product gas stream for examination and evaluation of sulfur recovery in the process

## 2. Numerical Efforts

In this section we summarize the progress of our numerical efforts. These efforts started with an equilibrium study for the optimum Claus reactor temperature, where we also introduced a study of the change of optimum temperature with the change in sour gas composition. Next, a kinetics study was performed. The reduction strategy for the hydrogen sulfide/oxygen reaction initiated with a sensitivity analysis for reducing the mechanism. However, since the sensitivity analysis turned out to be inefficient, we used the direct relation graph and error propagation methodology (DRGEP) as our reduction strategy.

### 2.1. Equilibrium Study

In this portion of the project we examined the effect of the temperature of the Claus reactor on the equilibrium mole fraction of S<sub>2</sub> as well as the conversion efficiency, which is defined as:

$$\text{Conversion Efficiency} = \frac{\text{Mass of recovered sulfur}}{\text{Mass of sulfur in inlet H}_2\text{S}}$$

Two selected cases were investigated:

Case (1): H<sub>2</sub>S gas with air  
 Inlet conditions: (3H<sub>2</sub>S+ 1.5O<sub>2</sub>+5.64N<sub>2</sub>)

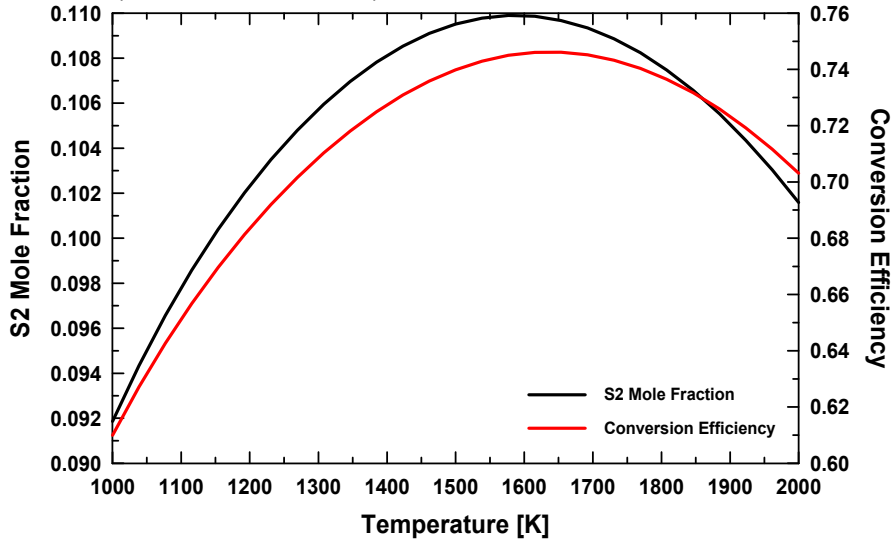


**Figure 1. Effect of reactor temperature on S<sub>2</sub> mole fraction and conversion efficiency with H<sub>2</sub>S gas only.**

The effect of change in the temperature on S<sub>2</sub> equilibrium mole fraction shows that the optimum temperature for the reaction is around 1600K.

Case (2): H<sub>2</sub>S and CO<sub>2</sub> gas mixture with air  
 Inlet conditions: (3H<sub>2</sub>S+ 1CO<sub>2</sub>+ 1.5O<sub>2</sub>+5.64N<sub>2</sub>)

The effect of changing the gas composition from H<sub>2</sub>S to a mixture of H<sub>2</sub>S and CO<sub>2</sub> mixture is shown in Figure 2.

In this case, effect of the CO<sub>2</sub> accompanying the hydrogen sulfide is to decrease the reactor temperature to around 1500K for achieving high sulfur recovery. This is of practical importance since the gas to be processed may have different gas stream compositions at times under certain conditions. This information allows one to change the reactor temperature based on the feed gas composition. Note that additional factors of flame chemistry with different mechanistic reaction pathways also provide a role when the gas composition and temperature of the reactor change. This leads one to examine detailed reaction mechanism and develop tools for reduced chemistry mechanism without losing key pathways. The reduced chemistry model can then be used in computational fluid dynamic calculations for detailed simulations of the process and process improvement.

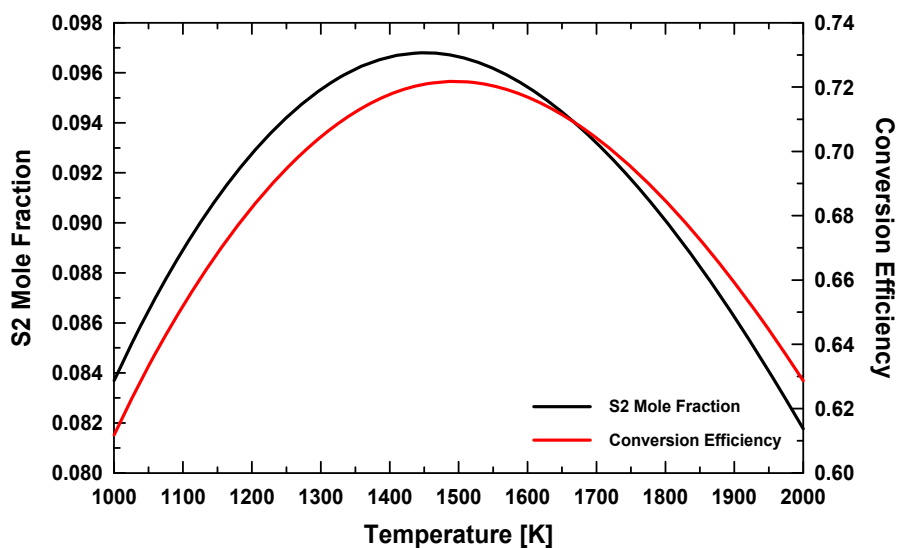


Figure 2. Effect of reactor temperature on  $S_2$  mole fraction and conversion efficiency with  $CO_2$  in  $H_2S$  gas.

## 2.2 Variation of optimum reactor temperature with sour-gas composition

Crude natural gas comes in sour form; i.e., it contains “sour” acid-forming gases like  $H_2S$  and  $CO_2$ , as well as undesired non-combustible impurities like  $N_2$ . Purification processes yield sour gas, which is a mixture of  $H_2S$ ,  $CO_2$ , and  $N_2$ . If the sour gas is to be thermally treated for sulfur recovery, the mole fractions of  $CO_2$  and  $N_2$  have to be taken into consideration, as the presence of either gas significantly affects both the rates and equilibrium conditions of sulfur-forming reactions. Since the goal is to maximize the sulfur-recovery efficiency, the corresponding reactor operating conditions (particularly temperature) have to be known and maintained. The presence of either  $CO_2$  or  $N_2$  affects the  $H_2S$  concentrations, partial pressures, and consequently the reaction rates. Therefore, in order to maintain peak sulfur recovery efficiencies, the reactor temperature has to be adjusted according to the given inlet concentrations of  $CO_2$  and  $N_2$  in the sour gas.

An analysis has been conducted to numerically determine the optimum reactor temperature (i.e., temperature yielding peak sulfur-recovery efficiency) for various combinations of  $CO_2$  and  $N_2$  inlet mole fractions. The following conditions were considered:

- $CO_2$  inlet mole fraction = 0 – 90% in steps of 10%
- $N_2$  inlet mole fraction = 0 – 50% in steps of 10%
- $H_2S$  inlet mole fraction  $\geq 10\%$
- $CO_2$  and  $N_2$  inlet numbers of moles, as well as total number of moles of sour-gas mixture, were changed to simulate different  $CO_2$  and  $N_2$  mole fractions. However, the inlet number of moles of  $H_2S$  was kept constant to maintain a fixed inlet mass of sulfur. This allows for a direct comparison of all analysis runs based on sulfur-recovery efficiency. Recall that this efficiency is defined as the ratio of recovered sulfur mass to the inlet sulfur mass within  $H_2S$ .
- For each combination of  $CO_2$  and  $N_2$  inlet mole fractions, a range of reactor temperatures was considered, and the recovery efficiency was plotted versus reactor temperature. This allowed for the determination of optimum temperature, corresponding to peak efficiency
- The detailed sulfur-reaction mechanism<sup>1</sup>, developed by Leeds University, was used.

<sup>1</sup> <http://www.chem.leeds.ac.uk/combustion/sox.htm>

### 2.2.1 Effect of nitrogen

To highlight the effect of nitrogen, two sour-gas compositions are considered, the first containing 90% reactants and 10% N<sub>2</sub>, and the second containing 90% reactants and 10% argon. Argon was chosen because it represents a purely inert gas that contributes to nothing but decreasing the mole fractions of reactants. As seen from the left efficiency-temperature plot in Figure 3, the presence of nitrogen has no significant effect on variation of conversion efficiency, which proves that nitrogen behaves as an inert gas, similar to argon, and does not affect the rates of H<sub>2</sub>S/O<sub>2</sub> reaction mechanism. If the inert gas concentration is increased to 50%, at the expense of decreasing reactants concentration down to 50%, both Ar and N<sub>2</sub> behave again very similarly. However, the optimum temperature (corresponding to peak efficiency) is slightly decreased. This is attributed to the fact that the lower partial pressures of all other species (S<sub>2</sub> included) in this latter case promote their tendency to dissociate. Therefore, the reactor temperature has to be decreased to hinder the dissociation and loss of S<sub>2</sub>, in order to maintain peak recovery efficiency.

### 2.2.2 Effect of carbon dioxide

In contrast to N<sub>2</sub>, the effect of the presence of CO<sub>2</sub> is more complicated. Unlike N<sub>2</sub>, CO<sub>2</sub> is not entirely inert. It has the capability to dissociate to CO and O radicals at elevated temperatures encountered in the Claus process<sup>11-12</sup>. If the same above analysis of the effect of nitrogen is repeated for carbon dioxide, the results obtained show that small quantities of CO<sub>2</sub> in acid gas slightly promote sulfur recovery, as shown in Figure 4a. In contrast, higher CO<sub>2</sub> concentrations result in decreased efficiency, as shown in Figure 4b.

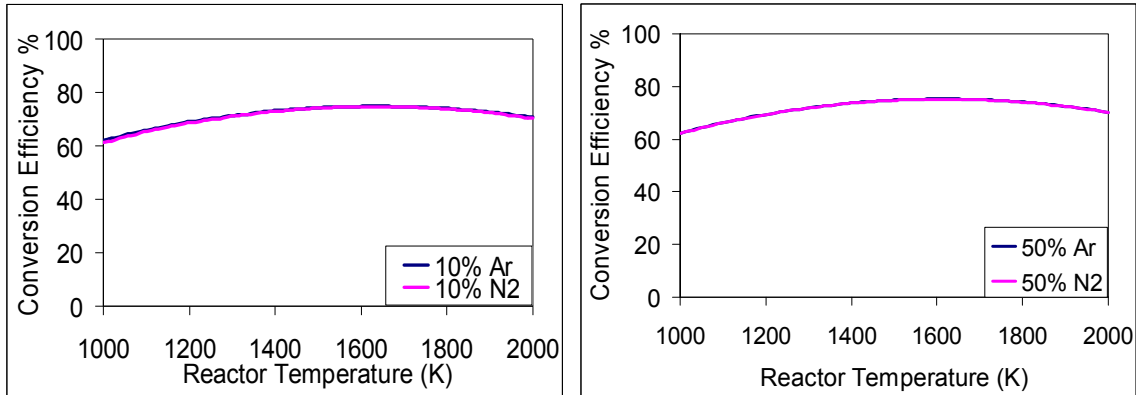


Figure 3. Effect of nitrogen presence in sour gas.

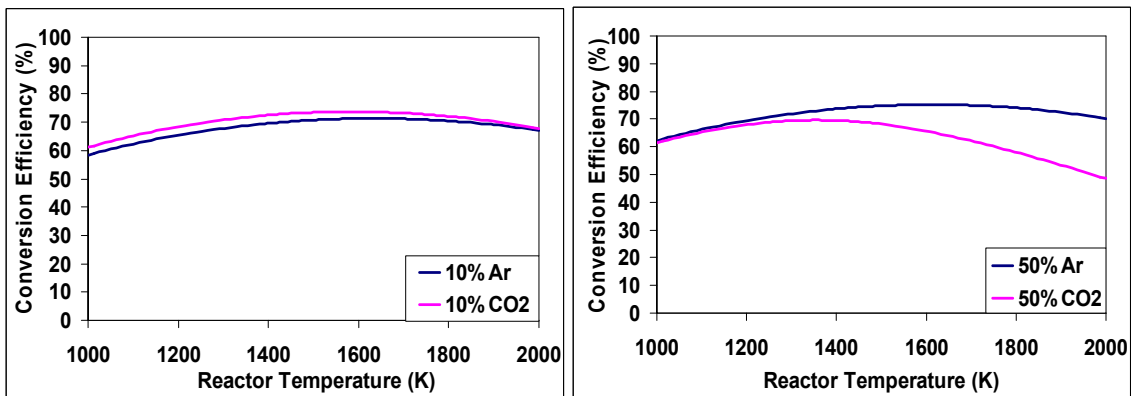
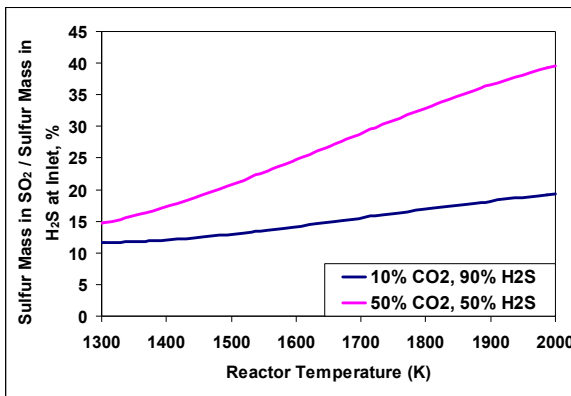


Figure 4. Effect of amounts of carbon dioxide or argon in acid gas on conversion efficiency (a) 10% concentrations (left), and (b) 50% concentrations (right).

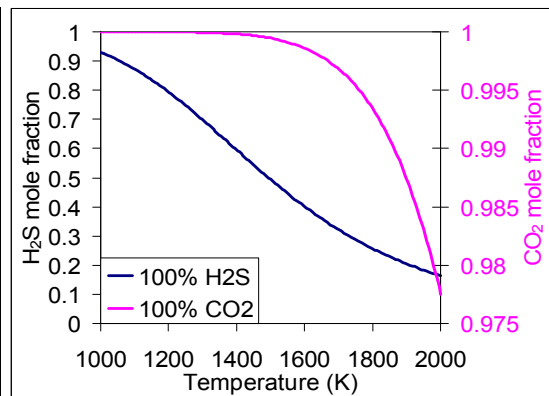
At low concentrations of CO<sub>2</sub> and Ar the conversion efficiencies are similar over a range of temperatures (see Figure 4a on left). However, at high concentrations (right Figure 4b) the behavior of carbon dioxide does not deviate much from that of argon until reactor temperature of about 1400K. Beyond this temperature of 1400 K, a steep decrease in the conversion efficiency is observed, as shown in Figure 4b. At these high temperatures the amount of oxygen radicals produced is considerably high. This oxygen radical is then free to attack hydrogen sulfide to form SH intermediately, which then eventually transforms to SO<sub>2</sub><sup>13</sup>. This will lead to an imbalance in the adjusted ratio of oxygen and SO<sub>2</sub> of the Claus process mentioned previously. Figure 5 shows the ratio of mass of sulfur in SO<sub>2</sub> to the mass of sulfur (constant) versus the reactor temperature at two different concentrations of CO<sub>2</sub>. The effect of increased temperature leads to increased mass of SO<sub>2</sub> in the products gases for both 10% and 50% CO<sub>2</sub> in the inlet gas stream, as shown in Figure 5. The rate of increase is higher at 50% CO<sub>2</sub> as compared to 10% CO<sub>2</sub> due to higher tendency of dissociation at higher temperatures. Note that increase in temperature also leads to increased dissociation, including S<sub>2</sub>, which will impact the conversion efficiency. The effect of CO<sub>2</sub> dissociation is negligible at temperatures up to about 1400K, while that of H<sub>2</sub>S is significant even at 1000K, as shown in Figure 6. This suggests that at higher temperatures the available oxygen radicals will be higher at higher combinations of CO<sub>2</sub> and N<sub>2</sub>.

### 2.2.3 Combined effect of carbon dioxide and nitrogen

By combining the effect of carbon dioxide and nitrogen, the efficiency-temperature plots can be obtained for all runs considered in acid gas analysis, as shown in Figure 7. As described before, the nitrogen behaves as an inert gas, while an increase in CO<sub>2</sub> concentration results in decreasing the recovery efficiency. The results show that the conversion efficiency increases at low reactor temperatures, which is due to the higher tendency of the H<sub>2</sub>S to dissociate in the reactant to form S<sub>2</sub>. Increasing the reactor temperature will affect carbon dioxide, as mentioned previously, to form oxygen radical, which then attacks hydrogen sulfide to form higher amounts of SO<sub>2</sub>. The effect of H<sub>2</sub>S dissociation is dominant at low reactor temperatures since the rate of dissociation of H<sub>2</sub>S is much higher than CO<sub>2</sub>, as shown in Figure 6, while the conversion efficiency keeps increasing till reaching the maximum conversion efficiency point at the optimum operating temperature. If the reactor temperature is increased beyond this reactor temperature, the effect of oxygen radical dissociated from carbon dioxide will dominate the process. At higher values of N<sub>2</sub> and CO<sub>2</sub> the optimum temperature shifts leftward because of the higher tendency for CO<sub>2</sub> to dissociate and form oxygen radicals which would attack H<sub>2</sub>S in order to form SO<sub>2</sub> instead of S<sub>2</sub>.



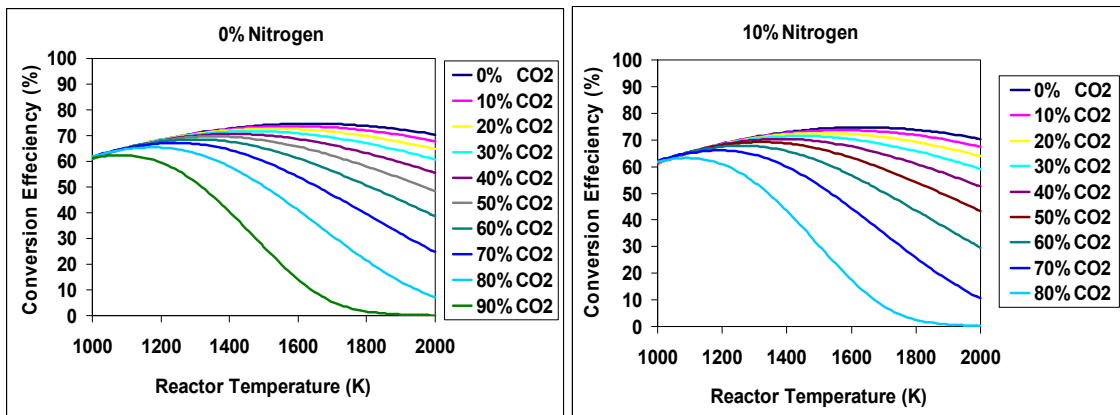
**Figure 5. Effect of carbon dioxide concentration in acid gas on the generated mass of SO<sub>2</sub> at different reactor temperature.**



**Figure 6. Effect of the reactor temperature on the dissociation of H<sub>2</sub>S and CO<sub>2</sub>.**

Figure 8 shows how the value of optimum temperature is affected by concentrations of CO<sub>2</sub> and N<sub>2</sub> in sour gas. This figure directly shows the variation of optimum temperature as a function of CO<sub>2</sub> and N<sub>2</sub> concentrations. The following three key observations can be made from these results:

1. At constant N<sub>2</sub> concentration, if the CO<sub>2</sub> mole fraction is increased, the optimum temperature must decrease. This is attributed to the fact that CO<sub>2</sub> provides an oxidizing environment after dissociation, where most of the sulfur ends up in the form of SO<sub>2</sub> as shown in Figures 5 and 6. Therefore, to prevent sulfur oxidation and to obtain peak recovery efficiency, the reactor temperature must be lowered, in order to decrease CO<sub>2</sub> dissociation and release of excess “O” radicals.
2. At constant CO<sub>2</sub> concentration, if the N<sub>2</sub> mole fraction is increased, the optimum temperature has to be decreased. This is again attributed to the fact that higher N<sub>2</sub> concentrations result in lower partial pressures of all other species (including S<sub>2</sub>), which promotes their tendency to dissociation. Therefore, the optimum reactor temperature has to be decreased to hinder the dissociation and loss of S<sub>2</sub>, in order to maintain peak recovery efficiency.
3. Lines of constant N<sub>2</sub> concentration do not have equal slopes. Higher N<sub>2</sub> mole fractions decrease the partial pressures of all other species and promote their dissociation. This is one reason it is necessary to decrease reactor temperature. CO<sub>2</sub>, among those other species, suffers being at lower partial pressures in the presence of higher N<sub>2</sub> concentrations. This increases the CO<sub>2</sub> tendency to dissociate, thus providing the undesired oxidizing medium, which is a second reason it is necessary to decrease the reactor temperature. Therefore, the combined effect of high CO<sub>2</sub> and N<sub>2</sub> concentrations lies in a sharper decrease in reactor temperature in order to maintain the conditions needed to attain peak sulfur-recovery efficiency.



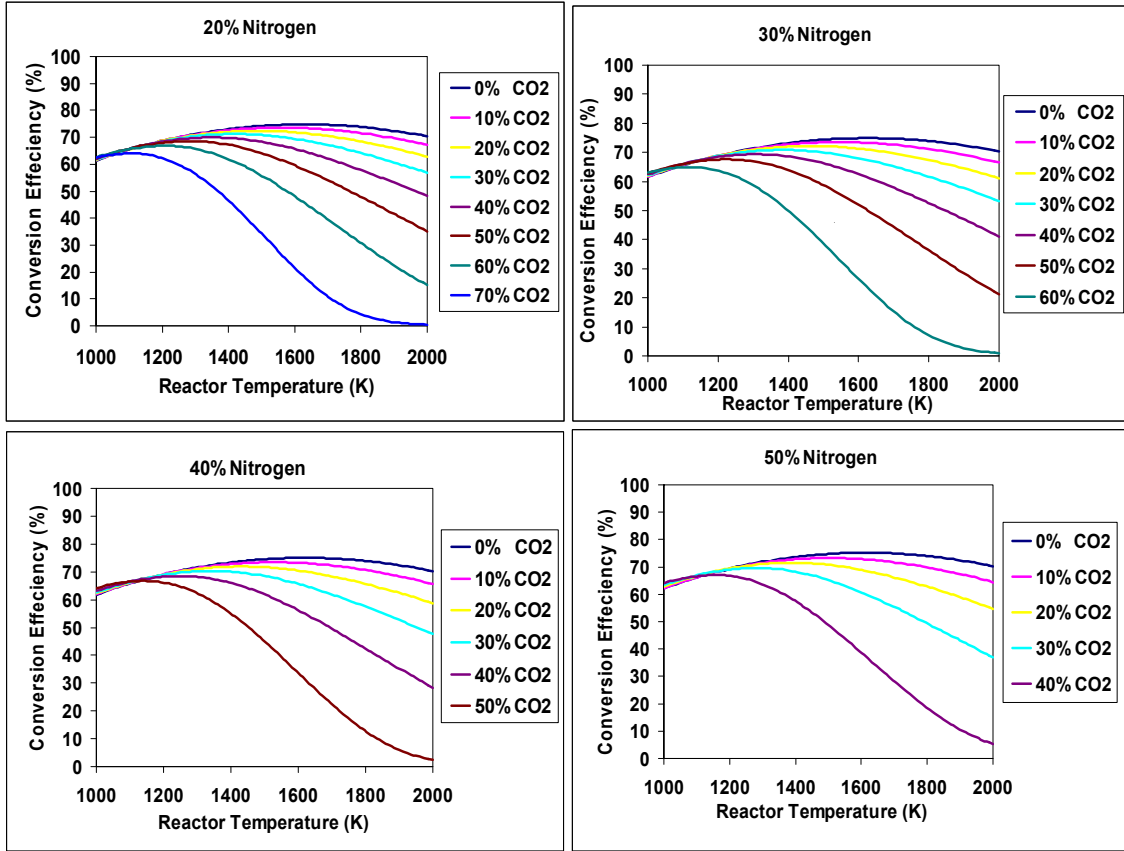


**Figure 7. Effect of carbon dioxide and nitrogen in acid gas on conversion efficiency. The CO<sub>2</sub> is changed from 10% to 90% and nitrogen changed from 10% to 50% in the acid gas with the remainder gas being hydrogen sulfide.**

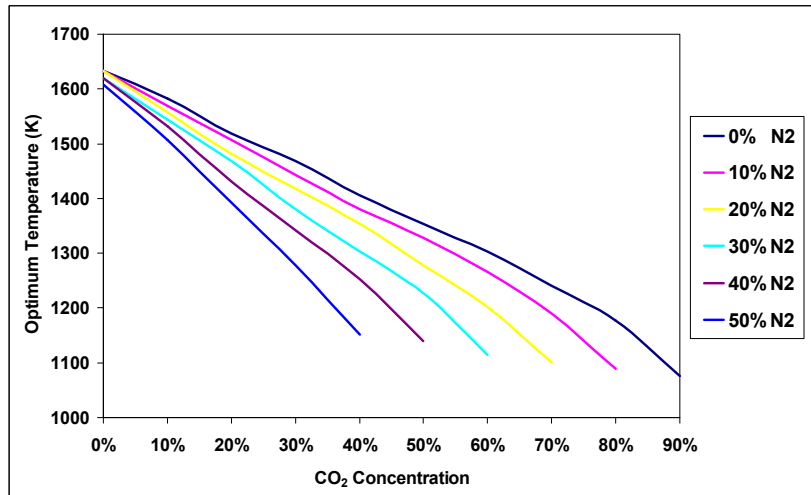


**Figure 8. Effect of CO<sub>2</sub> and N<sub>2</sub> in acid gas on the optimum operating temperature of reactor.**

To conclude the analysis of variation of optimum reactor temperature with acid gas composition, a color map of this temperature is depicted in Figure 9a within the investigated ranges of CO<sub>2</sub> and N<sub>2</sub> mole fractions (0 – 90% and 0 – 50%, respectively). Figure 9a (left figure) shows direct results from the equilibrium calculations, while Figure 9b (right figure) shows results obtained from the correlation equation given by:

$$T[K] = -556 \left( \frac{CO_2}{0.9 - N_2} \right) + 1659.5$$

This equation provides value of optimum temperature directly for a given sour-gas composition. The maximum error associated with this fit equation is calculated to be 4%.

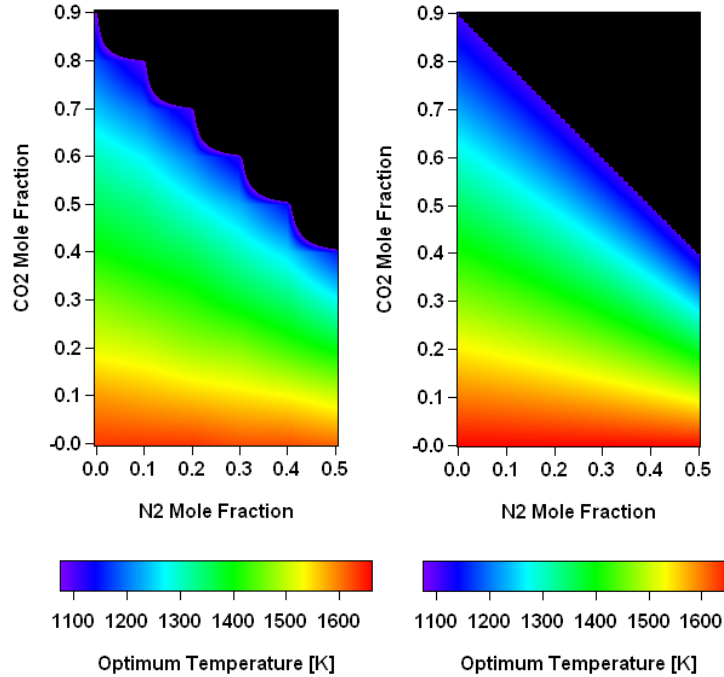


**Figure 9. Mapping of optimum reactor temperature at different sour-gas composition**  
**(a) Numerical results obtained from equilibrium calculations (left);**  
**(b) Results from fit equation given above (right).**

### 2.3 Kinetics study

In this section we discuss the reduction strategy that was used to give a representative reduced mechanism for the hydrogen sulfide oxidation reaction. In our investigations we started with the sensitivity analysis in order to reduce the mechanism by Leeds University<sup>1</sup>. It was very time consuming to remove every single reaction from the whole mechanism and to monitor its sole effect on the detailed mechanism, but it was beneficial that it gives us the sense of the important reaction in the mechanism. In this section we will discuss the technique followed for the hydrogen sulfide oxidation reaction.

#### Temperature range and the main species

In the beginning we determined the temperature range in which to examine our reduced mechanism. Since the Claus process is a prominent application for H<sub>2</sub>S treatment in order to hinder its harmful effect, the temperature range was chosen to achieve the highest conversion efficiency for the Claus process that could be obtained from Figure 1. Figure 1 demonstrates that the maximum conversion efficiency lies between 1600 and 1700 K. During our study for the reduced mechanism we broadened this range in order to maximize the range of applicability of our reduced mechanism. Therefore the range of our study was 1400-1800 K.

On the other hand, it is very important to define the main species in our mechanism. The main species are those we are interested in maintaining their values and their trends almost the same after reducing the mechanism with the minimum possible error. Generally, the main

species would be the reactants and the main products. In our case, we have chosen our main species to be H<sub>2</sub>S, O<sub>2</sub> as the reactants, and SO<sub>2</sub>, H<sub>2</sub>, S<sub>2</sub>, and H<sub>2</sub>O as the main species.

#### Preliminary reduction step

Before starting the implementation of the reduction approach, an insight on the conditions for specific application may reduce the mechanism with a good margin. Since this reduced mechanism will be used for examining the reactions that occur in a Claus process, which requires very rich conditions, nitrogen is not likely to react under these conditions, as it will find severe competition with other active reactants. Although nitrogen is not considered an inert gas within our temperature range, the very rich conditions will relentlessly reduce the likelihood of its reaction, where the oxygen is not sufficient to burn H<sub>2</sub>S. Moreover, it is not favorable to burn H<sub>2</sub>S with air while nitrogen is considered a burden in terms of reducing the overall mixture temperature, which subsequently leads to lower conversion efficiency. On the other hand, we were not interested in studying the combustion of CH<sub>4</sub>/H<sub>2</sub>S mixture. We assume that H<sub>2</sub>S had been separated previously from CH<sub>4</sub> in the amine extraction process. Considering these two facts, any reaction that has nitrogen or carbon will be discarded from the mechanism, as well as any species. In conclusion, applying this preliminarily process in this study reduced the detailed mechanism to 86 elementary reactions, and 25 species.

#### Direct relation graph and error propagation methodology (DRGEP)

The DRGEP is used to form a reduced skeletal mechanism from a detailed and long one. This approach depends on removing the species that do not have significant effect on the trend as well as the asymptotic values of the main species in the reaction mechanism. This is achieved by applying two main steps in the reaction mechanism. The first one is the direct relation graph (DRG), which aims to find a direct relation between the main species and each species in the mechanism. This relation is usually governed by the so called direct interaction coefficient. The second step is the error propagation (EP) which gives a relation between the main species and species that are not directly related to them in the detailed mechanism. These steps are illustrated in detail later.

#### *A- Direct relation graph (DRG)*

The direct relation graph is mainly concerned with finding a relation between the main species and each species that is directly related to them in the whole mechanism. This relation would be based on the reaction rate analysis. It is called direct relation because each relation between two species can be represented by a curve on a graph.

#### Direct interaction coefficient ( $r_{AB}$ )

The direct interaction coefficient is the parameter that is used to find the relation between every main species and any other one. Assuming that we have two species A and B in the detailed mechanism, we need to know the effect of species B on species A, given that they might be directly related in some elementary reactions, so the direct interaction coefficient can be defined as:

$$r_{AB} = \frac{\left| \sum_{i=1, n_R} \nu_{i,A} \omega_i \delta_B^i \right|}{\max(P_A, C_A)} \quad (1)$$

where,

$$P_A = \sum_{i=1, n_R} \max(0, \nu_{i,A} \omega_i) \quad (2)$$

$$C_A = \sum_{i=1, n_R} \max(0, -\nu_{i,A} \omega_i) \quad (3)$$

$$\omega_i = \omega_{f,i} - \omega_{b,i} \quad (4)$$

$$V_{i,A} = V''_{i,A} - V'_{i,A} \quad (5)$$

In these equations  $\omega_i$ ,  $\omega_{f,i}$ , and  $\omega_{b,i}$  are the net, forward, and backward reaction rates respectively, and  $V''_{i,A}$ ,  $V'_{i,A}$  are the stoichiometric coefficients of species A in reaction i, while

$\delta_B^i$  equals 1 if reaction i contains species B, and equals zero elsewhere. From Equations 2 and 3 we can notice the denominator of equation 1 should be positive. This denominator of Equation 1 denotes the total reaction rate of all the elementary reactions that contains species A. On the other hand, the numerator is the reaction rate of only the elementary reactions that contains species A and species B together. If the reaction does not contain species A, then  $V_{i,A}$  will be zero, and if the reaction does not contain species B, then  $\delta_B^i$  will be zero, so the definition of the numerator assures that the elementary reactions that count are those that have A and B together. The physical meaning of  $r_{AB}$  is the error that would appear in species A if species B is discarded from the detailed mechanism, so by defining a reasonable threshold ( $\epsilon$ ) we can discard any species (B) with  $r_{AB}$  less than this threshold.

Figures 10 and 11 show the direct interaction coefficient of  $\text{SO}_2$  and  $\text{H}_2\text{S}$ , respectively, with some minor species along the temperature range of our concern, where j denotes any minor species. The reaction rates have been calculated using CHEMKIN-PRO software assuming the inlet condition are the same as Claus process where hydrogen sulfide reacts with oxygen in a continuously stirred tank reactor (CSTR) under steady state conditions.

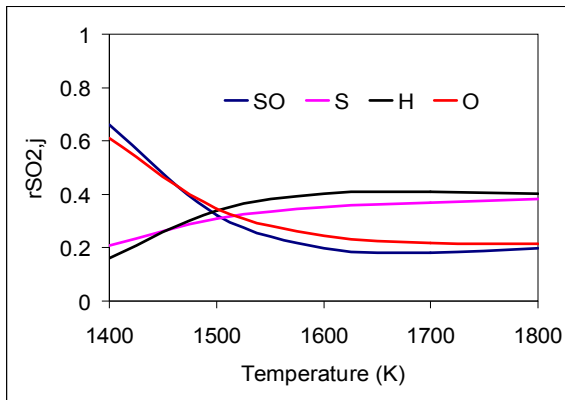


**Figure 10. Direct interaction coefficient of  $\text{SO}_2$  with minor species (SO, S, H, and O) at different reactor temperature.**

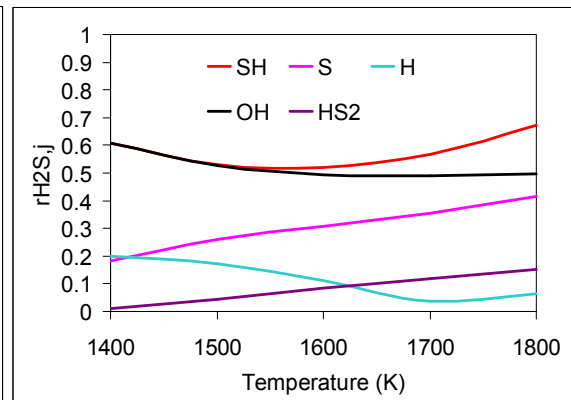


**Figure 11. Direct interaction coefficient of  $\text{H}_2\text{S}$  with minor species (SH, S, H, OH, and  $\text{HS}_2$ ) at different reactor temperature.**

By applying this approach in the detailed mechanism and by defining a threshold of 0.005 we can reduce the detailed mechanism with a great margin. The threshold has been chosen after trying several values and comparing the gain (number of removed species) to the obtained corresponding error. It was found that increasing the threshold value above the aforementioned one will not be that rewarding. We also note that the discarded species do not have direct interaction coefficient value above the threshold for any main species. For instance, the error corresponding to remove HOS from the mechanism will not be more than 0.5% for any main species. After implementing this approach the mechanism has been reduced to 37 elementary reactions with 14 species included. The discarded species are  $\text{SO}_3$ ,  $\text{HOSO}_2$ , HOS, HSOH,  $\text{H}_2\text{SO}$ , HOSHO,  $\text{H}_2\text{S}_2$ ,  $\text{H}_2\text{SO}_4$ ,  $\text{HSO}_2$ , HOSO, and  $\text{HO}_2$ .

#### B- Error propagation (EP)

The second step that was used to reduce the hydrogen sulfide/oxygen reaction is the error propagation technique. Although we already discarded the minor species that do not noticeably affect the main species, it is possible to shrink the number of minor species even further by applying the error propagation approach. The key of this approach is that not all the minor species are directly related to the main species, but some species can be found in the mechanism that react only with minor species. This does not mean that they do not affect the reaction mechanism, or we can remove them blindly without rational reason.

However, we have to study the relation between those species and the main ones, and this could be achieved by the implementation of the error propagation approach. Figure 12 shows the main idea of the error propagation approach. Assuming that A is a main species and is directly related to B and C, by using the DRG approach we can quantify  $r_{AB}$  and  $r_{AC}$ , and eventually we can determine if they are crucial to this mechanism or not. Concerning species D and E, there is no direct relationship between them and A; hence  $r_{AE}$  and  $r_{AD}$  are zero. However, E and D affect species B and C, which conclusively affect the main species A. Therefore, removing species E or D will cause error in species B or C by  $r_{BE}$  or  $r_{CD}$  respectively, which will affect by its role with the main species A. The mathematical relation of the error associated with the removal of species E or D will be as follows:

$$r_{AE} = r_{AB} \times r_{BE}$$

$$r_{AC} = r_{AC} \times r_{CD}$$

It is most likely, but not always true, that removing species that are not directly related to the main species will cause a smaller error than removing directly related species.

This approach in the error propagation technique may not be useful in all cases, where it is not always possible to remove species that do not have contact with main ones without affecting the mechanism with noticeable error, especially for light fuels where the number of species and elementary reactions are not enormous, and also after discarding the majority of redundant species by the DRG technique. However, we might have some unimportant elementary reactions in the mechanism that do not strongly affect the mechanism. Therefore, some tweaking should be made in the error propagation approach to reap its benefits in reducing the mechanism. The following equation can give the corresponding error to the removal of reaction  $i$ :

$$DERE_{A,i} = \sum_{j=1,N} \left( \left( \frac{v_{i,B}\omega_i}{\sum_{i=1,n_R} |v_{i,B}\omega_i|} r_{jB} \right) r_{Aj} \right) + \frac{v_{i,A}\omega_i \lambda_A^i}{\sum_{i=1,n_R} |v_{i,A}\omega_i|}$$

where  $DERE_{A,i}$ , direct elementary reaction error, is the error that appears in main species A after removing elementary reaction  $i$ , while  $j$  is any species in the reaction mechanism (it could be even A or B).  $N$  is the number of species in the mechanism.  $r_{jB}$  is the direct interaction coefficient between species  $j$  and B, or the error appears in species  $j$  because of discarding species B, where B is a species that is included in the removed elementary reaction.  $\lambda_A^i$  is equal to 1 if the main species A is included in the removed elementary reaction  $i$ , and equals to zero elsewhere. The term P denotes the error produced in the minor species B by removing this elementary reaction, by multiplying term P by  $r_{jB}$ , we can calculate the propagated error by removing this equation for every single species in the mechanism.

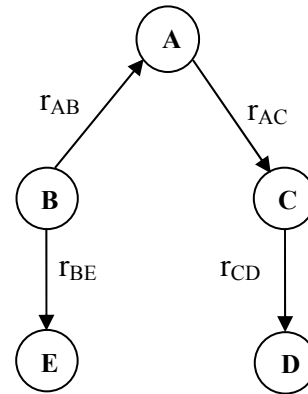


**Figure 12. Five species reaction mechanism, Species A is main species; species B, C, D, and E are minor ones.**

This error in each species will propagate further to affect the main species A by  $r_{Aj}$ . We should consider that if this elementary reaction contains species A itself, a direct error propagation in species is one that can be monitored by the second term with  $\lambda_A^i$  equals to unity.

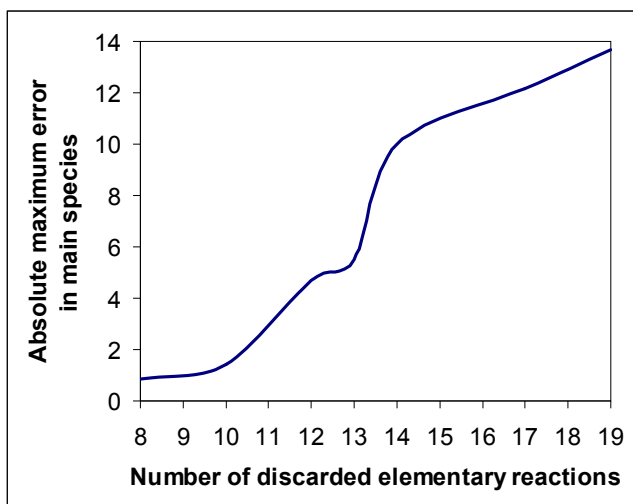


**Figure 13. Relation between the maximum error and the number discarded elementary reactions**

This approach should be used for every species B included in elementary reaction  $i$ . The implementation of this approach would be very effective in our case rather than the error propagation approach for removing some minor species. We can find in the detailed mechanism some reactions are not influential, but they are not identifiable because other active reactions are more prominent. In this case, the first approach will not be able to reduce the mechanism any further. However, the approach introduced here would be able to weight the contribution of each single reaction. By defining an acceptable threshold we will be able to discard the slow reactions. After using the aforesaid approach we were able to reduce the skeletal mechanism to be 24 elementary reactions with 14 species as shown in Appendix A. The threshold was chosen to be 7%, which corresponds to maximum error in the main species of 5.5%, as is the case in  $H_2$ . Figure 13 presents the relation between the number of discarded elementary reactions and the absolute maximum error in the main species. We can notice that the maximum error keeps increasing monotonically up to 12 discarded elementary reactions, then it barely increases until we reach 13 discarded reactions, when it increases abruptly with even only one more discarded reaction. Therefore, the most appropriate number of discarded equations is 13. The almost-constant behavior in the error between 13 and 14 discarded reactions is attributed to the discarded reaction at this point that acts as a trigger point to some species and as an inhibitor to others. In some situations like this one these effects cancel out with each other so that its overall effect on the main species in both directions is equal.

### 2.3.1 Reduced mechanism testing

The results obtained here are presented on the comparison between the 24-elementary reactions reduced mechanism and the detailed mechanism by Leeds University<sup>1</sup> for different reaction conditions. Since we assume that the temperature field and the conditions are Claus process conditions during the reduction steps, we will start the comparison with Claus process reactant condition. The main assumptions and reaction conditions are as follows: Mole fractions of the inlet stream are 0.333 for oxygen and 0.667 hydrogen sulfide. This resulted in an equivalence ratio of 3. The flow speed of 1 cm/s flows into plug flow reactor was maintained at constant temperature that varied for each run from 1400K up to 1800K in 100K step. The reactant pressure is atmospheric. We compared the results obtained from both the detailed mechanism and the reduced mechanism at two temperatures (1400K and 1800K) to make sure it gives reasonable results over this chosen temperature range.

#### First case T=1400K

Figures 14 and 15 show the behavior of the main species in the reaction under Claus conditions. The results have been obtained under conditions of both the detailed Leeds<sup>14</sup> mechanism and reduced mechanism. The focus in these figures is on the first millisecond of the reaction with specific focus on the evolution of main species and decay of the reactants. The trends are similar from a qualitative point of view. From the quantitative point of view the maximum error at this section occurs in O<sub>2</sub> which is fairly insignificant, where it is totally consumed and it has a minimal effect on the reaction downstream. The reason for having maximum error in O<sub>2</sub> instead of H<sub>2</sub> is due to the reduction strategy that caused prominent weakness in the radical pool in the reaction zone.

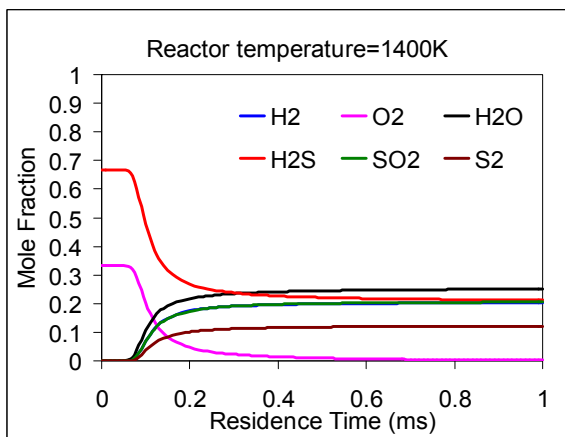


**Figure 14. Behavior of main species obtained from detailed Leeds mechanism<sup>1</sup> within the first 1 ms of the reaction,  $\phi=3$ .**

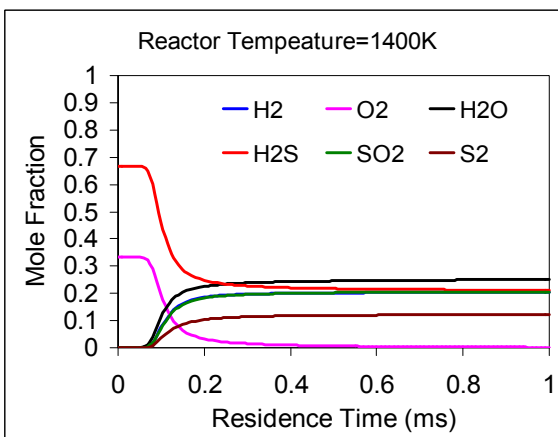


**Figure 15. Behavior of main species obtained from reduced mechanism within the first 1 ms of the reaction,  $\phi=3$ .**

#### Second case T=1800K

Figures 16 and 17 show the behavior of main species during the first millisecond of reactions at the highest temperature of 1800 K examined here. The results show a prominent deviation from the detailed mechanism, except in the hydrogen mole fraction, which is slightly over-predicted. According to the aforementioned in the reduction strategy, hydrogen has the maximum error among the main species. This relative error is -3.5% which is less than the

maximum error observed before. Besides, the reduced mechanism gives representative and acceptable results as compared to the detailed mechanism.

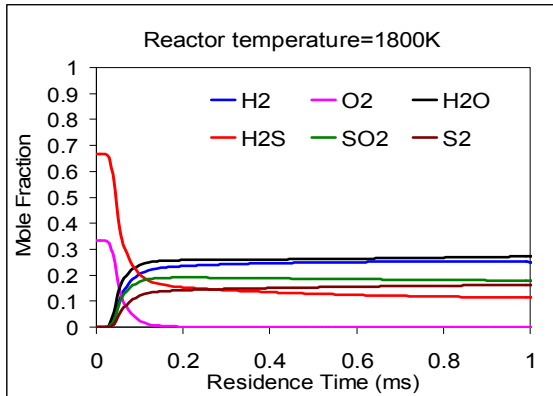


**Figure 16. Behavior of main species obtained from detailed Leeds mechanism<sup>1</sup> within the first 1 ms of reaction,  $\phi=3$ .**

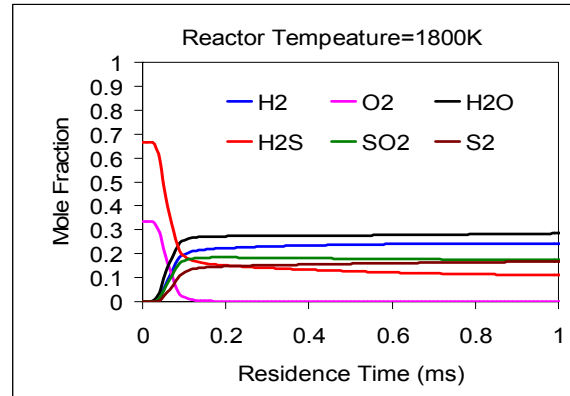


**Figure 17. Behavior of main species obtained from the reduced mechanism within the first 1 ms of reaction,  $\phi=3$ .**

Since we applied the reduced mechanism for Claus conditions which are extremely rich, we will go to the extremely lean conditions to examine the ability of the reduced mechanism to give reasonable results under these conditions. In this case the inlet conditions will be pretty much the same except for the reactants mole fractions; it will be 0.75 O<sub>2</sub> and 0.25 H<sub>2</sub>S, with equivalence ratio of 0.5. Meanwhile, the comparison will be held at the same temperatures.

First case T=1400K

Figures 18 and 19 present the behavior of mains species for lean conditions at an equivalence ratio of 0.5. The results show very good agreement between our reduced mechanism and the detailed mechanism. There are some deviations in O<sub>2</sub> and H<sub>2</sub> mole fractions, but maximum error is acceptable. On the other hand, the behavior of the main species has changed as compared to the rich case. For instance, the S<sub>2</sub> mole fraction became very minimal; the results show that it spikes with a very small value then decays to zero value everywhere. This is because of the tendency for the reactions to proceed in the direction of producing SO<sub>2</sub> rather than S<sub>2</sub>. In other words, the reaction between H<sub>2</sub>S and O<sub>2</sub> is much faster than the reaction between SO<sub>2</sub> and H<sub>2</sub>S. Since the mixture is lean, the reaction proceeds in the direction to produce SO<sub>2</sub>. The advantage of our reduced mechanism is its ability to track the changes associated with any changes in the reaction conditions, and to give reasonable results.

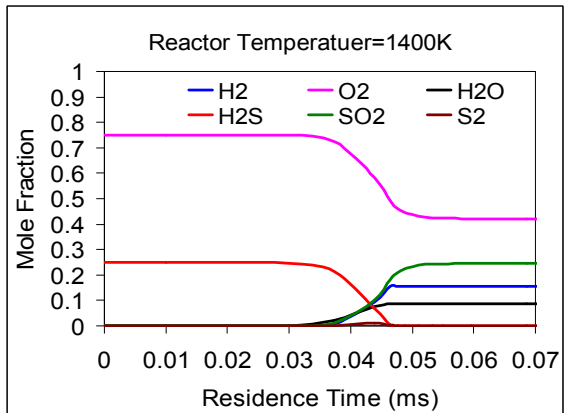
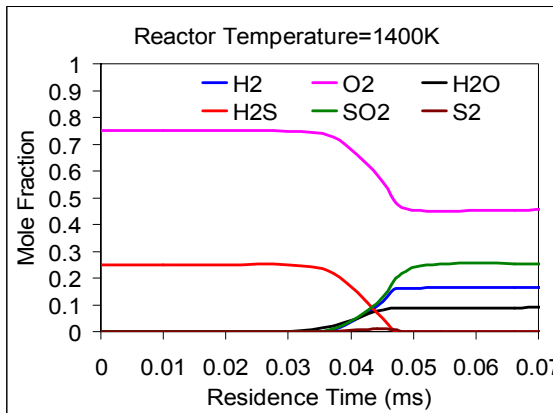


**Figure 18. Behavior of main species obtained from the detailed Leeds mechanism<sup>1</sup> within the first 0.07 ms of the reaction,  $\phi=0.5$ .**

**Figure 19. Behavior of main species obtained from the reduced mechanism within the first 0.07 ms of the reaction,  $\phi=0.5$ .**

**Second case  $T=1800K$**

Figures 20 and 21 show the evolution of the main products in the reaction between  $H_2S$  and oxygen under lean conditions at a reactor temperature of 1800 K. The results obtained from reduced mechanism show good agreement with the detailed mechanism at these conditions. The deviation in the hydrogen and oxygen mole fraction increased and even exceeded the threshold value assigned before to the new value of around 12%. This is because we used the Claus conditions as our reference during the reduction steps. We notice that the reduced mechanism is more coherent with Claus conditions than the lean conditions. On the other hand, the data obtained for the other species, such as,  $SO_2$ ,  $S_2$ , and  $H_2S$  give good agreement with the data obtained from the detailed mechanism. These results showed that our reduced mechanism can give reasonable results with high accuracy for the other species in terms of qualitative trend and asymptotic values for most of the main species.

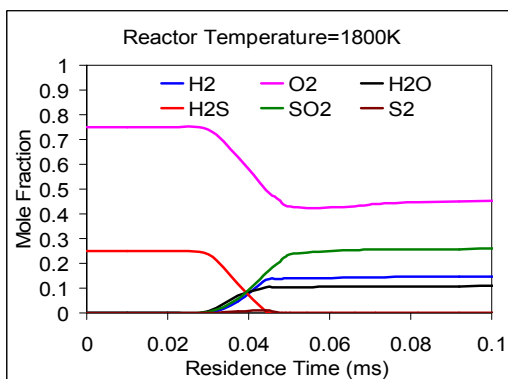


**Figure 20. Behavior of main species obtained from the detailed Leeds mechanism<sup>1</sup> within the first 0.1 ms of reaction,  $\phi=0.5$ .**

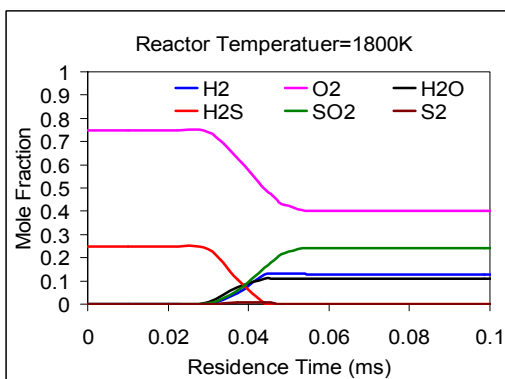


**Figure 21. Behavior of main species obtained from the reduced mechanism within the first 0.1 ms of reaction,  $\phi=0.5$ .**

**2.3.2 Pathways for Skeletal Mechanism**

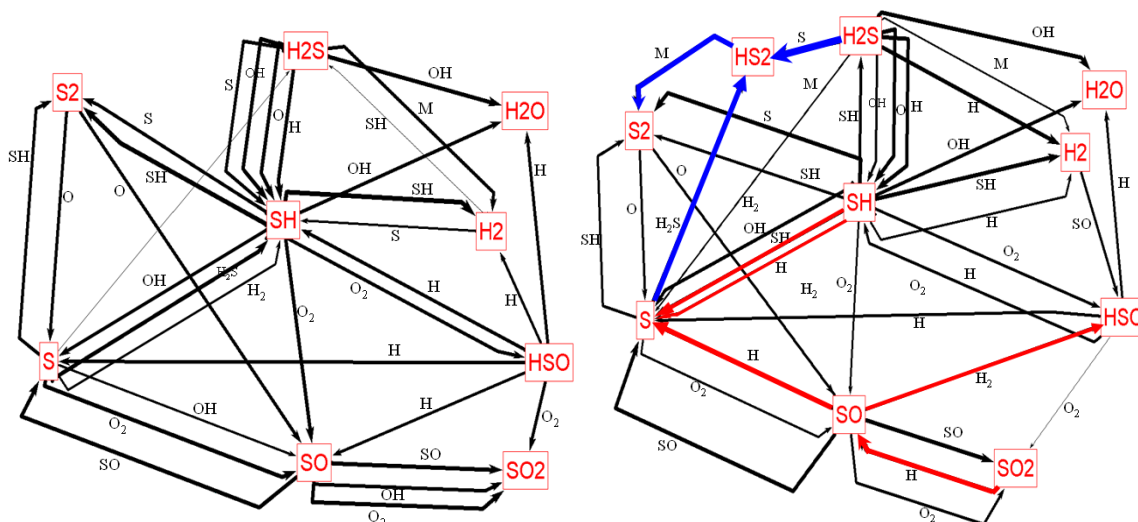


**Figure 22. Skeletal mechanism pathways for Claus conditions at  $T=1600 K$ , at residence time of 0.0832 ms (left); and 0.8 ms (right).**

Figure 22 shows the reduced-mechanism pathways for Claus conditions at different residence time values. The left figure shows the skeletal mechanism pathways at residence time of 0.0832 ms, where the oxygen and hydrogen sulfide mixture still exists. This figure depicts the chemical kinetics during the reaction between  $\text{H}_2\text{S}$  and  $\text{O}_2$  while the resultant reaction goes in the direction of forming  $\text{SO}_2$ , as the fastest reactions contribute in this direction. However, the right figure presents a totally different fact, where at residence time of 0.8 ms there is no oxygen left over. The red arrows denote the reactions that reverse their direction compared to the left figure, while the blue arrows denote new reactions appearing in the pathways. Concerning the red arrows, their directions now contribute mainly in the direction of forming  $\text{S}_2$  rather than  $\text{SO}_2$ . For instance, one of the three reactions that connect SO and  $\text{SO}_2$  reverses its direction to form SO instead of  $\text{SO}_2$ ; also the two reactions that connect SH and S became in the direction of forming S. This means that the only way for S to produce another species is to produce  $\text{S}_2$ . Moreover, considering the weakness occurring in the reactions that depend on  $\text{O}_2$ , which are the main reactions responsible for forming  $\text{SO}_2$ , we can assure that the reaction will go in the direction of forming  $\text{S}_2$ . Meanwhile, a new intermediate species appears at this residence time ( $\text{HS}_2$ ) which creates a direct link between  $\text{H}_2\text{S}$  and  $\text{S}_2$ . These facts explain, from the kinetics point of view, the tendency for the reaction to go in the direction of producing  $\text{S}_2$  in the absence of oxygen.

### 3. Experimental Efforts

In this section we illustrate the progress of our experimental efforts. A full description of the experimental facility as well as diagnostics is given. In addition, some preliminary results are presented which are the non-reactive test for mixedness investigation and the temperature profiles in the secondary reactor at different flow rates.

#### 3.1. Experimental Facility

Our experimental facility at the UMD Combustion Laboratory was designed and fabricated to allow for the investigation of both flame and flameless modes of sulfur recovery. The test rig comprises two reactors, a  $\text{CH}_4/\text{O}_2$  reactor followed by an  $\text{H}_2\text{S}/\text{O}_2$  reactor, as shown schematically in Figure 23. In the flameless mode of operation,  $\text{CH}_4$  and  $\text{O}_2$  are injected into the methane reactor in chemically-correct proportions through a coaxial injector. The combustion of methane and oxygen yields hot products that provide the necessary high-temperature environment for flameless reaction of hydrogen sulfide in  $\text{H}_2\text{S}$  reactor. The amount of oxygen needed to satisfy the Claus-process stoichiometry is accounted for and injected along with oxygen needed for methane combustion.

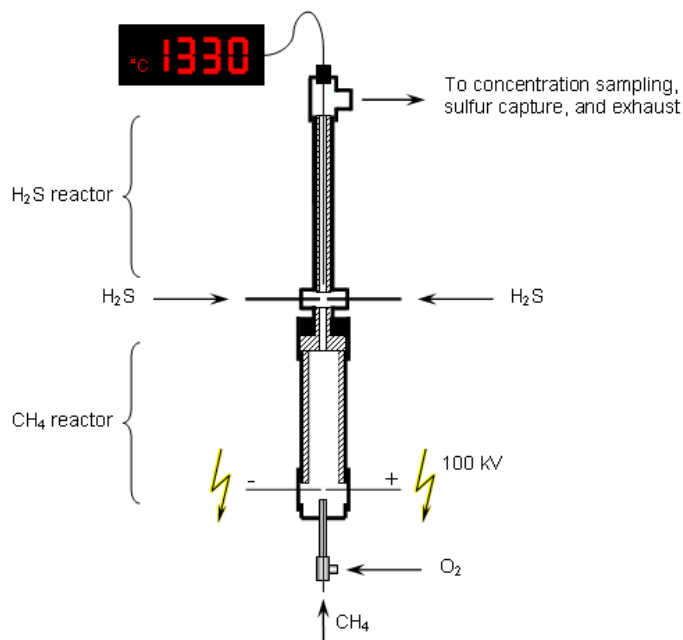


**Figure 23. Schematic of test rig.**

The two reactors of the test rig are connected through a 4-legged cross-connection. While two legs connect the reactors, the other two legs are utilized for H<sub>2</sub>S injection. Following the recommendations of our last report, the injection tubes of H<sub>2</sub>S extend up to few injection-diameters from the test-rig centerline to allow for traverse injection at centerline. Based on the findings of the last report, this injection geometry is expected to have the advantages of good mixing and minimum radical quenching and heat loss, as compared to the previously studied injection geometries.

To minimize heat loss from test rig, the interior of entire rig is coated with zirconia (ZrO<sub>2</sub>) insulation. Zirconia has a very low thermal conductivity of 0.2 W/m.K and withstands temperatures as high as 2500 K. Using considerable zirconia thickness, the 1600-K optimum temperature of sulfur recovery at peak efficiencies was easily achieved at half the maximum flow rates of reactants the facility can safely endure. The 3-inch methane reactor is coated by a ½-inch thick zirconia layer over its entire length of 9 inches, allowing for an enclosed volume of 2 inches diameter. The reactor diameter and insulation thickness have been carefully chosen to simultaneously increase the resistances to convective heat transfer from hot gases to zirconia and from reactor exterior to ambient surroundings. The hydrogen-sulfide reactor, on the other hand, is 12 inches long, has an inner diameter of 1 inch, and comprises a zirconia tube of 1-inch OD and ½-inch ID. The dimensions of H<sub>2</sub>S reactor and its zirconia tube have been chosen to (a) match geometries of previous experimental research from the literature and (b) decrease heat losses to ambient surroundings.

The operation of test rig is controlled through a sophisticated control board; see Figure 24. The flow rates of CH<sub>4</sub>, O<sub>2</sub>, and H<sub>2</sub>S are controlled by means of digital, normally-closed flow meters/controllers. Independent of upstream pressure, the controllers are capable of achieving their set points with an accuracy of 0.15% of full-scale within a 5-second response time. The full-scale flow rates of reactants are 10, 20, and 1 lit/min for CH<sub>4</sub>, O<sub>2</sub>, and H<sub>2</sub>S, respectively. The individual set points are set remotely through digital DC power sources, which provide the necessary electromotive forces across the set-point terminals of the controllers. The sensitivity of each power source is 0.1 V, which divides the 5-V set-point range of each controller into 50 increments. When no set point is provided, the controllers shut off the flows completely to prevent leakage of any non-combusted gas into the test rig.

Ignition of the reactants is attained safely inside the test rig by means of a stun gun. The gun (hidden behind the control board in Figure 24) creates a 100-kV electrical potential, enough to generate a spark across a 1.5-inch air gap. This potential is harnessed and channeled through electrical wiring to two ceramic-coated electrodes inserted into the upstream section of methane reactor, as seen in Figures 23 and 25. The tips of electrodes approach each other at the reactor centerline, leaving a gap of 0.25 inches. The generated spark is approximately 0.5 inches above the exit of CH<sub>4</sub>/O<sub>2</sub> coaxial burner. This choice of spark length and location ensures that a locally ignitable mixture of CH<sub>4</sub> and O<sub>2</sub> is stricken by the spark, so that the reactants ignite shortly after leaving injector without any accumulation of unburned combustible mixture within methane reactor. The initiation of sparking is managed through the ignition switch within facility control board. The switch closes the power-input circuitry of stun gun, which results in spark generation; see Figure 26.

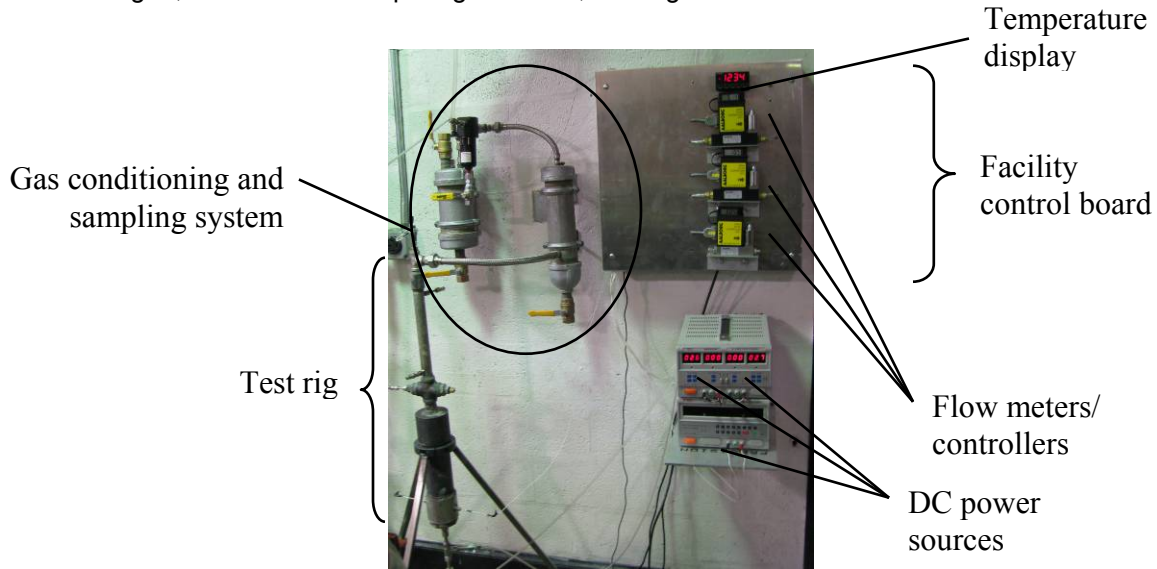


Figure 24. Photo of test rig.

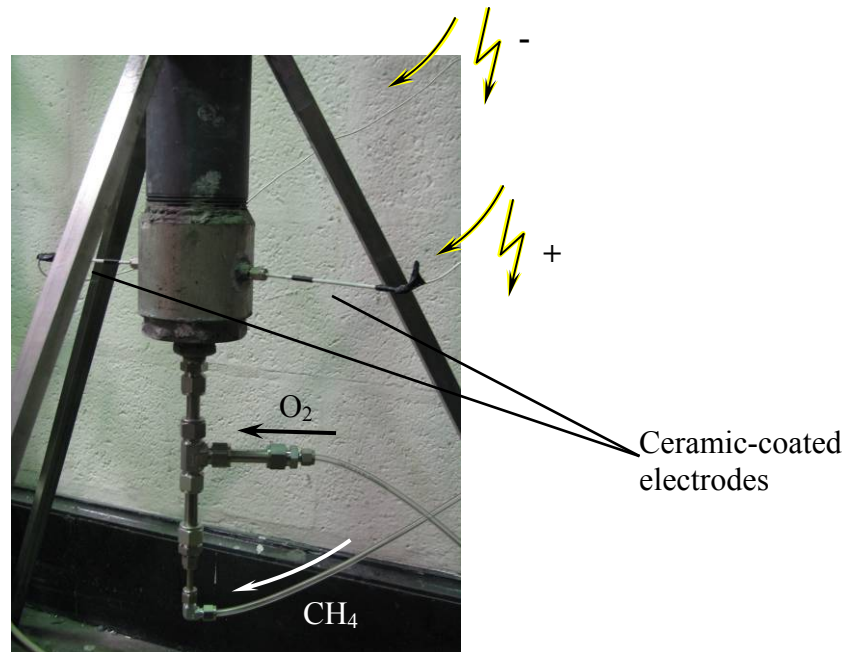
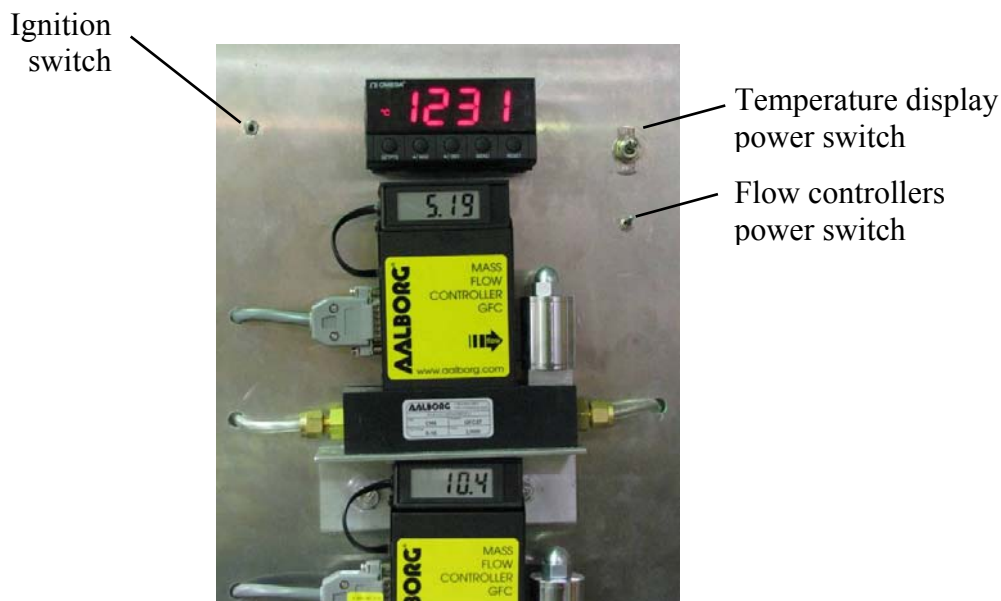


Figure 25. CH<sub>4</sub>/O<sub>2</sub> burner and ignition system.



**Figure 26. Facility control board.**

Temperature measurement can be performed along the centerline of H<sub>2</sub>S reactor by means of an 18-inch-long type-K Omega<sup>®</sup> thermocouple; see Figures 23, 24, and 27. The thermocouple is connected to a temperature display unit that is calibrated to give temperature value directly for K-type thermocouples and to internally simulate zero-junction. The thermocouple wiring is protected inside a 1/8-inch metal tube that is filled with isolative material. The entire thermocouple assembly is movable along the H<sub>2</sub>S-reactor centerline inside a bored-through Swagelok<sup>®</sup> fitting to ensure concentricity while scanning the axial temperature distribution.

At the end of H<sub>2</sub>S reactor the gases leave through a 1/2-inch 18-inch-long flexible connection that connects the test rig to the gas-conditioning and sampling system. This system starts with a 3-inch 12-inch-long tank for capture of recovered sulfur. The dimensions of flexible connection and sulfur-capture tank were chosen to ensure that the gases leaving test rig are cooled down to about 500 K, which is an adequate temperature for sulfur capture, where it is in liquid form and has the lowest viscosity. The sulfur-capture tank is internally equipped with multiple baffles to reduce the velocity of incoming flow and facilitate better capture efficiency of sulfur from gas stream, as sulfur deposits on baffles and tank inner walls. As the gases leave the tank sulfur-free, they are forwarded to another tank filled with an aqueous alkaline solution, where the acid-forming gases, like SO<sub>2</sub>, CO<sub>2</sub>, and any residual H<sub>2</sub>S, get neutralized. The effluent gas, if any, exiting the alkaline-solution tank, contains primarily hydrogen and is discharged into the lab exhaust system. A small portion of the gas stream is sampled between the sulfur-capture and alkaline-solution tanks for analysis in an Agilent<sup>®</sup> gas chromatograph. A water trap at the beginning of sample line captures most of the sample moisture, before the sample passes through an ice-cooled condenser that removes the remaining moisture. The dry sample is then fed to the gas chromatograph for analysis.



**Figure 27. Gas conditioning and sampling system.**

### 3.2 Injection Schemes of H<sub>2</sub>S

According to our previous numerical findings, maintaining a uniform reactor temperature is of critical importance for attaining peak sulfur-recovery efficiency. The uniform HiTAC environment results in flameless reaction of H<sub>2</sub>S with hot incoming O<sub>2</sub> to recover sulfur at greater efficiencies. Since the injected H<sub>2</sub>S is of lower temperature compared to O<sub>2</sub> stream, a considerable temperature gradient exists in the vicinity of injection point. Thermal and mass diffusion take place downstream of injection to homogenize the temperature distribution. Therefore, the goal is to promote mixing of H<sub>2</sub>S with incoming stream, in order to minimize the volume of non-uniform temperature downstream of injection.

Two injection schemes of H<sub>2</sub>S were investigated experimentally as well as numerically, and the results of both schemes are compared to each other in this report based on the achieved degree of mixedness. The first scheme utilizes coaxial injection, as shown in Figure 28, whereas the second scheme implements traverse injection, as depicted in Figure 29.

For both injection schemes the investigated geometry comprises a cross-connection with a characteristic leg inner diameter of 0.56" (14.2 mm). This cross-connection provides a means for H<sub>2</sub>S injection and joins a methane preliminary reactor (where methane is burned with excess oxygen to provide the necessary HiTAC environment) with the H<sub>2</sub>S reactor. Both reactors are vertical; thus the hot gases from methane reactor enter the cross-connection from below, mix, and react with injected H<sub>2</sub>S in the H<sub>2</sub>S reactor connected to the top leg of the cross-connection. This reactor is a pipe of 0.56" (14.2 mm) inner diameter and 12" (305 mm). The injection tube has outer and inner diameters of 0.25" (6.4 mm) and 0.125" (3.2 mm), respectively. Figures 28 and 29 depict the internal volume (occupied by gases) of the cross-connection, H<sub>2</sub>S reactor, and injection tube.

Due to the non-axisymmetric nature of the investigated geometries, the problem has been tackled numerically in a three-dimensional fashion, as seen in Figures 28 and 29. A total of 331167 and 215085 cells were used for the coaxial- and traverse-injection geometries, respectively. Tetrahedral meshing was utilized for most parts of the meshed volumes to account for irregularities. The standard K-ε viscous model was implemented with standard wall functions. Local values of all thermodynamic properties were computed based on incompressible ideal-gas mixing laws. Second-order upwind discretization was used for higher accuracy. The initial conditions were set equal to those of steady-state main-stream

flow in absence of injection, which allowed for faster convergence. Criteria of convergence were based on  $10^{-5}$  residuals.

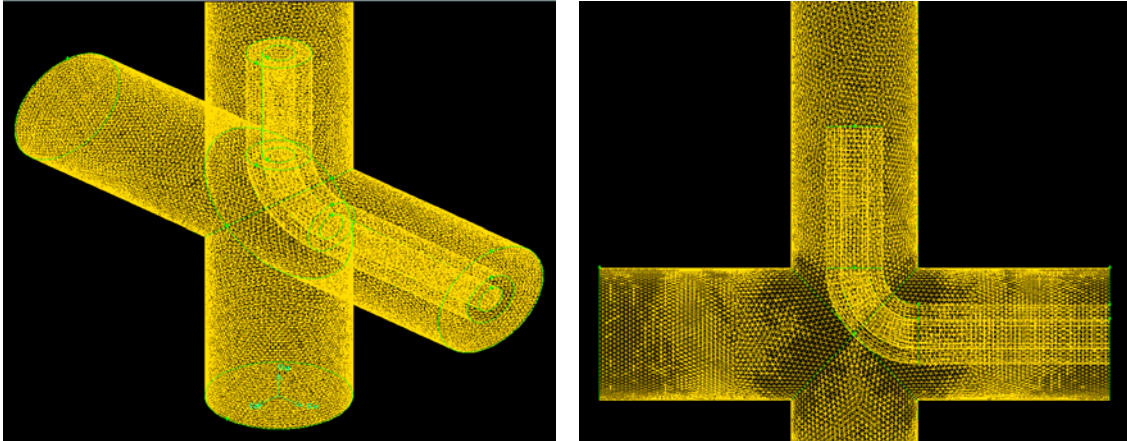


**Figure 28. Coaxial injection of  $H_2S$ .**

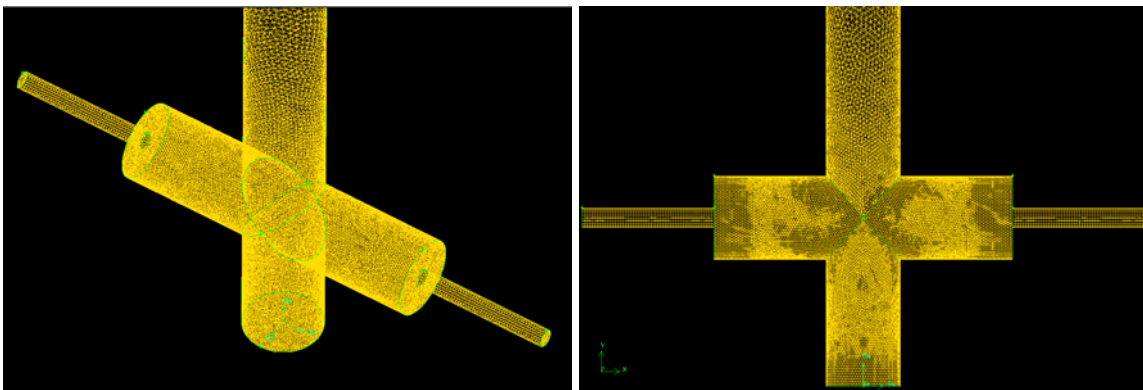


**Figure 29. Traverse injection of  $H_2S$ .**

Since thermal and mass diffusion, flow turbulence, and kinetics of chemical reactions all affect the flowfield downstream of injection point, the analysis of this report focuses just on mixing under isothermal (300 K) non-reacting conditions.  $H_2S$  has been simulated both experimentally and numerically by inert benign  $CO_2$ , as both gases have close molecular weights. A laminar Reynolds-number of 880 was maintained for the main stream in both geometries. Based on correct Claus-process  $H_2S/O_2$  stoichiometry, the momentum ratio (main stream to injected  $CO_2$ ) was 12 for coaxial injection, whereas the dynamic-pressure ratio was 13 for traverse injection. It is to be noted that the momentum ratio is the key parameter for judging mixedness in coaxial-injection geometries, while dynamic-pressure ratio is key parameter in traverse-injection ones.

Figure 30 shows the distribution of  $CO_2$  mole fraction within a centerline plane inside  $H_2S$  reactor of coaxial-injection geometry. This plane coincides with the single plane of symmetry of entire geometry. The distribution was found to be almost axisymmetric, so that this center-plane could represent all others. Also shown in Figure 30 are ten axial locations ( $z/D_{jet}$ ) where radial experimental measurements of  $CO_2$  mole fraction were conducted within the highlighted centerline plane.  $D_{jet}$  is the diameter of injected  $CO_2$  jet, which is equal to inner diameter of injection tube (3.2 mm). It can be noticed that it takes up to 25 jet diameters downstream of injection point for complete mixing to take place. This statement is concurred by Figure 31, where the radial distribution of  $CO_2$  mole fraction is plotted at these specific ten axial locations. Figure 31 also shows that the flow is almost symmetric with peak  $CO_2$  concentrations along the centerline.

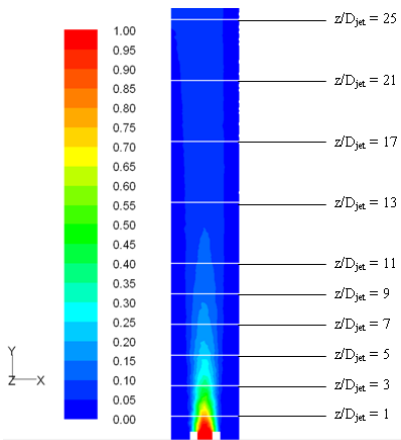


**Figure 30. Distribution of CO<sub>2</sub> mole fraction within centerline plane of symmetry of coaxial-injection geometry. Axial locations of experimental measurements are indicated.**

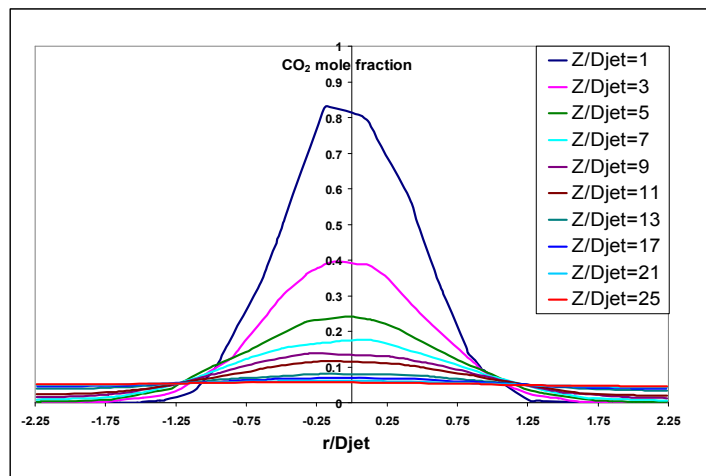


**Figure 31. Radial distribution of CO<sub>2</sub> mole fraction at ten axial locations of Figure 30.**

To validate the numerical findings of Figures 30 and 31, experimental data of CO<sub>2</sub> mole fraction are compared to the corresponding numerical results at each axial location in Figures 32a – j. Good agreement is observed.

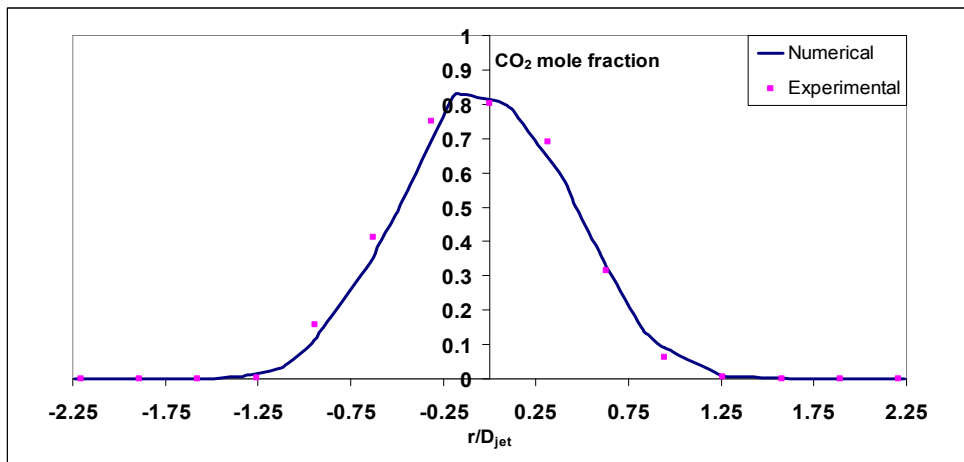


**Figure 32a. Radial distribution of CO<sub>2</sub> mole fraction at  $z/D_{jet} = 1$ .**

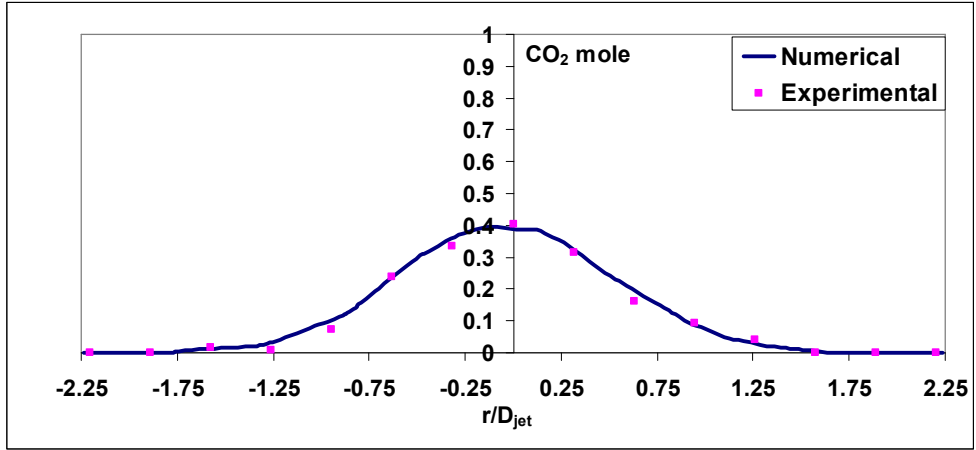


Figure 32b. Radial distribution of CO<sub>2</sub> mole fraction at  $z/D_{jet} = 3$ .

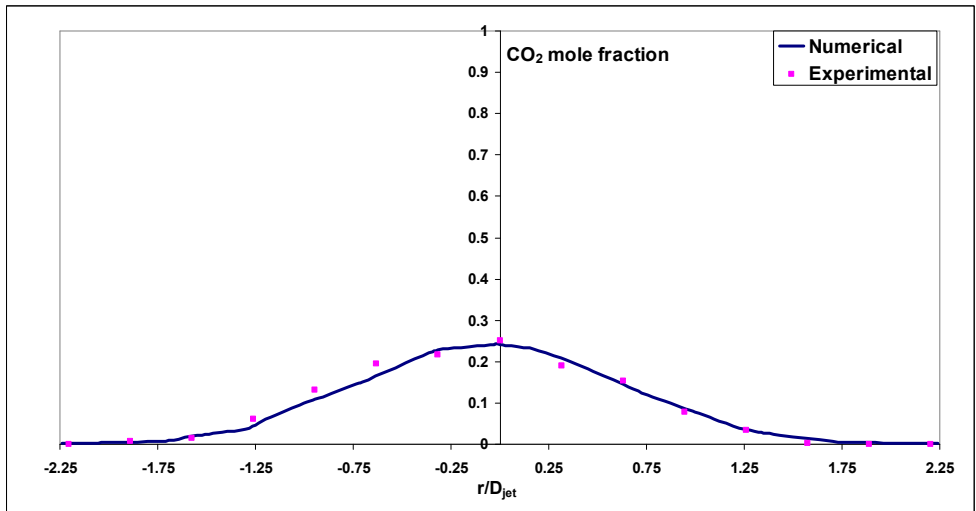


Figure 32c. Radial distribution of CO<sub>2</sub> mole fraction at  $z/D_{jet} = 5$ .

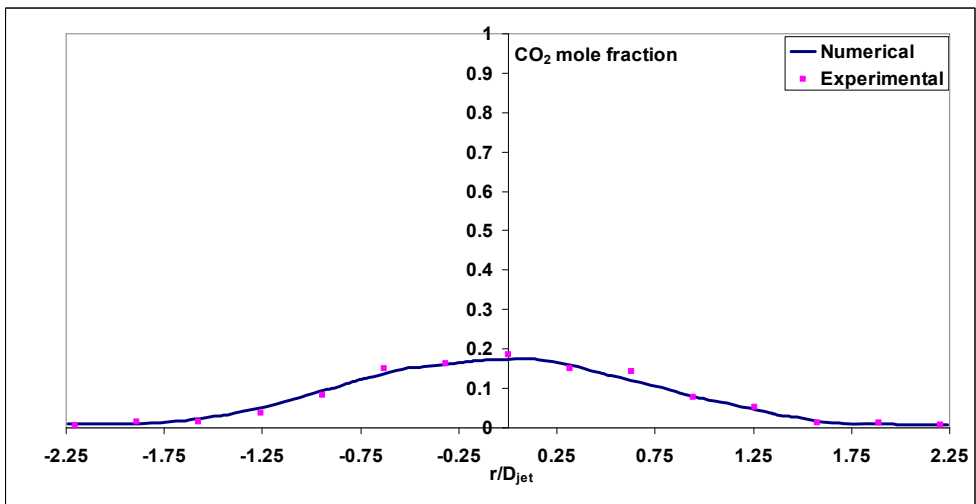


Figure 32d. Radial distribution of CO<sub>2</sub> mole fraction at  $z/D_{jet} = 7$ .

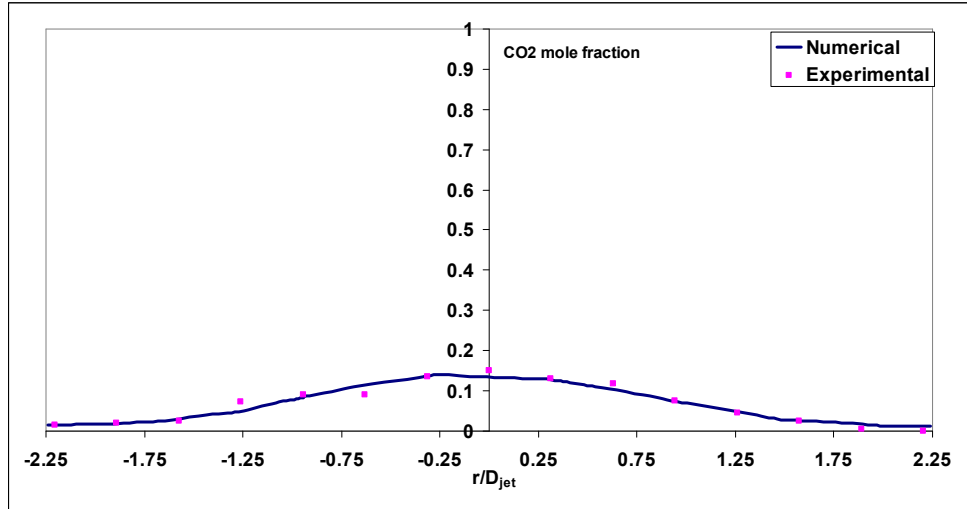


Figure 32e. Radial distribution of CO<sub>2</sub> mole fraction at  $z/D_{jet} = 9$ .

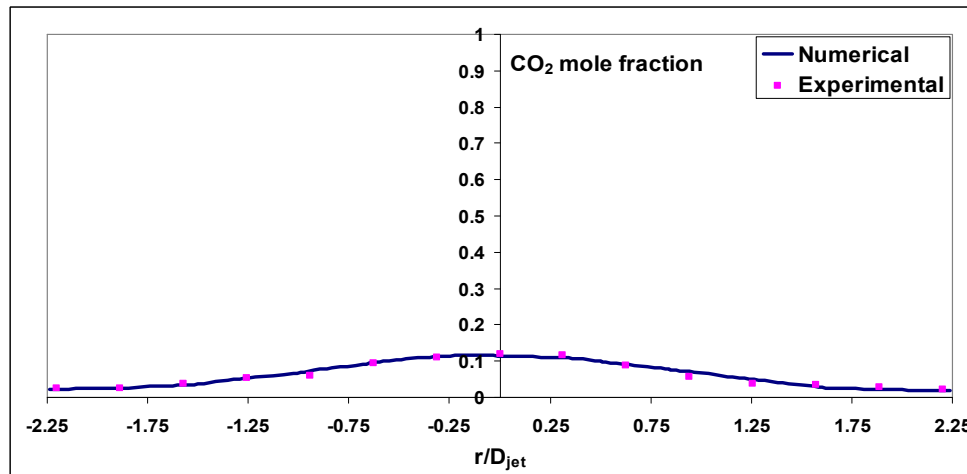


Figure 32f. Radial distribution of CO<sub>2</sub> mole fraction at  $z/D_{jet} = 11$ .

The mixing under traverse-injection conditions is shown in Figure 33 below. Shown again is the numerical CO<sub>2</sub> mole fraction distribution. The contours on the left are within the centerplane of symmetry of the investigated geometry, whereas those to the right are along the test rig walls. Also shown are seven axial locations where experimental measurements were done to validate the numerical findings. It is to be noted that the injected tubes are flush mounted to the side faces of the left and right legs of the cross-connection, i.e., they do not extend to the interior of the cross-connection close to the centerline of H<sub>2</sub>S reactor.

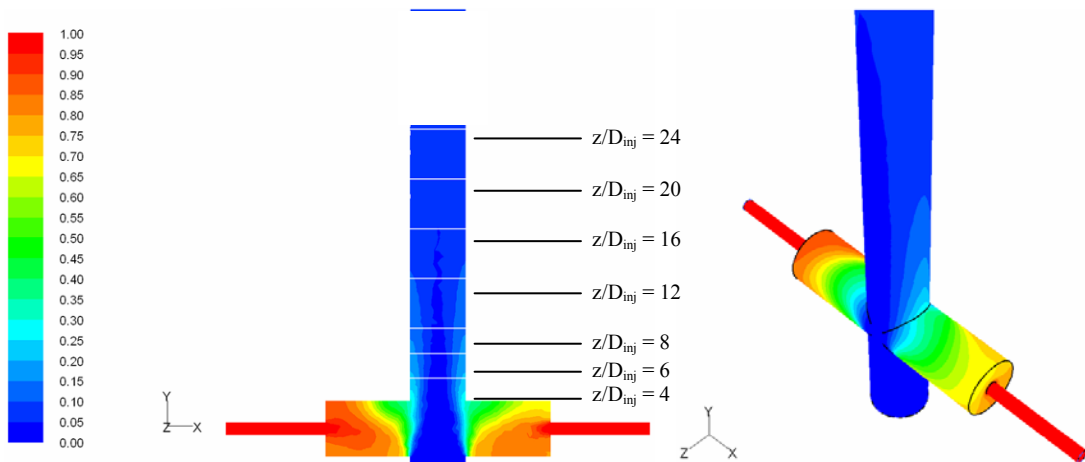
Figure 33 shows that volume within the side legs of cross-connection is dominated by high CO<sub>2</sub> concentrations, as expected. A CO<sub>2</sub>/O<sub>2</sub> shear layer exists at the planes where the side legs meet the central vertical stem of the cross-connection. Within the top leg and H<sub>2</sub>S reactor this shear layer is confined to a thick boundary layer vertically above the side legs, as observed from Figure 33. Higher CO<sub>2</sub> concentrations are always confined to the boundary layer in a non-axisymmetric fashion, whereas centerline concentrations are minimal.

These findings are strengthened by Figures 34 and 35. Figure 34 shows the numerical radial distribution of CO<sub>2</sub> mole fraction spanning the cross-connection between the left and right side faces at two axial locations,  $z/D_{inj} = 0$  (aligned with centerline of injection tubes) and  $z/D_{inj} = 2$ . It can be clearly observed that the side legs of cross-connection are rich with CO<sub>2</sub>

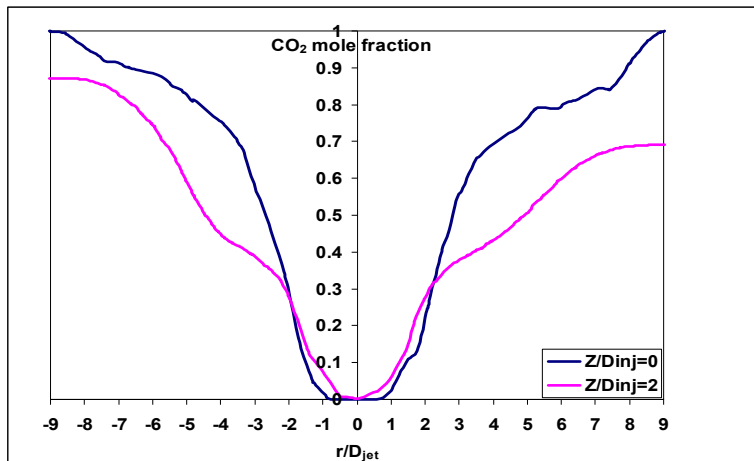
(radial regime between  $r/D_{inj} = 2.25$  and 9). The shear layer at  $r/D_{inj} = 2.25$  is clearly identifiable by the steep gradient in  $CO_2$  concentration.

Figure 35 shows the numerical radial distribution of  $CO_2$  mole fraction within the cross-connection top leg and  $H_2S$  reactor. Seven axial locations are depicted, which are also indicated on Figure 33. It can be observed that an axial distance of about 24 injection diameters is needed for achieving almost complete mixing; similar to what was observed for coaxial injection.

All numerical findings of Figures 33 and 35 were validated experimentally by measuring radial distribution of  $CO_2$  mole fractions at axial locations highlighted in Figure 33. The experimental data are compared to the corresponding numerical findings in Figures 36a – g. Good agreement is again observed.



**Figure 33.  $CO_2$  mole fraction distribution within centerplane of symmetry (left) and along the walls (right) of traverse-injection geometry.**



**Figure 34. Radial distribution of  $CO_2$  mole fraction at axial locations  $z/D_{jet} = 0$  and 2.**

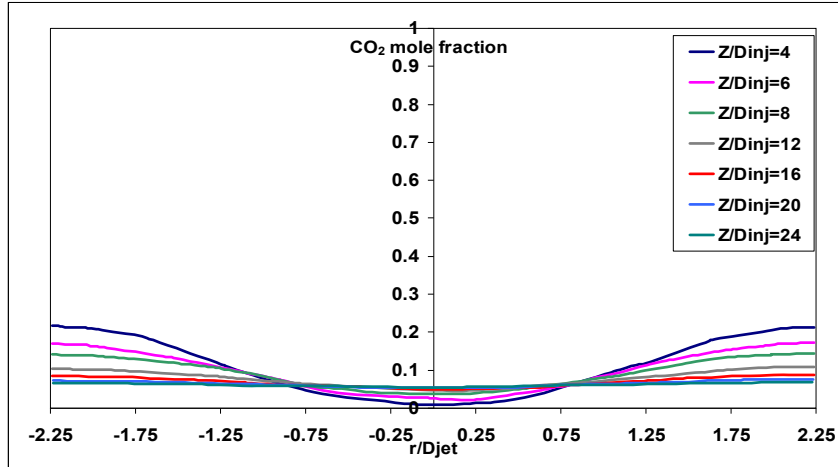


Figure 35. Radial distribution of CO<sub>2</sub> mole fraction at seven axial locations of Figure 33.

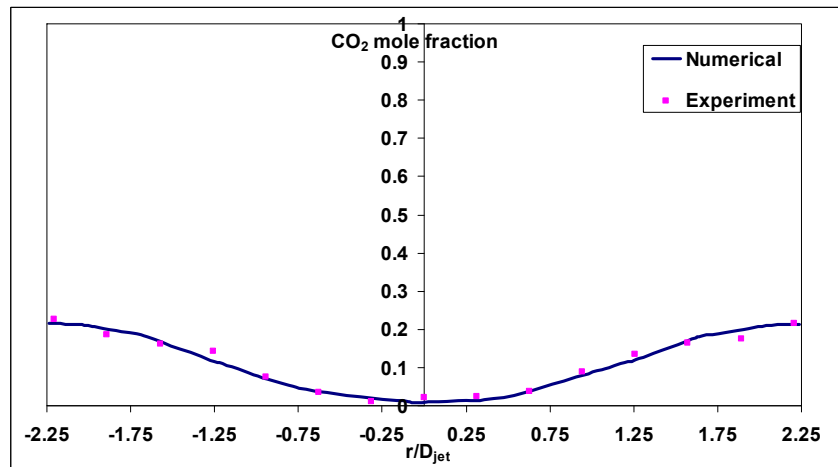


Figure 36a. Radial distribution of CO<sub>2</sub> mole fraction at  $z/D_{jet} = 4$ .

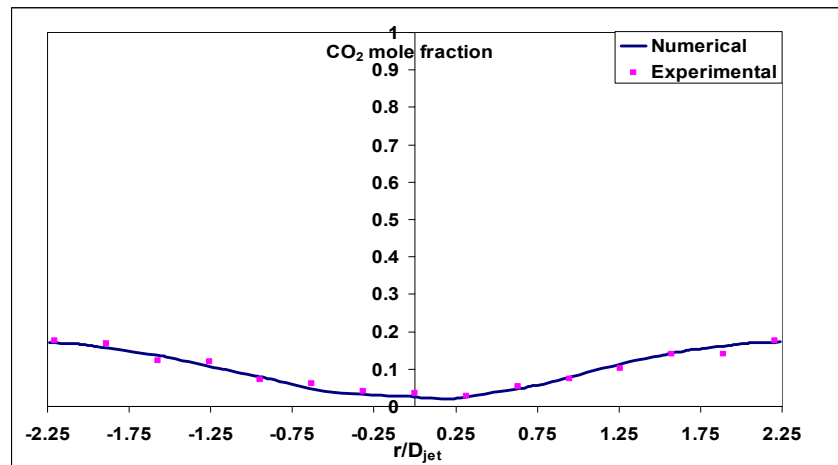


Figure 36b. Radial distribution of CO<sub>2</sub> mole fraction at  $z/D_{jet} = 6$ .

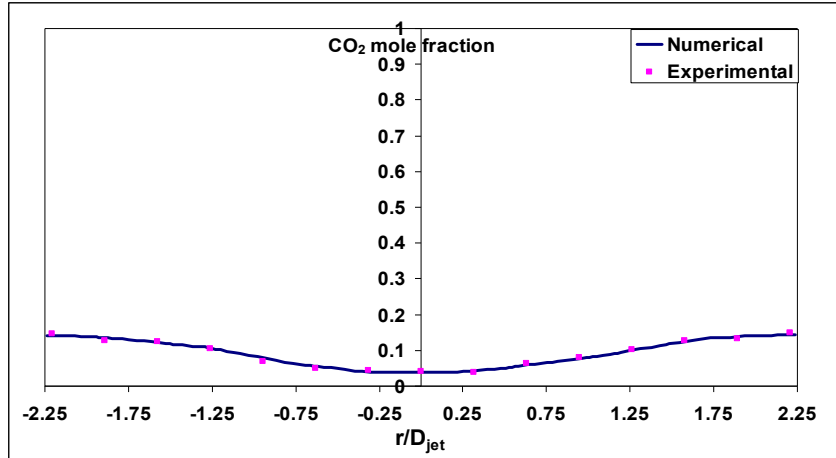


Figure 36c. Radial distribution of CO<sub>2</sub> mole fraction at  $z/D_{jet} = 8$ .

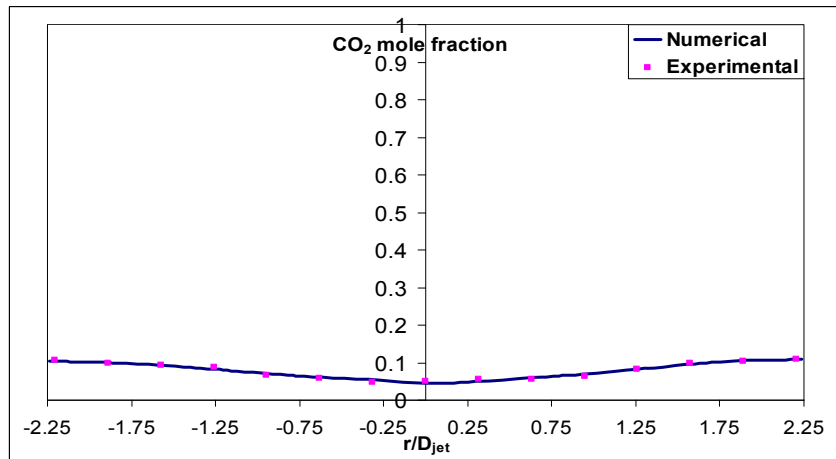


Figure 36d. Radial distribution of CO<sub>2</sub> mole fraction at  $z/D_{jet} = 12$ .

To conclude the analysis of injection schemes, neither configurations investigated here yielded the desired degree of mixedness, since a considerably long distance was needed downstream of injection point to achieve near-complete mixing. In terms of H<sub>2</sub>S reactor length this distance is about 25%, which is high enough, in order not to consider the reactor an acceptable uniform-temperature environment for high-efficiency sulfur recovery.

On a more specific basis, each configuration shows a certain advantage over the other. Coaxial injection is superior in the sense that the injected H<sub>2</sub>S is confined to the vicinity of reactor centerline with lower concentrations near the walls. This prevents wall quenching of critically important intermediate species of H<sub>2</sub>S/O<sub>2</sub> reaction mechanism, since O<sub>2</sub> stream wraps the injected H<sub>2</sub>S jet, and reactions take place mostly away from the wall. Traverse injection, on the other hand, results in high H<sub>2</sub>S concentrations confined to the creeping boundary layer adjacent to reactor walls, where radical wall quenching is expected to take place at a much larger magnitude.

Traverse injection is, however, superior in the sense that the 90°-elbow in injection tube (characteristic of coaxial injection) is missing. This allows for earlier injection of H<sub>2</sub>S (i.e., at heart of cross-connection), which effectively increases the H<sub>2</sub>S reactor length by that of the cross-connection top leg. Therefore, the ratio of mixing length to reactor length decreases, resulting in better uniformity of temperature on a global scale.

In order to benefit from advantages of both injection configurations, our near-term plans involve investigating a modified traverse-injection geometry, in which the two injection tubes extend inside the cross-connection, until they approach each other close to the H<sub>2</sub>S reactor centerline. This modified geometry allows for earlier injection of H<sub>2</sub>S and promotes injection close to the centerline away from the walls. It is to be noted that a new parameter should be taken into consideration, namely the radial location of injection tube tip. This location is expected to vary based on operating and flow conditions and will be investigated thoroughly under both non-reacting and reacting conditions. From a mixing non-reacting point-of-view, injection closer to the centerline is expected to be more favorable (up to a certain limit), as to avoid radical quenching at reactor walls. However, under actual reacting conditions, deeper insertion of injection tubes is not favorable, because (a) the tubes will be subject to harsh thermal stresses at the elevated temperatures, and (b) the tubes themselves will promote radical quenching, since their temperature is lower than flow temperature, due to the colder H<sub>2</sub>S flow they deliver.

We mentioned previously that the temperature of the Claus reactor is a very crucial factor in enhancing the sulfur recovery from hydrogen sulfide. Therefore, we have done a preliminary temperature scan for the experimental facility at different oxygen/ hydrogen sulfide flow rates with the same equivalence ratio of 3, the runs were mainly concern with the temperature homogeneity.

Figure 37 shows the technique used to measure the radial temperature distribution. The axial locations that we have measured were the same as those given in our previous report for axial temperatures. The thermocouples were moved radially using a traverse mechanism in steps of 0.05 inch. Every reading was taken after making sure that the temperature was settled and the variations did not exceed 0.5 K.

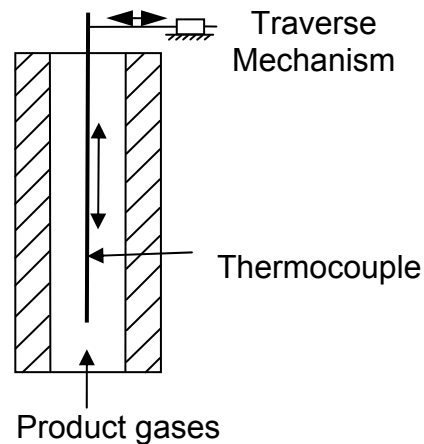


**Figure 37. A schematic diagram for temperature measurement setup.**

Figure 38 shows the radial temperature distribution at different axial locations.

Increasing the fuel and air flow rates will increase the temperature variation in the facility but this was still within the acceptable range. In order to highlight the temperature variation we have calculated the standard deviation ( $\sigma$ ) for each case to determine how much the temperatures deviate from the reactor average temperature. We found the following:

Case (1):  $V_{\text{CH}_4}$  = 2.05 lit/min,  $V_{\text{O}_2}$  = 4.1 lit/min, and  $\sigma$  = 6.85 K

Case (2):  $V_{\text{CH}_4}$  = 3.2 lit/min,  $V_{\text{O}_2}$  = 6.5 lit/min, and  $\sigma$  = 6.87 K

Case (3):  $V_{\text{CH}_4}$  = 3.8 lit/min,  $V_{\text{O}_2}$  = 7.6lit/min, and  $\sigma$  = 8.65 K

Case (4):  $V_{\text{CH}_4}$  = 4.6 lit/min,  $V_{\text{O}_2}$  = 9.2 lit/min, and  $\sigma$  = 15.1 K

One can see that the worst-case scenario is with the highest fuel and air flow rates which results in highest temperatures. However, the standard deviation was still found to be 15.1 K which is better than using normal combustion conditions.

Figure 39 presents the temperature contours in the hydrogen sulfide reactor for the different cases. One can notice that the potential core for the temperature gets shorter with increase in oxygen and fuel flow rates. This could be attributed to the higher heat convection that takes place at the higher flow rates due to the increased the velocity.

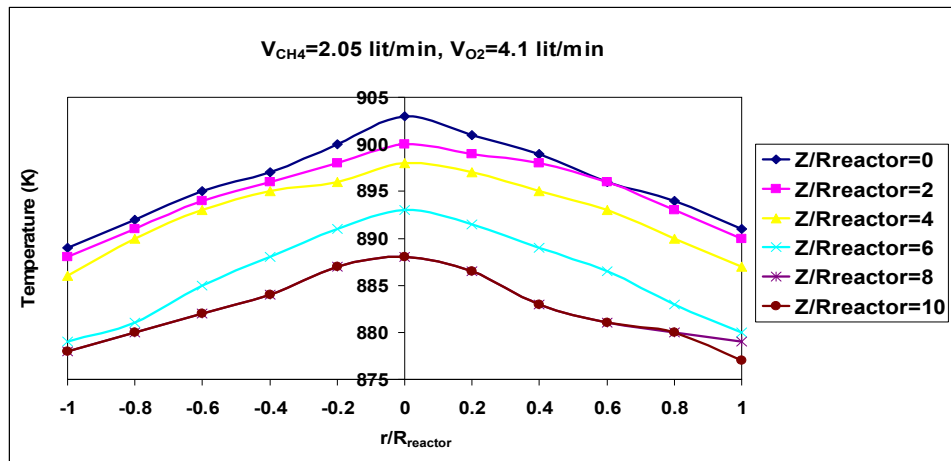


Figure 38a. Radial temperature profiles at different axial locations with  $V_{CH_4}= 2.05 \text{ lit/min}$  and  $V_{O_2}= 4.1 \text{ lit/min}$ .

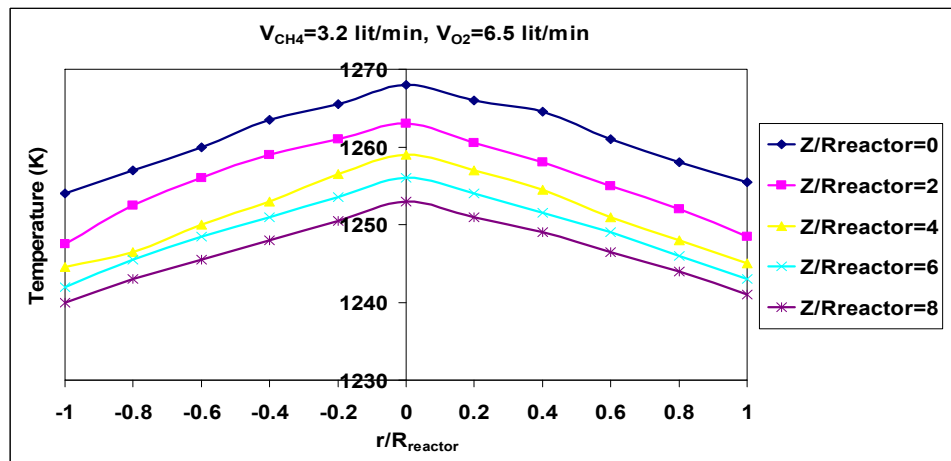


Figure 38b. Radial temperature profiles at different axial locations with  $V_{CH_4}= 3.2 \text{ lit/min}$  and  $V_{O_2}= 6.5 \text{ lit/min}$ .

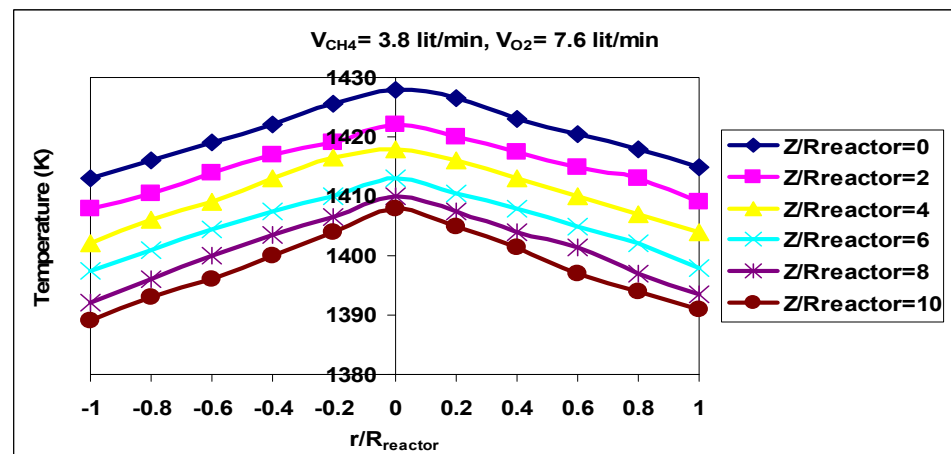


Figure 38c. Radial temperature profiles at different axial locations with  $V_{CH_4}= 3.8 \text{ lit/min}$  and  $V_{O_2}= 7.6 \text{ lit/min}$ .

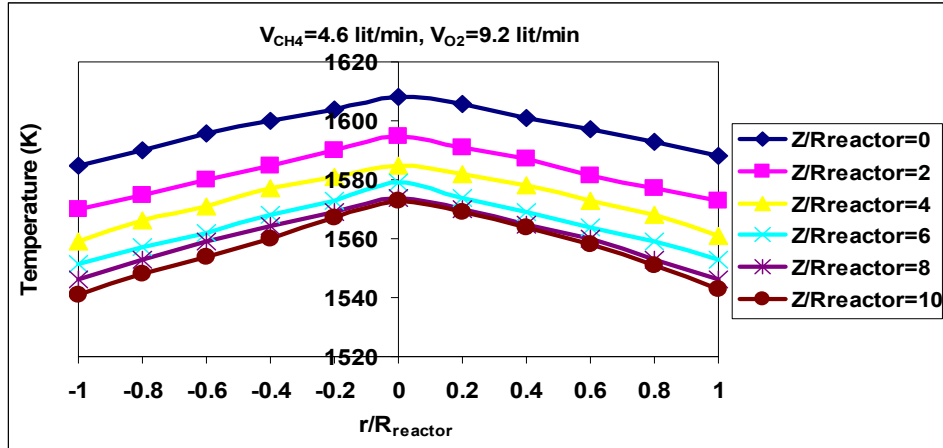


Figure 38d. Radial temperature profiles at different axial locations with  $V_{CH_4}= 4.6 \text{ lit/min}$  and  $V_{O_2}= 9.2 \text{ lit/min}$ .

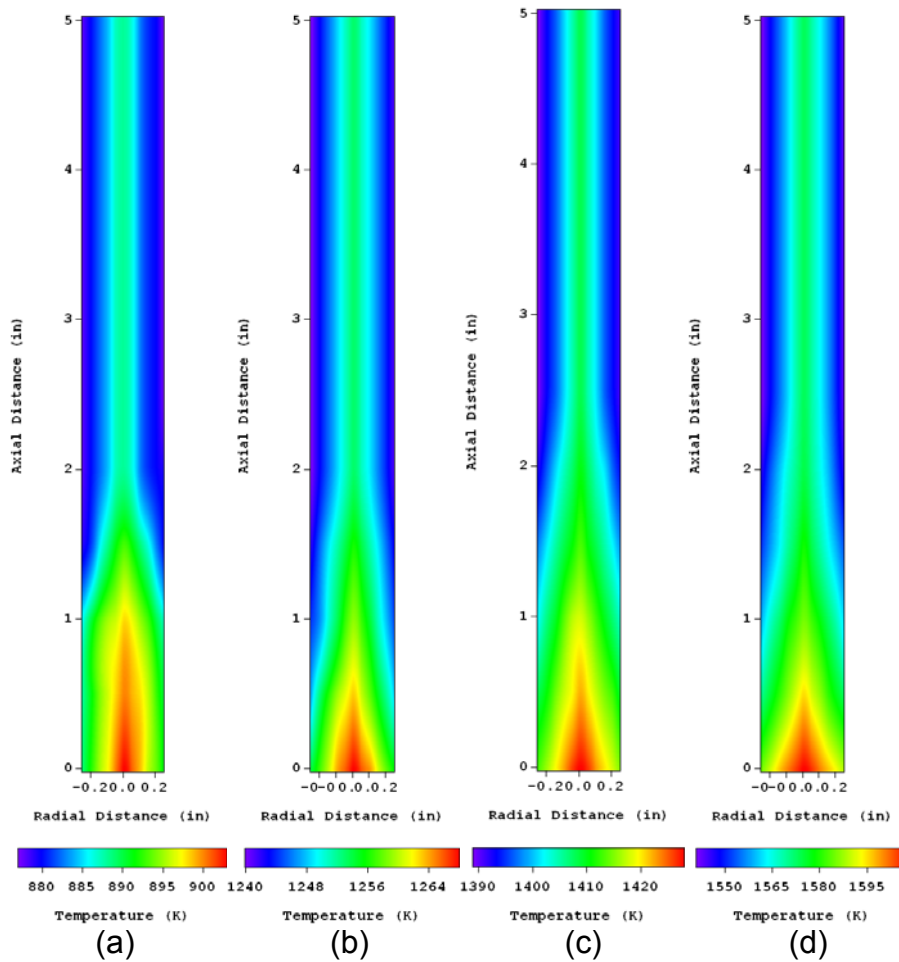


Figure 39. Temperature contours at different flow rates:  
 (a)  $V_{CH_4}=2.05 \text{ lit/min}, V_{O_2}=4.1 \text{ lit/min}$ , (b)  $V_{CH_4}=3.2 \text{ lit/min}, V_{O_2}=6.5 \text{ lit/min}$ ,  
 (c)  $V_{CH_4}= 3.8 \text{ lit/min}, V_{O_2}= 7.6 \text{ lit/min}$ , (d)  $V_{CH_4}=4.6 \text{ lit/min}, V_{O_2}=9.2 \text{ lit/min}$ .

#### 4. Conclusions

In this report the numerical and experimental efforts of the project to date have been listed cumulatively. Specific emphasis was on the main steps of the progress.

The numerical efforts show the importance of the equilibrium study in determining the most favorable temperature of Claus reactor, and the change of this temperature according to the change of the sour gas composition. Meanwhile, a chemical-kinetics study depicts the steps of reducing the detailed mechanism by Leeds University<sup>1</sup> down to less than quarter of the total reactions and species with an error less than 10%, which is beneficial for reducing the computational costs and increasing the likelihood of definite CFD code convergence.

As for the experimental approach, we provided a detailed description of the experimental facility and used diagnostics. Meanwhile, some preliminary results were introduced, in order to assure the capability of the facility of providing the required conditions. First, we examined the mixedness of the injected gases non-reactively by injecting CO<sub>2</sub> and N<sub>2</sub> instead of H<sub>2</sub>S and combustible gases. The results showed that cross injection is more efficient than parallel injection in assuring better mixedness of H<sub>2</sub>S in the combustible gases. Moreover, we examined the temperature homogeneity of the secondary reactor at different heat loads. The results showed the ability of our experimental facility to provide a very homogenous temperature medium with small standard deviation at the different heat loads.

#### 5. Future Plans

- Examine sulfur removal from hydrogen sulfide using flameless combustion at different reactor temperatures.
- Compare the flameless and flame combustion modes.
- Experimentally investigate the effect of sour gas composition on conversion efficiency.
- Numerically determine and monitor the behavior of the reaction kinetics of hydrogen sulfide oxidation at different reaction conditions.

Appendix A

#	Elementary Reaction	A	n	E/RT
1	$H_2S+M = S+H_2+M$	1.60E+24	-2.61	44800
2	$H_2S+H = SH+H_2$	1.20E+07	2.1	350
3	$H_2S+O = SH+OH$	7.50E+07	1.75	1460
4	$H_2S+OH = SH+H_2O$	2.70E+12	0	0
5	$H_2S+S = 2SH$	8.30E+13	0	3700
6	$H_2S+S = HS_2+H$	2.00E+13	0	3723.84
7	$S+H_2 = SH+H$	1.40E+14	0	9700
8	$SH+O = H+SO$	1.00E+14	0	0
9	$SH+OH = S+H_2O$	1.00E+13	0	0
10	$SH+O_2 = HSO+O$	1.90E+13	0	9000
11	$S+OH = H+SO$	4.00E+13	0	0
12	$S+O_2 = SO+O$	5.20E+06	1.81	-600
13	$2SH = S_2+H_2$	1.00E+12	0	0
14	$SH+S = S_2+H$	1.00E+13	0	0
15	$S_2+M = 2S+M$	4.80E+13	0	38800
16	$S_2+H+M = HS_2+M$	1.00E+16	0	0
17	$S_2+O = SO+S$	1.00E+13	0	0
18	$SO+OH = SO_2+H$	1.08E+17	-1.35	0
19	$SO+O_2 = SO_2+O$	7.60E+03	2.37	1500
20	$2SO = SO_2+S$	2.00E+12	0	2000
21	$HSO+H = SH+OH$	4.90E+19	-1.86	785
22	$HSO+H = S+H_2O$	1.60E+09	1.37	-170
23	$HSO+H = SO+H_2$	1.00E+13	0	0
24	$HSO+O_2 = SO_2+OH$	1.00E+12	0	5000
25	$SH+O_2 = SO+OH$	1.00E+12	0 503	2.48

## Solid Oxide Fuel Cells for CO<sub>2</sub> Capture and Enhanced Oil Recovery

UMD Investigators: Prof. Greg Jackson

Senior Research Associates: Dr. Serguei Dessaitoun

GRA's: Paul Jawlik and Siddharth Patel

PI Investigator(s): Prof. Valerie Eveloy, Prof. Ali Almansoori

Start Date: October 2006

FINAL REPORT

### 1. Objective/Abstract

This multi-faceted project will investigate the feasibility of implementing advanced solid oxide fuel cell (SOFC) technology for producing power from oil well off-gases while providing a source of concentrated CO<sub>2</sub> for sequestration and enhanced oil recovery. This project will explore fundamental issues in identifying preferred material combinations for durable SOFC anode operation with typical oil well off-gas composition. Along with these fundamental issues, multi-scale modeling will include detailed models for assessing SOFC membrane electrode assembly architectures for optimal operation with hydrocarbons, and higher-level system models for evaluating integrated systems with all accessory equipment within the context of oil well operation. System models will assess the economic viability of such a system and thereby determine technology performance requirements for successful implementation of SOFC-based systems for enhanced oil recovery with CO<sub>2</sub> injection.

### 2. Approach

Four tasks identified for this project are presented here.

#### *Task 1: Experimental study of SOFC MEA's for hydrocarbons*

UMD has high-temperature single-cell rigs with electrochemical characterization tools, electronic flow controls, and data acquisition for studying SOFC MEA's. This project will expand these capabilities to study porous MEA architectures of ceria-based anodes for stable operation on C<sub>3</sub>-C<sub>5</sub> gases. Experiments will explore the role of metal doping of the ceria for improved electronic conductivity and activity for fuel breakdown to avoid carbon build-up. The experiments will include V-I measurements as well as impedance spectroscopy to validate models developed in Task 2, as well as post-testing microscopy and surface characterization to evaluate the durability of the SOFC anodes for the different fuels. After being established at UMD, these capabilities will be duplicated at the Petroleum Institute (PI) with the aid of UMD researchers such that faculty at the PI will also participate in this effort while providing PI students a chance to explore SOFC technology. A UMD graduate student will assemble the experimental facilities at PI by the end of the first year of the project. This will permit, in the second year of this project, the PI Team to commence assessing the reproducibility of experimental measurements performed at UMD.

#### *Task 2: Numerical modeling for design of SOFC architectures*

Modeling of membrane electrode assemblies will explore optimal design of SOFC's for hydrocarbon operation and high fuel conversion efficiency to provide optimal CO<sub>2</sub> capturing by eliminating downstream combustion of unburned fuel. This work will build on detailed Matlab/Cantera-based models developed at UMD for SOFC MEA analysis. New efforts will involve the development and validation of hydrocarbon kinetic models on preferred anode materials identified in Task 1. Depending upon the availability of a RA/Graduate Student which PI plans to recruit for the project, and computational hardware/software resources at PI, the PI Team may i) expand the parametric analysis space explored at UMD using Matlab/Cantera-based models provided by the UMD Team,

and/or ii) investigate numerical modeling methodologies and software to explore the feasibility of implementing multi-physics models used in the UMD Team's Matlab/Cantera models, into commercially-available computational fluid dynamics (CFD)-based software to improve the simulation of SOFC MEA's having complex geometries.

*Task 3: System level analysis of integrated SOFC plants*

The economic and engineering viability of an integrated SOFC plant for CO<sub>2</sub> sequestration and efficient power production will be investigated numerically by the UMD Team, and possibly the PI Team - if compatible with man-power, and computational hardware and software resources available at PI - within the context of petroleum production, using Matlab-based system level modeling tools developed at UMD and possibly other process analysis software to be identified for use at PI. These tools will be used to explore overall balance of plant, adequacy of fuel supplies, and power requirements for CO<sub>2</sub> capture. If possible, this work will be done in consultation with ADNOC experts.

*Task 4: Identification of multi-university research team for SOFC's in the petroleum industry.*

The UMD/PI team will spend a portion of his time developing a broader-base team for pushing this project further toward implementation. Industrial partners may also be considered for participating in larger-scale demonstration and design efforts.

### 3. Two-Year Schedule

Year 1:

- Begin experiments for identifying preferred material systems using ceria-based anodes for hydrocarbon SOFC operation.
- Perform post-testing material characterization for evaluation.
- Acquire equipment for assembly rig at the PI.
- Adopt SOFC models at UMD for hydrocarbon studies.
- Undertake CFD modeling at PI.

Year 2:

- Perform experiments with preferred material systems for typical off-gas compositions (with varying team loadings).
- Validate models and perform SOFC design for both MEA microstructure and overall all fuel cell size.
- Establish system level models at both institutions, and Identify preferred system configurations for overall balance of plant.

### 4. Summary of Results

***Task1: Experimental study of SOFC MEA's for hydrocarbons***

UMD has spent significant effort exploring fabrication methods for developing optimal micro-architectures for metal-doped ceria anodes. Figure 1a shows the experimental configuration for single-cell SOFC's in which these anode architectures are being explored. Figure 1b shows a completed cell (minus the anode current collector and lead) before placing in the furnace. These single cells included the following:

- Ni/YSZ or Ni/CeO<sub>2</sub>/YSZ porous anodes with both functional layers ( $\approx 20 - 40 \mu\text{m}$  thick) near the electrolyte membrane for high electrocatalytic activity and support layers for effective gas transport ( $\approx 1 \mu\text{m}$  thick),

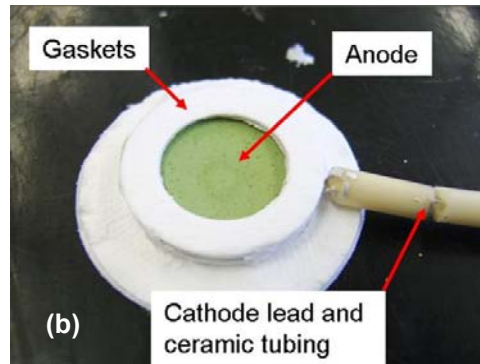
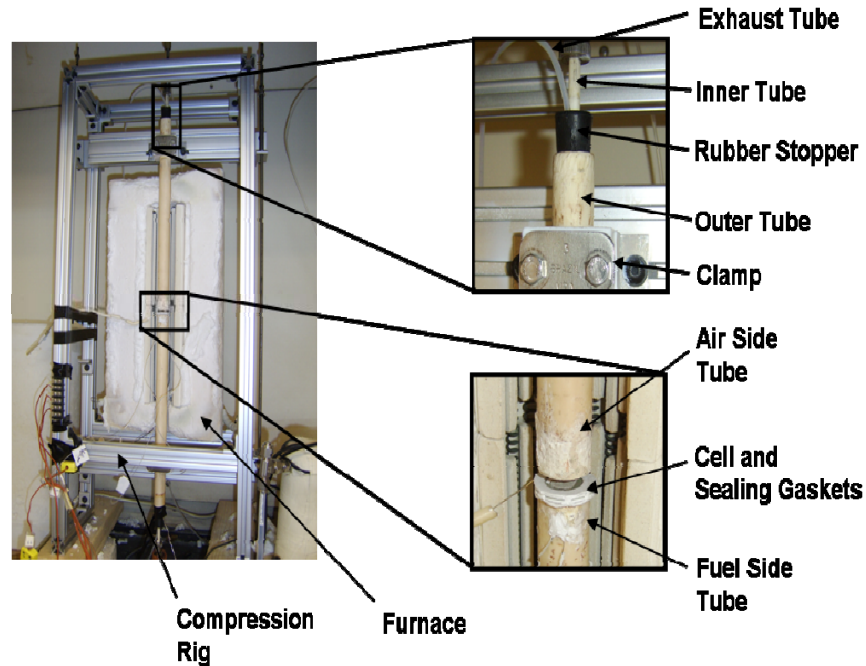


**Figure 1. (a) Photographic image of single-cell SOFC test rig showing the furnace, the mounted cell with the seals, and the feed tubes in the compression rig. (b) A photographic image of a completed cell showing the anode side before pasting the current collector on the anode and before the *in situ* Ni reduction.**

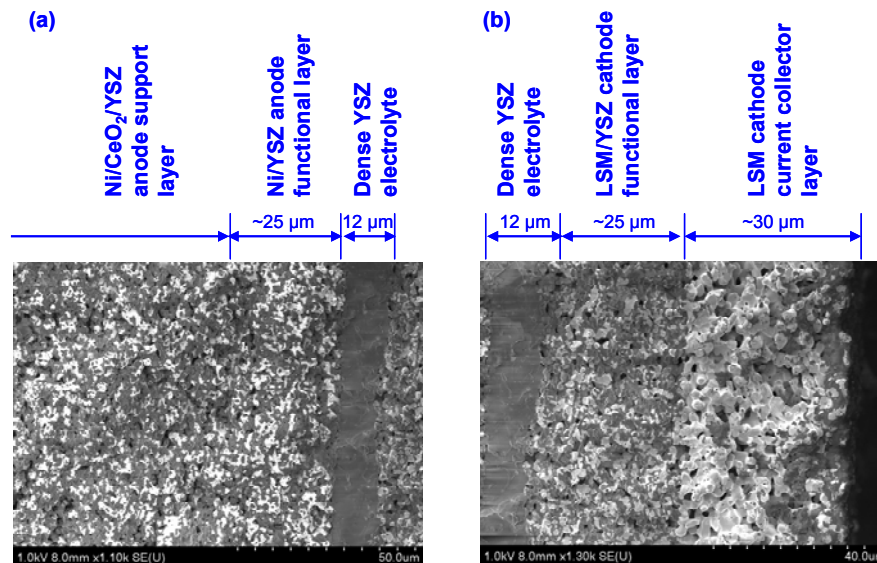
- Dense YSZ electrolytes ( $\approx 10 - 20 \mu\text{m}$  thick) for low bulk resistance of  $\text{O}^{2-}$  ion transport from the cathode to the anode,
- LSM/YSZ porous cathodes ( $\approx 50 \mu\text{m}$  thick) sometimes with a porous LSM overlayer,
- Porous Ag mesh current collectors attached to each electrode with porous Ag paste and 1 mm diam Ag wire for leads.

Various processes have been tested for fabricating the cell and in particular the porous anode with  $\text{CeO}_2$ , which was unique to this program. An in-house method adapted and modified from the work of Armstrong and Rich [1] provided reliable cells, and the full method is reported in detail in Paul Jawlik's M.S. thesis [2]. The protocol has been summarized in previous quarterly reports. The final method relied on starting with base material powders and using carbon-based pore forms to control porosity in the anode and cathode layers. The final cell fabrication process produced reliable cells that performed well over several days of testing. Electrolyte cracking, which was a problem off and on during testing for the first year and a half of the

testing, was found to be caused by excessive sealing on the cathode side, and testing over the last half year has been reliable when the cathode sealing was not applied and air was allowed to pass around the cell and into the furnace. The resulting cell performance under these conditions matched past performance and was reliable.

The testing showed that the addition of  $\text{CeO}_2$  through a co-firing method (simultaneous  $\text{NiO}/\text{YSZ}/\text{CeO}_2$ ) produced the most stable cells and provided the best performance, particularly with hydrocarbon feeds. The co-firing of  $\text{CeO}_2$  powders with  $\text{NiO}$  and  $\text{YSZ}$  powders in a single step provided larger  $\text{CeO}_2$  particles than impregnation methods as used by Gorte et al. in their work [3]. The impregnated  $\text{CeO}_2$  shows loose aggregates of  $\sim 100$  nm diameter particles, whereas the co-fired  $\text{CeO}_2$  shown in the support layer of Figure 2a is more integrated into the  $\text{Ni}/\text{YSZ}$  structure of the anode support layer. The less-structured nanoparticles from the impregnated ceria may provide higher surface area but do not provide superior performance, perhaps due to the reduced conduction pathways between the  $\text{CeO}_2$  particles and the  $\text{Ni}$  metal. Another key difference in the two fabrication approaches is that the impregnated  $\text{CeO}_2$  particles penetrate into the functional layer, whereas in the co-fired method the  $\text{CeO}_2$  remains in the structural layer where it is needed to suppress carbon formation during reforming of hydrocarbons.

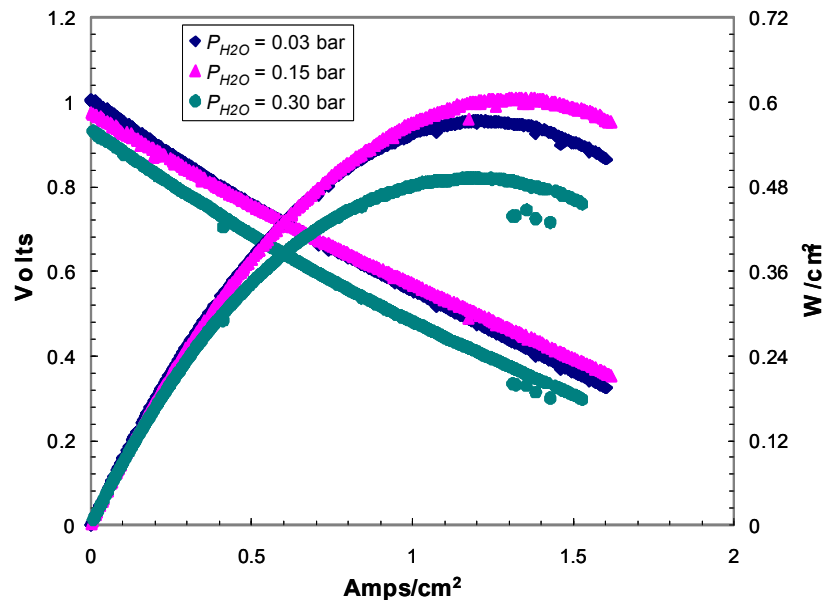
Improvements to the cathode have also contributed to the improved performance presented below. The addition of a conductive LSM layer between the cathode current collector (now a silver mesh and paste) and the LSM/ $\text{YSZ}$  cathode functional layer has helped to reduce the overall bulk resistance of the cells and thereby provide improved performance. This layer is seen on the far right of Figure 1b. Further improvements to the cathode were achieved by adding the graphite pore formers to improve  $\text{O}_2$  transport into the depths of the functional layer. This has resulted in a lower cathode contribution to the polarization resistance and thereby led to improved MEA performance. The added porosity due to the graphite pore formers in the cathode layers is illustrated in Figure 2b.



**Figure 2. Post-testing SEM images of microstructure for an MEA operated on hydrogen, syngas, and butane: a) anode/electrolyte interface with  $\text{Ni}/\text{YSZ}$  functional layer and  $\text{Ni}/\text{CeO}_2/\text{YSZ}$  support layer (entire 1 mm thickness not shown) and b) cathode/electrolyte interface with  $\text{LSM}/\text{YSZ}$  functional layer and  $\text{LSM}$  current collecting layer.**

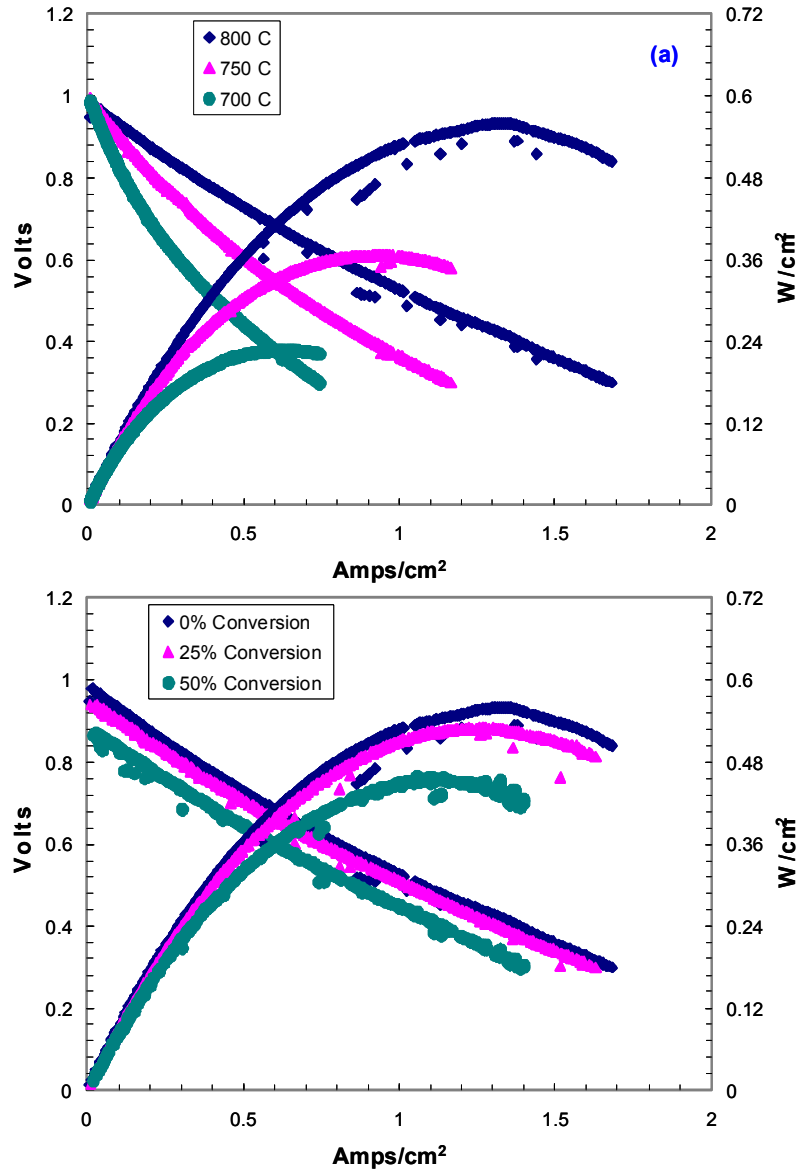
### Testing of the Anode-Supported Thin-Electrolyte Cells

The co-fired Ni/CeO<sub>2</sub>/YSZ anode-supported, thin-electrolyte MEA's with various microstructures were tested for temperatures  $T_{cell}$  ranging from 700 to 800 °C on various fuels including 1) humidified H<sub>2</sub> at a variety of H<sub>2</sub>O partial pressures, 2) syngas for a variety of fuel conversions, and 3) n-butane with H<sub>2</sub>O added at a 1.5-to-1 and a 1-to-1 steam-to-carbon (S/C) ratio. The MEA's were characterized with voltammetry measurements and with electrochemical impedance spectroscopy at overall overpotentials  $\eta_{tot}$  of 100-300 mV. While numerous results were obtained for other cells, the discussion here will focus on results with the co-fired Ni/CeO<sub>2</sub>/YSZ MEA's, which were deemed to be the most promising system for larger-system development. Voltage vs. current density ( $V-i$ ) curves for these cells running at 800 °C on H<sub>2</sub>/Ar/H<sub>2</sub>O anode feeds at various humidity levels are shown in Figure 3. Power densities exceeded the desired performance of 0.5 W/cm<sup>2</sup> for the  $P_{H_2O} < 0.20$  bar, and as shown below the desired power densities were also achieved with such syngas representing reformed light hydrocarbons. They were not achieved with direct butane-steam feeds which relied on internal hydrocarbon reforming in the SOFC anode.



**Figure 3. Voltage and associated power density vs. current density curves for Ni/CeO<sub>2</sub>/YSZ anode-supported thin-electrolyte MEA's operating at 800 °C with anode feeds of H<sub>2</sub>/Ar/H<sub>2</sub>O ( $P_{H_2,anode} = P_{Ar,anode}$ ) and cathode feeds of dry air.**

Cells were also run on a range of conditions for syngas with the  $V-i$  results shown in Figure 4a and 4b. The syngas conditions were selected based on equilibrium calculations of a steam reformer running on n-butane with an S/C of 1.5 and an outlet temperature of 800 °C. Initial experiments were run at syngas conditions with 0% fuel conversion, as shown in Figure 4a, and the results show that the desired 0.5 W/cm<sup>2</sup> have been achieved for syngas at  $T_{cell} = 800$  °C with cell voltages  $V_{cell} = 0.63$  V. At a reasonable stable  $V_{cell} = 0.75$  V at 800 °C, current and power densities are 0.45 A/cm<sup>2</sup> and 0.35 W/cm<sup>2</sup> respectively. As  $T_{cell}$  is reduced to 750 and 700 °C, current densities drop to about 0.29 and 0.15 A/cm<sup>2</sup>, respectively, with power densities of 0.22 and 0.13 W/cm<sup>2</sup>. These results suggest that lower  $T_{cell}$  down to 700 °C could be used to still achieve reasonable power densities on reformed hydrocarbons if a larger SOFC power plant were tolerable. The lower  $T_{cell}$  greatly simplifies SOFC sealing issues in a large-scale plant.



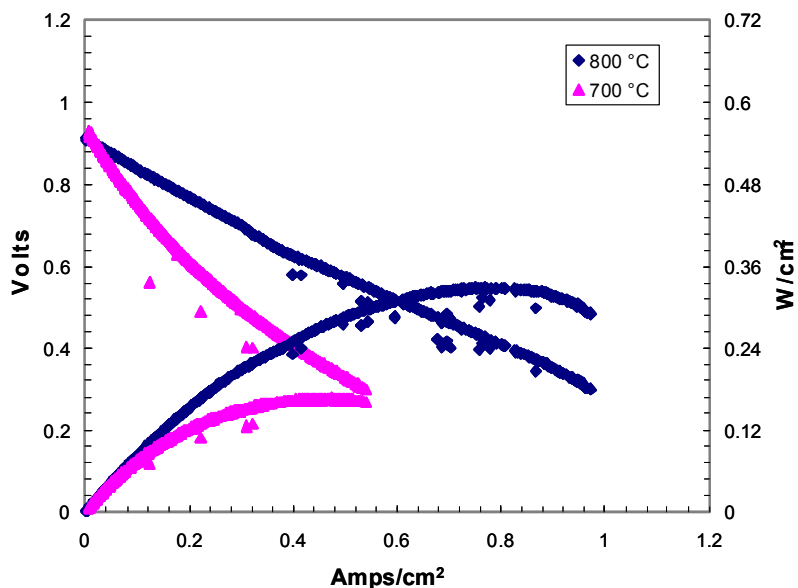
**Figure 4. Voltage and power density vs. current density curves for Ni/CeO<sub>2</sub>/YSZ anode-supported thin-electrolyte MEA's a) operating on 0% conversion syngas for a range of T<sub>cell</sub> and b) operating at T<sub>cell</sub> = 800 °C for a range of syngas conversions (as indicated in Table 1).**

Figure 4b shows the performance of the cell at T<sub>cell</sub> = 800 °C and various syngas conditions simulating along an SOFC channel as conversion rises (increasing P<sub>H<sub>2</sub>O</sub> and P<sub>CO<sub>2</sub></sub> partial pressures while reducing P<sub>H<sub>2</sub></sub> and P<sub>CO</sub> as shown in Table 1). Tests were restricted to 50% conversion. The results in Figure 3b are encouraging, as they show that for up to 50% syngas conversion, power densities at a stable operating voltage of 0.75 V do not drop by more than about 30%. This suggests that in an SOFC channel fed with butane reformat, power densities would be maintained down the length of the channel. Figure 3b indicates that overall cell resistance is not a strong function of syngas conversion. Rather, the drop in power densities with increased conversion seems to be largely driven by the necessary drop in open circuit voltage (OCV) with the increased syngas conversion.

**Table 1. Compositions of syngas at various degrees of conversion (to H<sub>2</sub>O and CO<sub>2</sub>). 0% conversion corresponds to equilibrium reformat from n-butane reforming with S/C = 1.5 and exhaust T = 800 °C.**

Syngas Conversion	P <sub>H<sub>2</sub></sub> (bar)	P <sub>H<sub>2</sub>O</sub> (bar)	P <sub>CO</sub> (bar)	P <sub>CO<sub>2</sub></sub> (bar)
0%	0.651	0.082	0.215	0.052
25%	0.499	0.234	0.151	0.116
50%	0.328	0.405	0.105	0.162

Further testing on the co-fired Ni/CeO<sub>2</sub>/YSZ-anode MEA's was performed with n-C<sub>4</sub>H<sub>10</sub>/H<sub>2</sub>O feeds with a S/C ratio of 1.5 as well as at 1.0. This S/C ratio is lower than a typical value of 2.5 for a hydrocarbon steam reformer because the production of steam in the SOFC allows for a carbon-resistant catalyst (like the CeO<sub>2</sub> additive) to be effective at suppressing surface carbon formation, which has been the weakness of conventional Ni/YSZ anodes without CeO<sub>2</sub>. The steam created from the O<sup>2-</sup> flux to the anode suppresses surface C build-up in the Ni/YSZ/CeO<sub>2</sub> cells, even though the inlet C-H-O ratio is initially in the region where such surface C build up might be expected [4]. Performance at T<sub>cell</sub> = 700 and 800 °C of the cells on n-C<sub>4</sub>H<sub>10</sub> anode feeds at S/C of 1.5 for the MEA's are shown in Figure 4. The 800 °C results indicate peak power densities of 0.33 W/cm<sup>2</sup> and a power density of 0.20 W/cm<sup>2</sup> at an operating voltage of 0.75 V. Performance at T<sub>cell</sub> = 800 °C and S/C of 1.0 was found to be comparable in power density to the S/C = 1.5 condition. Lowering T<sub>cell</sub> to 700 °C reduced the power density to 0.075 W/cm<sup>2</sup>. Beyond just the performance in Figure 5, some exploratory work was done on stability of the n-C<sub>4</sub>H<sub>10</sub> performance at 800 °C and 0.75 V. Tests for > 3 hours showed no degradation in current density at these conditions, although there were periodic and regular oscillations signified by mild drops in current density that were recovered in a few minutes. This behavior has not yet been explained and requires further investigation. Upon removal from testing, the Ni/CeO<sub>2</sub>/YSZ anode showed no C build-up, including in the post-test SEM imaging as exemplified in Figure 2a. Energy dispersive X-ray analysis (EDAX) did not indicate significant carbon build-up.



**Figure 5. Voltage and power density vs. current density curves for Ni/CeO<sub>2</sub>/YSZ anode-supported thin-electrolyte MEA's operating directly on n-butane and H<sub>2</sub>O at an S/C = 1.5.**

While the 800 °C performance on n-C<sub>4</sub>H<sub>10</sub> feeds is lower than the target 0.5 W/cm<sup>2</sup>, the benefits of removing a steam reformer from a light hydrocarbon recovery process make these results significant. The characterization with impedance spectroscopy has been helpful in identifying areas where improvement can be made in the MEA micro-architecture. The impedance spectra at a total cell overpotential  $\eta_{tot} = 0.2$  V for the MEA's are shown in Figure 6 for operation with n-C<sub>4</sub>H<sub>10</sub> feeds. The spectra illustrate the high-frequency bulk resistance and the two primary arcs characteristic of the anode (high-frequency) and cathode (low-frequency) at both 700 and 800 °C.

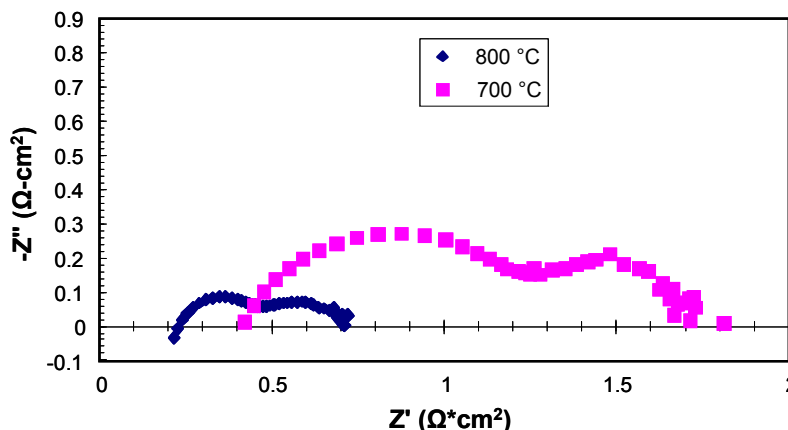


**Figure 6. Electrochemical impedance spectra at a total cell overpotential  $\eta_{tot} = 0.2$  V for the Ni/CeO<sub>2</sub>/YSZ anode-supported thin-electrolyte MEA's operating directly on n-butane and H<sub>2</sub>O at an S/C = 1.5.**

### **Task 2- Numerical modeling for design of SOFC architectures**

Non-isothermal, through-the-MEA models were developed on this program and used to study performance of the SOFC MEA microarchitecture's performance on syngas and on CH<sub>4</sub>/H<sub>2</sub>O steam feeds. The models implemented detailed H<sub>2</sub>/CO/CH<sub>4</sub> (on Ni/YSZ) oxidation chemistry adopted from previous references and UMD work [5,6] allowed for several tests of the energy equation to determine expected thermal gradients perpendicular to the electrolyte. The internal (endothermic) reforming of methane in the anode support layer causes some temperature losses in the MEA, and the drops in internal temperatures (from the flow channel temperature) increase with power density.

An example of the modeling results is shown in Figure 6 in this case for internal (endothermic) reforming of a near-pure natural methane gas stream (95% CH<sub>4</sub>, 3% H<sub>2</sub>, 2% H<sub>2</sub>O by mole) in the anode support layer. The high CH<sub>4</sub> concentrations cause a temperature loss in the MEA until currents approach 1.0 A/cm<sup>2</sup> when the heat release of the subsequent reformat offsets the heat loss due to the internal reforming. The higher current densities at temperatures  $\geq 800$  °C provide adequate H<sub>2</sub>O concentrations to encourage catalytic reforming on Ni surfaces and the production of H<sub>2</sub> and CO for eventual electrochemical oxidation in the anode functional layer. Figure 6a shows the predicted V-i curve for a Ni/YSZ-anode-supported MEA operating at 800 °C with the simulated natural gas feed under non-isothermal cell conditions but with 800 °C gas feeds. The  $V_{cell}$ -i curves in Figure 7a identify points where species profiles are shown in Figure 7b for all major species. As shown in Figure 7c, the production of H<sub>2</sub> and CO increases in the porous anode support layer, and then those intermediate species are consumed near the electrolyte due to electrochemical oxidation.

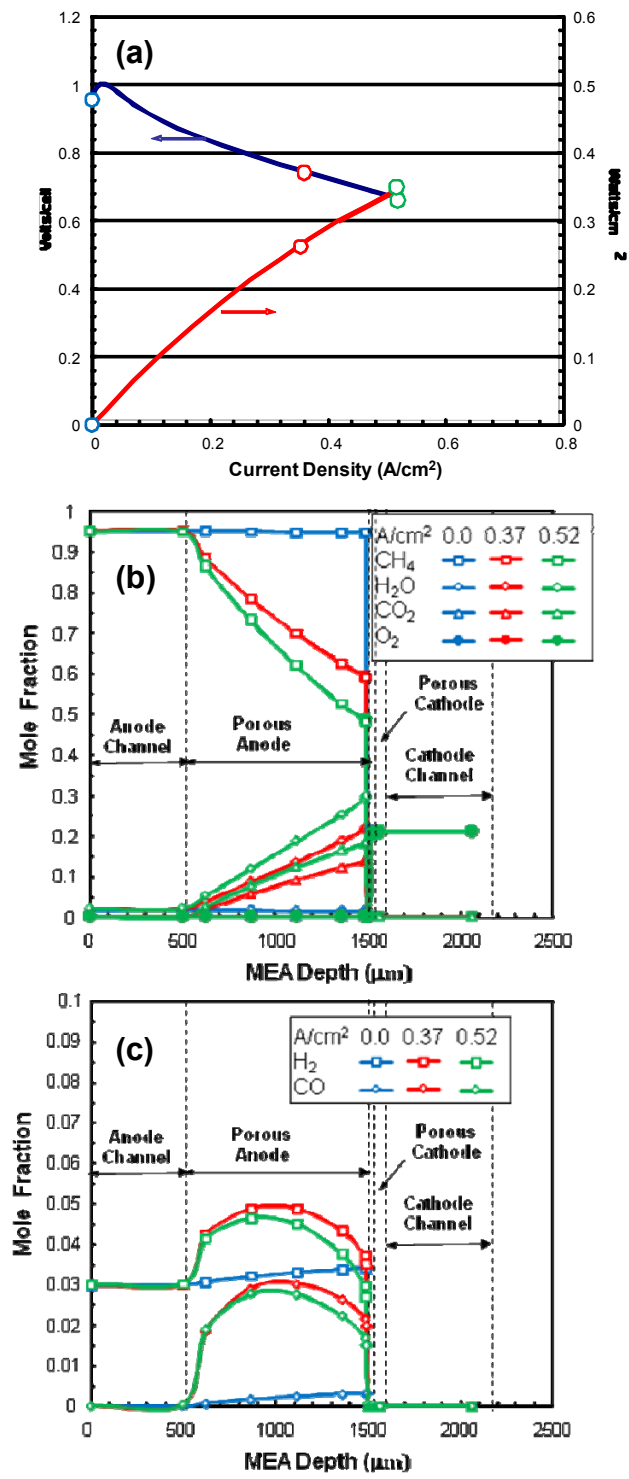


Figure 7. a) Predicted  $V_{cell}$  vs. current density curve, b) and c) species profiles for an Ni/YSZ anode-supported MEA with 1020  $\mu m$  thick anodes, 10  $\mu m$  thick YSZ electrolytes, and 50  $\mu m$ -thick LSM/YSZ cathodes operating at 800 °C flow temperatures with a 95%  $CH_4$ , 3%  $H_2$ , and 2%  $H_2O$  feed at 800 °C. Points indicate operating conditions for profiles in b) and c).

A down-the-channel model with heat transfer has been created for further studies. This model was used to predict current, species, and temperature profiles in a tubular fuel cell running on syngas created from catalytic partial oxidation of butane. The model, which predicts heat transfer along the channel and across the MEA, shows that current densities vary strongly with distance along the channel. Results on the cell operating on a reformat stream show that heat generation at higher current densities can be important for heating the cell and thus providing higher power. The down-the-channel model with heat transfer has been developed further and used in system studies as described in the following section.

Further modeling efforts for follow-on efforts were discussed with Prof. Nandakumar from the PI. Proposals were discussed to improve microarchitecture models by combining recent work by Nandakumar's group on cermet particle packing with UMD's fundamental kinetic models and measurements on microfabricated patterned anodes. The use of this particle-packing model for anode microstructures may also be combined with UM's work on ceria kinetics to explore the mechanisms for  $\text{CeO}_2$  for providing improved performance with carbonaceous fuels. This model may also allow for microstructure optimization of Ni/ $\text{CeO}_2$ /YSZ anodes for performance with oil-well off gases. Further discussions were held on furthering the model efforts when Prof. Jackson from UM visited the PI during the workshop in Abu Dhabi during the first week of November.

### ***Task 3: System-level analysis of integrated SOFC plants***

The UMD group began some system-level analysis work by furthering its study on the impact of possible impurities from petroleum off-gases on SOFC anode performance and on assessing various designs for mitigating such impacts. This work was an extension of a recent review paper by UMD researchers and coauthors [7]. Expected fuel impurities such as  $\text{H}_2\text{S}$  and perhaps some chlorinated species (likely converted to HCl) can significantly affect SOFC anode performance. For Ni/YSZ anodes, this is particularly true for species that can react with the Ni to form new phases with poor electrochemical activity [8]. Other trace impurities can also appear but are not expected to be as significant. The importance of gas clean-up for the system level studies will be increasingly important for designs that seek high fuel utilization for efficient operation and ease of downstream  $\text{CO}_2$  sequestration for enhanced oil recovery.

Significant work has been pursued to understand the effects of  $\text{H}_2\text{S}$  on various anode materials. These include efforts to develop new anode materials with higher sulfur tolerance [9, 10]. Sulfur concentrations as low as a few parts per million can deactivate Ni catalysts, which significantly reduces conventional Ni/YSZ anode performance. This has led to considering alternative electrolyte-phase materials, notably GDC, which decreases the rate of Ni degradation. The effects of  $\text{CeO}_2$  nanoparticle addition to Ni/YSZ anodes have been shown to dramatically improve sulfur tolerance, and this remains a promising approach for syngas applications with low  $\text{H}_2\text{S}$  concentrations. Alternative electronically conducting perovskite materials can replace Ni/YSZ-cermets altogether, and surprisingly good performance has been achieved with perovskite anode electrocatalysts when using syngas with relatively high concentrations of  $\text{H}_2\text{S}$ . However, because questions remain as to the long-term durability of these anodes for SOFC applications, this project has taken the approach of  $\text{CeO}_2$  addition as a preliminary approach for handling this project. More work has been proposed in a follow-on program to address this issue.

The UMD group also did some system-level analysis work by adapting modeling tools for smaller-scale SOFC systems using catalytic partial oxidation fuel processing and anode exhaust combustion for waste-heat recovery. While such a system is not

preferred for some petroleum processing, catalytic partial oxidation processing of light hydrocarbons is being considered in some applications which are off-shore and are volume-constrained. Preliminary system studies provided an understanding of how non-isothermal effects in an SOFC channel can cause non-monotonic efficiency and power densities with respect to SOFC operating-voltage per cell. This behavior arises because increased voltage can increase operating temperatures, which tends to lower overpotentials, particularly in the cathode and electrolyte.

#### **Task 4: Identification of multi-university research team for SOFC's**

Due to decisions of management at PI and UMD, this task was not implemented in this study. It will be included in follow-on efforts if the effort is to be broadened beyond the PI/UMD collaboration

### **6. Recommendations for Future Work**

Future work is recommended in the following areas.

- Further testing of cells with carbonaceous fuel feeds with inclusion of potential poisons ( $H_2S$  primarily and  $HCl$  secondarily) expected from petroleum process feeds.
- Expansion of the down-the-channel models into CFD codes for SOFC stack level design studies (particularly for thermal management).
- ASPEN-Hisys modeling in a petroleum processing plant scenario in collaboration with potentially interested ADNOC parties.
- Increased collaboration with PI on microarchitecture modeling studies and on fuel cell control modeling studies.
- Demonstration of small (< 5 kW) pilot-plant-scale stacks with an industrial partner to show the potential of stack operation in plant environment

### **7. Conclusion**

This project achieved the goals on the experimental side of the study and showed that with Ni/CeO<sub>2</sub>/YSZ anodes, stable high-power-density performance can be achieved with direct hydrocarbon steam feeds as well as with syngas feeds. Translation of these results into stack performance remains uncertain and will likely need larger investment in stack studies. The modeling effort has laid the basis for developing models to be integrated into CFD codes and into ASPEN-Hisys modeling. These goals were put into this project and not completed to date. More extensive PI-UMD collaboration is expected to achieve these goals in any follow-on work. This should be able to show the promise of using SOFC's to generate power and dense CO<sub>2</sub> streams for enhanced-oil-recovery (and carbon sequestration) from petroleum processing off-gases.

### **8. References**

1. Armstrong, T.J. and Rich, J.G., *J. Electrochem. Soc.* 2006. **153**(3): A515-A520.
2. Jawlik, P. "Effects of Ceria Addition on Ni-YSZ Anodes in Solid Oxide Fuel Cells Operating on Hydrogen and Syngas Fuel Feeds", M.S. Thesis, University of Maryland, College Park, MD, December 2008.
3. O. Costa-Nunes, R. J. Gorte, and J. M. Vohs, *Journal of Power Sources*, 141:241 (2005).

4. Sasaki, K. and Teraoka, Y., J. Electrochem. Soc., 150:A878 (2003).
5. V.M. Janardhanan and O. Deutschmann, J. Power Sources, 162:1192 (2006).
6. B. Habibzadeh, Ph.D. Dissertation, Univ. of Maryland (2007).
7. Kee, R.J., Zhu, H., Sukeshini, A.M., and Jackson, G.S., Combust. Sci. Tech., 180:1205 (2008).
8. Trembly JP, Gemmen RS, Bayless DJ. 2007. Journal Of Power Sources 171: 818-25
9. Aguilar L, Zha SW, Li SW, Winnick J, Liu M. 2004. Electrochemical and Solid-State Letters 7: A324-A6
10. 13. Cheng Z, Zha SW, Liu ML. 2006. Journal Of The Electrochemical Society 153: A1302-A9

## 9. Publications

1. Maxey, C., Jackson, G.S., Reihani, S.-A.S., DeCaluwe, S.C., Patel, S., Veeraragavan, A., and Cadou, C.P., "Integration of Catalytic Combustion and Heat Recovery with Meso-Scale Solid Oxide Fuel Cell System", ASME Paper # IMECE-2008-67040, presented at IMECE-2008, Boston, MA, November 2008.
2. DeCaluwe, S.C., Zhu, H., Kee, R.J., and Jackson, G.S., "Importance of anode microstructure in modeling solid oxide fuel cells". *Journal Of The Electrochemical Society*, Vol. **155**(6): 2008. pp. B538-B546.
3. Jawlik, P. "Effects of Ceria Addition on Ni-YSZ Anodes in Solid Oxide Fuel Cells Operating on Hydrogen and Syngas Fuel Feeds", M.S. Thesis, University of Maryland, College Park, MD, December 2008.
4. Jawlik, P., Patel, S., and Jackson, G.S. "Ni/CeO<sub>2</sub>/YSZ anodes for direct butane feeds in SOFC's" *in preparation*.
5. Patel, S., DeCaluwe, S., and Jackson, G.S. "Detailed modeling performance of SOFC's on syngas operation" *in preparation*.

## 10. Visits to PI and to UMD

1. Jawlik, P. to PI for Energy 2030, November 2006
2. Jackson, G. to PI for program review, March 2007.
3. A. Al Mansoori to UMD for program review, August 2007.
4. Jackson, G. to PI for 1<sup>st</sup> EERC workshop, January 2008.
5. Nandakumar, K. to UMD for program review, September 2008.
6. Jackson G. to PI for 2<sup>nd</sup> EERC workshop, January 2008.

## 11. GRAs (names, degrees, graduation)

Paul Jawlik, M.S. graduated December 2008  
 Young Jo, Ph.D. did not finish program  
 Siddharth Patel, M.S. will graduate May 2009.

## Fundamental Immiscible Porous Media Studies for Improved Reservoir Models

UM Investigators: K. Kiger, A. Riaz, A. Shooshtari

GRA's: M. Al Hebsi

PI Investigators:

Start Date: Sixth Quarter

FINAL REPORT

### 1. Objective/Abstract

Current reservoir simulation models are based on an empirical extension of porous media single-phase flow, which is known to poorly represent flow behavior in a wide range of relevant operating conditions. Experiments and numerical simulations are proposed to study the detailed mechanics of immiscible two-phase flow in porous media, with the intent to explore the nonequilibrium mechanisms responsible for the breakdown of traditional continuum equations used for reservoir simulation. The experiments will be conducted with an index-matched visualization facility, which will permit both microscopic (pore scale) and mesoscopic measurements of the constituent phases and the local velocity field. The simulations will be conducted with a combination of simple pore network models and direct numerical simulation of the micropore dynamics. The outcomes of this research will enable the rational modeling extension of the traditional equilibrium relative permeabilities to account for the non-equilibrium conditions which occur for unstable displacement conditions.

### 3. Approach

#### *Short-Term Goals*

The current funding represents an initiation seed program in anticipation of a fully funded project during Phase II. As such, the efforts have been directed towards developing the computational tools, techniques, and test facility that will be needed for the successful completion of the project. We plan to initiate the following short-term goals for the experimental work over the first six months of the initial investigation:

1. Determination of working fluids compatible with viscosity ratio and index of refraction requirements for the experimental technique
2. Design and construction of the initial version of the test cell required for the experiments

In addition to the above experimental program, a computational effort was conducted in collaboration with Dr. Amir Riaz and Dr. Amir Shooshtari as part of a summer intern project for Mr. Mohamed Al Hebsi, visiting for 7 weeks from the Petroleum Institute. Mr. Hebsi was responsible for implementing a pore-network simulation model developed by Dr. Riaz, with the goal of extending its functionality to a broad range of parametric space. The development of the pore-network model is a complementary tool to the pore-scale tests to be completed as part of the experimental program, as well as the direct numerical simulation tool. The short-term goals for the numerical work include:

1. Demonstration of the operation of the pore-network model to replicate simple known physics

2. Extension of the pore-network model to include the effects of pore morphology.
3. Development of iterative linear solvers for larger problems.

### **Long-Term Goals**

Experimental work will be conducted to study the details of both the micro- and macroscopic behavior of the displacement process in the intermediate viscosity and capillary regime during the onset of fingering instabilities. Knowledge of the detailed pore-scale dynamics (interface configuration) and the resulting macroscopic evolution (relative phase saturation and velocity field) are needed in order to advance the current state of continuum modeling to cover a broader range of parametric space. Specifically, recent work has proposed generalized extensions to the standard relative permeability coefficients, which include permeability interaction terms to account for nonlinear phase interactions. To assess the development of these models, interaction of the capillary forces with the flow-induced viscous effects in the vicinity of the incipient finger need to be characterized.

Toward this goal, a laboratory scale, two-phase porous flow visualization facility is under construction. The working fluids (aqueous salt solutions and various grade silicone oils) and porous media will be selected to generate an index-of-refraction matched system, which will allow for a clear view of the interior processes with minimal optical distortion. Separate fluorescent dyes will be used to mark both working fluids, which when combined with appropriate filters, will allow unambiguous measurements of each phase volume fraction, interface geometry, and the porosity of the media. Use of two different optical configurations will permit visualization of the microscale and macroscale behavior. These imaging systems will be mounted on a traversing stage to allow for a three-dimensional reconstruction of the fluid configuration from the sampled two-dimensional images. Lastly, the phases will also be seeded with neutrally buoyant micron-sized tracer particles, which will be used to measure the local velocity field of both phases. Our lab has expertise in developing and applying particle image velocimetry techniques to the study of multiphase systems, which can be leveraged to the proposed work.

The concurrent numerical work will produce a complementary set of results that will be used to obtain detailed flow field information difficult to access through the experiments. This includes the determination of phase saturation distribution, interfacial area, film thickness on solid surfaces, contact angle variation with capillary number, and viscosity ratio. Numerical simulations will also be used to explore a wider range of parameters and flow conditions than those possible with experiments.

Numerical simulations will be calibrated rigorously through a detailed comparison with experimental observations and the velocity field data obtained with particle image velocimetry. Together, numerical simulations and experiments will produce detailed flow field data that will be utilized to determine the average behavior of the flow process over various length scales containing different pore configurations. The average behavior of the flow statistics will determine the validity of the standard multi-phase flow models as well as suggest new averaging strategies for derivative-based quantities such as pressure and temperature fields.

Numerical simulations will be based on the Volume of Fluid, finite element method. This method will be extended to take into account the discontinuous nature of the interface separating the fluids. The standard implementation is based on the introduction of a source term representing the interfacial forces into the momentum equations. This methodology results in an interface that is not smooth in the gradient and hence does not accurately represent the interfacial curvature terms. The new implementation will use the level set function to model the interface. The interfacial conditions will then be determined from the exact interface representation to produce accurate flow conditions across the interface.

### 3. Five-Year Schedule

- Year 1: Facility construction, regime identification, preliminary visualizations, development of image reconstruction routines;
- Year 2: Testing of initially selected conditions, development of PIV method for porous media application
- Year 3: Testing phase: influence of capillary number and viscosity ratio under various conditions; start construction on demonstration rig for PI; application of test results toward model development.
- Year 4: Continued testing at UM, shakedown and initial testing at PI; continued model development
- Year 5: Final testing based on feedback from earlier model assessment; final model development

### 4. Results

We are continuing work on determining the proper fluids and solid matrix material that will permit the index-matched experiments. Candidate fluids are aqueous mixtures of zinc iodide and microscopy oils.

We investigated the various imaging options available for determining the high-resolution measurements needed for these flows. Both optical coherence tomography (OCT) and fluorescent confocal microscopy have been identified as potential options.

#### **Synergistic Activities**

In addition to the above technical work, Dr. Riaz and Dr. Kiger traveled to Abu Dhabi to visit the Petroleum Institute, ADNOC and ADCO. The purpose of the trip was to stimulate discussion about problems of common interest related to the physics and modeling of reservoir production and enhanced oil recovery. Two external collaborators, Dr. Hamdi Tchelepi of Stanford University, and Dr. Fathi Boukadi of the University of Louisiana at Lafayette, also made the trip. The group visited the faculty and staff of the Petroleum Institute as well as several managers from ADNOC and the director of operations from ADCO. Continued talks are currently underway with staff from ADCO and faculty at the PI.

### 5. Recommendations for Future Work

The current funding represents an initiation seed program in anticipation of a fully funded project during Phase II or a separate project outside the currently established agreement. As such, the efforts are directed towards developing the computational tools, techniques and test facility that will be needed for the successful completion of the project. The following experimental work will be completed over the next six months:

1. Determine working fluids compatible with viscosity ratio and index of refraction requirements for the experimental technique.
2. Design and construct the initial version of the test cell required for the experiments.
3. Develop the image processing routines needed to determine the interface location and local fluid motion within the pore volumes.

### 6. Publications:

Two papers were submitted for poster presentation at the Energy 2030 conference:

- 1) "Stability of two-phase vertical flow in EOR applications," by A. Riaz & H. Tchelepi
- 2) Turbulent dynamics of particle-laden pipeline flow," by K. Kiger and C.-H. Pan

## Solar Cooling

UM Investigators: Professor Reinhard Radermacher, Dr. Yunho Hwang

GRA's: Ali Al-Alii

PI Investigator(s): Dr. Isoroku Kubo, Dr. Peter Rodgers

Start Date: August 01, 2007

FINAL REPORT

### 1. Abstract/Objectives

The main objective of this project was to design, fabricate and test a solar cooling system with the highest possible cooling COP measured to date. The approach involved combining a very efficient concentrating PV-T collector with a separate sensible and latent cooling approach developed at CEEE. This solar cooling system is expected to operate under the UAE's harsh climate conditions with COPs that are essentially twice as high as those of conventional solar cooling technologies.

### 2. Approach

The electric power generated by the C-PVT collector will be used to produce only sensible cooling at very high COPs of 5 to 6 by using high evaporator temperatures. If, for example, the collector's electric efficiency is 0.15, then this value multiplied by the COP of 6 will yield an overall COP of 0.9 for the sensible portion. The latent load will be accommodated using desiccants regenerated by the solar heat from the C-PVT collector. Assuming the solar thermal efficiency is also 0.4, with a desiccant COP of 0.5, the overall efficiency is for the latent portion is 0.2. The combined COP for both cooling services, latent and sensible, is 1.1. This value is essentially double as high as that for conventional solar cooling technology as shown next.

### 3. Summary of results

- The fundamentals of solar radiation, thermal collectors, PV and thermal cooling processes have been reviewed. A review paper on solar cooling technologies has been published. In addition, the solar thermal collector and the PV technology has been compared to the performance of the photovoltaic/thermal hybrid collector. The best combination between the solar technology and cooling technology has been modeled in TRNSYS.
- The main system components (collector array, vapor compression cycle and desiccant wheel) have been reconsidered and resized separately. Then the modified sub-systems were coupled to design the complete system. The components were redesigned based on Abu Dhabi design conditions.
- The collector array was sized to provide 8 kW<sub>e</sub> and 34 kW<sub>th</sub>. The storage and necessary components to deliver the collector output to the load have also been resized accordingly. Moreover, the VCC was modeled based on a 5-ton unit using R410A from TRANE. Previously, the VCC was modeled in EES, and TRNSYS had to call EES at every time step. To avoid this, the manufacturer's catalog data was arranged in a format that TRNSYS can recognize. In addition, the desiccant wheel cycle has been sized based on ASHRAE's 1% design conditions for Abu Dhabi. Finally, the whole system was simulated by coupling the two sub-systems, and the monthly performance was investigated.
- The expected efficiencies were observed and appear to be realistic based on our model results.

## 4. Results

### Coupling the Solar and Cooling Technologies

A comparison of possible combinations is shown in Figure 1 based on the information gathered on the cooling processes and the various solar collectors.

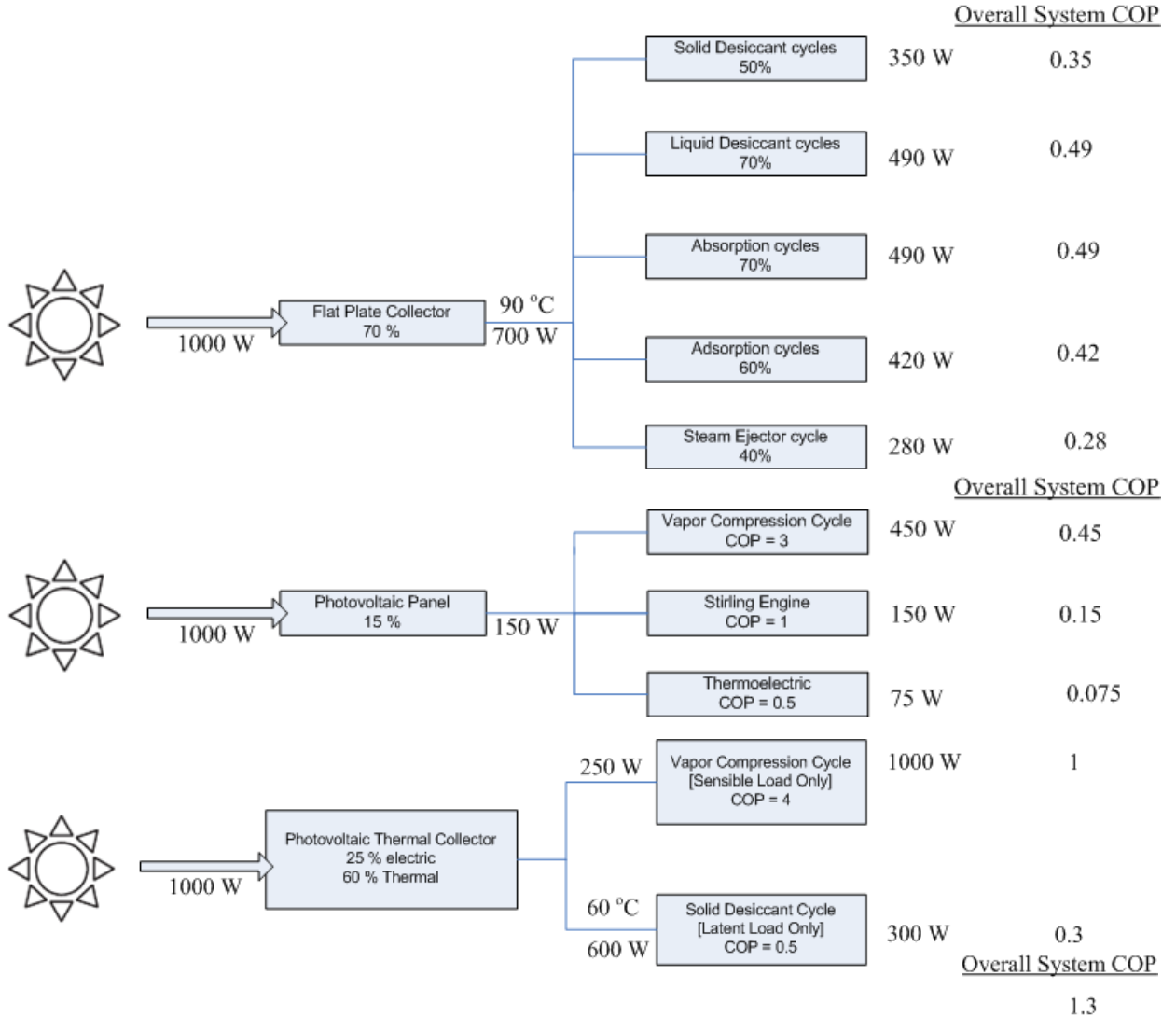


**Figure 1. Various combinations between solar and cooling processes.**

It can be seen that the highest possible overall cooling COP can be achieved by coupling the PV/thermal collector with two cooling processes. The reason for choosing these particular cooling cycles is to accommodate the latent load and the sensible load separately. A solid desiccant cycle, which is derived from the thermal output of the collector, is used to accommodate the latent load. A vapor compression cycle, which is powered by the electric output of the collector, is used to accommodate the sensible load.

The novelty of this combination is that minimal external energy source is needed since the collector is used to provide the electricity and thermal energy required to derive the two cooling cycles. The desiccant cycle lowers the vapor content of the inlet air, allowing the vapor compression cycle to operate at a higher evaporator temperature and pressure, which

decreases the pressure ratio, hence increasing the compressor efficiency. The whole system might be configured as shown in Figure 2.

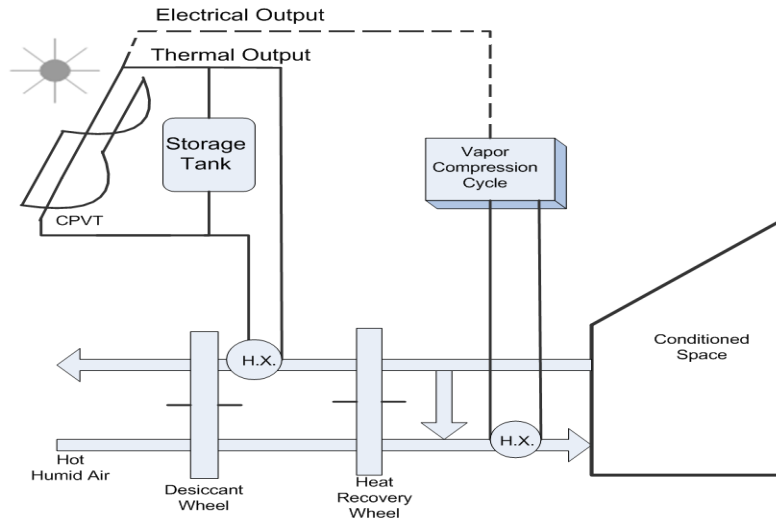


**Figure 2. Possible system configuration.**

### Modeling Methodology

This system is modeled based on Abu Dhabi weather data. Four cities in different US climate zones were also chosen for the investigation of the system performance in various climate conditions. The cities are shown in Figure 3 with their respective latitudes, longitudes and elevations.

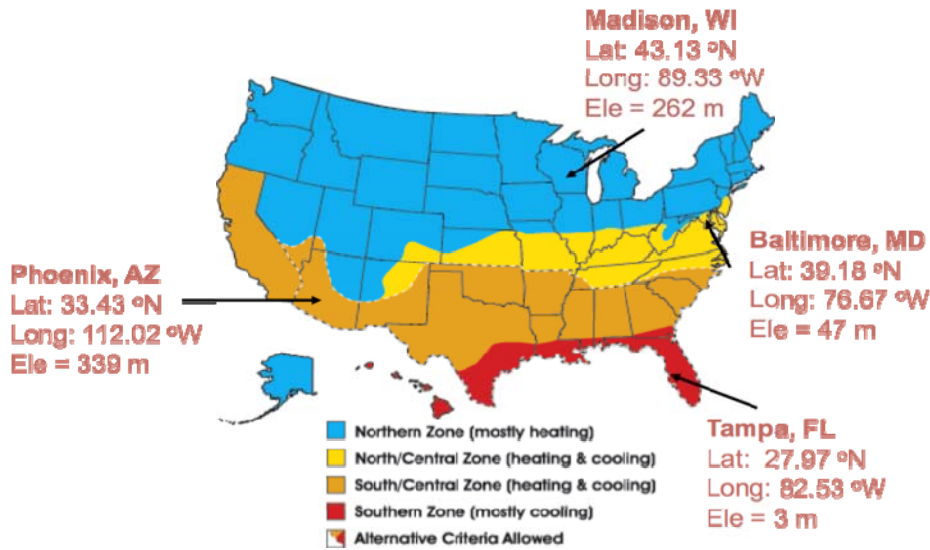


**Figure 3. The selected cities in different US climate zones.**

The modeling approach is shown in Figure 4. By calculating the electrical and thermal supply of the solar sub-system and the required heating and power by the cooling processes, one can calculate the solar fraction of each type of energy provided. For example, a thermal solar fraction and an electrical solar fraction can be calculated as shown below.

$$\text{Thermal solar fraction} = Q_{\text{provided}} / Q_{\text{required}}$$

$$\text{Electrical solar fraction} = E_{\text{provided}} / E_{\text{required}}$$

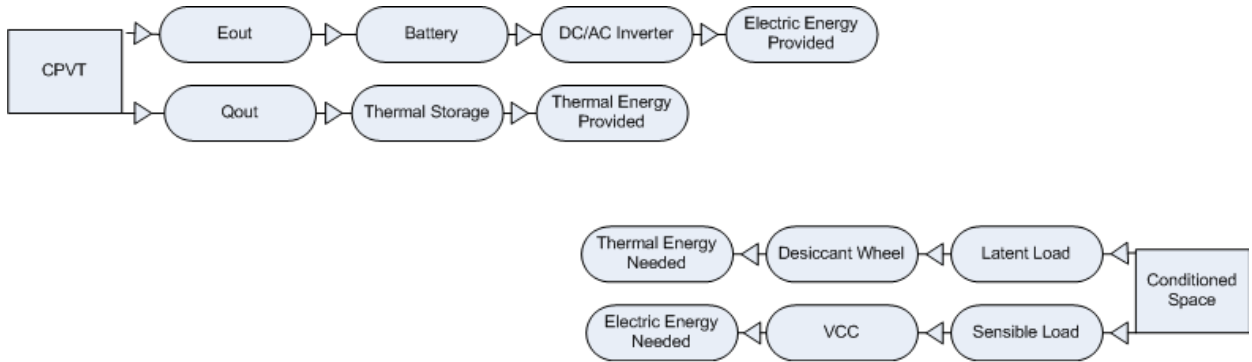


Figure 4. Modeling approach.

The system is modeled with the well-known TRNSYS program. TRNSYS consists of many subroutines that model subsystem components. It is necessary to construct an information flow diagram for the system once all the components of the system have been identified. The information flow diagram for the whole system was created as shown in Figure 5. The purpose of the information flow diagram is to facilitate identification of the components and the flow of information between the various components.

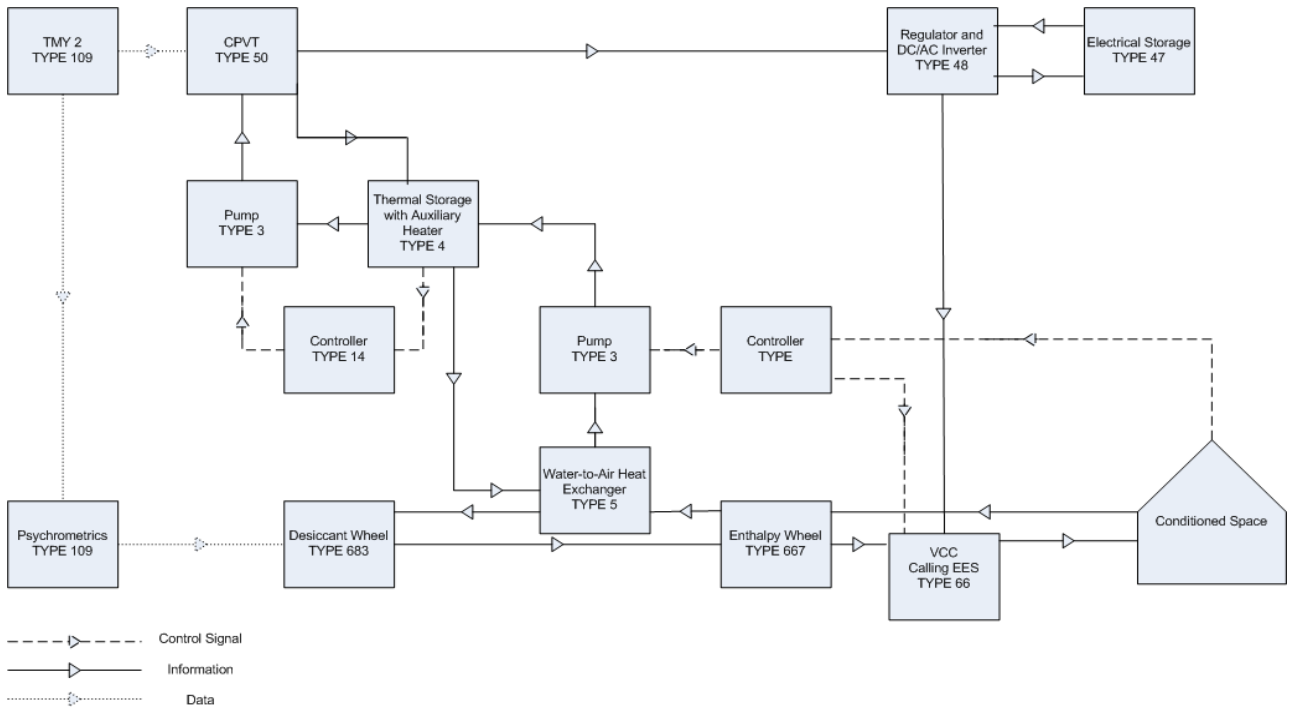
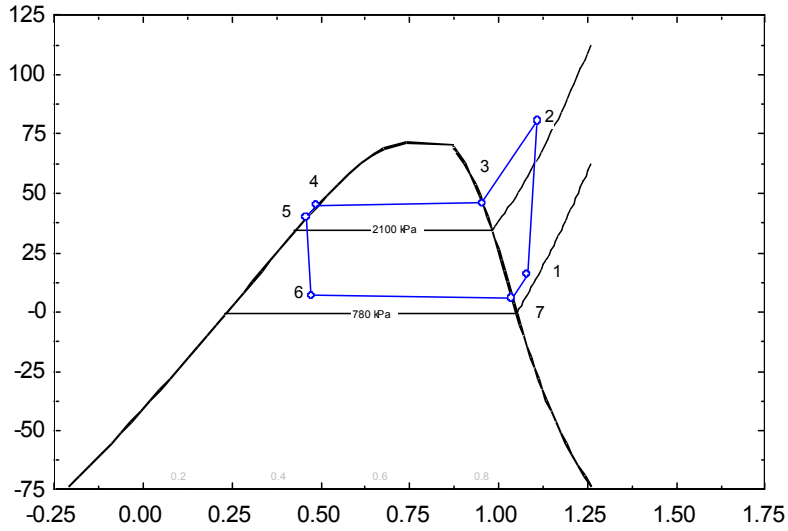
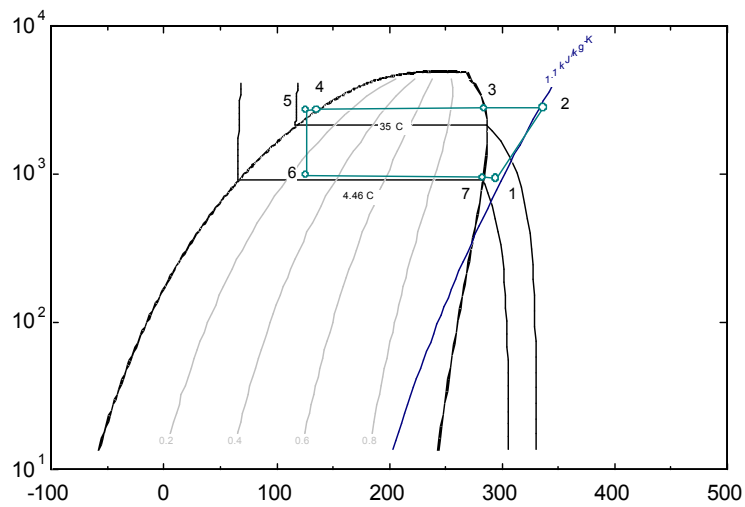


Figure 5. System flow diagram.





**Figure 7. VCC T-S diagram.**



**Figure 8. VCC P-h diagram.**

The desiccant wheel cycle was then modeled in TNRYS. It consists of the desiccant wheel, the enthalpy wheel and two fans. After the two cooling processes were modeled, the conditioned space and the two sub-systems were coupled as shown in Figure 9.

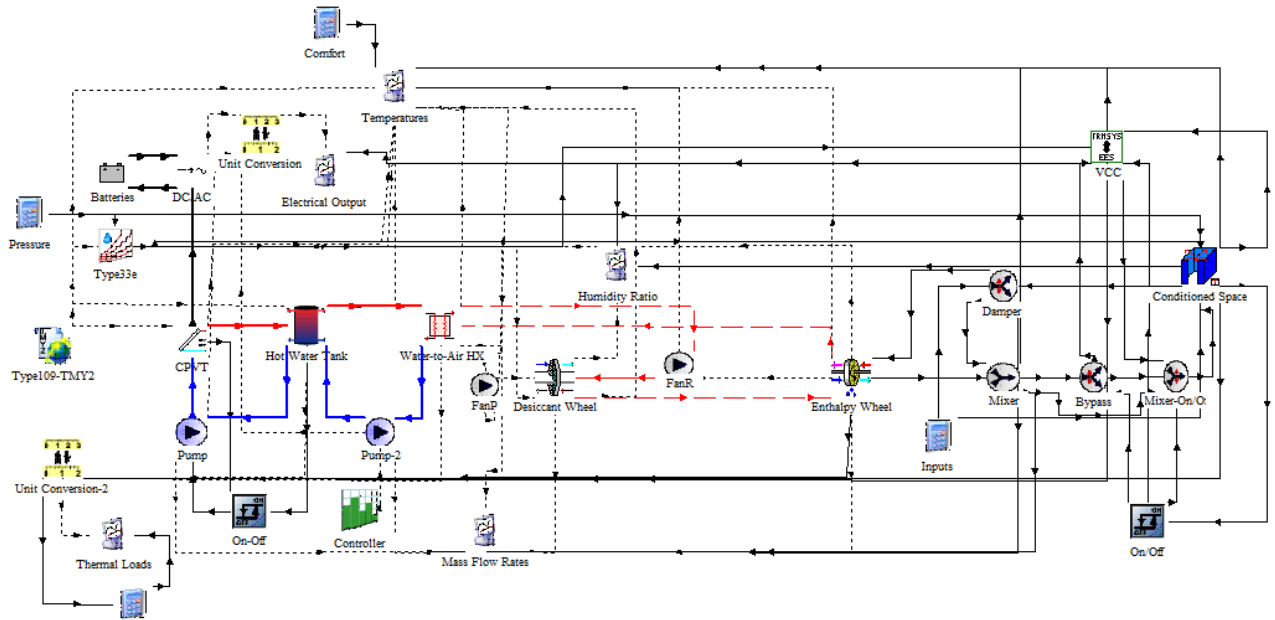


Figure 9. The whole system in TRNSYS.

A brief description of each component's parameters and the TRNSYS module, TYPE, used to model each component, is shown in Table 1.

Table 1. TRNSYS Components

Component	Parameter	value
Weather Data Reading and Processing TYPE 109	Tracking mode	4: Two-axis tracking
	External file [TMY2]	AE-Abu-Dhabi-Intl-412170
Solar Collector TYPE 50	Collector Area	6.5 m <sup>2</sup>
	Plate absorptance dimensionless	0.9
	Thermal conductance between cells and absorber Overall Loss Coeff.	720 kJ/hr.K
	Heat transfer coefficient Heat Transfer Coeff.	20 W/m <sup>2</sup> .K
	Cover plate transmittance	0.9
Thermal Storage Tank TYPE 4	Front loss coefficient for cells Heat Transfer Coeff.	3 kJ/hr.m <sup>2</sup> .K
	Fixed inlet positions	
	Tank volume Volumetric Flow Rate	0.35 m <sup>3</sup>
	Fluid specific heat Specific Heat	4.190 kJ/kg.K
	Fluid density Density	1000.0 kg/m <sup>3</sup>
		-3.0
	Tank loss coefficient	kJ/hr.m <sup>2</sup> .K
	Number of nodes	10
	Height of node Length	0.05 m
	Node containing heating	1
Node containing thermostat	2	
Set point temperature for element 1	45 oC	

Pump TYPE 3	Maximum flow rate Maximum power	100 kg/hr 60 kJ/hr
Desiccant Wheel TYPE 683	Dehumidifier F1 effectiveness Dehumidifier F2 effectiveness	0.08 0.95
Enthalpy Wheel TYPE 667	Rated power	671.1 kJ/hr
Controller TYPE 14	Turns on from 6 AM to 6 PM	
Water-to-Air HX TYPE 5	Specific heat of hot side fluid Specific heat of cold side fluid	4.19 kJ/kg.K 1.005 kJ/kg.K
Batteries TYPE 47	Cell Energy Capacity Cells in parallel Cells in series Charging efficiency Max. current per cell charging Max. current per cell discharge Max. charge voltage per cell	16.7 Ah 12 6 0.9 3.33 A -3.33 A 2.5 V
On-Off TYPE 2	Turns on and off based on pre-set values	
DC/AC Inverter and Regulator TYPE 48	Regulator efficiency Inverter efficiency High limit on fractional state of charge (FSOC) Low limit on FSOC charge to discharge limit on FSOC Inverter output power capacity	0.78 0.96 1 0 0.85 10800 kJ/hr
Unit Conversion TYPE 57	Converts kJ/hr to kW	
Fan TYPE 112	Rated flow rate Rated power Motor efficiency	300 kg/hr 2684 kJ/hr 0.9
Conditioned Space TYPE 660	Total heat loss coefficient Capacitance of zone Volume of zone Initial temperature	1000 kJ/hr.K 24000 kJ/K 250 m <sup>3</sup> 20 °C

Initial humidity ratio	0.005 kgw/kg
Number of adjacent zones	0
Infiltration flow rate	75 kg/hr
Dehumidification set point	0.01 kgw/kg
Corresponds to RH =50% at T = 25 C	

Mixer  
TYPE 11                      Used to mix to stream of moist air

VCC  
TYPE 66                      Calls EES where the VCC with R410A is modeled

It should be mentioned that the purpose of the preliminary code is to insure that there are no errors in running the program and joining all the components. Therefore, the values in the previous table will be modified once the whole system is sized. An example of the system performance under the UAE's climate conditions for the first two weeks of July is shown in Figure 10.

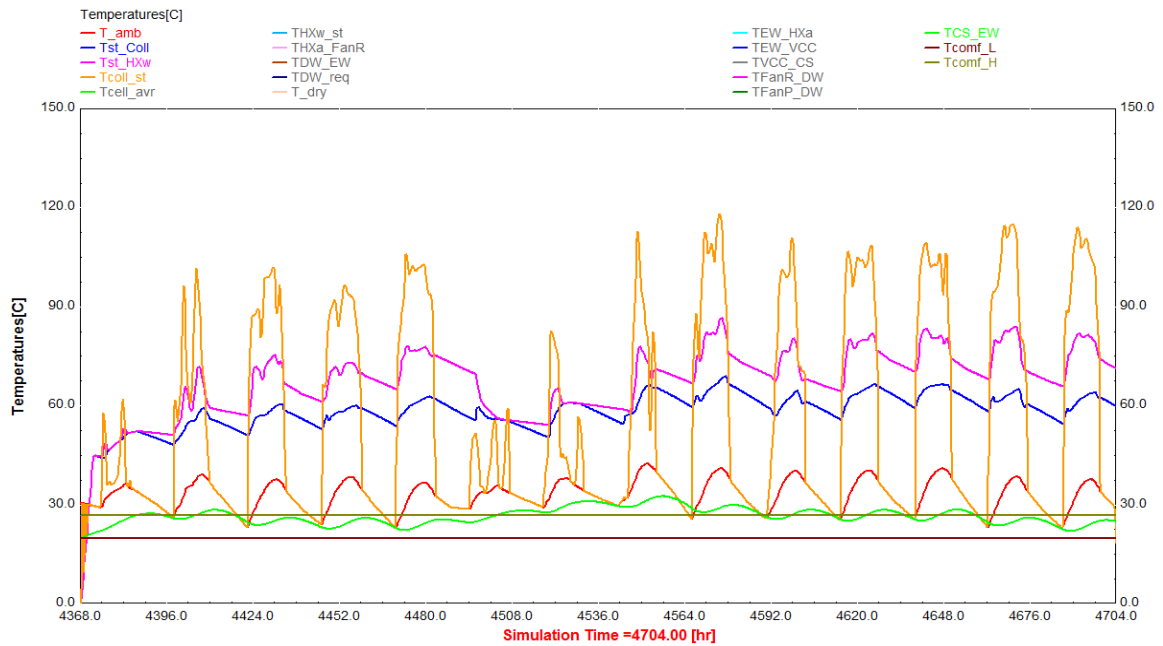


**Figure 10. Temperatures at different locations of the system.**

Orange → Collector outlet temperature  
 Red → Ambient temperature  
 Blue → Temperature of water leaving the storage tank going to the collector  
 Pink → Temperature of water leaving the storage tank going to the water-air heat exchanger  
 Green → Condition space temperature  
 The two straight lines represent the comfort zone in the conditioned space.

The VCC COP is shown below in Figure 11.

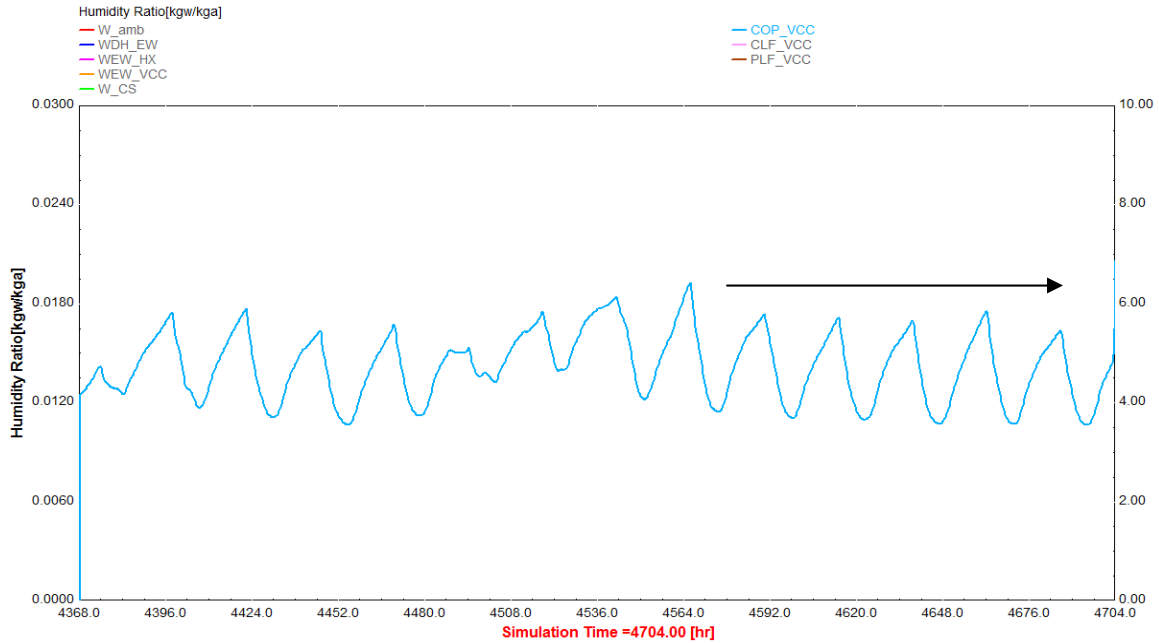


**Figure 11. VCC COP.**

The following main parameters were monitored during each simulation:

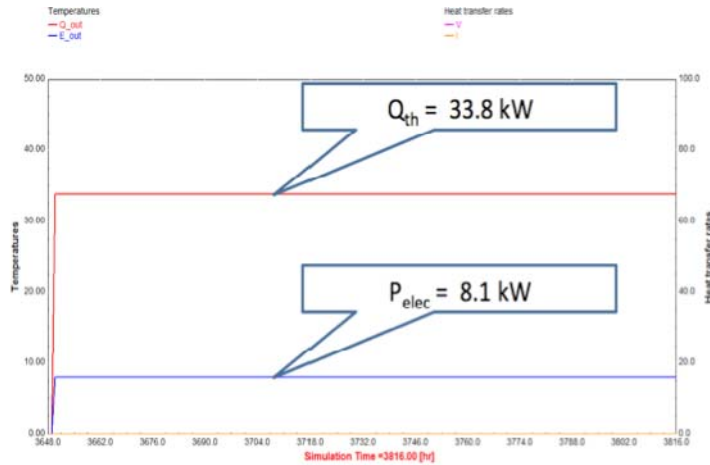
- Mass flow rates
- Temperatures
- Humidity ratio
- Electrical loads
- Thermal loads

### Sizing the Solar Sub-System

The solar sub-system was sized to deliver 8 kW<sub>e</sub> and the 34 kW<sub>th</sub>. In order to achieve this output, different configurations—parallel and series collector arrangements—were tried. The collector was sized based on the following conditions:

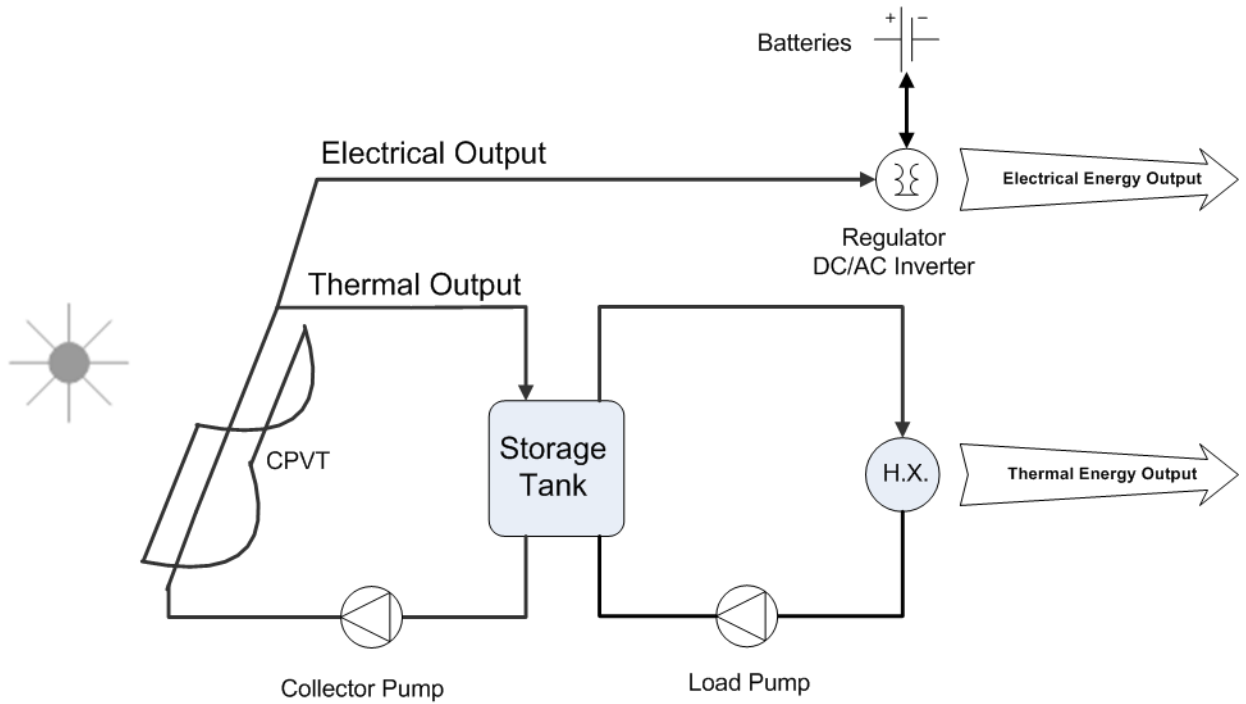
$$\begin{aligned} \text{Total Solar Radiation} &= 800 \text{ W/m}^2 \\ T_{\text{Ambient}} &= 25^{\circ}\text{C} \end{aligned}$$

Figure 12 shows the thermal and electrical outputs of the collectors at the design conditions.



**Figure 12. The CPVT outputs.**

The various electrical components needed to deliver the electrical output to the load were added. In addition, a battery array was used to store excess electrical output. Hot-water storage was also added to store the thermal output. The solar sub-system can be seen in Figure 13.



**Figure 13. Solar sub-system.**

The thermal and electrical performances of the solar sub-system can be seen in Figure 14 and Figure 15, respectively.

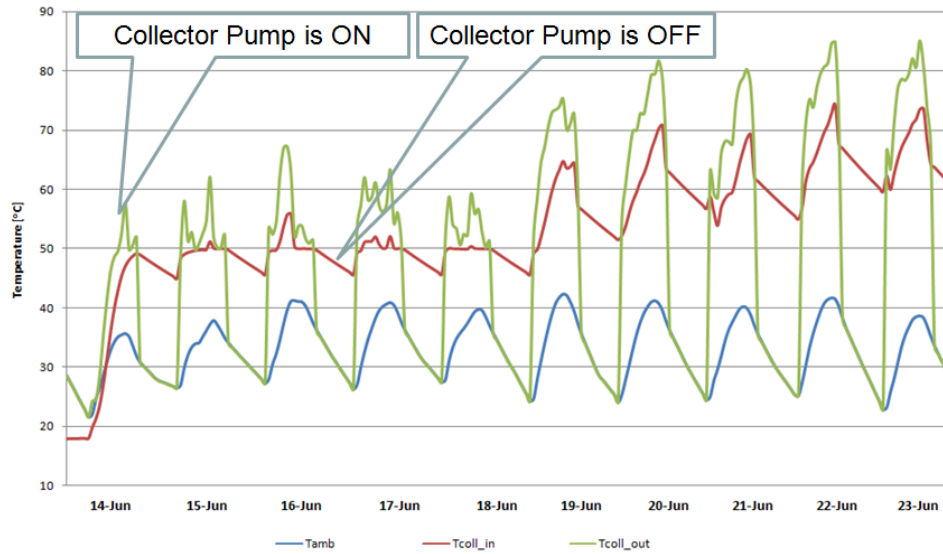


Figure 14. Thermal performance of the solar sub-system.

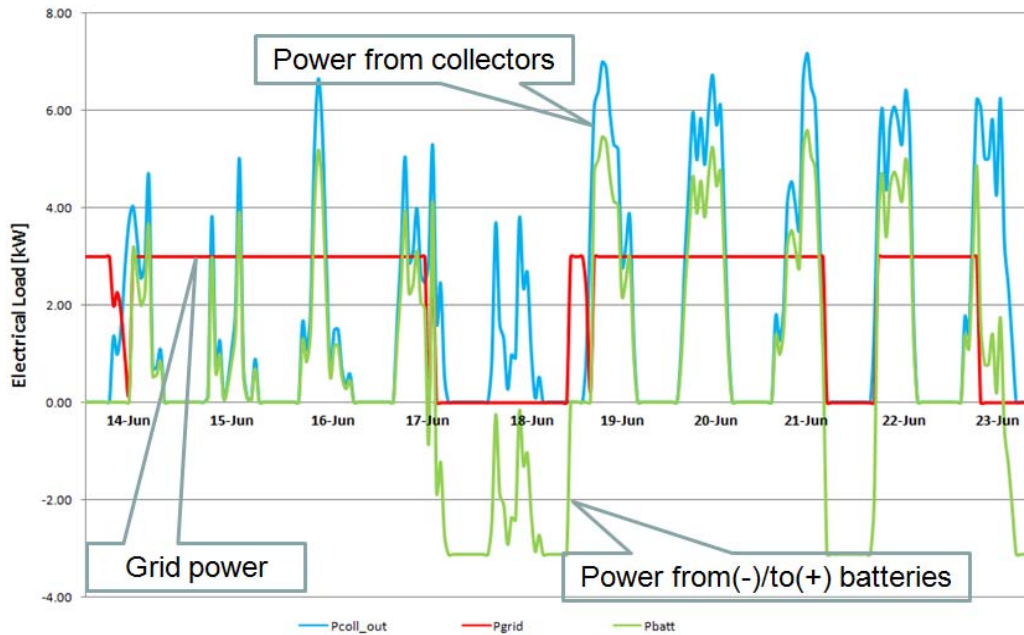


Figure 15. Electrical performance of the solar sub-system.

### Sizing the Cooling Sub-System

A brief survey of the commercially available VCC, using R410A with a cooling capacity of 5 tons, has been conducted and is summarized in Table 2. One major modification to the system is the use of TRNSYS to model VCC instead of EES. The TRNSYS model is capable of calling external files containing the unit's testing data. Therefore, the VCC TRNSYS model will be based on an actual product.

**Table 2. Commercially available VCC using R410A**

Company	Commercial Name	Capacity [Tons]	Price [\$]	Data
Trane	XB13/4TTB3060A	5	Contacted	Contacted
	XR13/4TTR3060A	5		
	XR14/4TTR4060C	5		
York	CZH	5		Available
	CZE	5		
	CZB	5		
Carrier	24ANA1, 24ANA7	5		
	24APA5, 24APA3	5		
	38HDR	5		
	24ACA3, 24ACA4, 24ACR3	5		

The unit chosen is made by TRANE and can provide heating and cooling during the winter and summer, respectively. The data was converted to SI units and arranged in a format that TRNSYS could recognize. A sample of the heating and cooling data files created can be seen in Figure 16.

```

TRANE-R410A_5tons_Cooling - Notepad
File Edit Format View Help
825.91 943.89 1061.88 !Air flow rates in liters per second (l/s)
15.00 17.22 19.44 21.67 !Return air wet bulb temperatures (C)
22.22 23.33 25.56 26.67 !Return air dry bulb temperatures (C)
29.44 35.00 40.56 46.11 !Outdoor air dry bulb temperatures (C)
15.5 13.3 4.3 !Total Cooling(kw), Sensible Cooling(kw) and Power(kw) at 825.91\15\22.22\29.44
14.6 12.9 4.8 !Total Cooling(kw), Sensible Cooling(kw), and Power(kw) at 825.91\15\22.22\35
13.7 12.6 5.2 !Total Cooling(kw), Sensible Cooling(kw), and Power(kw) at 825.91\15\22.22\40.56
12.8 12.2 5.6 !Total Cooling(kw), Sensible Cooling(kw), and Power(kw) at 825.91\15\22.22\46.11
15.5 13.3 4.3

TRANE-R410A_5tons_Heating - Notepad
File Edit Format View Help
825.91 943.89 1061.8
15.56 21.11 23.89 26.67
-16.67 -13.89 -11.11 -8.33 -5.56 -2.78 0.00 2.78 5.56 8.33 11.11 13.89 16.67 19.44 22.22
6.74 3.51 !Heating Capacity(kw) and Power(kw) at 825.91/15.56/-16.67
7.81 3.51 !Heating Capacity(kw) and Power(kw) at 825.91/15.56/-13.89
8.88 3.61 !Heating Capacity(kw) and Power(kw) at 825.91/15.56/-11.11
9.95 3.61 !Heating Capacity(kw) and Power(kw) at 825.91/15.56/-8.33
10.12 3.61 !Heating Capacity(kw) and Power(kw) at 825.91/15.56/-5.56
10.33 3.61 !Heating Capacity(kw) and Power(kw) at 825.91/15.56/-2.78
10.50 3.61 !Heating Capacity(kw) and Power(kw) at 825.91/15.56/0
11.57 3.61 !Heating Capacity(kw) and Power(kw) at 825.91/15.56/2.78
13.97 3.80 !Heating Capacity(kw) and Power(kw) at 825.91/15.56/5.56
16.40 3.90 !Heating Capacity(kw) and Power(kw) at 825.91/15.56/8.33
17.47 4.00 !Heating Capacity(kw) and Power(kw) at 825.91/15.56/11.11
18.54 4.00 !Heating Capacity(kw) and Power(kw) at 825.91/15.56/13.89
19.61 4.10 !Heating Capacity(kw) and Power(kw) at 825.91/15.56/16.67
20.68 4.10 !Heating Capacity(kw) and Power(kw) at 825.91/15.56/19.44
21.75 4.19 !Heating Capacity(kw) and Power(kw) at 825.91/15.56/22.22

```

**Figure 16. Cooling and heating test data files.**

Many TRNSYS runs were carried out to double-check the data files. Then, the vapor compression cycle VCC was sized to provide 15 kW of cooling at 1% ASHRAE design conditions for Abu Dhabi, as shown in Figure 17.

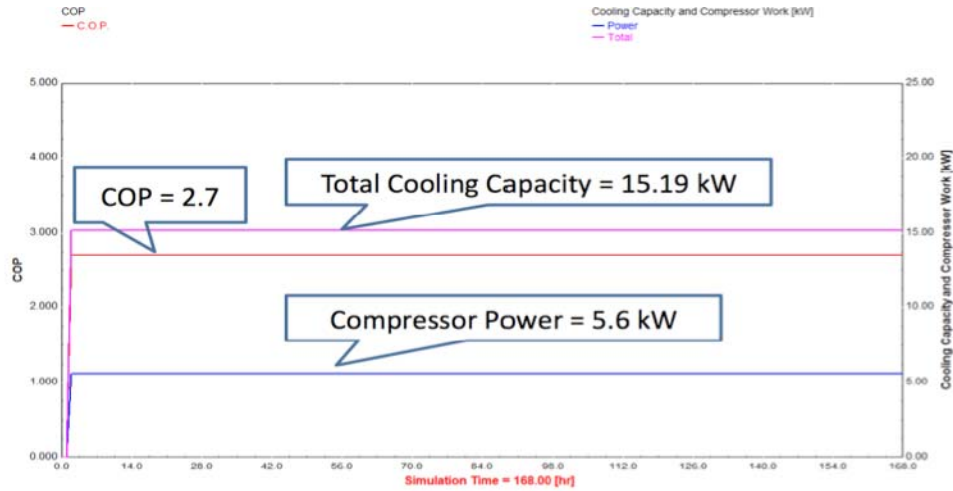


**Figure 17. VCC performance at 1% ASHRAE design condition for Abu Dhabi.**

The sensible and latent loads on the VCC can be seen in Figure 18.

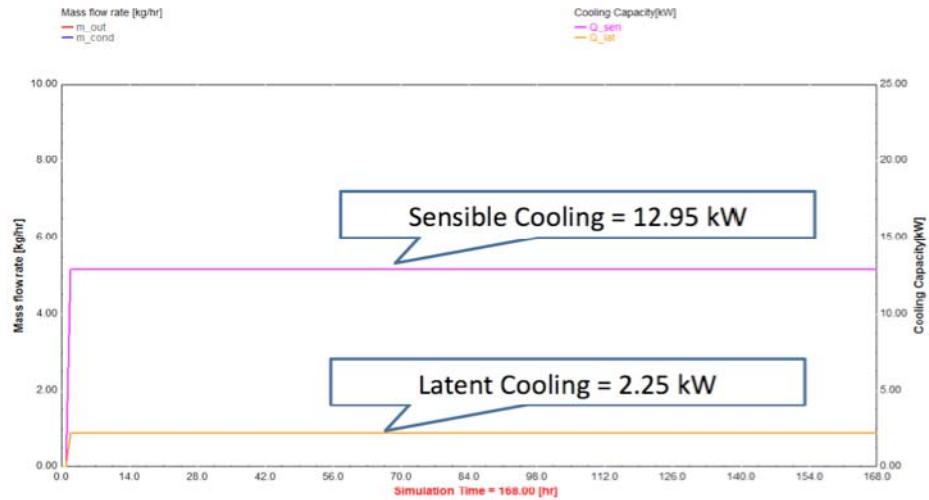


**Figure 18. Sensible vs. latent load on VCC.**

In addition, the desiccant wheel cycle (DWC) was sized to deliver 5 kW at Abu Dhabi 1% ASHRAE design conditions and air mass flow rate of 700 kg/hr. The properties of the inlet-processed air and outlet-processed air are shown in Table 3.

**Table 3. Processed air properties**

	Pro. Air In	Pro. Air Out
T_db [C]	32.8	45.8
W [kgw/kga]	0.0253	0.0099
h [kJ/kg]	98.1	71.7

The DWC was coupled with the VCC to be added to the conditioned space to form the cooling sub-system as shown in Figure 19. The performance of the cooling sub-system was then investigated. The system was sized based on the following conditions:

$$T_{\text{amb}} = 45 \text{ }^{\circ}\text{C}$$



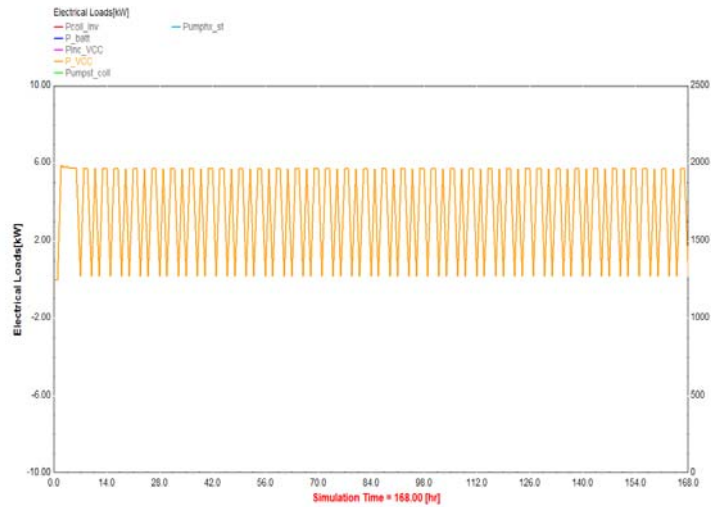


**Figure 21. The VCC power consumption.**

The advantage of the pretreatment of the air by the DWC before entering the VCC can be seen very clearly in Figures 22 and 23. Figure 22 shows the sensible and the latent loads on the VCC when the DWC is on. This figure shows that the DWC accommodates the latent load, whereas the VCC accommodates only sensible load. By treating latent and sensible loads separately, the VCC can be operated at higher evaporator pressure, hence reducing the cycle pressure ratio and increasing the compressor efficiency. Figure 23 shows the case when the DWC is turned off. In this case, more loads have to be taken care of by the VCC latent and sensible loads, which increase the power consumption.

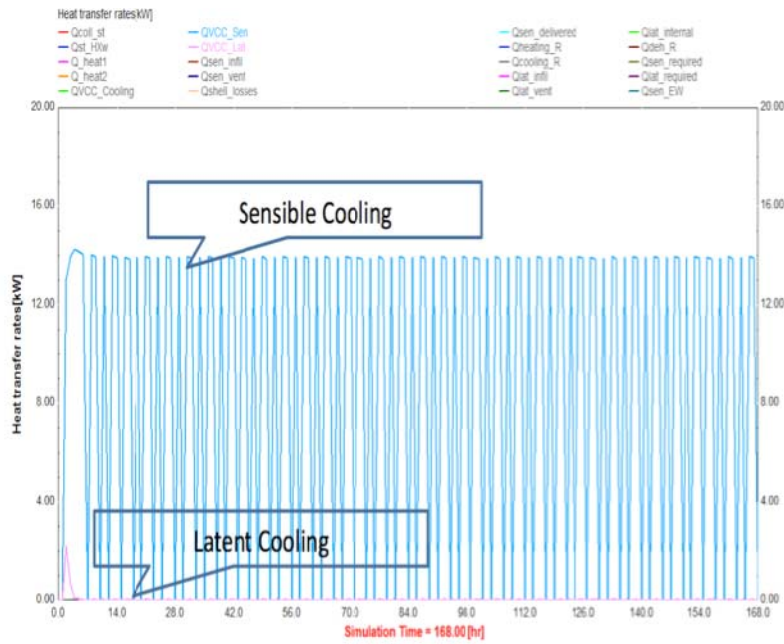


**Figure 22. VCC loads when DWC is ON.**

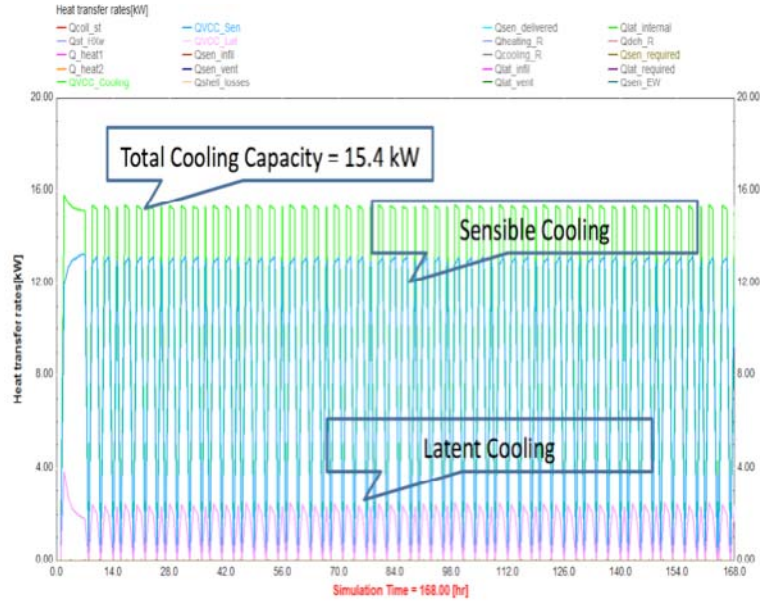


**Figure 23. VCC loads when DWC is OFF.**

The temperature and humidity ratios at various points in the cooling sub-system are recorded, as shown in Figure 24. The processes that the air goes through can be seen in Figure 25.

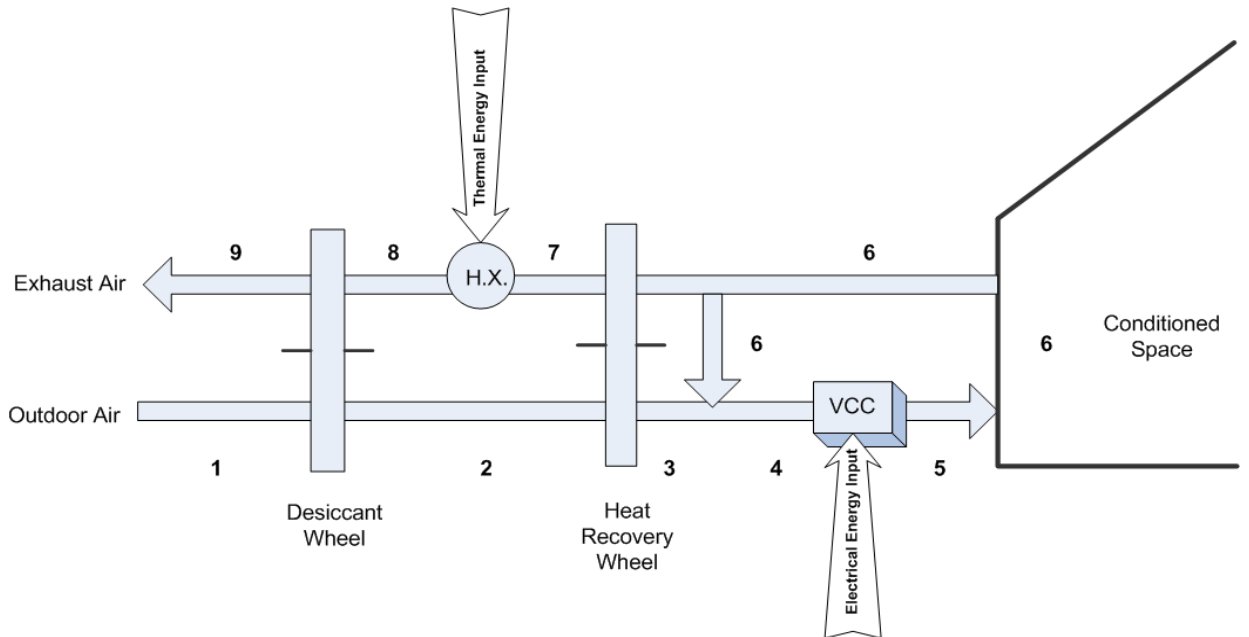


**Figure 24. State points in the cooling sub-system.**

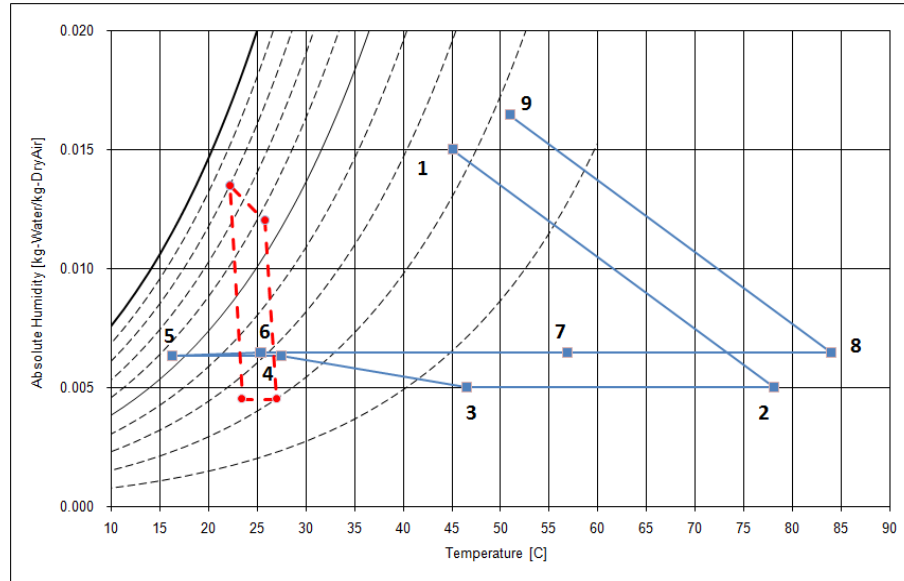


**Figure 25. Air state points in various locations in the cooling sub-system.**

The ambient air, state 1, goes through dehumidification and heating when it passes through the desiccant wheel. The air then is sensibly cooled by the rejected heat from the conditioned space's ventilation air through the heat recovery wheel. After that, the air is mixed with the recirculating air, state 4. The fresh air is cooler and drier than the ambient conditions even before going through the VCC. State 5 is the state of the air leaving the VCC going into the conditioned space. State 6 represents the conditioned space, and state 7 is the regeneration air leaving the building after the heat recovery wheel. The purpose of the thermal output of the solar collector is to move the air from state 7 to 8 by using the water-air heat exchanger. Finally, the regeneration air is heated and humidified after passing through the desiccant wheel.

### Constructing the Solar Cooling System

The solar sub-system is coupled with the cooling sub-system to form the complete system, as illustrated in Figure 26.

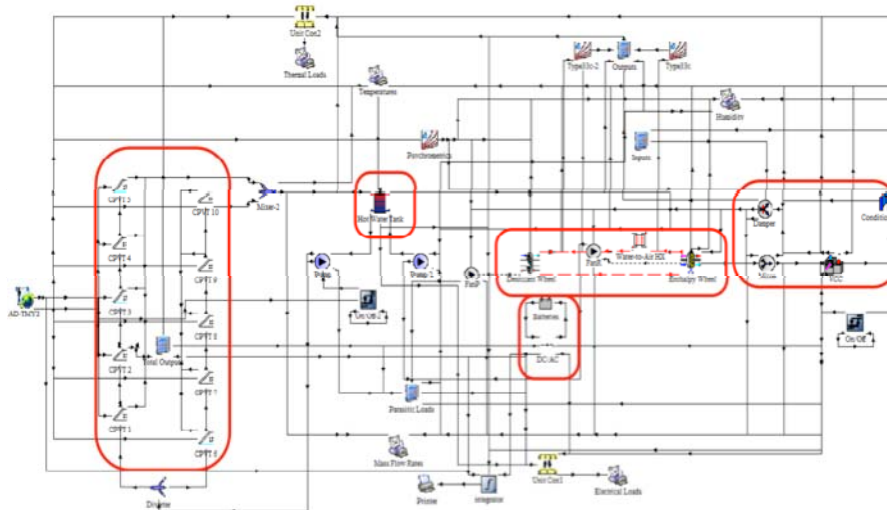


**Figure 26. Complete solar cooling system.**

The difference between the monthly total solar radiation on a horizontal surface and a surface with a two-axis tracking system for Abu Dhabi is shown in Figure 27.

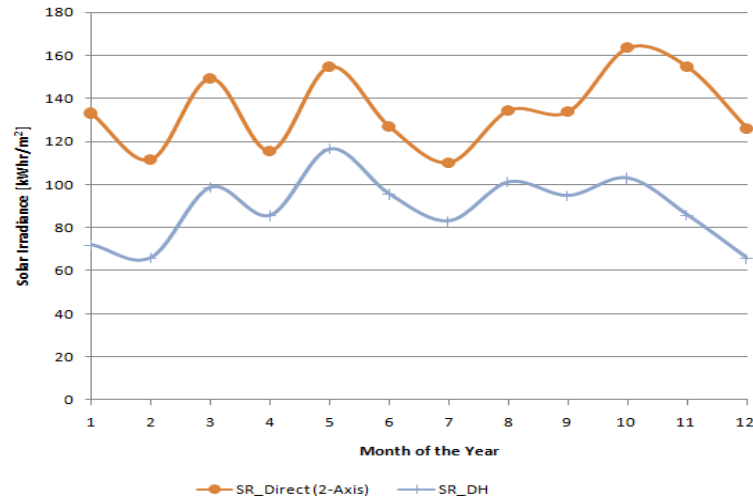


**Figure 27. Monthly solar radiation.**

The monthly thermal performance of the whole solar cooling system is shown in Figure 28.

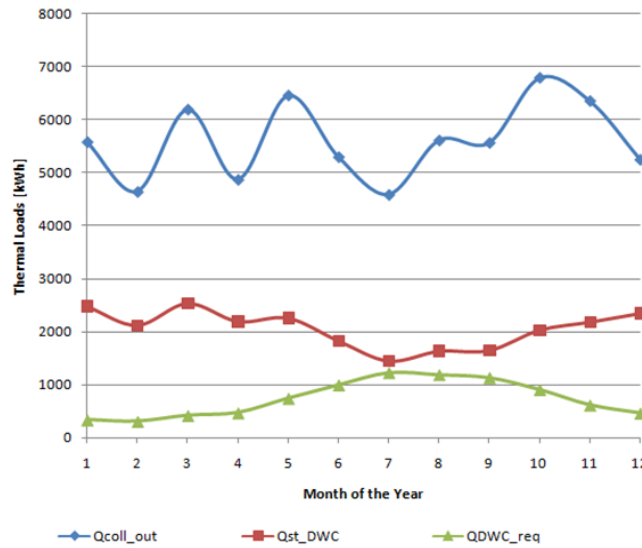


**Figure 28. Thermal performance of the solar cooling system.**

The figure shows that the total amount of heat provided by the hot water storage tank is higher than what is required to regenerate the DWC.

The monthly electrical performance of the solar cooling system is shown in Figure 29. The figure shows that grid power is needed only in July and August, due to the increase in the VCC required electricity during these two months and the lower solar radiation available.

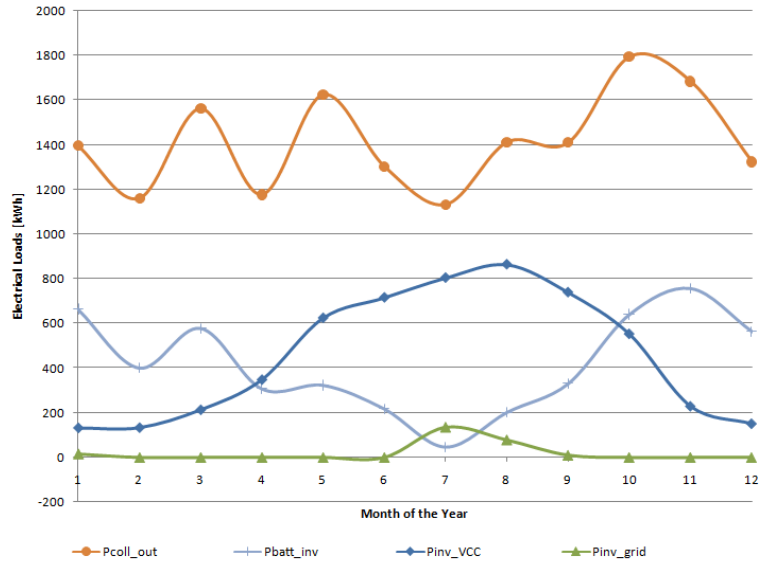


**Figure 29. Electrical performance of the solar cooling system.**

The monthly variation of the latent and sensible loads on the VCC is shown in Figure 30. It can be seen that the latent load represents a small fraction of the VCC load even during summer.

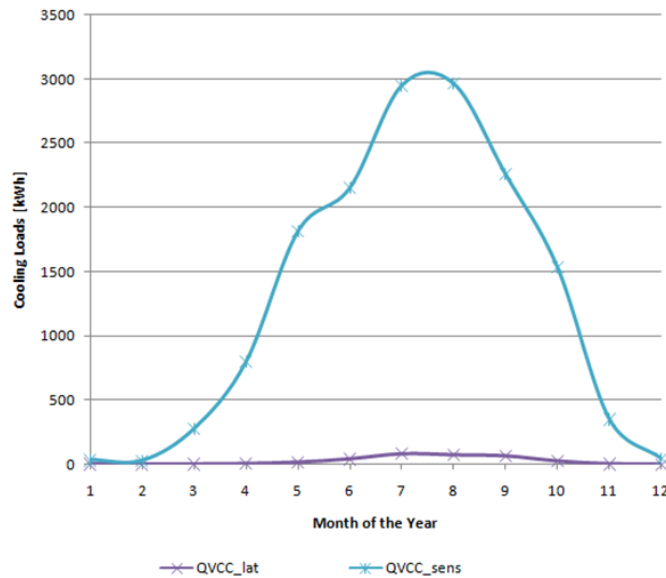


**Figure 30. Monthly latent and sensible loads on the VCC.**

The hourly temperature and humidity ratio of the conditioned space is plotted in Figure 31. The summer and winter comfort zones are defined based on ASHRAE guidelines. It can be seen that the conditions inside the space are always kept within the comfort zones.

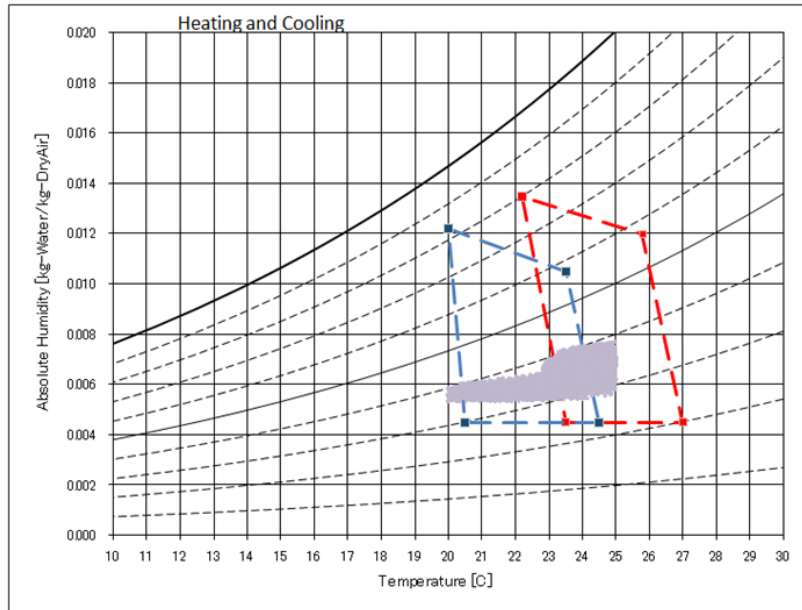


**Figure 31. Space conditions.**

The main system components (collector array, vapor compression cycle and desiccant wheel) have been reconsidered and resized separately. Then the modified sub-systems were coupled to construct the complete system. The components were redesigned based on Abu Dhabi design conditions.

The collector array was sized to provide 8 kWe and 34 kWth. The storage and necessary components to deliver the collector output to the load have also been resized accordingly. Moreover, the VCC was modeled based on a 5-ton unit using R410A from TRANE. Previously, the VCC was modeled in EES, and TRNSYS had to call EES at every time step. To avoid this, the manufacturer's catalog data was arranged in a format that TRNSYS can recognize. In addition, the desiccant wheel cycle has been sized based on ASHRAE's 1% design conditions for Abu Dhabi. Finally, the whole system was constructed by coupling the two sub-systems, and the monthly performance was investigated.

## 5. Recommendations for Future Work

Future work should focus on the experimental verification of the proposed new solar cooling technology. The data will then be used to verify the model. The next step would be to design and fabricate a prototype that will then be installed in a field test in the UAE.

## 6. Conclusion

The model results have borne out the expectation that the proposed system is feasible and that the expected high efficiencies seem realistic and can be reproduced in an experimental setting. Experimental verification is the next most important step.

## 7. References

- [1] Stine, W.B., Geyer, W.B., 2001, Power from the sun, [www.powerfromthesun.net](http://www.powerfromthesun.net).
- [2] Threlkeld, J, Kuehn, T., Ramsy, J., 1998, Thermal Environmental Engineering, Prentice-Hall, Inc, USA
- [3] [http://www.nrel.gov/rredc/solar\\_data.html](http://www.nrel.gov/rredc/solar_data.html)
- [4] [http://rredc.nrel.gov/solar/old\\_data/nsrdb/tmy2/State.html](http://rredc.nrel.gov/solar/old_data/nsrdb/tmy2/State.html)

- [5] Notton, G., Poggi, P., Cristofari, C., 2006, Predicting hourly solar irradiations on inclined surfaces based on the horizontal measurements: Performances of the association of well-known mathematical models, *Energy Conversion and Management*, 47 1816–1829
- [6] [http://rredc.nrel.gov/solar/old\\_data/nsrdb/1991-2005/siteonthefly.cgi?id=724060](http://rredc.nrel.gov/solar/old_data/nsrdb/1991-2005/siteonthefly.cgi?id=724060)
- [7] ASHRAE, 1999, Applications Handbook, CH.32
- [8] Kreith, F. and Kreider, J.F., 1978, Principles of solar engineering, *Hemisphere publishing corporation* Washington USA
- [9] Kalogirou, S., 2004, Solar thermal collectors and applications, *Progress in Energy and Combustion Science* 30 pp. 231–295
- [10] Goswami, Y., Kreith, F. and Kreider, J.F., 2000, Principles of solar engineering, *Taylor and Francis*, PA, USA,
- [11] Duffie, J.A., Beckman, W.A., 1991, *Solar engineering of thermal processes*, Second edition, John Wiley & Sons, Inc., New York, ISBN: 0-471-51056-4.
- [12] Pasupathy, A., Velraj, R., Seeniraj, R.V., 2008, Phase change material-based building architecture for thermal management in residential and commercial establishments, *Renewable and Sustainable Energy Reviews*, pp.39–64
- [13] Dieng, A., Wang, R. , 2001 Literature Review on Solar Adsorption Technologies of Ice-making and Air Conditioning Purposes and Recent Developments in Solar Technology, *Renewable and Sustainable Energy Reviews* 5 pp.313–342
- [14] Sumathy, K., Yeung, K, Yong, L., 2003, Technology Development in the Solar Adsorption Refrigeration Systems, *Progress in Energy and Combustion Science* 29 pp 301–327
- [15] Roger, A. Messenger, J. V., 2005, Photovoltaic Systems Engineering, 2nd ed. Taylor & Francis
- [16] <http://www.nfpa.org/>
- [17] <http://ieeexplore.ieee.org/iel5/7946/21930/01019771.pdf?arnumber=1019771>

## Publications

### Journal Papers:

1 - Hwang, Y., Radermacher, R. ,Al Alili, A., Kubo, I., 2008, Review of Solar Cooling Technologies, *HVAC&R RESEARCH*, VOLUME 14, NUMBER 3, pp. 507-528

### Conference Papers:

Submitted to ENERGY 2030:

2 - Al-Alili, A., Hwang, Y., Radermacher, R., Kubo, I. and P. Rodgers, 2008, "High Efficiency Solar Cooling Technique" *Energy 2030*, Abu Dhabi, UAE

## Visits

Reinhard Radermacher visits to PI:

July 25-28, 2006: With Mike Ohadi visiting German Universities

June 16-20, 2006, Commencement

October 28-11/03, 2006 Energy 2030

October 20-23, 2007 Research Collaboration

January 03-06, 2008: Collaboration Workshop

November 01-04, 2008 Energy 2030

## GRAs (names, degrees, graduation)

Ali Al-Alili, PhD, December 2010

## Waste Heat Utilization in the Petroleum Industry

UM Investigators: Professor Reinhard Radermacher, Dr. Yunho Hwang

GRA's: Amir Mortazavi, Chris Somers

PI Investigator(s): Dr. Saleh Al Hashimi, Dr. Peter Rodgers

Research student: Sahil Popli

Start Date: December 1, 2006

FINAL REPORT

### 1. Objective/Abstract

The main objective of this project is to minimize overall energy consumption of gas or oil processing plants by utilizing waste heat and/or improving cycle design. Consideration will include use of absorption chillers and two-phase expanders, among other options.

Model thermal systems that serve as waste heat sources and/or users

1. Modeling of propane chillers
2. Modeling the APCI LNG plant
3. Modeling of the gas turbine at different ambient and part load conditions.
4. Modeling of various absorption chiller designs

### 2. Justification and Background

Waste heat utilization opportunities are abundant in the oil and gas industry. Proper use of waste heat could result in improved cycle efficiency, reduced energy usage, reduction in CO<sub>2</sub> emissions, and increased production capacity.

CEEE at the University of Maryland has extensive experience in the design and implementation of integrated combined cooling, heating, and power (CCHP) projects. The faculty at PI has experience in the design and operation of petroleum processing plants. Jointly the team is well equipped to address the challenge posed by this project.

### 3. Approach

1. Assess waste heat (WH) sources (PI)
2. Assess WH conversion processes (UM)
3. Assess utility requirements (PI)
4. Match WH sources/processes and utility requirements (PI, UM)
5. Develop/implement of software for system analysis (PI, UM)
6. Rank and propose implementation of 1 or 2 preferred systems (PI, UM)
7. Define additional R&D as needed (PI, UM)

### 4. Two-Year Schedule

June 1, 2007	Report assessing WH sources and utility requirements
June 1, 2007	WH conversion options report
Oct. 1, 2007	Useful version of software
Apr. 31, 2008	Ranking of systems and selection
Nov. 31, 2008	Report recommended steps forward

### 5. Summary of Results

1. Overall, as much as 40MW of cooling capacity can be saved, reducing electricity demand by 15MW for a single plant.

2. Relevant gas turbine-related research  
Two gas turbines, the GE MS6001 and MS9001 were modeled for future use. Both models had very small discrepancies with vendor data (less than 2%).
3. APCI base cycle-related research  
The APCI cycle was chosen because it is the most commonly used design. Modeling the base cycle allows for a base design for comparison when improvements are being considered.
4. Enhancements to APCI cycles  
The APCI base cycle could be improved by replacing valves with expanders. Depending on the types of expanders used, nearly 5 MW could be saved, while LNG production could be increased by over 1 kg/s. In the future, absorption chiller models will be used to supplement the cooling load in the propane cycle, which will result in further energy reduction.
5. Single and double effect water/Lithium Bromide absorption chillers and single effect Ammonia/Water chiller Simulation in ASPEN  
The three chiller models were verified against EES models and found to have less than 5% discrepancy. Each model requires only known values (evaporator temperature, ambient temperature, etc) and gives all desired results (COP, capacity, etc.) These models can be used as part of a larger strategy to investigate energy savings in LNG plant design.
6. Driver/chiller integrated models in ASPEN  
These models will give an estimate of the amount of cooling available when an absorption chiller is used to recover waste heat from a large gas turbine that might be used in an LNG plant. They will also be used to conduct parametric studies.

### Gas Turbine Model

GE MS6001 gas turbine was modeled for:

- Quantifying the available of waste heat from one of the gas turbines at TAKREER refinery.
- Driving propane cycle.

The schematic diagram of the model is shown in Figure 1. In Table 1 the model results are compared with vendor data. It should be noted combustion process was considered in this model.

**Table 1. The MS 6001 gas turbine model results in comparison with vendor data.**

	Vendor Data	Model	Discrepancy
Output Power [MW]	43.53	42.84	1.58 %
Exhaust Temperature ° C	544	548	4 ° C
Efficiency %	33.3	34.4	3.22 %
Exhaust flow rate kg/sec	140	140	---



## Natural Gas Liquefaction and Fractionation Modeling

The APCI liquefaction process was selected for modeling because ADGAS and about 77% of LNG plants are utilizing this technology for natural gas liquefaction. Therefore, the improvements could be applicable to the majority of LNG plants. The schematic diagram of process is shown in Figure 3.

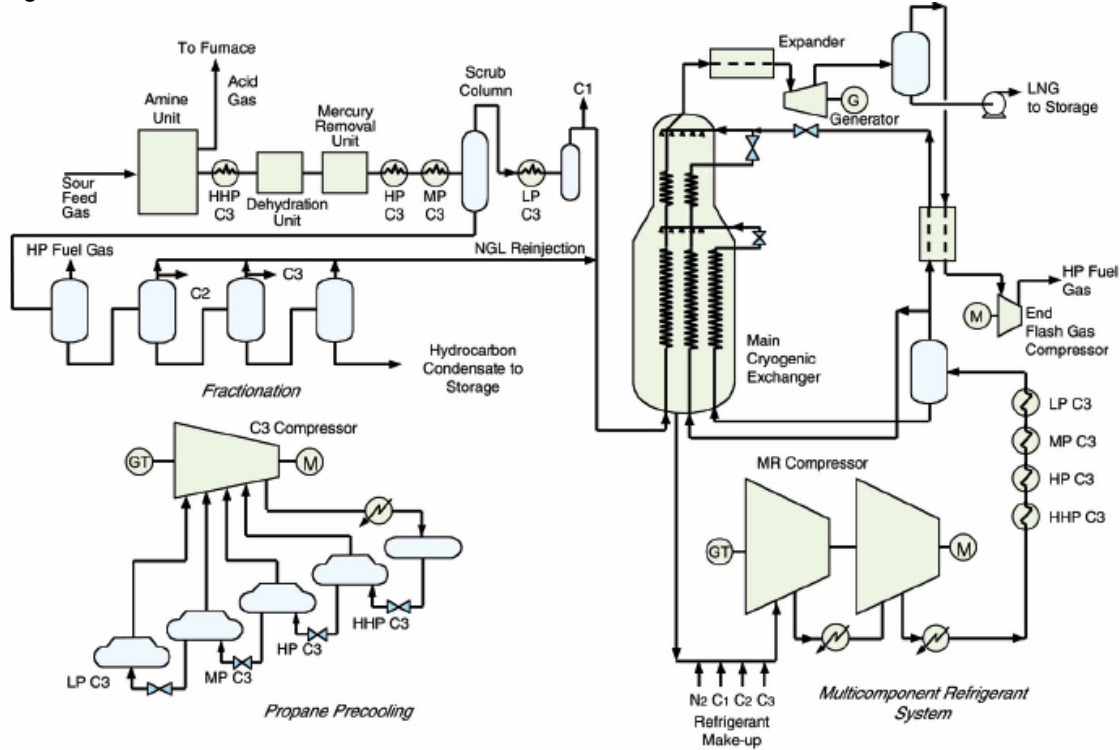


**Figure 3. Schematic diagram of APCI Liquefaction process[3].**

For the sake of simplicity, the gas sweetening process and flash gas utilization were not considered in modeling. The schematic diagram of the model is shown in Figure 4. The model is capable of simulating:

1. Different natural gas compositions liquefaction and fractionation processes
2. Process for different product purity requirements
3. Different vapor fraction at LNG process.
4. The effect of ambient temperature on performance of the LNG plant
5. The effect of new components on plant efficiency and capacity
6. The effect of plant components' efficiency degradations on performance of the LNG plant

An example of natural gas composition is shown in Table 3, and the assumptions are shown in Table 4. The results are given in Tables 5 and 6.

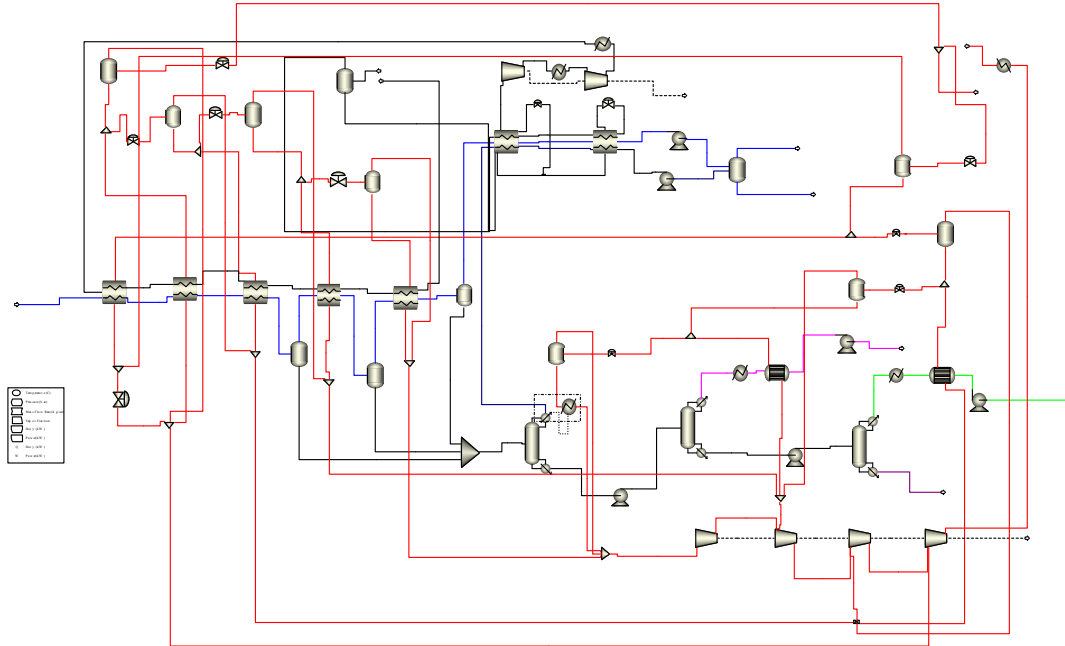


**Figure 4. Schematic diagram of ASPEN model.**

**Table 3. Assumed feed gas composition**

Gas composition after sweetening	
Component	Mole percent
Nitrogen	0.1
Carbon Dioxide	0.005
Methane	85.995
Ethane	7.5
Propane	3.5
i-Butane	1
n- Butane	1
i-Pentane	0.3
n-Pentane	0.2
Hexane Plus	0.4
total	100

**Table 4. Model assumptions**

Sea water temperature	35 ° C
Propane compressor efficiency	83 %
Mixed refrigerant compressor efficiency	86%
Feed gas mass flow rate [kg/s]	111.11

**Table 5. Product composition results**

Component	Mole fraction
Nitrogen	0.00101821
Carbon dioxide	5.1739e-05
Methane	0.88945969
Ethane	0.07694433
Propane	0.02459356
Iso- butane	0.00417114
N- Butane	0.00322346
N-Pentane	0.00016162
Iso-Pentane	0.00033784
N-Hexane	9.1746e-06
Iso-Hexane	2.9206e-05

**Table 6. Plant results**

Propane compressor power [MW]	35.34
Mixed refrigerant compressor power [MW]	66.535
Propane cycle cooling capacity [MW]	115.466
Mixed refrigerant cycle cooling capacity [MW]	165.475
Propane cycle COP	3.267
Mixed refrigerant Cycle COP	2.487
LNG Vapor fraction after the expander %	0.05

## APCI Cycle Enhancements

Cycle efficiency could be improved by replacing expansion valves with expanders. These options were modeled in ASPEN and were evaluated based on both energy efficiency and capacity improvements. Gas expanders are a readily available technology and typically exist at high efficiencies (>70%). Liquid turbines are a well-developed technology, and may be available with efficiencies over 90%. Two-phase expanders are under development with current efficiencies in the vicinity of 80%. The effect of replacing expansion valves with liquid turbines and gas expanders was examined. These results are shown in Table 7. To illustrate the difference between the APCI base liquefaction cycle and the cycle improved with LNG, MXR\* and propane expanders, the improved cycle ASPEN model diagram is shown in Figure 5.

**Table 7. The effects of replacing expansion valves with expanders**

Option	Compressor Power [MW]	Power Generation [MW]	LNG Production [kg/s]
APCI base cycle	101.875	-----	98.831
APCI improved with LNG expanders	101.875	0.648	100.06
APCI improved with both LNG and MXR* expanders	101.188	1.849	100.06
APCI improved with LNG, MXR* and propane expanders	100.706	3.911	100.06

\* MXR: Mixed Refrigerant

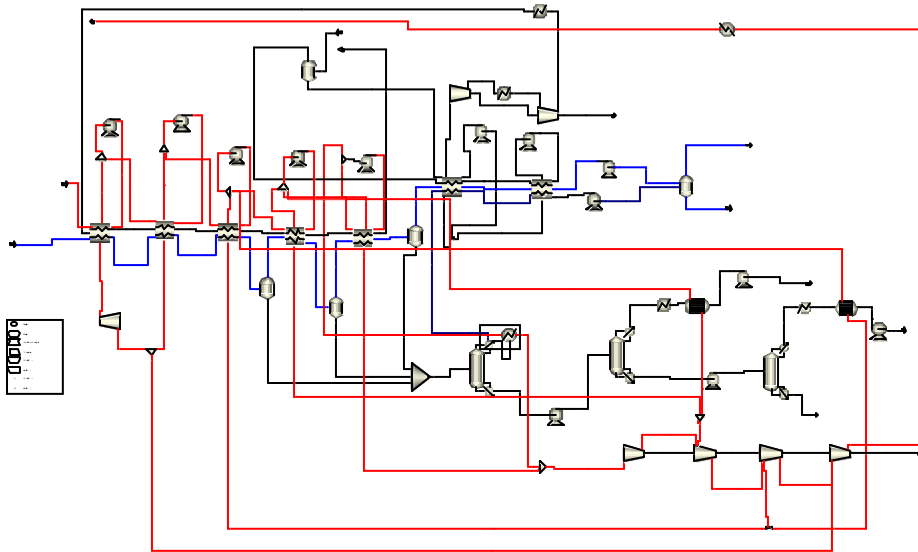


**Figure 5. ASPEN model diagram for APCI cycle improved with LNG, MXR\* and propane expanders.**

## Absorption Chiller Modeling

Absorption chillers were modeled as a means of utilizing waste heat. They take waste heat from a gas turbine and convert it into a cooling load to reduce the energy demands of the propane chiller cycle.

The two main designs employ ammonia/water and water/lithium bromide, respectively, each with various advantages and disadvantages. Additionally, either design can be single- or double-effect. The double-effect sacrifices simplicity for higher COP. For this project, both single- and double-effect water/LiBr and single-effect ammonia/water were modeled.

The main obstacle in modeling chillers in ASPEN was finding a suitable property method. This was an issue because absorption chillers operate at subcooled temperatures, for which limited property data were available. Beyond finding a suitable property method, the main challenge was decomposing the chiller into suitable components that ASPEN could model. The model is shown in Figure 3. The desorber was particularly complicated because it is where the solution and water are separated.

Now that these models have been completed, they will be integrated into the plant cycle models as part of a larger optimization strategy.

## Single-Effect Water/Lithium Bromide Cycle

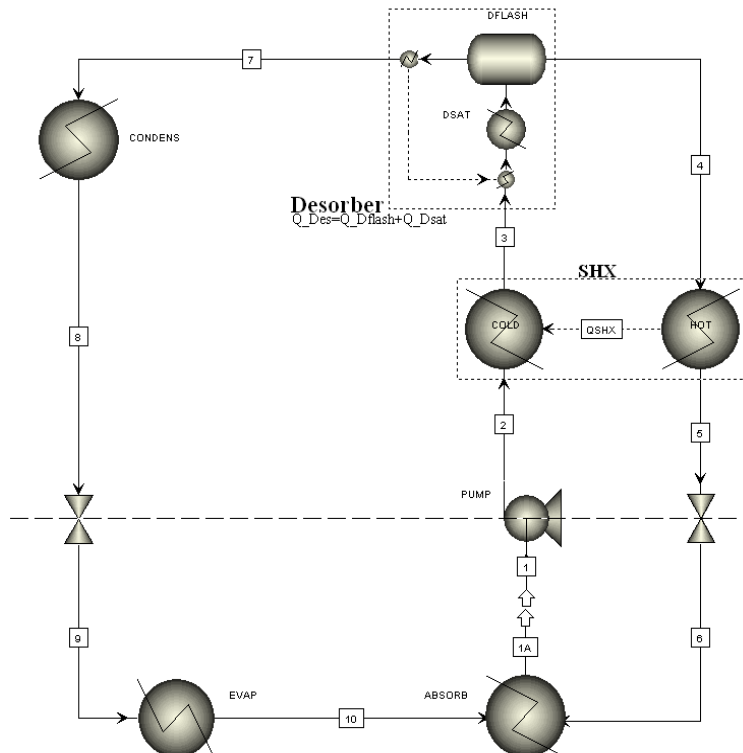


Figure 6. Single-effect water/lithium bromide model.

The model was compared to the EES model as summarized in Table 2. The errors are acceptable, being in the range of 4% or less.

**Table 8. Single-effect water/lithium bromide model accuracy.**

Parameter	Units	EES	ASPEN	% Error
Q absorber	kW	14.297	13.700	4.18%
Q condenser	kW	11.427	11.393	0.30%
Q desorber	kW	14.952	14.350	4.03%
Q evaporator	kW	10.772	10.746	0.24%
COP	N/A	0.720	0.749	3.94%

### Double-Effect Water/Lithium Bromide Cycle

Using a similar technique, a double-effect absorption chiller was also modeled. Double-effect chillers provide higher COP's but have more components and require higher-temperature waste heat.

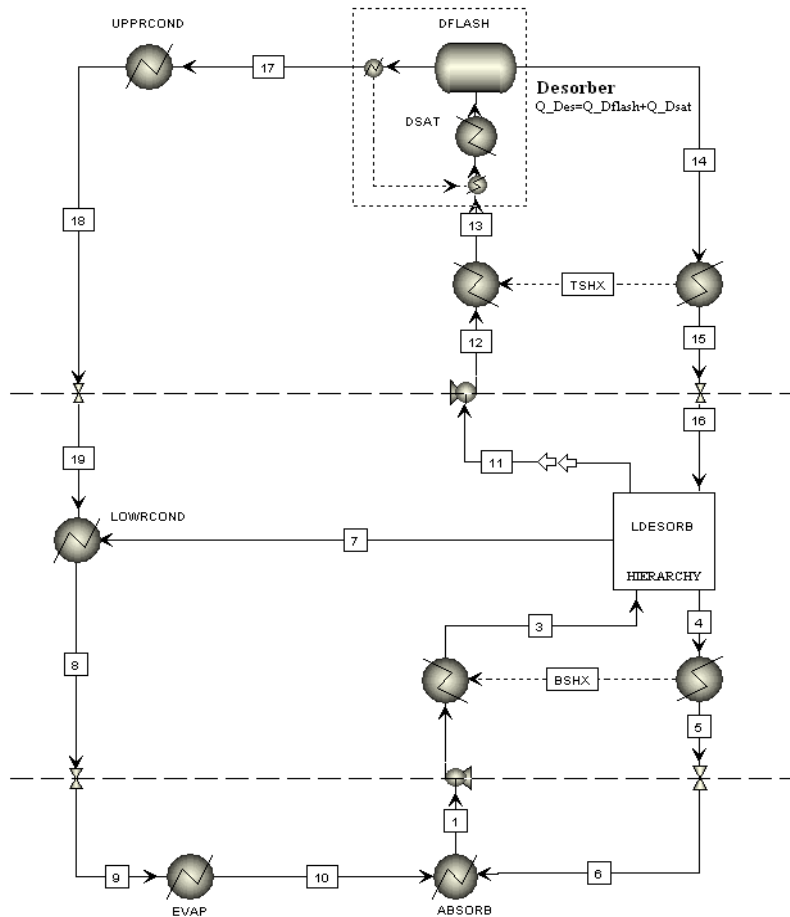


**Figure 7. Double-effect water/lithium bromide model.**

The double-effect model was compared to predicted EES values, as shown in Table 3.

**Table 9. Double-effect water/lithium bromide model accuracy**

Parameter	Units	EES	ASPEN	% Error
Absorber	kW	436.18	421.155	3.44%
Upper Condenser	kW	192.78	193.447	0.35%
Lower Condenser	kW	185.7	185.579	0.07%
Evaporator	kW	354.37	354.737	0.10%
Desorber	kW	267.49	259.335	3.05%
COP		1.325	1.368	3.24%

### Single-Effect Ammonia/Water Cycle

Finally, a single-effect ammonia/water model was completed in ASPEN, as shown in Figure 7. While the COP of the ammonia/water cycle tends to be lower than that of a water/lithium bromide cycle, ammonia/water can deliver lower cooling temperatures. A second cycle adding a pre-cooler was also modeled but is not shown.

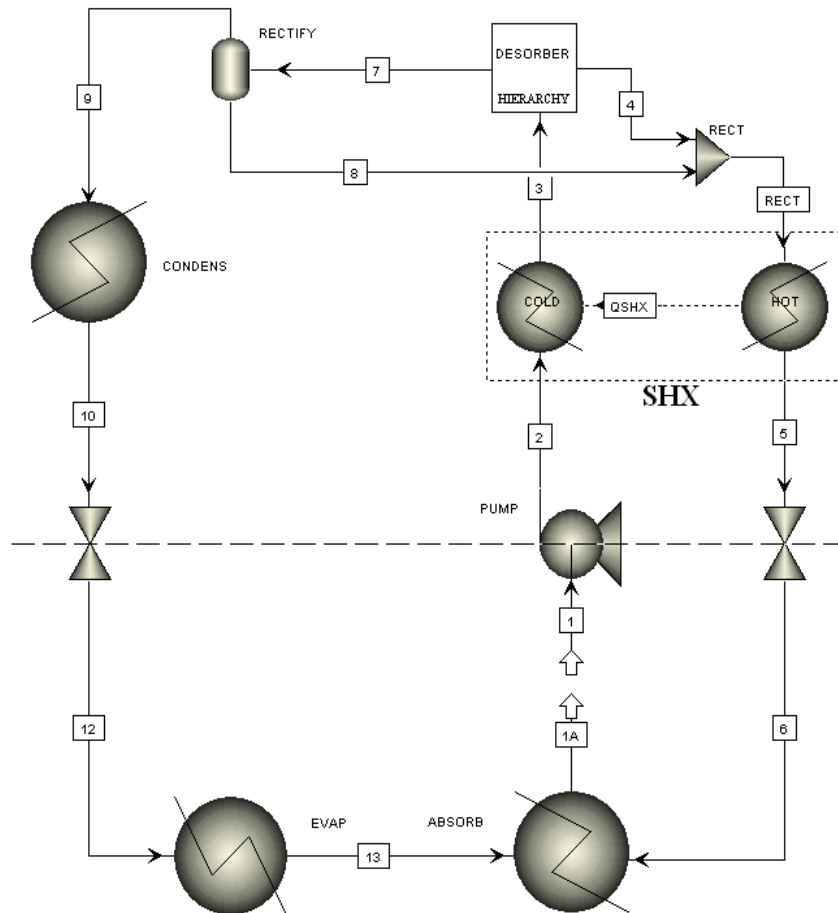


**Figure 8. Single-effect ammonia/water model.**

The comparison with the EES model is shown in Table 10.

**Table 10. Single-effect ammonia/water model accuracy**

Component	Units	EES	ASPEN	% Error
Desorber	kW	266	253.8	4.6%
Absorber	kW	235	219.3	6.7%
Condenser	kW	173	175.8	1.6%
Evaporator	kW	168	167.7	0.2%
<b>COP</b>		<b>0.632</b>	<b>0.661</b>	<b>4.6%</b>

### Integration of Chiller Models with Gas Turbine Model

Each chiller design was integrated into a model with a gas turbine. This allows the benefit of using chillers to recover waste heat to be quantified. Currently, parametric studies are being conducted to study the effects of varying cycle parameters like evaporator temperature and ambient temperature. Additionally, the various chiller designs will be compared at different operating conditions to show which produces the most cooling. Finally, a seasonal study using Abu Dhabi weather data will be conducted using the best design to quantify the savings over an entire year.

### Using Absorption chillers to improve APCI LNG plant Efficiency

Double effect water lithium bromide absorption chillers run by gas turbine exhaust were considered to replace the 22°C and 9°C propane evaporators and cooling propane cycle compressor at 27°C. This chiller design was chosen because it had the highest COP for these evaporator temperatures. The model schematic diagram is shown in Figure 9. The results are shown in Table 11, which shows that the total plant power consumption could be reduced by 10.9% by utilizing 74.5% of gas turbine waste heat. This amount of power saving could lead to a significant reduction in fuel consumption and CO<sub>2</sub> emissions. Further savings could be achieved by fully utilizing the gas turbine waste heat, which will be considered in the future.

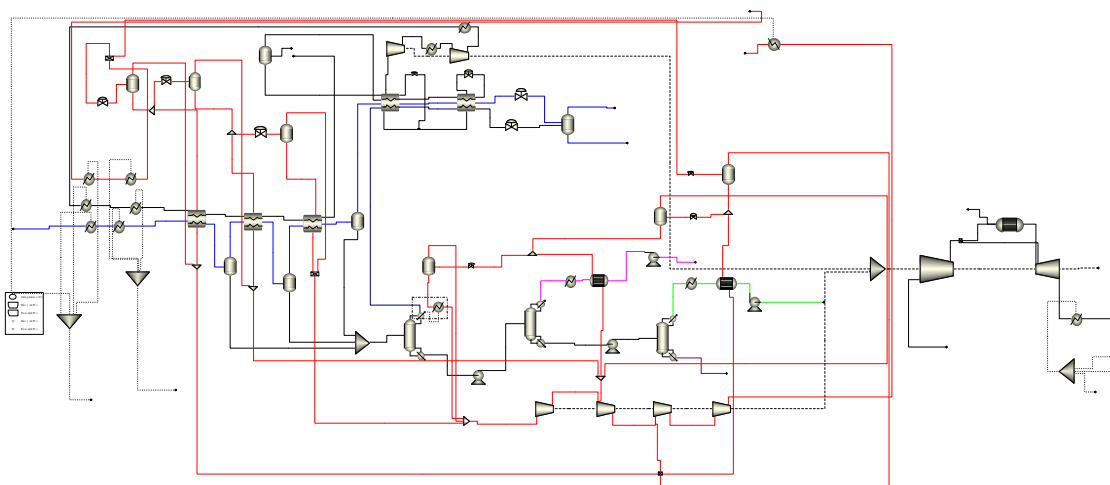


**Figure 9. ASPEN model diagram for APCI cycle improved absorption chiller.**

**Table 11. The power reduction in total plant energy consumption by utilizing waste heat by absorption chillers.**

Power consumption reduction	Required amount of waste
11.075 MW(10.87%)	92.917MW(74.46%of the available waste heat)*

\*Available waste heat is referred to the amount of waste from reduction of gas turbine exhaust to 200C

### Key References

- [1] Alefeld, G., Radermacher, R., 1994, "Heat conversion systems", CRC Press, Boca Raton.
- [2] Al-Hamdan, Q.Z., Ebaid, M.S.Y., 2006, "Modeling and simulation of a gas turbine engine for power generation", ASME Journal of Engineering for Gas Turbines and Power, Vol. 128, pp. 302-311.
- [3] LNG technology selection, [http://www.fwc.com/publications/tech\\_papers/files/TariqLNG.pdf](http://www.fwc.com/publications/tech_papers/files/TariqLNG.pdf), Last access, June, 2008
- [4] Haring, H., 2008, "Industrial Gas Processing", Wiley-VCH, Weinheim
- [5] ASHRAE, 2002, "ASHRAE Refrigeration Handbook", American Society of Heating, Refrigeration and Air-Conditioning Engineers, Atlanta, GA, USA.
- [6] ASHRAE, 2005, "ASHRAE Fundamentals Handbook", American Society of Heating, Refrigeration and Air-Conditioning Engineers, Atlanta, GA, USA.
- [7] Brant, B., Brueske, S., Erickson, D.C., Papar, R., 1998, "New waste-heat refrigeration unit cuts flaring, reduces pollution", Oil & Gas Journal, May 18, pp.61-64.
- [8] Brooks, F.,J., 2000 "GE gas turbine performance characteristics", GE Power Systems Schenectady, NY, GER-3567H.
- [9] Cohen, H., Rogers, G.F.C., Saravanamuttoo, H.I.H., 1996, "Gas turbine theory", 4<sup>th</sup> edition, Longman Scientific & Technical, Singapore.
- [10] Erickson, D.C., 2000 "LPG recovery from reformer treat gas", US Patent 6,158,241.
- [11] Erickson, D.C., Anand, G., Papar, R.A., Tang, J., 1998, "Refinery waste heat powered absorption refrigeration – cycle specification and design," Proceeding of the ASME Advanced Energy System Division, AES-Vol. 38, pp.391-402.
- [12] Erickson, D.C., Kelly, F., 1998, "LPG recovery from refinery by waste heat powered absorption refrigeration", IECEC-98-079, 33<sup>rd</sup> Intersociety Engineering Conference on Energy Conversion, Colorado Springs, CO.
- [13] Giampaolo, T., 2003, "The gas turbine handbook: principles and practices", 2<sup>nd</sup> edition, The Fairmont Press, Lilburn, GA.
- [14] Herold, K.E.; Radermacher, R., Klein, S, 1996, "Absorption chillers and heat pumps", CRC Press, Boca Raton.
- [15] Kim, T.S., Hwang, S.H., 2006, "Part load performance analysis of recuperated gas turbine considering engine configuration and operation strategy", Energy, Vol. 31, pp., 260-277.
- [16] Klein, S.A., 2005, "Engineering Equation Solver" F-Chart Software.
- [17] Kurz, R., 2005, "Gas turbine performance", 44<sup>th</sup> Turbomachinery Symposium, pp.131-146.

- [18] Kurzke, J., 2003, "Model based gas turbine parameter corrections", GT2003-38234, Proceedings of 2003 ASME TURBO EXPO: Power for Land, Sea, & Air, Atlanta, GA, USA.
- [19] Li, Y.G., Pilidis, P., Newby, M.A., 2006, "An adaptation approach for gas turbine design-point performance simulation", Journal of Engineering for Gas Turbines and Power, Vol. 128, pp. 789-795.
- [20] Orlando, J.,A., 1996, "Cogeneration design guide", American Society of Heating, Refrigeration and Air-Conditioning Engineers, Atlanta, GA.
- [21] Pande, M., 1996, "Tools for fractionator design in ammonia-water absorption machines", Master Thesis, University of Maryland, College Park.
- [22] Walsh, P.P., Fletcher, P., 1998, "Gas turbine performance", Blackwell Science, Oxford.

## 6. Publications

- Kalinowski P., Hwang Y., Radermacher R., Al Hashimi S., Rodgers P., Waste Heat Powered Absorption Refrigeration System In The LNG Recovery Process, International Sorption Heat Pump Conference 2008, 23-26 September, 2008, Seoul, KOREA
- Mortazavi, A., Hwang, Y., Radermacher, R., S. Al-Hashimi, and P. Rodgers ,*Performance Enhancement of APCI LNG Plant*, Energy 2030 conference November, 2008.
- Mortazavi, A., Hwang, Y., Radermacher, R., S. Al-Hashimi, and P. Rodgers, *Enhancement of LNG Propane Cycle through Waste Heat Powered Absorption Cooling*, Energy 2030 conference November, 2008.
- C. Somers, A. Mortazavi, Y. Hwang, R. Radermacher, S. Al-Hashimi, and P. Rodgers, *Modeling Absorption Chillers in ASPEN*, Energy 2030 conference November, 2008.

## 7. Visits

Reinhard Radermacher visits to PI:

July 25-28, 2006: With Mike Ohadi visiting German Universities  
 June 16-20, 2006, Commencement  
 October 28-11/03, 2006 Energy 2030  
 October 20-23, 2007 Research Collaboration  
 January 03-06, 2008: Collaboration Workshop  
 November 01-04, 2008 Energy 2030

## 8. GRA (names, degrees, graduation)

- a. Chris Somers, MS, February 2009
- b. Amir Mortazavi, MS, May 2009

## ***4.2. Energy Efficient Transport Processes Projects***

## Thermally Enhanced Polymer Heat Exchanger for Seawater Applications

UM Investigator(s): Prof. Avram Bar-Cohen, Prof. S.K. Gupta

GRA(s): Juan Cevallos, Patrick Luckow

PI Investigator(s): Dr. Peter Rodgers, Dr. Ahmed Abdala

Start Date: October 2006

FINAL REPORT

### 1. Objectives/Abstract

The two-year study addressed the fundamental thermal performance issues associated with the use of thermal high-conductivity polymer materials, addressing their advantages and limitations and defining the heat exchanger configurations that optimize the unique characteristics of high conductivity polymer materials.

To achieve optimum thermal performance, a clear understanding of the thermal engineering characteristics of fiber-enhanced polymer tubes/channels and the fundamental thermo-fluid predictive relations that underpin heat exchange in such configurations was developed.

This effort provides fundamental thermofluid modeling relations for thermally enhanced polymer tubes and channels; it also provides the basis for determining the environmental, weight, and cost advantages resulting from future applications of this technology to seawater heat exchangers for shipboard heat exchangers and for the petroleum and power industries.

### 2. Approach

1. Review the available compact liquid-liquid heat exchanger concepts, e.g., shell-in-tube and plate-coil, and identify their strengths and weaknesses.
2. Define the relevant heat exchange metrics, e.g., kW/m<sup>3</sup> and COP (kW heat/kW pumping), and rank the concepts by these metrics.
3. Review and tabulate the thermal, chemical, and mechanical properties of thermally enhanced polymer materials suitable for use in liquid-to-liquid heat exchangers.
4. Apply the selected metrics to conventional polymer and thermally enhanced polymer heat exchangers, and re-rank the heat exchanger concepts.
5. Develop new polymer nanocomposite materials and compare their thermal, chemical, and mechanical properties to the best-known thermally enhanced polymeric materials.
6. Select the most promising polymer materials and configuration(s) for seawater heat exchange and determine the theoretical performance limits for these configurations/materials.
7. Fabricate and test polymer tube/channel heat exchanger “building blocks” to determine the pressure drop and heat transfer coefficients achievable.
8. Correlate baseline thermofluid data for “building block” tube/channels and compare to theoretical predictions.
9. Develop a test loop for testing of pilot scale polymer heat exchangers, representative of industrial applications.
10. Develop recommendations for seawater-cooled, thermally enhanced polymer heat exchangers for specific applications, such as in the power industries, refineries, and aboard ships.

### 3. Two-Year Schedule

#### Year 1:

- Conduct literature review on: (i) the strengths and weaknesses of various

commercially available heat exchanger designs and (ii) current usage of polymer heat exchangers.

- Assess the thermal, chemical, and mechanical properties of thermally-enhanced polymer materials suitable for use in liquid-to-liquid heat exchangers.
- Assess theoretical performance limit of polymer candidate materials and configuration(s).
- Construct laboratory-scale test apparatus for thermal characterization of polymer heat exchanger “building block” tube/channels.
- Fabricate polymer nanocomposite materials suitable for polymer heat exchangers.
- Characterize thermal properties of polymer “building block” tube/channel heat exchanger test vehicles.
- Correlate baseline thermofluid data for “building block” tube/channel with theoretical predictions.

Year 2:

- Construct a test loop for thermal characterization of pilot-scale polymer heat exchangers representative of industrial applications.
- Characterize thermal properties of pilot-scale polymer heat exchangers.
- Recommend seawater-cooled, thermally enhanced polymer heat exchangers for specific applications.

**4. Summary of results**

**Literature Review:**

A thorough literature review was conducted at the start of the project. Available compact liquid-liquid heat exchanger concepts, e.g., shell-in-tube and plate-coil, and their strengths and weaknesses were identified. Current uses and applications for low-k polymer heat exchangers in the cooling processes of highly corrosive or chemically aggressive fluids where the chemical inertness of the polymers is beneficial were also identified.

Metallic materials most commonly used in heat exchangers for use with corrosive fluids were identified. The properties of these materials (Table 1) can be used to assess the performance of thermally conductive thermoplastics. For seawater applications, the most commonly used heat exchanger metals are Cu-Ni alloys and titanium.

**Table 1. Commonly used metals for heat exchangers having corrosive fluids.**

<b>Material</b>	<b>Density (<math>\times 10^{-3}</math> kg/m<sup>3</sup>)</b>	<b>Specific heat (J/kg.K)</b>	<b>Thermal Conductivity (W/m.K)</b>	<b>Yield Strength (MPa)</b>	<b>Tensile Strength (MPa)</b>	<b>CTE (<math>\times 10^{-6}</math> m/m.K)</b>	<b>Melting range (°C)</b>
SS 304	7.92	502	16	207	586	4.4	1399- 1454
SS 316	8.08	502	16	276	621	4.9	1371- 1399
Titanium	4.51	582	17	517	621	2.6	1691
Cu-Ni 90/10	8.9	377	50	140	320	17	1100- 1145
Cu-Ni 70/30	8.95	377	29	170	420	16	1170- 1240

**Assessment of thermal, chemical, and mechanical properties of thermally-enhanced polymers**

Table 2 is a compilation of the mechanical and thermal properties of commercially available thermally conductive polymers. This data can be used to assess the performance limits of candidate polymeric materials for heat exchanger applications. Material vendors include Cool Polymers, GE Plastics, PolyOne, Ticona, and Saint Gobain. The materials offered range in thermal conductivity from 1 W/m.K to 20 W/m.K.

**Table 2. Commercially available thermally conductive polymeric materials.**

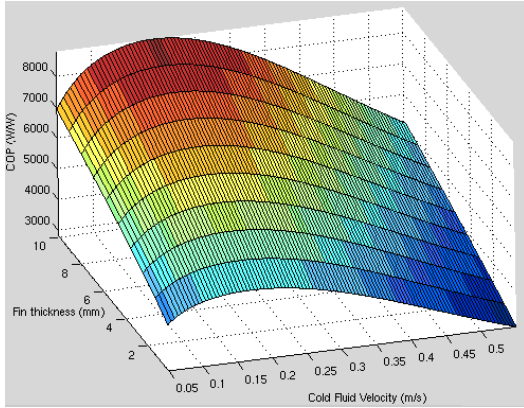
Company	Resin	Thermal Conductivity (W/m K)	Tensile Strength (MPa)	Tensile Modulus (MPa)	Density (g/cc)	HDT (°C) @ 1.8 MPa
Cool Polymers	PPS	20	45	13000	1.7	260
Cool Polymers	PP	5	25	5200	1.38	
GE Plastics	PA 6	1.1	81	10160		174
GE Plastics	PA 6/6	1.2	95	11920	2.04	226
GE Plastics	PPS	7/2.2	139	27586	1.74	270
PolyOne	PPS	10-11	100	26200	1.82	282
PolyOne	PA 6/6	10-12	60.7	14479	1.58	254
PolyOne	LCP	18-20	103.4	20684	1.82	277
PolyOne	PA 12	20-25	39.3	14479	1.68	185
RTP	LCP	18.01	45	24132	1.7	232
RTP	PPS	2.31	62	26201	1.7	260

**Note:** HDT = heat deflection temperature.

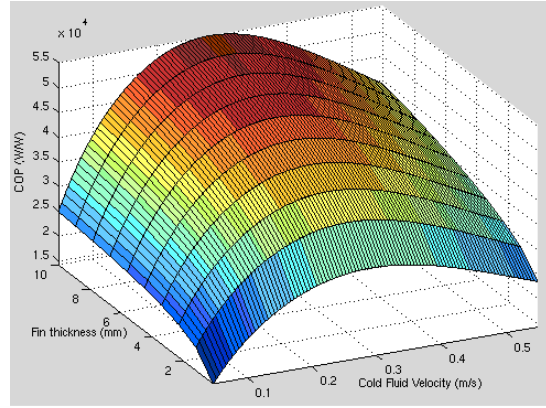
**Assessment of theoretical performance limits of polymer candidate materials and configurations**

- Modeled the thermo-fluid performance of a counterflow seawater-fresh water heat exchanger module, consisting of a double-finned plate, using basic equations from heat exchanger theory.
- Evaluated the performance of doubly-finned polymer counterflow heat exchanger modules, from un-enhanced ( $k=0.25\text{W/m.K}$ ) through thermally enhanced polymer ( $k=20\text{W/m.K}$ ), and compared their performances to the thermal performance of an aluminum module ( $k=168\text{W/m.K}$ ) over a range of liquid velocities from 0.5 m/s to 2 m/s. In the parametric range studied, the results are as follows:
  - At maximum flow velocities, thermal conductivities of 0.25 W/m.K and 20 W/m.K yield 86% and 36% reduction, respectively, relative to the thermal performance of aluminum (168 W/m.K).
  - The addition of fins to the un-enhanced, low conductivity polymer produces an adverse effect on performance, while for higher conductivities ( $\sim 20\text{ W/m.K}$ ) the addition of fins to the plates leads to an improvement in thermal performance.
  - Least-material optimization can be used to improve the thermal performance of a double-finned polymer heat exchanger module, when the thermal conductivity is in the range of 20 W/m.K. If the conductivity is substantially lower, no benefit is derived from such an optimization.
  - COP thermal performance findings for low-k polymer (0.25 W/m.K), high-k polymer (20 W/m.k), and aluminum alloy (168 W/m.K) are illustrated in **Error! Reference source not found.** The COP values for the high-k polymer are seen

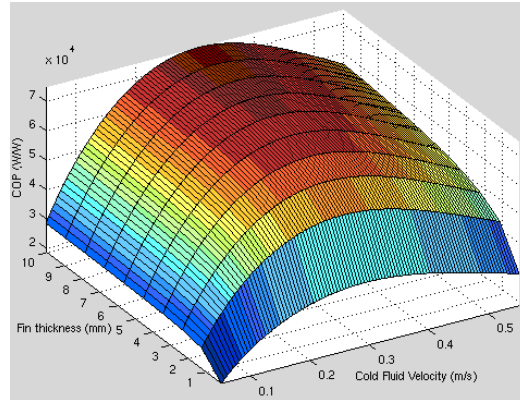
to fall some 30% below those of the aluminum module and to drop off more steeply than the aluminum, but they reach their peak values at similar liquid velocities of approximately 0.3m/s.



(a) Low-k polymer (0.25 W/m.K),



(b) High-k polymer (20 W/m.k)

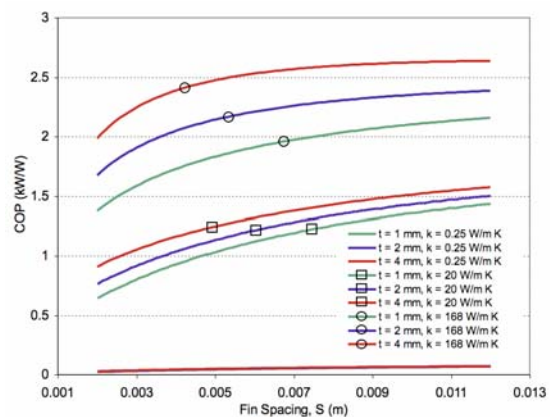
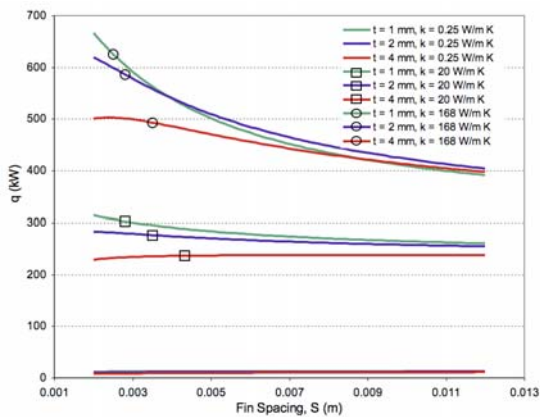


(c) Aluminum alloy (168 W/m.K)

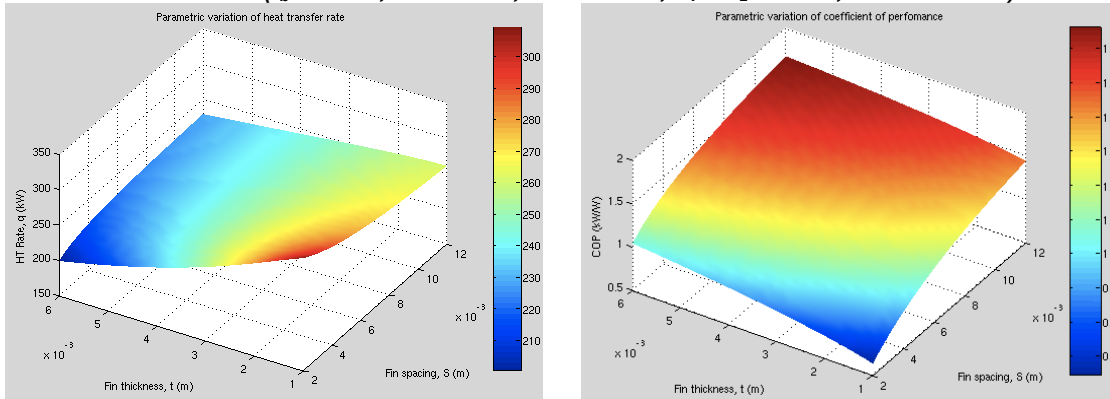
Note: Hot fluid velocity = 0.5 m/s

**Figure 1. COP of a double-finned polymer heat exchanger module as function of thermal conductivity, fin thickness and cold fluid velocity.**

Figure 2 and Figure 3 illustrate the variation of overall heat transfer rate and COP as a function of fin spacing and fin thickness. It is evident that the optima for these metrics often lie in opposite sides of the parametric space.



(a) Heat Transfer Rate (b) Coefficient of Performance  
**Figure 2 . Doubly finned counterflow heat exchanger performance as a function of fin spacing and fin thickness ( $t_b = 1 \text{ mm}$ ,  $H = 10 \text{ mm}$ ,  $W = L = 1 \text{ m}$ ,  $u_1 = u_2 = 2 \text{ m/s}$ , turbulent flow).**



(a) Heat Transfer Rate (b) Coefficient of Performance  
**Figure 3. Parametric optimization of heat transfer rate and COP within a set rectilinear volume ( $k = 20 \text{ W/m-K}$ ,  $t_b = 1 \text{ mm}$ ,  $H = 10 \text{ mm}$ ,  $W = L = 1 \text{ m}$ ,  $u_1 = u_2 = 2 \text{ m/s}$ , turbulent flow).**

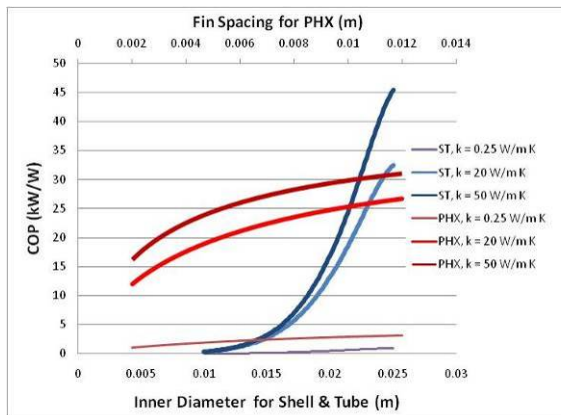
**Thermal-fluidic analysis of shell and tube heat exchanger design:**

- Identified key functional differences between two candidate heat exchanger designs, i.e. finned plate and sheel-and-tube, with sample comparisons illustrated in Table 3.

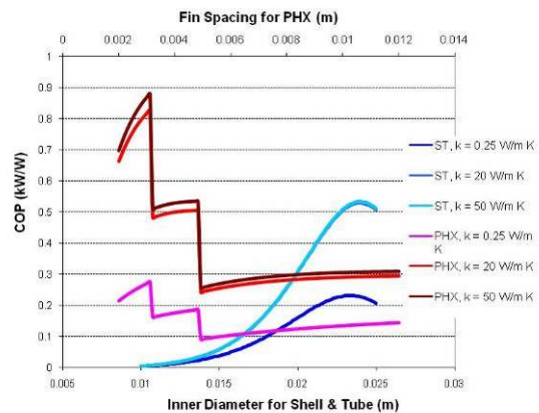
**Table 3. Heat Exchanger Comparison.**

	Plate HX	Shell-and-tube HX
<b>Approach <math>\Delta T</math></b>	$\sim 1^\circ\text{C}$	$\sim 5^\circ\text{C}$
<b>Hold up Volume</b>	Low	High
<b>Normalized Heat Transfer</b>	$\sim 3\text{-}5$	1
<b>Normalized Volume</b>	1	$\sim 2\text{-}5$
<b>Thermal Performance Modification</b>	Easy	Difficult
<b>Maximum Operating Temperature</b>	Low	High
<b>Maximum Operating Pressure</b>	Low	High

- Developed coefficient of performance (COP) comparisons for both a standard water/water heat exchanger, and for actual conditions at coastal UAE petroleum refineries and gas liquefaction plants, using seawater and methane as heat exchanger fluids (see Figure 4).



(a) Water/Water:  $u_1 = u_2 = 0.5 \text{ m/s}$  for PHX, shell-and-tube  $u_1$  and  $u_2$  set to match flow rate of plate heat exchanger.



(b) Seawater/Methane:  $u_1 = 10 \text{ m/s}$ ,  $u_2 = 0.5 \text{ m/s}$  for PHX, shell-and-tube  $u_1$  and  $u_2$  set to match flow rate of plate heat exchanger.

**Figure 4. COP as a function of HX geometric parameters ( $t = 1 \text{ mm}$ ) and thermal conductivity compared for plate (PHX) and shell-and-tube (ST) heat exchangers.**

**Energy content analysis:**

- Energy content values were determined for carbon fiber and various polymers, as well as for conventional heat exchanger materials, to develop appropriate metrics to compare the polymer composites with conventional metals used for heat-exchangers.
- The energy content of the thermally conductive polymers was determined by use of the Nielsen equation to determine the relationship between the thermal conductivity and the filler concentration.
- We applied a new metric, the “total coefficient of performance,” or  $COP_T$ , which incorporates the energy required to manufacture a heat exchanger along with the pumping power expended over the lifetime of the heat exchanger, to compare HX fabricated of conventional materials to HX fabricated of thermally conductive polymers (see Figure 5).

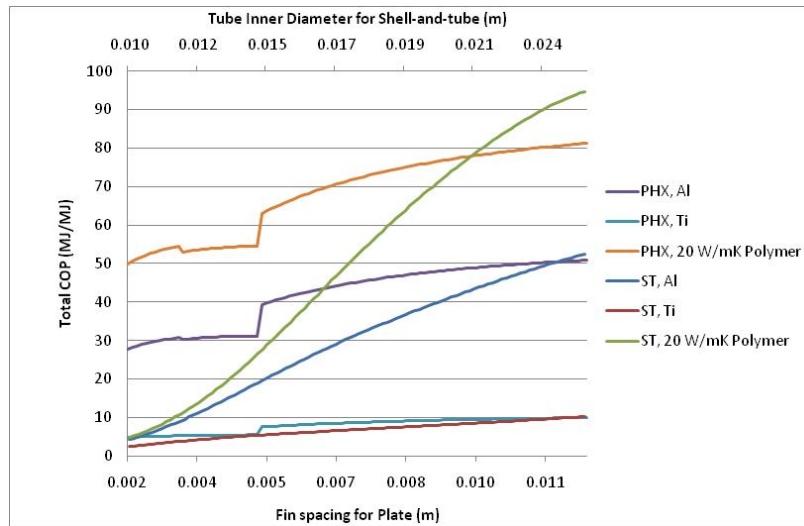


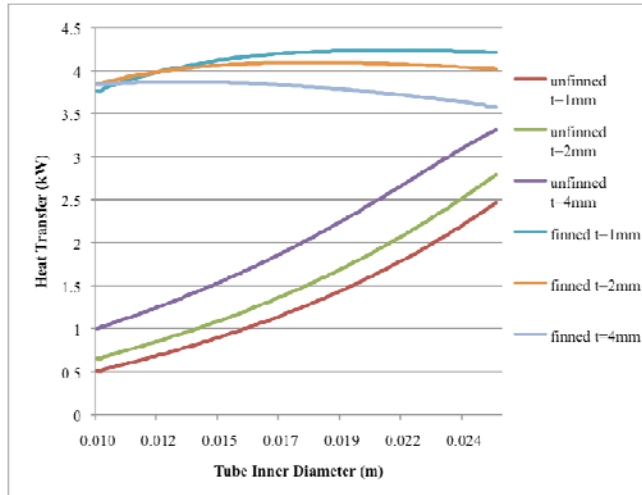
**Figure 5. Total coefficient of performance comparison ( $t=1\text{mm}$ ) as a function of heat exchanger design and material. Plate Heat Exchanger (PHX),  $u_1=10\text{m/s}$ ,  $u_2=0.5 \text{ m/s}$ , compared to Shell-and-Tube Heat Exchanger (ST),  $u_1$  and  $u_2$  set to match plate heat exchanger flow rate.**

**Optimization of heat exchanger design:**

- Optimized the fin height and fin spacing of finned-plate heat exchangers for total COP. The fin thickness was optimized for the least material design using the Kern & Kraus relation.
- For shell-and-tube heat exchanger, shell diameter and tube pitch were optimized.
- Total COP was also investigated for the shell-and-tube heat exchanger with the shell material. The shell thickness was optimized for least material design using the hoop stress equation.

**Investigation of the feasibility of gas-side heat transfer coefficient enhancements up to a level comparable to that of the seawater-side:**

- In gas-to-liquid heat exchangers, the gas-side thermal resistance is significantly larger than that of the water-side. Thermal enhancements to a shell-and-tube heat exchanger were investigated to reduce the thermal resistance of the gas-side down to the level of the water-side. These enhancements were in the form of annular fins on the outside of the tubes, as shown in Figure 6.

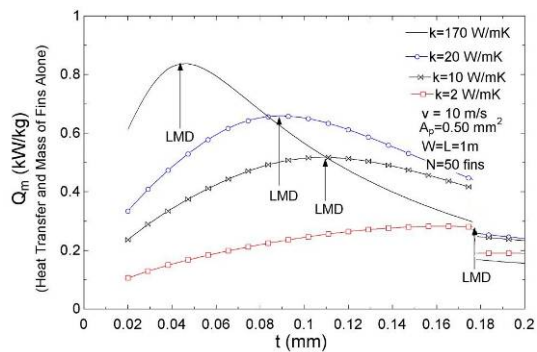
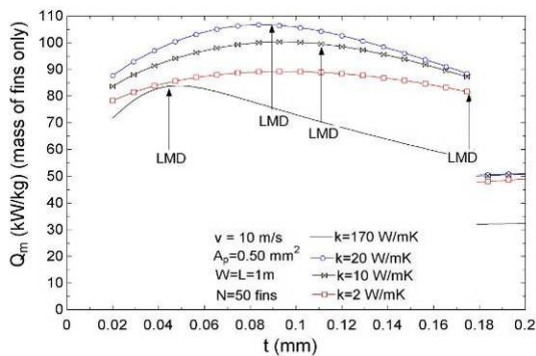


(a) Tubular annular fin geometry. (b) Heat transfer rate comparison for an annular finned versus unfinned tubular design, for three different tube wall thicknesses.

Figure 6. Shell-and-tube heat exchanger analysis (fin height = 8 mm, fin thickness = 0.5 mm, fin spacing = 1 mm).

### Assessment of the applicability of least-material optimization analysis for plate heat exchangers

- It was found that for low thermal conductivity finned-plate arrays, the least material condition accurately predicts the point of maximum heat transfer per unit mass of the fins alone (Figure 7), but since for low fin conductivity the heat transfer through the base plays a significant role, the least-material fin condition may not correspond to the peak of the mass-based heat transfer rate.

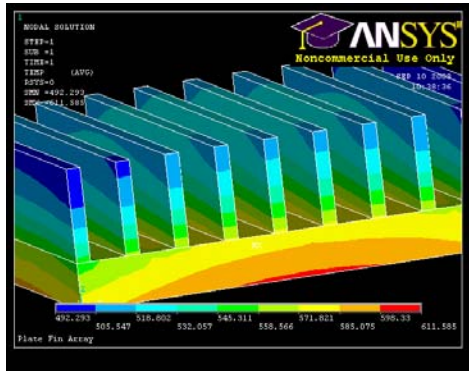


(a) Total array heat transfer (fins and inter-fin spacings, per unit fin mass). (b) Heat transfer from fins only, per unit fin mass.

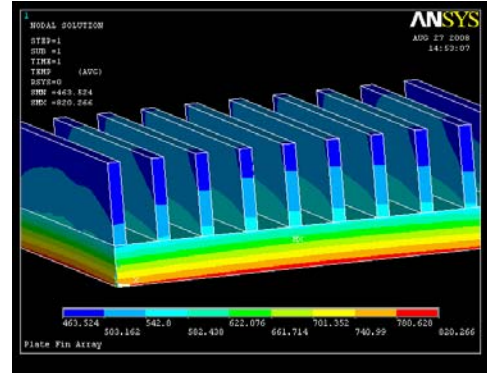
Figure 7. Gas/liquid heat exchanger least-material fin analysis as a function of fin thickness for various thermal conductivities ( $L = W = 1\text{ m}$ ,  $A_p = 0.50\text{ mm}^2$ ,  $v = 10\text{ m/s}$ ,  $\theta_b = 55\text{ K}$ ,  $N_{fins} = 50$ ).  
Study of anisotropic fins

Finite element models (Figure 8) were developed to understand the behavior of fins and fin arrays with anisotropic thermal conductivity.

Development of an analytical model for the heat conduction in a two-dimensional anisotropic fin is in progress, with finite-element verification in Ansys.



(a) Isotropic,  $k=20 \text{ W/mK}$ .



(b) Anisotropic; Fins:  $k_x = k_y = 20 \text{ W/mK}$ ,  $k_z = 2 \text{ W/mK}$ ; Base:  $k_x = k_y = 2 \text{ W/mK}$ ,  $k_z = 20 \text{ W/mK}$ .

Figure 8. Finned array with constant base heat flux;  $W=L=5\text{cm}$ ,  $H_{fin}=1\text{cm}$ ,  $N_{fin}=10$ ,  $t_b=5\text{mm}$ ,  $t_{fin}=1.5\text{mm}$ ,  $h=30 \text{ W/m}^2\text{K}$ ,  $q_{flux}=1e5 \text{ W/m}^2$ .

### Assessment of the impact of molding thermally conductive thermoplastics on the thermal and mechanical characteristics of plate heat exchangers, by simulating the injection molding process in Moldflow:

- A comprehensive parametric analysis was conducted to study the effects of four chosen variables on mold filling of a square finned plate. The finned plate was chosen as an example of a heat exchanger module that could be mass-produced. The variables are:
  - Plate length,  $A_b$
  - Plate thickness,  $t_b$
  - Fin spacing,  $S$
  - Fin thickness,  $t$
- The motivation for the parametric analysis arose from the need to obtain cost correction factors to account for the limited filling ability of a part molded with thermally conductive polymers. With this in mind, the overall cost of a heat exchanger can be written as:

$$\text{Manufacturing Cost} = \text{Material Cost} + \text{Tooling Cost} + \alpha \cdot \text{Production Cost}$$

$$\text{Assembly Cost} = \beta \cdot (\text{Heat load required} / \text{Heat transferred by single module})$$

$$\text{Overall Cost} = \text{Manufacturing Cost} + \text{Assembly Cost}$$

where  $\alpha$  is the correction factor for limited filling, and  $\beta$  is the rate for assembling HX modules.

- The approaches to model material properties of a thermally conductive material were reviewed with the major findings found to be:
  - The shear-temperature dependence of the viscosity must be defined using a model that also accounts for the filler content given that these are highly filled materials.
  - The density changes with pressure/temperature must be corrected for the presence of the filler by using a rule of mixtures found in the literature.
  - Similarly, the melt thermal conductivity can be calculated using a common rule of mixtures suggested by Knappe.

- The filler properties can be defined using previous morphological analysis of a thermally conductive resin found in the literature.
- Material properties, including shear rate viscosity and melt thermal conductivity, were obtained from PolyOne Corp. for a thermally enhanced Nylon 12-based composite. This data will be used for the mold flow parametric analysis that is currently underway.

### Experimental validation of Moldflow filling predictions

- A spiral aluminum mold was machined using CNC equipment. The cross-section of the spiral is 2.286 mm wide by 1.27 mm tall.
- The spiral mold was used to conduct filling experiments using the Babyplast injection machine to create parts with PolyOne's thermally enhanced Nylon 12 (NJ 6000 TC). The parts were injected at two different pressures: 150 MPa and 180 MPa, with a melt temperature of 270 C. The measured length of the spirals was compared with the length predicted by Moldflow under similar conditions. Figure 9 below shows a plot comparing the experimental results to those predicted by Moldflow. Moldflow predictions are approximately within 20% of the experimental measurements.

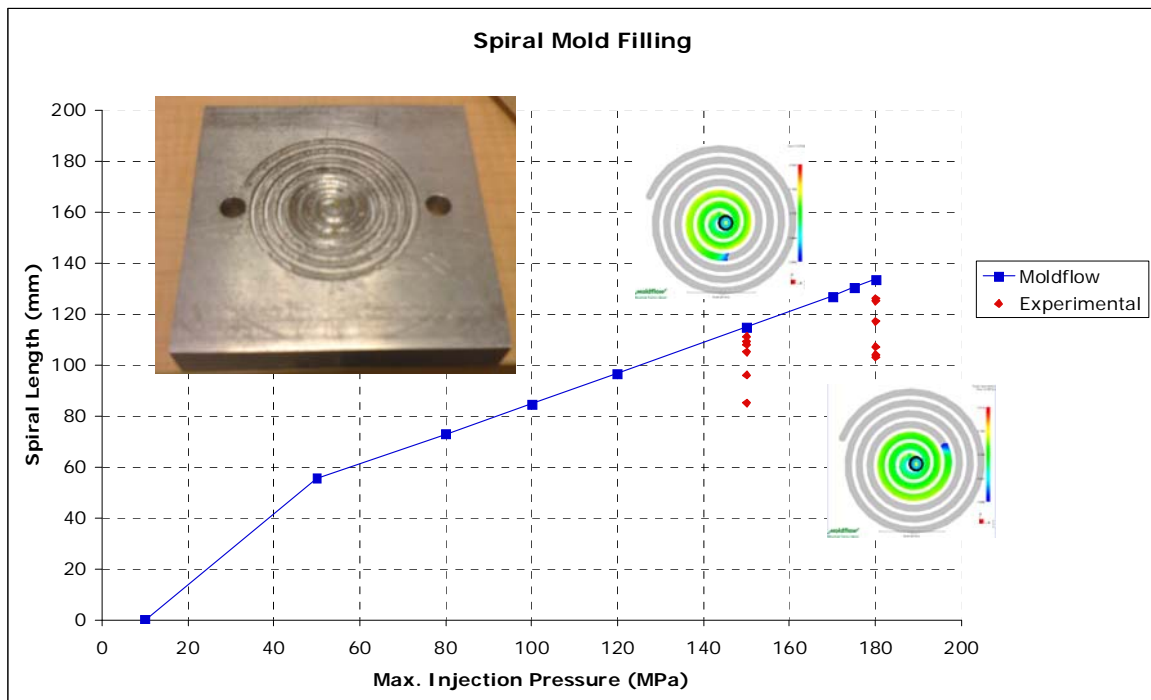
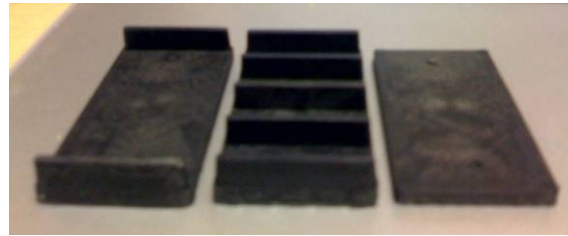


**Figure 9 Experimental verification of Moldflow filling predictions.**

- A finned-plate mold was machined (Figure 10a), and full parts were successfully molded with PolyOne's thermally enhanced Nylon 12 (Figure 10b).



(a) Aluminum mold



(b) Molded parts

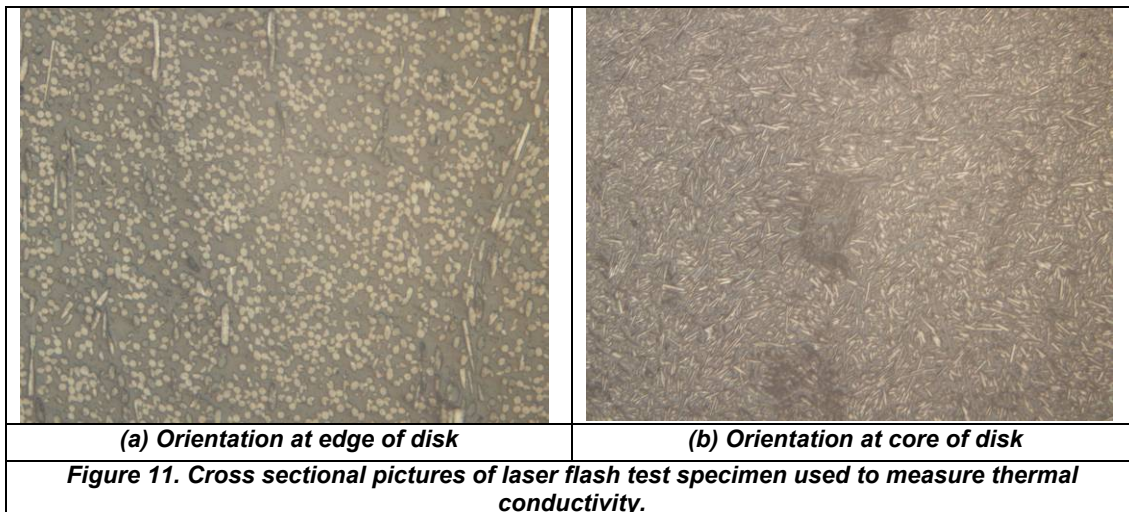
Figure 10 . Fabrication of a molded ABS polymer finned plate.

### Experimental validation of fiber orientation Moldflow prediction

A preliminary validation was performed to confirm Moldflow predictions of fiber orientation. A molded finned plate (Figure 10b) was cross-sectioned, and the process-induced fiber orientation was observed and measured. The observed orientation was then compared to predictions obtained from Moldflow simulations, and good agreement was found near the top of the fin, across its length. More extensive measurements are needed to fully validate Moldflow predictions.

### Thermal conductivity of PolyOne thermally enhanced Nylon 12

- A disk (12.7 mm diameter) was injection-molded, and the thermal conductivity was measured using the laser flash test. However, Moldflow simulations revealed a flow pattern—extensional flow in the core—that causes the fiber orientation and the conductivity to vary with location. The micro-images, shown in Figure 11, confirm these predictions. More experiments are needed to address this issue.



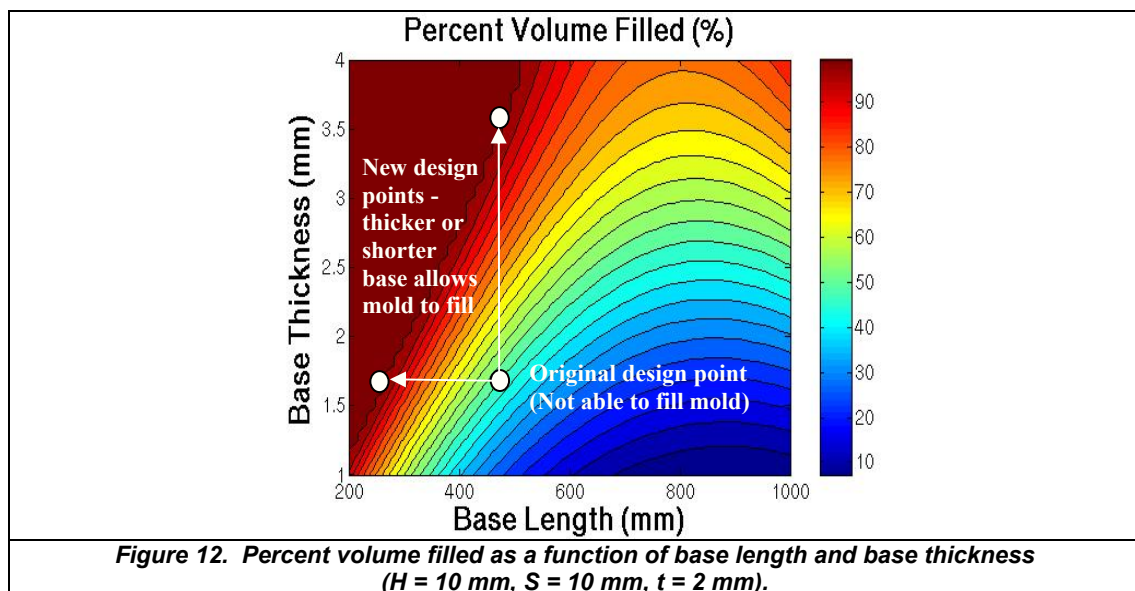
- The out-of-plane conductivity has been measured using the laser flash method and the results are shown in Table 4 below:

**Table 4. Thermal conductivity measurements using laser flash method for out-of-plane samples**

Sample	$\rho$ (g/cm <sup>3</sup> )	$\alpha$ (cm <sup>2</sup> /s)	$C_p$ (J/Kg.K)	$k$ (W/m.K)
1	1.513	0.02398	1.030	3.737
2	1.500	0.02196	1.100	3.625
3	1.503	0.02404	1.155	4.172

**Moldflow-filling parametric analysis and response surface models.**

- Numerous Moldflow simulations have been performed, and the data obtained from these were used to develop a meta-model for predicting filled volume percentage of a finned plate with single-gate injection. Figure 12 shows a plot of percent volume filled and illustrates the use of the meta-model as a design tool.



- Cost models for materials, production, and tooling have been created for injection molding of a finned plate, based on existing models ([www.custompartnet.com](http://www.custompartnet.com)). These cost models were modified to reflect the parameters of PolyOne’s thermally enhanced Nylon 12.
- Moldflow simulation data have been compiled to develop meta-models for 2-gate and 4-gate injection. These models, along with the cost models, will serve to assess the manufacturability of a finned plate using a thermally-enhanced material.
- The dataset (~60 points), obtained from Moldflow simulations, was used to construct a quadratic meta-model to predict the percent volume filled in the mold for single-gate injection. The quadratic model fits the dataset with residual errors of less than 10%.

**Design and construction of a laboratory-scale test apparatus module.**

- A design stage uncertainty analysis has been conducted to minimize experimental measurement error using the test apparatus.
- Expected convective heat transfer rates have been calculated for both fully developed and

developing flow conditions. Based on this analysis, the appropriate air and water flow rates have been determined.

- Fused Deposition Modeling (FDM) was used to construct prototypes of both the actual test piece (Figure 13a) and the finned plates (Figure 13b) that will be assembled to form the test piece.



*(a) Test piece prototype*



*(b) Finned plates prototypes*

**Figure 13. Fused deposition modeling (FDM) rapid prototyping**

- Crossflow heat exchanger and manifolds were built with Stratasys Dimension FDM equipment, using FDM-grade ABS plastic.
- A second heat exchanger, made of thermally-enhanced thermoplastic material-filled Nylon 12 from PolyOne, was injection-molded in small pieces and assembled with epoxy. Figure 14 shows the assembled heat exchanger.



**Figure 14. Cross-flow heat exchanger made with thermally enhanced Nylon 12.**

- Test equipment was purchased and installed, as shown schematically in Figure 15. Labview code was written to collect and process thermocouple and fluid flow data measurements. Initial calibration was done using built-in calibration functions in the thermocouple DAQ module, and refined calibrations were done using ice baths and boiling water.

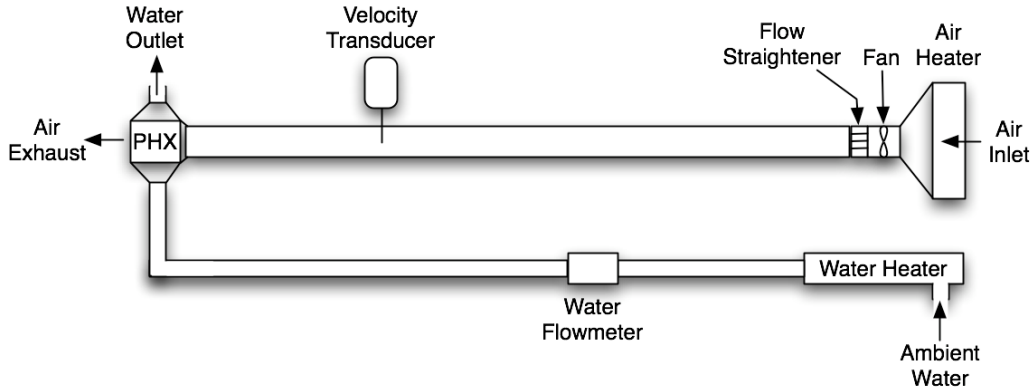


**Figure 15. Polymer heat exchanger test apparatus.**

- Data were collected for the unfilled polymer heat exchanger, and results are presented in Figure 16. Error analysis revealed an overall 15.7% uncertainty, reflected in the figure.

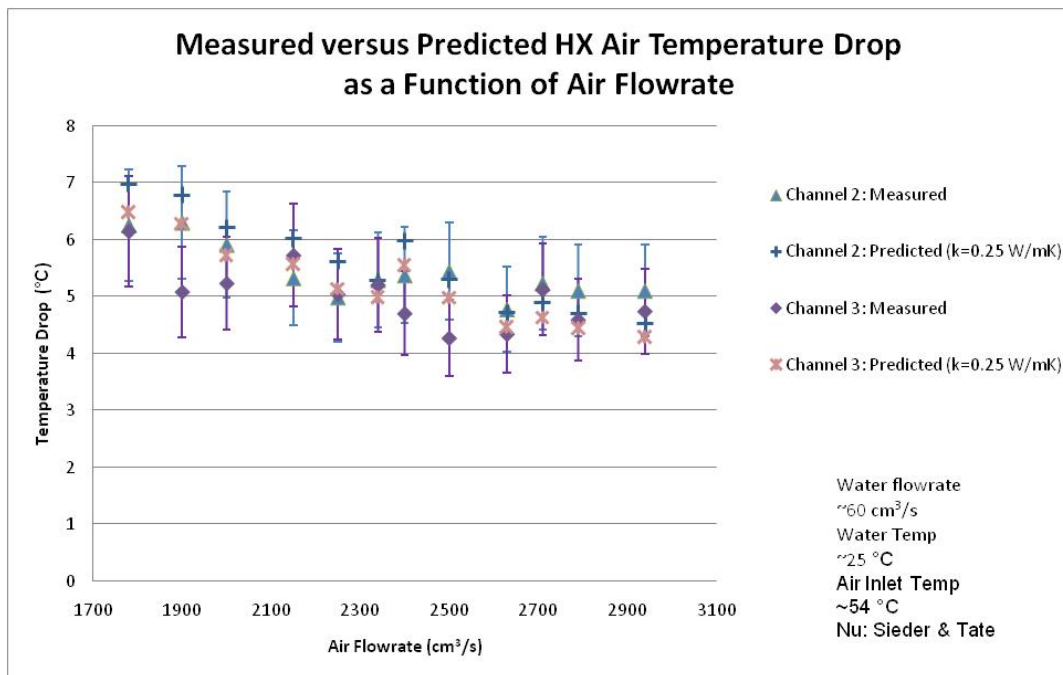
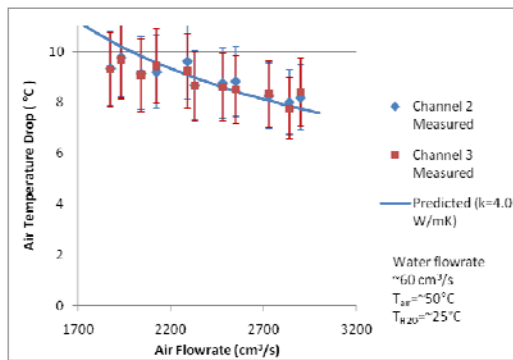


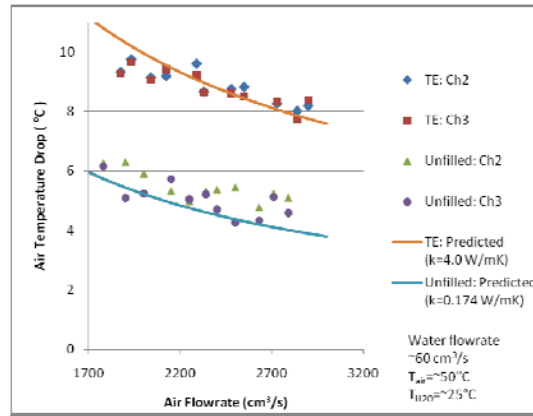
**Figure 16. Experimental temperature drop over unfilled polymer heat exchanger, compared to predicted results.**

### Thermally enhanced PolyOne polymer heat exchanger

- Experimental apparatus (Figure 15) was assembled with the PolyOne polymer heat exchanger.
- Data was collected for the PolyOne polymer heat exchanger, with results shown in Figure 17a, well within experimental uncertainty.
- Results of ABS and PolyOne heat exchangers were plotted and compared to theoretical predictions (Figure 17b). PolyOne heat exchanger showed approximately 70% performance gain over ABS.



(a) PolyOne heat exchanger results



(b) Comparison of PolyOne to ABS heat exchanger

Figure 17. Cross-flow heat exchanger made with thermally enhanced Nylon 12.

### Fabrication of polymer nano-composite materials suitable for heat exchangers

- Polyphenylene sulfide (PPS) and polycarbonates have been selected as the polymer matrices for the polymer-graphite nanocomposite materials based on thermal, chemical and mechanical considerations.
- Graphite nanosheets have been prepared via thermal exfoliation of graphite oxide.
- The morphologies of both graphite oxide and exfoliated graphite oxide were characterized using X-ray diffraction (XRD) and a scanning electron microscope (SEM), with the latter analysis presented in Figure 18.
- PPS-graphite oxide and PPS-exfoliated graphite oxide composites have been prepared by coating graphite nanosheets with polymer chains.
- The thermal degradation behaviors of PPS, graphite oxide, and their composites have been characterized by thermal gravimetric analysis (TGA), with results shown in Figure 19.

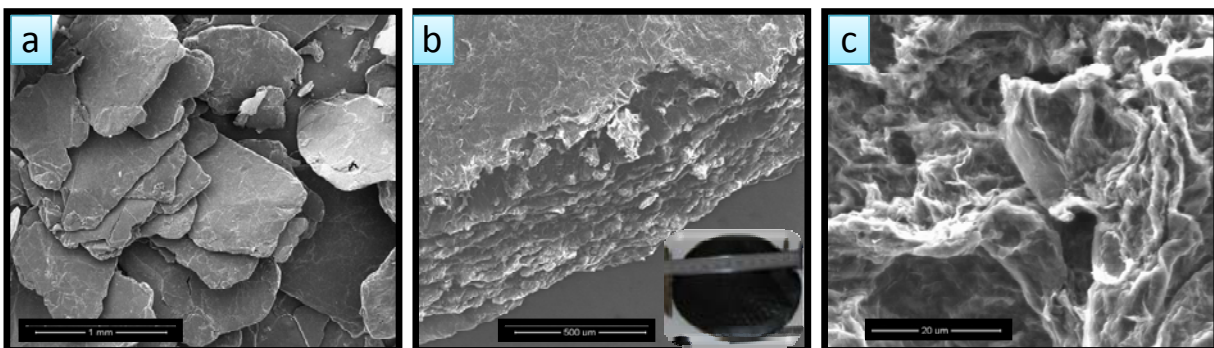
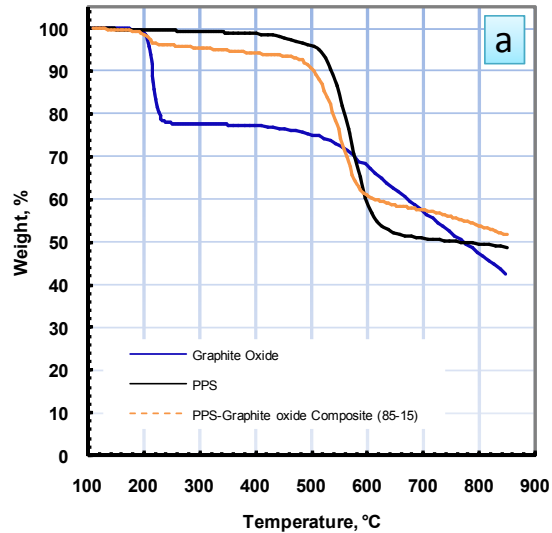
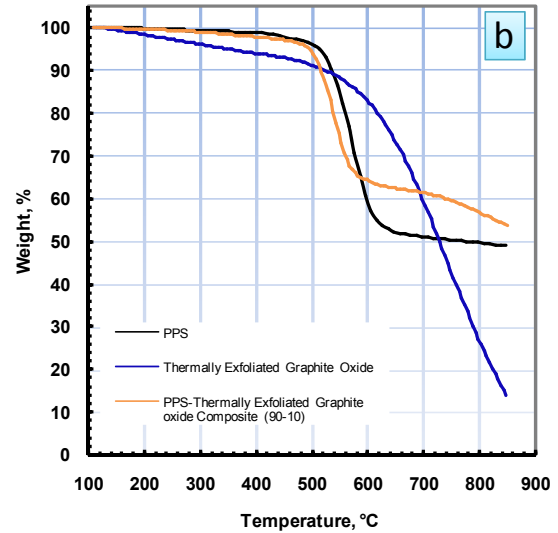


Figure 18. SEM images of: (a) natural flake graphite, (b) 0.5 mm thick graphite oxide film, and (c) thermally exfoliated graphite oxide.



**(a) Polyphenylene sulfide (PPS), graphite oxide (GO) and their composite (85% PPS, 15% GO).**



**(b) Polyphenylene sulfide (PPS), thermally exfoliated graphite oxide (TEGO) and their composite (90% PPS, 10% TEGO).**

**Figure 19. Thermal gravimetric analysis.**

- Polycarbonate-exfoliated graphite oxide composites have been prepared with different loading of exfoliated graphite oxide, i.e. 0.5, 1, 2, 3, 4, 5, and 10% (by weight).
- The thermal stability of these composite samples were characterized using thermal gravimetric analysis (TGA) to estimate the operating range of the polymer composite, as shown in Figure 20. Differential scanning calorimetry (DCS) analysis was also performed to assess glass transition and melting behavior. These analyses revealed:
- The temperature onset for thermal degradation of the polymer and polymer composite samples is 325°C.
- The glass transition temperature of the polymer and the composite samples is approximately 140°C.
- The polymer composite samples were processed to produce test samples to characterize both the mechanical behavior and thermal conductivity.

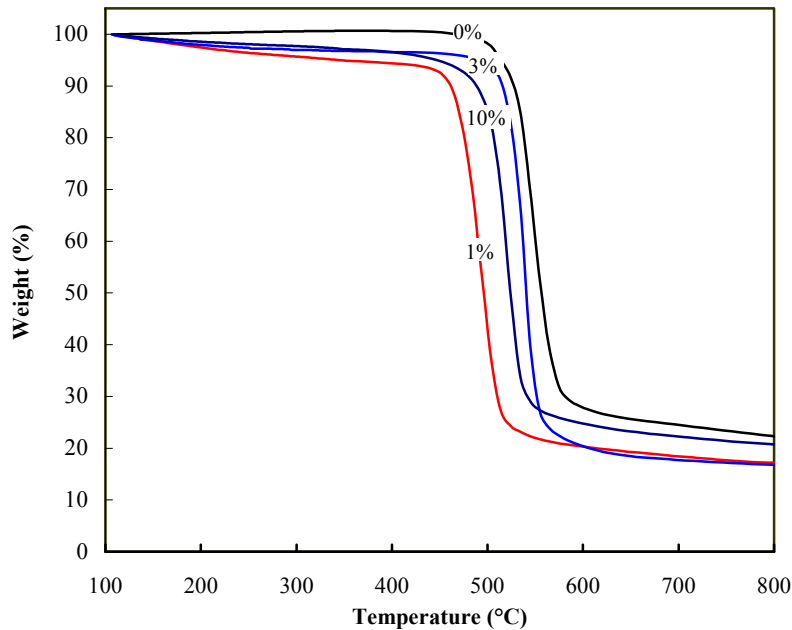


**Figure 20. Thermal gravimetric analysis traces of polycarbonate and polycarbonate-thermally exfoliated graphite oxide composites with different loading of thermally-exfoliated graphite (0%, 1%, 3%, 10% by weight).**

- Test specimens of polycarbonate-graphene composites with graphene loading between 0.5 to 3 wt.% have been processed via extrusion followed by hot pressing the composite samples into 0.5" disks for thermal conductivity measurement. Standard dogbone samples have also been made for mechanical testing. Due to the high surface area of the graphene sheets and the limited power of the microcompounder used for processing the samples, difficulties were encountered in processing samples with high graphene loading (4-10 wt.%). These samples were processed by directly hot pressing them into the required specimen dimensions.
- Test samples of polyphenylene sulfide-graphene composites with graphene loading 1 to 20 wt.% were scheduled for processing at Case Western Reserve University to make test specimens for thermal conductivity and mechanical properties testing.

## 5. Conclusion

Recently developed carbon-fiber polymer composites, with thermal conductivities equal to or higher than corrosion resistant titanium, can be applied to the development of low-cost and low-weight compact heat exchangers for corrosive fluids. These attributes, combined with the low energy investment in the formation and fabrication of these polymer and their ease of manufacturing, motivated this pioneering two-year effort to explore the viability of using thermally-enhanced polymers in gas-liquid and liquid-liquid seawater heat exchanger applications for the oil and gas industry. Mathematical models, based on thermofluid correlations for laminar and turbulent flow in channels, were developed for finned-plate and tube-and-shell heat exchangers. These models were used to study and compare the performance of heat exchangers using polymers of various thermal conductivities and operating with seawater at the temperatures and salinity levels typical of the UAE coastline. A laboratory water-air polymer heat exchanger, molded with a carbon-filled PolyOne Nylon, was tested and its performance compared to theoretical predictions and to the empirically determined characteristics of an unfilled polymer heat exchanger.

Optimizing the heat exchanger designs requires characterization of the moldability over the design space. However, molding actual parts to explore the design space would be time consuming and costly. Hence, a more suitable approach is to explore the design space using mold flow simulation software such as Moldflow. However, mold flow simulations can also be time consuming and not directly useful for design exploration. Hence, the simulation was conducted for discrete points in the design space and a meta-model was constructed based on the simulation results. As part of this study, Moldflow filling predictions were validated using a spiral mold test. The moldability analysis model developed as a part of this work can be used to identify regions of infeasible designs within the parametric space. Maps like that of Figure 12 can be used to elucidate possible changes, which can be made to make designs feasible. This model provides a computationally fast analysis tool (running time is less than 1 second) when compared to Moldflow predictions (running time is greater than 2 hrs).

The results of the numerical and experimental aspects of this study suggest that thermally-enhanced polymers can be applied to the development of low-cost and low-weight compact heat exchangers for seawater cooling of hot gas streams in LNG processing at considerable savings in weight, cost, and invested energy.

## 6. Recommendations for Future Work

The goal of the proposed extension of this polymer heat exchanger project is to develop the science and technology needed to underpin the systematic design of polymer heat exchangers for the fossil fuel industry. Successful development of cost-effective, high-performance polymer heat exchangers will require a detailed understanding of the limitations imposed on the thermal performance of such heat exchange devices by the selection of the polymer and fill materials and concentration, molding limitations, failure mechanisms, and the energy investment in the fabrication and formation of the heat exchangers. The fabrication and testing of pilot-scale polymer heat exchangers, along with the development, experimental and numerical validation, and delivery of a computerized design methodology, would provide PI with a unique capability to develop low life-cycle-cost heat exchange systems for the petroleum and gas industries.

## 7. References

- [2] Zaheed, L., and Jachuck, R.J.J., 2004, "Review of polymer compact heat exchangers, with special emphasis on a polymer film unit," *Applied Thermal Engineering*, Vol. 24, No. 16, pp. 2323-2358.
- [3] Bahadur, R., and Bar-Cohen, A., 2005, "Thermal Design and Optimization of Polymer-Based Pin Fin Natural Convection Heat Sinks," *IEEE Transactions on Components and Packaging Technologies*, Volume 28, Issue 2, pp 238-246.
- [4] Zweben, C., 2003, "Emerging High-Volume Commercial Applications for Thermally Conductive Carbon Fibers," *Sixth International Business Conference on The Global Outlook for Carbon Fiber*, San Diego, California, USA, November 5 – 7.
- [5] Shah, R.K., 2006, "Advances in science and technology of compact heat exchangers," *Heat Transfer Engineering*, vol. 27, no. 5, pp. 3-12.
- [6] Pugh, S. J., et al, 2005, "Fouling During the Use of Seawater as Coolant—the Development of a User Guide," *Heat Transfer Engineering*, vol. 26, no. 1, pp. 35-43.
- [7] Zweben, C., 2004, "Emerging High-Volume Commercial Applications for Advanced Thermally Conductive Materials," *SAMPE 49th International Symposium and Exhibition*, Long Beach, California.
- [8] Bahadur, R., and Bar-Cohen, A., 2005, "Thermal Design and Optimization of Polymer-Based Pin Fin Natural Convection Heat Sinks," *IEEE Transactions on Components and Packaging Technologies*, Volume 28, Issue 2, pp 238-246.
- [9] Suzuki, T. and Takahashi, J., 2005, "Prediction of energy intensity of carbon fiber reinforced plastics for mass-produced passenger cars," *9th Japan International SAMPE Symposium JISSE-9*, Tokyo, Japan, 29 November–2 December, 2005.
- [10] Wang, L., and Sundén, B., and Manglik, R.M., 2007, "Plate Heat Exchangers: Design, Applications and Performance," *WIT Press*, Volume Billerica, MA.
- [11] Kampe, S.L., 2001, "Incorporating Green Engineering in Materials Selection and Design," *2001 Green Engineering Conference*, Roanoke, Virginia, July 29-31 2001.
- [12] Osswald, T.A., and Hernández-Ortiz, J.P., 2006, "Polymer Processing: Modeling and Simulation," *Hanser Gardner*, Cincinnati, OH.

## 8. Publications

- [1] Bar-Cohen, A., Rodgers, P., and Cevallos, J., 2008, "Application of Thermally Conductive Thermoplastics to Seawater-Cooled Liquid-Liquid Heat Exchangers," *Proceedings 5th European Thermal-Sciences Conference*, Eindhoven, Netherlands, paper HEX\_10 .
  - [2] Bar-Cohen, A., Rodgers, P., and Cevallos, J., 2008, "Application of Thermally-Enhanced Thermoplastics to Seawater-Cooled Liquid-Liquid Heat Exchangers," *Proceedings 2nd International Energy 2030 Conference*, Abu Dhabi, United Arab Emirates, pp. 354-364.
  - [3] Luckow, P., Bar-Cohen, A., Rodgers, P., and Cevallos, J., 2008, "Energy Efficient Polymers for Gas-Liquid Heat Exchangers," *Proceedings ASME 2nd International Conference on Energy Sustainability*, Jacksonville, FL.
  - [4] Luckow, P., Bar-Cohen, A., Rodgers, P., and Cevallos, J., 2008, "Energy Efficient Polymers for Gas-Liquid Heat Exchangers," *Proceedings 2nd International Energy 2030 Conference*, Abu Dhabi, United Arab Emirates, Poster Presentation, pp. 138-141 (abstract).
  - [5] Bar-Cohen, A., Gupta, S.K., Rodgers, P., Cevallos, J., and Adi, M., "Mold Filling Metamodel for Polymer Composite Heat Exchangers," *Proceedings 2nd International Energy 2030 Conference*, Abu Dhabi, United Arab Emirates, Poster Presentation, pp. 319-321 (abstract)
- In Preparation:
- [6] Bar-Cohen, A., Luckow, P., Rodgers, P., 2009, "Minimum Mass Polymer Seawater Heat Exchangers for LNG Applications," *International Symposium on Convective Heat and Mass Transfer in Sustainable Energy*. Yasmine Hammamet, Tunisia.
  - [7] Bar-Cohen, A., Cevallos, J.G., Bergles, A., Gupta, S.K., Rodgers, P., *Polymer Heat Exchangers: Past, Present, Future Prospects*.
  - [8] Cevallos, J.G., Gupta S.K., Bar-Cohen, A., *Mold Filling Metamodel for Polymer Composite Heat Exchangers (tentative title)*.

## **9. Visits**

- Juan Cevallos visited the Petroleum Institute in Abu Dhabi in the summer of 2007, and worked alongside Prof. Peter Rodgers to prepare his first publication, and to meet with ADGAS officials regarding their heat exchanger needs
- Patrick Luckow visited the Petroleum Institute during the summer of 2008 to work on two of his publications.
- Mahmoud Adi, a senior undergraduate at The Petroleum Institute, conducted the Moldflow simulations as part of a two-level factorial design experiment during his 2008 summer internship at UMD and will return for a 1-month internship in January 2009

## **10. GRAs (names, degrees, graduation)**

Juan Cevallos, PhD, 2011(expected)  
Patrick Luckow, MS, 2009 (expected)

## Study of Condensing Flows in a Micro-scale Channel with a Micro-element Array and Visual Techniques

UM Investigators: Dr. S. Dessiatoun, Dr. A. Shoostari

GRA's: Ebrahim Al-Hajri

PI Investigator(s): Dr. M. Ohadi, Dr. A. Goharzadeh

Start Date: December 2006

FINAL REPORT

### Abstract/Objectives

With the development of new manufacturing technologies and fluid maintenance techniques, miniaturization of heat transfer systems has proven to be possible and economical. Two orders of magnitude of reduction in system weight and volume with significant reductions in cost have become feasible. Furthermore, micro-channels can support high heat fluxes with small temperature gradients and thus minimize the failure risks due to thermal stress. This is especially important for cooling high flux electronics and the next generation of microprocessors. Sufficient data and advanced modeling are available to characterize boiling processes in microchannels. However, such data are lacking for condensing flows in microscale passages and are necessary for the development of predictive models and correlations in the future.

This study investigated the fundamentals of the two-phase condensing flow phenomenon in a sub-millimeter microchannel by using different experimental techniques. In order to understand the mechanism of the flow, measurements of heat flux, temperature, pressure drop and flow velocities are necessary.

The specific objectives of this research are (1) to generate, through experimentation, comparisons of heat transfer rates and pressure drops for two identified refrigerants in a flat plate, single-channel, microscale condenser; (2) to develop correlations of heat transfer coefficient and pressure drop using the experimental data obtained in this project together with data obtained in the literature; (3) to determine whether there is any deviation in heat transfer and pressure drop compared to macroscale, conventional heat exchangers and if there is, to quantify it; and (4) to study the structure of flow regimes at small scales using flow visualization.

### Approach

In the present study, we design, fabricate and test a microscale single-channel flat plate condenser with a channel width of 0.4 mm and channel height of 2.8 mm. The corresponding aspect ratio is 7 and the hydraulic diameter is 0.7 mm. Experiments are designed to quantify the effects of saturation temperature, refrigerant mass flux, and inlet superheating temperature on the heat transfer and pressure drop of the refrigerant in the micro condenser. Experiments are carried out in an experimental loop consisting of test section module, a coolant loop with accessories, and a data acquisition system. The collected experimental data, are analyzed, correlated, and compared against commonly used correlations for macroscale condensation. The flow visualization technique is used to investigate the collapse of micro-bubbles and underlying physics behind the phenomena are studied and utilized to improve the knowledge-base of the field. Energy balance and uncertainty analysis are performed according to available standard procedures.

This combined data set is intended to serve in future predictive models and correlations, which will pave the way for optimization of two-phase, high-performance heat transfer systems.

### Two-Year Schedule

UM-side participation

Year 1.

Literature review and summary.

Fabrication of experimental setup.

Experimental parametric study  
Year 2.  
Final fabrication of visualization prototype and loop.  
Visualization study.  
Development of correlations  
Final report.

PI-side participation  
Year 1.  
Literature review and summary.  
Development of optimum visualization setup.  
Year 2.  
Experimentation on visualization setup designed and fabricated in UM.  
Final report.

### Literature Review

Existing empirical results of two-phase flows in micro channels are limited to out-dated refrigerants and are for high uncertainty data collection. To design accurate microdevices, it is necessary to know the behavior of the fluid flow and values of the transport parameters as precisely as possible (Bontemps (2005)). A considerable amount of researchers have been investigating the evaporation phenomena in microchannels and very little work has been done on condensation. Although these two processes have similar flow patterns, the absence of nucleation in condensation make the physics of these processes significantly different.

Riehl et al. (1998) performed a literature survey of experimental single-phase and two-phase heat transfer data in microchannels and compared them to the available analytical models. The comparisons showed large discrepancies. The models that the authors examined were not able to predict the experimental data. Furthermore, correlation of microchannel convective flow also showed wide discrepancies. Riehl et al. (2002) presented experimental results of condensation for miniature systems with a restricted heat dissipation area while using methanol as the working fluid. The experiments were conducted for two different saturation temperatures, and heat dissipation ranging from 20 to 350 W for four microchannel condensers with channel diameters between 0.5 to 1.5 mm. All the channels had aspect ratios of 1. Their results showed high heat transfer capabilities with Nusselt number ranging from 15 to 600. They also obtained a Nusselt number correlation which was able to predict 95% of the data within a 25% error band.

Garimella et al. (2005) experimentally evaluated different shapes and sizes of micro and mini-channels for pressure drop and heat transfer of a condensing flow. The channels' hydraulic diameters ranged from 0.4 to 5 mm for qualities ranging from 0% to 100% and mass fluxes between 150 kg/m<sup>2</sup>s and 750 kg/m<sup>2</sup>s. The authors developed a model for pressure drop, which is able to predict 90% of the measured data within 28%; however, the model depends on flow visualization information, which is not practical for use as a general correlation for condenser design. Coleman and Garimella (2000-I & II and 2003) identified wavy, intermittent and dispersed flow regimes inside round and square channels with a hydraulic diameter ranging from 1 to 5 mm, using R134a as the refrigerant. They developed an equation describing transition criteria between the regimes.

El Hajal et al. (2003) studied condensation of 15 different fluids amongst which were pure refrigerants and refrigerant blends. They used Kattan et al. (1998-I; 1998-II; 1998-III) studies of evaporating refrigerants to develop a flow regime map and a heat transfer model. In this study, they observed the following regimes: slug flow, intermittent, annular, stratified wavy, fully stratified and mist. However, the model did not include the bubbly flow regime. They claimed that heat transfer occurred due to two mechanisms: film condensation and convective condensation. The regimes that contributed to convective condensation were annular, mist and intermittent flow, whereas stratified-wavy and stratified flows were governed by both mechanisms. The developed

heat transfer correlation was governed by the interfacial friction factor, Prandtl number and Reynolds number.

Baird et al. (2003) developed a model that agreed with their experimental data more than other models by using a simple shear-driven annular flow model to predict the condensation heat transfer coefficient.

Other researchers (Kim et al. (2003) and Wang et al. (2002)) suggested that the condensation phenomena in minichannels may be different from those in macrochannels. Kim et al. (2003) found that the existing heat transfer correlations fall short of predicting their experimental investigation data of R134a condensing inside a single round tube with an inner diameter of 0.691 mm, and at low mass fluxes the disagreement was more obvious. The existing correlations that Wang et al. (2002) have tested over-predicted their heat transfer data obtained in a horizontal rectangular multi-channel condenser with 1.46 mm hydraulic diameter of channels.

Cavallini et al. (2002) investigated condensation of R123a, R125, R410a, R32, R236ea and R22 inside a round tube with 8 mm inner diameter while varying mass flux from 100 to 750 kg/m<sup>2</sup>s. The study intended to improve Friedel's (1979) correlation in the annular regime. They also used the dimensionless vapor velocity to distinguish between the different flow regimes that exist in condensation. New coefficients were fitted to the Friedel's correlation from the study of the annular regime. Due to the insignificant effect of gravitational forces in the annular flow regime, Froude number was not used in the two-phase multiplier of the correlation. However, the correlation poorly described the transition of flow regimes.

From the above reviews, it is clear that some of the researchers focused only on the heat transfer aspect of the condensation, others reviewed the pressure drop part of the phenomena, while some looked at both. They also evaluated different channel sizes and shapes using a wide range of fluids. All the studies described above are based on channels with an aspect ratio close to one. Very few have examined condensation in high aspect ratio microchannels. However, high aspect ratio microchannels are widely used by industry, and some difference in condensation process, such as much earlier collapse of annular regime and liquid bridges cross flow, is expected. The effect of such differences may substantially effect heat transfer and pressure drop of condensation. In addition, the majority of studies have been done on multiple channels where flow maldistributions effect heat transfer and pressure drop significantly. To compliment prior studies, this work focuses on condensation of R134a and R245fa in a single microchannel with hydraulic diameter of 0.7 mm and an aspect ratio of 7:1.

### **Experimental Apparatus**

In a single microchannel, heat exchange is relatively small. Heat exchange with the environment can significantly affect the accuracy of experimental results. Therefore, the experimental set-up was designed and built such that heat losses were minimal. A schematic diagram of the test facility is shown in Figure 1. The testing setup consists of two loops: (1) the refrigerant loop and (2) the water-chilling loop. The refrigerant loop consists of a high precision Coriolis flow meter, variable-speed gear pump, pre-heater, heater, test section, reservoir, and sub-cooler. The refrigerant is circulated by the gear pump with precise flow rate control and then passes through a flow meter where the refrigerant flow rate is measured. The use of a gear pump instead of a compressor allows testing a pure refrigerant without the influence of the oil leakage from the compressor. This is especially important in order to accurately quantify the heat transfer coefficient and pressure drop in the micro condenser. It is also convenient to set and adjust small mass flow rates of the refrigerant across a broad range.

The microchannel was fabricated from a long HCOF copper block. A slitting saw in a milling machine is used to construct the microchannel. For the inlet and outlet of the condenser, two 1/8" holes are drilled at each end, and two stainless steel tubes are inserted in the holes constructed. In addition, two 1/16" holes are constructed, each at the ends of the channel, for pressure drop measurements. Then, the channel is filled with jeweler's wax, and the top surface is scraped flat

and chemically cleaned in preparation for electroplating the channel. Then the three inactive faces are painted with a nonconductive paint to resist deposition during electroplating. Next, the top of the wax-filled portion is painted with a thin strip of silver solution to make it electrically conductive. The channel is then submerged into a copper-sulfate solution to be plated to the desired thickness on the remaining open surface of the channel. After electro-plating, the wax in the channel is melted and drained by heating the channel. The channel is then chemically cleaned to remove traces of wax or silver paint. On the outer surface of the channel, five single Constantan wires and one copper wire are soldered to act as T-type thermocouples. The fabricated copper micro-channel is shown Figure 2 & 3.

The evaporator consisted of a copper tube with a resistance wire wound around the tube from the outside. By adding the desired amount of heat, a desired inlet quality could be achieved.

To control the operation pressure of the test loop, two electrical heaters were attached on the surface of the liquid reservoir. The heaters are connected to a Watlow ® PID controller as a means of pressure stabilization. The controller received a 0-5 Volt output signal from the absolute pressure transducer, determined the corresponding system pressure, and controlled the power input to the heaters on the reservoir, thereby controlling the system pressure by increasing and adjusting the reservoir temperature.

To minimize the heat losses, an insulation of Dewar cylinders shells consisting of two concentric glass cylinders of diameters 1 in. and 2 in., respectively, with a high vacuum between the walls is used. The condenser and evaporator Dewars spanned the length of the condenser channel and evaporator tube, respectively, Figure 4. In addition, the inner cylinder of the condenser Dewar acted as a water jacket. The vacuum provides good insulation from heat loss or gain. In addition, a copper elbow connecting the Dewar cylinders is equipped with Kapton ® heaters controlled by a PID temperature controller. The heaters keep the surface temperature of the elbow equal to that of the inlet refrigerant thus minimizing heat loss from the inlet T-connection acting as an adiabatic thermal shield.

The water loop is used to cool both the micro condenser and the sub-cooler. It consists of a refrigerated bath/circulator with pump which supplies flow to the condenser water jacket and the sub-cooler. The bath/circulator was used to provide constant water flow at the designated test conditions. For water flow rate measurements, a highly accurate capillary water flow meter was used to decrease the overall error of data measurement. The inlet and outlet water temperature are directly measured by four K-type thermocouples on each side. Averaging the reading of the four thermocouples on the water side inlet and outlet produced  $T_{water\_in}$  and  $T_{water\_out}$ , respectively.

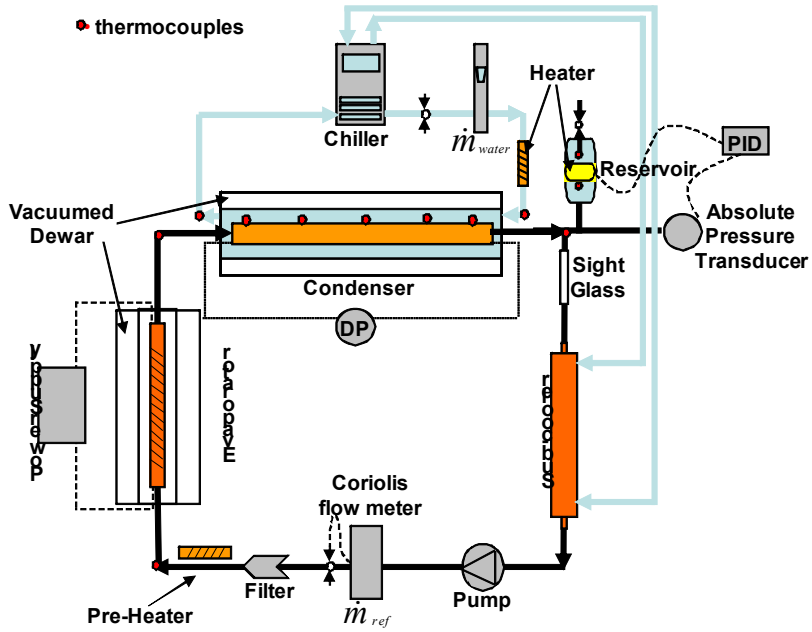


Figure 1 Schematic of experimental test setup

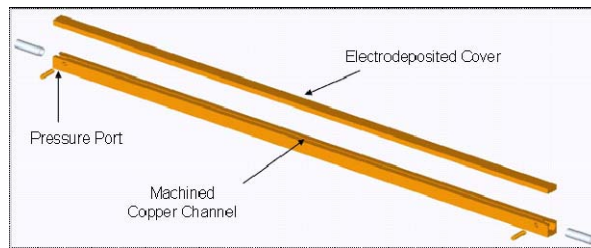


Figure 2 A drawing of the fabricated micro-channel

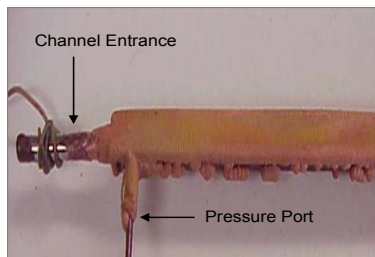
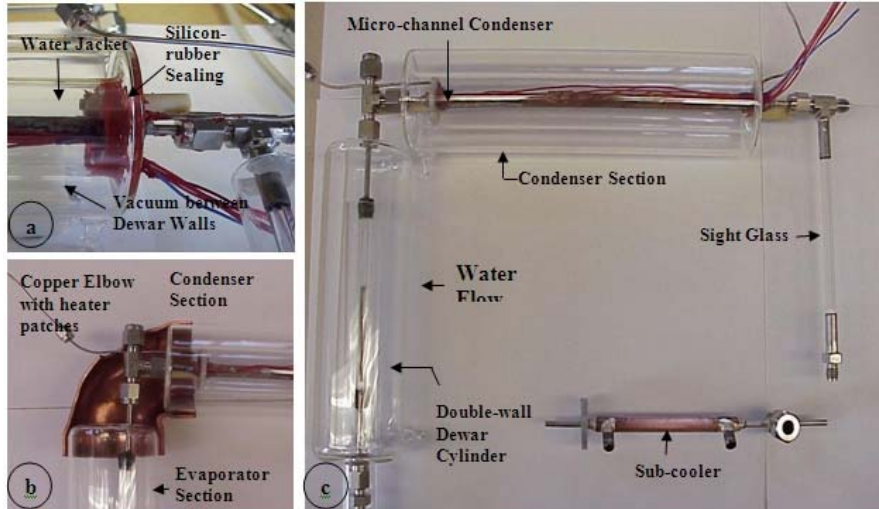


Figure 3 Electroplated micro-channel



**Figure 4** Details of test section: (a) details of the joint between condenser section and sight-glass (b) details of the joint between evaporator Dewar and condenser Dewar (c) view of the arrangement of various parts in the refrigeration loop.

### Testing Refrigerants

Two different refrigerants are used in this investigation (R134a and R245fa), which provides a wide band of physical properties difference to explore in this investigation its effects on both heat transfer and pressure drop (Table 1) Refrigerants R245fa is low pressure refrigerant and has a slightly higher latent heat than R134a, and different density and surface tension.

**Table 1** Physical properties of tested refrigerants

	$T_{sat}$ (°C)	$P_{sat}$ (kPa)	Conductivity (mW/m.K)		Viscosity ( $\mu$ Pa.s)		Density ( $kg/m^3$ )		Enthalpy (kJ/kg)		Surface Tension (mN/m)
			liquid	vapor	liquid	vapor	liquid	vapor	liquid	vapor	
R134a	30	770	79.0	14.33	185.8	12.04	1187.5	37.53	241.7	414.8	7.42
	70	2116	61.7	20.45	106.4	14.65	996.2	115.6	304.3	428.7	2.61
R245fa	30	179	79.2	12.52	376.4	10.51	1325.1	10.11	239.6	427.5	13.41
	70	610	70.2	14.78	226.8	12.0	1204.7	33.43	295.7	456.6	8.35

### Data Reduction

Once the steady state conditions are established, all the temperatures, pressure drops, heating powers, and flow rates are measured and stored.

The average heat transfer coefficient of condensation is calculated based on average refrigerant saturation temperature, average wall temperature and water-side extracted heat by:

$$h_{avg} = \frac{Q_{water}}{A_{channel\ surface} (T_{sat,avg} - T_{wall,avg})} \quad (1)$$

Where,  $A_{channel\ surface}$  is the total heat transfer surface area of the microchannel in refrigerant side..  $T_{sat,avg}$  refers to the saturation temperature of the refrigerant corresponding to the average absolute pressure along the microchannel. It takes in account that the saturation temperature along the microchannel changes due to pressure drop  $T_{wall,ave}$  represents the average temperature of the micro-channel outer walls in the waterside. This temperature is calculated

based on the readings of five single-wires, calibrated, T-type thermocouples, equally spaced and embedded in the outer wall of the micro-channel condenser.

Considering the thermal resistance of channel walls, the corrected average temperature of inner walls is calculated as

$$T_{\text{wall-avg}}^{\text{corrected}} = T_{\text{wall-avg}} + \frac{Q_{\text{water}}}{k_{\text{Cu}} A_{\text{channel surface}}} \quad (2)$$

$Q_{\text{water}}$  is the total heat transfer amount from the refrigerant to cold water. It is determined from an energy balance on the waterside:

$$Q_{\text{water}} = \dot{m}_{\text{water}} (h_{\text{GT}=\text{T}_{\text{out}}}^{\text{out}} - h_{\text{GT}=\text{T}_{\text{in}}}^{\text{in}}) \quad (3)$$

Where

$$\Delta h = C_p \Delta T + v \Delta P \quad (4)$$

The pressure drop on the water side was not measured during experiments; however, when calculated the result was in fractions of Pascal. In addition, the specific volume of water is relatively small, 0.001 m<sup>3</sup>/kg, which makes the second term in the right side of equation (4) negligible. Thus reduces the  $Q_{\text{water}}$  to:

$$Q = Q_{\text{water}} = \dot{m}_{\text{water}} C_p (T_{\text{water-out}} - T_{\text{water-in}}) \quad (5)$$

$\dot{m}_{\text{water}}$  refers to the mass flow rate of water entering the test section.  $T_{\text{water-out}}$  and  $T_{\text{water-in}}$  represent temperatures of water at the outlet and inlet of the water jacket, respectively.

## Experimental Results

Experimental tests were conducted to study the effect of three different parameters on average heat transfer coefficient and pressure drop for two refrigerants selected in this study, namely R143a and R245fa. The range of parameters variations is presented in Table 2.

**Table 2 Ranges of testing parameters**

Testing Parameters	Range
Mass Flux (kg/m <sup>2</sup> s)	50 – 500
Saturation Temperature (°C)	30 – 70
Super Heat (°C)	0 - 15

### Effect of Mass Flux

#### Average Heat Transfer Coefficient

Figures 5 and 6 show the effect of mass flux on average heat transfer for the refrigerants R134a and R245fa at a fixed saturation temperature of 50 °C, respectively. This saturation temperature is chosen as the midpoint of the experimental range (30 – 70 °C). As seen in the figures, the heat transfer coefficient is positively affected by increasing the mass flux in the range of 50 – 500 kg/m<sup>2</sup>s. This is because the velocity is increased, enhancing the convection effects. The heat transfer coefficient is dominated by the thin-film condensation process, and when the velocity is increased, the annular flow regime becomes longer, therefore contributing to the increase in heat transfer.

When comparing the performance of the two refrigerants in terms of average heat transfer coefficient, it is clear that R245fa has on average 20% better heat transfer than that of R134a.

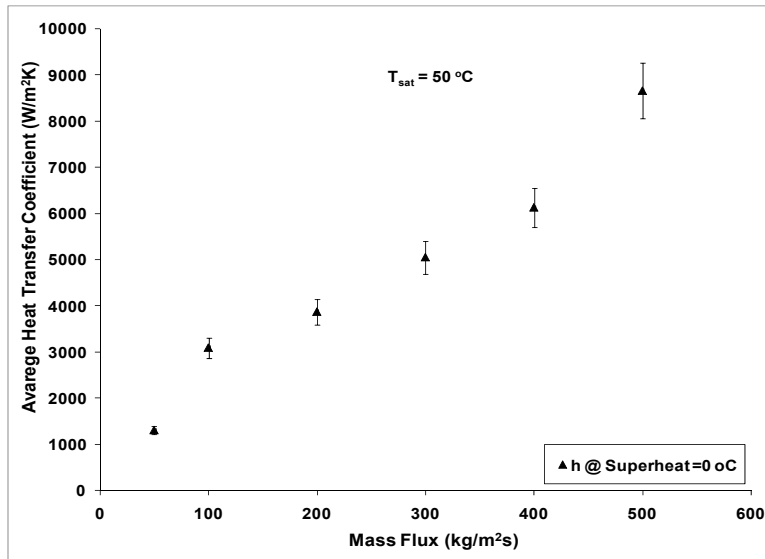


Figure 5 Effect of mass flux on average heat transfer coefficient for R134a at  $T_{sat} = 50\text{ }^{\circ}\text{C}$

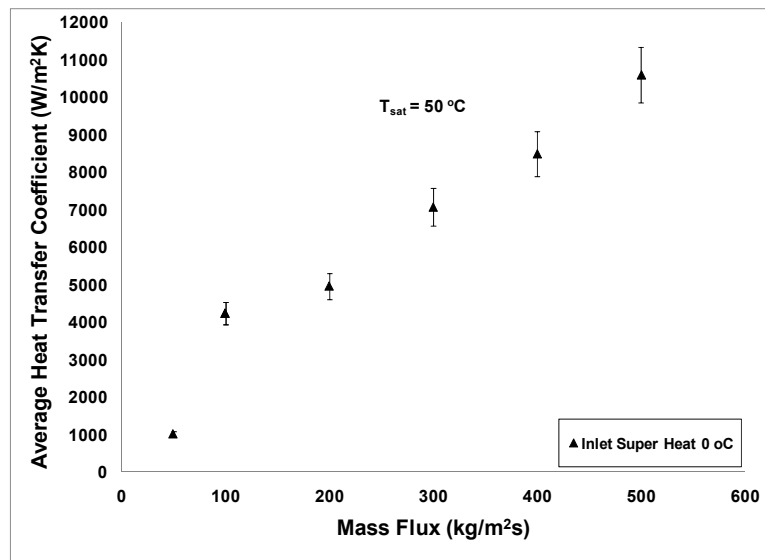


Figure 6 Effect of mass flux on average heat transfer coefficient R245fa at  $T_{sat} = 50\text{ }^{\circ}\text{C}$

#### Pressure Drop

It is known that pressure drop has a squared power relation with the velocity and hence is significantly affected by increase in the mass flux, Figure 7 and 8. It is noteworthy that R245fa has almost three times higher pressure drop as R134a does. This is mainly due to the higher surface tension, liquid viscosity and vapor density values of R245fa. However, from these properties vapor density contributes the most to the increase in pressure drop because vapor is dominant in the channel. This can be sensed when comparing the vapor density of the two testing refrigerants, where the vapor density of R245fa is more than three times lower than that of R134a ( Table 1); therefore, the magnitude of pressure drop of R245fa compared with R134a at the same mass flux is three times higher.

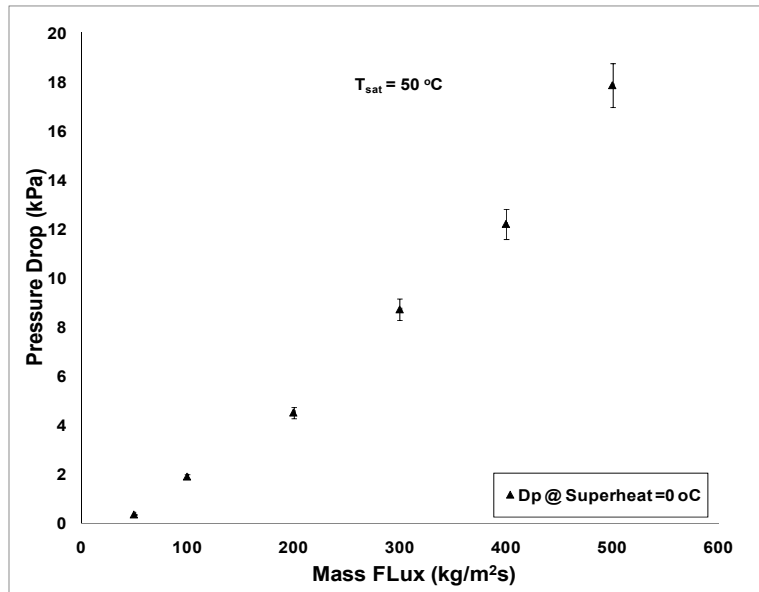


Figure 7 Effect of mass flux on pressure drop R134a at  $T_{sat} = 50\text{ }^{\circ}\text{C}$

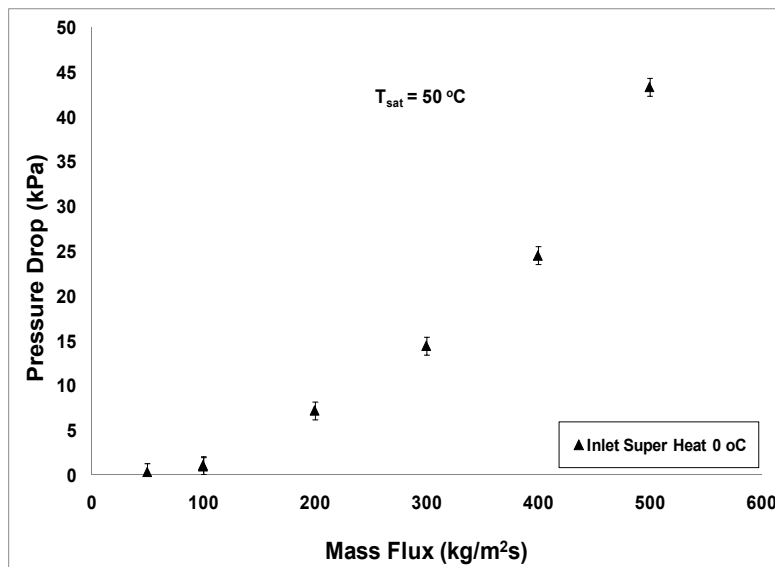


Figure 8 Effect of mass flux on pressure drop R245fa at  $T_{sat} = 50\text{ }^{\circ}\text{C}$

### Effect of Saturation Temperature

#### Average Heat Transfer Coefficient

Average heat transfer coefficient shows a descending trend with increasing the saturation temperature, as shown in Figure 9 and 10. This is mainly due to increases in system pressure when increasing the saturation temperature, because the specific volume decreases, and as a result, the vapor velocity decreases due to increase in vapor density, which reduces the heat transfer. Therefore, the heat transfer is higher at lower saturation temperatures.

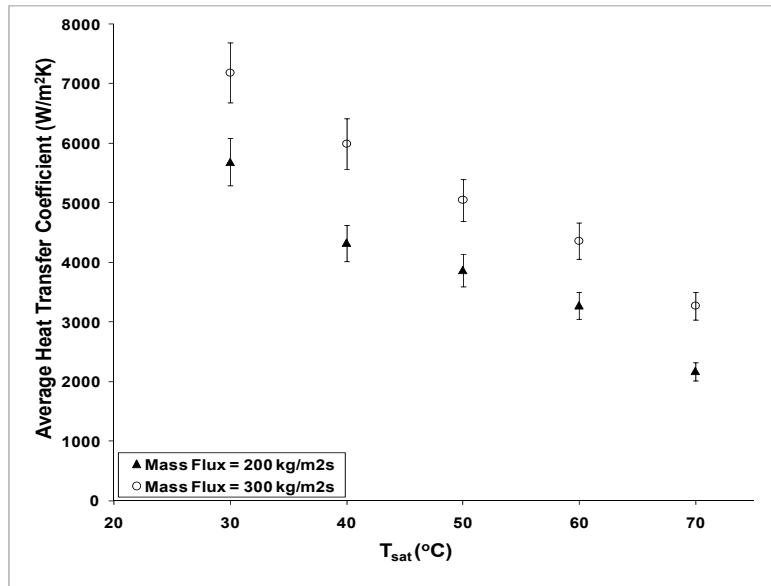


Figure 9 Effect of saturation temperature on average heat transfer coefficient for R134a

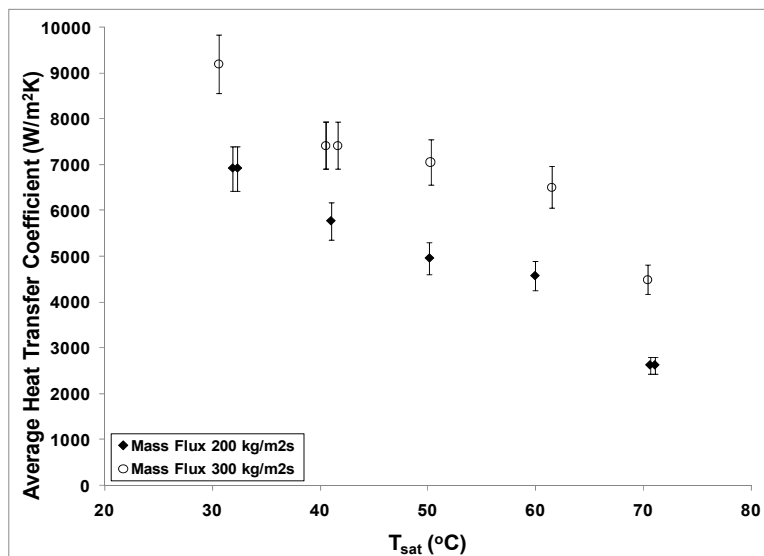


Figure 10 Effect of saturation temperature on average heat transfer coefficient for R245fa

### Pressure Drop

As for the pressure drop, increasing the saturation temperature has a significant effect on decreasing the pressure drop, as seen in Figure 11 and 12. This is due to the sensitivity of pressure drop to liquid viscosity and vapor density; because liquid viscosity is higher and vapor density is lower at 30 °C than at 70 °C, as can be seen in Table 1 when the saturation temperature increases, the volumetric flow rate decreases therefore the velocity is lower. In another word, vapor is dominant in the channel and as saturation temperature increases, vapor density increases; thus decreasing the velocity; as a result, decreasing the pressure drop. The magnitudes of the effect of each of these properties are illustrated in Figure 13 and 14. It is obvious that more than one fluid property is affected by changing saturation temperature, and then these properties have an effect on pressure drop. However, only one or two properties significantly affect the pressure drop such as: liquid viscosity and vapor density. Where on average the liquid viscosity of R245fa is twice of that of R134a and decreases about 40% when the saturation temperature is changed from 30 to 70 °C. On the other hand, vapor density of

R134a on average is three times higher than that of R245fa and the lower vapor density, the higher volumetric flow, thus the higher the pressure drop. In addition, it is believed that vapor is dominant in the channel; therefore, the effect of liquid viscosity is small compared to the effect of vapor density on pressure drop. This explains why the pressure drop of R245fa is three times larger than that of R134a.

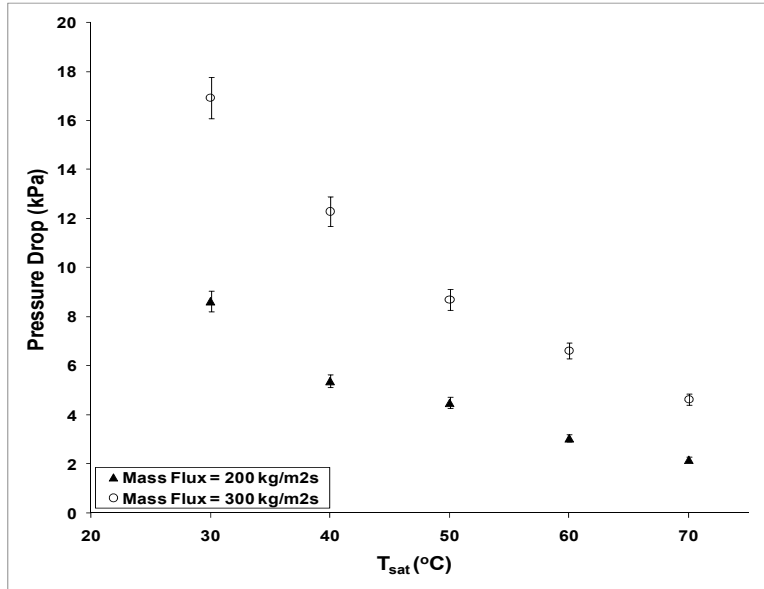


Figure 11 Effect of saturation temperature on pressure drop for R134a

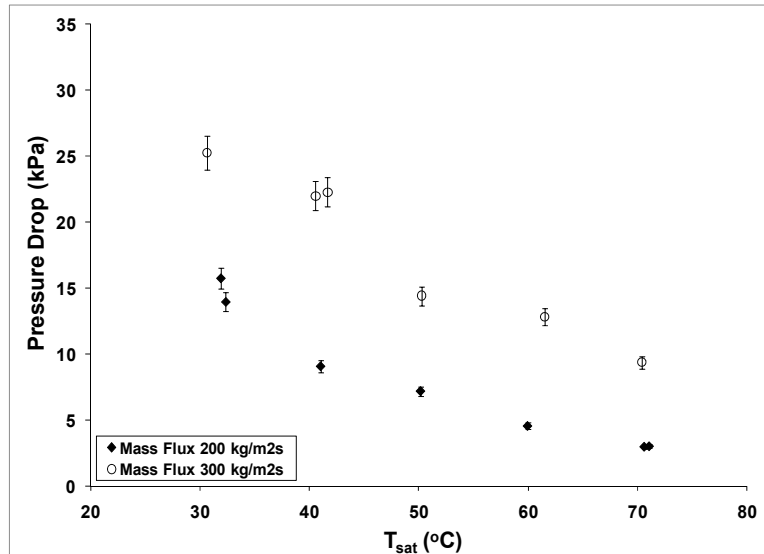


Figure 12 Effect of saturation temperature on pressure drop for R245fa

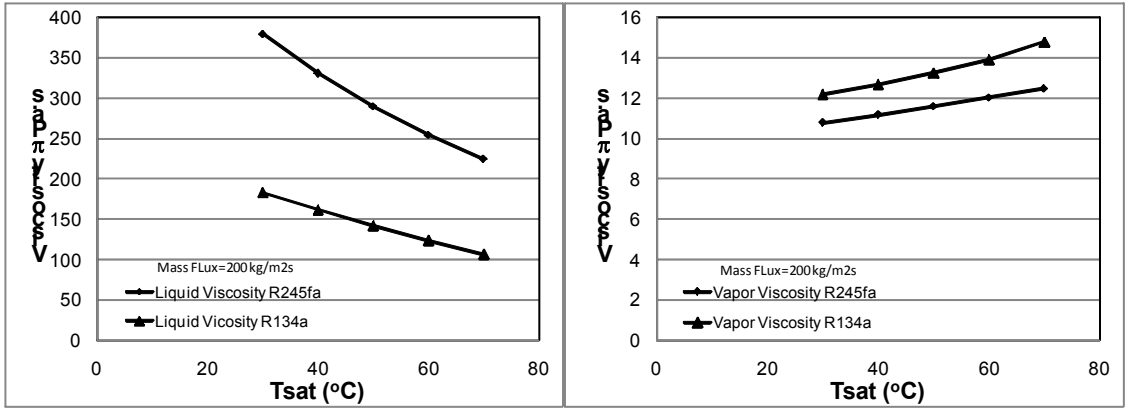


Figure 13 The change of liquid & vapor viscosity with saturation temperature for R134a & R245fa

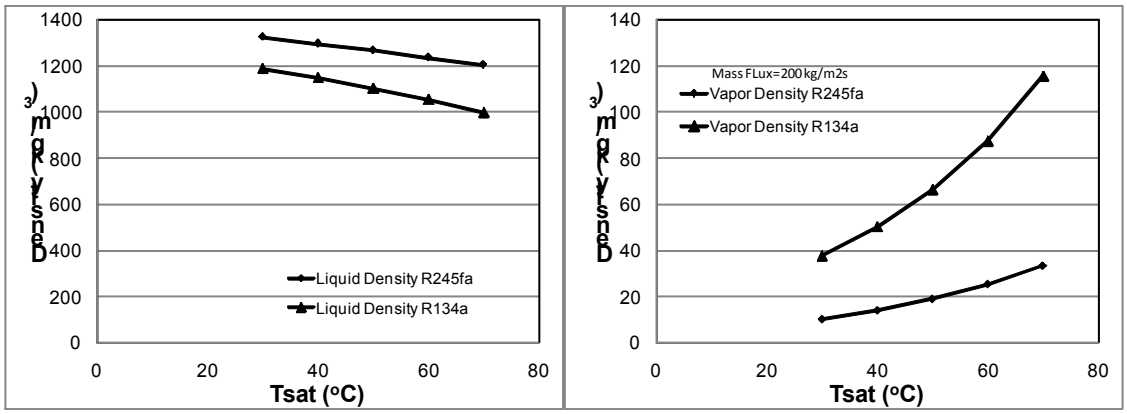


Figure 14 Change of liquid & vapor density with saturation temperature for R134a & R245fa

Effect of Inlet Superheat

Average Heat Transfer Coefficient

It is worth mentioning here that saturation temperature is used in calculating the average heat transfer coefficient. Since only the average heat transfer coefficient was measured in this study, it was difficult to find the heat transfer in the superheated region. Local heat transfer coefficient is required to calculate the length of the superheated region, from which heat transfer in that region can be estimated.

Figure 15 and 16 illustrate that as inlet superheat increases; the average heat transfer modestly increases. This could be because we used the saturation temperature to calculate the heat transfer coefficient in superheated conditions or because of the length of the annular flow region, which would cause more heat to be transferred than the heat transferred at the lower inlet superheat. The heat transfer difference between 0 and 15 °C superheat is insignificant (10-15% of total heat transfer in the channel); and the local heat transfer coefficient at the inlet is significantly high; hence, the “extra” heat due to inlet superheat is quickly absorbed in the initial part of the channel. Since the figure shows average heat transfer, the inlet superheat is not obvious.

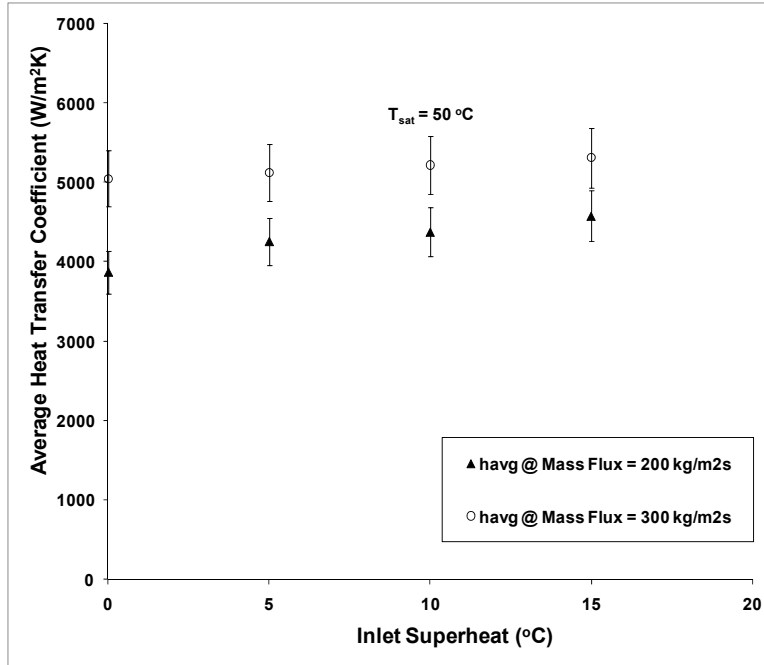


Figure 15 Effect of inlet superheat on average heat transfer coefficient at  $T_{sat} = 50\text{ }^{\circ}\text{C}$  for R134a

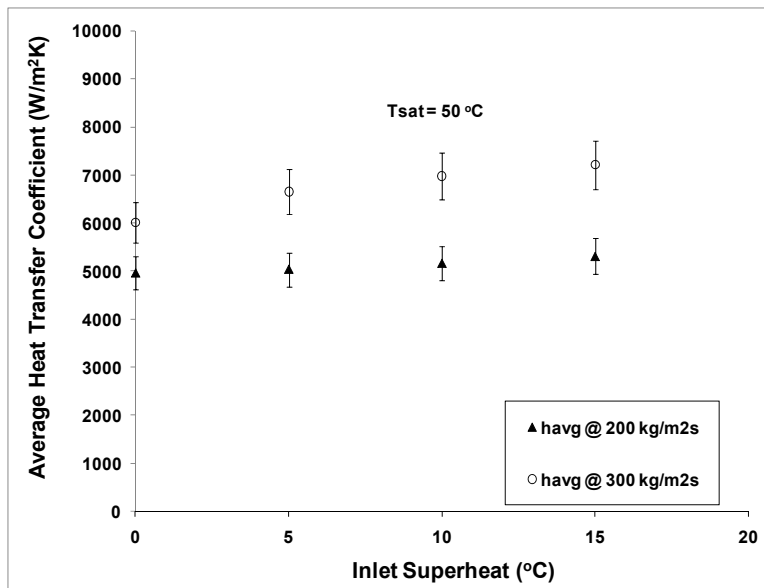


Figure 16 Effect inlet superheat on average heat transfer coefficient at  $T_{sat} = 50\text{ }^{\circ}\text{C}$  for R245fa

### Pressure Drop

The variation of pressure drop as a function of degree superheat at a given mass flux (200 & 300 kg/m<sup>2</sup>sec) and at 50 °C saturation temperature, the pressure drop is almost constant at different superheats as shown in Figure 17 and 18. It is known that pressure drop of two phase flows differs - It is known that pressure drop is dependant of flow regime. Thus, it is believed that the flow pattern in the significant remaining length of the channel (after the annular flow zone) is more or less the same as in the zero-superheat case. Moreover, variation of pressure drop with superheat at a given mass flux is negligible. Since all the tests

were conducted under the condition of having 100% quality entering the condenser and 0% quality leaving the condenser, then the overall flow pattern is not much different at various superheats and can be expected to be almost the same except at the inlet where the annular flow is expected to be a bit longer in higher superheats.

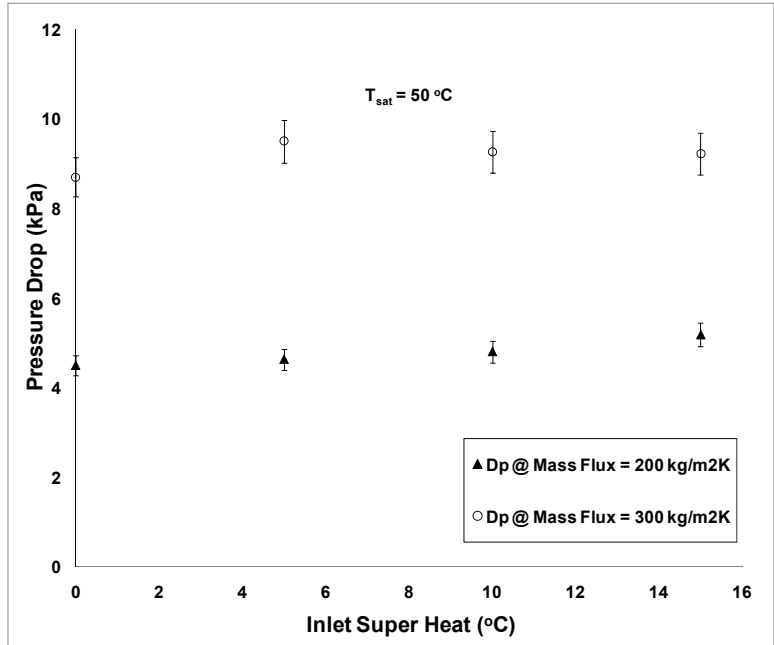


Figure 17 Effect of inlet superheat on pressure drop at  $T_{sat} = 50\text{ }^{\circ}\text{C}$  for R134a

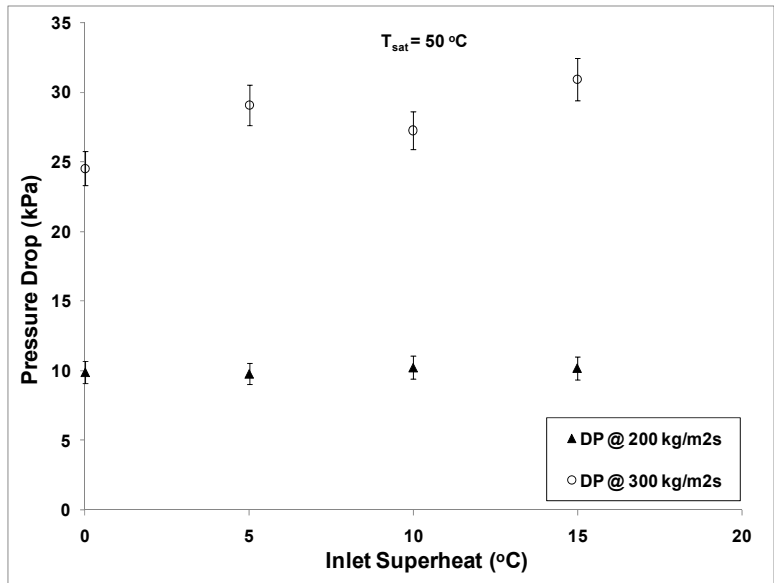


Figure 18 Effect of inlet superheat on pressure drop at  $T_{sat} = 50\text{ }^{\circ}\text{C}$  for R245fa

### Correlations

One of the objectives of this study was to develop empirical correlations for average heat transfer and pressure drop coefficients of condensation in micro-channels applicable for heat exchangers design. As a starting point, several widely used and well-known correlations for both heat transfer and pressure drop coefficients were collected from the literature. The vast majorities of these correlations have been developed for local heat transfer and pressure drop; however, the data

collected in this investigation are average values of heat transfer coefficient and the overall pressure drop of the channel.

### Heat Transfer Coefficient Correlations

Since the data collected in this study for heat transfer coefficient were average values, a comparison between the data and correlation of local heat transfer coefficients would not be adequate. Therefore, a technique was developed to compare the average local values obtained from experiments with the average values calculated from the correlations. In order to calculate the averages from the local value correlations, the channel was divided into nine segments as shown in Figure 19.

Both the pressure and the temperature of the condenser inlet were measured using an absolute pressure transducer and T-type thermocouple, respectively. Also, the temperature of the condenser outlet, five temperature measurements along the channel wall, and the differential pressure were obtained experimentally. On the water side, inlet and outlet water temperatures and the water flow rate were also obtained from the experiments. All this information was then used in the correlations to calculate by iterative means the local heat transfer coefficient. Once the local HTC's were attained from the calculations, the mean average of the local HTC's was compared with the average heat transfer coefficient directly obtained from the experiments.

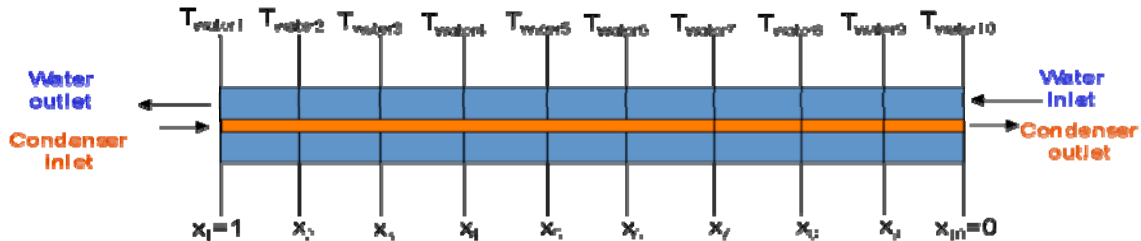


Figure 19 Schematic of the micro-channel divided to nine segments

The correlations that are studied in this investigation are developed for macro- and micro scale-channels, such as Dobson et al. (1998), Shah (1978), and the void fraction model correlation by El Hajal et al. (2003). The Dobson-Chato correlation is one of the recent correlations that was developed based on testing R12 and R134a (Dobson et al. 1998) using the Martinelli parameter. D. Jung et al. (2002) have modified the Dobson-Chato correlation, and this correlation was also used as a comparison to the experimental data of this investigation. Shah's (1978) correlation was developed by using nine different fluids, three different orientations, and a wide variety of tube diameter sizes. Thus, it was appealing to compare this macro-channel correlation with our micro-channel results to quantify any difference between the macro- and micro-channel results. The void fraction model correlation was also evaluated in this study due to the physics that this model employs and the different approach that this model takes from the previous two models.

### Shah Correlation

The Shah correlation (1978) was generated from his former correlation for saturated boiling by eliminating bubble nucleation (Shah, 1976). To find the heat transfer coefficient for condensation, Shah adopted two approaches to reach the best-fitting correlation for his data. In the first approach, a vapor-liquid density ratio was used, Equation 11:

$$C_o = \left( \frac{1}{x} - 1 \right)^{0.8} \left( \frac{\rho_v}{\rho_l} \right)^{0.8} \quad (11)$$

Then the two-phase heat transfer coefficient was defined as the superficial heat transfer coefficient of the liquid-phase divided by the constant  $C_o$ , Equation 12:

$$h_{tp} = \frac{1.8 h_l (1-x)^{0.8}}{C_o^{0.8}} \quad (12)$$

where  $h_l$  is the heat transfer coefficient, assuming all the flowing mass is liquid:

$$h_t = 0.023 Re_t^{0.8} Pr_t^{0.4} \frac{k_t}{D_t} \quad (13)$$

The second approach that Shah developed to replace the vapor-to-liquid density ratio ( $\rho_v/\rho_l$ ) by the reduced pressure, which is the ratio of saturation pressure to critical pressure,

$$p_{red} = P_{sat}/P_c \quad (14)$$

A new parameter was also defined to fit his data to the correlation, which is defined as:

$$Z = \left(\frac{1}{x} - 1\right)^{2.9} p_{red}^{3.4} \quad (15)$$

Then the two-phase heat transfer coefficient yields:

$$h_{tp} = \frac{1 + 3.8}{Z^{0.98}} h_t (1-x)^{0.8} = h_t \left( (1-x)^{0.8} + \left( \frac{3.8 x^{0.76} (1-x)^{0.04}}{p_{red}^{0.88}} \right) \right) \quad (16)$$

Shah (1978) went a bit further and defined a mean heat transfer coefficient, assuming negligible change in transport properties of liquid phase and pressure drop along the channel. This was achieved first by finding the relation of the vapor quality distribution to length. Then, integrating the later two-phase heat transfer coefficient, defined above, over the length of the channel. This led to developing Equation 17 for the case of  $x = 1$  to  $x = 0$ :

$$h_{tp-Mean} = h_{l1} \left( 0.55 + \left( \frac{2.09}{p_{red}^{0.88}} \right) \right) \quad (17)$$

All the above three heat transfer coefficient correlations that Shah (1978) developed for two-phase heat transfer coefficient were compared with the data collected in the present study. The comparisons are shown in Figure 18 and 17.

The reduced pressure and the mean methods were able to predict the R134a data fairly well; however, the density method under-predicted all the data, as shown in Figure 21.

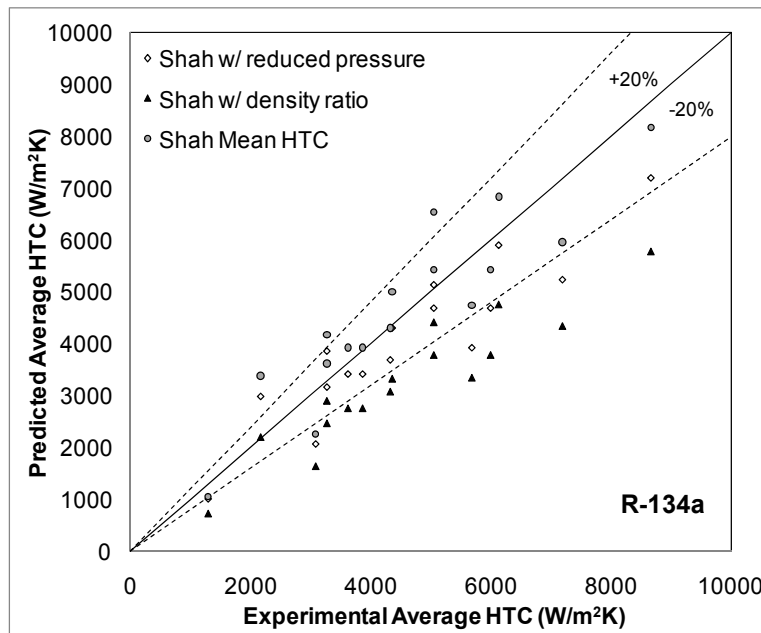


Figure 20 Comparison of Shah HTC correlations versus the current data of R134a

Figure 21 shows the comparison between the R134a data and the correlation and on Figure 21 the same for R245fa. It is obvious from the figure that the correlation under-estimated the majority of the data.

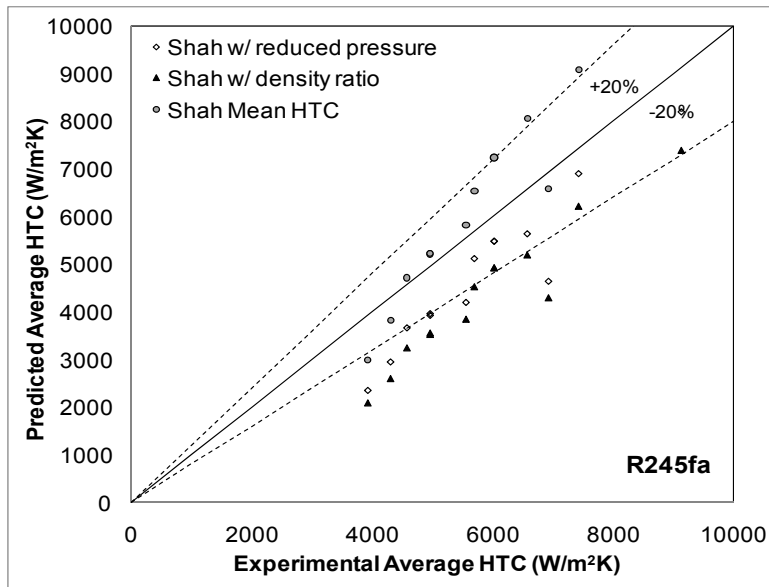
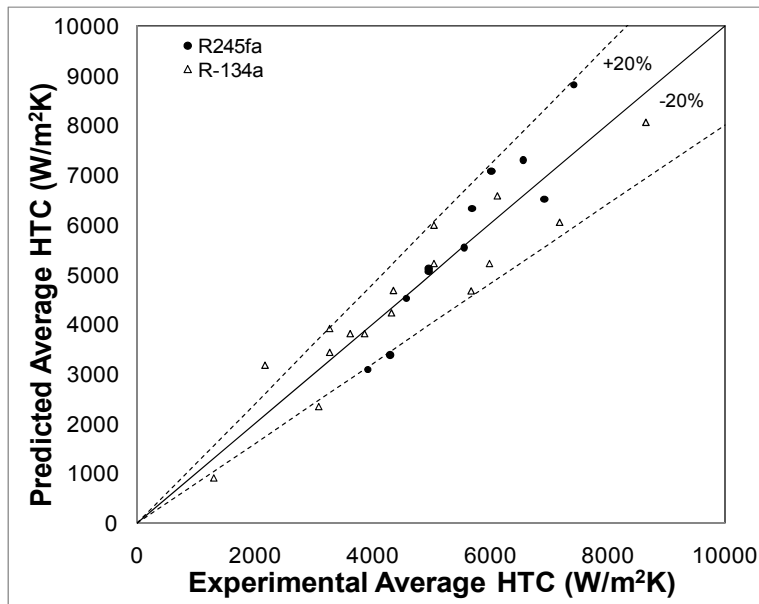


Figure 21 Comparison of Shah HTC correlations against the current data of R245fa

In an effort to fit the current study data to this correlation, since the reduced pressure model predicted the R134a data well, this model was modified. In addition, since the refrigerants have different critical pressures, it was clear that the disagreement between the R245fa results and the correlation was most likely due to its fluid properties. When modifying the power of the predicted pressure in the Shah two-phase heat transfer coefficient correlation from 0.38 to 0.53, the data for both refrigerants were in good agreement with the correlation, as seen in Figure 22.



**Figure 22 Comparison of the newly modified Shah's HTC correlation against the present data of R134a & R245fa**

Void Fraction Model

The void fraction is defined as the cross-sectional area occupied by the vapor with respect to the total cross-sectional area of the channel. El Hajal et al. (2003) have reported several prediction methods of void fractions. Amongst those methods is the homogenous model, which assumes the two phases travel at same velocity,  $e_h$ , and the drift flux, which takes into account the effect of surface tension and the mass velocity,  $e_{ra}$ . The drift flux model was developed by Rouhani et al. (1970) for flow boiling. These models are defined as

$$e_h = \left( 1 + \left( \frac{1+x}{x} \right) \left( \frac{\rho_v}{\rho_l} \right) \right)^{-1} \quad (18)$$

and

$$e_{ra} = \left( \frac{x}{\rho_l} \right) \left( [1 + 0.12(1-x)] \left( \frac{x}{\rho_l} + \frac{1-x}{\rho_v} \right) + \frac{1.18(1-x)[g_s \sigma (\rho_l - \rho_v)]^{-0.25}}{G \rho_l^{0.75}} \right)^{-1} \quad (19)$$

The homogenous model is mostly applicable at very high reduced pressures because the density of the vapor approaches that of the liquid (El Hajal et al. 2003). Whereas for the drift flux model it is mainly effective at low to medium pressures and as pressure approaches to the critical point, this model does not work towards the homogenous void fraction limit (El Hajal, et al. 2003). Both models are sensitive to saturation pressures; however, they produce reversed trends, as the investigators found. Therefore, a more general void fraction model was developed by El Hajal et al. to correct the effect of pressure on the models, which involved interpolation between the values of the models, the homogenous and the drift flux. The model was developed by taking the logarithmic mean void fraction between the values of  $e_h$  and  $e_{ra}$ , which is defined as

$$e = \frac{e_h - e_{ra}}{\ln \left( \frac{e_h}{e_{ra}} \right)} \quad (20)$$

This method gave the best fit to the data used in their investigation (El Hajal et al. 2003). Since this correlation comprises different physics from the previous two correlations by Dobson-Chato and Shah, it was considered in this study.

The heat transfer coefficient (Equation 19) that was used in El Hajal et al. (2003) is for the convective evaporation of Kattan et al. (1998) that includes two empirical constants  $c$  and  $n$ :

$$h_{cep} = c Re_l^n Pr_l^{0.3} \frac{k_l}{\delta_f} \quad (21)$$

Where  $c$  and  $n$  are the empirical constants and are 0.0039 and 0.734, respectively.  $Re_l$  and  $\delta_f$  are the liquid film Reynolds number and the liquid film thickness for annular flow, respectively, and they are defined as, (assuming  $\delta_f \ll Dh$ ),

$$Re_l = \frac{G(1-x)D_h}{\mu_l} \quad (22)$$

and

$$\delta_f = D_h \frac{(1-e)}{4} \quad (23)$$

Figure 23 shows how the data from this investigation fit the correlation. In the case of R134a, it is obvious from the figure that the majority of the data points fall into the 20% error lines and that the correlation under-predicted the data results. As for R245fa, it seems like the correlation was very poor in predicting the data as well (Figure 24). The correlation did not generate as much discrepancy as the other two correlations produced when compared with the current data of R134a, which motivated us to modify the correlation to fit these data as well.

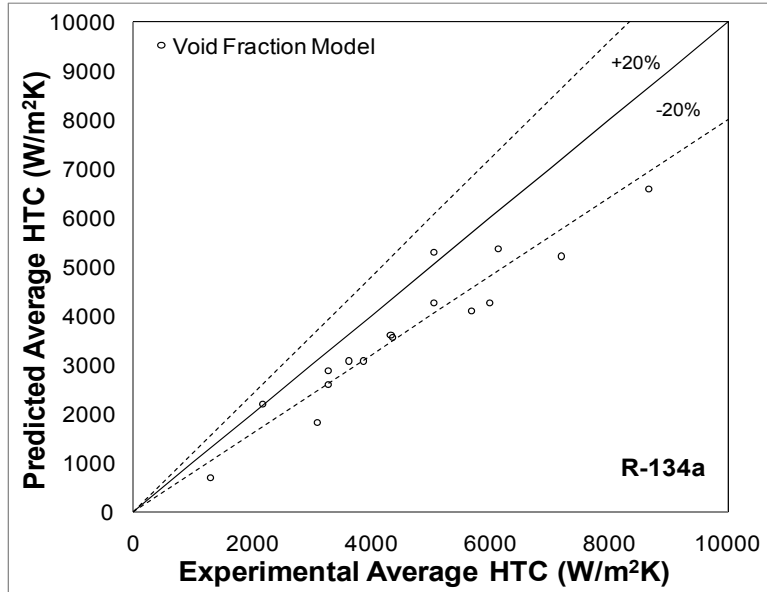


Figure 23 Comparison of the void fraction model against the current data of R134a

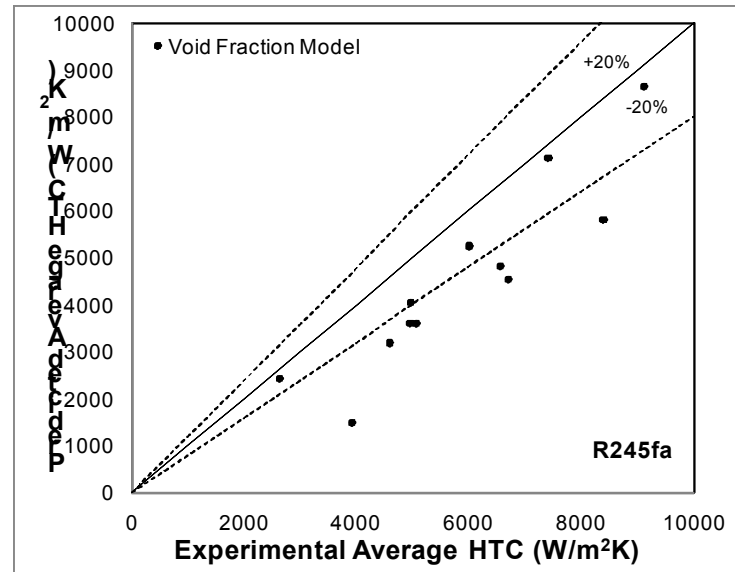
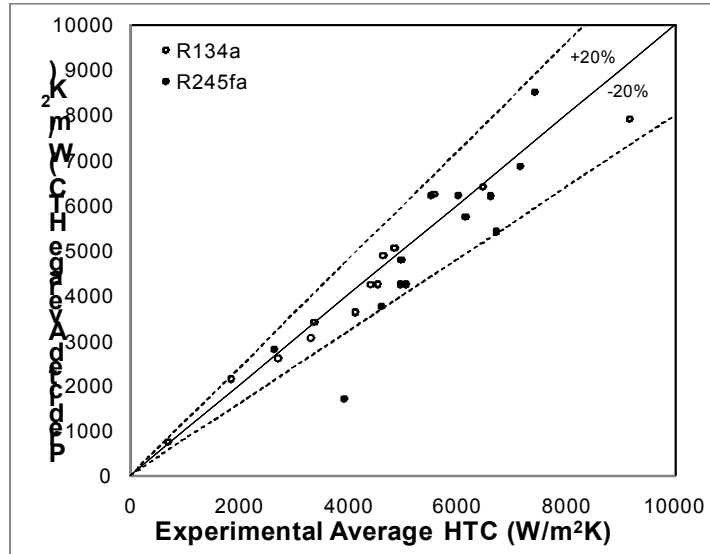


Figure 24 Comparison of the newly modified void fraction model against the current data of R134a

In order to improve the correlation to fit the data, the constants  $c$  and  $n$  were changed to 0.0045 and 0.75, respectively; thereafter, the modified correlation was compared with the data, Figure 25. It is apparent from the figure that the modification to the empirical constant has improved the correlation to fit the current data well.



**Figure 25 Comparison of the newly modified void fraction model against the current data of R134a & R245fa**

### Pressure Drop Correlations

Similar to the heat transfer coefficient case, the average value for pressure drop correlations was obtained from experiments. The pressure drop measured from experiments was the total pressure drop of the entire micro-channel. As explained earlier in the experimental setup section, an accurate differential pressure transducer was used to measure the pressure difference from the inlet and the outlet of the micro-channel. It is acknowledged that in two-phase flows different regimes have different pressure drops, and, in this study only the overall pressure drop was measured.

The correlations introduced in this section are for local pressure drops. Again, using these correlations directly to correlate our data was not adequate unless local information were obtained using the same technique used to obtain the local heat transfer coefficient above. Given the saturation pressure at the inlet of the condenser, the temperatures of the condenser walls, and the pressure drop across the condenser, local pressure drops were obtained where the channel was divided into nine segments by using the correlations. The local pressure drops were averaged and compared with the overall pressure drop acquired from experimentation.

Most of the descriptive two-phase pressure drop correlations that take into account the effect of different flow regimes make use of flow mapping information. It is important to obtain and study the flow regime pattern to develop an accurate two-phase flow model (Thome et al. 2003), (El Hajal et al. 2003), (Garimella et al. 2003), (Baker, 1954) and (Coleman et al. 2003). Since this investigation did not develop a flow mapping due to the fact that this work only considered the condensation case where 100% quality enters the condenser and 0% quality leaves out of the condenser, one data point ( $T_{sat}=50\text{ }^{\circ}\text{C}$ , mass flux =  $300\text{ kg/m}^2\text{s}$  and a rectangular channel shape with  $D_h = 0.7\text{ mm}$ ) of the current study was compared with one data point of Garimella et al. (2005) that was obtained at similar testing conditions and channel size, ( $T_{sat}=50\text{ }^{\circ}\text{C}$ , mass flux =  $300\text{ kg/m}^2\text{s}$  and a square channel shape with  $D_h = 0.76\text{ mm}$ ). The comparison was done in order to determine whether Garimella et al. (2005) flow mapping could be used in the current work to find a more accurate pressure drop model. However, the heat transfer of the current study was 25% higher than that of Garimella, et al. Thus, no flow map was used in this study to develop pressure drop correlation. However, the pressure drop correlations presented in this section are derived from physical and classical approaches.

### Lockhart-Martinelli Model

This model considers different velocities for each phase and assumes that the velocity of each phase is uniform at any axial cross section. For one-dimensional, adiabatic flow in a constant cross sectional area channel, the total pressure drop is defined as

$$\frac{dP}{dz} = \left[ \Phi_l^2 \left( \frac{dP}{dz} \right)_l - ((1 - \alpha)\rho_l + \alpha\rho_v)g_s \right] \quad (24)$$

where  $\left( \frac{dP}{dz} \right)_l$  indicates the pressure gradient of only liquid flowing in the channel, and  $\Phi_l^2$  is the Lockhart and Martinelli key multiplier, which was defined by Martinelli et al. (1948) and Lockhart et al. (1949), and which compares the two-phase frictional pressure gradient  $\left( \frac{dP}{dz} \right)_{tp}$  with a single-phase frictional pressure gradient  $\left( \frac{dP}{dz} \right)_l$  assuming only one phase in the tube:

$$\Phi_l^2 = \frac{\left( \frac{dP}{dz} \right)_{tp}}{\left( \frac{dP}{dz} \right)_l} = \left[ 1 + \frac{20}{X_{tt}} + \frac{1}{X_{tt}^2} \right] \quad (25)$$

where  $X_{tt}$  is a parameter that Lockhart et al. (1949) developed and is the square root of the ratio of liquid frictional pressure drop to the vapor frictional pressure drop:

$$X_{tt} = \left[ \frac{\left( \frac{dP}{dz} \right)_l}{\left( \frac{dP}{dz} \right)_v} \right]^{1/2} = \left( \frac{1-x}{x} \right)^{0.875} \left( \frac{\rho_v}{\rho_l} \right)^{0.5} \left( \frac{\mu_l}{\mu_v} \right)^{0.125} \quad (26)$$

where the frictional gradient for a separated two-phase flow model can be defined as

$$\left( \frac{dP}{dz} \right)_l = -\frac{1}{2} f_l \frac{G^2 (1-x)^2}{\rho_l D_h} \quad (27)$$

$$\left( \frac{dP}{dz} \right)_v = -\frac{1}{2} f_v \frac{G^2 (1-x)^2}{\rho_v D_h} \quad (28)$$

where  $f_l$  and  $f_v$  are the fanning friction factor, assuming that only liquid or only vapor is flowing alone at the same superficial velocity of the phase. They are presented as

$$f_l = 0.316 \left( \frac{G(1-x)D_h}{\mu_l} \right)^{-0.25} \quad (29)$$

$$f_v = 0.316 \left( \frac{GxD_h}{\mu_v} \right)^{-0.25} \quad (30)$$

Although this model assumes adiabatic condition, the physics of each flow regime in condensation is captured using the proper quality and void fraction to find the corresponding local pressure drop. The void fraction is obtained from the quality and the densities of both liquid and vapor, which is defined as

$$x = \frac{\rho_v \alpha}{(1-\alpha)\rho_l + \alpha\rho_v} \quad (31)$$

A comparison of the correlation and the experimental results are shown in Figure 26 and 27. As seen in these graphs, it is obvious that the Lockhart and Martinelli model was very poor in predicting the pressure drop for the micro-channel condensation for both refrigerants.

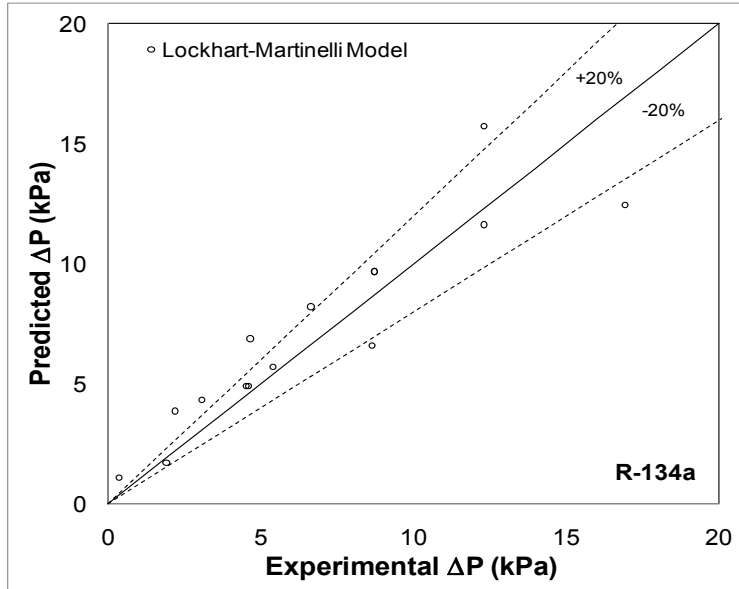


Figure 26 Comparison of Lockhart-Martinelli pressure drop model against the current data of R134a

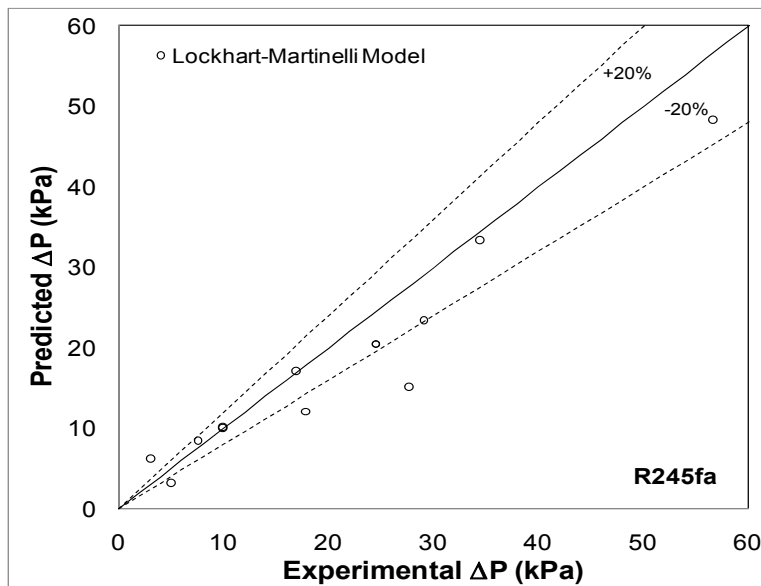


Figure 27 Comparison of Lockhart-Martinelli pressure drop model against the current data of R245fa

#### The Classical Pressure Drop Model

This model consists of several effects, such as friction, acceleration or deceleration due to momentum changes, and gravitational components (Shao et al. 2000). The total pressure drop for two-phase flow is presented as follows:

$$\left(\frac{dP}{dz}\right) = \left(\frac{dP}{dz}\right)_f + \left(\frac{dP}{dz}\right)_m + \left(\frac{dP}{dz}\right)_g \quad (32)$$

Since the experiments were conducted on a horizontal plane, the gravitational component can be neglected. Thus the total pressure drop is reduced to

$$\left(\frac{dP}{dz}\right) = \left(\frac{dP}{dz}\right)_f + \left(\frac{dP}{dz}\right)_m \quad (33)$$

The subscripts  $f$  and  $m$  indicate the pressure drop due to friction and momentum, respectively.

### Friction Term

This term uses the Lockhart-Martinelli correlation to find the two-phase pressure gradient due to friction by using the Lockhart and Martinelli two-phase pressure drop key parameter:

$$\Phi_v = \left[ \frac{\left(\frac{dP}{dz}\right)_f}{\left(\frac{dP}{dz}\right)_v} \right]^{-0.5} \quad (34)$$

where the vapor pressure drop is defined as:

$$\left(\frac{dP}{dz}\right)_v = -2f_o \frac{(xG)^2}{\rho_v D_h} \quad (35)$$

$f_o$  is the friction factor for the adiabatic two-phase flow and is estimated here by Colburn's equation as follows:

$$f_o = \frac{0.045}{Re_v^{0.2}} \quad (36)$$

Here the Reynolds number of the vapor flow is defined as:

$$Re_v = \frac{xGD_h}{\mu_v} \quad (37)$$

Lockhart et al. (1949) analyzed pressure drop data of adiabatic flows of different fluids and obtained the following key multiplier and parameter:

$$\Phi_v = 1 + 2.85X_{tt}^{0.323} \quad (38)$$

Azer et al. (1972) and Shao et al. (2000) were able to correlate key multipliers for two-phase condensation data instead of adiabatic flow data. Azer's correlation was as follows:

$$\Phi_v = 1 + 1.09X_{tt}^{0.289} \quad (39)$$

Whereas Shao's correlation was as follows:

$$\Phi_v = 1 + 0.8X_{tt}^{0.1} \quad (40)$$

### Momentum

The contribution of momentum transfer to the total pressure drop is negligible in adiabatic two-phase flows (Shao et al. 2000). However, the momentum transfer contribution becomes more noticeable in condensation heat transfer due to the mass transfer present at the vapor-liquid interface and also due to the change in kinetic energy, which is defined as

$$\left(\frac{dP}{dz}\right)_m = \left[ \frac{x^2 G^2}{\rho_v} + \frac{(1-x)^2 G^2}{\rho_l(1-\varepsilon)} \right]_{x=0} + \left[ \frac{x^2 G^2}{\rho_v} + \frac{(1-x)^2 G^2}{\rho_l(1-\varepsilon)} \right]_{x=1} \quad (41)$$

Here the void fraction  $\varepsilon$  was developed by Smith (1971) as

$$\varepsilon = \left( 1 + \left(\frac{\rho_v}{\rho_l}\right) \left(\frac{1-x}{x}\right) \left[ 0.4 + 0.6 \left( \frac{x(\rho_l/\rho_v) + 0.4(1-x)}{x + 0.4(1-x)} \right) \right]^{0.5} \right)^{-1} \quad (42)$$

After obtaining the frictional and momentum terms, the total pressure drop was calculated and then compared with the current data. Figure 28 and 29 show the comparison of classical pressure drop correlation with the three different key multipliers,  $\Phi_v$ , that were introduced earlier, against the current data. The key multiplier developed by Shao shows a better agreement and consistency with the current data of R134a than the key multipliers developed by Lockhart and Martinelli, and Azer. Whereas for R245fa data, the key multiplier developed by Azer shows a better agreement than the other two.

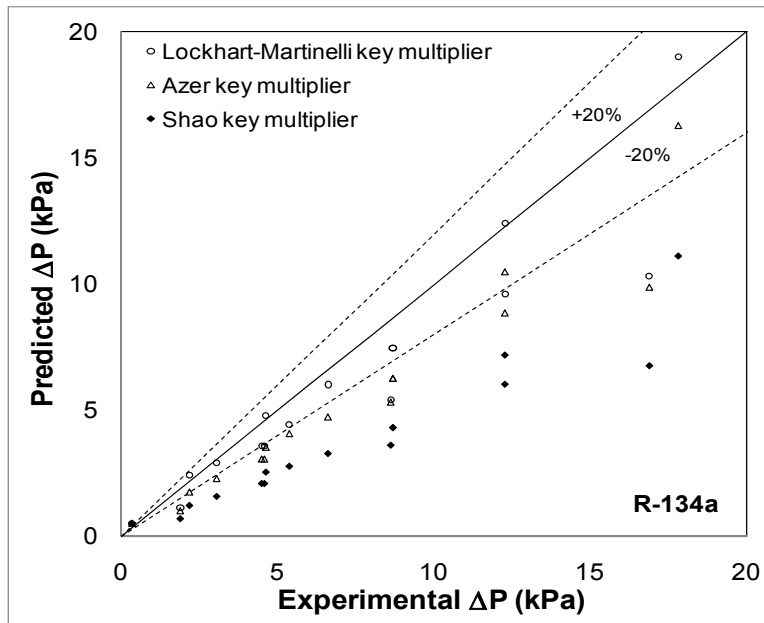


Figure 28 Comparison of the classical pressure drop model using three different key multipliers against the present data of R134a

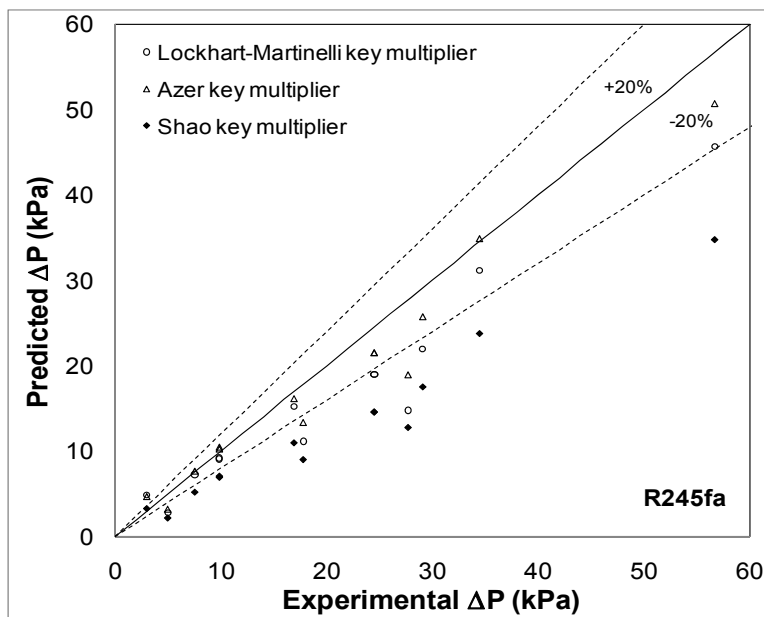
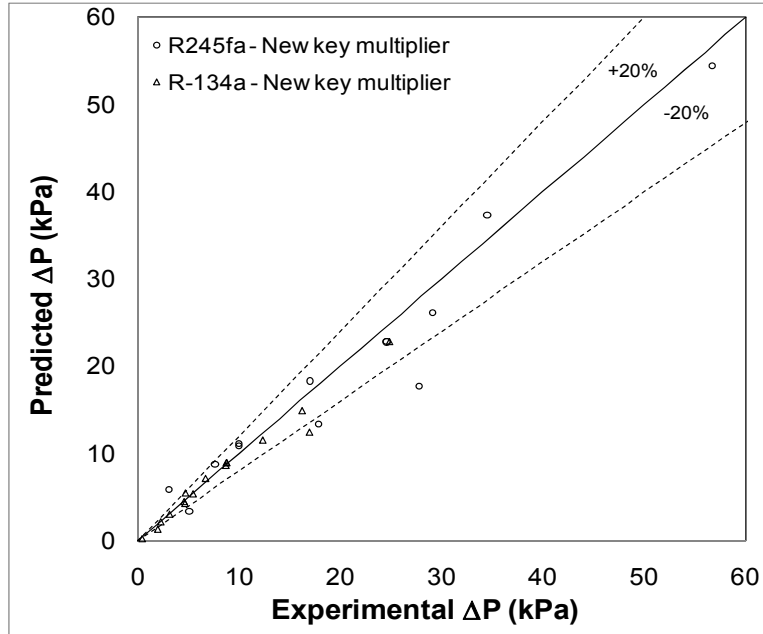


Figure 29 Comparison of the classical pressure drop model using three different key multipliers against the present data of R245fa

To reach a better agreement between the correlation and the data for this study, the key multiplier was modified. The newly modified key multiplier is defined as follows:

$$\Phi_{s, \text{new}} = [1 + 0.25x_{cc}^{-0.055}]^{1.98} \quad (43)$$

Figure 30 shows the comparison between the current data and the correlation using the newly developed key multiplier, where a better fit is apparent.



**Figure 30 Comparison of the classical pressure drop model using the newly modified key multiplier with the current data of R134a & R245fa**

### Visualization Study

Two test sections were built for this visualization study. One was with a window opening equal to the width of the channel and a second window equal to the height of the channel. Both channels have the same length of 25.4 mm.

#### Visualization section 1

In this test section, a microchannel 0.4 mm deep and 2.8 mm wide was machined on a copper block, as shown in Figure 31. A groove around the channel was also machined to house the gasket for sealing purposes. Two 1/16" holes are located on each end of the microchannel for the inlet and outlet. To seal the top of the channel, an aluminum clamp was designed and built to house the glass that will press on the gasket to seal the micro-channel from the top. The micro-channel, the glass and the clamp will be assembled using bolts. In order to cool the saturated vapor to condense to saturated liquid, a copper tube will be soldered on the backside of the microchannel.

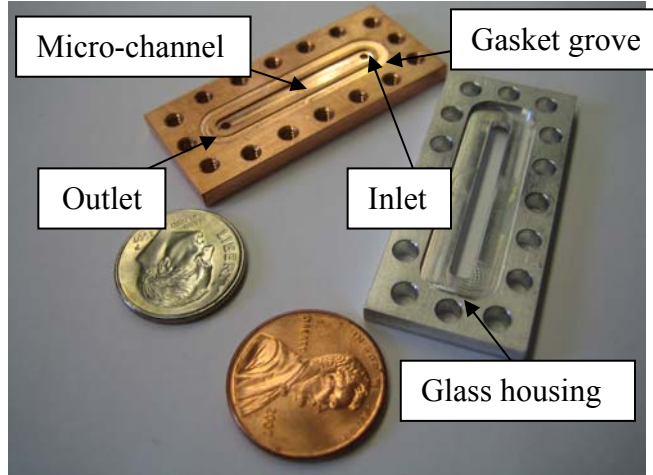


**Figure 31. Micro-channel for visualization of condensing refrigerant flow**

Figure 32 shows a picture of the condenser. The visualization tests for this micro-channel condenser were conducted in two different orientations to observe whether there was any gravitational effect on the flow. In the first orientation, the channel was placed on the horizontal plain, and the camera was positioned to take videos from the top. In the second orientation, the channel was rotated 90° from its previous position, and the camera was set to take videos from the side.

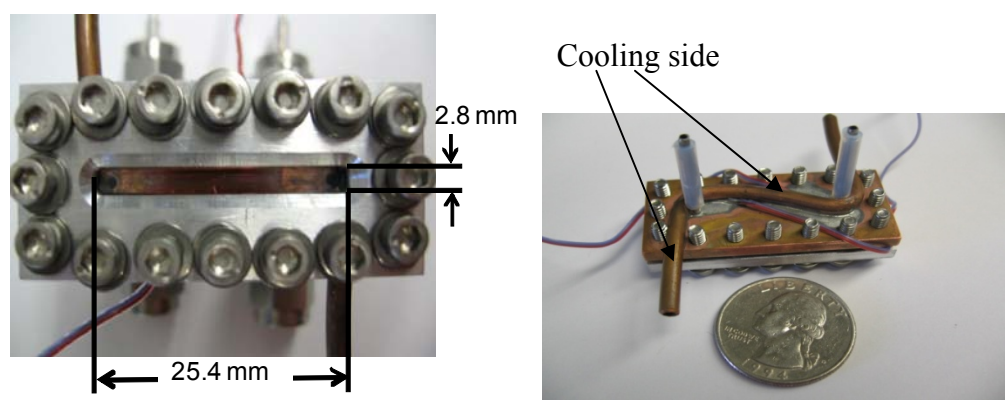


**Figure 32 Microchannel condenser with viewing window of 2.8mm.**

Visualization tests according to the parametric study table, Table 1, were conducted. All the tests have been completed for this channel, and pictures of the results are shown in Table 1,

**Table 3 Visualization results of channel with viewing window of 2.8mm**

x	300 kg/m <sup>2</sup> s
0.02	
0.05	
0.08	
0.1	

0.2	
0.3	
0.4	
0.5	
0.6	
0.7	
0.8	
0.9	

The results in the table are for different qualities varying from 0.02 to 0.9 for a flow with a mass flux of  $300 \text{ kg/m}^2\text{s}$  and  $50 \text{ }^\circ\text{C}$  saturation temperature. It is clear from the results that at low qualities (from 0.02 to 0.1) the flow is mostly bubble and slug flows. In this range of qualities, swirling, necking and axe-directional movements of the fluid were observed, which was quite interesting to see. This is believed to be due to the high aspect ratio of the channel, which gives the fluid freedom to move in different directions inside the channel, which then causes the swirling and necking of the flow.

Another interesting observation was that the annular flow developed very early at qualities from 0.1 to 0.2. After increasing the quality to 30%, a liquid film began to form at the bottom of the channel where vapor began to flow on top of the liquid film, which created waves. The waves changed from discrete to disperse waves as the quality was increased due to the vapor velocity flowing at higher velocities than the liquid, which was due to the decrease in vapor density with increasing quality.

The results for both orientations were very similar and no difference in flow is reported.

### [Visualization section 2](#)

Figure 33 shows a picture of the second visualization channel. This channel has a viewing window of 0.4 mm and a depth of 2.8 mm. Two identical channels were built, one to be tested at UM and the other at PI. The visualization performed using this channel showed similar regimes at similar conditions as condenser 1. However, it was much easier to observe film bridging and transition from annual to intermittent and slug regimes.



**Figure 33 Micro-condenser with viewing window of 0.4 mm.**

### **Conclusion**

To characterize condensation heat transfer and pressure drop coefficients in micro channels with small hydraulic diameter and high aspect ratio, a micro-channel made of copper with the dimensions of 190 mm × 2.8 mm × 0.4 mm was fabricated. Parametric tests were conducted and analyzed for refrigerants R134a and R245fa. Correlations of average heat transfer coefficients and pressure drops were developed utilizing available correlations.

From analysis of the results the following conclusions were drawn:

- For both refrigerants the heat transfer and pressure drop coefficients decreased with an increase in the saturation temperature.
- As expected, increase in both heat transfer coefficient and pressure drop was observed as mass flux increased.
- While the heat transfer coefficients were slightly affected by changes in the inlet superheat, the corresponding effect on pressure drops was insignificant.
- Refrigerant R245fa on average demonstrated a 15%-better heat transfer than that of R134a; thus, it can provide lower thermal resistance for two-phase thermal management systems.
- The pressure drop for R245fa is almost three times higher than that of R134a for the same operating conditions.
- The best match model for heat transfer is the Void Fraction Model and the Classical Pressure Model for pressure drops.
- Heat transfer and pressure drop models for macroscale channels under- predict the data obtained in high aspect ratio microchannel. However, with adjusted coefficients, they describe the data reasonably well.
- Cross flow patterns and earlier film bridging observed in high aspect ratio microchannels may be responsible for higher heat transfer and pressure drop compared to low aspect ratio microchannels.
- .

### Recommendations for Future Work

- Map the flow in high aspect ratio microchannel and compare it with flow maps in the low aspect ratio microchannels.
- Further evaluate the effect of the cross flow and earlier film bridging on the flow map, heat transfer and pressure drop.
- Based on obtained flow maps further improve heat transfer and pressure drop correlations.

### References

- Azer, N.Z., L. V. Abis, and H. M. Soliman. "Local Heat Transfer Coefficient During Annular Flow Condensation." *ASHRAE Transactions* 78, no. 2 (1972): 135-134.
- Baird, J.R., D.F. Fletcher, and B.S. Haynes. "Local Condensation Heat Transfer Rate in Fine Passages." Edited by 4466. *Int. J. of Heat and Mass Transfer* 46 (2003): 4453.
- Baker, O. "Simultaneous Flow of Oil and Gas." *Oil and Gas Journal* 53 (1954): 185-195.
- Bontemps, A. "Measurements of Single-Phase Pressure Drop and Heat Transfer Coefficients in Micro and Minichannels." *Microscale Heat Transfer* (Sipringer), 2005: 25-48.
- Cavallini, A., G. Censi, D. Del Col, L. Doretti, G.A. Longo, and L. Rossetto. "Condensation of Halogenated Refrigerants inside Smooth Tubes." *HVAC&R Research* 8, no. 4 (2002): 429-451.
- Chen, J. "Correlation for Boiling Heat Transfer for Saturated Fluid in Convective Flow." *Ind. Eng. Chem. Process Des. Dev.* 5, no. 3 (1966): 322-329.
- Coleman, J.W., and S. Garimella. "Two-Phase Flow Regime Transitions in Microchannel Tubes: The Effect of Hydraulic Diameter." *In: Proceedings of ASME Heat Transfer Division (ASME IMECE2000)* 4 (2000-I): 71-83.

Coleman, J.W., and S. Garimella. "Two-Phase Flow Regimes in Round, Square and Rectangular Tubes During Condensation of Refrigerant R134a." *International Journal of Refrigeration* 26, no. 1 (2003): 117-128.

Coleman, J.W., and S. Garimella. "Visualization of Two-Phase Refrigerant Flow During Phase Change." In: *34th National Heat Transfer Conference, 2000-II*: nHTC2000-12115.

Dobson, M. K., and J. C. Chato. "Condensation in Smooth Horizontal Tubes." *ASME Journal of Heat Transfer* 120 (1998): 193-213.

El Hajal, J., J. Thome, and A. Cavallini. "Condensation in Horizontal Tubes, Part I: Two-Phase Flow Pattern Map." *International Journal of Heat and Mass Transfer* 26 (2003): 3349-3363.

Friedel, L. "Improved Friction Pressure Drop Correlations for Horizontal and Vertical Two Phase Flow." *3R International* 18, no. 7 (July 1979): 485-491.

Garimella, S., A. Agarwall, and J. D. Killion. "Condensation Pressure Drop in Circular Micro-Channels." *Heat Transfer Engineering* 26, no. 3 (2005): 28-35.

Garimella, S., J. D. Killion, and J. W. Coleman. "An Experimentally Validated Model for Two Phase Pressure Drop in the Intermittent Flow Regime for Noncircular Micro-Channels." *Journal of Fluid Engineering* 125 (2003): 887-894.

Kattan, N., J. R. Thome, and D. Favrat. "Flow Boiling in Horizontal Tubes: Part I - Development of a Diabatic Two-Phase Flow Pattern Map." *Journal of Heat Transfer, Transactions ASME* 120, no. 1 (1998-I): 140-147.

Kattan, N., J. R. Thome, and D. Favrat. "Flow Boiling in Horizontal Tubes: Part II - New Heat Transfer Data for Five Refrigerants." *Journal of Heat Transfer, Transactions ASME* 120, no. 1 (1998-II): 148-155.

Kattan, N., J. R. Thome, and D. Favrat. "Flow Boiling in Horizontal Tubes: Part III Development of a New Heat Transfer Model Based on Flow Pattern." *Journal of Heat Transfer* 120, no. 1 (1998-III): 156-165.

Kim, M.H., J.S. Shin, C. Huh, T.J. Kim, and K.W. Seo. "A Study of Condensation Heat Transfer in a Single Mini-Tube and a Review of Korean Micro- and Mini-Channel Studies." *Proc. of the First International Conference on Microchannels and Minichannels, Rochester, April 2003*: 47-58.

Lockhart, R. W., and R. C. Martinelli. "Proposed Correlation of Data for Isothermal Two-Phase, Two Component Flow in Pipes." *Chem. Eng. Prog.* 45, no. 1 (1949): 39-48.

Martinelli, R. C., and B. Nelson. "Prediction of Pressure Drop During Forced-Circulation Boiling Water." *Trans. ASME* 70 (1948): 695-702.

Riehl, R. R., and J. M. Ochterbeck. "Comparison of Heat Transfer Correlations for Single- and Two-Phase Microchannel Flows for Microelectronics Cooling." *ITherm'98 – Sixth Intersociety Conference on Thermal and Thermomechanical Phenomena in Electronic Systems, May 1998*: 409-416.

Riehl, R., and Jay M. Ochterbeck. "Experimental Investigation of the Convective Condensation Heat Transfer in Microchannel Flows." *Proceedings of the ENCIT. Caxambu-MG, Brazil, 2002. CIT02-0495.*

Rouhani, Z., and E. Axelsson. "Calculation of Void Fraction in the Sub-cooled and Quality boiling Regions." *International Journal of Heat and Mass Transfer* 13 (1970): 383-393.

Shao, D. W., and E. G. Granryd. "Flow Pattern Heat Transfer and Pressure Drop in Flow Condensation Part I: Pure and Azeotropic Refrigerants." *International Journal of HVAC&R Research* 6, no. 2 (2000): 175-195.

Shah, M. "A general Correlation of Heat Transfer During Film Condensation Inside Pipes." *International Journal of Heat Transfer* 22 (1978): 547-556.

Shah, M. "A New Correlation for Heat Transfer During Boiling Flow Through Pipes." *ASHRAE Transactions* 82, no. 2 (1976): 66-86.

Smith, S. L. "Void Fraction in Two-phase Flow: A Correlation Based Upon an Equal Velocity head Model." *Heat Fluid Flow* 1 (1971): 22-39.

Thome, J. R., J. El Hajal, and A. Cavallini. "Condensation in Horizontal Tubes Part II: New Heat Model Based on Flow Regimes." *International Journal of Heat and Mass Transfer* 46 (2003): 3365-3387.

Wang, W.W., T.D. Radcliff, and R.N. Christensen. "A Condensation Heat Transfer Correlation for Millimeter-Scale Tubing With Flow Regime Transition." *Exp. Thermal Fluid Sci.* 26 (2002): 472-485.

## Publications

12. "Performance Characterization of Two Selected Refrigerants in a Flat-Plate Micro-Tube Condenser", E. Al-Hajri, S. Dessiatoun, A. Shooshtari, M. Ohadi and A. Goharzadeh, Second International Energy 2030 Conference, Abu-Dhabi, UAE, Nov. 2008.
13. "An Experimental Study of Condensation Heat Transfer and Pressure Drop in a Single High Aspect Ratio Micro-channel for Refrigerant R134a", S. Chowdhury, E. AL-Hajri, S. Dessiatoun, A. Shooshtari, M. Ohadi and A. Goharzadeh, 4th International Conference on Nanochannels, Microchannels and Minichannels, ASME, June 19-21, 2006, Limerick, Ireland
14. "Studies on Condensation of Refrigerants in a High Aspect Ratio Minichannel and in a Novel Micro-groove Surface Heat Exchanger-Development of Micro-condensers in Compact two Phase Cooling Systems", S. Dessiatoun, S. Chowdhury, E. Al-Hajri, E. Cetegen, M. Ohadi and A. Goharzadeh, Proceedings of the Fifth International Conference on Nanochannels, Microchannels and Minichannels ASME ICNMM2007, June 18-20, 2007, Puebla, Mexico
15. "Performance Characterization of Two Selected Refrigerants in a Flat-Plate Micro-Tube Condenser", E. Al-Hajri, S. Dessiatoun, A. Shooshtari, M. Ohadi and A. Goharzadeh, (Pending to be published in ASHRAE HCAV&R Journal).
16. "Studies on Condensation of Refrigerants in a High Aspect Ratio Minichannel and in a Novel Micro-groove Surface Heat Exchanger-Development of Micro-condensers in Compact two Phase Cooling Systems", S. Dessiatoun, S. Chowdhury, E. Al-Hajri, E. Cetegen, M. Ohadi and A. Goharzadeh, Submitted to the International Journal of Heat Transfer, 2008.

## Visits

- Amir Shooshtari, 1 month working visit to PI, May 2007
- Afshin Goharzadeh, 2 weeks working visit to University of Maryland, July 2007.
- Mohamed Alshehhi, Serguei Dessiatoun visited P.I., GASCO and ADGAS from Dec 8 -13 2007
- Mohamed Alshehhi, Serguei Dessiatoun visited P.I., GASCO, ADGAS, Habshan Plant and Das Island from May 3 -9 2008

## GRA( names, degrees, graduation)

17. Ebrahim AL-Hajri, Ph.D. candidate; expected to graduate in 2009

## An EHD-Enhanced Gas-Liquid Separator

UMD Investigators: Dr. Serguei Dessiatoun, Dr. Amir Shooshtari

GRA's: Mohamed Alshehhi

PI Investigator(s): Dr. Michael Ohadi, Dr. Afshin Goharzadeh

Start Date: October 2006

FINAL REPORT

### Abstract/Objectives

Development of effective techniques for separation of fine liquid droplets from moving gaseous mediums has grown significantly in recent years. Separation processes have applications in many industrial systems, particularly in the refrigeration, process, petrochemical, and cryogenics industries. The efficiency and reliability of this equipment appreciably suffers due to mal-distribution of lubricant oil in the system. Electro-hydrodynamic (EHD) separation can correct this mal-distribution and improve the efficiency of this refrigeration and air-conditioning equipment. Similarly, vapor compression equipment with lubricant circulation is also used in oil refinery processes. This circulation can be significantly improved using EHD separators to increase heat-pumping efficiency.

However, the fundamentals of this separation mechanism must be better understood to enable optimization of the working design. There is also a need to explore the feasibility of separation of gas-and-conductive liquid mixtures, which poses additional challenges. This study, therefore, will investigate the hybrid inertia-EHD gas-liquid separation phenomena for electrically conductive (water) and nonconductive (oil) liquid particles suspended in a moving gaseous medium. This is useful in a variety of applications including petrochemical and process industries, refrigeration and cryogenics, and micron/sub micron air filtration and clean room applications.

### Approach

#### Literature Review

A thorough review of previous literature was conducted on two main areas:

- Gas-liquid separation technique
- EHD phenomena

#### Numerical Modeling

A custom user defined function code was written to simulate the effect of EHD separation on particles.

#### Experimental Work

Parametric study was conducted on air-oil separation.

### Two- Year Plan

UMD-side participation

Year 1

- Literature review and summary
- Simulation of EHD effect on droplets in gas flow through numerical modeling
- Fabrication of experimental prototype and experimental loop

Year 2

- Finalized experimental setup
- Experimental results

Final report

PI-side participation

Year 1

Input on literature review and summary  
Discussion and assistance in design of test prototype  
Concentrator design

Year 2

Discussion and assistance in experimentation  
Concentrator fabrication or participation in fabrication  
Testing of concentrator and cooling system in UAE conditions  
Input on final report and recommendation

## Literature Review

### Gas-Liquid Separation

Separation of liquid droplets from gas flows comprises a significant part of process industries including HVAC and refrigeration systems. Failure to have highly efficient separation techniques will lead to a reduction in performance, lower efficiency and increased operation costs. The separation of lubricant oil that leaks from compressors as droplets of micron and submicron sizes and mixes with refrigerant is very important to maintain system's performance and functionality. Statistics show that the oil concentration in a refrigerant after leaving a compressor ranges between 2.0 – 4.5 wt.%. About 50% of these droplets are below 1  $\mu\text{m}$  in diameter size. If the oil droplets are not separated from the gas flow, they will cause a reduction in the system's cooling capacity once they enter a heat exchanger, usually the evaporator. In fact, they will be deposited on the inner surface of the heat exchanger and while accumulating, they form a heat transfer insulation layer on the walls. This will cause an increase of the pressure drop of the systems, a decrease in the heat transfer coefficient and a reduction in the refrigerant volumetric flow rate that goes into the heat exchanger. Much research in refrigeration field is devoted to study of the impact of increasing oil concentration in refrigerants. It has been found that increasing oil concentration in refrigerant will increase pressure drop and decrease cooling rate. There are a variety of methods of separating oil droplets from process streams using different principles, such as inertial separation as applied in cyclones, impaction and diffusion as used in coalescence force-based filters, and so on. However, many industrial and conventional gas-liquid separators are limited in terms of separating fine droplets from gas streams. For example, the conventional cyclone's efficiency falls dramatically when the diameter of oil droplets are below 1  $\mu\text{m}$ . This is because the cyclone's performance depends on the mass difference between the suspended liquid droplets and the carrier gas, and this factor becomes insignificant in submicron droplets. Although coalescence-based separators are more efficient, their performance also decreases when the droplet size is below 0.5  $\mu\text{m}$ . In addition, this type of separator has very high pressure drop and a high maintenance cost.

### EHD Mechanism

EHD separation operates on the basic principle of gas-borne aerosols that are passed through a corona or charged field, where they receive an electric charge. Then the charged particles are deflected by the electric field and move across the gas stream from an emitter electrode to a collector electrode, where they are removed from the gas stream. Two distinct mechanisms are active in charging the particles, diffusion charging and field charging. The aerosol's size plays an important role in determining the dominant charging mechanism. For a submicron aerosol, diffusion charging is more dominant, while field charging becomes the prevailing factor when the aerosol's diameter is in the micron range.

Figure 1 shows diffusion charging in a charging and collecting particles process. The charging process starts when liquid aerosols enter a region filled with randomly moving ions created by a high voltage difference between two electrodes. The thermal motions of the ions cause them to

diffuse through the gas and to collide with aerosols. Such ions will generally adhere to aerosols due to the attractive electrical-image forces which come into play as the ions approach the particles. The accumulation of electric charge on an aerosol gives rise to a repelling field, which tends to prevent additional ions from reaching the aerosol. Thus, the rate of charging decreases as charge accumulates on a particle and will ultimately proceed at a negligible rate. As charge builds up, the aerosols move to the electrode that has the opposite charge. Unlike the electric field intensity, the charge density of the ions has a direct influence on this type of charging mechanism. Also, the temperature of the flow affects the charging process, but aerosol material to a first approximation plays no role in this process.

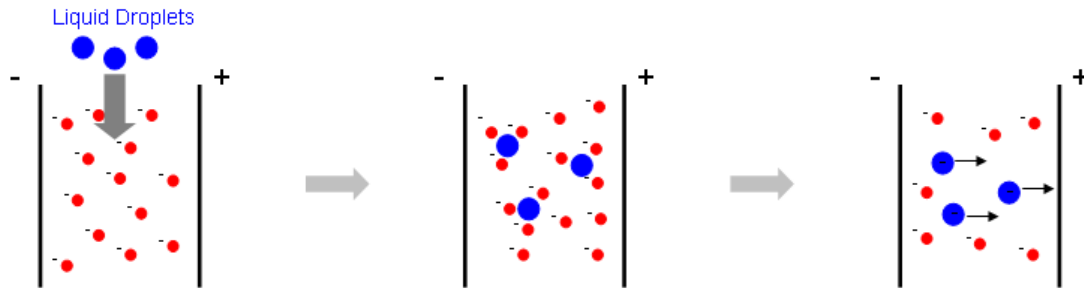


**Figure 1. Diffusion charging mechanism. Aerosols enter a region of moving ions, the aerosols absorb the charge after colliding with ions, the aerosols move to the opposite charge surface.**

In field charging, as depicted in Figure 2, a liquid aerosol enters a region of traveling ions between electrodes. The presence of the aerosol disturbs ions traveling along electrical field lines, so the ions strike the aerosol and transfer their charge to the aerosol's surface. After the aerosol gets charged, it moves to the opposite-charge electrode. Unlike the diffusion charging process, this type of charging is affected greatly by the electric field.

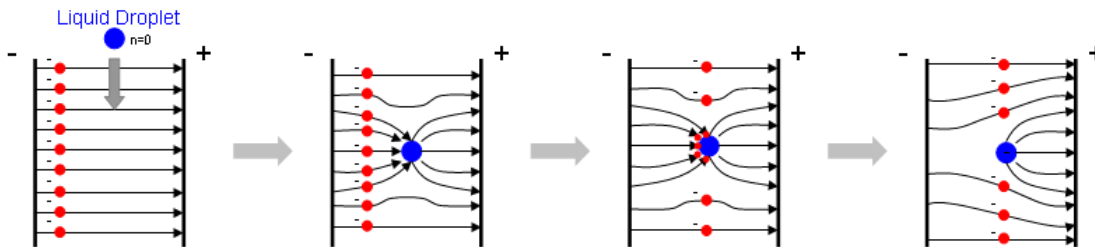


**Figure 2. Field charging mechanism. An aerosol enters a region of traveling ions along field lines because of a gradient in electric field. The aerosol's size is big enough to be stroked by ions and absorb the charge, and the aerosol moves to opposite charge.**

## Numerical Modeling

In this section, the performance of a wire-cylinder ESP has been studied numerically. A mathematical model has been developed based on a modified Lagrangian approach to simulate the ESP performance on separating water aerosols from an air flow when applied voltage, ESP geometry and flow conditions have been changed. Also, the accumulated charge on droplets has been obtained and shows that their breakup due to the charge accumulation is unlikely.

### Mathematical Model

To develop the mathematical model, the following simplifying assumptions were made:

1. All the particles are spherical.
2. The accumulated charge on each particle does not affect the local electric field.
3. Due to low concentration, there is no interaction among the particles.

4. The temperature of the particles and fluid are the same.
5. The fluid flow field is not affected by the motion of the particles.

Next, we consider an aerosol subject to electric and fluid flow fields. The trajectory can be determined from the momentum balance applied to this particle.

$$\frac{d\mathbf{u}_p}{dt} = F_D(\mathbf{u} - \mathbf{u}_p) + \frac{\mathbf{g}(\rho_p - \rho)}{\rho_p} + \mathbf{F}_e \quad [1]$$

The Stokes drag force is given as

$$F_D = \frac{18\mu}{\rho_p} \frac{C_D \text{Re}}{d_p^2} \quad [2]$$

where the drag coefficient ( $C_D$ ) for spherical particles is calculated for different ranges of Reynolds numbers. The Reynolds number can be defined as

$$\text{Re} = \frac{\rho d_p |\mathbf{u}_p - \mathbf{u}|}{\mu} \quad [3]$$

For submicron particles, drag force acting on the particles is independent of the Reynolds number. Stokes's law assumes that the relative velocity of the gas at the surface of a droplet is zero. Since this assumption is not accurate for submicron aerosols, the Cunningham correction factor must be included in the calculation of the drag force.

$$F_D = \frac{18\mu}{C_c \rho_p d_p^2} \quad [4]$$

where Cunningham correction factor,  $C_c$ , is

$$C_c = 1 + \frac{2\lambda}{d_p} \left[ 1.257 + 0.4e^{-\frac{1.1d_p}{2\lambda}} \right] \quad [5]$$

The velocity of fluid,  $\mathbf{u}$ , can be obtained from continuity and the Navier-Stokes equations.

$$\nabla \cdot \mathbf{u} = 0 \quad [6]$$

$$\rho(\mathbf{u} \cdot \nabla \mathbf{u}) = -\nabla p + \mu \nabla^2 \mathbf{u} + \mathbf{F}_{EHD} \quad [7]$$

where  $\mathbf{F}_{EHD}$  is the electrohydrodynamic body force applied to the aerosol carrier fluid and is given as

$$\mathbf{F}_{EHD} = \rho_i \mathbf{E} \quad [8]$$

$\rho_i$  and  $\mathbf{E}$  are the ionic charge density and the electric field, respectively.

The last term in Eq. (1) represents the electrostatic body force exerted on charged aerosol, given as

$$\mathbf{F}_e = \frac{q_p \mathbf{E}}{1/6 \pi d_p^3 \rho_p} \quad [9]$$

To calculate this body force, the local electric field in vicinity of aerosol particle ( $\mathbf{E}$ ) and the charge accumulated on the particle ( $q_p$ ) must be determined. The total particle charge is the summation of diffusion charging and field charging.

$$q_p = q_{diff} + q_{fld} \quad [10]$$

Assuming that every ion that strikes an aerosol droplet due to Brownian motion is captured, the amount of accumulated diffusion charge on a given spherical particle is given by

$$q_{diff} = \frac{d_p k T}{2 k_E e} \ln \left( 1 + \frac{\pi k_E d_p \bar{C}_i \rho_i t}{2 k T} \right) \quad [11]$$

where  $\bar{C}_i$  is the mean thermal speed of the ions,  $t$  is time interval and  $T$  is fluid temperature. As can be seen, the diffusion charging mechanism is not directly affected by the electric field intensity, and as time passes, the rate of charging gradually slows down. The amount of charge acquired by an aerosol particle due to the field charging process is

$$q_{fld} = \left( \frac{3 \varepsilon_p}{\varepsilon_p + 2} \right) \left( \frac{\mathbf{E} d_p^2}{4 k_E} \right) \left( \frac{\pi k_E Z_i \rho_i t}{1 + \pi k_E Z_i \rho_i t} \right) \quad [12]$$

where  $\varepsilon_p$  is the relative permittivity of the particle and  $Z_i$  is the mobility of ions. Aerosols charged by the field charging mechanism reach saturation charge status as time passes, wherein they repel any additional ions from reaching the aerosols. The amount of charge at saturation state is

$$q_{fld,sat} = \left( \frac{3 \varepsilon_p}{\varepsilon_p + 2} \right) \left( \frac{\mathbf{E} d_p^2}{4 k_E} \right) \quad [13]$$

In order to determine the ion charge density,  $\rho_i$ , and electric field intensity,  $\mathbf{E}$ , the Poisson's and conservation of charge equations must be solved:

$$\nabla^2 \phi = -\frac{\rho_i}{\varepsilon} \quad [14]$$

$$\frac{\partial \rho_i}{\partial t} + \nabla \cdot \mathbf{J} = 0 \quad [15]$$

where  $\phi$  is the potential field,  $\varepsilon$  is the permittivity of fluid, and  $\mathbf{J}$  is the current density. The relation between potential and electric fields is given by

$$\mathbf{E} = -\nabla \phi \quad [16]$$

The current density is the summation of ionic mobility, conduction and convection components, respectively, given as

$$\mathbf{J} = \rho_i Z_i \mathbf{E} + \sigma_i \mathbf{E} + \rho_i \mathbf{u} \quad [17]$$

Since the electrical conductivity of gases is negligible, and the velocity of fluid,  $\mathbf{u}$ , is much less than ion velocity,  $Z_i \mathbf{E}$ , the last two terms in Eq. (17) can be dropped out. Therefore,

$$\mathbf{J} = \rho_i Z_i \mathbf{E} \quad [18]$$

The total electrical current passing from the charged electrode (emitter) to the ground electrode (collector) is given by

$$i = \int_{A_0} \mathbf{J} \cdot d\mathbf{A} \quad [19]$$

where  $A_0$  is any closed area that encloses the emitter or collector electrodes.

The boundary conditions must also be specified to be able to solve the set of governing equations and determine the trajectory of every aerosol particle entering the computational domain. The boundary condition for Eq.(1) at the injection point is given by

$$\mathbf{u}_p = \mathbf{u}_{inj} \quad [20]$$

where  $\mathbf{u}_{inj}$  is the velocity of the particle which must be specified.

The boundary conditions for Eq. (7) depend on the given geometry and are straightforward. For example, on walls, the no-slip condition is imposed. For Eq. (14) following boundary conditions are enforced.

$$\left\{ \begin{array}{ll} \phi = \phi_{emitter} & \text{on the charged electrode (emitter) surface} \\ \phi = 0 & \text{on the ground electrode (collector) surface} \\ \frac{d\phi}{dn} = 0 & \text{on all other surfaces} \end{array} \right.$$

where  $\phi_{emitter}$  is the applied voltage to the emitter electrode and  $n$  is local unit vector normal to the surface. Here it is assumed that, except the emitter and collector electrodes, all other surfaces are perfectly insulated.

The boundary conditions for charge density calculated from Eq. (15) are more involved, and various approaches have been suggested. In the current work, it is assumed that

$$\left\{ \begin{array}{ll} \rho_i = \rho_{emitter} & \text{on the charged electrode (emitter) surface} \\ \frac{d\rho_i}{dn} = 0 & \text{on the ground electrode (collector) surface and all other surfaces} \end{array} \right.$$

where  $\rho_{emitter}$  is the charge density on the emitter surface and its value is assumed to be known. If the current-voltage characteristic (CVC) of the separator is known, the  $\rho_{emitter}$  can be set such that the calculated current from Eq. (19) matches the experimental current for a given voltage. When dealing with charging liquid droplets, the issue of droplets breaking up due to the charge accumulation on their surfaces arises (Hinds 1999). The reason for this behavior is that the mutual repulsion force of the electric charges at the droplet's surface exceeds the confining force of the surface tension. At this point, the droplet will be broken into smaller drops in order to create more surface area for the charge. The maximum amount of charge that a liquid particle can have is called the Rayleigh limit and depends on particle's type and size. This limit generally cannot be reached except in the case of small droplets. The limiting charge is given by

$$q_R = \sqrt{\frac{2 \pi \gamma d_p^3}{k_E}} \quad [21]$$

The performance of the electrostatic separation is characterized based on its efficiency defined as

$$\eta = 1 - \frac{\text{No. of Escaped Particles}}{\text{No. of Injected Particles}} \quad [22]$$

#### Numerical Method

The commercial CFD code Fluent (version 6.2, Lebanon, NH) was used to solve the governing equations. Since the Fluent code does not provide a built-in solver for potential and charge conservation equations (i.e. Eqs. (14) and (15)), a user-defined program determining the charge density and the electric fields as well as the aerosols charging was written and incorporated with main source code (Shooshtari 2004). The electrostatic force influence on aerosol droplets was modeled through an applied body force as described in Eq. (1). The major steps of numerical solution are as follows:

1. Solve for the electric and ion charge density fields using Poisson's and charge conservation equations.
2. Solve for the flow field using Navier-Stokes and continuity equations.
3. Track particles using momentum equations and determine temporal charge accumulation on particles as they travel.

This numerical method can be applied to various ESP geometries to study their performances. Since this method is based on the Lagrangian approach, the polydisperse aerosol particle injection can easily be incorporated.

#### Wire-Cylinder Separator

The numerical method was used to perform a parametric study on classic wire-cylinder geometry. This is a simple geometry that conveniently represents many industrial applications. Moreover, from a modeling perspective, the advantage of this geometry is the availability of analytical solutions for electric field governing equations (i.e., Eqs. (14) and (15)). The numerical results of aerosol tracking can be used to investigate the efficiency of this class of separators for separation of fine droplets. The schematic configuration of the wire-cylinder separator is shown in Figure .

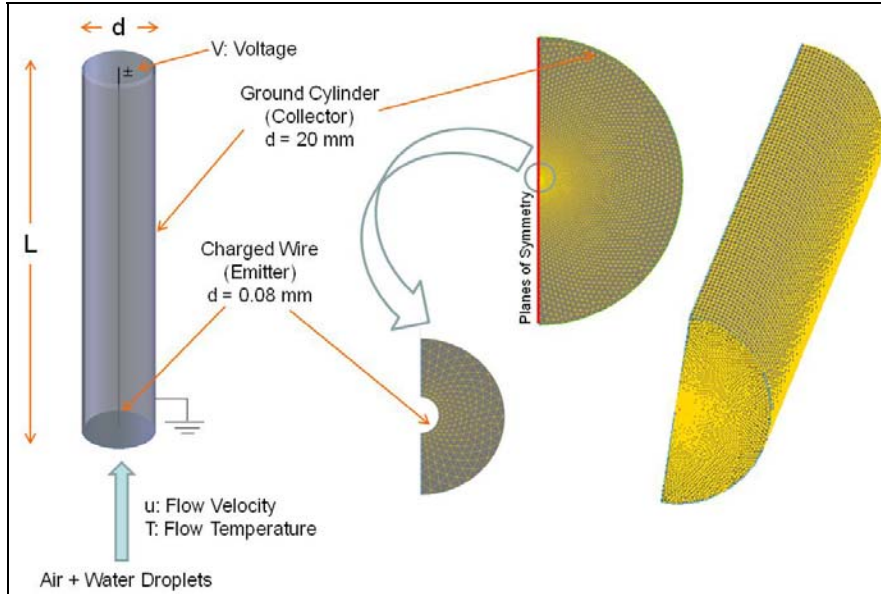


**Figure 3. Wire-cylinder schematic where  $L$ : separator length,  $d_c$ : cylinder diameter (grounded),  $u$ : flow velocity,  $T$ : flow temperature,  $\phi$ : applied electric potential at the wire.**

In this modeling the particles were water aerosol droplets carried with the air stream. The modeling input parameters listed in Table 1 and Table 2 summarize the selected range of parameters used in this study. For each modeling case, only one parameter changed at a time.

**Table 1. Modeling Input Variables**

Cylinder diameter (m)	$d_c = 0.02$
Wire diameter (m)	$d_w = 0.00008$
Fluid density ( $\text{kg}/\text{m}^3$ )	$\rho = 1.18$
Fluid viscosity ( $\text{kg}/(\text{m}\cdot\text{s})$ )	$\mu = 1.86 \times 10^{-5}$
Fluid permittivity (F/m)	$\varepsilon = 8.854 \times 10^{-12}$
Aerosol relative permittivity	$\varepsilon_p = 80$
Ions mean thermal speed (m/s)	$\bar{C}_i = 240$
Ions mobility ( $\text{m}^2/(\text{V}\cdot\text{s})$ )	$Z_i = 1.5 \times 10^{-4}$

**Table 2. Modeling Varied Parameters**

Wire electric potential (kV)	$\phi = 4, 5, 6, 7, 8$
Average air flow inlet velocity (m/s)	$\mathbf{u} = 0.3, 0.6, 0.9, 1.2, 1.5$
Air flow temperature (K)	$T = 280, 300, 320$
Separator length (m)	$L = 0.05, 0.075, 0.1, 0.125, 0.15$

Due to symmetry, only half of the cylindrical tube was considered as the computational domain. Also, since the electric force exerted on the airflow was axisymmetric, no recirculation was created, and air fluid flow was not affected by EHD interaction. Therefore,  $F_{EHD}$  in Eq. (7) was not considered.

The computational domain was discretized to 487520 computational cells using Tri-Pave meshing scheme in each cross-section as well as uniform meshing in axial direction. To capture the high intensity electric field, a high concentration of cells was created in the vicinity of the wire electrode.

For the fluid flow boundary condition, the fully developed parabolic velocity profile was imposed at the tube inlet such that average inlet velocity was equal to those values given in Table 2. For electric field, the wire electric potential was set based on values given in Table 2, and the tube wall was always grounded. The charge density on the wire electrode was set using the analytical solutions of Eqs. (14) and (15).

The particles were injected using uniform surface distribution injection. Preliminary tests of the model showed that the number of injected particles affects the separation efficiency significantly if it is lower than 200 particles. To minimize any error and to insure the efficiency independence on the particle number, 500 equally distant particles were injected in each study. The particles were assumed to be at a halt once they were injected, and they gradually accelerated along the airflow due to the drag force. The particles that were deflected by the electric field force and which collided with the tube wall were totally collected, and no reflection existed.

### Results

The first step in generating results was to obtain the current vs. voltage curve (CVC) to characterize the separator performance and to calculate the power consumption. Figure shows the CVC for the given separator geometry. The minimum voltage to sustain a corona discharge for the conditions studied here was 4 kV.

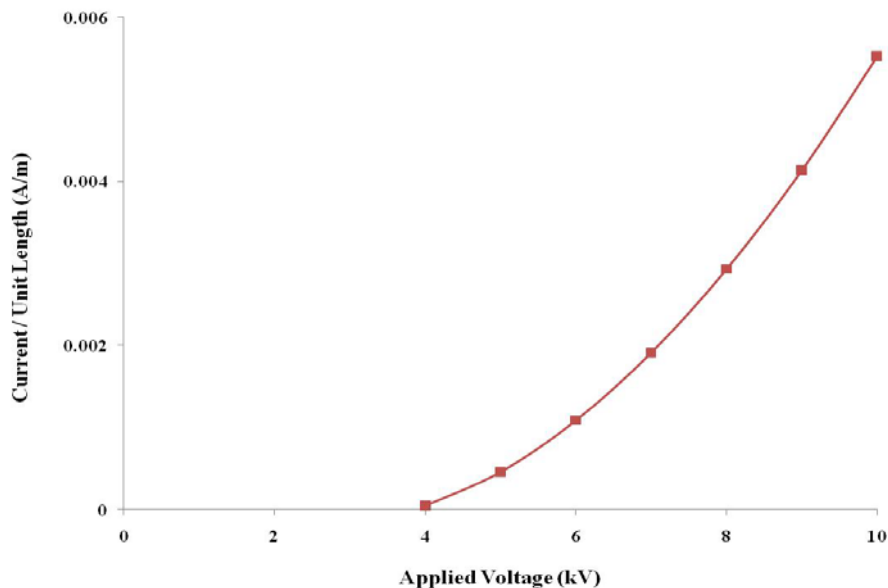


**Figure 4. Current-voltage characteristics for the wire-cylinder separator at  $T = 300$  K.**

First, the numerical model solution for potential field and charge density had to be verified against the analytical solution. Figure 5 and Figure 6 show comparisons between both numerical and analytical results for the electric potential and charge density distribution along the radial

distance, respectively. As seen there, a favorable agreement between the results was obtained. The results show that the charge density decreases more than four-fold as one moves from the emitter to collector surfaces.

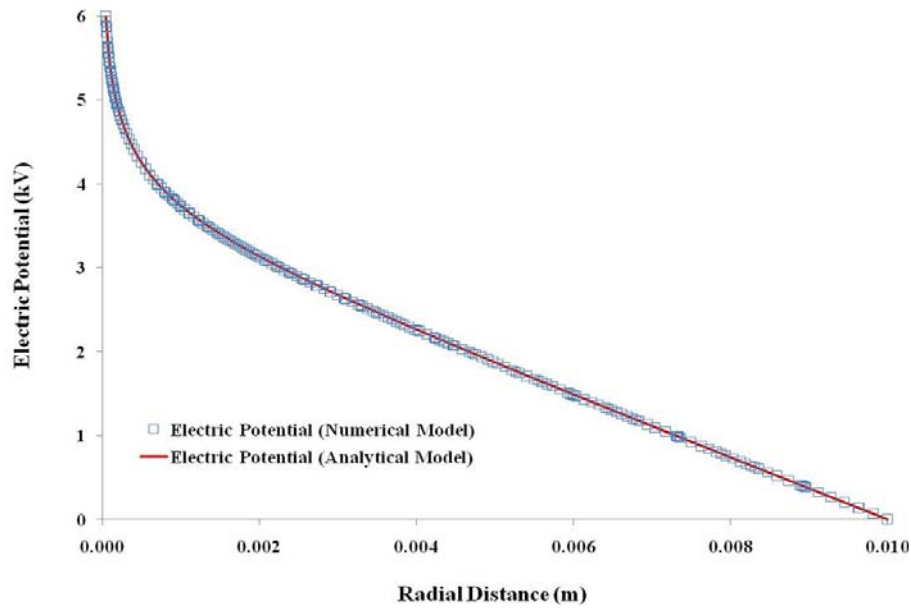


**Figure 5. Comparison in electric potential field between numerical and analytical models at  $\phi = 6.0$  kV,  $u = 1.0$  m/s,  $T = 300$  K and  $L = 0.15$  m.**

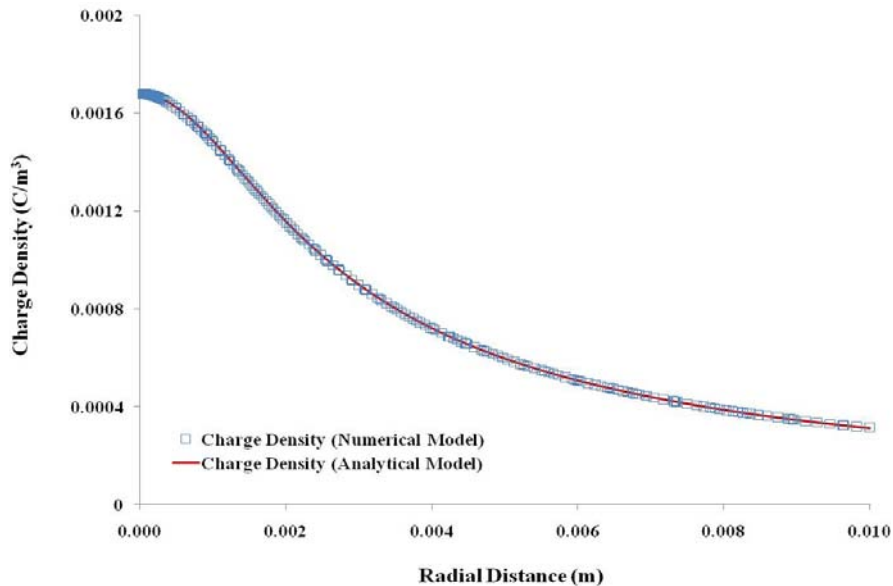


**Figure 6. Comparison in charge density between numerical and analytical models at  $\phi = 6.0$  kV,  $u = 1.0$  m/s,  $T = 300$  K and  $L = 0.15$  m.**

Particle size plays an important role in how the particle is charged. Figure 7 shows the average of number of charges accumulated on injected particles as they travel inside the separator by each of the two different charging mechanisms as well as the combined effect. It can be seen from the figure that particles of less than  $0.5 \mu\text{m}$  are charged mainly through diffusion charging, where particles of size greater than  $0.5 \mu\text{m}$  are predominantly charged through field charging.

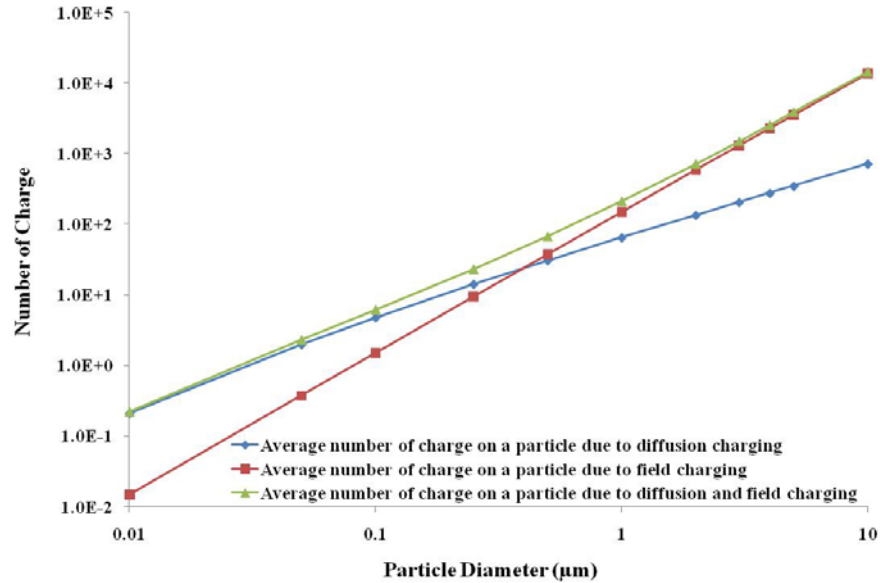


**Figure 7. Average number of charge accumulated on a particle due diffusion charging, field charging or diffusion and field charging. The varied parameters are  $\phi = 4.0$  kV,  $u = 1.0$  m/s,  $T = 300$  K and  $L = 0.15$  m.**

In order to ensure that the water aerosol droplets maintained their integrity and did not break into parts as they moved inside the high electric field, the number of accumulated charges had to be checked against the Rayleigh limit. Figure 8 shows the maximum, average and minimum number of accumulated charges over all the injected aerosol droplets. The difference ratio between the Rayleigh limit and the maximum accumulated charge on a particle ranged between 65-150. Therefore, the limit was not reached in this study.

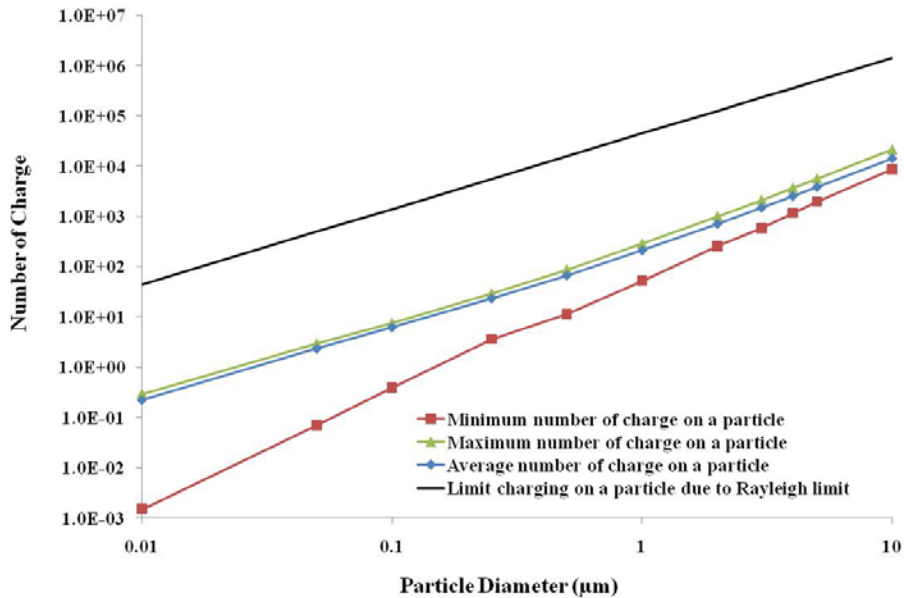


**Figure 8. Rayleigh limit vs. the number of charges accumulated on a particle due to diffusion and field charging. The varied parameters are  $\phi = 4.0$  kV,  $u = 1.0$  m/s,  $T = 300$  K and  $L = 0.15$  m.**

The first case in the parametric study investigated the effect of applied electric potential on separation efficiency defined by Eq. (22). Figure 9 shows five cases where a potential increase improved separation efficiency. The reason for this is that increasing the electric potential leads to

enhancement of the electric field intensity and an increase of charge density, which both enhance the charging process.

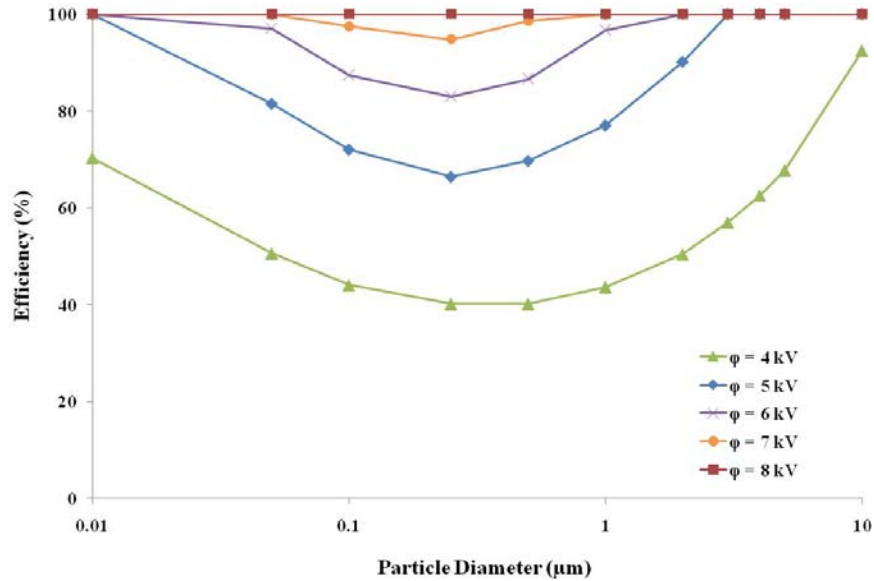


**Figure 9. Electric potential field effect on separation efficiency for five cases with the following input parameters:  $u = 0.9 \text{ m/s}$ ,  $T = 300 \text{ K}$  and  $L = 0.15 \text{ m}$ .**

The efficiency generally starts decreasing as the aerosol diameter size gets bigger than  $0.01 \mu\text{m}$ , and then it starts increasing once diameter size passes  $0.5 \mu\text{m}$ . The reason for this behavior is that the total charging is the summation of diffusion and field charging. The diffusion charging mechanism is the more dominant factor on small particles, while the field charging is more dominant on larger particles. However, the combined effects are less effective when the particle size is in-between. Looking at case (5) where the voltage is  $8 \text{ kV}$ ,  $100\%$  efficiency was reached at all different aerosol diameters. The power consumption in this case was about  $2.4 \text{ W}$ . The next case addressed the effect of flow rate on charging and collecting water aerosols. As expected, increasing the flow rate lowered the efficiency because of the shorter resident time available for the aerosols to receive charge, to travel to the collector electrode, and get trapped, as Figure 10 shows. For example, in case number (1), where the velocity was  $0.3 \text{ m/s}$ , the efficiency was  $100\%$  at all different diameter sizes, while for velocity  $1.5 \text{ m/s}$  the minimum efficiency decreased to  $66\%$  at diameter size  $0.25 \mu\text{m}$ .

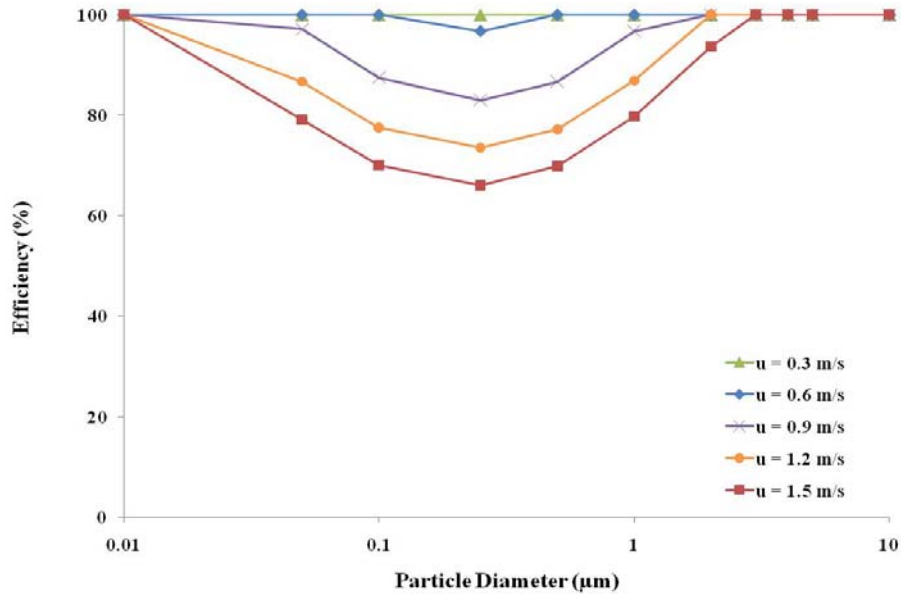


**Figure 10. Flow rate effect on separation efficiency for five cases with the following input parameters:  $\phi = 6.0$  kV,  $T = 300$  K and  $L = 0.15$  m.**

The third case investigated the effect of flow temperature on the separation efficiency. As mentioned earlier, in diffusion charging ions move due to Brownian motion. Based on Eq. (11), the flow temperature can affect this charging mechanism, the primary method of charging of small particles (i.e.  $< 0.5 \mu\text{m}$ .). The result of our study, presented in Figure 11, shows that over the investigated range of temperatures, the temperature influence is minimum and is only on small particles. Overall, the effect of temperature on the separation efficiency can be disregarded without any substantial error. The temperature change is considered on the thermophysical properties of gas and particles such as density and viscosity.

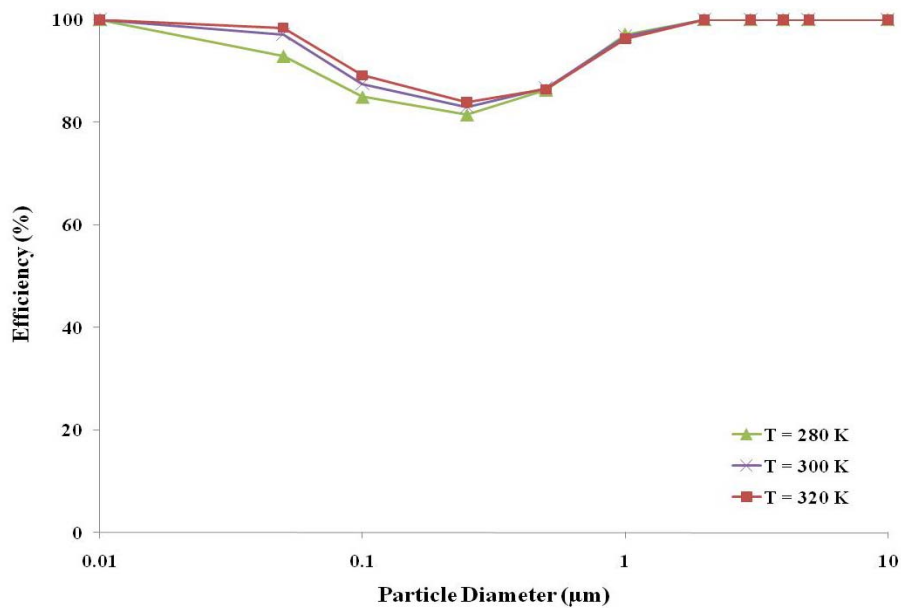


**Figure 11. Flow temperature effect on separation efficiency for three cases with the following input parameters:  $\phi = 6.0$  kV,  $u = 0.9$  m/s and  $L = 0.15$  m.**

The last case investigated the effect of the separator length on separation performance. Figure 12 shows that as the length increased, so did the separation efficiency. Increasing the length means increasing the aerosol residence time as well as the collection area, which eventually enhances the performance of the separator. As seen there, the minimum efficiency varied from 61% for 0.05 m separator to 100% for 0.15 m separator.

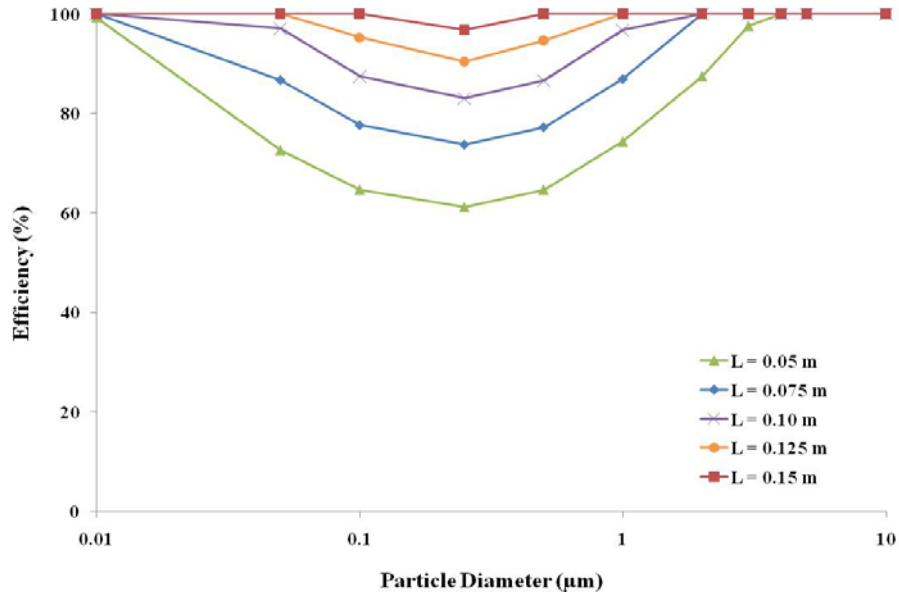


**Figure 12. Separator length effect on separation efficiency for five cases with the following input parameters:  $\phi = 6.0$  kV,  $u = 0.9$  m/s and  $T = 300$  K.**

### Mesh Study

A mesh study was conducted to investigate the independency of numerical model results with the number of computational cells. The study used the same meshing scheme, Tri-Pave, but with finer and coarser computational grids. Figure 13 shows a comparison between three cases that had the same input parameters with different cell numbers, where (a) was with decreased cell numbers, (b) was the standard case and (c) was with increased cell numbers. The average difference between cases (a) and (b) was about 0.5% where the difference between cases (b) and (c) was about 0.8%. Therefore, for the parametric study in this paper it can be concluded that within  $\pm 1\%$  the results are independent of the cell number. Thus, the computational cells number can be increased to improve the accuracy.

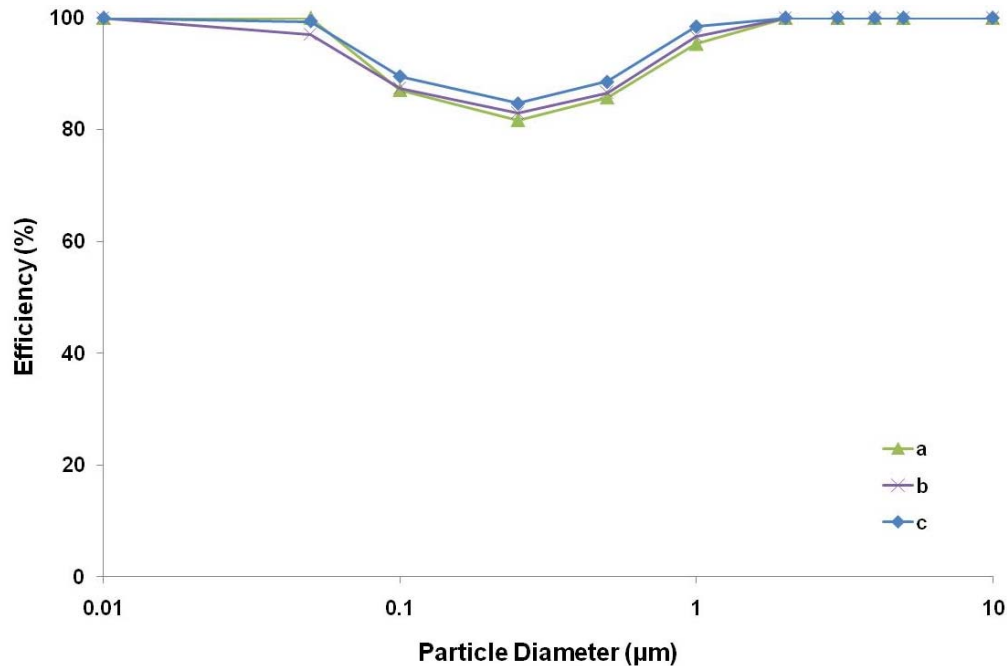


**Figure 13. Mesh study comparison between three cases that have the same parameters such as:  $\phi = 6$  kV,  $u = 0.9$  m/s,  $T = 300$  K, and  $L = 0.10$  m with different computational cell numbers, as  $a = 94655$  cells,  $b = 487520$  cells and  $c = 753840$  cells.**

### Conclusion

Based on the results obtained, increasing the applied voltage and separator length directly increases the separation efficiency. On the other hand, the efficiency decreases as the flow velocity increases. The effect of flow temperature on the performance of the separator was found to be insubstantial. Electrostatic separation can be considered an energy-efficient mechanism at low air velocities. Numerically, it can achieve 100% efficiency with reasonable power consumption, 2.4 W for a voltage of 8 kV and wire length of 0.1 m in the present study. Based on the collective findings of this study, electrostatic separation appears to be a promising solution to the separation area of water aerosols from airflow.

### **Experimental Work**

A lab scale test rig was constructed to test the performance of the oil separator using air as the gas phase. The oil that was used in this experiment was synthetic lubricant based with the properties shown in Table 3.

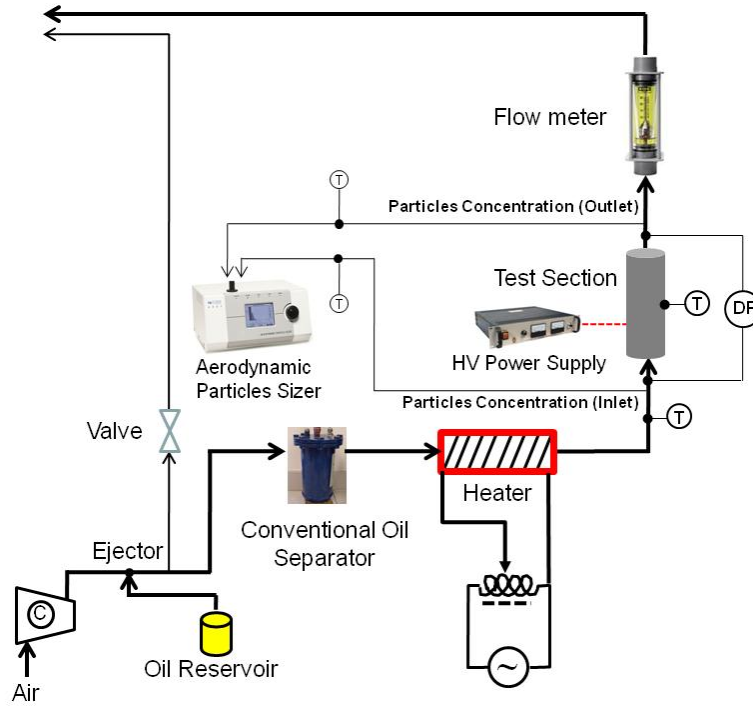
**Table 3. Oil Droplet Properties**

Oil type	Alkyl-benzene (synthetic lubricant)
Density ( $\text{kg/m}^3$ )	$\rho_p = 862$
Dynamic Viscosity ( $\text{N}\cdot\text{s/m}^2$ )	$\mu_p = 27 \times 10^{-3}$
Permittivity	$\epsilon_p = 2.2$

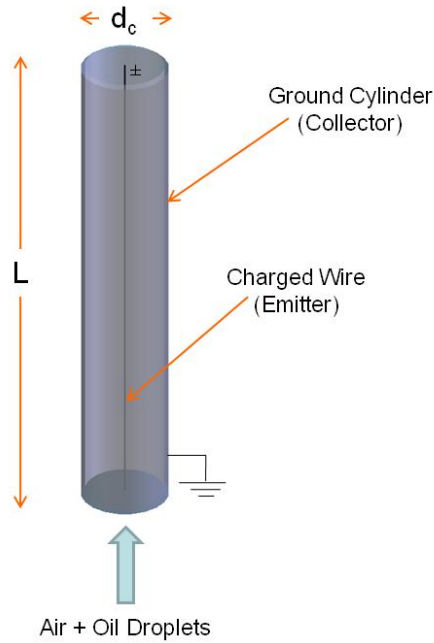
### Test setup and Procedures

Figure 14 shows a schematic of the test setup. Air enters the open test loop through a compressor. Then it passes through an ejector that is connected to an oil reservoir where the oil is injected as droplets. Then the two-phase flow passes through a bypass to control the bulk flow that goes into the test section. Next, the two-phase flow enters a conventional impactor-type oil separator to separate the large oil droplets. Then the air flow that contain oil droplets of micron size leaves the conventional oil separator for the test section passing through a heater that is used to study the effect of temperature on the separation efficiency of the test section.

Figure 15 shows the test section, which is an EHD wire-cylinder separator with a wire and cylinder diameters of 0.08 mm and 20 mm, respectively. The length of the separator is 150 mm. The wire (emitter electrode) is connected to a high voltage power supply where the cylinder (collector electrode) is grounded. An aerodynamic particle sizer (TSI 3321) is used to measure the particle diameters and weight concentrations before and after the separator. The sizer is capable of measuring particles ranging from 0.1-20  $\mu\text{m}$  in diameter and up to 10,000 particles/ $\text{cm}^3$  in particle concentrations with  $\pm 10\%$  in accuracy. Other monitoring devices are used, such as flow meter to measure the flow rate inside the EHD separator, thermocouples, T-type, to measure the temperature of the EHD separator and inlet gas, and a pressure transducer to measure the pressure drop of EHD across the EHD separator.



**Figure 14. Air-oil separation test setup.**



**Figure 15. Air-oil EHD separator.**

The current-voltage characteristics (CVC) and separation efficiency ( $\eta_{\text{separation}}$ ) are presented in the next section for the studied cases. The CVC summarizes the relation between current and voltage and how this relation changes when testing parameters are varied. This relation is very important to predict the performance of the separator and to identify the power consumption. The separation efficiency is calculated based on the total mass of oil droplets at the inlet and outlet of the separator based on Eq. 1.

$$\eta_{\text{separation}} = 1 - \frac{\text{Total Mass of Particles}_{\text{outlet}}}{\text{Total Mass of Particles}_{\text{inlet}}} \quad [23]$$

Table 4 summarizes the selected range of parameters used in this study.

**Table 4. Varied parameters**

Charged wire electric polarity	+, -
Wire electric potential (kV)	$\phi = 1, 2, 3, 4, 5, 6, 7$
Average air flow inlet velocity (m/s)	$u = 1, 2, 3, 4, 5$
Air flow temperature (K)	$T = 300, 315, 330$

### Experimental Results

The first experimental test for all cases was to obtain the CVC to characterize the separator performance and to calculate the power consumption. Then the separation efficiency vs. applied voltage was plotted to inspect how the performance was behaving when selected parameters were changed. The first case investigated polarity effect. Two high-voltage power supply devices with different polarity outputs were used in this study. Figure shows the CVC for positive and negative voltage polarities where the negative polarity has higher current. In positive charging there are much fewer free electrons than the negative one. The reason for this behavior is the way that ions are generated.

In positive charging ions are created by the gas surrounding the corona plasma region, the region surrounding the charged wire, whereas in the case of negative corona, ions are created by the emitter wire itself. Therefore, ions are traveling inward when wire positively charged; however, they traveling outward when negatively charged. Therefore, negative polarity achieves better efficiency, about 26 % higher efficiency at 7.0 kV, Figure 16, due to better electron emission and gas ionization (9). The minimum voltage to sustain a corona discharge ( $V_0$ ) for the studied conditions was 3.8 kV

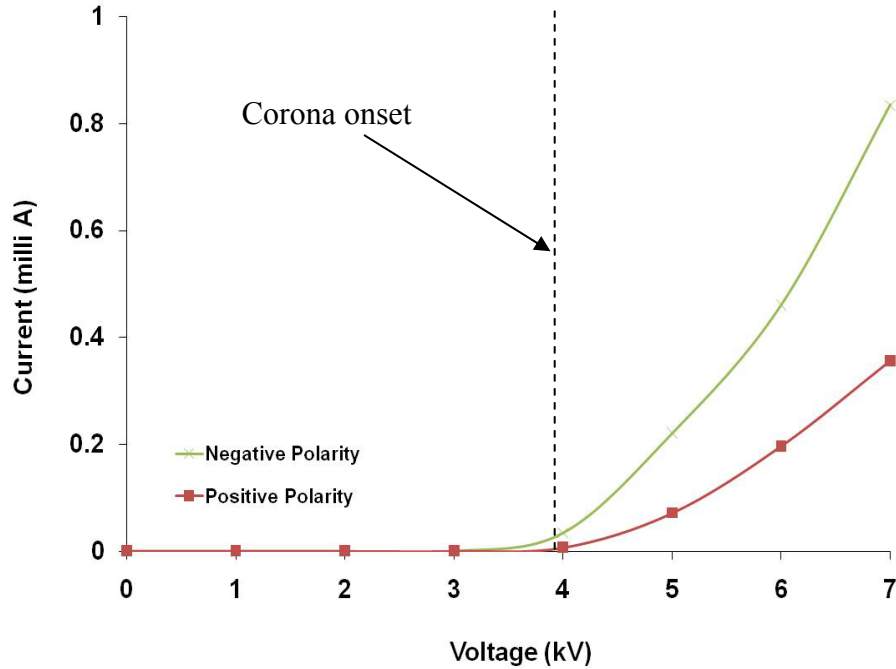


Figure 16. Polarity effect on CVC when  $v = 5.0$  m/s and  $T = 300$  K.

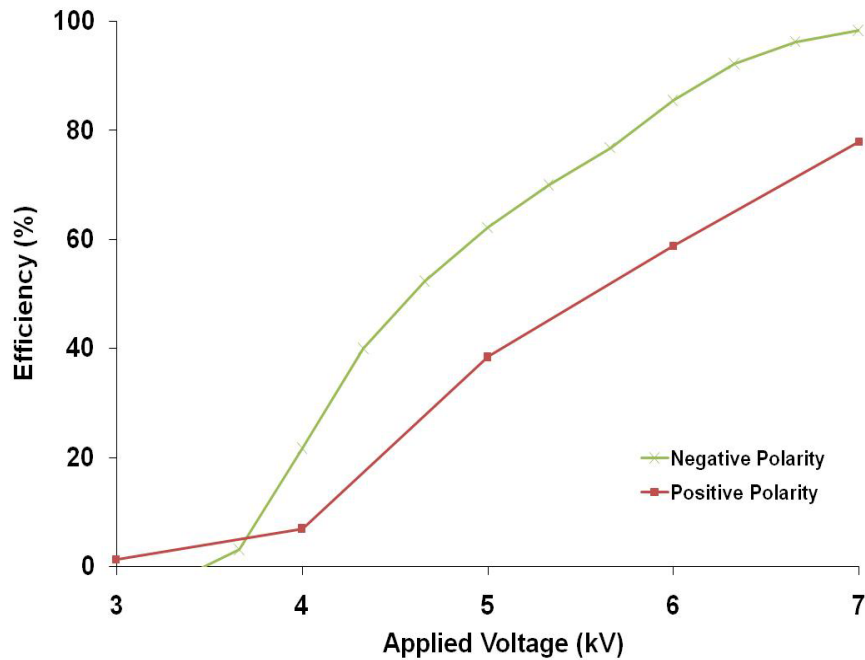


Figure 17. Polarity effect on separation efficiency ( $v = 5.0$  m/s and  $T = 300$  K).

The second study examined the gas velocity effect. It was observed that while varying velocity does not have any significant effect on the CVC, it had substantial impact on the separation efficiency. As the air velocity decreases, the separation efficiency increases. This happens because decreasing the speed of the flow increases particle resident time, time needed for charged particles to travel to the collector, and therefore the separation efficiency is enhanced. Looking at the two cases of lowest and highest air velocities in Figure 18, it can be noticed that the efficiency for  $v = 1.0$  m/s is 4 times larger than for  $v = 5.0$  m/s at 4.0 kV. Separation efficiency achieves near 100% at 5.0 kV for  $v = 1.0$  m/s where it achieves 98.3% for  $v = 5.0$  m/s at 7.0 kV. Overall, the average efficiency increases 24% when the velocity dropped from 5.0 to 1.0 m/s.

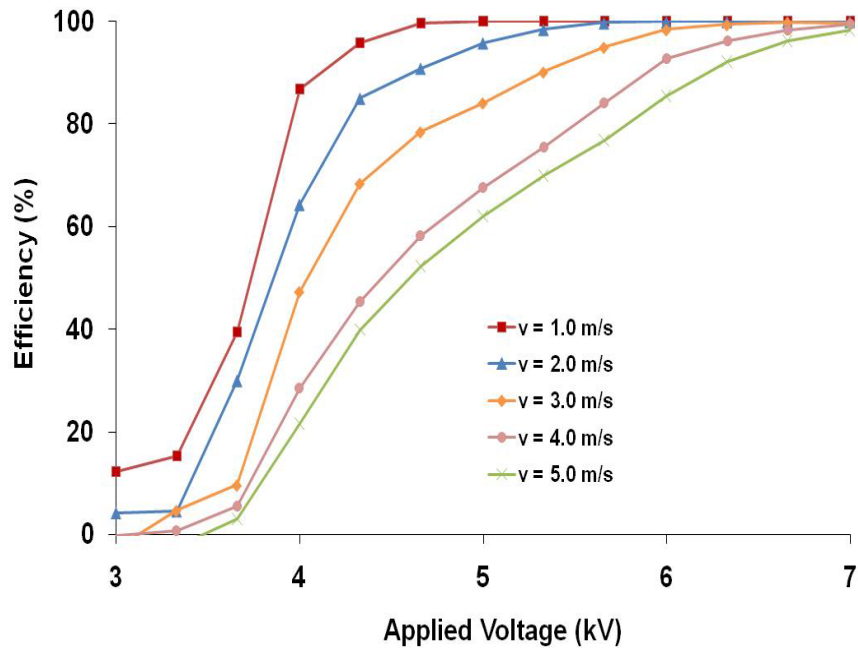


Figure 18. Flow velocity effect on efficiency when (negative polarity and  $T = 300$  K).

The last study involves the effect of temperature on CVC and separation efficiency. It can be seen from Figure 19 that as the flow temperature increases, the current increases too. This is due to a better ion emission from emitter. According to the Maxwell-Boltzmann distribution for the thermal speed of ions, it increases as the temperature is increased. The average separation efficiency is 15.4% higher when the temperature increases from 300 to 330 K, Figure 20.

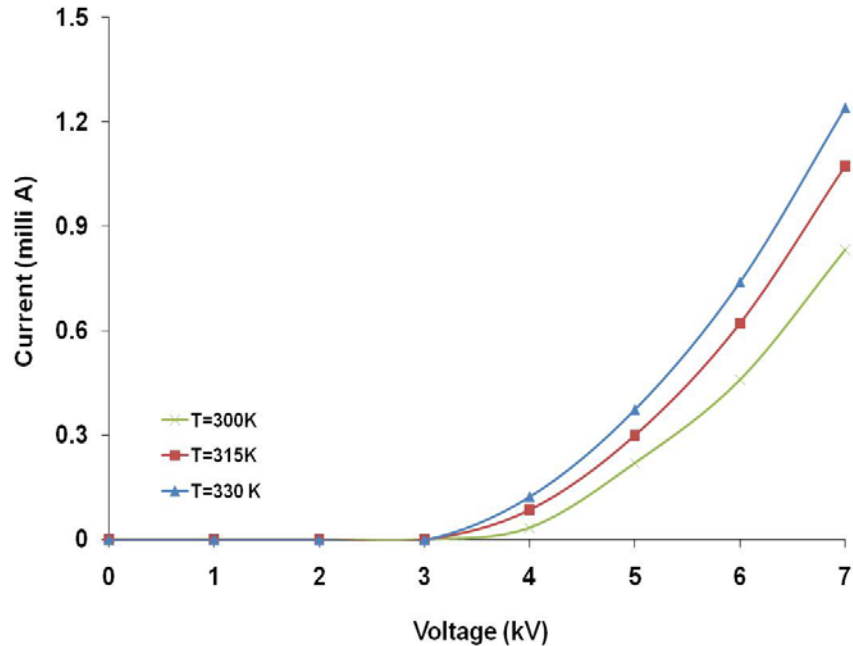


Figure 19. Flow temperature effect on CVC (negative polarity and  $v = 5.0$  m/s).

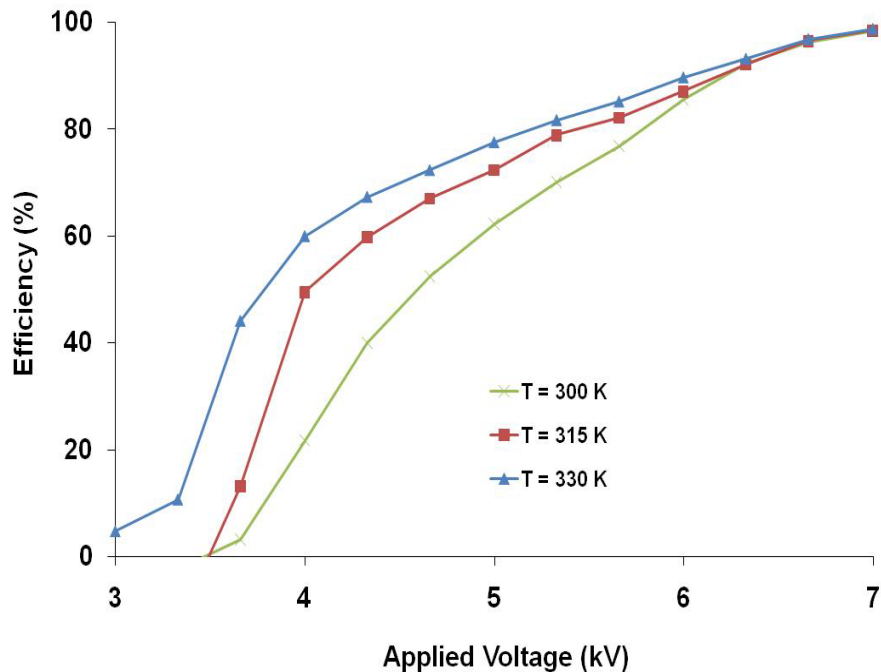


Figure 20. Flow temperature effect on efficiency (negative polarity and  $v = 5.0$  m/s).

A pressure drop analysis due to the EHD effect on the flow was obtained. The pressure drop increase due to EHD effect was a low as few Pascal (3.1 Pa) with the applied voltage at 9kV and gas velocity of 5 m/s.

### Conclusion

The results obtained from the experimental work in the current study show that the EHD technique can be utilized for effective separation of liquid droplets from gas flows and can push the technology beyond the limitation of conventional separators. There are many parameters that affect the performance of EHD separation phenomenon, including polarity of the emitter,

temperature and velocity of the flow, and the magnitude of applied voltage and current. The separation efficiency improves with using negative polarity due to an increase in electron emissions and gas ionization. Also, the higher temperature of the gas phase increases the efficiency due to the enhancement of ion thermal speed. As expected, as the flow velocity decreases, the efficiency increases since the residence time of droplets inside the separator increases. As shown earlier, one of the advantages that EHD has in the separation process stream is its low pressure drop, a few Pa for the experiments conducted in the current study. Also, the power consumption of EHD is very low, which makes it an energy efficient technique. The maximum power consumption measured in this study was 8.0 W at 7.0 kV and for negative charge polarity. Moreover, this mechanism can be combined with other conventional mechanisms for better performance.

### Concluding Remarks and Recommendations for Future Work

Utilizing the EHD mechanism in separation of liquid droplets from moving gaseous medium will overcome the limitation of conventional separation techniques. Besides its ability to remove droplets of micron and submicron droplets from gas flow, it also has very small pressure drop. With an optimum design, it can be an energy efficient device through consuming less power. These findings were obtained through numerical study and experimental work that were conducted at the University of Maryland.

Future work of this project is constructing a sophisticated test setup for air-water separation, since water droplets require humidity, temperature and pressure monitoring to prevent them from evaporating, where oil droplets do not require this. Also, it remains to be determined, in conjunction with ADNOC, the direct cases and applications to which this mechanism could be applied.

### Key References

- [1] Mo, B., Ohadi, M.M., and Dessiatoun, S.V., "Liquid vapor separation and thermal management in an EHD-enhanced capillary pumped loop," Heat Transfer 1998, Proceeding of 11th International Heat Transfer Conference, Vol. 2, Taylor & Francis Inc., Levittown, PA, pp.63-68.
- [2] Ohadi, M. M., Ivenkenko, I., and Dessiatoun, S., "Electrohydrodynamic Liquid-Vapor Separator," USA Pat.# 6,582,500.
- [3] Schrage, D.S., Shoemaker, J.M., and McQuillen, J., 1998, "Passive two-phase fluid separation," AIAA 36th Aerospace Sciences Meeting & Exhibit, Reno, NV, Jan. 1998, AIAA-98-0731.
- [4] Balachandran, W., Machowski, W., Ahmad, C.N. "Electrostatic atomization of conducting liquids using AC superimposed on DC fields," Industry Applications, IEEE Transactions on Volume 30, Issue 4, July-Aug. 1994 Page(s):850 - 855 Digital Object Identifier 10.1109/28.297899.

### Publications

*"Electrohydrodynamic (EHD)-Enhanced Separation of Fine Liquid Droplets from Gas Flows - Application to Refrigeration and Petro-chemical Processes"*, M. Alshehhi, S. Dessiatoun, A. Shooshtari, M. Ohadi and A. Goharzadeh, Second International Energy 2030 Conference, Abu-Dhabi, UAE, Nov. 2008.

*"Parametric Performance Analysis of an Electrostatic Wire-Cylinder Aerosol Separator in Laminar Flow Using a Numerical Modeling Approach"*, M. Alshehhi, S. Dessiatoun, A. Shooshtari, M. Ohadi and A. Goharzadeh, to be submitted to HVAC & R Journal

*"Electrohydrodynamic Enhanced Separation of Immiscible Oil Droplets from an Air Flow"*, M. Alshehhi, S. Dessiatoun, A. Shooshtari, and M. Ohadi, to be published in International Journal of Refrigeration

## Visits

- Amir Shoostari, 1 month working visit to PI, May 2007
- Afshin Goharzadeh, 2 weeks working visit to University of Maryland, July 2007.
- Mohamed Alshehhi, Serguei Dessiatoun visited P.I., GASCO and ADGAS from Dec 8 -13 2007
- Mohamed Alshehhi, Serguei Dessiatoun visited P.I., GASCO, ADGAS, Habshan Plant and Das Island from May 3 -9 2008

## GRA (names, degrees, graduation)

Mohamed Alshehhi, Ph.D. candidate; expected to graduate in 2009

### ***4.3. Energy System Management Projects***

## Robust Optimization of Petrochemical Systems

UM Investigator: Dr. Shapour Azarm

PI Investigators: Dr. Saleh Al Hashimi and Dr. Ali Almansoori

UM's GRA: Mr. Weiwei Hu

PI's GRA: Ms. Naveen Al Qasas

Acknowledgement: Dr. Mian Li

FINAL REPORT

### 1. Abstract

The overall objective of this research project was to develop a framework for robust optimization and sensitivity analysis of petrochemical systems. The investigation mainly focused on engineering decisions but also considered the effects of engineering decisions on business objectives such as cost and profit while maintaining the required product specifications as well as when there was uncertainty. The proposed models and approaches were considered in the context of two typical systems in a petrochemical plant, i.e., a single distillation column and an integrated reactor-distillation system, as part of the infrastructure case studies. Based on the developed system analysis models for these case studies, three methods were developed, implemented and discussed. These methods include: i) multi-objective robust optimization; ii) robust optimization with sensitivity analysis; and iii) approximation assisted optimization. Based on our close collaboration between UMD and PI researchers, joint papers on these methods have been co-authored and submitted. Possible future research directions have also been identified and presented.

Throughout this research, the PI and UMD researchers had close collaboration and numerous contacts and meetings. We regularly met (often on a bi-weekly basis by way of MSN) to discuss the results of our research and exchange ideas. The results of this collaboration are one (1) published journal article, another submitted journal article (currently under review), and finally a third article which is in the final stages of preparation (i.e., a working paper), which is expected to be submitted to a conference in January and eventually converted to a journal article. We also had an abstract/poster in the Energy 2030 conference in 2008.

### 2. Objective

The objective of this study was to develop a framework for analysis and robust optimization of petrochemical, systems such as a distillation column, while considering the net profit effects at the plant level. The investigation mainly focused on engineering decisions but also considered the effects of these decisions on business objectives while maintaining the required product specifications. The investigation explored tradeoffs between engineering objectives versus expected profit and other business goals when there was uncertainty. The research included three interrelated research models and/or methods: i) Multi-Objective Robust Optimization (MORO); ii) Robust Optimization with Sensitivity Analysis; and iii) approximation assisted (or Kriging-Directed) Multi-Objective Genetic Algorithm (KD-MOGA). The goal in MORO was to obtain the best system solutions as possible in a multi-objective sense; at the same time, their system performance had to be "insensitive" to uncertainty. We developed a new MORO approach for the case when uncertainty was irreducible. Compared to a previous (two-level) MORO approach, this new MORO approach was shown to produce comparable robust solutions but required an order-of-magnitude fewer simulation calls for the tested examples, including petrochemical case studies considered. For problems that had reducible uncertainty, we developed a new combined Robust Optimization and Sensitivity Analysis (ROSA) approach in which we not only obtained robust solutions but also determined the minimum amount of *investment* needed to reduce the effect of uncertainty on the system objectives. To implement the

new MORO and ROSA approaches efficiently, we developed a KD-MOGA which required approximately 50%~60% fewer function calls compared to a conventional MOGA.

There were two main tasks in the project. Both tasks began after a literature review in the respective domain was performed.

**Task 1 (PI):**

Develop and implement engineering analysis models for a petrochemical system:

Task 1.1: Develop a MATLAB-based multi-input, multi-output analysis model for a distillation column.

Task 1.2: Extend the above analysis model for the distillation column to include: (i) additional complexity, (ii) subsystem details; or, expand the model to include other subsystems in a refinery plant. The ultimate goal was to develop an integrated multi-subsystem petrochemical analysis model for a plant or a small number of units in a petrochemical plant. Our goal was to demonstrate the feasibility of the proposed techniques with a few case studies.

**Task 2 (UM):**

Develop and implement robust optimization and sensitivity analysis approaches with multi-objective optimization solvers:

**Task 2.1:** Develop and implement a MATLAB-based multi-objective robust optimization approach for the above mentioned case studies given the uncertainty in the system is irreducible.

**Task 2.2:** Extend the robust optimization approach to consider the case when a portion of uncertain parameters is reducible.

**3. Infrastructure: Case Studies**

In this section, two simulation analysis models—a single-disciplinary distillation column and a multi-disciplinary reactor-distillation system—are introduced which are used as part of the infrastructure (i.e., case studies) for verification and demonstration of the proposed approaches.

**3.1 Distillation Tower Example**

Distillation columns (or towers) are commonly used in the chemical process industries to separate a mixture of two or more chemicals based on the difference in their volatilities. In this example a mixture of toluene and benzene is fed to a distillation column where the two chemicals are separated into two high-purity streams. A simplified scheme of a binary distillation tower is shown in Figure.1

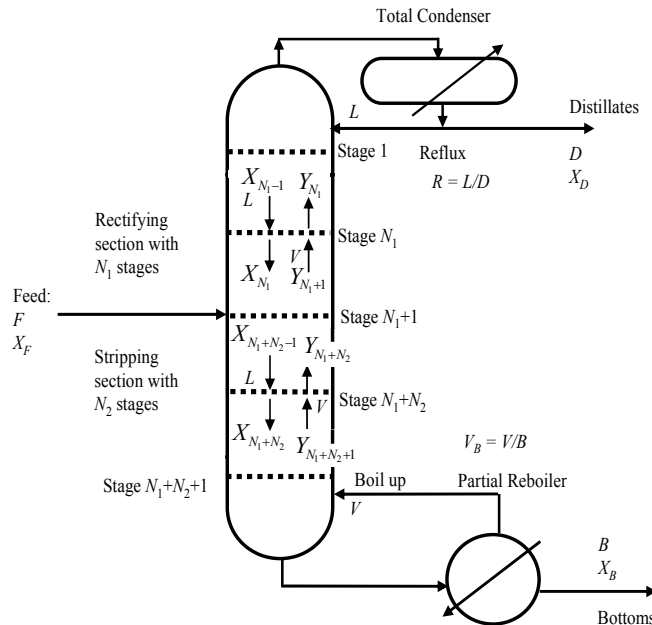


**Figure 1. Schematic of a binary distillation tower.**

In Figure -1,  $D$  and  $B$  are the flow rates of the distillate and bottom products, respectively;  $F$  is the feed flow rate per unit time and is fixed (100 mol/hour);  $L$  is the liquid reflux flow rate sent back to the column from the condenser to improve the overall separation power of the unit;  $N_1$  is the number of stages in the rectifying section (upper section, above the feed plate);  $N_2$  is the number of stages in the stripping section (bottom section, below the feed plate);  $P$  is the pressure of the column, which is fixed (1 atm);  $R$  is the reflux ratio defined as  $L/D$ ;  $T$  is the temperature of the feed stream and is assumed to be fixed (30°C);  $V$  is the vapor flow rate of the stream leaving the partial boiler and entering the bottom of the column;  $V_B$  is the vapor boil-up ratio defined as  $V/B$ ;  $X_B$  is the composition of the more volatile component, benzene, in stream  $B$ ;  $X_D$  is the composition of the more volatile component in stream  $D$ ; and  $X_F$  is the mole fraction of the more volatile component, benzene, in the feed, which is fixed (0.45).

In this simplified version of the distillation tower, the design variables are  $N_1$ ,  $N_2$ ,  $R$  and  $V_B$ . Especially the last two design variables reflect the quantity of liquid and vapor returned to the column respectively (e.g., [Douglas, 1988]). Typically, as the number of trays in the column increases, gas-liquid contact increases, and therefore mass transfer is enhanced, causing the distillate to become richer in the more volatile component (benzene in this case) and the bottoms to become richer in the less volatile component (toluene in this case). Therefore, as  $N_1$  and  $N_2$  increase,  $X_D$  increases and  $X_B$  decreases. Also, any increase in the gas-liquid traffic in the column increases the mass transfer coefficients, leading to an enhancement in the separation process. Thus, an increase in  $R$  and  $V_B$  would increase  $X_D$  and decrease  $X_B$  (e.g., [Douglas, 1988]; [Seader and Henley, 2006]).

### 3.2 Integrated Reactor-Distillation System Example

As shown in Figure 2, we also considered an integrated reactor-distillation refinery system. Two distillation columns are used to separate phthalic anhydride and malice anhydride from un-reacted o-xylene after the reaction (in the reactor subsystem) occurs. The operational conditions for the entire system, such as the reactor feed flow rate and column reflux ratios, are selected optimally to minimize the total cost and maximize the purity of the two distilled products.

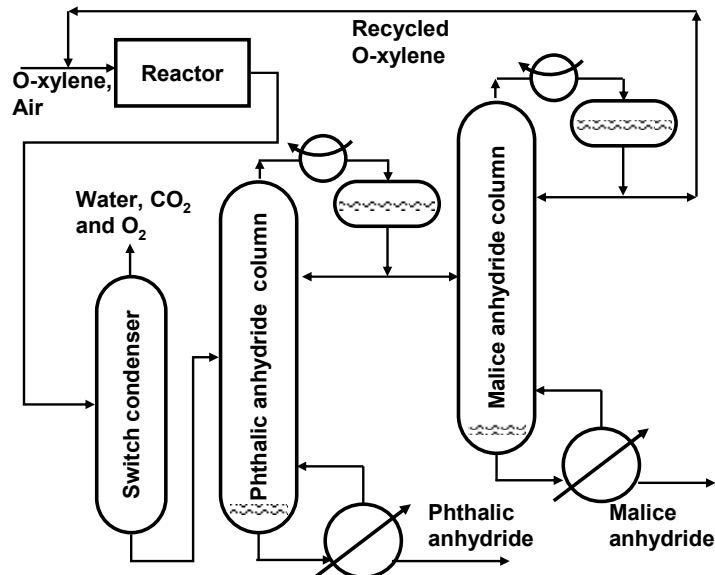


**Figure2 . The schematic of reactor distillation system.**

In the reactor-distillation process, the subsystems include reactor and two distillation columns. Raw materials, including o-xylene and air, are first combined with recycled o-xylene and then fed to the reactor. A switch condenser removes unwanted products such as  $\text{CO}_2$ ,  $\text{O}_2$ , and water. The

product stream leaving the switch condenser contains phthalic anhydride, malice anhydride and un-reacted o-xylene, from which the first two products can be obtained after a two-stage distillation.

The simulation model of each subsystem was developed at PI. We used an “all-at-once” optimization approach to obtain consistent operational conditions for the entire system and simultaneously optimize system outputs as shown in Figure 3

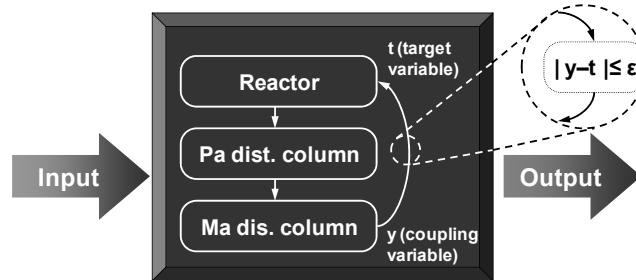


Figure 3. Handling couplings in the “all-at-once” approach.

Since the product/material flow in this integrated system forms a closed loop, we had to break up the feedback stream to run the simulation model sequentially [Li et al., 2008(b)]. Subsystem couplings in the model include  $F_{org}$ ,  $X_{org}$ ,  $D$ ,  $X_D$ , and  $DS_{dis}$  (i.e., distilled steam). We chose  $DS_{dis}$ , the flow rate of recycled o-xylene, to break up the coupling in this “all-at-once” formulation by adding its target (or dummy) value  $DS_{rct}$  as an additional design variable in the system. A convergence constraint was enforced by requiring that the difference between the coupling variable and its target be smaller than  $\epsilon$  where  $\epsilon$  is equal to 0.5% of  $DS_{dis}$ . The convergence condition was also enforced, as shown in Figure 3.

We will use these two case studies in the demonstration of our three methods in the next few sections.

#### 4. Multi-Objective Robust Optimization (MORO)

##### 4.1 Approach

Figure 4 gives a definition for our robust optimization problem with irreducible interval uncertainty. To obtain a robustly optimized solution, objective functions are optimized with respect to design variables  $\mathbf{x}$ , and for all values of  $\mathbf{p}$  within an interval of uncertainty (blue rectangle), constraints are to be satisfied and objective variations  $\Delta f$  are kept within an acceptable range (yellow rectangle).

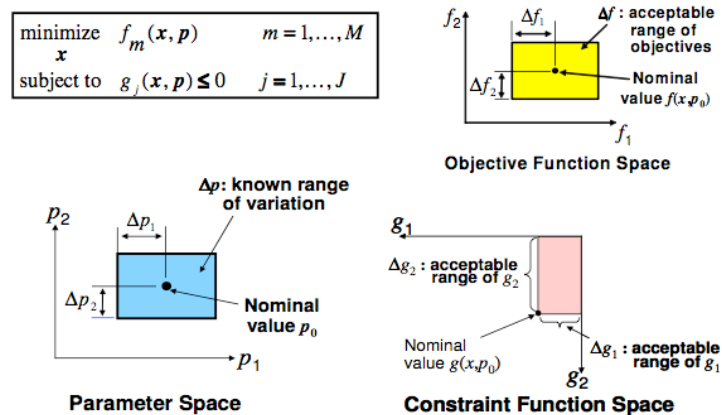
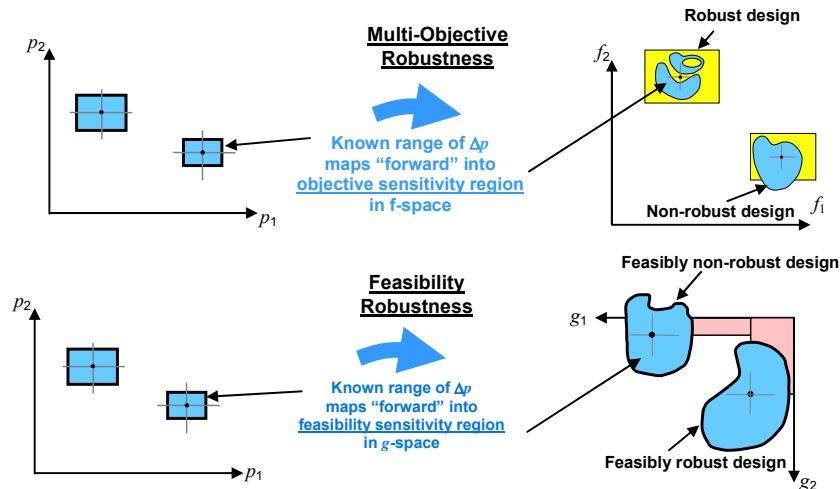


Figure 4 . Robust optimization problem with interval uncertainty.

Figure 5 conceptually describes how our robust optimization approach works for objective robustness (top two figures in Figure) and feasibility robustness (bottom two figures). It can be seen that objective variation for a robust design is kept within an acceptable range subject to parameter interval uncertainty (blue rectangles). Additionally, constraints are satisfied (for a feasibly robust design) subject to interval uncertainty for parameters.



**Figure 5. Objective and feasibility robustness.**

Two approaches were developed and applied for solving MORO problems. In the previously developed two-level MORO [Li et al., 2006], the upper level problem searches and solves for candidate solutions while the lower level problem applies a robustness assessment for every candidate solution generated in the upper level, as shown in Figure 6 (LHS). This iterative formulation in the two-level MORO between the upper and lower level problems can result in a large number of simulation calls (e.g., simulation of distillation tower). In order to handle MORO problems more efficiently, a single-level MORO approach was developed and implemented during the course of this project. In this single-level MORO, constraints have been iteratively added to the optimization problem. These constraints are devised using a worst case value of parameters which collectively help identify robust solutions. Because the single-level MORO approach involves only one level (or a sequence of two steps), it is considerably more efficient than the two-level MORO approach. The detailed discussion on this new single level MORO approach can be found in our working paper [Hu et al., 2008].

Next, some results from the above mentioned MORO approaches are presented.

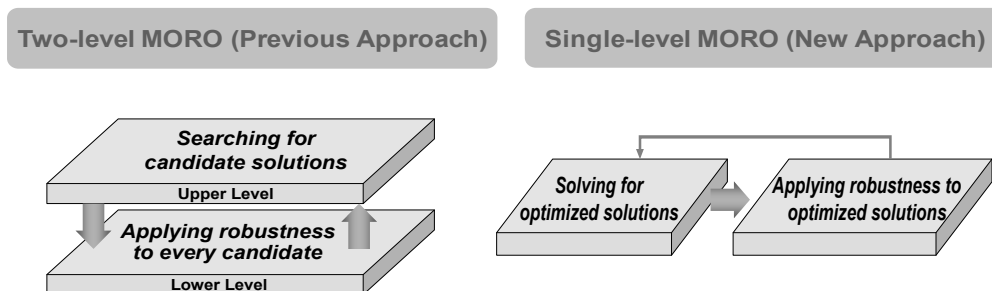


**Figure 6. Two approaches for MORO.**

## 4.2 Results

### 4.2.1 Distillation Column Optimization

#### 4.2.1.1 Initial Cost Model

Figure 7 gives a summary of the simulation model for the distillation column with a cost model. As shown in Figure 7, the inputs from the left are for design variables, and the top two inputs are for design parameters (these are fixed for the deterministic (or nominal) optimization model but have interval uncertainty for the robust optimization). The outputs from the simulation model are also shown in Figure 7, including the two objective functions considered (shown in red).

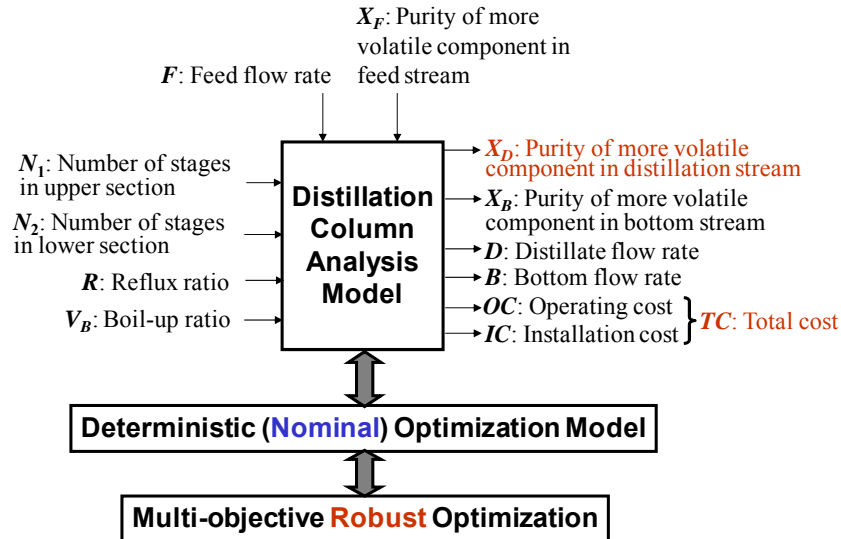


Figure 7. Simulation model for the distillation column analysis.

Figure 8 shows the corresponding optimization problem: both deterministic and robust cases with the corresponding settings are given.

## Deterministic + robust optimization model:

$$\begin{aligned} &\text{maximize } X_D = Y_1(N_1, N_2, R, V_B, F, X_F) \quad \left. \vphantom{\text{maximize}} \right\} \text{Purity } (X_D) \\ &\text{minimize } TC = Y_2(N_1, N_2, R, V_B, F, X_F) \quad \left. \vphantom{\text{minimize}} \right\} \text{Total Cost } (TC) \end{aligned}$$

subject to:

$$10 \leq N_1 \leq 100$$

$$10 \leq N_2 \leq 100$$

$$0 < R \leq 10$$

$$0 < V_B \leq 10$$

$$0.6 \leq X_D < 1$$

$$D \geq \lambda F$$

### Robust optimization settings:

- Known interval of uncertainty for  $F$  and  $X_F$  (from nominal):

$$\Delta F = \pm 4 \text{ and } \Delta X_F = \pm 0.03$$

- Acceptable variation range for objectives:

$$[\Delta X_D, \Delta TC] = \text{“ 4\% of nominal value”}$$

nominal  $F = 100$  Feed flow rate, uncertain parameter

nominal  $X_F = 0.45$  Purity of more volatile component in feed stream, uncertain parameter

Figure 8. Deterministic and robust optimization models for distillation column.

In this model, as shown in Figure 8, we introduced a design parameter  $\lambda$  and considered its effect on the objectives. The deterministic designs using three different values of  $\lambda$  are shown and compared in Figure 9. The parameter  $\lambda$  is introduced because it specifies the quantity of output  $D$  given the input  $F$ . In our previous attempts, we had noticed that when  $\lambda$  was not present, the optimizer would automatically seek high values of  $X_D$  while producing poor values for  $D$ . After the introduction of  $\lambda$ , we observed that it indirectly determines an upper bound for the mole fraction of the distillate  $X_D$ . The smaller the value that  $\lambda$  assumes, the larger the maximum mole fraction of distillate the optimum solution is able to have. When  $\lambda$  becomes too small, however, it has little practical value even if a higher mole fraction of distillate can be obtained. According to our numerical experiments, the best overall performance of the distillation column is reached when  $\lambda=0.4$ , as shown in Figure 9. Figure also shows that as  $\lambda$  is decreased, the optimized solutions shift to the right.

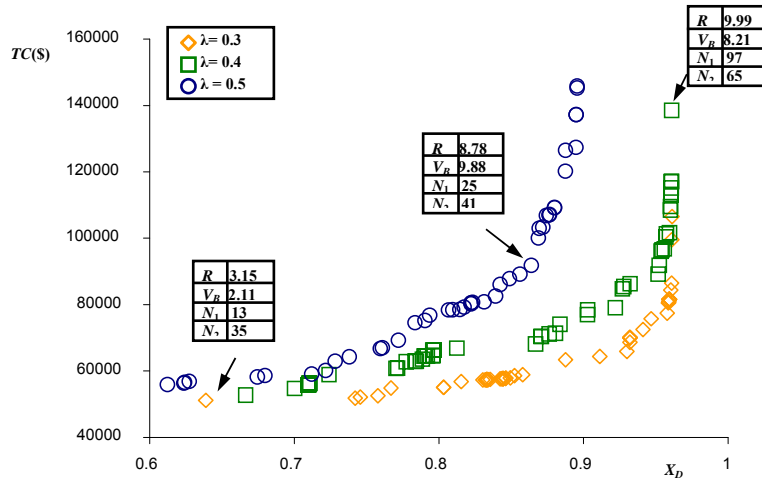


Figure 9. Deterministic Pareto optimum solutions for distillation column with different values of  $\lambda$ .

As shown in Figure 10, robust solutions are generated using the two-level MORO approach. Those robust solutions are generally inferior (or conservative) compared to the deterministic ones. Moreover, as before, when  $\lambda$  decreases, the Pareto frontier of both deterministic designs and robust designs shift together to the right and achieve a higher mole fraction.

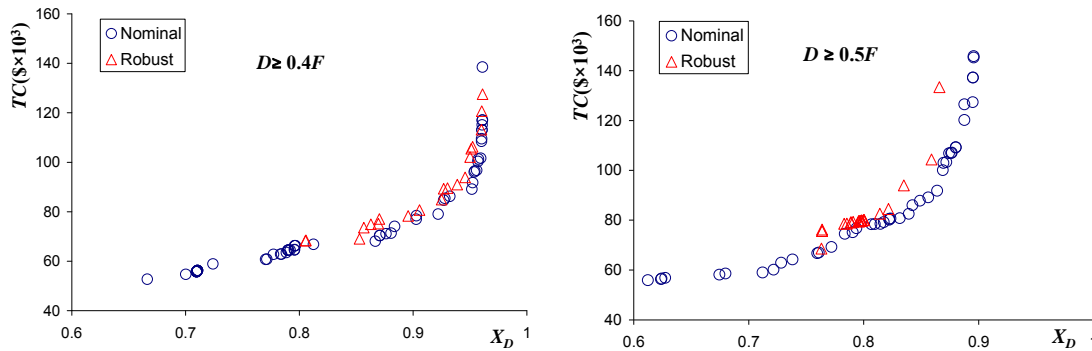


Figure 10. Pareto solutions for distillation column with and without parametric uncertainties

#### 4.2.1.2 New Profit Model

So far, one of the objectives considered was cost. Here, that objective is modified for the distillation column to consider profit, which accounts for the total cost (including capital and operating costs), product prices and the product flow rate. We added a new uncertain parameter for the distillation column optimization, i.e., the price of the distillate product, to the robust optimization model. MORO is conducted for the distillation column problem to obtain tradeoffs between the objectives of profit and purity of the distillate product.

Figure 11 summarizes the integrated profit based simulation model for the distillation column. As shown in Figure 11 design variables are the inputs from the left to the analysis model. The top three inputs are parameters (fixed for the deterministic optimization, but having interval uncertainty for robust optimization). The price of propylene, related to the total income, is considered as an uncertain parameter. Two outputs from the analysis model are considered as objective functions (shown in green), where profit depends on annual revenue and cost of the distillation process.

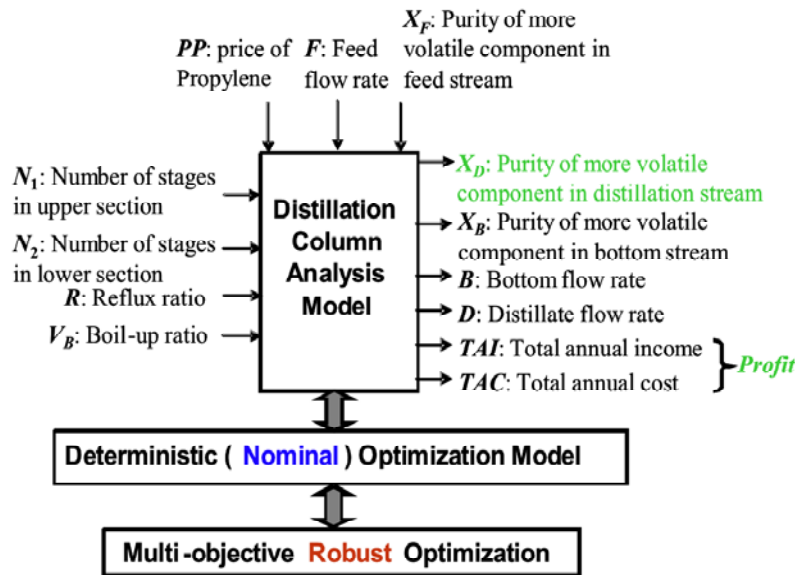
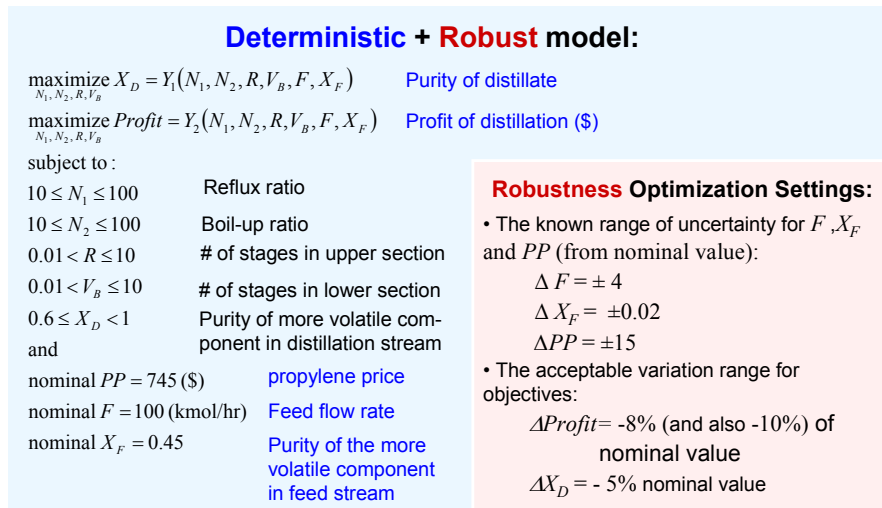


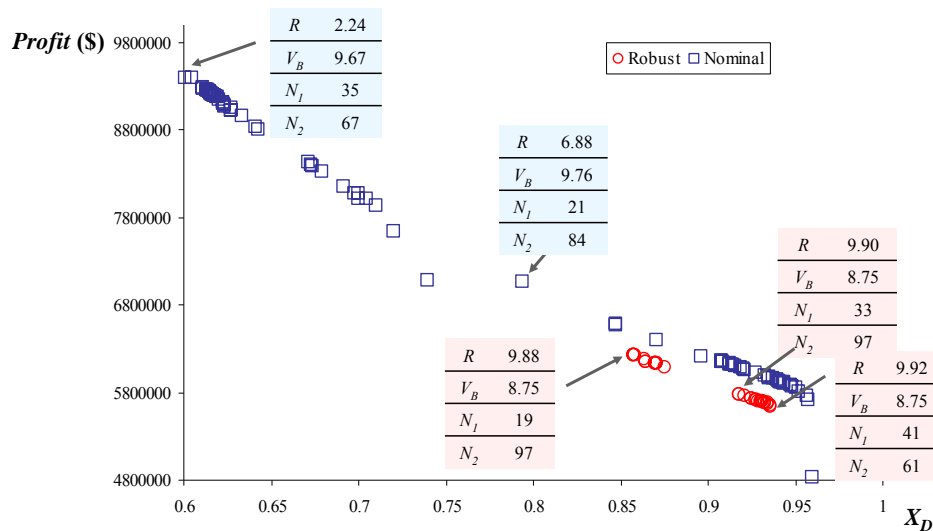
Figure 11 Integrated profit analysis model for the distillation column

Figure 12, summarizes the deterministic (nominal) and robust optimization problems of the distillation column, with the profit of distillation considered as one of the objective functions. Both deterministic and robust optimization models have the same objective functions. Design variables and constraints for the deterministic model are formulated in the blue box. Uncertain parameters are assumed to be fixed at the nominal values in the deterministic model but are subjected to interval uncertainties in the robust optimization study. The known range of uncertainty for these parameters is shown under the robust optimization settings in the pink box. Also shown in Figure is the acceptable variation range for the objectives. Note that the range only specifies the lower bound of the allowable tolerance for the objectives since the objectives are to maximize the purity and profit. That is, the variation that can give a higher value of the purity and profit does not degrade the performance of the system and will not violate the robustness requirement. Note also that for the profit we have considered two cases of acceptable variation range (i.e., -8% and -10%).



**Figure 12. Deterministic and robust optimization models for the distillation column.**

Figure 12, shows the nominal and robust optimum results for the optimization problems described in Figure. As shown in Figure 12, robust designs are still inferior (or more conservative compared) to the nominal designs. It is also observed that the robust optimum designs cover a smaller region in the objective space than the nominal ones. Note that in Figure 12, the acceptable variation range for profit is  $-8\%$  in the robust model.



**Figure 13. Pareto solutions for distillation column with and without interval uncertainties.**

Optimum results for the robust optimization problem using two different acceptable variation ranges of profit are compared in Figure 13. The red circles represent robust solutions with the acceptable variation range of profit of  $-8\%$ , and the red multiply symbols represent the solutions of  $-10\%$ . It should be clear that the robust optimization problem with a larger acceptable variation range of profit generally gives better solutions (with respect to both objectives) than that with a smaller acceptable variation range.

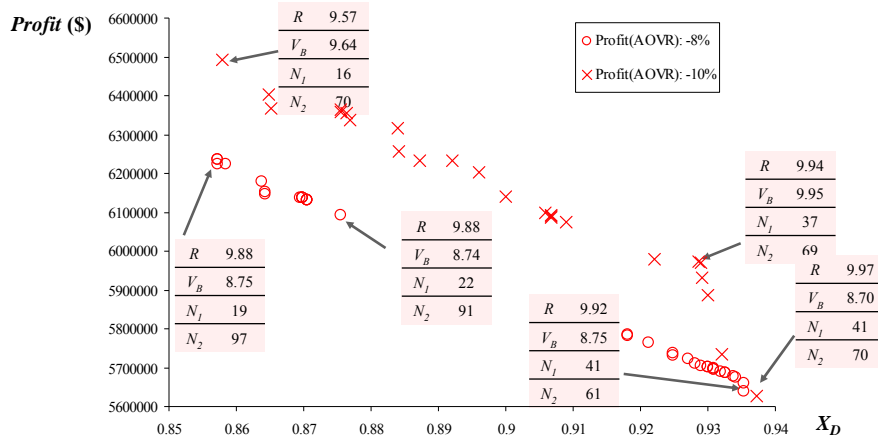


Figure 14. Robust Pareto solutions for distillation column with different acceptable variation range for objectives.

#### 4.2.1.3 Comparative Study: Single-Level MORO vs. Two-Level MORO

We used both the proposed single-level MORO and the two-level MORO approach to solve the previous distillation column optimization problem, as summarized in Figure 14. For comparison, the deterministic optimization problem with the nominal value of parameters was also solved. The Pareto solutions obtained from the two MORO approaches are in general agreement, as shown in Figure 14. More importantly, the number of function calls required by the single-level MORO approach was reduced by an order of magnitude (as shown in the table to the right of Figure 14) compared to the two-level MORO.

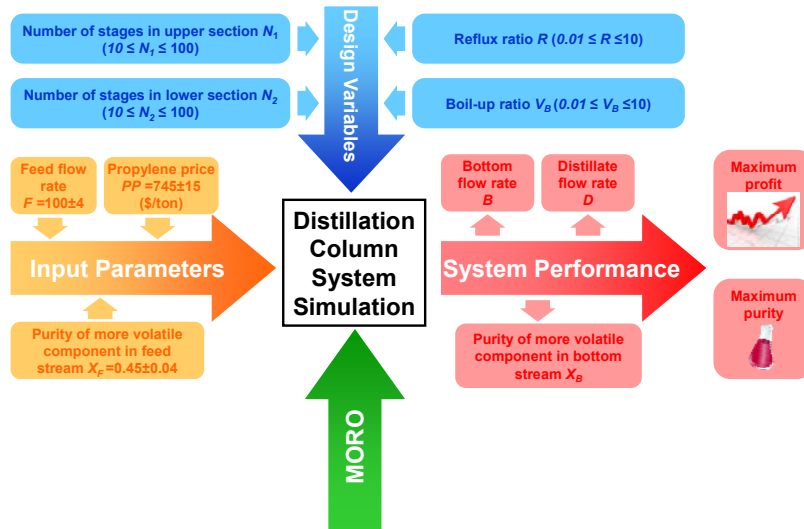


Figure 15. Implementing two MORO approaches for distillation column.

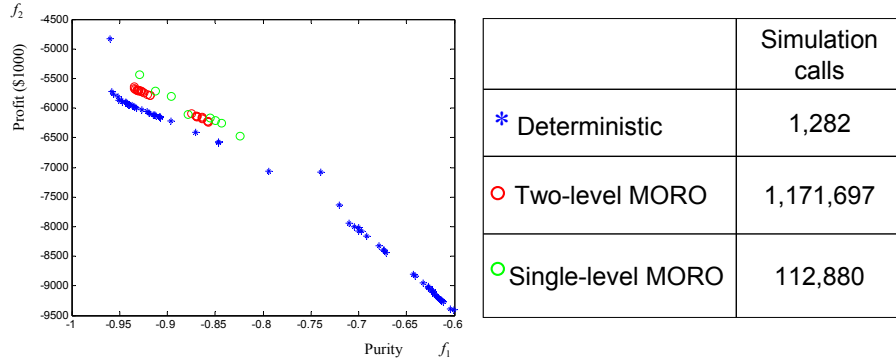


Figure 16. Deterministic and robust optimization results.

#### 4.2.1 Reactor-Distillation Optimization

##### 4.2.1.1 Deterministic Optimization

The objectives of the reactor-distillation system optimization were to maximize the purity of distillation stream and to minimize the total cost. Because there are three subsystems in the reactor-distillation analysis model, they must be consistent in such a way that the difference between the coupling variable and its target is small, as shown by the convergence condition in Figure 17. The optimization problem has ten design variables: four for the reactor subsystem, two for the first distillation column, and four for the second distillation column.

$$\begin{aligned}
 &\underset{\mathbf{x}}{\text{minimize}}: TC = f_1(\mathbf{x}) && \text{Total Cost} \\
 &\underset{\mathbf{x}}{\text{maximize}}: X_{pa} + X_{Ma} = f_2(\mathbf{x}) && \text{Total Purity} \\
 &\text{subject to: } |DS_{rct} - DS_{dis}| \leq \varepsilon && \text{Convergence Condition: } \varepsilon = 5\% \text{ and } 0.5\% DS_{dis}
 \end{aligned}$$
  

SS <sub>1</sub> reactor		$100 \leq F_{oxy} \leq 1000$	feed flow rate (kmol/hr)
		$200 \leq F_{air} \leq 2000$	Air flow rate (kmol/hr)
		$2 \leq Vol \leq 10$	Volume of the reaction chamber (m <sup>3</sup> )
		$100 \leq DS_{Rct} \leq 2000$	Target variable of the feedback to the reactor

SS <sub>2</sub> distillation1		$2 \leq N_{min} \leq 20$	Minimum number of stages of column 1
		$0.1 \leq R_{min} \leq 10$	Minimum reflux ratio of column 1

SS <sub>3</sub> distillation2		$5 \leq R \leq 10$	reflux ratio
		$5 \leq V_B \leq 10$	boil-up ratio
		$10 \leq N_1 \leq 100$	number of stages in upper section
		$10 \leq N_2 \leq 100$	number of stages in lower section

Figure 17. Formulation of reactor-distillation system as a multi-disciplinary optimization problem.

We obtained the Pareto optimum solutions using two different  $\varepsilon$  values, i.e.,  $|DS_{rct} - DS_{dis}| \leq 5\% DS_{dis}$  and  $|DS_{rct} - DS_{dis}| \leq 0.5\% DS_{dis}$ . The results obtained are shown in Figure 18. Particularly, the left figure in Figure 18 shows the relative trend of the two Pareto solutions obtained. A portion of the left figure is enlarged and shown on the right of Figure 18. The design variables for some selected optimal solutions from Figure 18 are shown in Table 1.

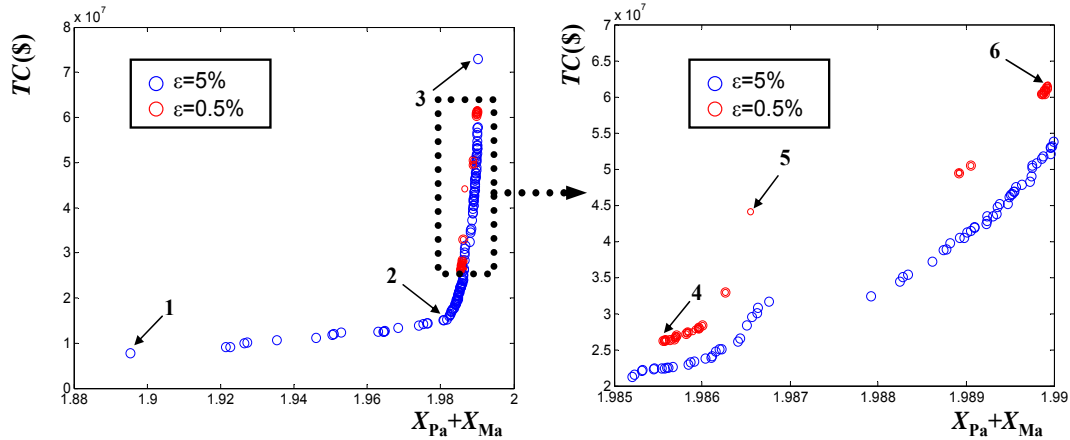


Figure 18. Deterministic optimal solutions for the reactor-distillation system.

Table 1. Design variables for select optimal solutions

#	$F_{oxy}$	$F_{air}$	$Vol$	$DS_{Rct}$	$R_{min}$	$R$	$V_B$	$N_{min}$	$N_1$	$N_2$	$TC$	$X_{Pa}+X_{Ma}$
1	100.66	1122.51	3.55	160.77	0.12	6.82	6.07	5	86	100	7.78E+06	1.895
2	100.41	224.01	4.78	263.98	0.12	8.86	6.00	5	94	71	1.51E+07	1.981
3	100.33	259.00	2.93	1884.81	0.12	6.44	6.06	5	85	76	7.30E+07	1.990
4	100.96	244.63	7.95	579.33	0.10	5.15	6.01	5	73	77	2.62E+07	1.986
5	104.70	356.78	3.95	1078.46	0.10	5.14	6.01	5	79	87	4.41E+07	1.987
6	100.05	242.87	7.70	1567.61	0.10	5.15	6.00	5	87	93	6.16E+07	1.990

#### 4.2.1.2 Robust Optimization

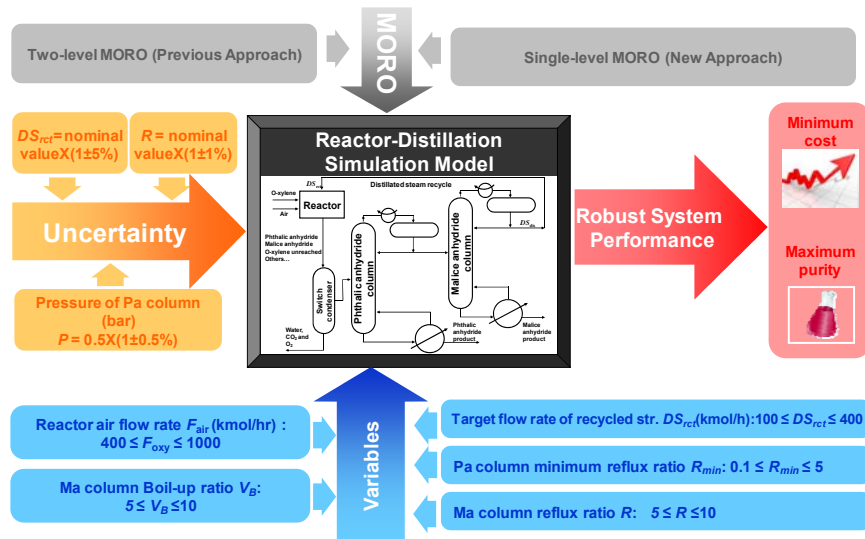


Figure 19. Robust optimization framework.

An overview of the model for this problem is shown in Figure 19 where distillation column 1 refers to the phthalic anhydride column and distillation column 2 refers to the malice anhydride column.

Uncertain factors in the system are the pressure  $P$  in the phthalic anhydride column, the reflux ratio  $R$  in the malice anhydride column, and the target variable  $DS_{rct}$ . The bounds of uncertain factors are described using percentages of their nominal values such as:  $\pm 1\%P$ ,  $\pm 5\%R$  and  $\pm 5\%DS_{rct}$ . We also assumed the following parameters are fixed for the sake of robust optimization, as shown in Table 2.

**Table 2. Fixed parameters in reactor-distillation robust optimization**

$F_{oxy}$ feed flow rate (kmol/hr)	100
$Vol$ Volume of the reactor (m <sup>3</sup> )	5
$N_{min}$ minimum number of stages of Pa column	5
$N_1$ number of stages of Ma column upper section	80
$N_2$ number of stages of Ma column lower section	80

The robust optimization problem was solved using both two-level and single-level MORO approach. The deterministic case of this example is also solved for the comparison purpose. The total number of function calls and the CPU time for the deterministic and robust optimization cases are shown.

It can be seen the two robust optimization approaches require much more computation efforts than the deterministic case. More importantly, as shown in Table 3, the number of functional calls for the two-level MORO approach is almost an order of magnitude higher than that for the single-level MORO approach. Settings for the genetic algorithm in the robust optimization are also shown in **Error! Reference source not found.** The population size and maximum iterations for the deterministic optimization are 50 and 40, respectively.

**Table 3. Comparative statistics of deterministic, two-level and single-level approach**

Deterministic		Two-level MORO		Single-level MORO	
Function Call	Time (min)	Function Call	Time (min)	Function Call	Time (min)
10596	706	1,171,697	30448	97994	6993

**Table 4. Setting for the genetic algorithm in the reactor-distillation optimization**

Two-level MORO			Single-level MORO		
GA parameters		Value	GA parameters		Value
upper level	Population size	50	relaxed problem (LHS block in Figure 6)	Population size	50
	Max iterations	40		Max iterations	40
	Elite number	2		Elite number	2
lower level	Population size	30	robustness assessment (RHS block in Figure 6)	Population size	30
	Max iterations	40	Elite number	40	1
Crossover probability		0.9	System iterations (iterations between two blocks of Figure 6)		5
Mutation probability		0.1	Crossover/Mutation	same as Two-level	

The optimal solutions obtained by the deterministic, single-level and two-level MORO approaches are plotted in the objective space in Figure 20. As expected, the robust optimal solutions are slightly inferior to the deterministic optimal solutions. However, the robust Pareto fronts from the single-level and two-level MORO approaches in general agree with each other.

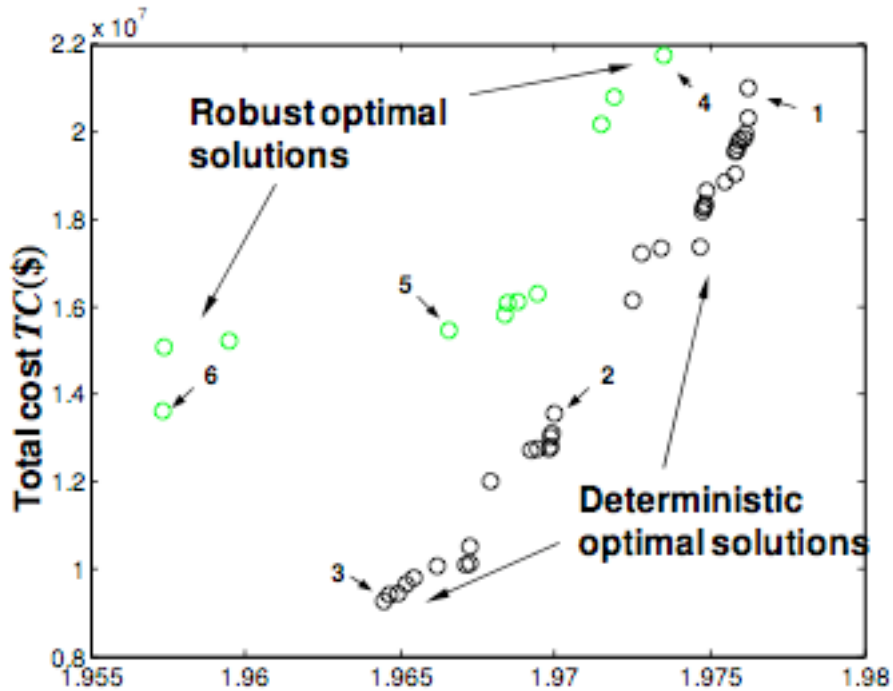


Figure 20. Optimal solutions for the reactor distillation system.

## 5. Robust Optimization and Sensitivity Analysis (ROSA)

Uncertainty considered in MORO is usually treated as irreducible uncertainty since it is not reduced during an optimization procedure. In contrast, uncertainty considered in sensitivity analysis approaches can be reduced partially or completely in order to quantify the effect of input uncertainty on the outputs of the system. Considering this, and the usual existence of both reducible and irreducible uncertainty, an approach that can perform robust optimization and sensitivity analysis simultaneously becomes much of particular interest. In this study, we developed a non-gradient based design approach that is used to perform both robust optimization and sensitivity analysis in a single procedure. The objective of ROSA is to obtain solutions that (i) are multi-objectively optimum, (ii) are insensitive to parameters that have irreducible uncertainty, and (iii) have minimum system output variation with respect to parameters that have reducible uncertainty.

### 5.1 Approach

This new integrated approach, or ROSA, incorporates two existing approaches into one optimization procedure: the two-level MORO approach discussed above and a global sensitivity analysis to deal with reducible uncertainty [Li, 2007]. However, in the ROSA approach, parameters will have both irreducible and reducible uncertainty. As shown in Figure 21 for a two-parameter case, we use darker grey rectangles to represent irreducible uncertainty in the tolerance region while lighter grey represents reducible uncertainty. Accordingly, the tolerance region (TR) of parameters might consist of two parts: Irreducible tolerance region and reducible tolerance region. We assume a parameter can have irreducible uncertainty, or reducible uncertainty, or both. As shown in Figure 21(a), uncertainty in both  $p_1$  and  $p_2$  is fully reducible, while in Figure 21(b) uncertainty in  $p_1$  is partially reducible and uncertainty in  $p_2$  is fully irreducible. In the case of Figure 21(b), the total amount of uncertainty that can be reduced is the lighter grey region.

A selectable retention factor called the Parameter Uncertainty Reduction Index (*PURI*),  $\alpha = (\alpha_1, \dots, \alpha_K)$  with  $\alpha^{lower} \leq \alpha \leq \alpha^{upper}$ , is adopted to control the intervals for both irreducible and reducible uncertainty. That is, each element of *PURI* vector is a retention factor and the amount of retained uncertainty in the corresponding parameter is then controlled by it.  $\alpha^{upper}$  is usually set equal to 1, representing the maximum possible range of the tolerance region. The irreducible and reducible tolerance regions are determined by setting the lower bounds of *PURI* accordingly. If the uncertainty in all parameters is fully reducible as shown in Figure 21(a),  $\alpha^{lower} = \mathbf{0}$  and the tolerance region collapses to become the nominal point  $p_0$ . As shown in Figure 21(C), Retained Tolerance Region (*RTR*) is a symmetric hyper-rectangle in the parameter space, representing the amount of uncertainty that parameters possess after uncertainty reduction.

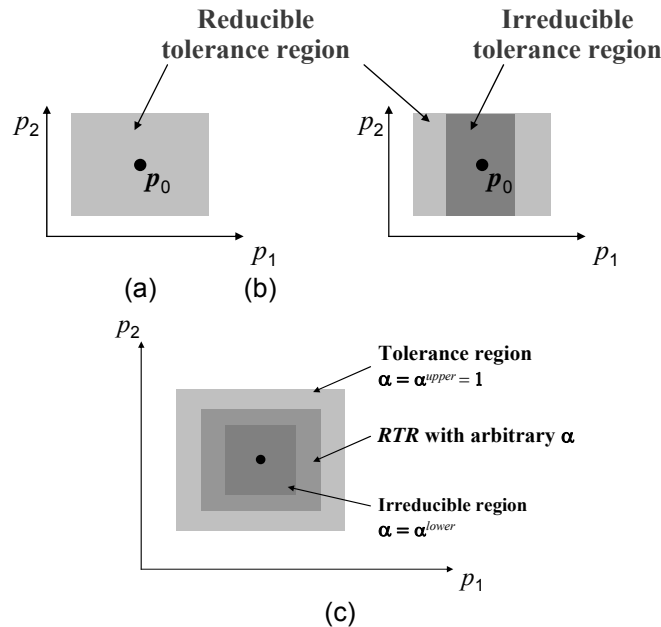


**Figure 21. Sensitivity analysis terminology.**

However, extra but limited “costs” must be absorbed or “resources” should be allocated (i.e., costs of new material investigations, conducting surveys, new manufacturing machines, etc.) to efficiently reduce epistemic (or reducible) uncertainty for the most critical parameters. Those parameters that can impart substantial variation reduction in one or multiple system outputs are deemed the most critical. We define this effort in uncertainty reduction as an *Investment* and quantify the investment’s cost in terms of parameter uncertainty reduction. As in Figure 21(c), and for the purpose of this study, the *Investment* is defined as the volume and perimeter difference between the original tolerance region (lighter grey rectangle in Figure 21(C) and any *RTR*. Essentially, *Investment* here provides a simple interface to connect the amount of inputs uncertainty to the uncertainty reduction in the system outputs, which can be easily replaced by any specific cost model for the petrochemical system of interest.

As shown in Figure 22 (lower right), the distance measure used in the two-level MORO approach above is also used to measure the variation in multiple objectives for designs under consideration when input parameters have different levels of interval uncertainty.

Moreover, the optimizer (or population based optimizers) assigns a fitness value or a rank to each design point in the population to represent its relative goodness in a Pareto sense. This fitness value can be used as a performance measure of the design alternatives. As shown in **Error! Reference source not found.** (upper right), black dots are used for non-dominated points which consist of the first non-dominated frontier.

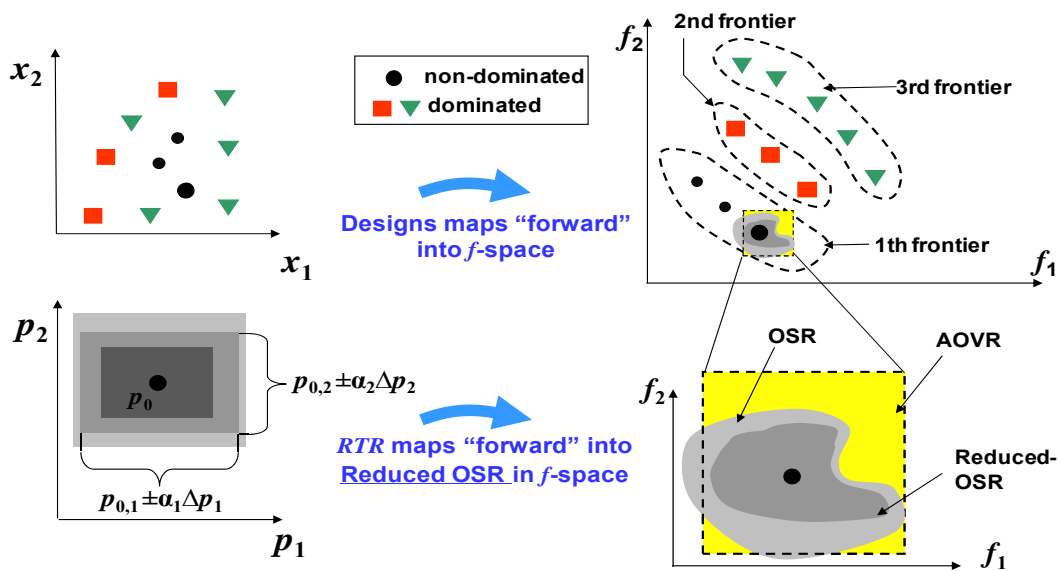


Figure 22. Robust optimization with sensitivity analysis.

Given the above mentioned definitions, a three-objective optimization problem is formed to demonstrate the tradeoff between the performance (i.e., the fitness value of designs in terms of their objectives and constraints), the variation in system outputs (represented by a measure called robustness index  $\square$ ) and the Investment used in reducing uncertainty in input parameters. This approach not only obtains robustly optimal designs which are insensitive to the retained uncertainty consisting of irreducible and reducible uncertain parameters, but also optimum solutions in terms of investment levels. These solutions provide the designer with multiple choices for reducible uncertain parameters and their corresponding ranges. The approach can also optimally determine which reducible uncertainty should be eliminated or partially reduced from the model inputs in order to achieve the desired robustness in system objective and constraint functions. Compared to classic robust optimization and SA methods, the approach efficiently provides the optimal designs for robust optimization as well as the optimal choices on uncertainty reduction. The detailed discussion about his approach can be found in the submitted journal article [Li et al., 2008(c)].

## 5.2 Results

We applied the ROSA approach to the deterministic and robust optimization models for the distillation column example, shown in

*Figure.* In this case, the tolerance region of parameters  $F$  and  $X_F$  (from nominal value) is  $\square F = \pm 4$  kmol/hr and  $\square X_F = \pm 0.02$ ; both assumed reducible. The acceptable variation range for objectives in this example is  $[\square X_D \square TC] = \pm 5\%$  of their nominal value.

The obtained nominal and robust Pareto solutions from a typical run of the integrated ROSA approach are shown Figure 23. As expected, the robust Pareto solutions with reducible

uncertainty are dominated by the nominal solutions. All robust Pareto solutions obtained from ROSA are Pareto optimal. We also show the obtained Pareto  $\square$  solutions for the robustness index  $\square$  vs. *Investment* in Figure 24. As *Investment* increases (i.e., decreasing of *RTR*), the robustness index  $\square$  value (i.e., the variation in objective and constraint values) for optimal robust designs becomes smaller. Three typical solutions, indicated as  $X_I$ ,  $X_{II}$ , and  $X_{III}$ , are selected and shown in Figure 23 and **Error! Reference source not found.** to illustrate the corresponding *RTR*.

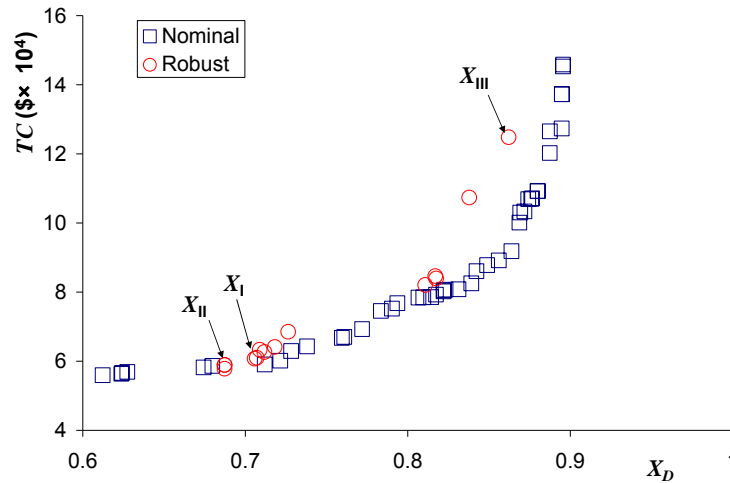


Figure 23. Robust Pareto frontier from ROSA.

For instance in Figure 24  $\square$  value for  $X_I$  is about 0.36, which means the variation in this design's outputs is very small and that the approach can eliminate a significant amount of uncertainty in parameters at a significant cost (i.e., *Investment* = 0.72). On the contrary, a large amount of uncertainty in the other extreme case,  $X_{III}$ , remains due to limited investment. Between the extreme points,  $X_{II}$  and other solutions provide different robustness values for different level of investment. With the combination of uncertainty reduction in both parameter  $F$  (87.7% of original retained) and  $X_F$  (43.9% of original retained), the robustness index  $\square$  for  $X_{II}$  is reduced to approximately 0.62, compared to 0.89 for  $X_{III}$ .

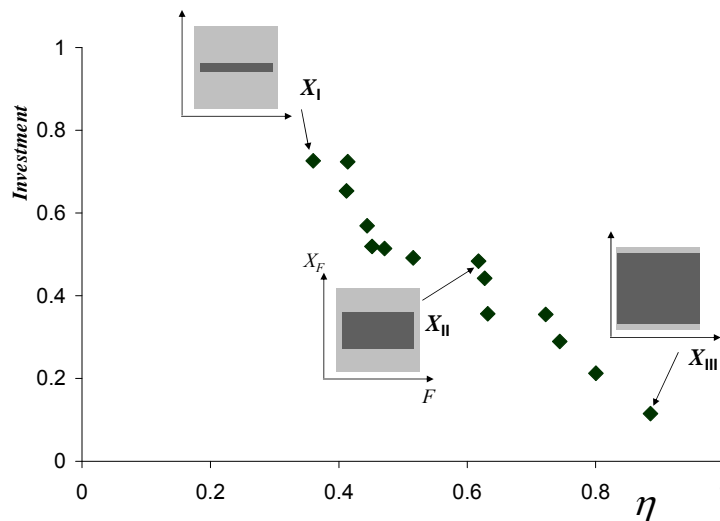


Figure 24. Obtained solutions for robustness index ( $\square$ ) vs. *Investment*.

As expected, robust distillation column designs with different levels of the retained tolerance regions are obtained and can be selected according to the designer's preference to satisfy the robustness requirements. In the same optimization procedure, the proposed method additionally identifies the uncertain parameters whose reduction or elimination will produce the largest payoffs in uncertainty reduction for any given investment. Prior- or post-SA procedures are not necessary, and thus computational effort for SA is eliminated.

## 6. Kriging-Directed Multi-Objective Genetic Algorithm (KD-MOGA)

To facilitate the proposed MORO and ROSA approach, we proposed a Kriging-Directed Multi-Objective Genetic Algorithm (KD-MOGA) or called improved MOGA. Compared to a conventional MOGA, KD-MOGA was shown to require about 50%~60% fewer function calls. The details of this approach can be found in the published journal article [Li et al., 2008(a)].

### 6.1 Approach

A conventional MOGA for solving engineering optimization problems usually requires numerous function calls. Figure 25 shows the framework of a conventional MOGA.

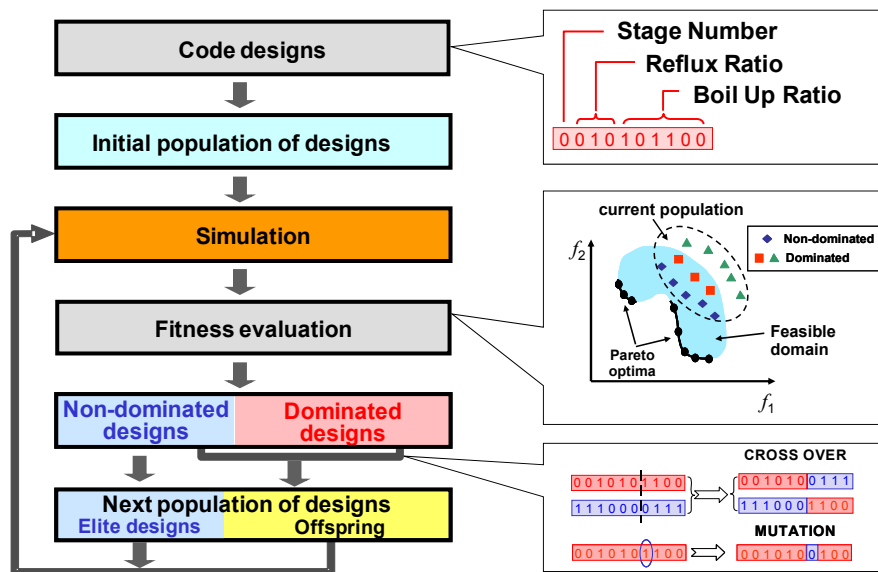
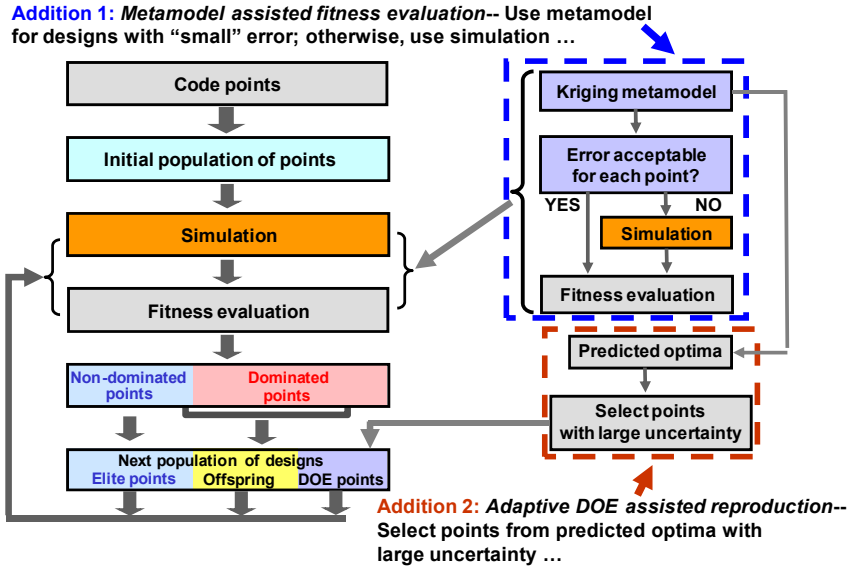


Figure 25. Framework for a conventional MOGA.

One way to reduce the number of function calls is to use approximation. A typical approximation approach involves two steps: Design of Experiments (DOE) and metamodeling. A new approach where both DOE and metamodeling are integrated with a MOGA was developed and is shown in Figure 26. Compared with the conventional MOGA, the new approach contains two additions where the DOE addition reduces the number of generations in the MOGA procedure, while the metamodeling addition reduces the number of function calls in each generation. The DOE locates a subset of design points that are estimated to better sample the design space, while the metamodeling assists in estimating the fitness of design points.



**Figure 26. Framework for Kriging-directed MOGA.**

In the metamodeling addition, as shown in Figure 26, a metamodel-assisted fitness evaluation objectively chooses either a metamodel or simulation to evaluate a design, depending on the error in the design’s estimated objective values. The main concept behind the proposed metamodel assisted fitness evaluation is shown in Figure 27. The error in the predicted objective values for a design is considered acceptable if the design’s “dominance” status does not change because of using the metamodel.

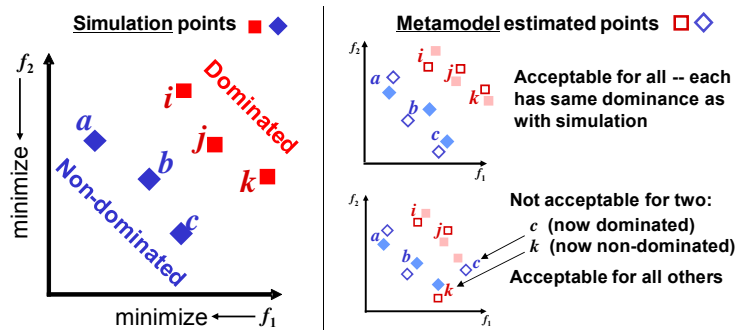


**Figure 27. Metamodel-assisted fitness evaluation.**

For the completeness of the report, the concept of kriging metamodeling is also shown in Figure 28. It can be seen that kriging predicts the performance (or objective value)  $f$  for “unobserved” design  $x$ , given the actual performance for “observed” designs. Kriging also estimates “variance” (i.e., the error) for the performance of unobserved design  $x$ . Variance is large when that design is far from observed designs. With prescribed confidence levels, error in predicted performance can be estimated by a range:  $\pm 2s$ , where  $s$  is the standard deviation of the predicted values.

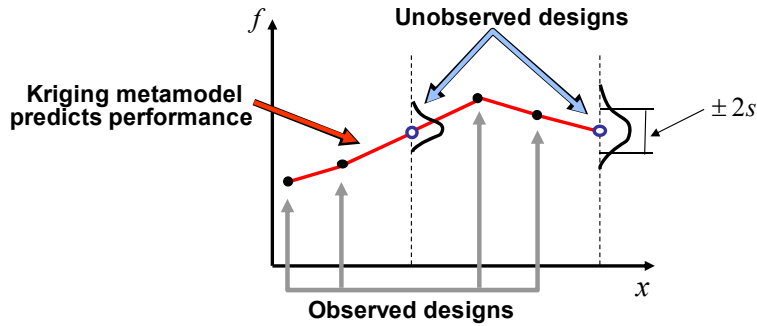


Figure 28. Kriging metamodeling.

Figure 29 shows acceptable error criterion. If the sum of variance intervals for two designs (e.g.,  $a$  and  $i$ ) is smaller than the distance between these two points in each objective (e.g.,  $f_1$  or  $f_2$ ), the error is acceptable. Otherwise, the error is not acceptable, because the dominance status might be changed.

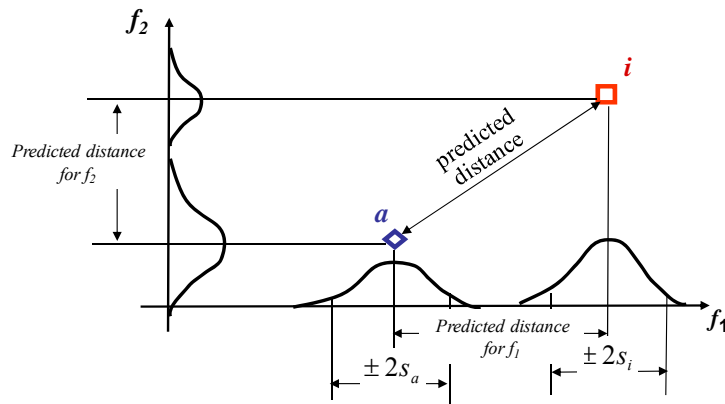


Figure 29. Acceptable error criterion.

The adaptive DOE-assisted reproduction (addition 2 in Figure 26) is separately shown in Figure 30 in which designs from predicted optima with large errors are selected and added into the population so that the metamodel accuracy around these designs is improved in the later generations.

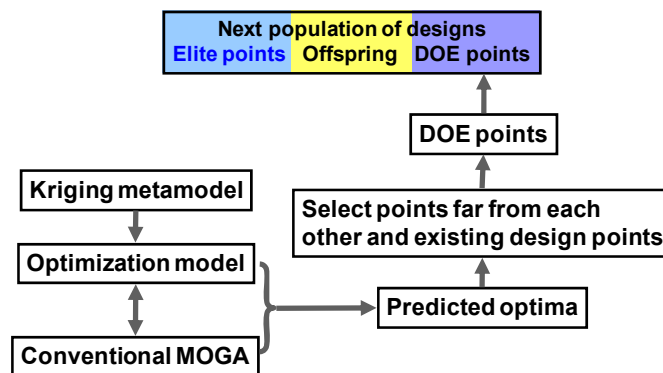
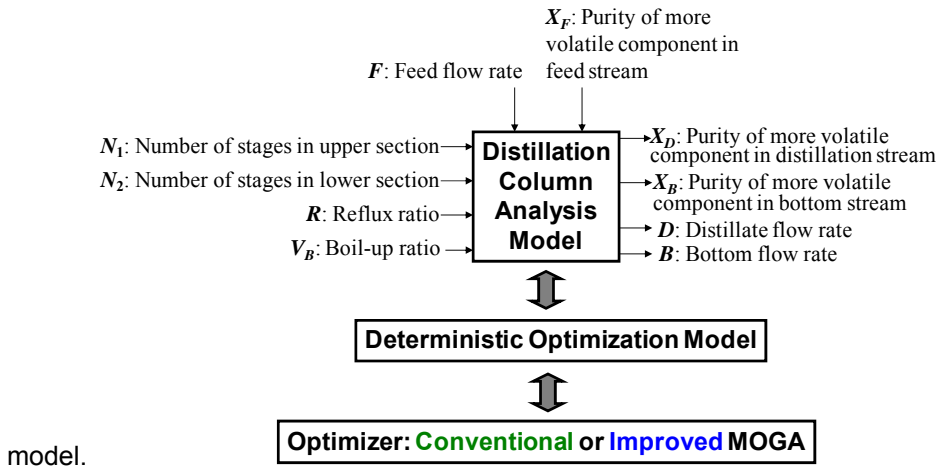


Figure 30. Adaptive DOE-assisted reproduction.

## 6.2 Result

Figure 31 shows implementation of conventional and improved MOGA on the distillation column analysis model. Parameters in this distillation column problem are fixed at their nominal values and design variables are the inputs from the left to the analysis



model.

**Figure 31. Implementation of conventional and improved MOGA on distillation column.**

The objectives of this problem are to simultaneously maximize the product yield ( $D$ ) and purity ( $X_D$ ), which are conflicting objectives. This optimization model is solved using the conventional MOGA and the improved MOGA (or KD-MOGA). Figure shows the obtained Pareto fronts from both approaches.

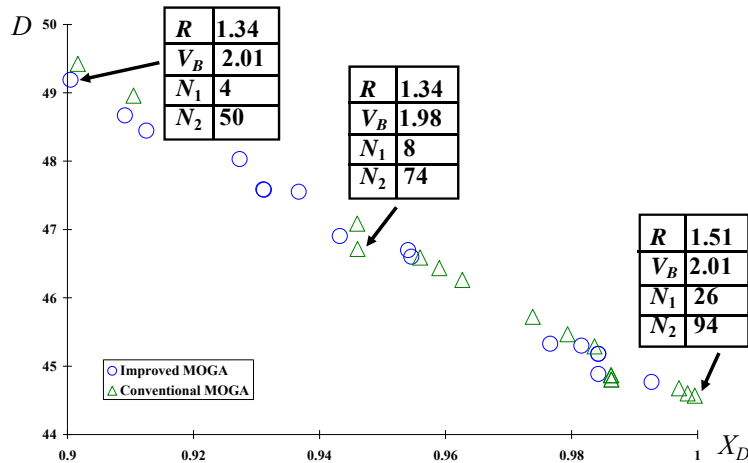


**Figure 32. Pareto solutions for distillation column design using the conventional MOGA and the improved MOGA.**

It is observed from Figure that the Pareto frontiers from both approaches agree with each other. It also shows that as the purity, and thus the quality of the distillate, improves (higher  $X_D$ ) the quantity of the final product  $D$  available for sale is reduced. A higher purity also requires a larger number of total stages.

Additionally, several numerical and engineering examples are also tested to demonstrate the applicability of this new approach. Figure 33 below shows the improvements obtained from our new KD-MOGA when compared to two other previous optimizers, a previous K-MOGA and a conventional (full analysis) MOGA. As shown in Figure 33 the number of function calls required

by KD-MOGA is about 50% fewer than the other two optimizers for the standard test problems given in Figure 33 while the solutions obtained are in general agreement.

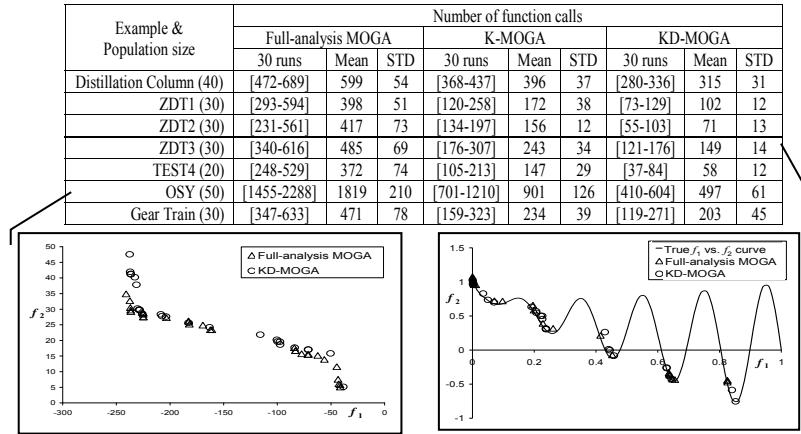
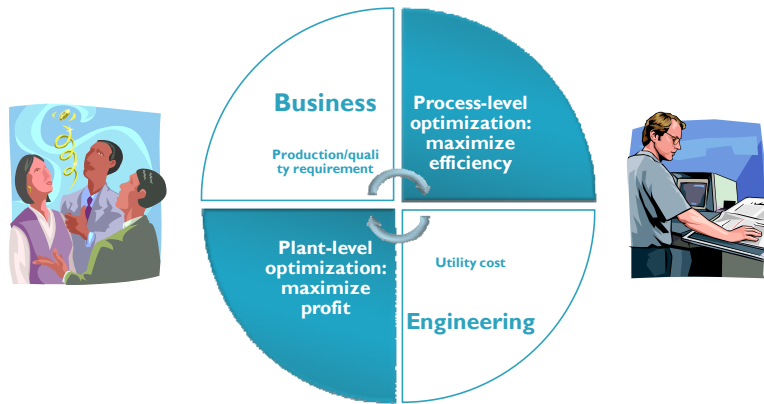


Figure33. Number of function calls for KD-MOGA vs. K-MOGA and MOGA.

## 5. Recommendations for Future Work

A preliminary review of the literature has revealed that the previous methods considered for the design and/or operational optimization of petrochemical systems were mainly based on either engineering or business decisions. The literature is sparse for the cases when these two types of decisions are integrated. However, given that operational decisions should be based on both engineering and business considerations, research is needed for methods and models that facilitate integration of these two domains with ultimate goal of increasing profitability.

Current research in the literature on business-based optimization usually considers supply chain, demand and market forces to maximize a measure of profit. One limitation of business-based optimization is that the process performance that is based on engineering models is not directly considered in the business model. Along this line, an interesting research topic is an integration of business and engineering optimization models over the entire refinery. However, considering both business and engineering issues in a single optimization model may lead to a large-scale optimization problem. As shown in Figure 34, two optimization problems are formulated in the business and engineering domains, which are interrelated by the production/quality requirements and utility cost. The engineering optimization is subject to the production and quality and other engineering requirements, which can be determined only after the business model is considered. And the business model is dependent upon the engineering performance, energy loss, etc., which depends on the engineering model. These optimization problems will have to be solved in an integrated manner and will be considered as part of our future research directions.



**Figure 34. Integration between business and engineering decisions.**

## 6. Conclusion

In this research, petroleum refining process optimization is studied using black-box analysis models and multi-objective genetic algorithms (MOGAs). We considered two typical refining process models as case studies: a single binary distillation column and an integrated reactor-distillation system. Using these models, multi-objective optimization was performed to identify their Pareto optimal solutions. These Pareto solutions can be used for trading-off the most profitable design and operational decisions, including distillation purity. As a population based optimization approach, MOGA can involve a large number of simulation calls. To address this issue, online metamodeling for both fitness estimation and reproduction was integrated within a conventional MOGA. It was observed that, after solving the distillation column and other examples, on the average the number of simulation calls can be significantly reduced using the improved MOGA compared to a conventional MOGA.

The research also involved multi-objective optimization under uncertainty. To ensure that the distillation product quality was within acceptable specifications in view of process uncertainty, robust optimal solutions were obtained using a previously developed two-level robust optimization. The robust optimal solutions have an additional benefit of controlling the variation in the system outputs due to the uncontrollable input uncertainty. In spite of these advantages over the deterministic optimization, the two-level robust optimization was a computationally intensive approach that required a large number of simulation calls. To overcome this limitation, we developed a new and novel single-level robust optimization approach which fundamentally breaks down the nested structure of the two-level approach. Based on our results, we found that the number of simulation calls required by the single-level robust optimization approach can be an order-of-magnitude less than that required by a two-level approach. More encouragingly, it was found through this study that the obtained solutions from the single-level optimization approach generally agreed with those obtained from the previous two-level approaches. A new robust optimization and sensitivity analysis has also been developed to deal with both reducible and irreducible uncertainty. This new approach performed both robust optimization and sensitivity analysis in a single procedure for problems that have irreducible and reducible uncertainty, multiple objectives and mixed continuous-discrete variables. In this approach, robust solutions and important reducible and/or irreducible uncertain parameters are considered and accounted for in one procedure, where the decision maker can obtain the optimal and robust solutions as well as a combination of parameters for uncertainty reduction.

Throughout this research, the PI and UMD researchers worked in close collaboration and made numerous contacts. We regularly met (often on a bi-weekly basis) to discuss the results of our research and exchange ideas. The results of this collaboration are one published journal article,

another submitted journal article (currently under review), and finally a third article which is in the final stages of preparation. We also had an abstract/poster in the Energy 2030 conference in 2008.

## References

- [1] Douglas, J.M. *Conceptual Design of Chemical Processes*, McGraw-Hill Science, 1998.
- [2] Du, X.P., A. Sudjianto, and B.Q. Huang, Reliability-based design with the mixture of random and interval variables. *Journal of Mechanical Design*, 127(6): 1068-1076, 2005.
- [3] Forbes, R.J., *Short History of the Art of Distillation*, E.J. Brill, Leiden, 1948.
- [4] Grossmann, I. E., Sargent, R. W. H., "Optimum Design of Chemical Plants with Uncertain Parameters," *AIChE Journal*, 24(6): 1021-1028, 1978.
- [5] Halemane K. P., Grossmann I. E., "Optimal Process Design under Uncertainty," *AIChE Journal*, 29 (3): 425-433, 1983.
- [6] Hu, W. Li, M., Azarm, S., Al Hashimi, S., Almansoori, A., and Al Qasas, N., "An Efficient Single-level Robust Approach for Multi-objective Optimization with Interval," 2008 (working paper, under preparation).
- [7] Inamdar, S. V.; Gupta, Santosh K.; Saraf, D. N, "Multi-Objective Optimization of an Industrial Crude Distillation Unit Using the Elitist Non-Dominated Sorting Genetic Algorithm," *Chemical Engineering Research and Design*, 82(5): 611-623, 2004.
- [8] Janak, S. L., Lin, X., Floudas, C. A., "A New Robust Optimization Approach for Scheduling Under Uncertainty: II. Uncertainty with Known Probability Distribution," *Computers and Chemical Engineering*, 31: 171-195, 2007.
- [9] Li, G., Li, M., Azarm, S., Al Qasas, N., Al Ameri, T., and Al Hashimi, S., "Improving Multi-Objective Genetic Algorithms with Adaptive Design of Experiments and Online Metamodeling," *Structural and Multidisciplinary Optimization* (published online, 5 April 2008(a)).
- [10] Li, M. "Robust Optimization and Sensitivity Analysis with Multi-Objective Genetic Algorithms: Single- and Multi-Disciplinary Applications," Ph.D. Dissertation, University of Maryland, College Park, Maryland, November, 2007.
- [11] Li, M., and Azarm, S., "Multiobjective collaborative Robust Optimization (McRO with Interval Uncertainty and Interdisciplinary Uncertainty Propagation)," *Journal of Mechanical Design*, 130(8): 081402/1 - 081402/11, 2008(b).
- [12] Li, M., Azarm, S., and Boyars, A., "A New Deterministic Approach using Sensitivity Region Measures for Multi-Objective and Feasibility Robust Design Optimization," *Trans. ASME, Journal of Mechanical Design*, 128(4): 874-883, 2006.
- [13] Li, M., Azarm, S., Williams, N., Al Hashimi, S., Almansoori, A., and Al Qasas, N., "Integrated Multi-Objective Robust Optimization and Sensitivity Analysis with Irreducible and Reducible Interval Uncertainty," *Engineering Optimization*, 2008(c) (submitted).
- [14] Lin, X., Janak, S. L., Floudas, C. A., "A New Robust Optimization Approach for Scheduling Under Uncertainty: I. Bounded Uncertainty," *Computers and Chemical Engineering*, 24: 1069-1085, 2004.
- [15] Seader JD, Henley EJ, *Separation Process Principles*, 2nd edition. Wiley, New York, 2006.

## Publications that had full/partial support of this project:

- Li, G., Li, M., Azarm, S., Al Qasas, N., Al Ameri, T., and Al Hashimi, S., "Improving Multi-Objective Genetic Algorithms with Adaptive Design of Experiments and Online Metamodeling," *Structural and Multidisciplinary Optimization* (published online, 5 April 2008).
- Li, M., Azarm, S., Williams, N., Al Hashimi, S., Almansoori, A., and Al Qasas, N., "Integrated Multi-Objective Robust Optimization and Sensitivity Analysis with Irreducible and Reducible Interval Uncertainty," *Engineering Optimization*, 2008 (submitted).
- Hu, W. Li, M., Azarm, S., Al Hashimi, S., Almansoori, A., and Al Qasas, N., "An Efficient Single-level Robust Approach for Multi-objective Optimization with Interval," 2008 (working

- paper, under preparation).
- W. Hu, N. Al-Qasas, M. Li, S. Al Hashimi, and S. Azarm, "Multi-Objective Robust Optimization of Energy Systems," Poster and Abstract, Energy 2030, Abu Dhabi, UAE, Nov 4-5, 2008.

#### **Visits by faculty & students to PI**

Prof. Azarm visited PI three times: in Nov 2007, January 2008 and Nov 2008.

#### **Hosting of PI faculty or students**

Professors Al Hasimi and Al Mansoori visited UMD and met with Dr. Azarm.

#### **Students working on this project, degrees sought or obtained**

Genzi Li received his PhD while being supported on this project during the last year of his PhD work. Weiwei Hu is currently being supported by this project. Mian Li is working voluntarily on this project.

## Dynamics and Control of Drill Strings on Fixed and Floating Platforms

UM Investigators: B. Balachandran  
GRA's: Chien-Min Liao (started in SPRING 2007)  
PI Investigator(s): Mansour Karkoub and Youssef Abdelmagid  
Start Date: 12/01/2006  
Report Date: 12/31/2008  
FINAL REPORT

### 1. Objective/Abstract

Drill-string dynamics need to be better understood to understand drill-string failures, control drill-string motions, and steer them to their appropriate locations in oil wells. Although a considerable amount of work has been carried out on understanding drill-string vibrations (for example, Spanos *et al.*, 2003), the nonlinear dynamics of this system are not well understood given that the drill strings can undergo axial, torsional, and lateral vibrations, and operational difficulties include sticking, buckling, and fatiguing of strings. In addition, the prior models focus on either bending or torsion or axial motions.

Research objectives of this project are the following: i) develop and study control-oriented models for the drill strings through analytical and numerical methods, ii) investigate the control of an under-actuated nonlinear system (drill string) with complex interactions with the environment, and iii) build drill-string test-beds at the Petroleum Institute (PI) & the University of Maryland (UMD) to validate the analytical findings and suggest possible strategies to mitigate drill-string failures.

### 2. Approach

A combined analytical, numerical, and experimental approach is being pursued at the University of Maryland and Petroleum Institute. Specifically, the drill string is being modeled as a reduced-order nonlinear dynamical system. Appropriate attention is also to be paid to the interactions with the environment. The experiments at UMD and PI are tailored to address specific aspects of the drill-string dynamics as well as complement each other. Actuator and sensor choices will also be explored to determine how best to control the system dynamics. The studies will be initiated with drill strings located on fixed platforms and later extended to systems located on floating platforms.

### 3. Two-Year Schedule

January 1, 2007 to July 31, 2007: Modeling of drill-string dynamics, computational models; analytical and numerical studies

August 1, 2007 to October 31, 2007: Analytical and experimental studies and initiation of experimental studies

November 1, 2007 to January 31, 2008: Experimental arrangement and calibration experiments and simulations of reduced-order models

February 1, 2008 to July 31, 2008: Continuation of experimental studies, studies on actuator and sensor configurations for control of drill-string dynamics, and investigations into the need for vibration control schemes

August 1, 2008 to December 31, 2008: Continuation of experimental and numerical studies

## 4. Summary of Results

Appropriate literature was identified, and reviewed, and reduced-order models were developed. These models have been numerically and analytically investigated with particular attention to stick-slip interactions. An experimental arrangement complementing one at PI has been designed and constructed for studying drill-string dynamics. This is a unique experimental arrangement available for this type of studies.

### 4.1 Analytical and Numerical Studies

#### 4.1.1 Modeling of Drill-String: Development of Reduced-Order Models

Derivation of equations of motion for a four degree-of-freedom (4DOF) system

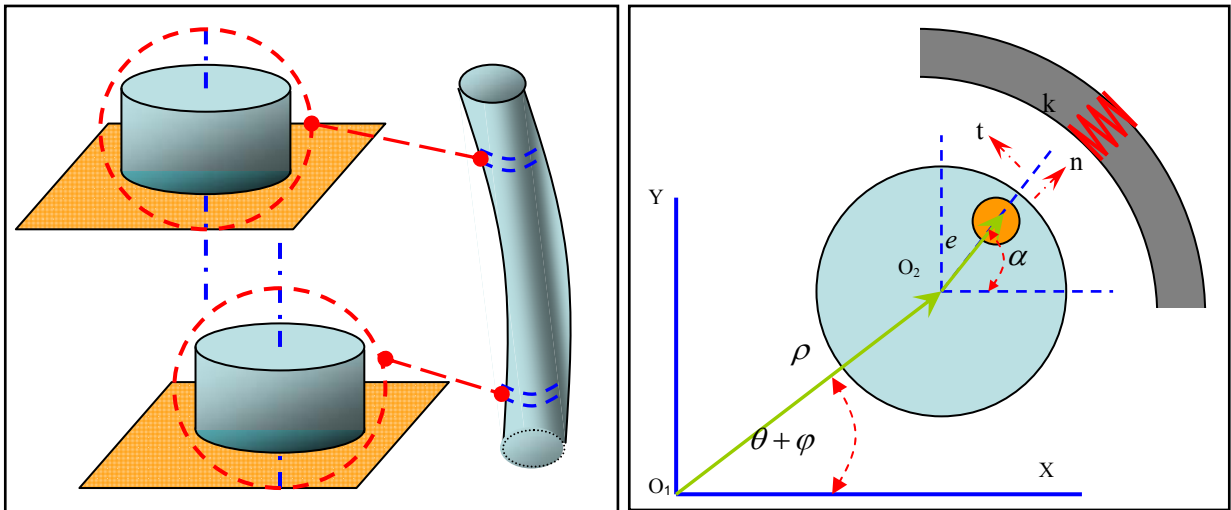
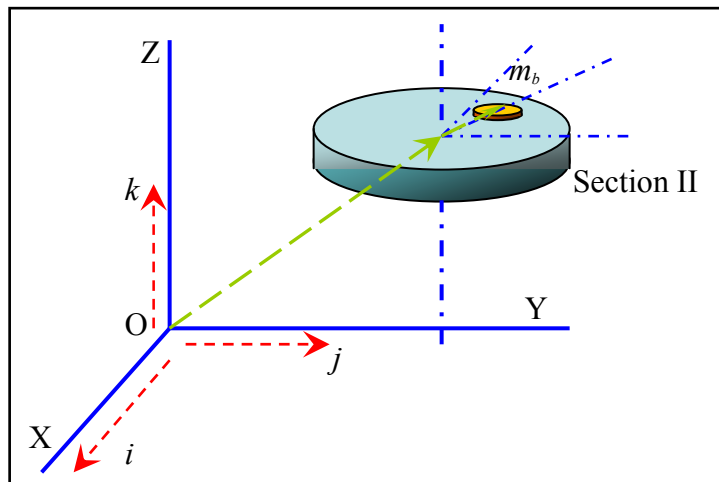


Figure 1. Drill string modeled as a system with two sections.



**Figure 2. Illustration for unbalanced mass in Section II.**

As shown in Figure 1, the drill string system is modeled as a system with two rotating sections and four degrees of freedom. Here,  $\rho$  is the radial displacement,  $\theta$  is the rotation of the first section,  $\varphi$  is the bending angle along the tangential direction, and  $\alpha$  is the torsion angle of the second section. In addition,  $m_b$  is the unbalanced mass located at a distance  $e$  from the axis of rotation of the second section, as shown in Figure 2.

For this system, the kinetic energy can be written as

$$T = \frac{1}{2} I_1 \dot{\theta}^2 + \frac{1}{2} m (\dot{\rho}^2 + \rho^2 (\dot{\theta} + \dot{\varphi})^2) + \frac{1}{2} I_2 \dot{\alpha}^2 + \frac{1}{2} m_b e^2 \dot{\alpha}^2 + m_b e \dot{\alpha} [\rho (\dot{\theta} + \dot{\varphi}) \cos(\beta) - \dot{\rho} \sin(\beta)] \quad (1)$$

where the different inertia parameters are appropriately defined; the potential energy is constructed as

$$U_{total} = \frac{1}{2} K_r (\rho - \rho_0)^2 + \frac{1}{2} K_t (\rho \varphi)^2 + \frac{1}{2} K_{tor} (\alpha - (\theta + \varphi))^2 + \frac{1}{2} \lambda K_p (\rho - (\frac{D}{2} - \frac{d}{2}))^2 \quad (2)$$

where the different stiffness constants are also appropriately defined and  $\lambda$  is a contact parameter.  $\lambda$  is zero when there is no contact and  $\lambda = 1$  when there is contact. The virtual work associated with the external forces and moments is given by

$$\delta W_{ext} = \lambda F_t [R(\delta\alpha) + \rho(\delta\theta + \delta\varphi)] + M_{ext} \delta\alpha \quad (3)$$

The work done by the external moment differs from that provided in the work of Melakhessou *et al.* (2003), which is presented in the following section.

#### **4DOF model of Melakhessou et al. (2003):**

Melakhessou *et al.* (2003) obtained the following equations after neglecting the rotary inertia associated with the unbalanced mass  $m_b e^2$  and considering the work done by  $M_{ext}$  as  $M_{ext} \delta\theta$  instead of how it is shown in Eq. (3).

$$\begin{aligned} m \ddot{\rho} - m \rho (\ddot{\theta} + \ddot{\varphi})^2 + K_r (\rho - \rho_0) + \lambda K_p (\rho - \delta) + K_t \rho \varphi^2 &= e m_b (\ddot{\alpha}^2 \cos(\beta) + \ddot{\alpha} \sin(\beta)) \\ I_1 \ddot{\theta} + m \rho^2 (\ddot{\theta} + \ddot{\varphi}) + 2m \rho \dot{\rho} (\dot{\theta} + \dot{\varphi}) &= -e m_b \ddot{\alpha} \rho \cos(\beta) + e m_b \rho \dot{\alpha}^2 \sin(\beta) + \lambda F_t \rho + M_{ext} \\ m \rho (\ddot{\theta} + \ddot{\varphi}) + 2m \dot{\rho} (\dot{\theta} + \dot{\varphi}) + K_t \rho \varphi &= -e m_b \ddot{\alpha} \cos(\beta) + e m_b \dot{\alpha}^2 \sin(\beta) + \lambda F_t \\ I_2 \ddot{\alpha} + K_{tor} (\alpha - \theta) &= -e m_b ([\rho (\dot{\theta} + \dot{\varphi}) + \rho (\ddot{\theta} + \ddot{\varphi})] \cos(\beta) + [\rho (\dot{\theta} + \dot{\varphi})^2 - \\ &\quad \dot{\rho}] \sin(\beta)) + \lambda F_t R \end{aligned} \quad (4)-(7)$$

where  $\beta = \alpha - (\theta + \varphi)$ .

#### **4DOF model of UMD:**

After making use of Eqs. (1)-(3) and the principle of virtual work, the following governing equations of motion are obtained:

$$\begin{aligned}
m \ddot{\rho} - m \rho (\dot{\theta} + \dot{\varphi})^2 + K_r (\rho - \rho_0) + \lambda K_p (\rho - \delta) + K_t \rho \dot{\varphi}^2 &= em_b (\ddot{\alpha} \sin(\beta) + \dot{\alpha}^2 \cos(\beta)) \\
I_1 \ddot{\theta} + m \rho^2 (\ddot{\theta} + \ddot{\varphi}) + 2m \rho \dot{\rho} (\dot{\theta} + \dot{\varphi}) - K_{tor} (\alpha - (\theta + \varphi)) \\
+ em_b \rho (\ddot{\alpha} \cos(\beta) - \dot{\alpha}^2 \sin(\beta)) + em_b \dot{\alpha} (\dot{\rho} \cos(\beta) + \rho (\dot{\theta} + \dot{\varphi}) \sin(\beta)) &= \lambda F_t \rho \\
m \rho^2 (\ddot{\theta} + \ddot{\varphi}) + 2m \rho \dot{\rho} (\dot{\theta} + \dot{\varphi}) + K_t \rho^2 \dot{\varphi} - K_{tor} (\alpha - (\theta + \varphi)) + em_b \rho (\ddot{\alpha} \cos(\beta) - \dot{\alpha}^2 \sin(\beta)) \\
+ em_b \dot{\alpha} (\dot{\rho} \cos(\beta) + \rho (\dot{\theta} + \dot{\varphi}) \sin(\beta)) &= \lambda F_t \rho \\
(I_2 + m_b e^2) \ddot{\alpha} - em_b \dot{\alpha} (\dot{\rho} \cos(\beta) + \rho (\dot{\theta} + \dot{\varphi}) \sin(\beta)) + K_{tor} (\alpha - (\theta + \varphi)) & \\
+ em_b [(2 \dot{\rho} (\dot{\theta} + \dot{\varphi}) + \rho (\ddot{\theta} + \ddot{\varphi})) \cos(\beta) + (\rho (\dot{\theta} + \dot{\varphi})^2 - \ddot{\rho}) \sin(\beta)] &= \lambda F_t R + M_{ext}
\end{aligned} \tag{8)-(11)$$

It is noted that the UMD form of the 4DOF model is different from that presented in the earlier work of Melakhessou *et al.* (2003).

### **Contact between the drill string and outer shell**

At UMD, the stick-slip interactions between the drill string and the outer shell are modeled along the lines of the work of Leine *et al.* (2002). The different cases considered are as follows: i) no contact between the outer edge of the string and the shell (i.e.,  $\lambda = 0$  in this case) and the normal contact force  $F_{normal}$  is zero in this case, ii) when there is contact and there is only rotation but no sliding, as shown in Figure 3, and iii) when there is contact and there is pure sliding but no rotation.

The equations used to determine and describe the contact between the drill string and the outer shell are given by Eqs. (12)-(17), and the tangential force to be used in the governing equations is determined from Eq. (15). The parameter  $\delta$ , which is shown in Eq. (12), is the radial separation between the shell and the drill string, and this parameter is used to judge whether there is contact or not. The relative velocity between the two contacting surfaces is used to determine whether there is sliding or not.

$$\delta = 0.5 * (D_{shell} - d_{string}) \tag{12}$$

$$\lambda = \begin{cases} 0; \rho \leq \delta \\ 1; \rho > \delta \end{cases} \tag{13}$$

$$F_{normal} = \begin{cases} 0 & \rho \leq \delta \\ K_{contact} * (\rho - \delta) & \rho > \delta \end{cases} \tag{14}$$

$$F_t = \begin{cases} Ft_{equ} & V_{relative} = 0 \quad \text{and} \quad |Ft_{max}| \geq |Ft_{equ}| \\ Ft_{max} & \text{else} \end{cases} \tag{15}$$

$$Ft_{max} = -Sgn(V_{relative}) * \mu * F_{normal} \tag{16}$$

$$Ft_{equ} = - \frac{M_{ext}}{\frac{I_2}{0.5 * m * d_{string}} + 0.5 * d_{string}} \quad (17)$$

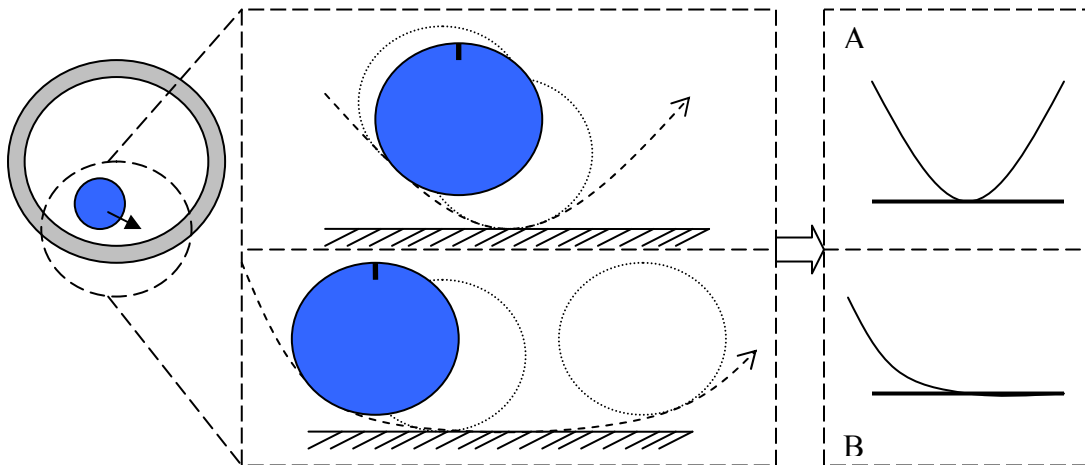
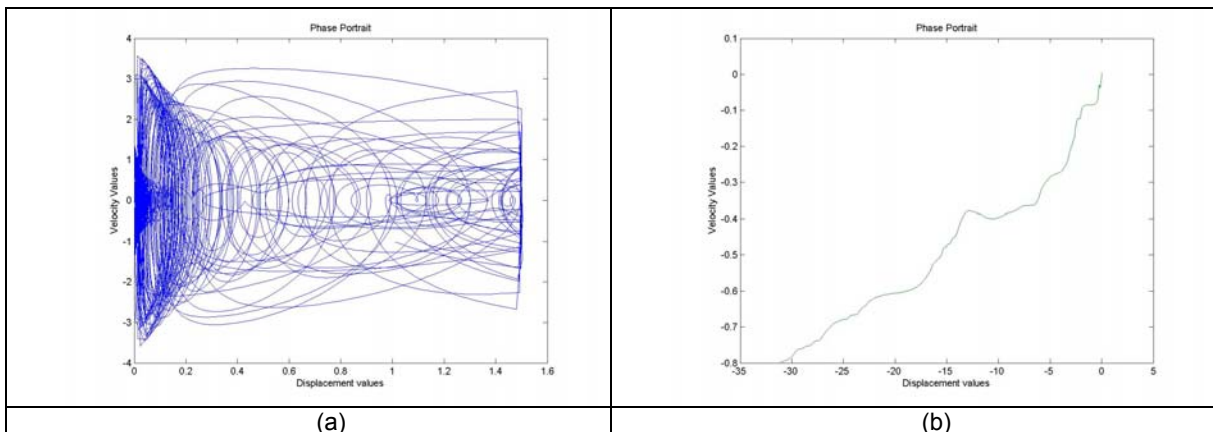


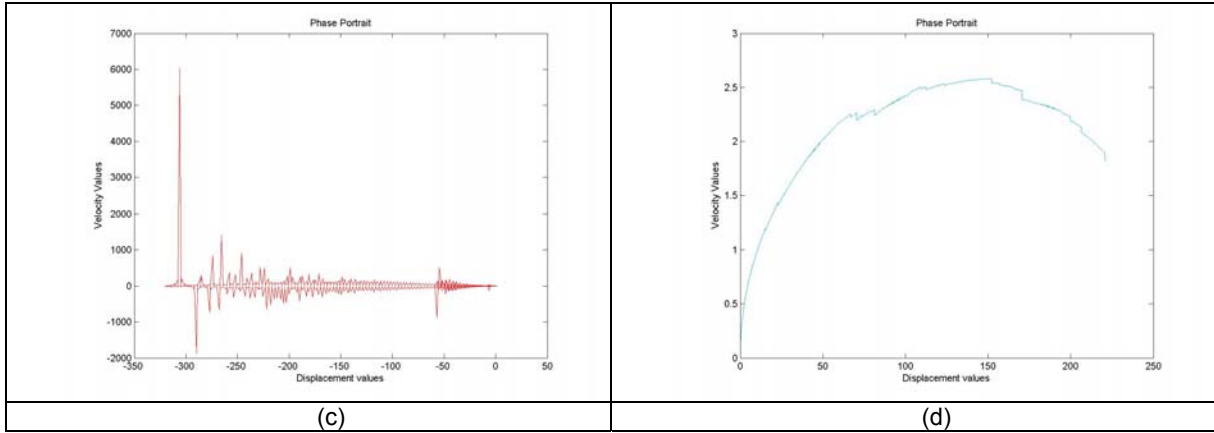
Figure 3. Illustrations of two contact scenarios between string and shell.

Simulation results for 4DOF model with constant, external torque:

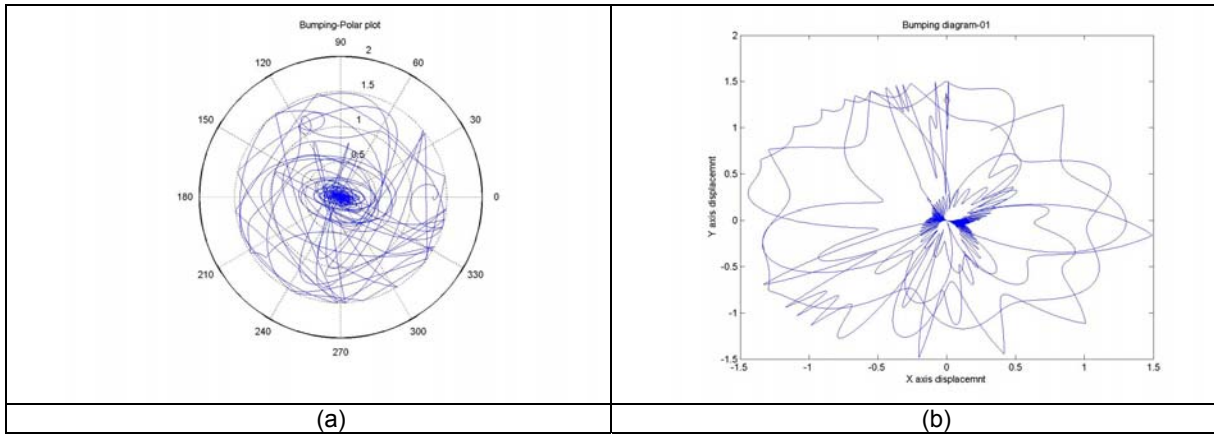
The parameter values used in the work of Melakhessou *et al.* (2003) are used to conduct simulations with Eqs. (4)-(7) to provide a flavor for the qualitative aspects of the drill-string dynamics. It is recalled that the ratio of  $m_b$  to  $m$  is  $0.5/2.05$ , which means the unbalanced mass is close to 25% of the section mass. The magnitude of the torque is selected as 5 units. Representative results obtained for two different values of the coefficient of friction  $\mu$  are shown in Figures 4 to 7. The initial position of the string is close to the outer shell in both cases. It is noted that the stiffness of the outer shell is orders of magnitude larger than that of the drill string itself.

**Case I: High friction coefficient  $\mu = 0.9$**



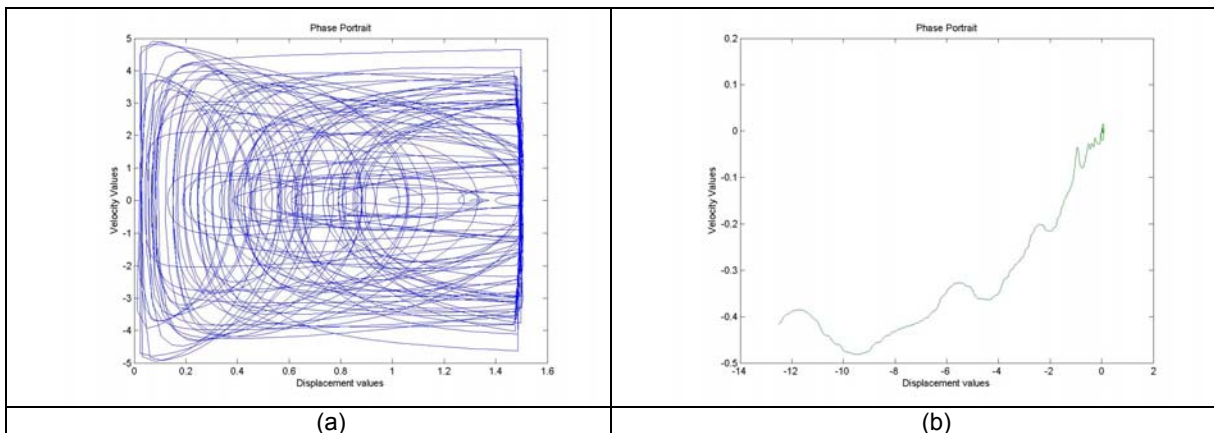


**Figure 4. Phase portraits: a) radial displacement of Section II versus radial speed, b) rotation angle of Section I versus rate of change of rotation angle, c) bending angle of Section II versus rate of change of bending angle, and d) rotation angle of Section II versus rate of change of rotation angle.**



**Figure 5. Trajectory of the center of Section II in horizontal plane: a) in polar coordinates ( $\rho, \theta$ ) and b) in Cartesian coordinates.**

**Case II: Low friction coefficient  $\mu = 0.1$**



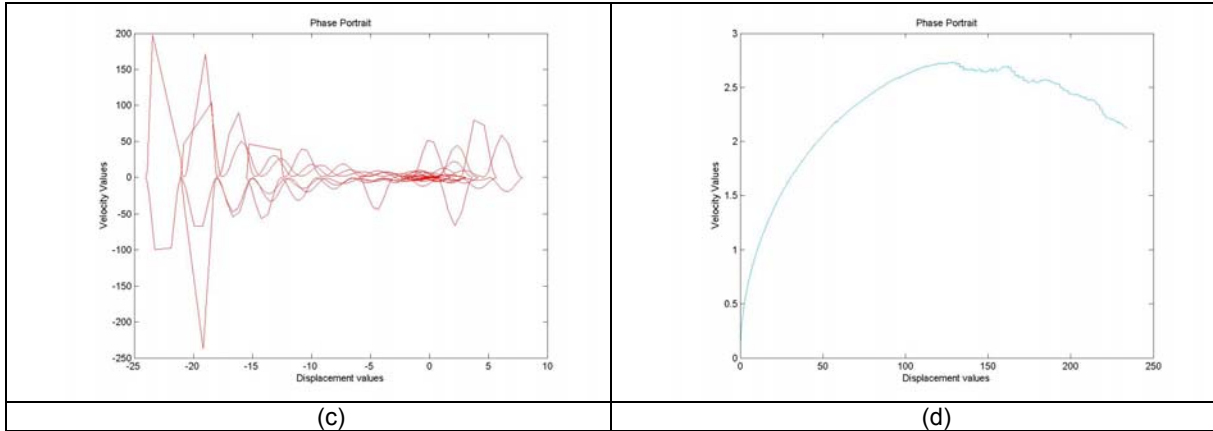


**Figure 6. Phase portraits: a) radial displacement of Section II versus radial speed, b) rotation angle of Section I versus rate of change of rotation angle, c) bending angle of Section II versus rate of change of bending angle, and d) rotation angle of Section II versus rate of change of rotation angle.**

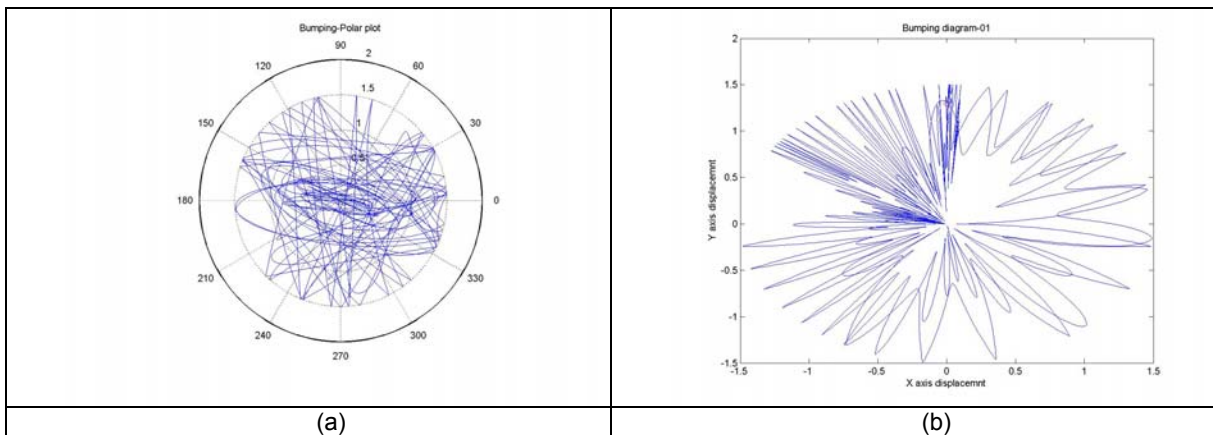


**Figure 7. Trajectory of the center of Section II in horizontal plane: a) in polar coordinates ( $\rho$ ,  $\theta$ ) and b) in Cartesian coordinates.**

Comparing the results obtained in Cases I and II, it is clear that when the coefficient of friction is high, the trajectory of the drill string stays closer to the center for longer periods than in the other case, where the drill string bounces from one end to the other. The results compare well with those presented in the work of Melakhessou *et al.* (2003).

**Five degree-of-freedom (5DOF) model of PI and simulation results for constant, external torque:**

A five degree-of-freedom model has been developed at PI. In addition to the four coordinates that were used in the 4DOF model (the radial displacement  $\rho$ , the rotation of first section or Section I  $\theta$ , the bending angle along the tangential direction  $\varphi$ , the torsion angle of the second section or Section II  $\alpha$ ), the additional coordinate is a tilt angle  $\psi$ , which is controllable angle at the bottom of the drill string. The equations of motion can be determined as previously outlined for the 4DOF model. They are of the following form:

$$\begin{aligned}
& \left[ m_b e^2 \cos^2(\alpha) + I_3 + \rho \cos(\beta) \{ 2m_b e \cos(\alpha) + m \rho \cos(\beta) \} \right] \ddot{\psi} \\
& + 2 \left[ (m_b e \cos(\alpha) + m \rho \cos(\beta)) (\dot{\rho} \cos(\beta) - \rho \dot{\beta} \sin(\beta)) \right] \dot{\psi} \\
& - 2 \left[ m_b e \dot{\alpha} \sin(\alpha) (e \cos(\alpha) + \rho \cos(\beta)) \right] \dot{\psi} \\
& = \lambda F_t (R + \rho)
\end{aligned}$$

$$\begin{aligned}
& (I_2 + m_b e^2) \ddot{\alpha} - m_b e \ddot{\rho} \sin(\alpha - \beta) + m_b e \rho \ddot{\beta} \cos(\alpha - \beta) \\
& + m_b e^2 \dot{\psi}^2 \cos(\alpha) \sin(\alpha) + 2m_b e \dot{\beta} \dot{\rho} \cos(\alpha - \beta) \\
& + m_b e \rho \dot{\beta}^2 \sin(\alpha - \beta) + m_b e \rho \dot{\psi}^2 \cos(\beta) \sin(\alpha) \\
& + K_{tor} (\alpha - \theta) = \lambda F_t R
\end{aligned}$$

$$\begin{aligned}
& m_b e \ddot{\alpha} \cos(\alpha - \beta) + m \rho \ddot{\beta} - m_b e \dot{\alpha}^2 \sin(\alpha - \beta) + m_b e \dot{\psi}^2 \cos(\alpha) \sin(\beta) \\
& + K_t \rho \dot{\varphi} + m \rho \dot{\psi}^2 \cos(\beta) \sin(\beta) + 2m \dot{\rho} \dot{\beta} - \lambda F_t + K_r \varphi = 0
\end{aligned}$$

$$\begin{aligned}
& I_1 \ddot{\theta} + m_b \rho e \ddot{\alpha} \cos(\alpha - \beta) + m \rho^2 \ddot{\beta} + m \rho^2 \dot{\psi}^2 \cos(\beta) \sin(\beta) + 2m \rho \dot{\rho} \dot{\beta} \\
& + 2m_b \rho \dot{\rho} \dot{\varphi} + \frac{1}{2} m_b \rho e \dot{\psi}^2 \sin(\alpha + \beta) - \frac{1}{2} m_b \rho e (2\dot{\alpha}^2 + \dot{\psi}^2) \sin(\alpha - \beta) \\
& + K_{tor} (\theta - \alpha) - \lambda F_t \rho = M_{ext}
\end{aligned}$$

$$\begin{aligned}
& m \ddot{\rho} - m_b e \ddot{\alpha} \sin(\alpha - \beta) - m_b e (\dot{\alpha}^2 \cos(\alpha - \beta) + \dot{\psi}^2 \cos(\alpha) \cos(\beta)) \\
& - K_r \rho_0 - K_c \lambda \delta + \rho (K_t \dot{\varphi}^2 + K_r + K_c \lambda - m(\dot{\beta}^2 + \dot{\psi}^2 \cos^2(\beta)))
\end{aligned} \tag{18)-(22)}$$

It is recalled that the ratio of  $m_b$  to  $m$  is 0.2/2.05, which means the unbalanced mass is close to 10% of the section mass. The magnitude of the torque is selected as 2 units. Representative results obtained for two different values of the coefficient of friction  $\mu$  are shown in Figures 8 and 9. The initial position of the string is close to the outer shell in both cases. It is noted that the stiffness of the outer shell is orders of magnitude larger than that of the drill string itself.

**Case III: High friction coefficient  $\mu = 0.9$**

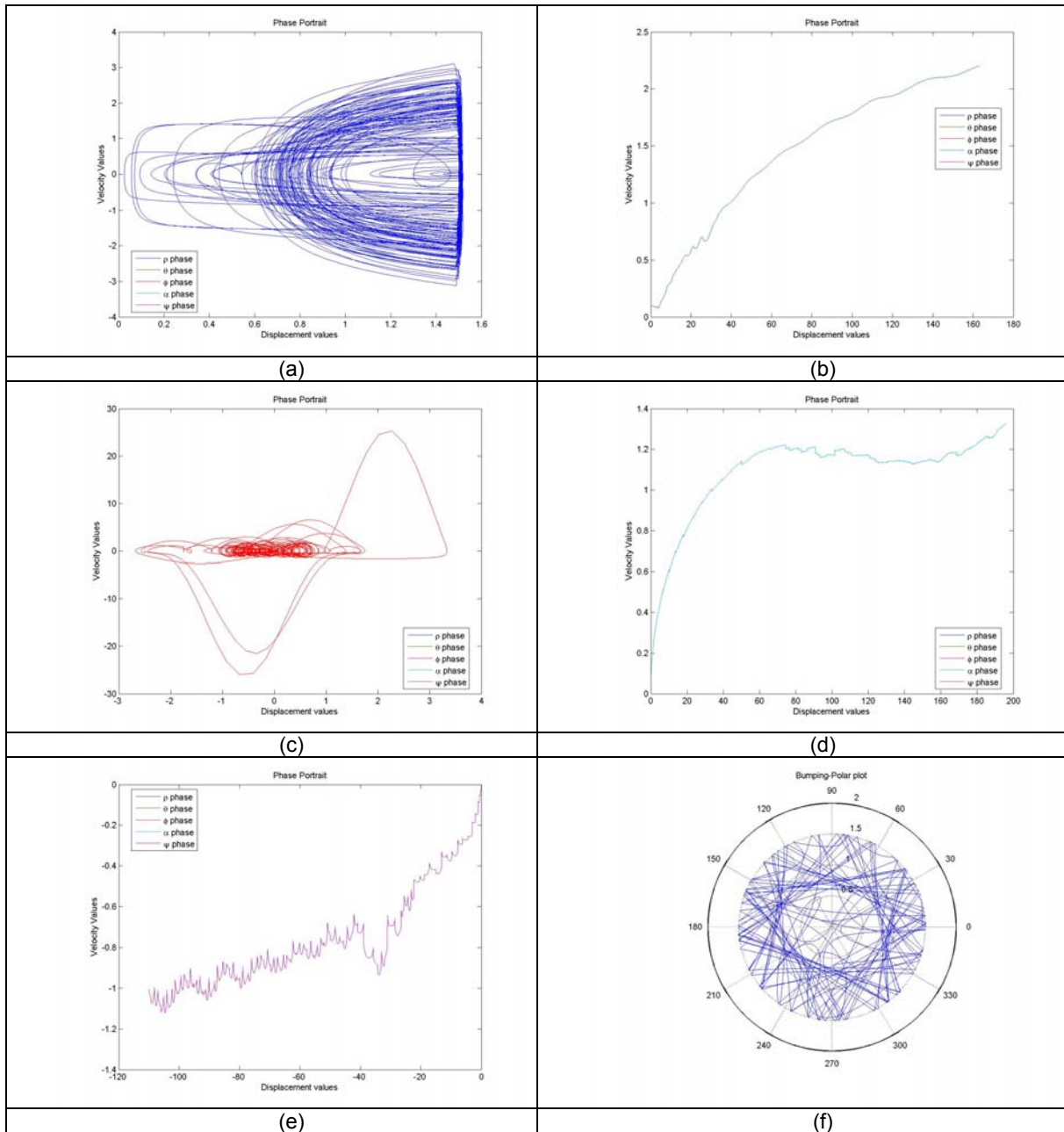


**Figure 8. a) radial displacement of Section II versus radial speed, b) rotation angle of Section versus rate of change of rotation angle, c) bending angle of Section II versus rate of change of bending angle, and d) rotation angle of Section II versus rate of change of rotation angle, e) tilt angle of the Section II versus rate of change of tilt angle, and f) trajectory of the center of Section II in horizontal plane, in polar coordinates ( $\rho$ ,  $\theta$ ).**

**Case IV: Low high friction coefficient  $\mu = 0.1$**

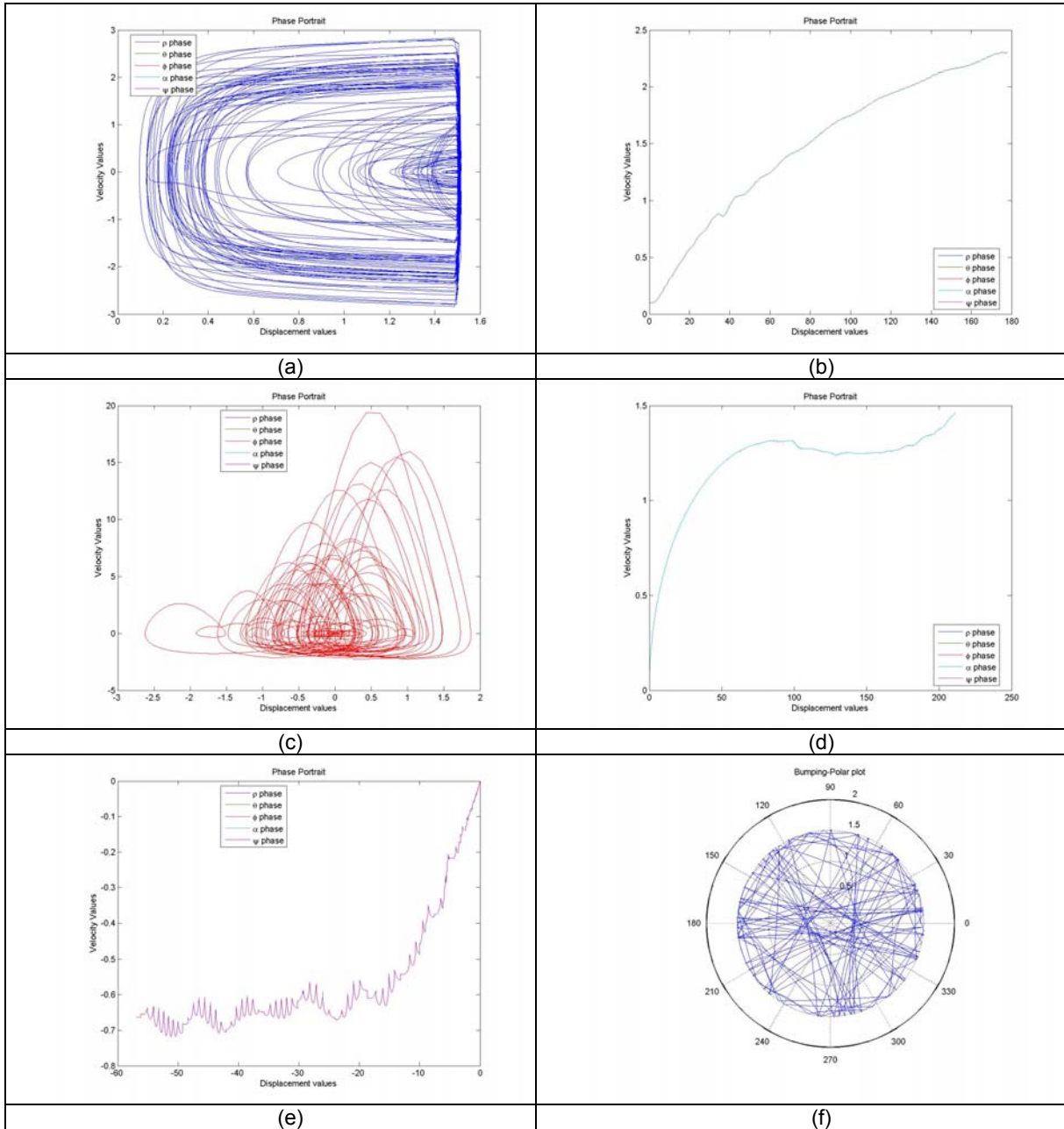


**Figure 9. a) radial displacement of Section II versus radial speed, b) rotation angle of Section versus rate of change of rotation angle, c) bending angle of Section II versus rate of change of bending angle, and d) rotation angle of Section II versus rate of change of rotation angle, e) tilt angle of the Section II versus rate of change of tilt angle, and f) trajectory of the center of Section II in horizontal plane, in polar coordinates ( $\rho, \theta$ ).**

From the results of the simulations shown for the 5DOF case, it is clear that the motions appear to be aperiodic for the two different values of friction considered. The drill string motions appear to exhibit sliding motions, without the stick and slip aspects seen in the system with 4DOF.

Comparisons of numerical results obtained in the current work with those obtained by Melakhessou *et al.* (2003),

It is recalled from the results reported in previous sections that when the coefficient of friction is high, the trajectory of the drill string stays closer to the center for longer periods than in the other case, in which the drill string bounces from one end to the other.

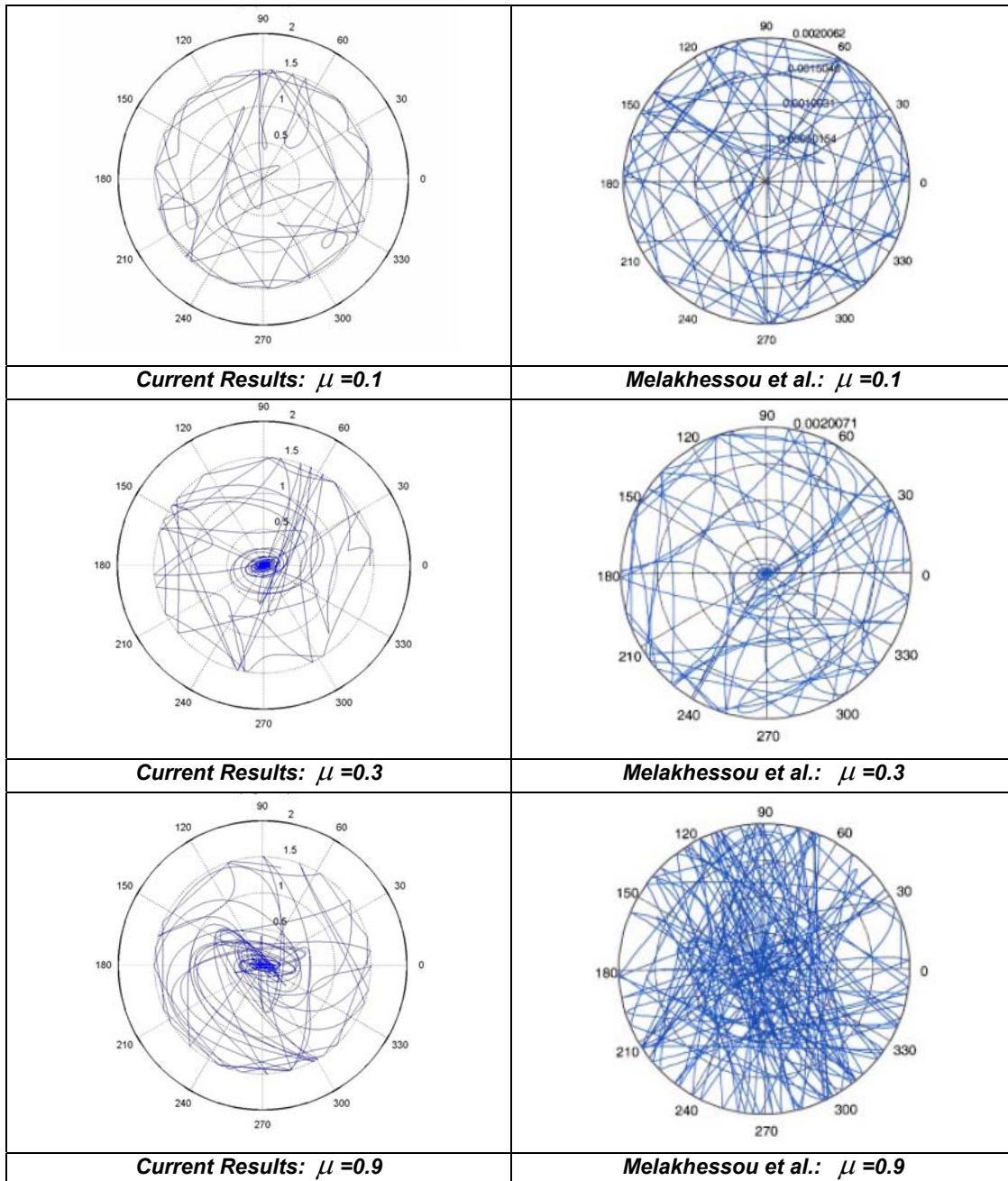


**Figure 10. Comparisons of simulation results for the trajectory of the center of Section II in horizontal plane, in polar coordinates ( $\rho, \theta$ ): trajectory of the center of Section II: (a) initial position close to the outer shell, friction coefficient =0.1; (b) initial position close to the outer shell, friction coefficient =0.3; and (c) initial position close to the outer shell, friction coefficient =0.9. The results obtained by using the modified four degree-of-freedom system are shown on the left column, and those obtained by using the model of Melakhessou *et al.* (2003) are shown on the right.**

In Figure 10, the results obtained for the trajectory of center of Section II for different values of friction are compared with those obtained by using the model of Melakhessou *et al.* (2003). The results are highly dependent on the value of the initial radial displacement  $\rho_0$ . The differences seen between the results obtained with the modified four degree-of-freedom model and those obtained with the model of Melakhessou *et al.* (2003) are attributed to the manner in which the contact between the drill string and the outer shell is modeled in the present research. As the friction coefficient is increased in the modified four degree-of-freedom system, the system exhibits sliding motions as opposed to the bumping motions seen in earlier work. For low-friction coefficients, the system appears to exhibit aperiodic motions, which possibly could be chaotic (Nayfeh and Balachandran, 1995). The manner in which stick-slip interactions are modeled here allows one to capture slipping and sticking motions that are possible at high values of friction. This is in contrast to what is observed in the work of Melakhessou *et al.* (2003) at high values of friction.

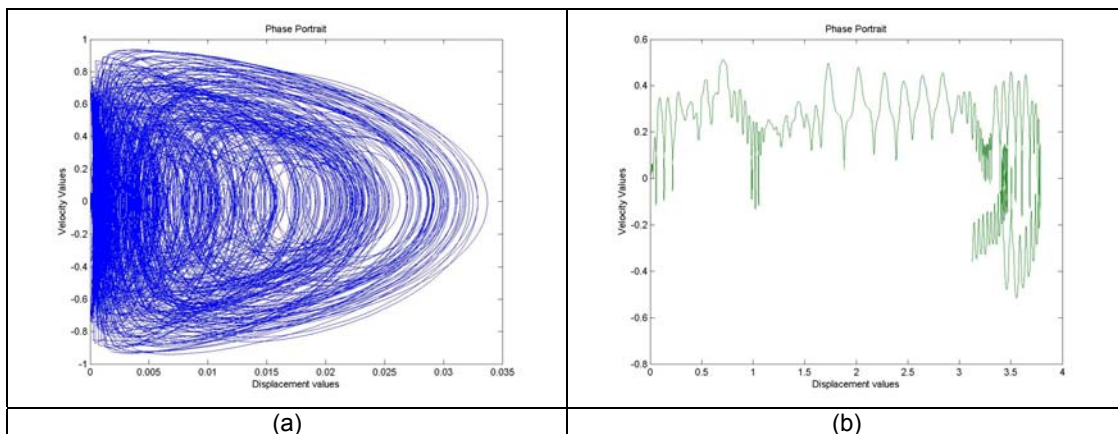
#### 4.1.2 Results for Different Contact Stiffness Values

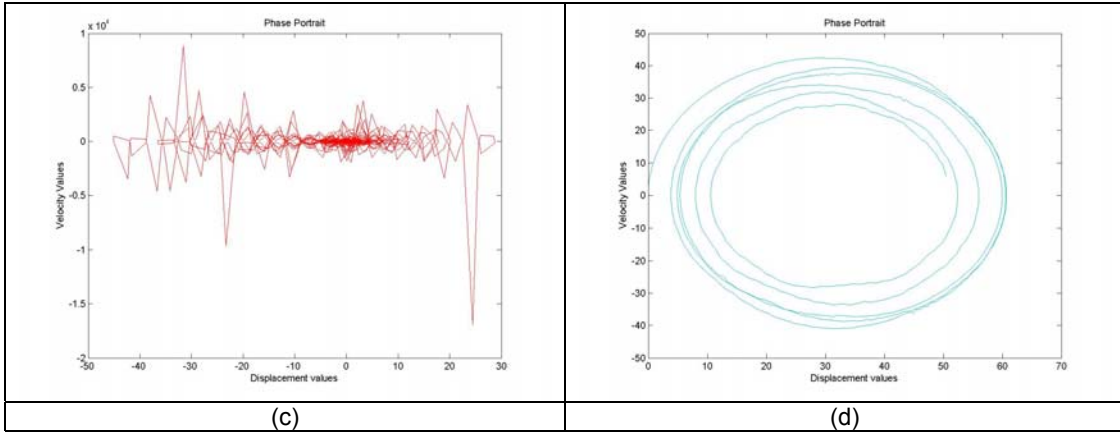
In addition to the parametric studies conducted in the previous section, additional studies are carried out to examine the effect of three representative contact stiffness values here. The results obtained for each of these cases when the friction coefficient is high or low are presented next and discussed. All of the simulations were carried out with the four degree-of-freedom model discussed in the previous section.

##### Low Friction at the Contact Surface

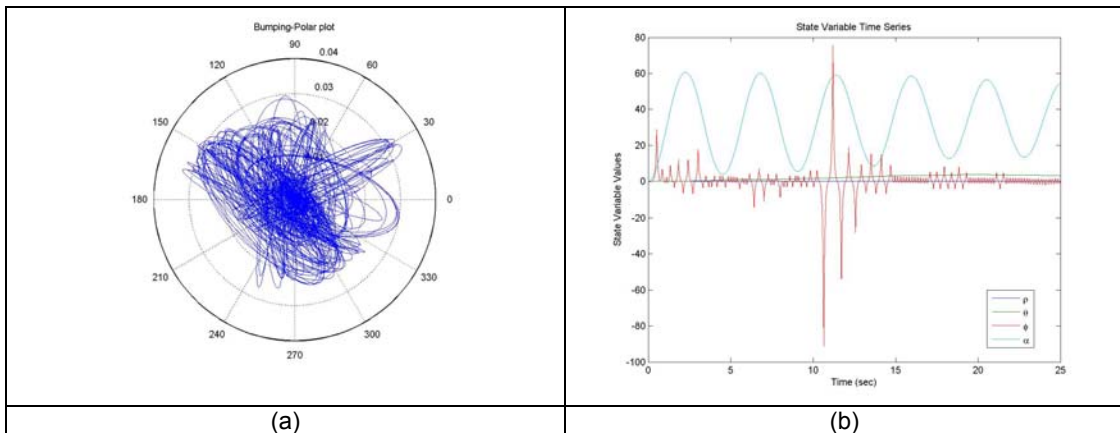
In Figures 11 and 12, the results obtained when the contact stiffness is low are presented, and in Figures 13 and 14, the results obtained when the contact stiffness is medium valued are presented. When the contact stiffness is low, the contact between the drill string and the outer shell is expected to be soft, and when the contact stiffness is high, as the case shown in Figures 15 and 16, the contact between the drill string and the outer shell is expected to be hard.

##### Case I: Low friction coefficient ( $\mu = 0.1$ ) and low contact stiffness



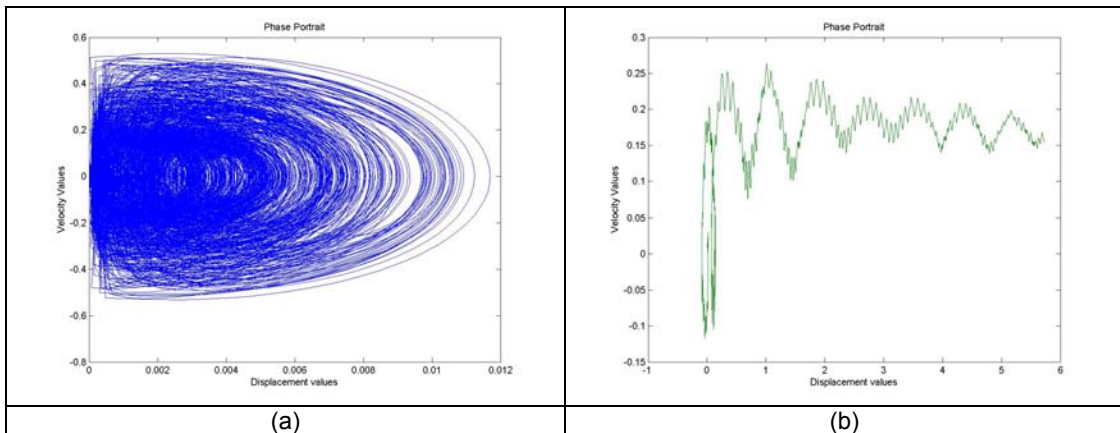


**Figure 11. Phase portraits: a) radial displacement of Section II, b) rotation angle of Section I, c) bending angle of Section II, and d) rotation angle of Section II.**



**Figure 12. a) Trajectory of the center of Section II in polar coordinates ( $\rho$ ,  $\theta$ ) in horizontal plane and b) displacement histories.**

**Case II:** Low friction coefficient ( $\mu = 0.1$ ) and medium contact stiffness



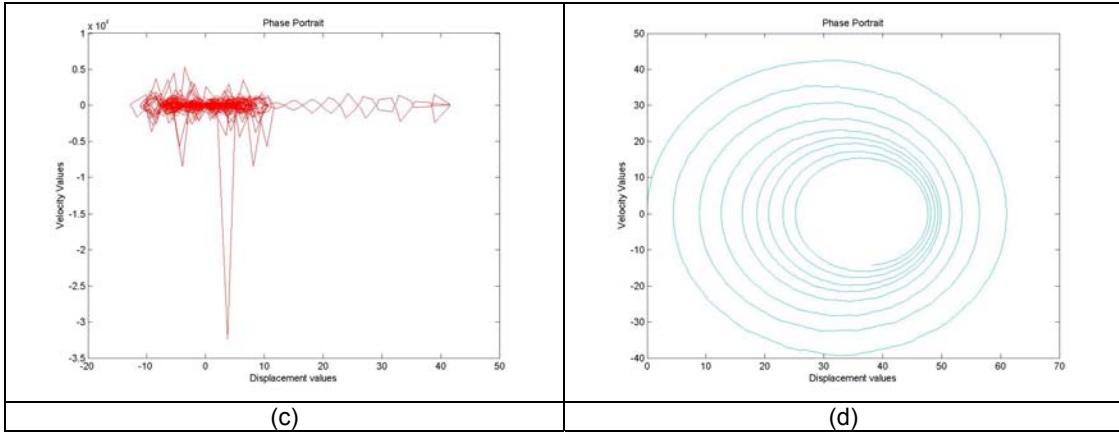


Figure 13. Phase portraits: a) radial displacement of Section II, b) rotation angle of Section I, c) bending angle of Section II, and d) rotation angle of Section II.

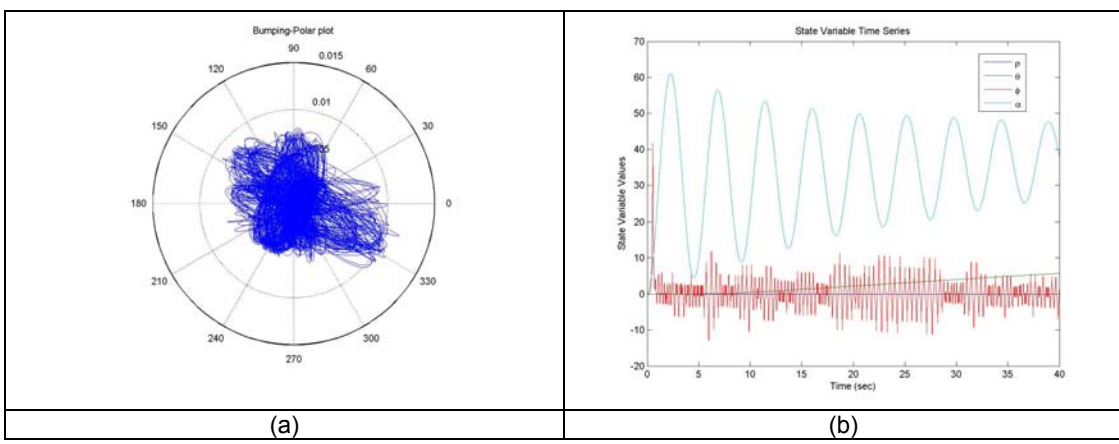
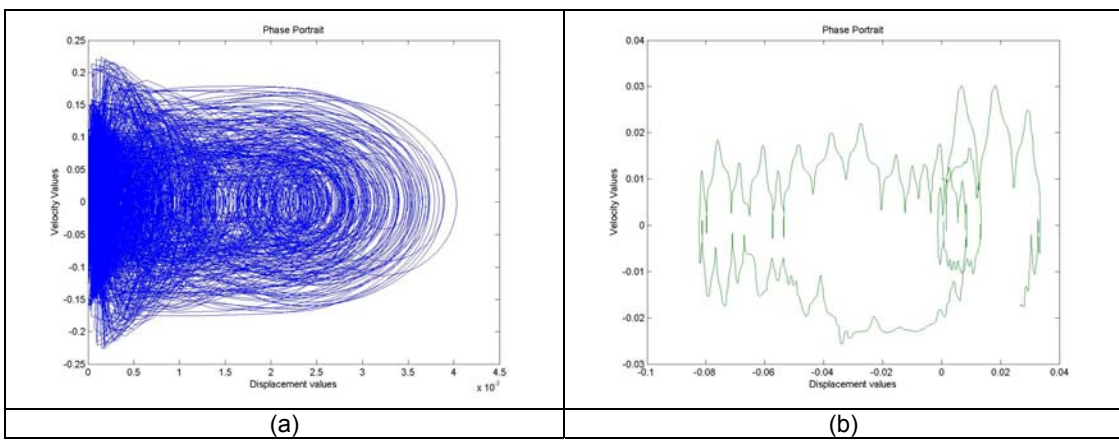
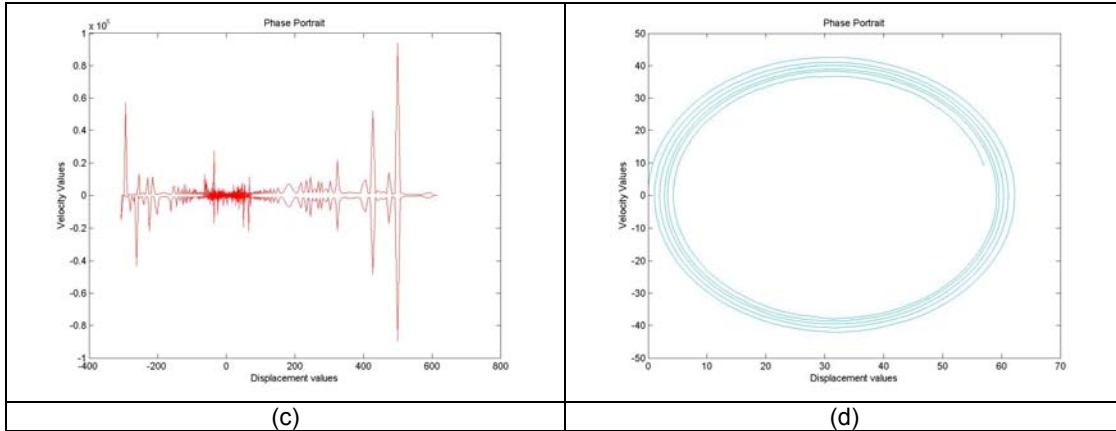


Figure 14. a) Trajectory of the center of Section II in polar coordinates ( $\rho$ ,  $\theta$ ) in horizontal plane and b) displacement histories.

**Case III:** Low friction coefficient ( $\mu = 0.1$ ) and high contact stiffness





**Figure 15. Phase portraits: a) radial displacement of Section II, b) rotation angle of Section I, c) bending angle of Section II, and d) rotation angle of Section II.**

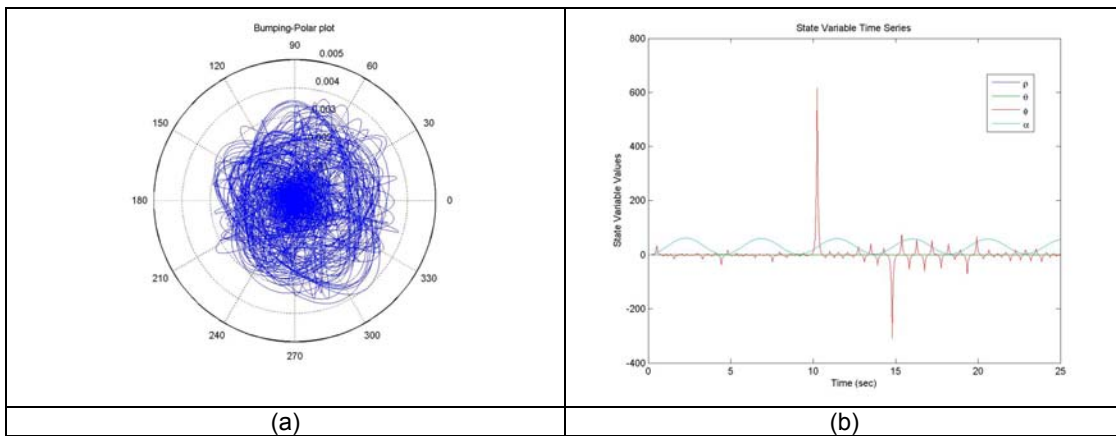


**Figure 16. a) Trajectory of the center of Section II in polar coordinates ( $\rho$ ,  $\theta$ ) in horizontal plane and b) displacement histories.**

As the contact stiffness is increased, the trajectory of the center of Section II tended stays closer to the center of the system. There is a pronounced increase in the bending angle displacement peaks as the contact stiffness value is increased.

### High Friction at the Contact Surface

The different results obtained in this case are shown in Figures 17 to 22. Apart from the features observed in the previous case, in this case, sticking motions are also observed because the friction coefficient is high.

**Case IV:** High friction coefficient ( $\mu = 0.9$ ) and low contact stiffness

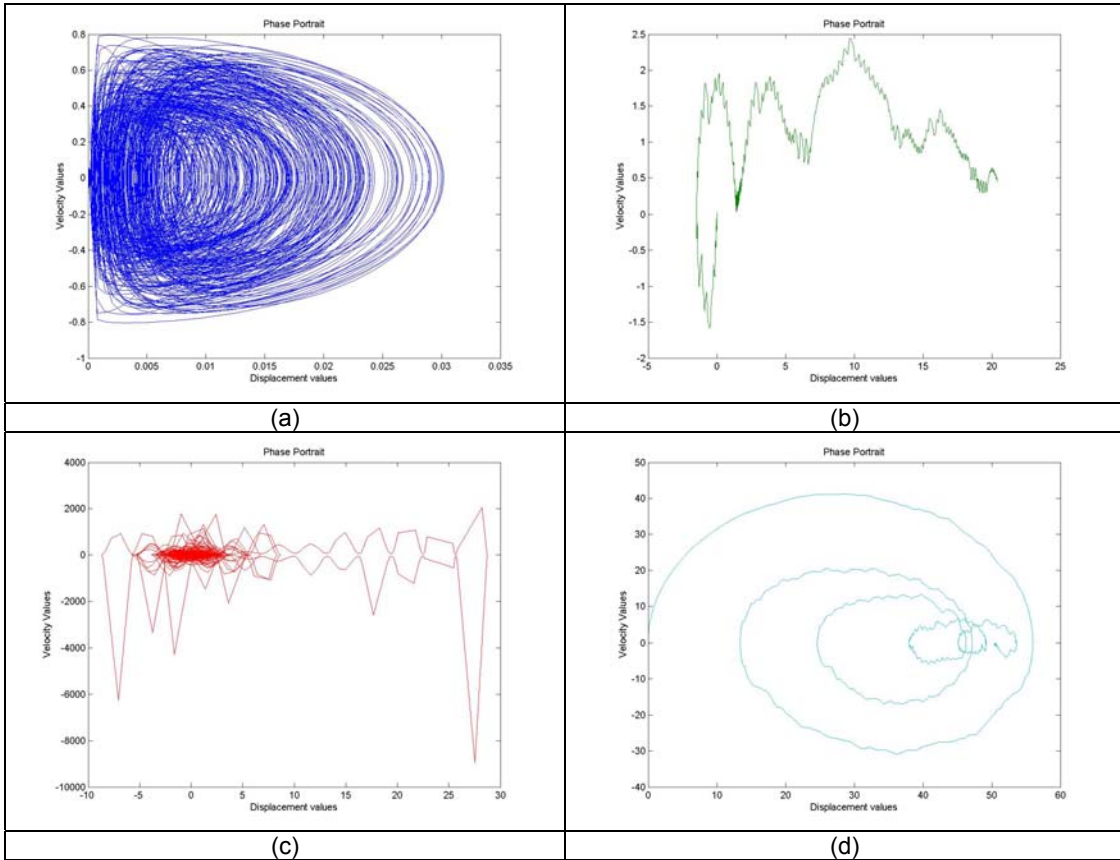


**Figure 17. Phase portraits: a) radial displacement of Section II, b) rotation angle of Section I, c) bending angle of Section II, and d) rotation angle of Section II.**

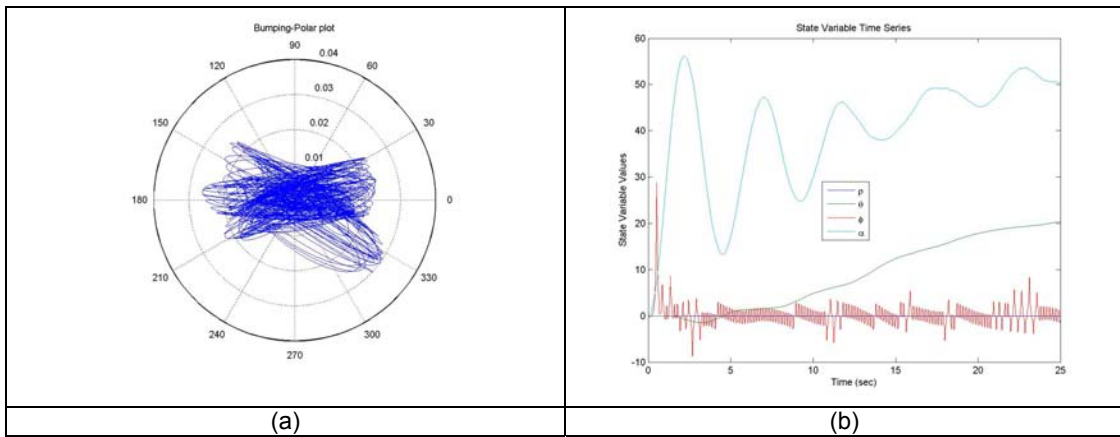


**Figure 18. a) Trajectory of the center of Section II in polar coordinates ( $\rho$ ,  $\theta$ ) in horizontal plane and b) displacement histories.**

**Case V:** High friction coefficient ( $\mu = 0.9$ ) and medium contact stiffness

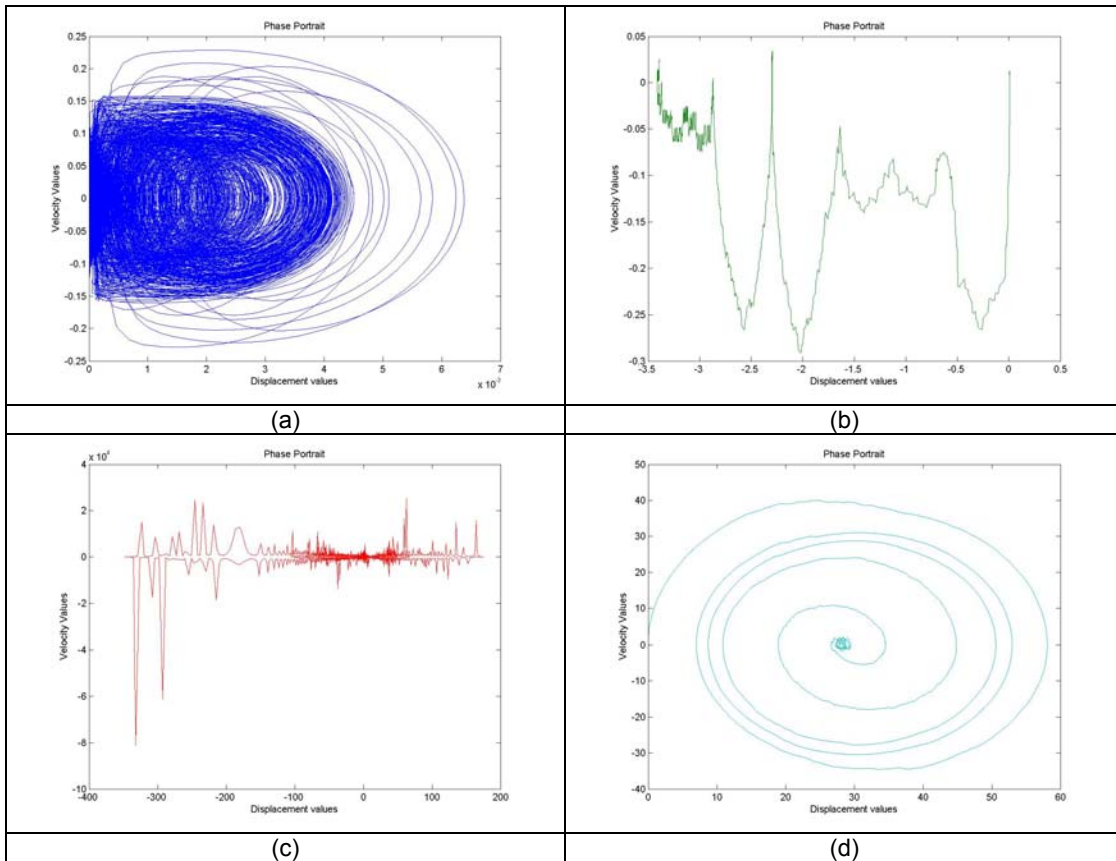


**Figure 19. Phase portraits: a) radial displacement of Section II, b) rotation angle of Section I, c) bending angle of Section II, and d) rotation angle of Section II.**

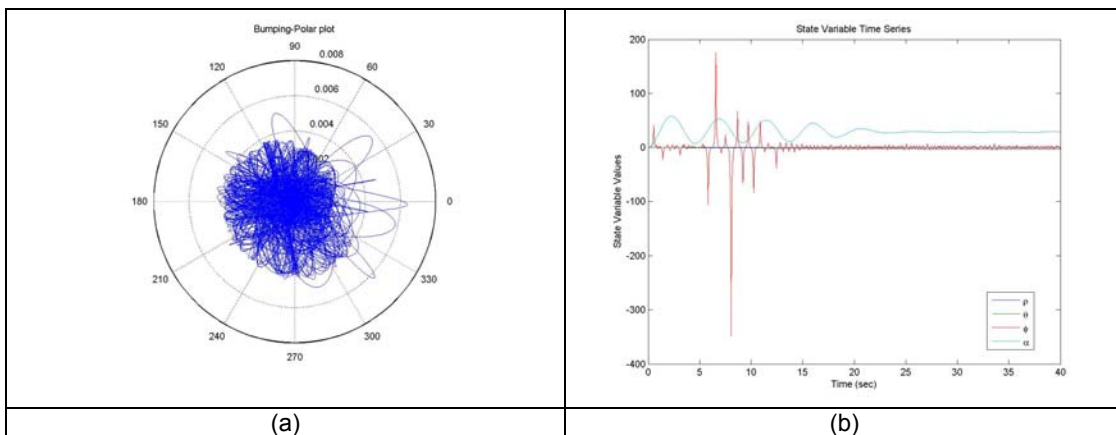


**Figure 20. a) Trajectory of the center of Section II in polar coordinates ( $\rho$ ,  $\theta$ ) in horizontal plane and b) displacement histories.**

**Case VI:** High friction coefficient ( $\mu = 0.9$ ) and high contact stiffness

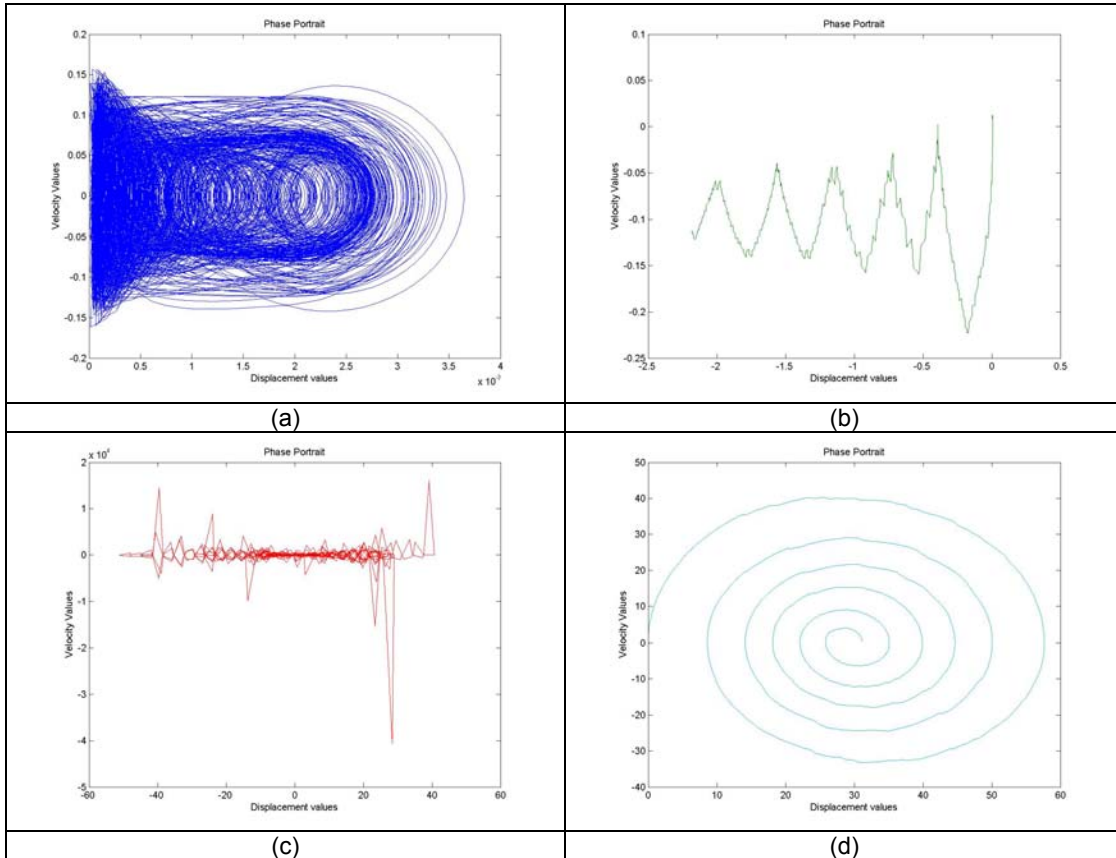


**Figure 21. Phase portraits: a) radial displacement of Section II, b) rotation angle of Section I, c) bending angle of Section II, and d) rotation angle of Section II.**

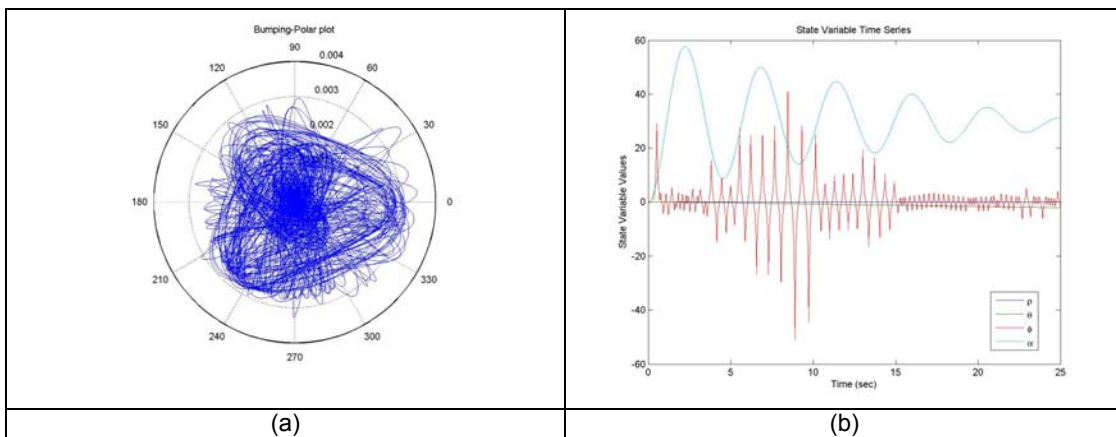


**Figure 22. a) Trajectory of the center of Section II in polar coordinates ( $\rho, \theta$ ) in horizontal plane and b) displacement versus time relations**

As seen from the results, with a high friction coefficient, one could possibly avoid “drill-string shocks” seen in the cases with a low friction coefficient. From an experimental standpoint, the contact stiffness value can be varied by changing the connection between the outer shell and the drill string. A rigidly bolted housing could be used to mimic the high contact stiffness case.

### 4.1.3 Examination of the Models:

#### Examination of the Four-degree-of-freedom Model

The equations derived in the previous sections are re-examined, corrected, and presented here.

$$(m + m_b) \ddot{\rho} - (m + m_b) \rho (\dot{\theta} + \dot{\varphi})^2 + K_r (\rho - \rho_0) + \lambda K_p (\rho - \delta) + K_t \rho \varphi^2 - em_b (\ddot{\alpha} \sin(\beta) + \dot{\alpha}^2 \cos(\beta)) = 0 \quad (23)$$

$$I_1 \ddot{\theta} + (m + m_b) \rho^2 (\ddot{\theta} + \ddot{\varphi}) + 2(m + m_b) \rho \dot{\rho} (\dot{\theta} + \dot{\varphi}) - K_{tor} (\alpha - \theta) - em_b \rho (\dot{\alpha}^2 \sin(\beta) - \ddot{\alpha} \cos(\beta)) = -\lambda F_t \rho \quad (24)$$

$$(m + m_b) \rho (\ddot{\theta} + \ddot{\varphi}) + 2(m + m_b) \dot{\rho} (\dot{\theta} + \dot{\varphi}) + K_t \rho \varphi - em_b (\dot{\alpha}^2 \sin(\beta) - \ddot{\alpha} \cos(\beta)) = -\lambda F_t \quad (25)$$

$$(I_2 + m_b e^2) \ddot{\alpha} + K_{tor} (\alpha - \theta) + em_b [-\dot{\rho} \sin(\beta) + \rho (\ddot{\theta} + \ddot{\varphi}) \cos(\beta) + \dot{\rho} (\dot{\theta} + \dot{\varphi})^2 \sin(\beta) + 2 \dot{\rho} (\dot{\theta} + \dot{\varphi}) \cos(\beta)] = M_{ext} - \lambda F_t R \quad (26)$$

where

$$\beta = \alpha - (\theta + \varphi)$$

The main differences between this modified model and that of Melakhessou *et al.* (2003) are as follows: i) the unbalanced mass  $m_b$  is not relatively small compared to the section mass  $m$ , and ii) there is an additional term related to the torsion stiffness in Eq. (24).

Disregarding all the external force terms, the system is determined to have one fixed or equilibrium point, and this fixed point is given by

$$\rho = \frac{K_r \rho_0 + \lambda K_p \delta}{K_r + \lambda K_p} \quad (27)$$

$$\theta = \alpha, \quad \varphi = 0 \quad (28)-(29)$$

The radial position of the equilibrium point depends on the initial radial displacement and the radial stiffness and contact stiffness. Also, this point can be determined for either  $\lambda=0$  or  $\lambda=1$ . For the system parameter values given in the work of Melakhessou *et al.* (2003) and studied in the prior section, the eigenvalues (Table 1) were determined from the Jacobian Matrix, but this equilibrium point was found to be unstable.

**Table 1. Eigenvalues of the Jacobian Matrix**

$\lambda = 0$	$0 + 114.018i$	$-1.24 \times 10^{-5} + 38.33i$	$-1.64 \times 10^{-5} + 33.35i$	$-8.34 \times 10^{-6}$
	$0 - 114.018i$	$-1.24 \times 10^{-5} - 38.33i$	$-1.64 \times 10^{-5} - 33.35i$	$-1.36 \times 10^{-9}$
$\lambda = 1$	$0 + 114.018i$	$-1.11 \times 10^{-4} + 38.33i$	$-1.51 \times 10^{-3} + 33.58i$	0
	$0 - 114.018i$	$-1.11 \times 10^{-4} - 38.33i$	$-1.51 \times 10^{-3} - 33.58i$	$-7.66 \times 10^{-5}$

Next, free oscillation results obtained through numerical integration are presented for different initial positions of Section II relative to Section I in Figures 23 to 25. When there is contact between the outer shell and Section II, the oscillations have characteristics similar to those observed in the case of forced oscillations. This is evident when the results of the present studies are compared to those presented in previous sections.

**Case I:** Initial position close to the center of the stator

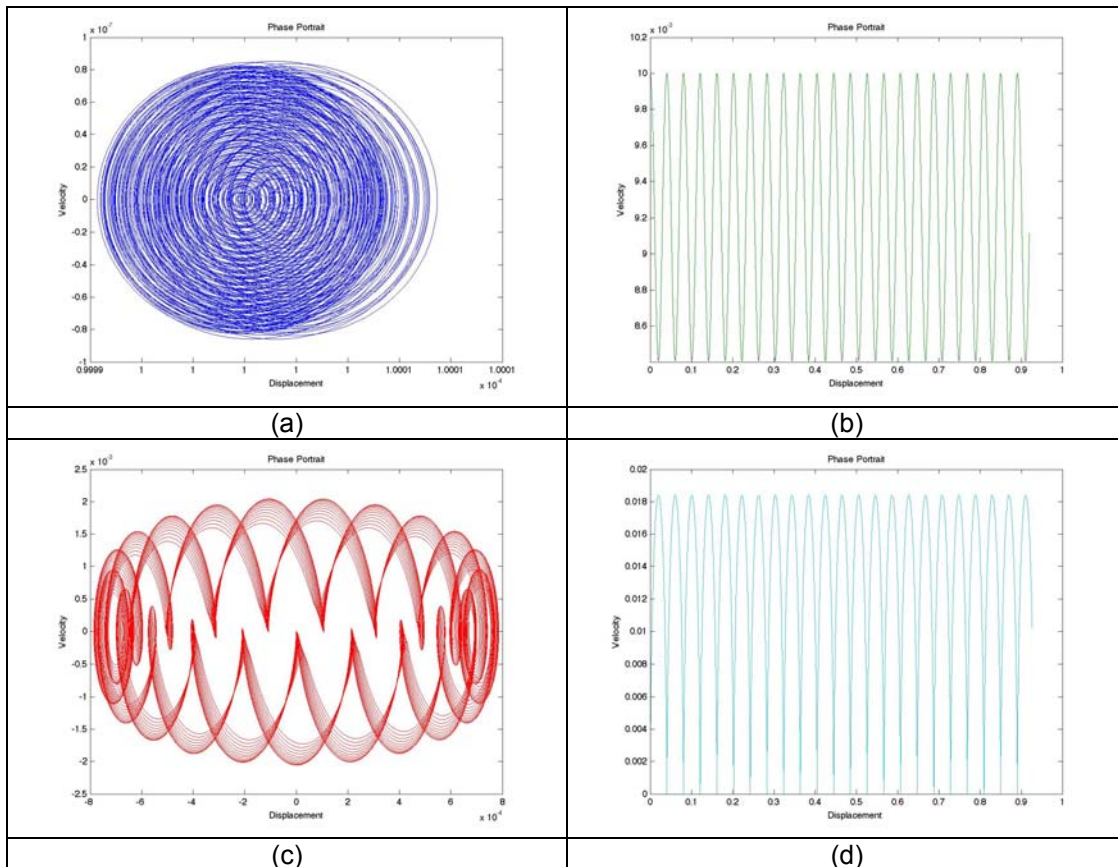


**Figure 23. Phase portraits: a) radial displacement of Section II, b) rotation angle of Section I, c) bending angle of Section II, and d) rotation angle of Section II.**

**Case II:** Initial position close to the outer shell

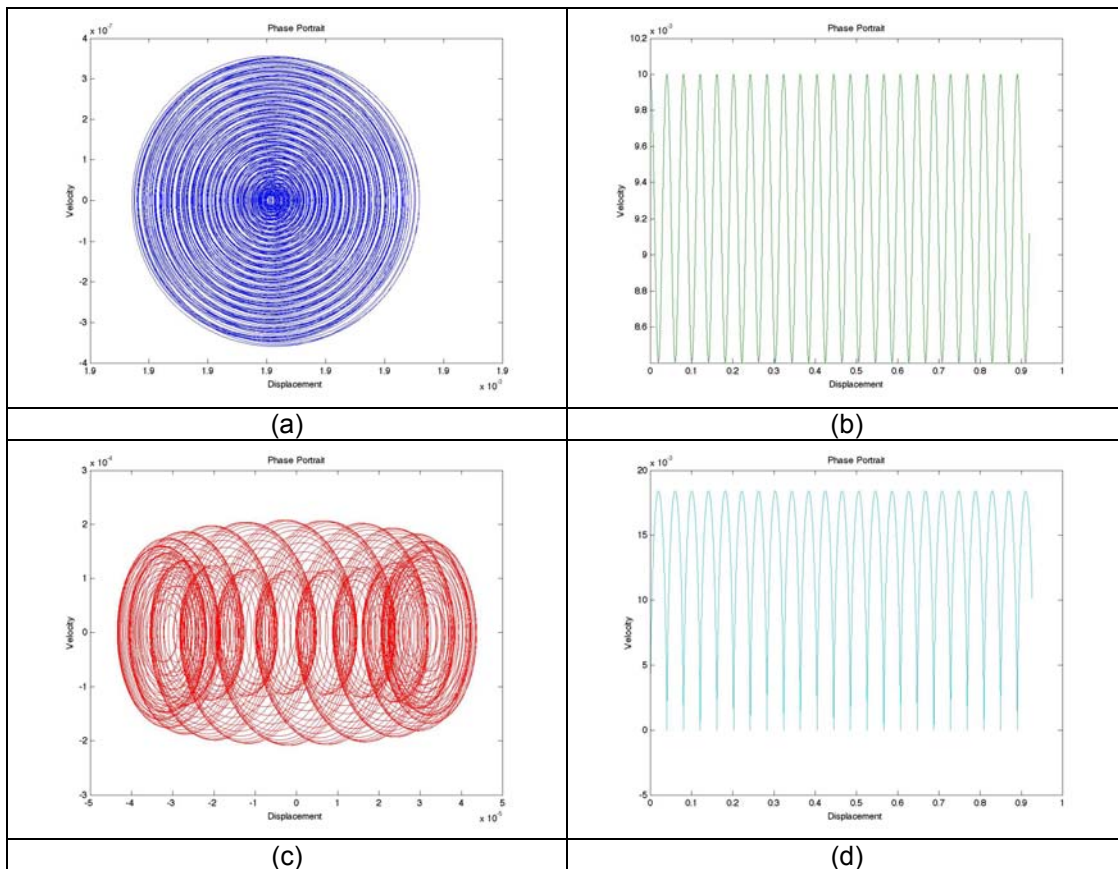


**Figure 24. Phase portraits: a) radial displacement of Section II, b) rotation angle of Section I, c) bending angle of Section II, and d) rotation angle of Section II.**

**Case III:** Initial position corresponds to contact with the outer shell

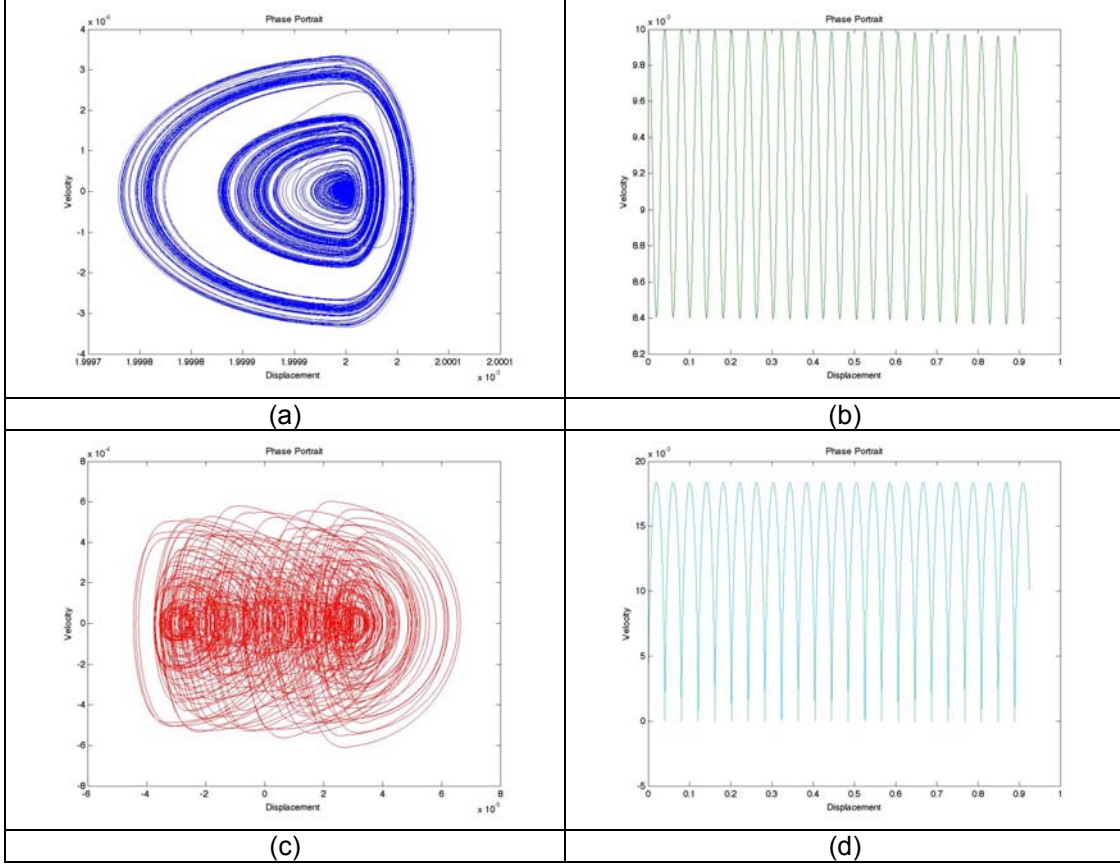


**Figure 25. Phase portraits: a) radial displacement of Section II, b) rotation angle of Section I, c) bending angle of Section II, and d) rotation angle of Section II.**

### Examination of the Five-Degree- of-Freedom Model

The corrected system with five degrees of freedom is presented next. With the additional tilt angle, the equations read as

$$\begin{aligned}
 (m + m_b) \ddot{\rho} - (m + m_b) \rho (\dot{\theta} + \dot{\varphi})^2 + K_r (\rho - \rho_0) + \lambda K_p (\rho - \delta) + K_t \rho \varphi^2 \\
 - m_b \rho \sin^2 (\theta + \varphi) \dot{\psi}^2 - m_b e \cos \beta \dot{\alpha}^2 - m_b e \sin \alpha \sin (\theta + \varphi) \dot{\psi} - m_b e \sin \beta \ddot{\alpha} = 0
 \end{aligned} \tag{30}$$

$$\begin{aligned}
 I_1 \ddot{\theta} + (m + m_b) \rho^2 (\ddot{\theta} + \ddot{\varphi}) + 2(m + m_b) \rho \dot{\rho} (\dot{\theta} + \dot{\varphi}) - K_{tor} (\alpha - \theta) - em_b \rho (\dot{\alpha}^2 \sin(\beta) - \ddot{\alpha} \cos(\beta)) \\
 - m_b \rho \dot{\psi}^2 \cos(\theta + \varphi) [e \sin \alpha + \rho \sin(\theta + \varphi)] = -\lambda F_t \rho
 \end{aligned} \tag{31}$$

$$\begin{aligned}
 (m + m_b) \rho (\ddot{\theta} + \ddot{\varphi}) + 2(m + m_b) \dot{\rho} (\dot{\theta} + \dot{\varphi}) + K_t \rho \varphi - em_b (\dot{\alpha}^2 \sin(\beta) - \ddot{\alpha} \cos(\beta)) \\
 - m_b \dot{\psi}^2 \cos(\theta + \varphi) [e \sin \alpha + \rho \sin(\theta + \varphi)] = -\lambda F_t
 \end{aligned} \tag{32}$$

$$(I_2 + m_b e^2) \ddot{\alpha} + K_{tor} (\alpha - \theta) + em_b [-\ddot{\rho} \sin(\beta) + \rho(\ddot{\theta} + \ddot{\varphi}) \cos(\beta) + \rho(\dot{\theta} + \dot{\varphi})^2 \sin(\beta) + 2\rho(\dot{\theta} + \dot{\varphi}) \cos(\beta)] - em_b \dot{\psi}^2 \cos \alpha [e \sin \alpha + \rho \sin(\theta + \varphi)] = M_{ext} - \lambda F_t R \quad (33)$$

$$[(I_3 + m_b e^2 \sin^2(\alpha)) + \rho m_b \sin(\theta + \varphi)(2e \sin \alpha + \rho \sin(\theta + \varphi))] \ddot{\psi} + [(2m_b e \dot{\alpha} \cos \alpha + 2m_b \sin(\theta + \varphi) \dot{\rho} + 2m_b \cos(\theta + \varphi) \rho(\dot{\theta} + \dot{\varphi})) \bullet (e \sin \alpha + \rho \sin(\theta + \varphi))] \dot{\psi} = -\lambda F_t (R + \rho) \quad (34)$$

where  $\beta = \alpha - (\theta + \varphi)$ . Again, for free oscillations of the system, the equilibrium points of the system are determined. The system is found to have one equilibrium or fixed point, which is given by

$$\rho = \frac{K_r \rho_0 + \lambda K_p \delta}{K_r + \lambda K_p} \quad (35)$$

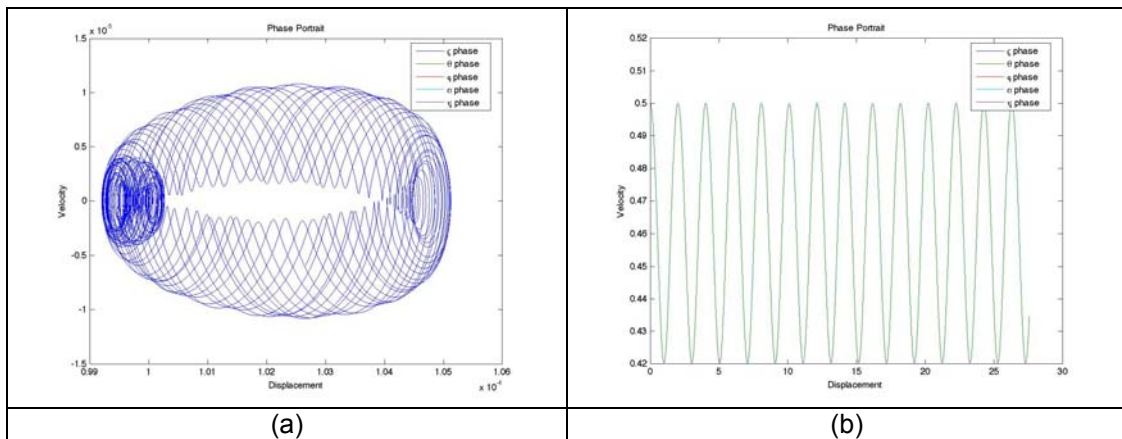
$$\theta = \alpha; \quad \varphi = 0$$

with the additional condition that the tilt angle

$$\psi = \text{arbitrary} \quad (36)$$

As with the four degree-of-freedom model, the free oscillations of the system are studied for different initial conditions and the results are presented in Figures 26 and 27. As in the system with the four degrees of freedom, the oscillatory characteristics are different in cases with contact and without contact. The inclusion of the tilt angle does include some oscillatory characteristics other than those observed previously.

**Case IV:** Initial position close to the center of the stator



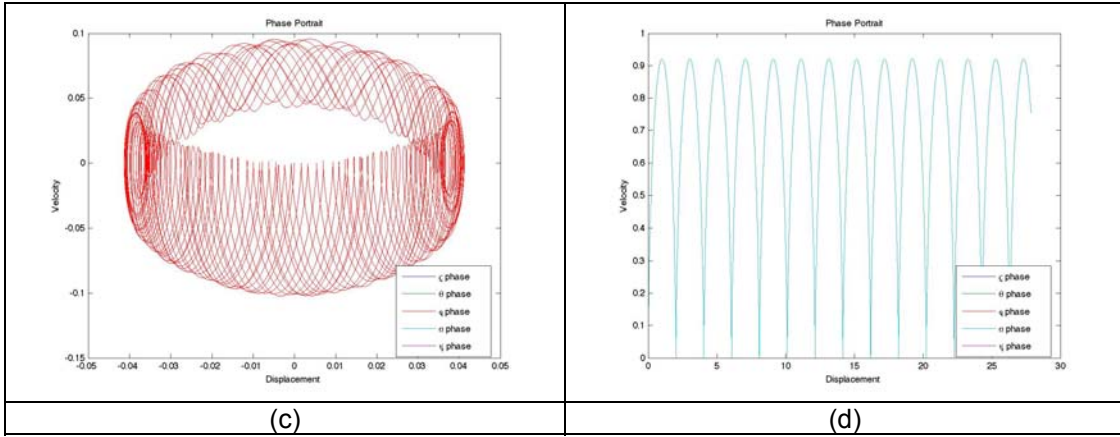


**Figure 26. Phase portraits: a) radial displacement of Section II, b) rotation angle of Section I, c) bending angle of Section II, and d) rotation angle of Section II.**

**Case V:** Initial position corresponds to contact with the outer shell

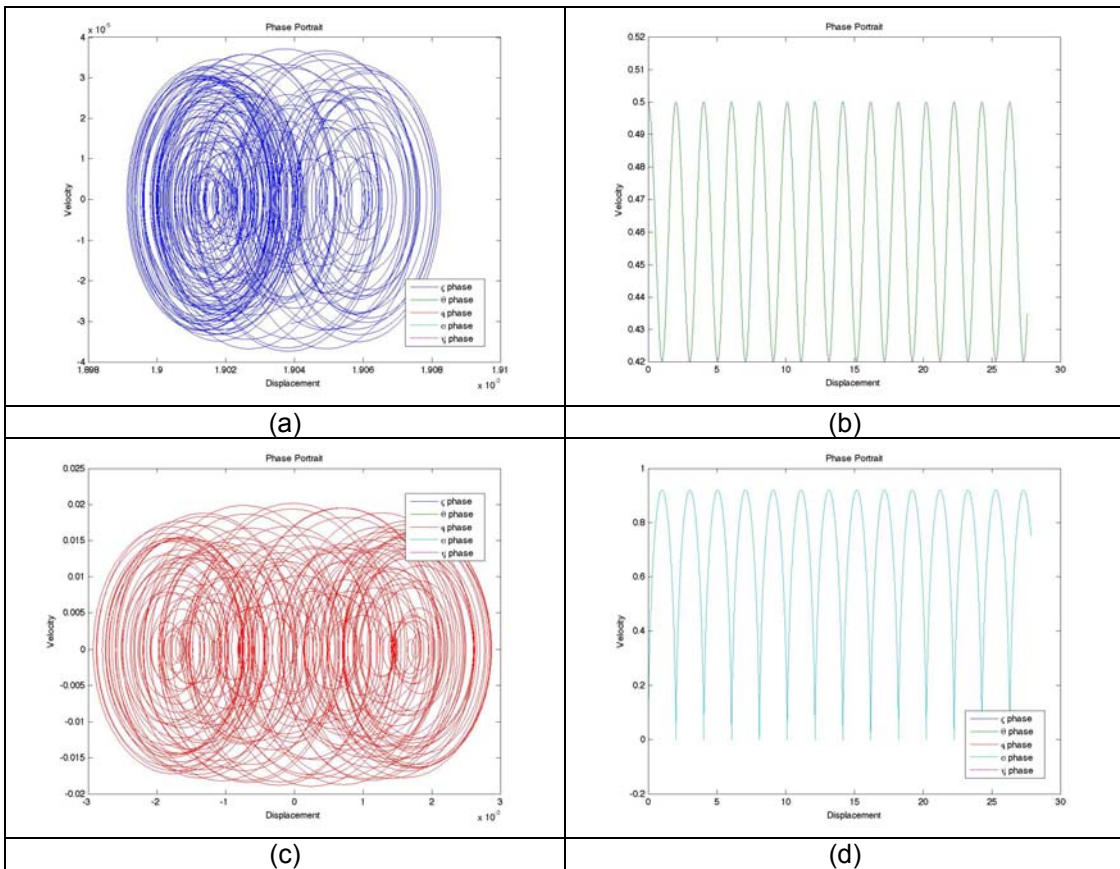


**Figure 27. Phase portraits: a) radial displacement of Section II, b) rotation angle of Section I, c) bending angle of Section II, and d) rotation angle of Section II.**

## 4.2 Experimental approach:

### 4.2.1 Experimental setting:

## Description

To facilitate the analysis of the drill string axial, whirl, and stick-slip vibrations, a laboratory scale drill string arrangement complete with sensors and actuators is being constructed at UMD to simulate the working conditions experienced by a drill string. The design is shown in Figure 28; in this arrangement, a slender metal string driven by a DC motor from the top of the rigid frame is used to mimic the drill string under the ground; together with the actuator at the bottom of the frame, brakes, springs, and an actuator are installed in the housing at the lower end of the string to generate resistive forces and axial vibrations such as those caused by rocks. Due to the eccentricity of the mass in the string, whirl is generated when the string rotates at critical speeds, and whirling motions are expected to occur at high speeds. When the lateral motion is large enough, it is expected that the drill string will collide with the outer pipe, causing stick-slip vibrations. Sensors are to be placed along the string to measure the axial, lateral, and rotational vibrations of the drill string. Measurements will also include the tilt angle between the drill string and the outer pipe. This measurement is expected to be challenging in the presence of applied lateral and axial forces.

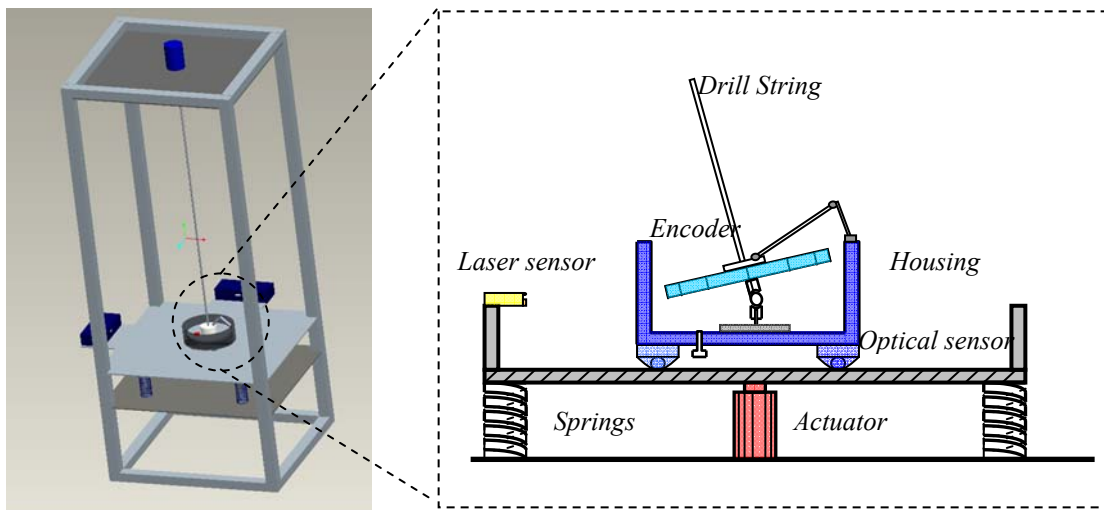


**Figure 28. Experimental arrangement to study bending-torsional vibrations (left), and detailed contact section design of the experiment (right)**

## Equipment

The main components used in this experiment are listed on the Table 4.2.1. and the details are shown as Figure 29 to 33.

**Table 2. Components of the experimental arrangement**

Item	Description	Figure
<b>DC Motor</b>	A DC motor is used to drive the drill-string system. This motor has the following features; i) maximum speed of 4000 rpm, ii) peak torque of 22.5 oz-in, and iii) a built-in rotary encoder.	4.2.2
<b>Rotating Disks</b>	The arrangement has an upper disk and a lower disk. The upper disk represents the rotary table of the drill string, and the lower disk represents the combination of the drill collar and drill bit. The diameters of the upper disk and lower disk are 12 inches and 6 inches, respectively.	4.2.3
<b>Encoder</b>	Absolute rotary encoders are used to measure the rotation angles of the disks.	4.2.4

	These encoders have a resolution of 360 pulses per revolution.	
<b>Actuator</b>	An electro-magnetic actuator will be used to realize an axial loading in the 0-2.5 kHz frequency range. This actuator is to be used to simulate the bearing capacity of the soil as well as to provide control input to the system.	4.2.5
<b>Laser Displacement Sensor</b>	A laser sensor is to be used to measure the lateral movement of the bottom end of the drill string. This end is connected to the lower rotating disk and brake housing.	4.2.6
<b>Optical Sensor</b>	An optical sensor is to be placed on the brake housing to measure the tilt angle of the lower rotating disk.	4.2.7

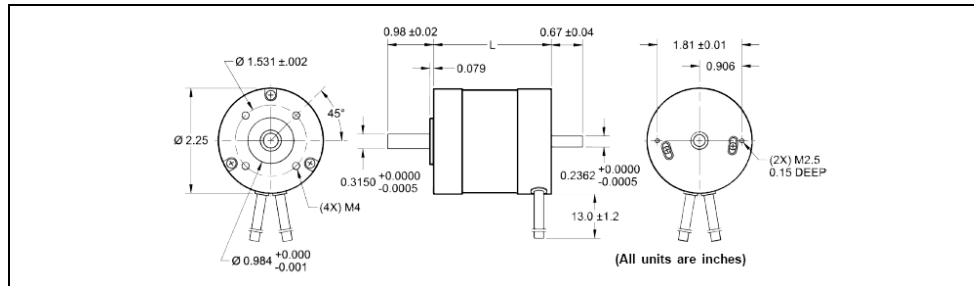


**Figure 29. DC Motor scale diagram (Ref. Anaheim Automation).**

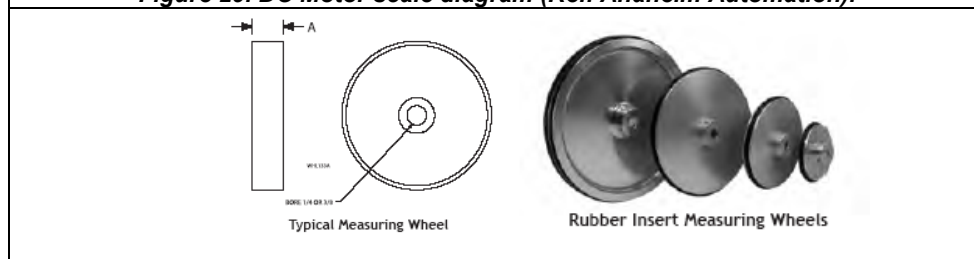


**Figure 30. Rotating Disk (Ref. Encoder Product Inc.).**

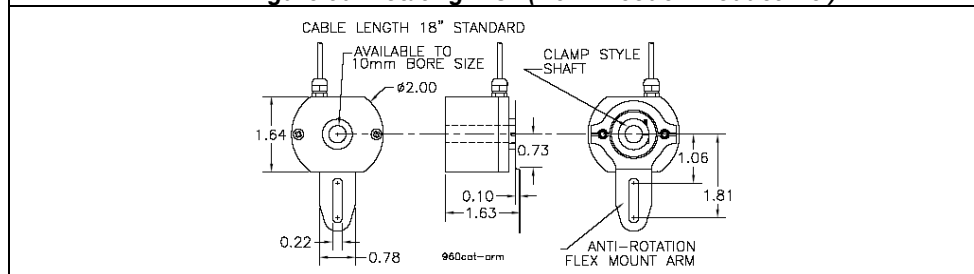


**Figure 31. Encoder Model 960 (Ref. Encoder Product Inc.).**

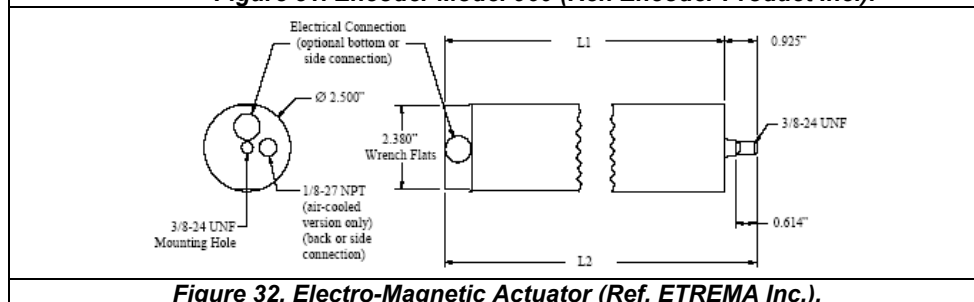
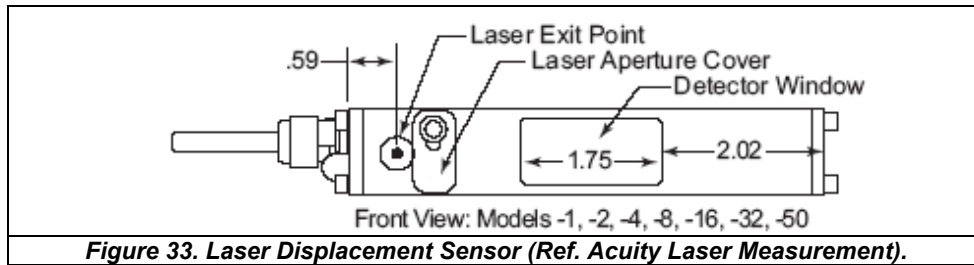


**Figure 32. Electro-Magnetic Actuator (Ref. ETREMA Inc.).**



In Figures 34 and 35, the different components that comprise the experimental arrangement housed by a 2'X2'X6' frame are shown. Details at the different levels are shown in Figures 36 to 41.



**Figure 34. Side view**



**Figure 35. Another view**



**Figure 36. Driving motor**



**Figure 37. Housing and bottom disk**

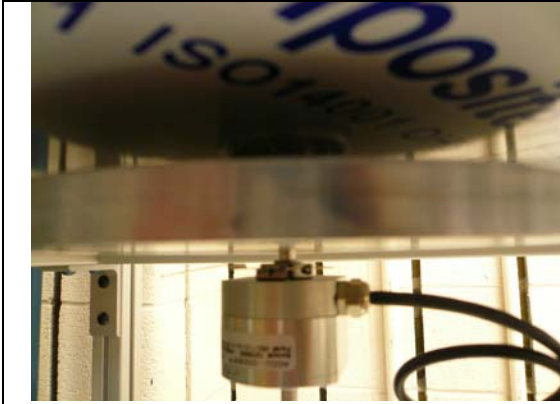


**Figure 38. Top disk with encoder**

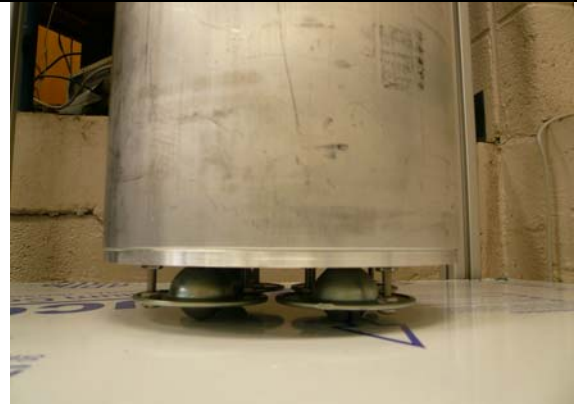


**Figure 39. Wheels under the housing**



**Figure 40. Encoder supporting frame**

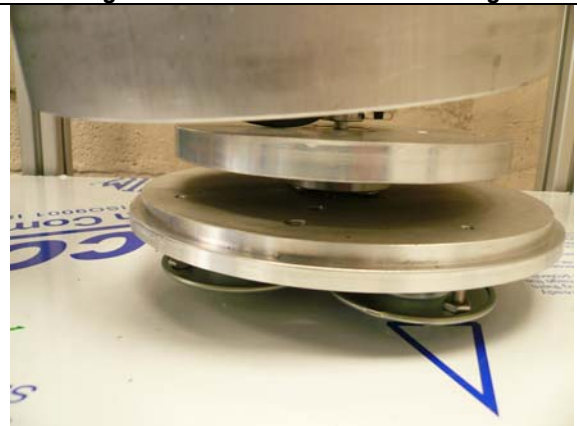


**Figure 41. Bottom disk with housing**

### Experimental Activities

Mihajlović *et al.* (2007) performed a series of experiments focusing on the interaction between friction-induced vibration and self-sustained later vibrations caused by a mass imbalance in an experimental rotor dynamic setup. The results of this work are being used as a basis for the planned experiments at UMD.

On the UMD side, a series of experiments are planned with the calibration experiments to be carried out in the beginning leading up to experiments similar to those of Mihajlović *et al.* (2007). Following that, experiments will be conducted to gain further insights and comparisons with the predictions of the four degree-of-freedom and five degree-of-freedom models. The details of experimental design and setup are shown in Figure 42.

These experiments will focus on the influence of stick-slip phenomena in the lateral direction only and at the bottom of the drill string. These experiments are also expected to help refine the model. The different activities to be carried out are detailed below.

- i.) **Calibration experiments:** The main purpose of these experiments is to address the basic performance of the designed experimental arrangement. Only the upper and lower disks with an unbalanced mass within an unmovable housing will be used for detecting the reaction of the lower disc whirling in the housing. Stick-slip characteristics along the lateral direction between the lower disc and outer shell will also be studied. Sensors and actuators will also be characterized.

- ii.) **Drill string performance at the bottom end section:** The lower rotating disk is used for representing the rotational behavior of the drill string excited through a DC motor. An attached unbalanced mass on the lower disk is to be used. The lower disk is also attached to a brake disk by using a universal joint, which could allow the brake disk to remain on the face of the housing and not be disturbed by the tilting of the lower disk. The friction force is the main excitation source for torsion vibration of the system, and further, this force could also be used to simulate the resistance of the soil and rock resistance.
- iii.) **Interaction between the rotating disk and stick-slip phenomena:** A housing that is allowed to move freely on the vertical plane will be established at the lower end, as shown in Figure 28 and 37. The edge side of the housing is designed to mimic the bumping or sliding performance of drill string with the drill pipe, and the bottom side is used to provide a friction force to the system. With a fixed housing, the stick-slip movement and the corresponding influence on the rotating disk could be studied. With a floating housing, the contact action of a drill bit with soil or rock will be another issue that can be investigated.
- iv.) **Rotating system under axial force applied by actuator:** At the bottom section, a set of actuator and springs has been designed to represent the stiffness of the contact material (i.e., rock and soil) for the drill bit. The actuator can also be used to provide a normal force for the friction brake or be used to provide axial inputs for a feedback control scheme to stabilize the system. By controlling actuator motions, the contact and non-contact effects will be studied to replicate realistic operating conditions.

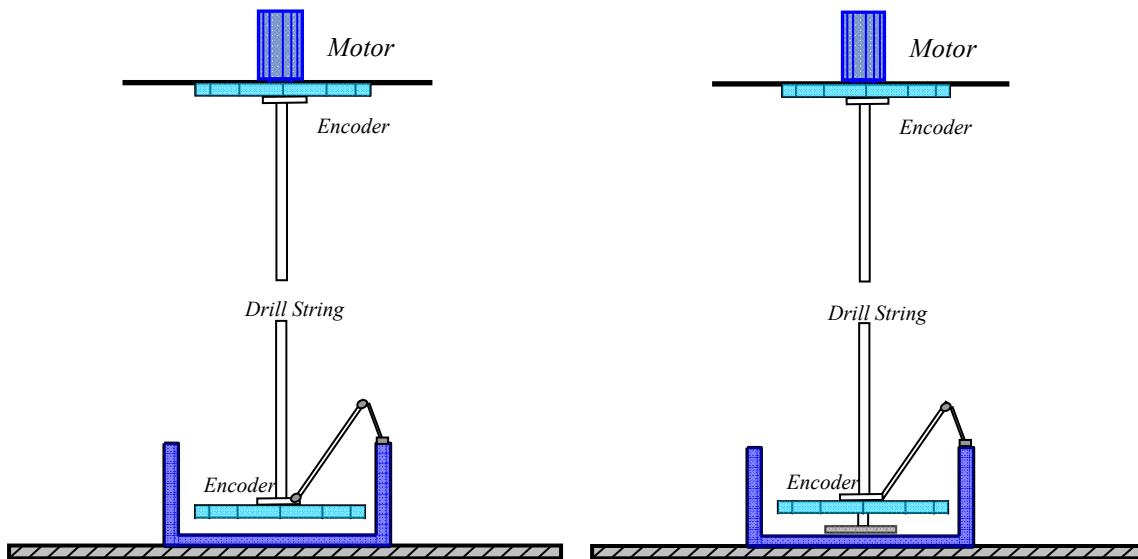


**Figure 42. Details of experimental contact section design. Lateral contact (left) and lateral with axial contact (right).**

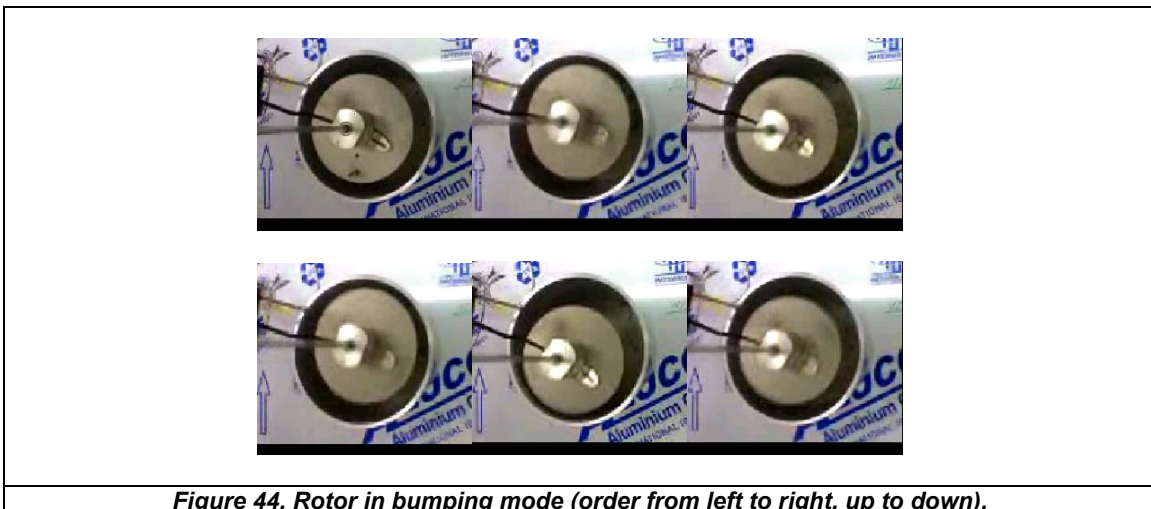
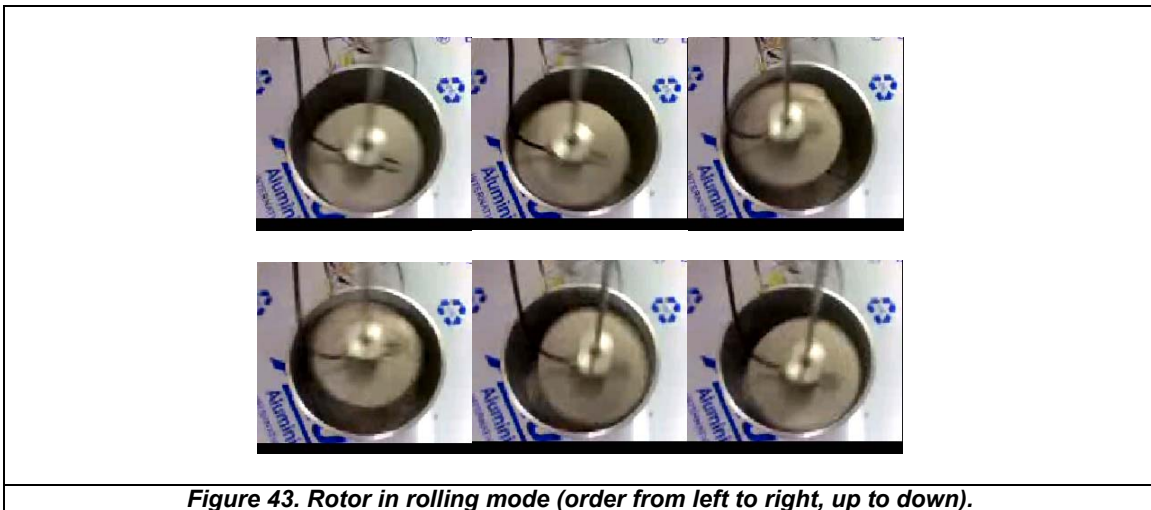
### Control Algorithms

In preliminary joint effort between UMD and PI, different controllers have been synthesized by using lead-lag compensators and PID controllers in conjunction with genetic algorithms for reducing the stick-slip induced vibrations. The controllers were designed with different

objective functions and parameter search limits. The designed controllers have been verified through numerical simulations, and the results are promising.

#### 4.2.2 Experimental Observations

In Figures 43 and 44, experimental observations of rolling motions and bumping motions made in the arrangement at the University of Maryland are shown. The first case corresponds to the higher rotation speed, while the second one corresponds to a lower rotation speed. With a heavier unbalanced mass, it is expected that one would observe rolling motions. These characteristics have been predicted previously in forced oscillations of four-degree-of-freedom and five-degree-of-freedom systems.



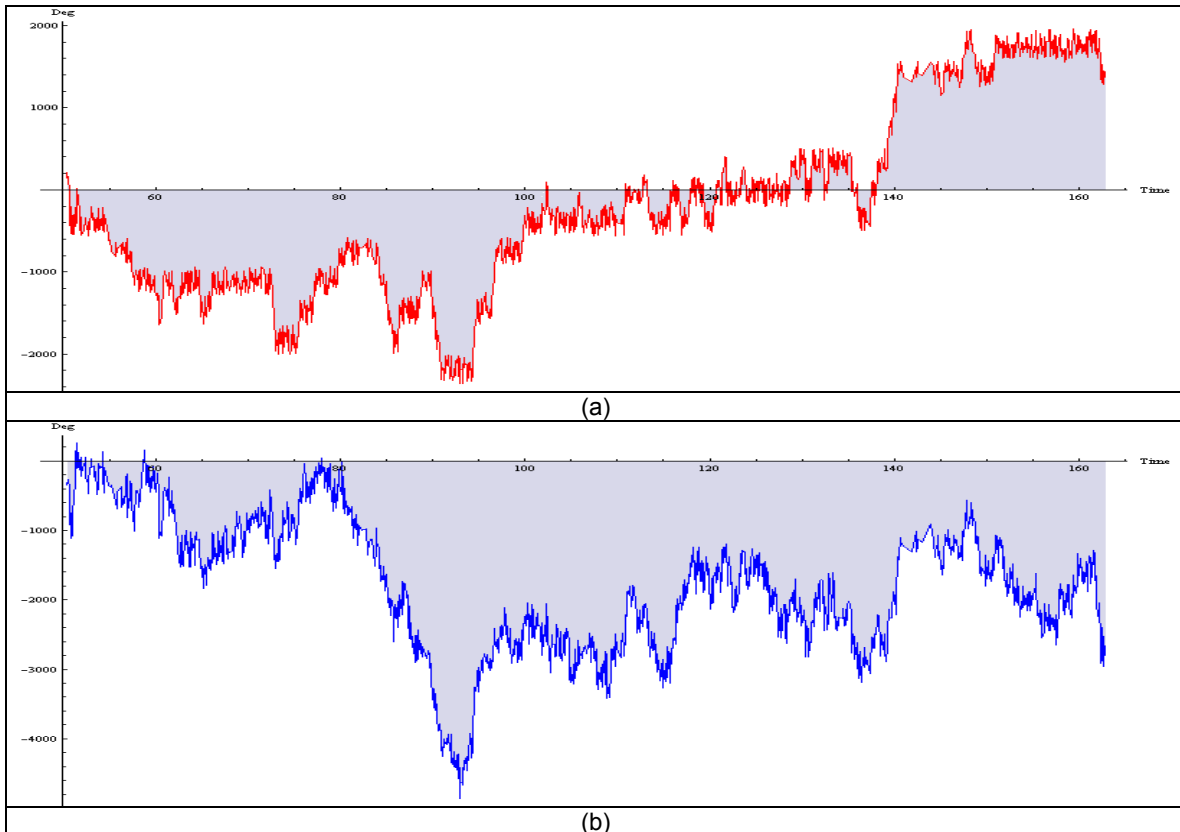
Experimentally observed rolling and bumping motions of the bottom disk are reported. Following these experiments, where the focus was on qualitative behavior, experiments have been conducted to calibrate the different sensors (encoders in particular) as well as to study

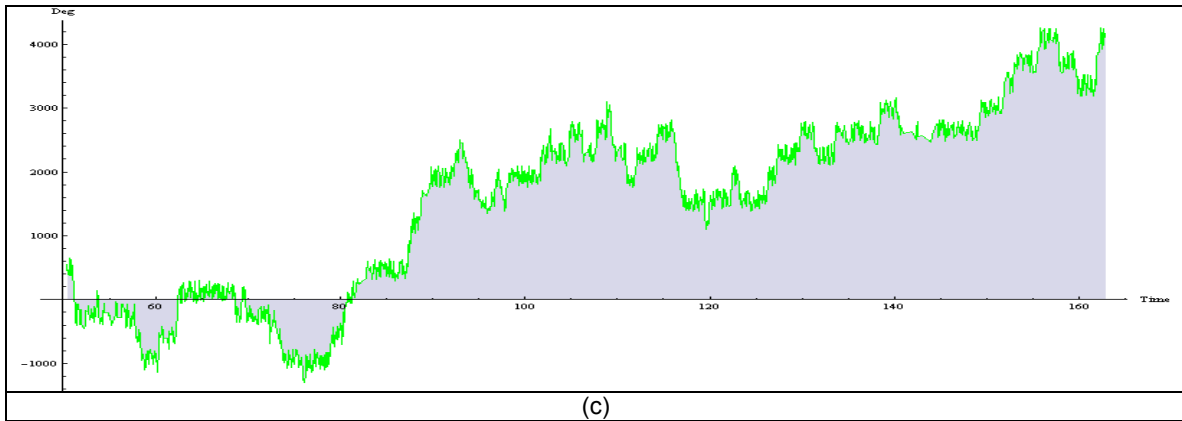
at what speeds the experiments could be conducted with an unbalanced mass. These experiments have been conducted as a first step towards collecting quantitative data for analysis and comparison with model predictions. In the following sections, the progress made towards this end is briefly detailed over three sections. In the first section, the results obtained from the low rotation speed experiments are discussed. In the second section, the results obtained from the high rotation speed experiments are presented. Following that, in the third section, the results obtained from the experiments with an unbalanced mass on the bottom disk are presented.

### Experimental results obtained at low rotation speed

A motor running at a constant rotation speed of 100 rpm is used in this experiment. The encoders used for measuring the angular positions at the two ends of drill string are absolute position encoders, each with 11 bits gray code output, which is decoded on a Labview<sup>®</sup> software platform.

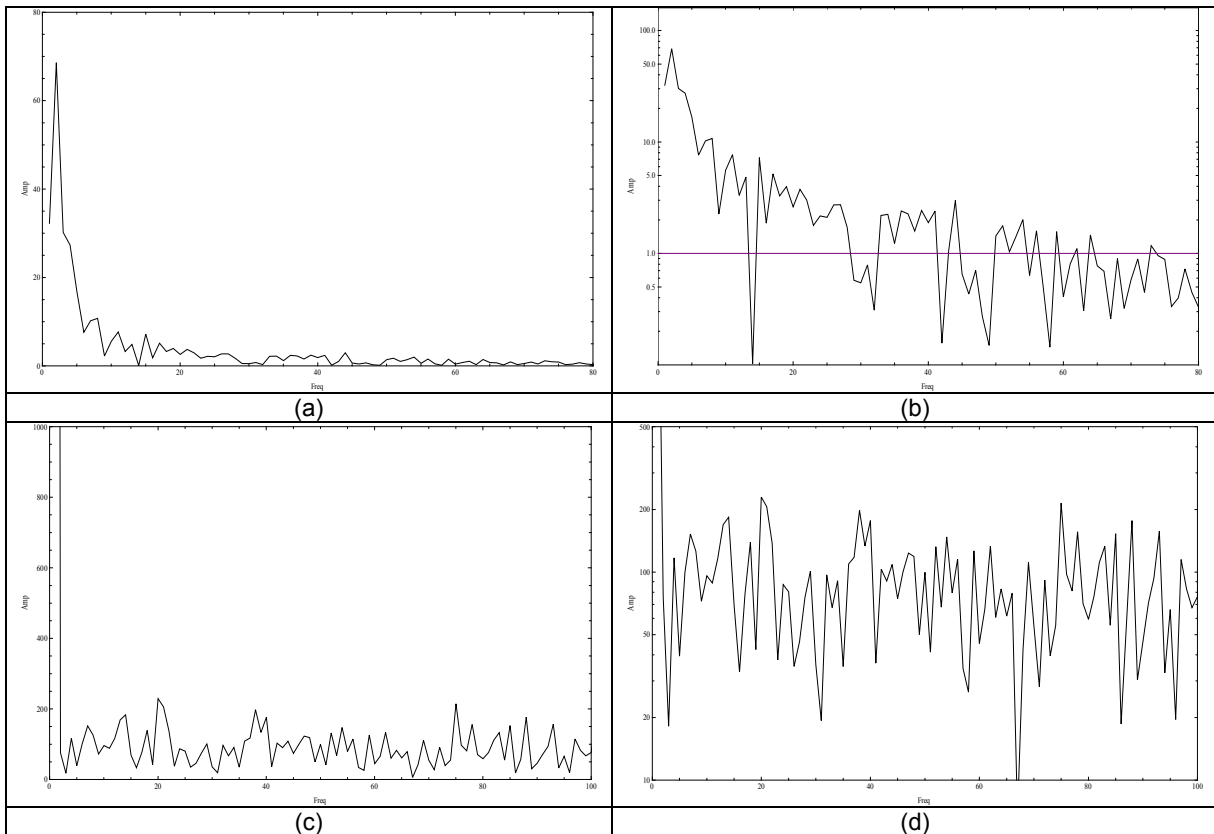
In Figure 45, the rotating angle time histories of the top and bottom of the drill string are presented along with the difference. The corresponding frequency domain information is shown in Figures 46 and 47. In Figures 46 a) and b), a prominent peak can be seen close to 1.5 Hz, which is at the excitation frequency, and another peak is noticeable close to 7 Hz. The same characteristics are also present in Figures 47 a) and b).



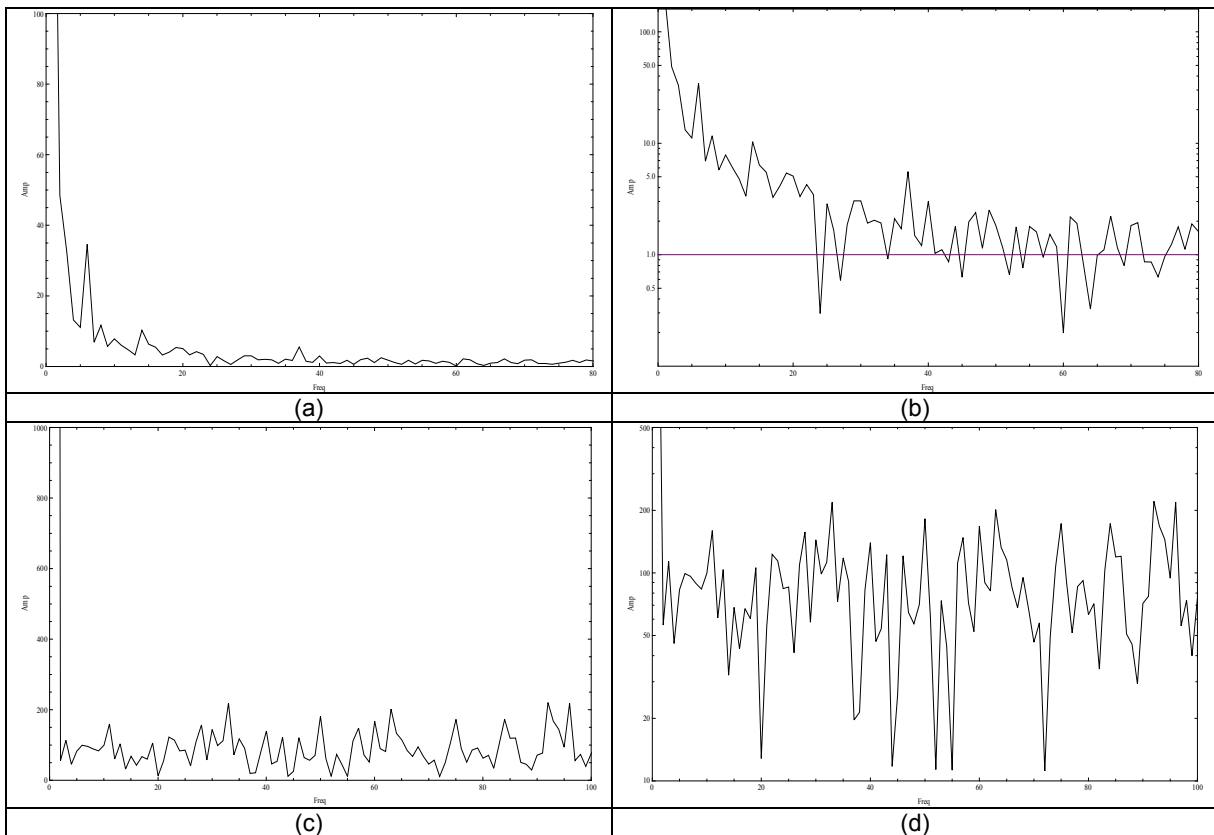


**Figure 45. Time histories: a) rotation angle of top disk, b) rotation angle of bottom disk, and c) difference between the rotations of the two disks. The rotation unit is degrees and the time unit is seconds.**

To generate the spectra shown in Figures c) and d) of Figures 46 and 47, the corresponding time histories were allowed to vary over a  $2\pi$  range. Some of the same features as seen in the corresponding Figures 46 a) and b) and Figure 3 can be seen. However, the peak close to 7 Hz is not dominant in Figures 47 c) and d).



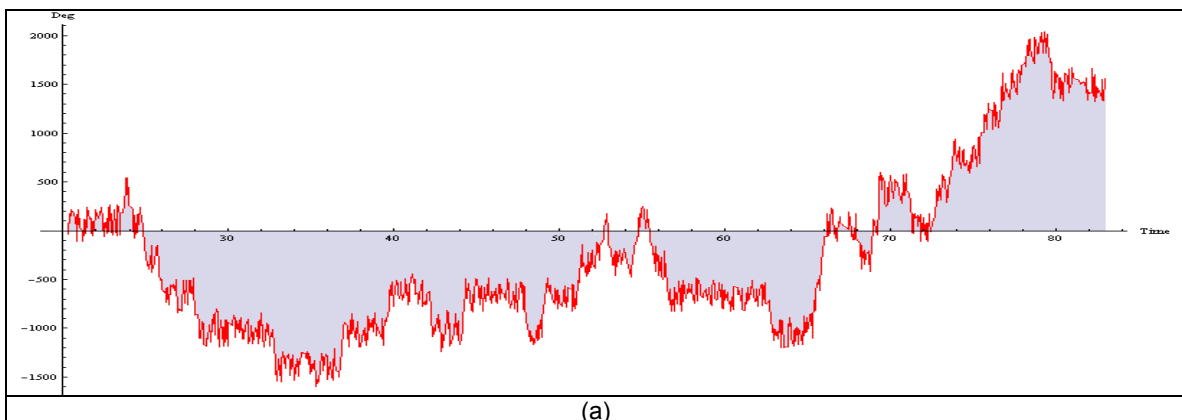
**Figure 46. Frequency spectra for top disk: a) spectrum on linear scale, b) spectrum on a log scale, c) spectrum on linear scale (complete spectrum of time history on  $2\pi$  scale); magnitude on , and d) spectrum on linear scale (expanded view of time history on  $2\pi$  scale).**

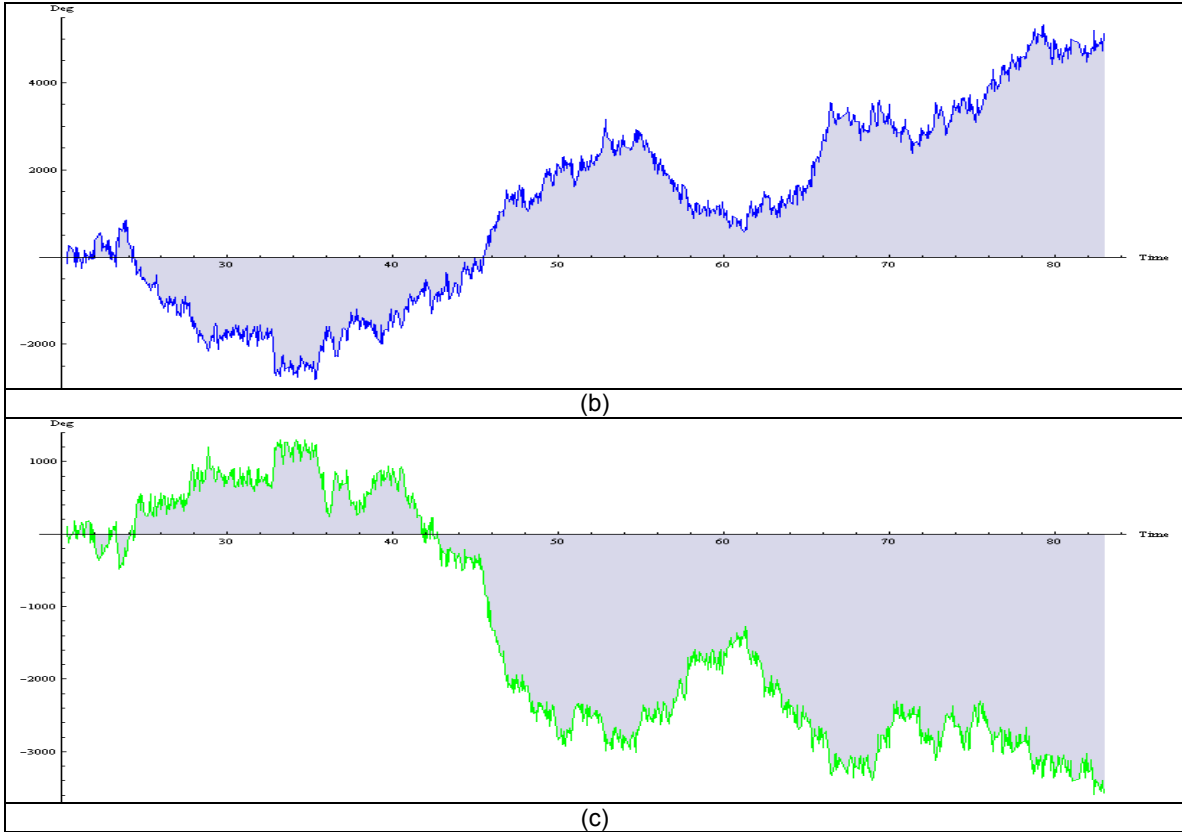


**Figure 47. Frequency spectra for bottom disk: a) spectrum on linear scale, b) spectrum on a log scale, c) spectrum on linear scale (complete spectrum of time history on  $2\pi$  scale); magnitude on ), and d) spectrum on linear scale (expanded view of time history on  $2\pi$  scale).**

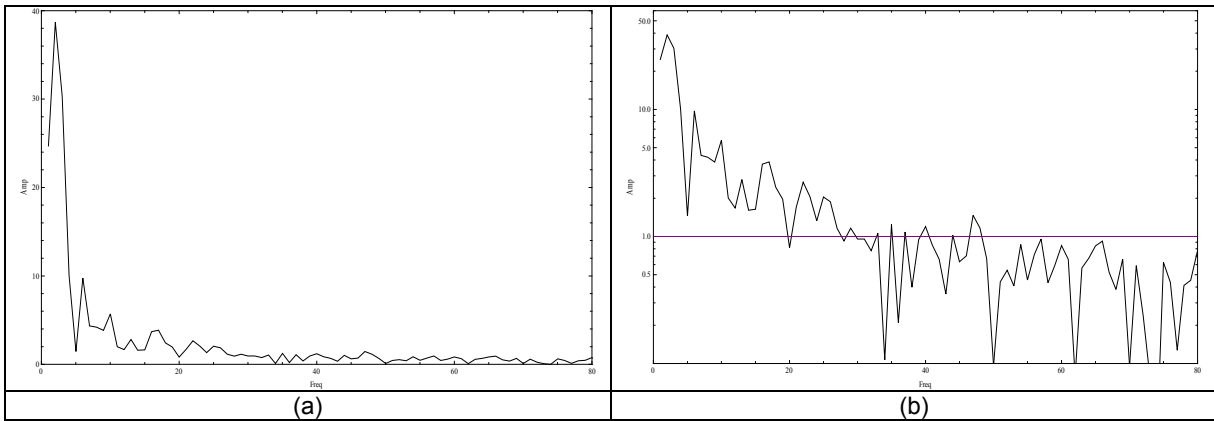
**Experimental results obtained at high rotation speed**

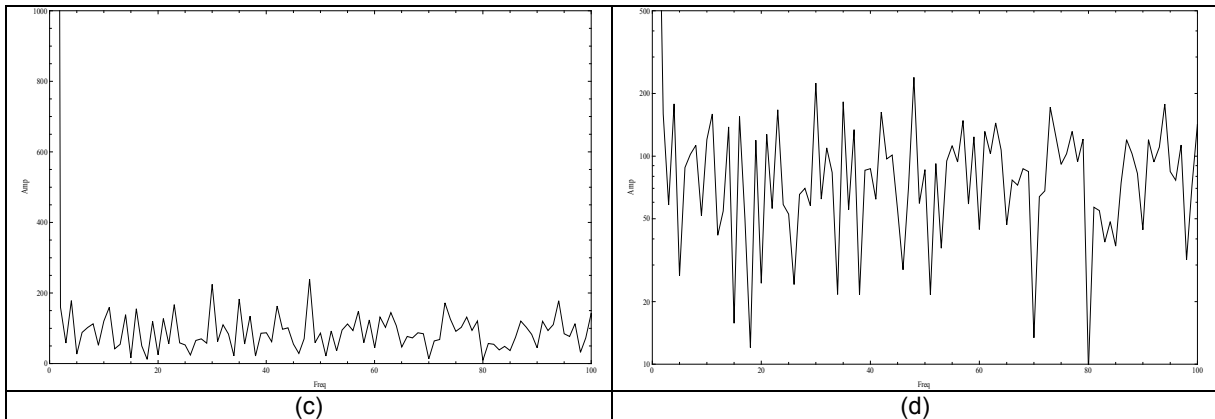
For this set of experiments, the rotation speed was increased to 200 rpm. Again, a peak close to 7 Hz is discernible in the observed rotations. Higher rotation speeds have not been tried so far, for safety reasons. The time histories are presented in Figure 48 and the associated spectra are shown in Figures 49 and 50. In the spectra, a prominent peak close to 3 Hz is seen.



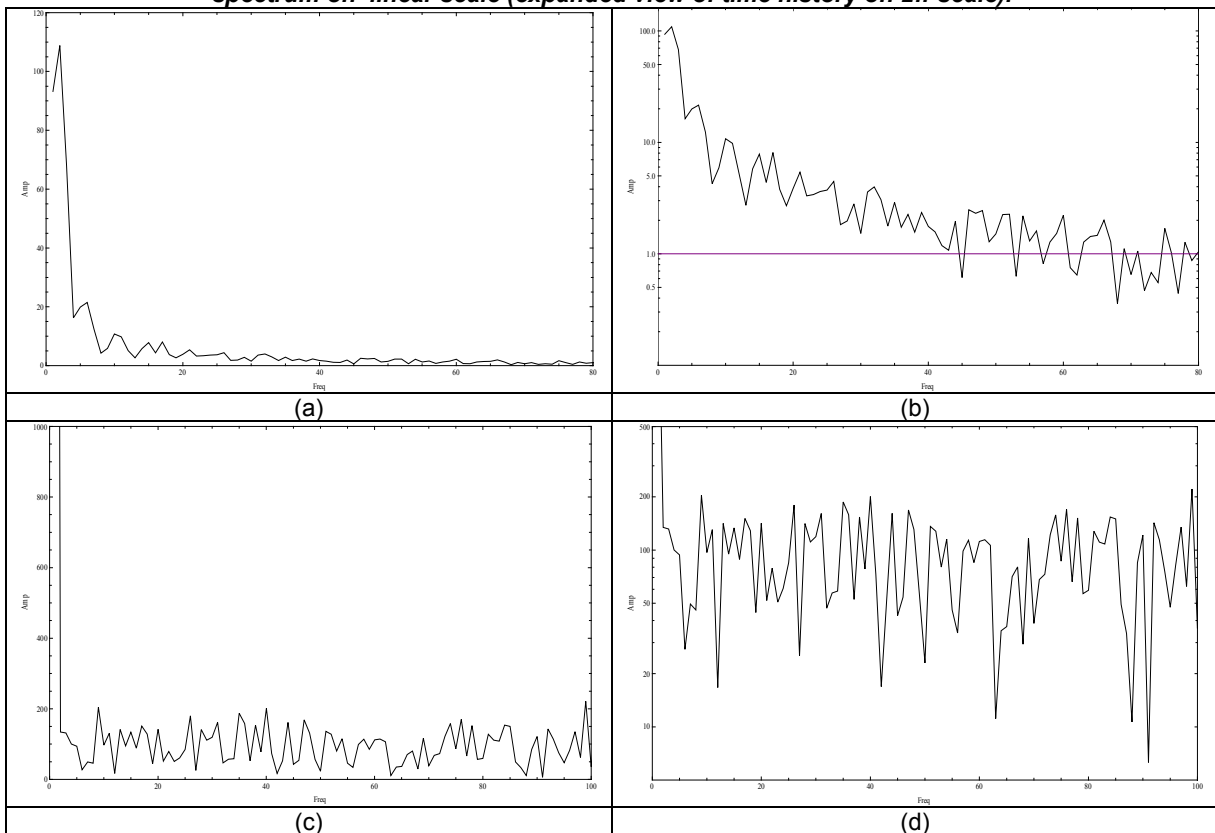


**Figure 48. Time histories: a) rotation angle of top disk, b) rotation angle of bottom disk, and c) difference between the rotations of the two disks. The rotation unit is degrees and the time unit is seconds.**





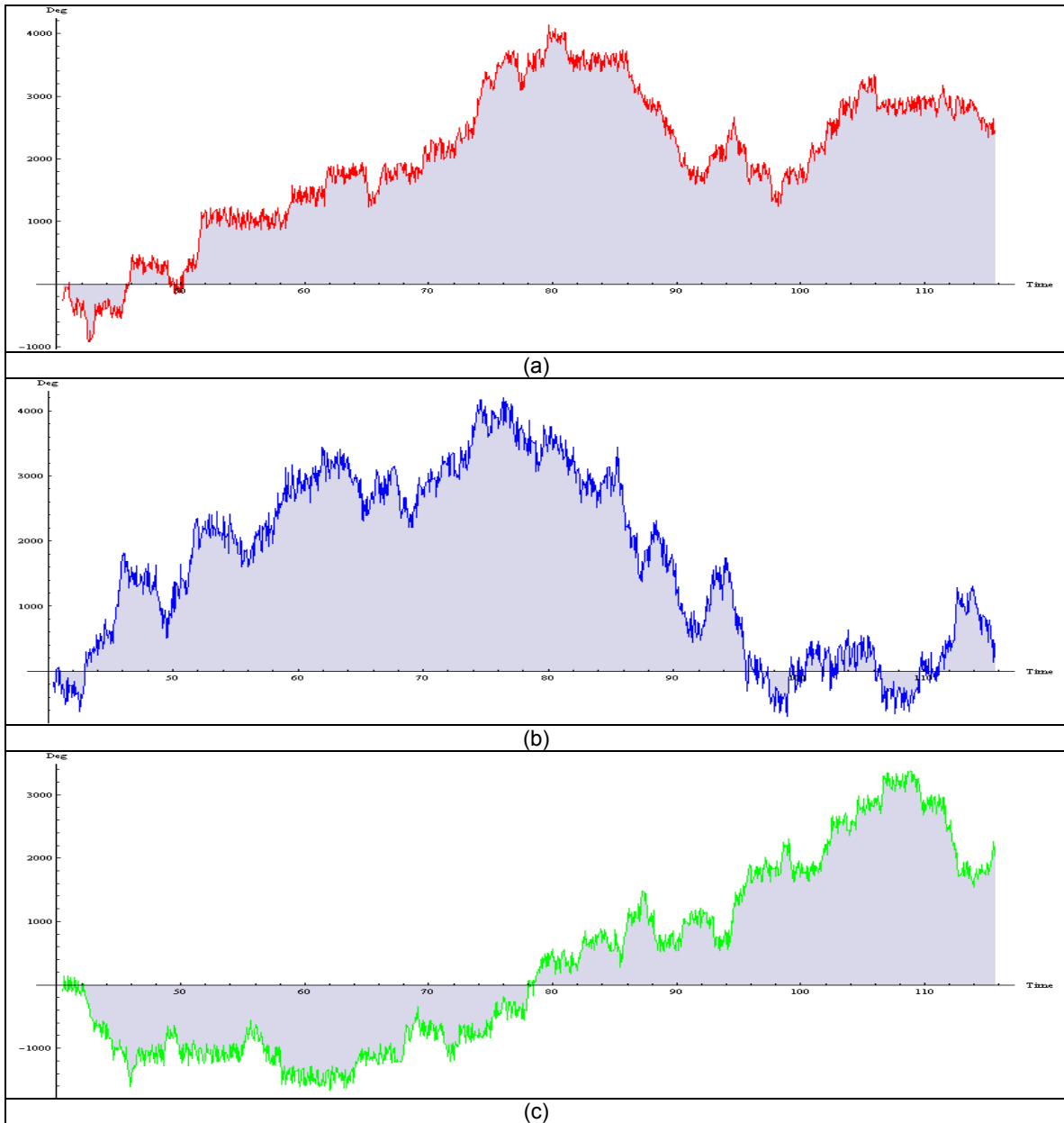
**Figure 49. Frequency spectra for top disk: a) spectrum on linear scale, b) spectrum on a log scale, c) spectrum on linear scale (complete spectrum of time history on  $2\pi$  scale); magnitude on , and d) spectrum on linear scale (expanded view of time history on  $2\pi$  scale).**



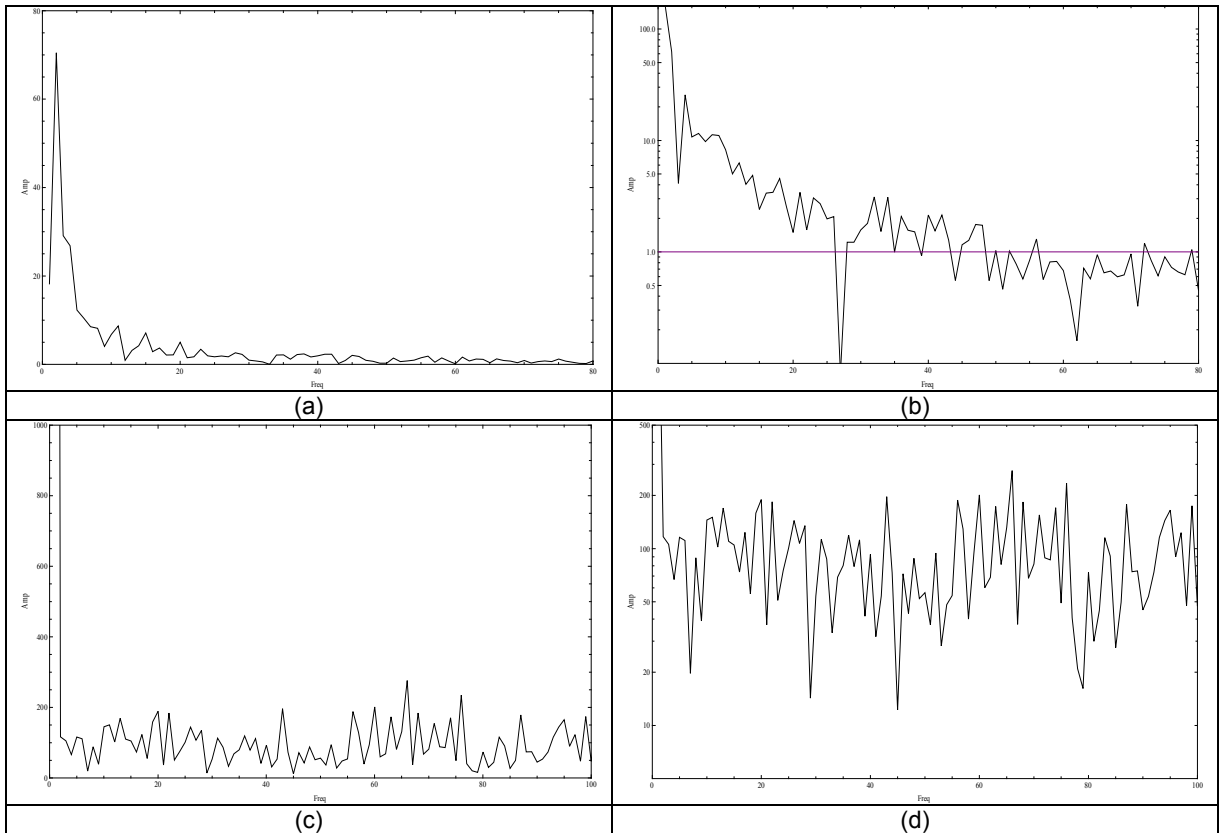
**Figure 50. Frequency spectra for bottom disk: a) spectrum on linear scale, b) spectrum on a log scale, c) spectrum on linear scale (complete spectrum of time history on  $2\pi$  scale); magnitude on , and d) spectrum on linear scale (expanded view of time history on  $2\pi$  scale).**

### Experimental results obtained with unbalanced mass attached to bottom disk

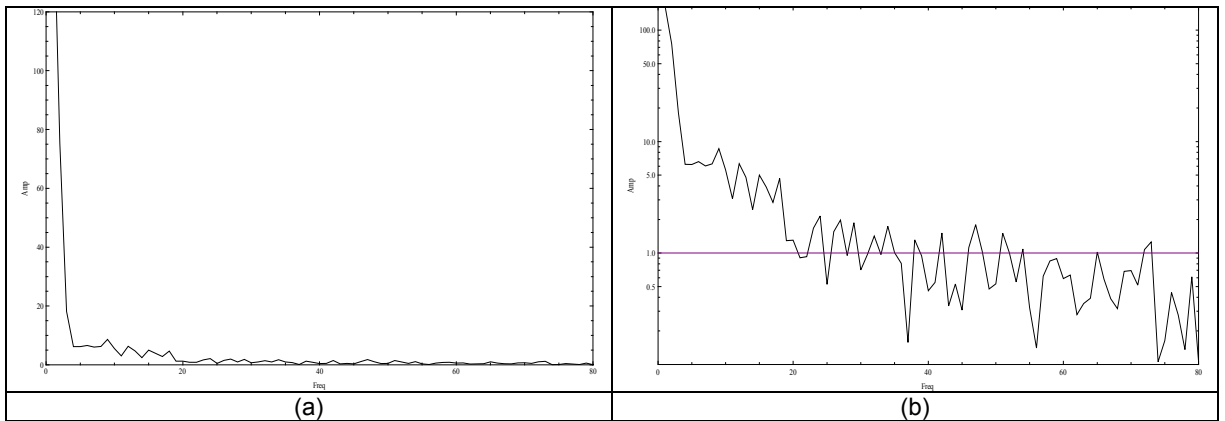
An unbalanced mass in the form of a bolt is attached to the bottom disk and the experiments are run at 100 rpm. The corresponding time histories and frequency spectra are shown in Figures 51 to 52. Due to the unbalance, the previously observed peak close to 7 Hz is shifted to the neighborhood of 8 Hz.



**Figure 51. Time histories: a) rotation angle of top disk, b) rotation angle of bottom disk, and c) difference between the rotations of the two disks. The rotation unit is degrees and the time unit is seconds.**



**Figure 52. Frequency spectra for top disk: a) spectrum on linear scale, b) spectrum on a log scale, c) spectrum on linear scale (complete spectrum of time history on  $2\pi$  scale); magnitude on ), and d) spectrum on linear scale (expanded view of time history on  $2\pi$  scale).**



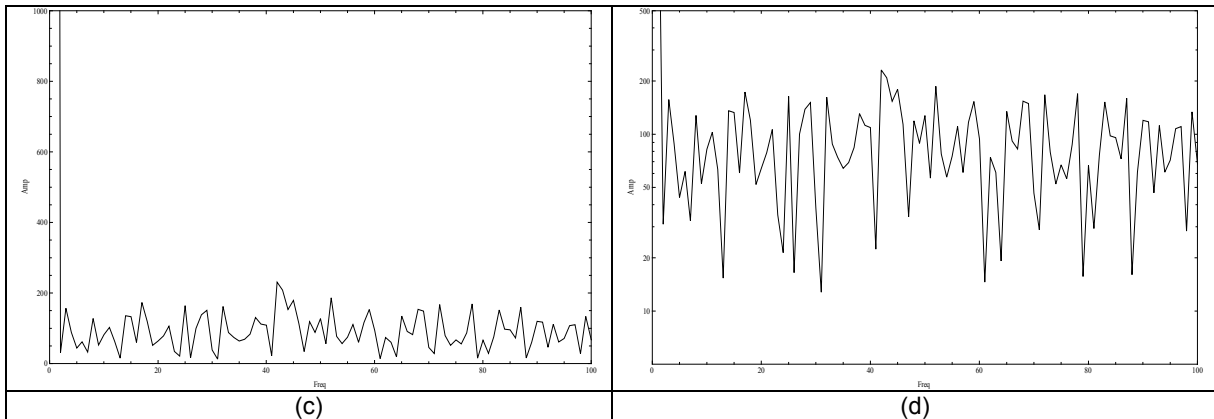


**Figure 53. Frequency spectra for bottom disk: a) spectrum on linear scale, b) spectrum on a log scale, c) spectrum on linear scale (complete spectrum of time history on  $2\pi$  scale); magnitude on ), and d) spectrum on linear scale (expanded view of time history on  $2\pi$  scale).**

### 4.3 Concluding Remarks and Recommendations for Future Work

Reduced-order models descriptive of drill-string dynamics with stick-slip interactions have been developed, and the results obtained from these models have been shown to qualitatively match experimental results. A unique experimental arrangement has been constructed at the University of Maryland to complement the experimental arrangement at the Petroleum Institute. It is believed that these experimental arrangements can be used to gain further insights into drill-string dynamics as well the means to control them. In future work, quantitative comparisons between the model predictions and the experimental observations can be made. It is also suggested that this arrangement be used to study horizontal drilling configurations as well.

### Key References

- [1] Leine, R. I., van Campen, D. H., and Keultjes, W. J. G. (2002). "Stick-Slip Whirl Interaction in Drill String Dynamics," *ASME Journal of Vibration and Acoustics*, Vol. 124 (2), pp. 209-220.
- [2] Melakhessou, H., Berlioz, A., and Ferraris, G. (2003). "A Nonlinear Well-Drillstring Interaction Model," *ASME Journal of Vibration and Acoustics*, Vol. 125 pp. 46-52.
- [3] Nayfeh, A. H. and Balachandran, B. (1995). *Applied Nonlinear Dynamics: Analytical, Computational, and Experimental Methods*, Wiley, New York.
- [4] Spanos, P. D., Chevallier, A. M., Politis, N. P., and Payne, M. L. (2003). "Oil and Gas Well Drilling: A Vibrations Perspective," *Shock and Vibration Digest* Vol. 35(2), pp. 85-103.
- [5] Mihajlović, N., van Veggel, A. A., van de Wouw, N., and Nijmeijer, H. (2004) "Analysis of Friction-Induced Limit Cycling in an Experimental Drill-String System," *ASME Journal of Dynamic Systems, Measurement, and Control*, Vol. 126(4), pp. 709-720.
- [6] Mihajlović, N., van de Wouw, N., Rosielle, P.C.J.N., and Nijmeijer, H. (2007) "Interaction between torsional and lateral vibrations in flexible rotor systems with discontinuous friction,"

*Nonlinear Dynamics*, published online.

### **Publications**

“*Drill String Dynamics*”, C.-M. Liao, B. Balachandran, M. Karkoub, and Y. Abdel-Magid, Twelfth Conference on Nonlinear Vibrations, Dynamics, and Multibody Systems, Blacksburg, VA, USA, June 1-5, 2008.

“*Reduced-Order Models of Drill String Dynamics*”, C.-M. Liao, B. Balachandran, M. Karkoub, and Y. Abdel-Magid, Second International Energy 2030 Conference, Abu-Dhabi, UAE, Nov. 2008.

“*Drill String Torsional Vibration Suppression Using GA Optimized Controllers*,” M. Karkoub, Y. Abdelmagid, and B. Balachandran, *Canadian Journal of Petroleum Technology*, submitted for publication, 2008.

“*Drill-String Vibrations: Reduced-Order Models and Experimental Results*,” C.-M. Liao, B. Balachandran, M. Karkoub, and Y. Abdel-Magid, *ASME Journal of Vibration and Acoustics*, in preparation for submission.

### **Visits**

Professor B. Balachandran visited PI and NDC from February 19 to February 24, 2006

Professor M. Karkoub visited UMD from Oct. 31 to Nov. 2, 2008.

### **GRA (names, degrees, graduation)**

Chien-Min Liao, Ph.D. candidate; expected to graduate in 2009; co-advised by Professors Balachandran and Karkoub.

## Developing Corporate Dashboards for Multi-Unit Firms/Plants: An Agent-Based Approach

UM Investigator: Dr. P. K. Kannan  
PI Investigators: Dr. Ali Almansoori, Dr. Saleh Al Hashimi, (Dr. Tareq Al Ameri, till August 2008)  
UM's GRA: Mr. Phillippe Kamaha  
Start Date: 15 May 2008  
FINAL REPORT

### 1. Abstract/Objectives

Multi-unit enterprises are defined as systems that are interconnected through complementary product/service categories and the markets they serve and through a common ownership of the enterprises that renders the problem of overseeing/managing these enterprises as a whole a complex task (see Figure 1 below). These units could be plants within a firm or firms within a multi-organizational setting.

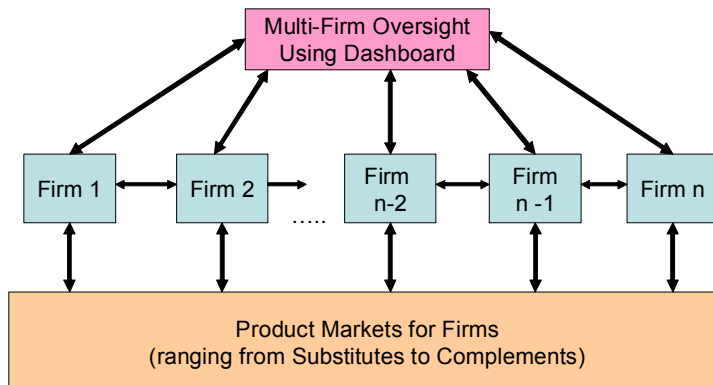


**Figure 1. Multi-unit oversight dashboard concept.**

Our project focuses on developing measurement systems that will incorporate interconnectedness among the units and provide clear guidelines at the multi-unit level through dashboards that will enable the management of such complex systems and improve the understanding of such systems. The project will also enable managers to understand the implications of their various policies and decisions at the multi-unit level through the use of agent-based models.

Given that the task of oversight is a complex one, our research focuses on (1) identifying the key performance variables, such as the impact of market forces and the management's own policies and decisions across units, from which the management would benefit most, (2) designing the measurement schemes across the multiple units that will encompass the areas of marketing metrics, new products/services, financial measures and key engineering performance measures, and (3) designing simulation studies to test the robustness of these measures under different markets and product-market scenarios (ranging from substitute markets to complement markets for the firms), and testing the sensitivity of these measures to policy changes and actions.

## 2. Justification and Background

In managing a multiple-unit firm (for example, a firm with multiple plants or a firm with multiple Strategic Business Units), the upper-level management needs a set of performance metrics to act as a dashboard, indicating how the different units are performing on key dimensions. Given the interaction between the different units and the interaction across customers they serve, designing such a dashboard is not an easy task. The dashboard cannot simply contain those metrics and measures that are used at the unit level because they might ignore such interactions. Finding the right set of measures for dashboard-based oversight of the multiple units is therefore a complex problem. Our objective in this project is to find the smallest set of metrics that are appropriately sensitive to the changes in the phenomena in which managers are interested in measuring. At the same time, the set of metrics must be robust to the noises in the environment, so that managers are able to “steer” the multiple units successfully in a turbulent environment.

## 3. Approach

The research team will start focusing on the multi-plant level problem with the following stages during the seed funding stage of the project:

- Stage 1:** Design of KPIs for multi-plant oversight. Plant level measures are being developed currently and will be shared with the PI team in the next meeting. These KPIs will enable the management of multiple plants at the corporate level using the developed dashboard.
- Stage 2:** Understanding robustness of corporate dashboard measures and specification for multi-plant oversight.
- Stage 3:** Agent-based simulations to understand the impact of market forces for the plants and firm.
- Stage 4:** Decision-support system for multi-plant oversight.

## 4. Summary of Results

### Project Activities (April-August 2008)

- UM and PI interacted through teleconference on May 20, 2008, during which the initial research ideas were presented to the PI team. The original research plan as presented later in this section was reviewed, and it was suggested that the problem might be modified to one of multi-plant problem within a firm to make the scope manageable.
- UM hired engineering student Phillipe Herve Kamaha to work on the project for the summer as well as for Fall 2008 and a high-school student, Wendell Shirley, for the summer 2008.
- Initial research activities focused on the first objective of the project as follows: determining key performance indicators (KPIs) across firms and understanding how they are impacted by market forces and interactions. Based on secondary research and refinement of the questions, the first phase of the two-phase project was developed as focusing on the skeletal design of the corporate dashboard. The specific areas we focused on were: (1) What should be measured and why? (2) Key measures and their interrelationships, (3) Integration of commonly used measures in marketing, finance, engineering and (4) Specifying the insides of the dashboard.
- Based on secondary research, the following areas of initial focus were identified:

### ***Interrelationship Between Firms***

- Focus on manufacturing and manufacturing-based relatedness, synergy, and coordination
- Focus on primary value activities of each firm
- Incoming logistics, operations, outbound logistics, market and sales, and service
- Supporting functions: technology development, procurement, human resources management, and administration
- Interrelationships based on the above value chain

The interrelationships in the manufacturing related activities will include (1) raw materials – that is, the types of and processes for acquiring raw materials; (2) product and process science/technology – specifically, the theoretical principles underlying the design and manufacture of products, and (3) resource conversion - the equipment, processes, and procedures used to apply the technical and scientific principles to the conversion of raw materials into end products. From the marketing and market related activities the interrelationships will focus on (1) marketing – the processes and methodologies used to market the products, and (2) market interrelationships – the degree to which customers are common for the firms, substitutability and complementarity of the products of firms, etc.

### ***Focus on Specific Measures***

The following measures were examined as candidates for the key performance indicators (KPIs) focusing on manufacturing and marketing/sales activities. These measures are used by each firm's management as well as by managements interested in multi-firm oversight across all firms. (These measures can also be tailored to the problem of multi-plant oversight within a firm, in which case these measures will be defined at the plant level and across plants).

#### ***Cost Drivers***

- Economies of scale – factories, equipment and logistics scale
- Capacity utilization – factory/plant utilization
- Linkages – with suppliers and distributors
- Integration – backward into supplies, forward into distribution
- Timing of new capacity, new facility, and new technology investments
- Location of plants, warehouses
- Discretionary policies that affect costs

#### ***Uniqueness drivers***

- Capacity or inventory available to provide delivery as requested
  - Quality specifications and tolerances
  - New product-process development processes
  - System-wide flexibility and responsiveness to design changes
- ***Revised Problem Formulation and Research Design:*** Given the discussion with PI and the objective of making the problem more manageable and focused, the problem context was changed to a ***multi-plant*** environment rather than a multi-firm environment. A sample framework has been developed as follows:
    - The problem considers production at an industrial chemical multi-plant facility. The initial focus is on determining production rates and schedules of multiple products in the multi-plant facility to meet customer orders and inventory targets. The plant process requirements and quality requirements are also considered.

- We consider four plants to start with – two plants of Type 1 and two plants of Type 2. Type 1 plants can produce multiple products – one at a time. Type 2 plants produce products which require input of final products from the Type 1 plants. The schematic can be shown as follows:

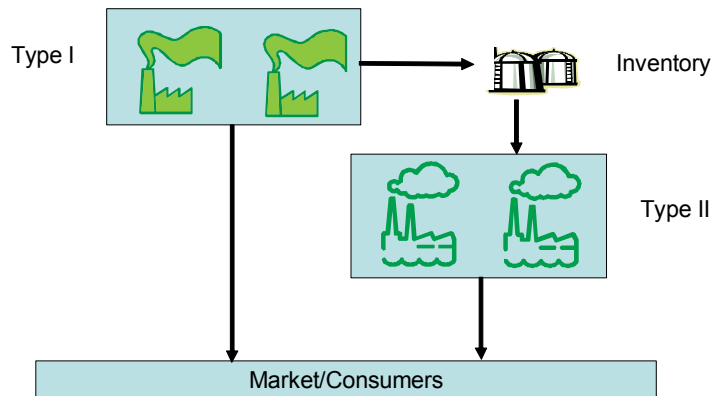


**Figure 2. Schematic of the multi-plant firm.**

- There are interdependencies between the plants as shown because of the intermediate products and shared resources. The problem we consider is one of planning and scheduling the products so that the customer demands are met and stock-outs are minimized. If the demand and constraints are known deterministically, this problem can be solved using optimization methods. However, we incorporate uncertainties and interactions among markets and consumers, so they cannot be solved easily using optimization techniques. (For example, the products could be substitutes/complements, in which case, if there is a stock-out of one, some consumers may choose to use another one instead of going away from the market). We will formulate the deterministic problem (using expected values of the uncertain distributions) as an optimization problem so that it can be used as a benchmark.
- The focus in this problem is on performance metrics. Given the above problem setup, we will determine a list of recommended performance metrics, submetrics, and sub-submetrics, both at the plant level and the overall firm level. These metrics could be related to the set of metrics identified in the previous bullet points. We will examine several questions at this stage: (1) which of the above metrics are used by different stakeholders (e.g., plant managers, firm level managers), and how do they relate? How often should these metrics be monitored: per month, per quarter, or in real time? (For example, at the strategic level they could be measured less often.) Which metrics are sufficient? When do the metrics enter a “danger zone” that require managerial action?
- The next step is the design of agent-based simulation model that would explain how the performance metrics react to environmental and managerial control factors. In addition to these, interaction among customers in the market will be taken into account. This simulation will be carried out in stages, starting from a simple model with few variables to gradually building a more sophisticated model with many variables and interactions.

- Based on the results of the simulation, we will perform sensitivity analysis, optimization and robustness analysis of the metrics simulation model. Sensitivity analysis, in addition to validating the simulation model, will provide insights into how the performance metrics help and will identify the critical performance metrics and the critical control factors. We will also examine the robustness of the performance metrics. Based on the analysis, the overall objective of this step is to identify the best set of performance metrics that should go into the dashboard of the upper management to optimally control the multi-plant setup.
- The UM team started examining the simulation test bed – NetLogo environment – so that the multi-plant setup can be modeled. Currently, the team is modeling simple setups of the problem with 4 plants and a closed market of customers, and examining the impact of various control variables on meeting customer demand and on stock-outs.

### **Project Activities (September-December 2008)**

- With the departure of Dr. Tareq Al Ameri from PI, the project team interacted with Dr. Ali Almansoori and Dr. Saleh Al Hashimi on continuing the project and discussed the model development with them. A framework for a multi-plant problem within a refinery setting has been developed to tie the research more closely with PI's research contexts based on the comments from Dr. Al Hashimi and Dr. Almansoori.
- UMD and PI interacted through teleconference on September 3<sup>rd</sup> and 17<sup>th</sup>. The revised research plan as presented later in this section was reviewed and it was suggested that the problem might be modified to one of multi-plant problem within a firm to have the scope manageable.
- UMD hired Engineering student Phillippe Herve Kamaha to work on the project for Fall 2008.
- **Revised Problem Formulation and Research Design:** Given the discussion with PI and with the objective of making the problem more manageable and focused, the problem context was changed to a multi-plant refinery environment. A sample framework has been developed as follows:
  - The problem considers production at a multi-plant refinery. The initial focus is on determining production rates and schedules of multiple distillates in the multi-plant facility to meet customer orders and inventory targets. The plant process yields and capacity constraints are also considered. The figure below (Figure 3) provides the outline of the model.

## Schematic of the Model

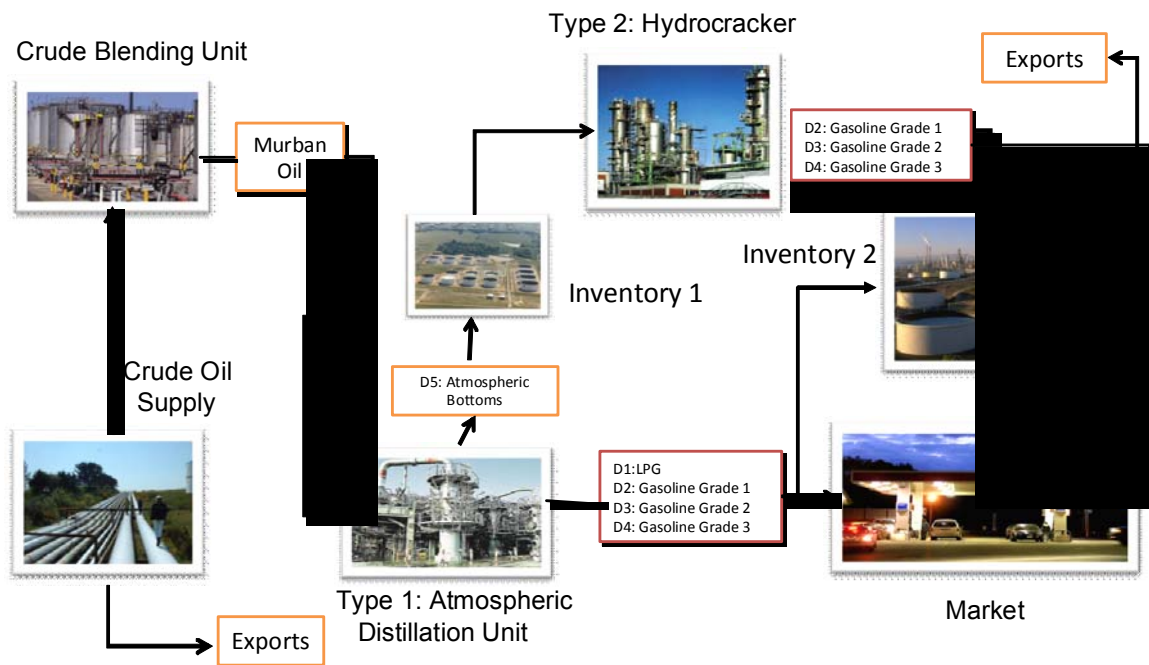


Figure 3. Schematic of the multi-plant refinery.

- There are interdependencies between the plants (Atmospheric Distillation Unit and the Hydrocracker) as shown because of the intermediate products and shared resources. The problem we consider is one of planning and scheduling the products so that the customer demands are met and stock-outs are minimized. If the demand and constraints are known deterministically, this problem can be solved using optimization methods. However, we incorporate uncertainties and interactions among markets and consumers, so they cannot be solved easily using optimization techniques. (For example, the products could be substitutes/complements in which case, if there is a stock-out of one, some consumers may choose to use another one instead of going away from the market). We will formulate the deterministic problem (using expected values of the uncertain distributions) as an optimization problem so that it can be used as a bench-mark.
- The benchmark optimization problem is formulated as below. First we provide the nomenclature and then provide a schematic of the problem.

**Table 1. Nomenclature**

<b>Index, Variables and Parameters</b>	<b>Description</b>
$t$	Index of Time, $t = 1, 2, \dots, T$
$T$	Maximum Planning Horizon
$x_t$	Input of Murban Oil – Volume/Time – in time $t$
$e_1$	Yield of Distillate D1 (LPG) from one unit volume of Murban oil
$e_2$	Yield of Distillate D2 (Gasoline Grade 1)
$e_3$	Yield of Distillate D3 (Gasoline Grade 2)
$e_4$	Yield of Distillate D4 (Gasoline Grade 3)
$e_5$	Yield of Distillate D5 (Atmospheric Bottoms)
$l-f_{1t}$	Fraction of Distillate D1 from Atmospheric Distillation Unit (ADU) inventoried at Inventory 2 in time $t$
$l-f_{2t}$	Fraction of Distillate D2 from ADU inventoried at Inventory 2 in time $t$
$l-f_{3t}$	Fraction of Distillate D3 from ADU inventoried at Inventory 2 in time $t$
$l-f_{4t}$	Fraction of Distillate D4 from ADU inventoried at Inventory 2 in time $t$
$l-g_t$	Fraction of Distillate D5 (atmospheric bottoms) inventoried at Inv 1 at time $t$
$l-h_{2t}$	Fraction of Distillate D2 from Hydrocracker inventoried at Inventory 2 at time $t$ .
$l-h_{3t}$	Fraction of Distillate D3 from Hydrocracker inventoried at Inventory 2 at time $t$ .
$l-h_{4t}$	Fraction of Distillate D4 from Hydrocracker inventoried at Inventory 2 at time $t$ .
$d_{it}$	Demand for Distillate $i$ ( $i=1,2,3,4$ ) from market at time $t$
$vs_{it}$	Supply from Inventory 2 to market of Distillate $i$ ( $i=1,2,3,4$ ) at time $t$
$ve_{it}$	Export from Inventory 2 of Distillate $i$ ( $i=1,2,3,4$ ) at time $t$
$C_o$	Cost of Murban Oil per unit volume
$p_{it}$	Price of Distillate $i$ ( $i=1,2,3,4$ ) in the market at time $t$ .
$pe_{it}$	Export price of Distillate $i$ ( $i=1,2,3,4$ ) at time $t$

In addition, we have capacity constraints on inventories at Inv 1 and Inv 2, capacity of Atmospheric Distillation Unit, Hydrocracker. For now, we have assumed the processing costs at AMU and Hydrocracker to be fixed and sunk (but these could be tied to the volume of Murban crude oil processed).

- o The benchmark optimization problem is as follows:

## Model with Input and Output

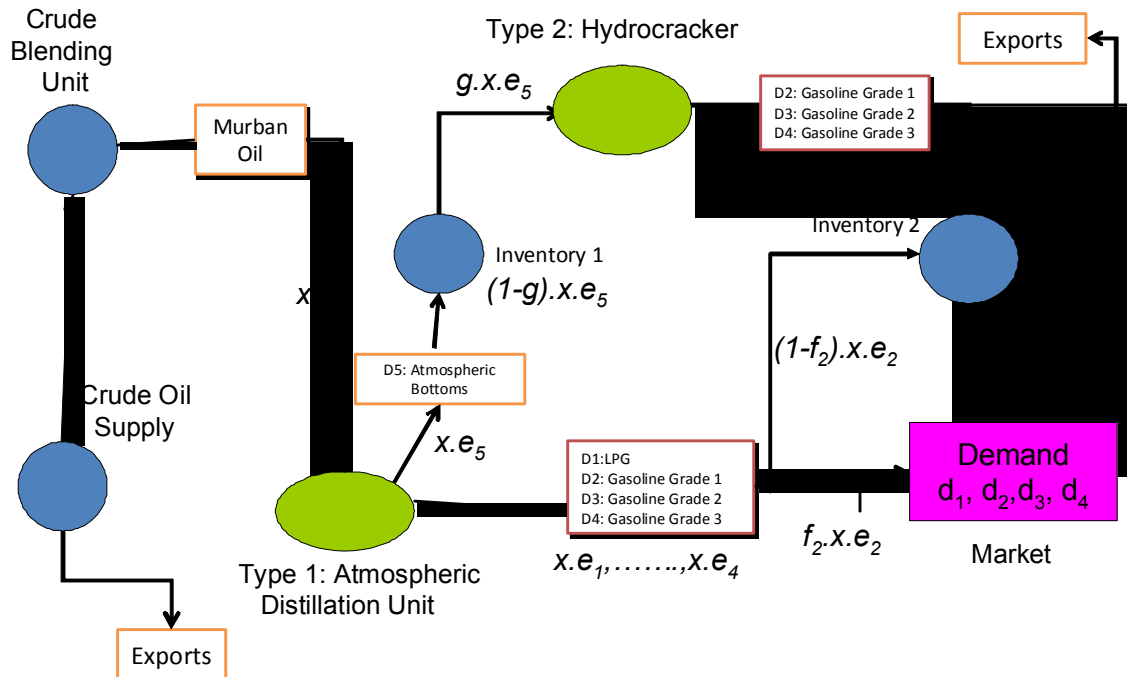


Figure 4. Model flows for the optimization problem

**Formulation of an optimization problem to meet the demand and maximize profits (revenues – cost):**

Revenues = Revenue from local market + Revenues from Export

Revenues from local market = price X demand for each distillate for each time period in the planning horizon

Revenues = Export prices X amount of each distillate exported

Costs = Cost of Murban oil X Volume processed for each time in the planning horizon

**Maximize:** Revenues – Costs

**Subject to Constraints**

1. Inventory Constraints
2. Meeting local demand constraints
3. Capacity constraints at AMU, Hydrocracker, Inventory 1 and Inventory 2

**Decision Variables:**

1. Volume of Murban Crude Oil to be processed in each period  $X_t$
2. Inventory decision variables – fraction of distillates to be inventoried at each inventory location – Inv 1 and Inv 2 – of the different distillates D1 through D5 for each time period
3. Volume of distillates exported in each period

The above optimization problem is deterministic. However, in actual practice, there are uncertainties in the yields which may vary over time, and uncertainties in demand which can vary over time. In addition, the prices of the distillates can change over time as a function of the demand, and there could be substitutability and complementarity relationships between the distillates demanded by the market. To model these complexities, we use an agent-based model.

Agent-based models can capture many complexities that an ordinary optimization formulation in a deterministic setting cannot capture. While the decision variables for the managers still remain the same, we are interested in exploring how they can dynamically set their decisions as a response to these demand and yield complexities.

- **Where do the dashboards come into picture?**
- Dashboards provide the measurements on the key variables in the system over time. Thus, some dashboards can provide the status of prices of the distillates in the local market and the demand information. Some may provide details on inventory levels of each distillate in each inventory locations. They can also provide instantaneous feedback on the impact of changing a decision variable on the system output such as revenues and profits. They become part of the decision support system that allows managers to understand the relationships between different variables and helps to guide them in making the appropriate decisions.
- Our objective, therefore, is to understand how to design these dashboards based on the model structure and the complexities we are considering and help design dashboard systems that will enable managers to make better decisions to optimize performance (maximize profits, for example).
- The focus in this problem is on performance metrics. Given the above problem setup, we will determine a list of recommended performance metrics, submetrics, and sub-submetrics, both at refinery level and overall firm level. These metrics could be related to the set of metrics identified in the previous bullet points. We will examine several questions at this stage: (1) which of the above metrics are used by different stakeholders (e.g., plant managers, firm level managers), and how do they relate? How often should these metrics be monitored: per month, per quarter, or in real time? (For example, at the strategic level they could be measured less often). Which metrics are sufficient? When do the metrics enter a “danger zone” as in a dashboard that require managerial action?
- The next step is the design of agent-based simulation model that would explain how the performance metrics react to environmental and managerial control factors. In addition to these, interaction among customers in the market will be taken into account. This simulation will be carried out in stages – starting from a

simple model with few variables to gradually building a more sophisticated model with many variables and interactions.

- Based on the results of the simulation, we will perform sensitivity analysis, optimization and robustness analysis of the metrics simulation model. Sensitivity analysis, in addition to validating the simulation model, will provide insights into how the performance metrics help, identify the critical performance metrics and the critical control factors. We will also examine the robustness of the performance metrics. Based on the analysis, the overall objective of this step is to identify the best set of performance metrics that should go into the dashboard of the upper management to optimally control the multi-plant setup.
- The UM team has started examining the simulation test bed – the NetLogo environment – so that the multi-plant setup can be modeled. Currently, the team is modeling simple setups of the problem with four plants and a closed market of customers, and we are examining the impact of various control variables on meeting customer demand and on stock-outs (customer service). A demonstration of the problem in Net Logo was presented to PI researchers during the November trip to Abu Dhabi.

## 5. Recommendations for Future Work

- The prototype of the agent-based model will be refined to create a demonstration tool so that the power of the methodology becomes evident to all (this is currently being carried out).
- During the visit of UMD PI – P. K. Kannan – to Abu Dhabi, there was discussion with both Dr. Almansoori and Dr. Al Hashimi, with regard to the scope of the problem. It was felt that while the suggested model will be a good example to showcase the power of agent-based models, it was necessary to understand the exact problem faced by managers in refinery setting to formulate a more realistic problem. It was decided that the UMD students working on the project will visit Abu Dhabi in the next few months to discuss and demonstrate the prototype to managers and study and model their actual problems better. The UMD PI may also visit Abu Dhabi in the near future to complement this work. It is important to understand clearly the decisions managers face and model those business decisions using agent-based models. The resulting dashboard will be much more useful in that context.
- UMD will also formulate the optimization problem that will serve as a benchmark based on the above metrics. The outline has been given above. It is also necessary to link the engineering/operation optimization problem with the business problem to make the model/application more realistic. This is being done currently in collaboration with Dr. Azarn and his student team.
- A research paper based on the above work in being written up currently and will be available for circulation in the next month. We hope that the project can be continued to have the working paper ready for journal submission.

## 6. Conclusion

This project was started about six months ago based on a seed-funding from EERC and in this span of time, the researchers have been able to demonstrate the usefulness of the agent-based methodology in tackling the design of decision support for a problem such as refinery decision making. While the research has so far focused on an example problem, the real contributions of this methodology will materialize once an actual decision situation in the refinery setting is studied and modeled. The recommendations for future work clearly focus on these issues and it is hoped that the project can be continued to make the intended impact for PI and its sponsors.

## 7. References

- [1] Jackson, Jennifer R, Jeanna Hoffman, John Wassick, and Ignacio E. Grossman, "A Nonlinear Multiperiod Process Optimization Model for Production Planning in Multi-Plant Facilities," Working paper, Carnegie Mellon University. 2002.
- [2] Kleijnen, Jack PC and Martin T Smits, "Performance Metrics in Supply Chain Management," Journal of the Operational Research Society, 2003.
- [3] Gargeya, Vidyaranya B, "Plant Level Performance Measurement: An Exploratory Case Study of a Pharmaceutical Encapsulation Company," Technovation, Vol. 25, Issue 12, 2005, p. 1457-1467.
- [4] Kaplan, Robert S. and David P. Norton, "Using the Balanced Scorecard as a Strategic Management System," Harvard Business Review, Jan-Feb, 1996, p. 75-85.
- [5] Birkinshaw, Julian and Mats Lingblad, " Intrafirm Competition and Charter Evolution in the Multibusiness Firm," Organization Science, Vol. 16, No. 6, Nov-Dec, 2005.
- [6] Robins, James and Margarethe F. Wiersema, "A Resource-Based Approach to the Multibusiness Firm: Empirical Analysis of Portfolio Interrelationships and Corporate Financial Performance," Strategic Management Journal, Vol. 16, No. 4 (May) 1995, p. 277-299.
- [7] NetLogo, <http://ccl.northwestern.edu/netlogo/>
- [8] Suresh S. Pitty, Wenkai Li, Arief Adhitya, Rajagopalan Srinivasan, I.A. Karimi, "Decision support for integrated refinery supply chains, Part 1. Dynamic simulation," Computers and Chemical Engineering 32 (2008) 2767–2786
- [9] Lee Ying Koo, Arief Adhitya, Rajagopalan Srinivasan, I.A. Karimi, "Decision support for integrated refinery supply chains, Part 2. Design and Operations," Computers and Chemical Engineering 32 (2008) 2787–2800

## 8. Publications

None currently, but a working draft is being prepared and will be ready in a month.

## 9. Visits

The UMD PI – P. K. Kannan – made a visit to Petroleum Institute on November 1-3, 2008 and discussed the progress on the project with Dr. Al Almansoori and Dr. Saleh Al Hashimi. It was decided at the meeting that, as part of the project, the UMD students and UMD PI will make a visit with the PI sponsors and learn more about their actual problem context in order to develop a more realistic decision model.

## 10. GRA (names, degrees, graduation)

Mr. Phillipe Herve Kamaha started on this project in Fall 2008 as a Ph. D. student in the Mechanical Engineering department. He will continue this program and will use this project as his dissertation work.

## **Development of a Probabilistic Model for Degradation Effects of Corrosion-Fatigue-Cracking in Oil and Gas Pipelines**

UMD Investigator: Prof. Mohammad Modarres

GRA : Mohamed Chookah

Faculty Research Assistant: Mohammad Nuhi

PI Investigator(s): Prof. Abdennour Seibi

Final Report

### **1. Objectives/Abstract**

This study involves developing and applying an engineering-based (mechanistic) probabilistic model for health management of oil pipelines in process plants. The study involves two interrelated projects. The first project, which is the topic for a PhD dissertation, focuses on model development and demonstration. The second project involves developing a degradation acceleration lab at PI and performing experiments to further validate the proposed models of the first project. The funds made available by the Petroleum Institute will facilitate building the experimental set-up. Mr. Mohamed Chookah is working on the first project. When the research equipment is ready to install, a new student will be added to perform validation experiments (that is, to work on the second project.) Mr. M. Nuhi was hired as a Faculty Research Assistant to support the mechanistic failure part of the research.

The overall objective of this study is to propose and validate a probabilistic mechanistic model based on the underlying degradation phenomena whose parameters are estimated from the observed field data and experimental investigations. Uncertainties about the structure of the model itself and parameters of the model will also be characterized. The proposed model should be able to capture wider ranges of pipelines rather than only the process ones. Thus, the proposed model will better represent the reality of the pipeline's health and can account for material and size variability. The existing probabilistic models sufficiently address the corrosion and fatigue mechanisms individually, but are inadequate to capture mechanisms that synergistically interact. Admitting the fact that capturing all degradation mechanisms will be a challenging task, the new model will address pitting corrosion followed by corrosion enhanced fatigue-crack growth.

### **2. Approach**

The researchers identified a focal point in one of ADNOC's operating companies, such as TAKREER, which provided data pertinent to the core activities of this research study. The study consisted of two interrelated projects that will run over a period of two years and a half. The first phase of Project 1 focused on the development of a PhD thesis proposal, which encompassed the latest technological development and ongoing research activities and outlined the subject of the research project. The second phase concentrated on the development of a probabilistic model for piping in process plants followed by model validation through collected experimental and field data. The second project, which started a year later, focused on the design, construction and commissioning of the corrosion-fatigue test cell. The test rig will be designed and built by the research team at the University of Maryland (UMD) with the assistance of Dr. Abdennour Seibi from the Petroleum Institute (PI). The third phase of this study will deal with model application to ADNOC process facilities in order to predict their remaining service life.

The test rig, which was to be built at PI, was delayed and temporary installed at UMD and was used by GRA-2 to conduct an accelerated degradation experimental study reflecting field conditions for model validation developed in project 1. The equipment consists of CORTEST corrosion-fatigue test cells, autoclaves, multiphase flow loops, and testing machines for slow

strain rate and crack growth testing. The equipment will be transferred to PI upon mutual agreement of timing and when a permanent laboratory space becomes available. This activity also requires a complete line of monitoring equipment for evaluation of corrosion, scaling, and chemical treatment for field and laboratory.

### 3. Two-Year Schedule

#### Project 1:

1. PhD thesis proposal, which will include a literature search (9/1/2006 - 6/30/2007)
2. Data collection from ADNOC process plants (1/1/2007 - 8/30/2007)
3. Prof. Modarres visit to PI to review progress and plan for accelerated lab development (3/2007).
4. Dr. Seibi visit to UMD to advise PhD student in his thesis work and assist in designing the accelerated Testing Facility (11 – 21 May/2007).
5. Empirical/Engineering-Based Model Development (9/1/2006 – 6/30/2007)
  - a. Streamlining of the model to pipeline/pressure vessel application.
  - b. Collection of appropriate data (data availability is at the discretion of ADNOC operating companies).
  - c. Actual model development.
6. Probabilistic estimation of model parameters (9/1/2007 – 12/31/2007)
7. Application example (11/1/2007 – 2/15/2008)
8. Dr. Seibi visit to UMD for thesis proposal defense and thesis defense (dates to be announced).

#### Project 2:

1. Design, construction, and commissioning of Accelerated Degradation Lab at PI. UMD research team will design the test facility with the assistance of Dr. A. Seibi from PI (6/1/2007 - 12/31/2007).
2. Test planning (8/1/2008 – 9/31/2008). Dr. Seibi will visit UMD for two weeks during this period to jointly develop the test plan with UMD researchers.
3. Experimental test for model testing/validation (1/1/2008 - 12/31/2008)
4. Examples of model applications (9/1/2008 – 12/31/2008)
5. Conference and archival paper.

### 4. Summary of Results

The following is a summary of the adopted simulation model.

#### Pitting Corrosion Model

To assess the influence of concurrent pitting corrosion, a simplified model for pit growth proposed by Harlow and Wei was used [9]. The model is patterned after that proposed by Kondo [10] and assumes a pit of hemispherical shape growing at constant volumetric rate in accordance with Faraday's law from an initial radius  $a_0$ . The rate of pit growth (with volume  $V = (2/3)\pi a^3$ ) is given as follows:

$$\frac{da}{dt} = \frac{da}{dV} \frac{dV}{dt} = \frac{1}{2\pi a^2} \frac{dV}{dt}$$

But assuming  $\rho$  is constant,

$$m = \rho V \Rightarrow \frac{dm}{dt} = \rho \frac{dV}{dt} \Rightarrow \frac{dV}{dt} = \frac{1}{\rho} \frac{dm}{dt}$$

From Faraday's Law,

$$m = \frac{MI_p t}{\eta F} \Rightarrow \frac{dm}{dt} = \frac{MI_p}{\eta F}$$

Hence by substitution,

$$\frac{da}{dt} = \frac{MI_p}{2\pi\eta\rho F} \frac{1}{a^2}$$

where,

$$I_p = I_{p_0} \cdot \exp\left(-\frac{E_a}{RT}\right)$$

and  $a$  is the pit radius at time  $t$ ;  $M$  is the molecular weight of metal;  $I_p$  is the pitting current;  $I_{p_0}$  is the pitting current coefficient;  $\eta$  is the metal's valence;  $\rho$  is the density of the metal;  $F = 96,514$  C/mole is Faraday's constant;  $E_a$  is the activation energy;  $R = 8.314$  J/mole-K is the universal gas constant; and  $T$  is the absolute temperature.

### **Corrosion Fatigue Crack Growth Model**

#### **Electrochemical Model**

For the electrochemical reaction contribution, the surface coverage  $\theta$  is identified with the ratio of the amount of charge transferred during each loading cycle ( $q$ ) to that required to completely "repassivate" the bared surface ( $q_s$ ), or, more conveniently,

$$\theta = (q / q_s)$$

For this purpose, a simplified model for the reaction is used: for example, it is assumed that the underlying electrochemical reaction consists of a single step and is represented by thermally activated, first-order kinetics [1, 11]. The bare surface reaction current and charge densities are represented in simple exponential forms,

$$i = i_0 \exp(-kt)$$

$$q = \frac{i_0}{k} \{1 - \exp(-kt)\}$$

$$q_s = \frac{i_0}{k}$$

$$k = k_0 \exp\left(-\frac{E_a}{RT}\right)$$

where  $i_0$  is the peak current density (initial rate of reaction on the clean (bare) surface), and  $k$  is the reaction rate constant in Arrhenius form. Thus,

$$\theta = 1 - \exp\left(-\frac{k}{\nu}\right) = 1 - \exp\left[-\frac{k_0}{\nu} \exp\left[-\frac{E_a}{RT}\right]\right]$$

where  $\nu = \text{frequency} = \frac{1}{t}$ .

### **Mechanistic Model**

For mechanistic understanding of the problem, the following mechanistic model for fatigue crack growth was chosen. It is assumed that both parts of the above superposition equation can be modeled by the power law (Paris-Erdogan relationship) [12] of the form,

$$\frac{da}{dN} = C(\Delta K)^n$$

*i.e.*

$$\left(\frac{da}{dN}\right)_r = C_r (\Delta K)^{n_r}$$

$$\left(\frac{da}{dN}\right)_c = C_c (\Delta K)^{n_c}$$

where

$$\Delta K = \beta \Delta \sigma \sqrt{(\pi a)}$$

with  $\Delta \sigma$  being the far field stress range, and  $\beta$  a geometric parameter.

The coefficients  $C_r$  and  $C_c$  reflect material properties, and the exponents,  $n_r$  and  $n_c$ , reflect the functional dependence of crack growth-rate on the driving force  $\Delta K$ .

Incorporating the electrochemical and mechanical relations yields a simple differential equation in that the variables  $a$  and  $N$  can be separated. Estimation of parameters  $n_r$  and  $n_c$  may require numerical integration [1].

### **Superposition Model**

A superposition model proposed by Wei [13] was adopted. In the most general form the fatigue crack growth rate is given by [7]:

$$\left(\frac{da}{dN}\right)_e = \left(\frac{da}{dN}\right)_{\text{cycle}} + \left(\frac{da}{dN}\right)_{\text{time}}$$

with a cycle-dependent rate and a time-dependent rate. Within each of these rates, the mechanical (deformation) and environmental contributions are treated as being from independent parallel processes.

The corrosion fatigue model becomes

$$\left(\frac{da}{dN}\right) = C_r \left(F \Delta \sigma \sqrt{(\pi a)}\right)^{n_r} (1 - \theta) + C_c \left(F \Delta \sigma \sqrt{(\pi a)}\right)^{n_c} \theta$$

From the solution of this equation, we can estimate the  $N$  as follows:

$$N_{cg} = \int_{a_{tr}}^{a_f} \frac{da}{C_r (F\Delta\sigma\sqrt{\pi a})^{n_r} (1-\theta) + C_c (F\Delta\sigma\sqrt{\pi a})^{n_c} \theta}$$

where  $a_f$  and  $a_{tr}$  are the final and initial crack sizes, respectively.

$a_{tr}$  could be calculated iteratively using the criterion set earlier,

$$(\Delta K)_{pit} \geq \Delta K_{th} \quad \text{and} \quad \left(\frac{da}{dt}\right)_{crack} \geq \left(\frac{da}{dt}\right)_{pit}$$

which reflects equality between the pitting and cracking rates at the onset of crack growth,

$$\begin{aligned} \left(\frac{da}{dt}\right)_{pit} &= \left(\frac{da}{dt}\right)_{crack} \\ \frac{MI_p}{2\pi\rho F a_{tr}^2} &= C(\Delta K)^n \\ a_{tr}^2 (\Delta K)^n &= \frac{MI_p}{2\pi\rho F C_F f} \\ a_{tr}^2 (\beta\Delta\sigma\sqrt{\pi a_{tr}})^n &= \frac{MI_p}{2\pi\rho F C_F f} \end{aligned}$$

The corrosion-fatigue life  $N_F$  is the sum of the number of loading cycles over which pitting and fatigue cracking dominates at a given stress level [7] and is given by

$$N_F = N_{pit} + N_{cg}$$

Generic data (from the related papers) was used to build and run the computer routine Matlab for corrosion fatigue according to Wei's superposition model.

**Table 1. Generic parameters for X70 steel used as deterministic values [1]**

Universal gas constant	R = 8.314 J/mol-K
Activation energy	$E_a = 35$ KJ/mol
Fatigue exponent	$n_r = 2$
Corrosion fatigue exponent	$n_c = 2$
Frequency	$\nu = 0.1 - 10$ Hz
Applied stress range	$\Delta\sigma = 100 - 500$ Mpa
Temperature	T = 293 - 723 K
Final crack size	$a_f = 25$ mm
Shape Factor	$\beta = 1.24$
Faraday's constant	F = 96,514 C/mole
Molecular weight	M = 55 g/mole
Valence	$\eta = 3$
Density	$\rho = 7.87$ g/cm <sup>3</sup>

**Table 2. Weibull distribution parameters for X70 steel used as probabilistic values [1]**

Random Variable	$\alpha$ (shape factor)	$\beta$ (scale factor)	$\gamma$
$C_r$	12	$4.0 \times 10^{-11}(\text{m/cyc})(\text{MPa}\sqrt{\text{m}})^{-2}$	0
$C_c$	8	$2.0 \times 10^{-10}(\text{m/cyc})(\text{MPa}\sqrt{\text{m}})^{-2}$	0
$\kappa_0$	10	$3.0 \times 10^5 (\text{s}^{-1})$	0

An exponential distribution is assumed for the Current Density ( $I_p$ ) using the data in [14]. The pdf of  $I_p$  is

$$f(I_p) = \frac{1}{4.44 \times 10^{-3}} e^{-4.44 \times 10^{-3} I_p}$$

The flowchart shown in Figure 1 outlines the steps followed in assessing the required variables in our proposed model:

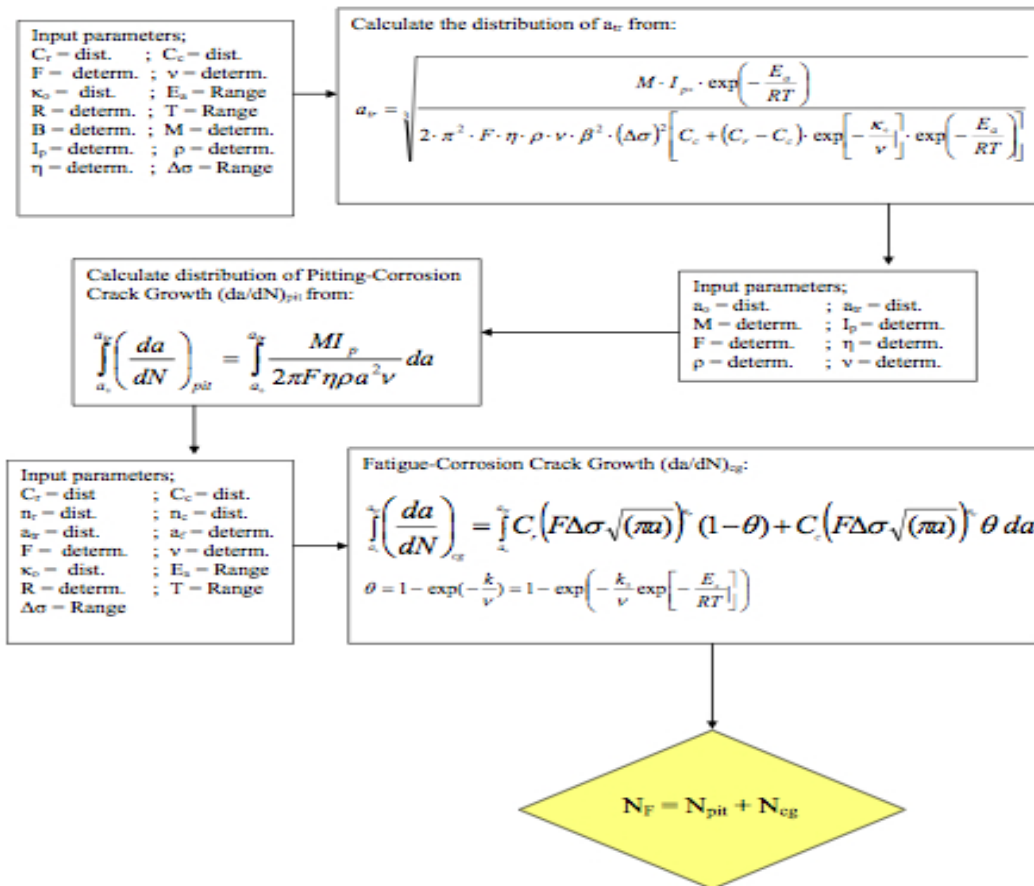


**Figure 1. Simulation algorithm of the computational method applied in the research.**

We developed simple empirical parametric models estimated from curve fitting of data obtained from the computer simulation, as shown below.

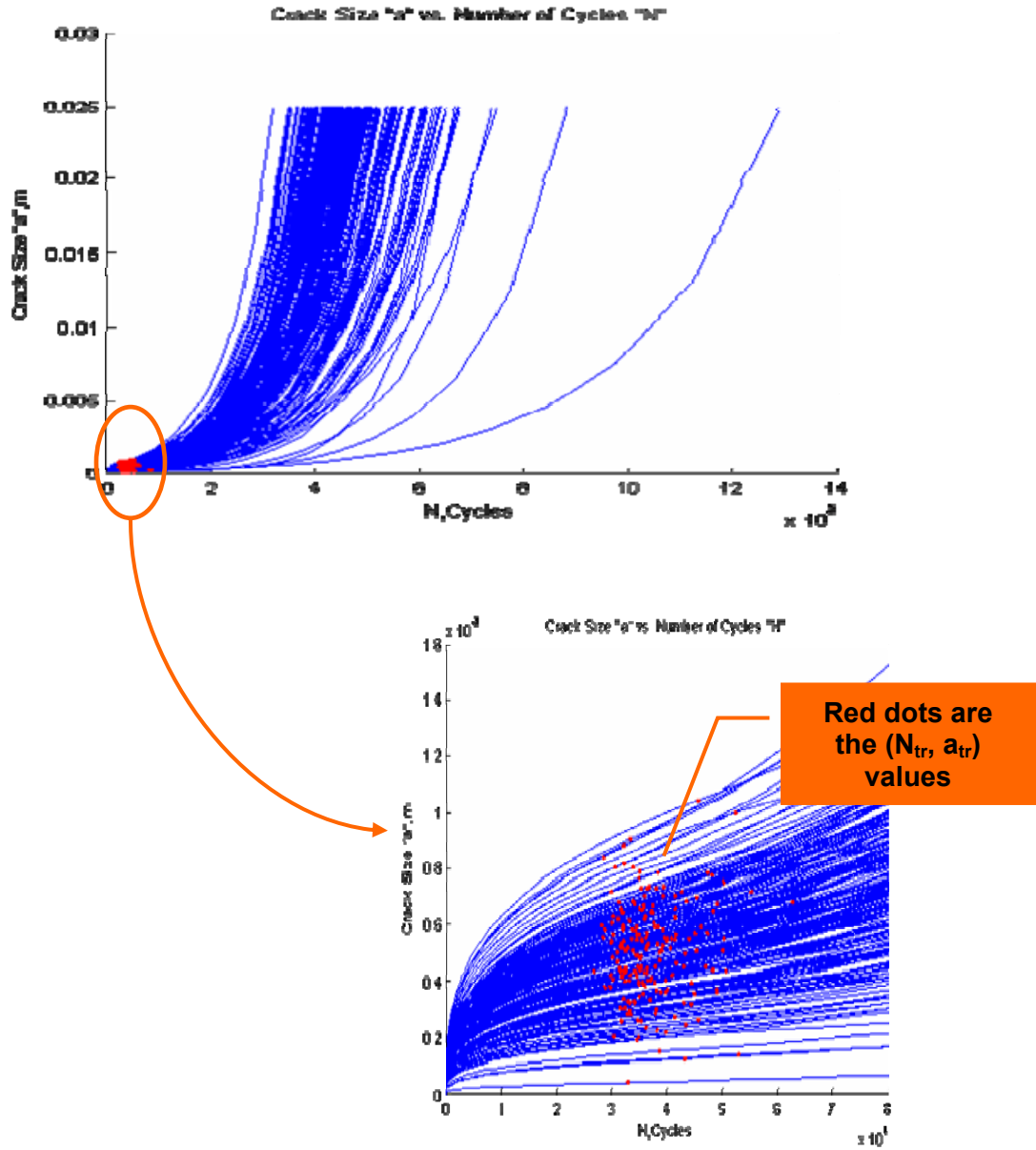


Figure 2. The results of the simulation.

Through an extensive trial and error process, a simplified general parametric empirical model is proposed as follows:

$$a = C_1 \cdot N^{1/3} + C_2 \cdot N^2 \cdot \exp(\varepsilon \cdot N)$$

$$\varepsilon = 0.45451 \times 10^{-5}$$

This model was checked against Wei's model, which has consistently shown a reasonable match, as shown for one such case in Figure 3.

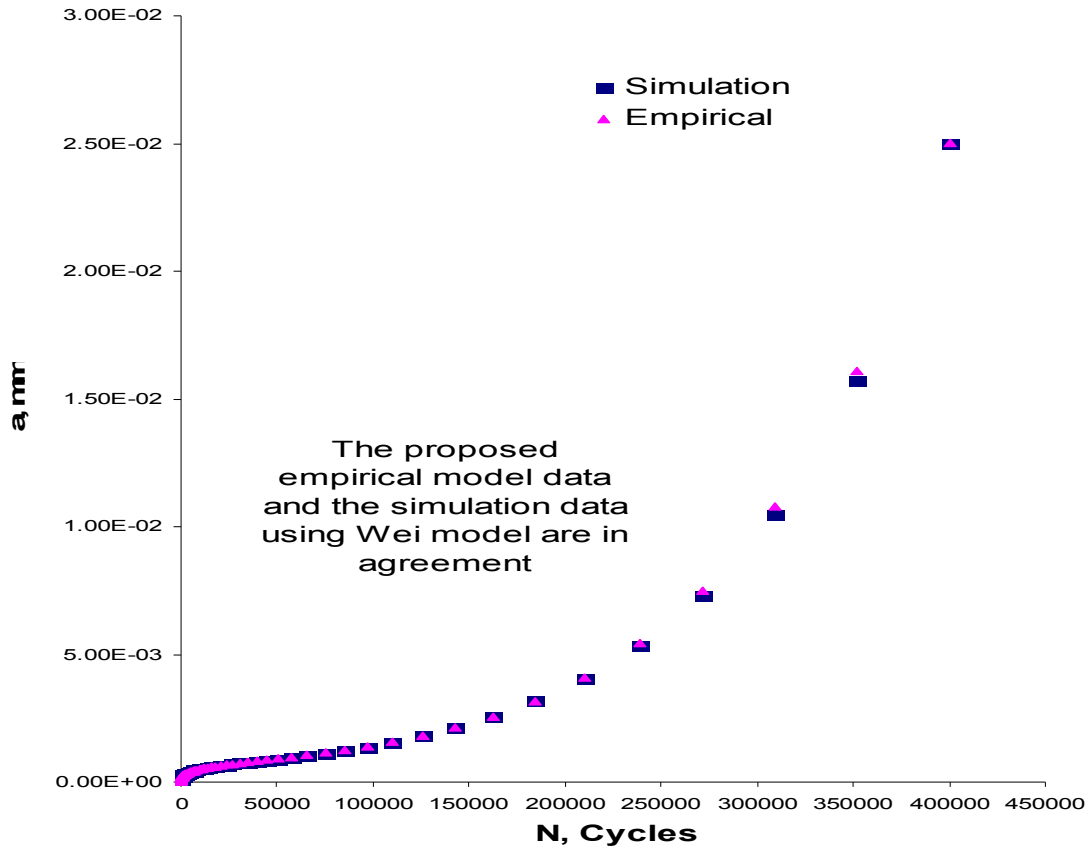


Figure 3. Graph of the simulation (Wei's model) and the proposed empirical model.

Assuming frequency, temperature, cyclic stress, & corrosion current are independent, the above general model is modified to the following form, which explicitly describes the environmental factors of stress, frequency and temperature:

$$a = A \cdot \sigma^{\varepsilon_1} \cdot \nu^{\varepsilon_2} \cdot I_p^{\varepsilon_3} \cdot N^{1/3} + B \cdot \sigma^{\varepsilon_4} \cdot \nu^{\varepsilon_5} \cdot I_p^{\varepsilon_6} \cdot N^2 \cdot e^{(\varepsilon_7 \cdot \sigma^{\varepsilon_8} \cdot \nu^{\varepsilon_9} \cdot N)}$$

where

$$\begin{aligned} \varepsilon_1 &= 0.182 ; \varepsilon_2 = -0.288 ; \varepsilon_3 = 0.248 ; \varepsilon_4 = 3.24 \\ \varepsilon_5 &= -0.377 ; \varepsilon_6 = 0.421 ; \varepsilon_7 = 4 \times 10^{-10} ; \varepsilon_8 = 2.062 \\ \varepsilon_9 &= 0.024 \end{aligned}$$

Based on the uncertainties of the three random variables ( $C_c$ ,  $C_r$ ,  $k_0$ ) used in this simulation, best estimates of the constant parameters A and B are presented as two parameter Weibull distributions as follows:

$$A \begin{cases} \beta = 3.32 \\ \alpha = 4.01 \times 10^{-7} \end{cases} \quad B \begin{cases} \beta = 1.7 \\ \alpha = 2.48 \times 10^{-22} \end{cases}$$

Similarly, this modified model has been verified against Wei's model, where once again a good match is secured as shown in Figure 4:

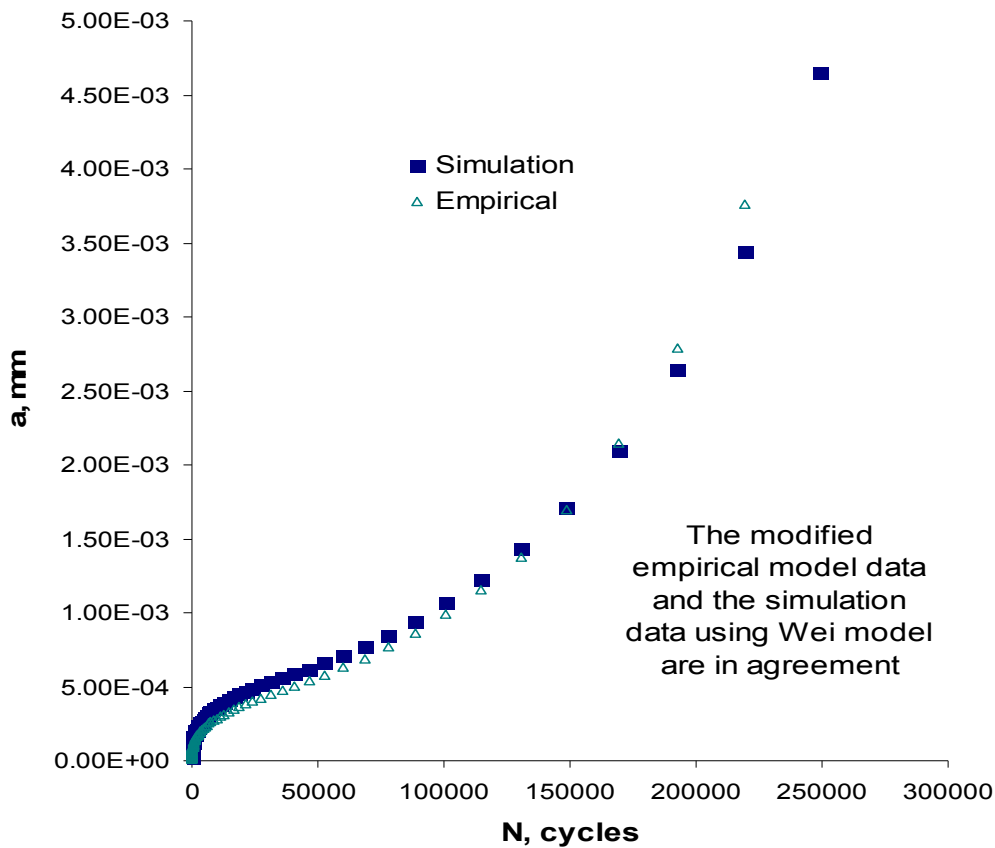


Figure 4. Graph of the simulation (Wei's model) and the proposed empirical model.

### Estimation of the Empirical Model Parameters A & B Probability Distribution Functions

Here we have verified the distribution of A and B parameters of the proposed empirical model structure against the variable environmental conditions. Utilizing **ReliaSoft-Weibull++ 5.32** program to analyze the distribution of each parameter respectively, it was possible to obtain the following, shown in Figures 5 and 6.

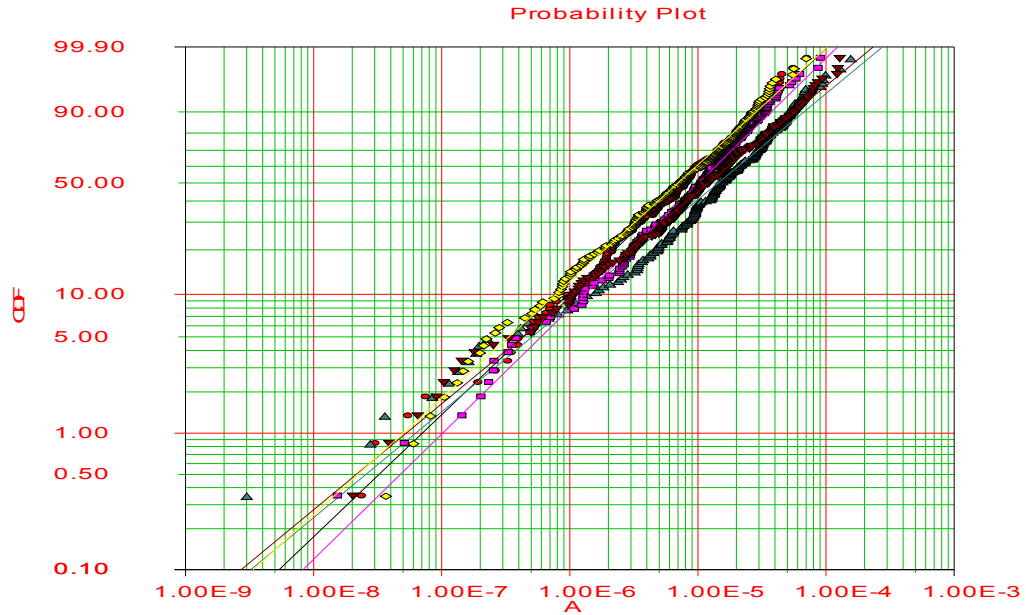


Figure 5. The CDF (Weibull) of parameter "A" distribution.

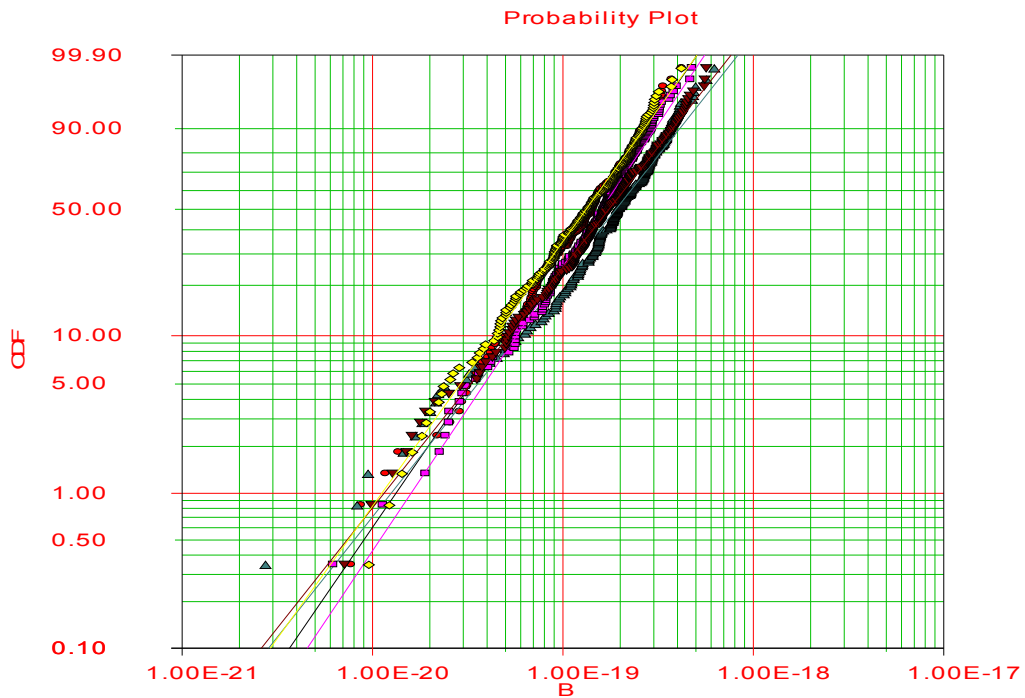


Figure 6. The CDF (Weibull) of parameter "B" distribution.

The environmental conditions used to run the simulation to build the above distributions are shown in Table 3.

**Table 3. Randomly selected environmental conditions to run the Monte Carlo Simulation to estimate A & B distributions**

Data set	T, K	$\sigma$ , MPa	$v$ , Hz	$I_p$ , A
1	373	10	10	$1 \times 10^{-5}$
2	673	20	7	$1 \times 10^{-6}$
3	473	30	5	$1 \times 10^{-5}$
4	273	40	4	$1 \times 10^{-6}$
5	573	50	3	$1 \times 10^{-5}$

The most noticeable evidence from Figures 5 & 6 is the negligible impact of environmental condition variations on the A and B distributions. This evidence implies that A and B are independent of the pipeline's surrounding environmental conditions, allowing us to focus on material properties as the main source of variability.

### Corrosion Model

Corrosive species in the pipeline flow streams play an important role in the overall degradation mechanism. Among all of the possible corrodents, the modeling shall concentrate on only two significant corrosive species in the oil refinery fields [15-28]:

1. Corrosion due to chloride concentration [Cl<sup>-</sup>]
2. Corrosion due to H<sub>2</sub>S concentration [H<sub>2</sub>S].

### Chloride Corrosion

Most chloride salts in crude oil are inorganic (sodium, magnesium, or calcium chlorides) and are effectively removed by the desalter. The non-extractable chlorides are not removed in the desalter, but can break down from downstream heating and processing to form hydrochloric acid (HCl). They cause corrosion and fouling problems. The forms of these chlorides are still being investigated and it is possible that they could be of organic types. Even with as little as 1% of the non-extractable chlorides, a major increase in the atmospheric tower overhead HCl and chloride levels can occur and cause severe corrosion and fouling problems [29].

Attempts to model the effects of chloride concentration have been well documented in literature. Table 3 lists some of the most promising models.

**Table 4. Chloride concentration effect models**

Proposed Model	Respective References
$I_p = A \exp(-B E_{pit})$ $I_{corr} = E \exp(-F \times [pH])$ $CR = G \exp(H \times [pH])$	[30],[31],[34] [33],[37] [33]
$E_{pit} = -C \log [Cl^-] + D$ $E_{corr} = -R [pH] (+,-) S$	[31],[32],[33],[34],[35],[36] [33],[36],[37]
$pH = -P \ln [Cl^-] + Q$	pH decreases with increasing Chloride concentration.[30],[32]
$I_p = M \exp(N \log [Cl^-])$	The current density increases with the increasing of Chloride concentration [30],[31],[34],[37]

The coefficients A,B,C,D,E,F,G,H,M,N,P,Q,R,S are constant values.

The effect of [Cl<sup>-</sup>] on E<sub>pit</sub> follows the following relation [38, 39]:

$$E_{\text{pit}}(T) = E_{\text{pit}}^{\circ}(T) + B(T) \log [\text{Cl}^-]$$

where E<sub>pit</sub><sup>°</sup> is the pitting potential at 1M chloride concentration, and B(T) is the slope of E<sub>pit</sub> dependence on [Cl<sup>-</sup>], with T the absolute temperature.

Similar to chloride [Cl<sup>-</sup>], increasing the temperature generally results in decreasing E<sub>pit</sub> values.

Examining the pitting behavior of carbon steel in bicarbonate solutions containing chloride, the following relations were found for E<sub>pit</sub><sup>°</sup> (mV) and B(T) as a function of temperature [38]:

$$E_{\text{pit}}^{\circ}(T) = -584.8 + 3.92 T, \quad \text{and } B(T) = -24.5 - 1.1 T$$

The general dependency is expressed as

$$I_p = A \exp(-B E_{\text{pit}}), \text{ and } E_{\text{pit}} = -C \log [\text{Cl}^-] + D,$$

We can combine this relation with I<sub>p</sub> values related to E<sub>pit</sub> and get:

$$I_p = A^* \exp(B^* \log [\text{Cl}^-])$$

## H<sub>2</sub>S Corrosion

Sulphur is one of the foremost corrodents which cause problems in the refinery industry. It occurs in crude petroleum at various concentrations, and forms a variety of chemical compounds, including hydrogen sulphide, mercaptans, sulphides, polysulphides, thiophenes, and elemental sulphur. Because of the strong influence of hydrogen sulphide on the corrosion behaviors of the steels, two forms of sulphide corrosion are distinguished [29, 40]:

1. Without hydrogen present, and
2. With hydrogen present.

### Sulphide corrosion without hydrogen present

Sulphur contained in hydrocarbon fractions in atmospheric and vacuum distillation units, catalytic cracking units, and hydro-treating and hydro-cracking units upstream of the hydrogen injection line destroys steel structures. Heat exchangers tubes, furnace tubes and piping are generally made of carbon steel. Although the data given by respondents were incomplete and scattered considerably, they were combined with earlier reported corrosion rates and presented as the so-called original McConomy curves [29, 40].

We tried to estimate our corrosion rate for carbon steel for the case of corrosion without hydrogen present from these curves and got a relation for corrosion rate dependent on temperature as,

$$\ln(CR) = 2 \times 10^{-6} \exp(2.09 \times 10^{-2} T[K])$$

For 6 wt% sulfur content.

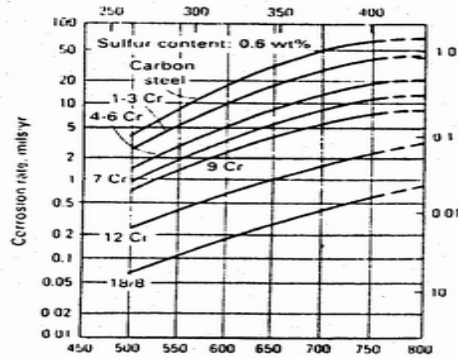


Figure 7. Modified McConomy curves showing the influence of temperature on sulphide corrosion rates of steels (without hydrogen present) [29, 40].

### Sulphide corrosion with hydrogen present

Basic information for material selection for refinery hydrogen units is provided by the so-called Couper-Gorman curves [29, 40], shown in Figure 8.

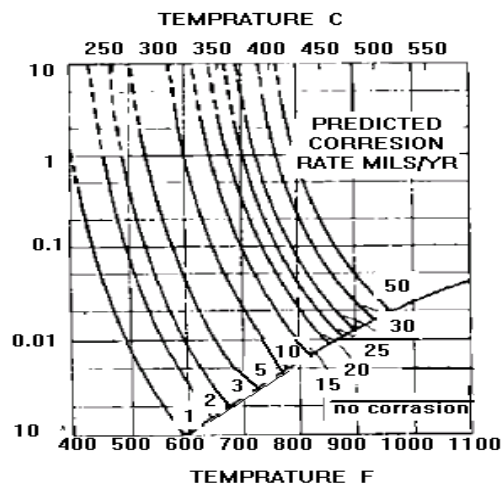


Figure 8. Effect of Temperature and Hydrogen Sulfide Content on High-Temperature  $H_2S/H_2$  Corrosion of Carbon Steel (Naphtha Desulpharizers)  
1 mil/yr = 0.025 mm/yr [29, 40].

Table 5. Corrosion Data of Carbon Steel in Naphtha

H <sub>2</sub> S [ mol% ]	Corrosion rate(CR) in [mm/yr]	$i_{corr}$ [ uA ]
0.1	$6E-5 \exp(0.0134 T[K])$ T[K]	$(2.5979E-2)\exp(0.0134 T[K])$
0.2	$2E-5 \exp(0.0155 T[K])$ T[K]	$(0.8660E-2)\exp(0.0155 T[K])$
...	...	.....
1.0	$1E-5 \exp(0.0170 T[K])$ T[K]	$(0.4330E-2)\exp(0.0170 T[K])$
...	...	.....
10.0	$8 E-6 \exp(0.0179 T[K])$ T[K]	$(0.3464E-2)\exp(0.0179 T[K])$

Using the data in Table 4, the general relation for the corrosion of carbon steel looks like:

$$CR(T) \approx I_p = M \times \exp(N \times T[K])$$

The H<sub>2</sub>S concentration effect on the corrosion current is affected by temperature, partial pressure, and cyclic conditions.

### Temperature

As shown above, temperature is the most important variable, and nearly all investigators report a rapid increase of corrosion with rising temperature. The majority of the data indicates that a temperature rise of 38°C (311 K) can be expected to approximately double the rate of attack. This relationship is illustrated by exponential curves by the M.W.Kellogg Co by G. Sorell et al. [41-45], which can be given by the following equation:

$$\text{Corrosion rate [In/yr]} = K * \exp(A T[K])$$

where K is a constant (~ 0.0014 ), A is a constant (~ 0.0062 ), and T is the temperature in Kelvin. Although Backensto et al. [46] have described a notable exception to this trend, in which the rates go through a maximum above 1000 °F (811 K), maximum corrosion rates typically result in the range from 672 K to 755 K. According to this literature, the collected data show without exception that under constant temperature the corrosion rate increases with higher hydrogen sulfide content. This explanation strengthens our suggestion that the corrosion rate increases exponentially with the hydrogen sulfide concentration, and this tendency, like the chloride corrosion relation, can be given in the following form:

$$\text{Corrosion rate [in / yr]} = 0.2138 \exp(0.0348 * [\text{H}_2\text{S (vol. \%)}])$$

The corrosion rate and the current in conversion [m A/ cm<sup>2</sup>] are given by in the literature. Another interesting fact in the literature [41] is that in attempting to relate the rate of attack to some measure of hydrogen sulfide content, it becomes apparent that often-used measures like weight, volume or molar percentage do not correlate as well as does the partial pressure of the hydrogen sulfide in the gas mixture. This illustrates the synergetic effects of hydrogen sulfide content, hydrogen sulfide partial pressure, and total pressure on each other and their effects on the corrosion rate, for which the following relation for corrosion rate can be derived:

$$\ln ( CR[\text{In/yr.}] ) = -5.73895 + 0.00665 T [K] + 0.0174 [\text{H}_2\text{S}]$$

and

$$[\text{H}_2\text{S}] = 0.0909 * (\text{partial pressure of hydrogen sulfide})$$

### Pressure

The total pressure appears to be an important corrosion variable only in as much as it determines the partial pressure of the hydrogen sulfide in a given gas mixture.

### Cyclic conditions

Another reason these cyclic conditions accelerate the corrosion rate is because they tend to deteriorate the sulfide scale, which is at least partially protective. The types of cyclic conditions of the greatest practical interest are cyclic heating and cooling, alternately reducing and oxidizing atmospheres, and forgetting the cyclic applied loading from the pumps to the pipelines in a refinery.

### Combination of chloride and hydrogen sulfide corrosion

In addition, in a sour (H<sub>2</sub>S) and chlorinated environment, the synergetic effect of chloride concentration and hydrogen sulfide concentration can increase the corrosion rate. Chloride in the presence of hydrogen sulfide tends to make localized corrosion attacks, and the synergetic effect of the two chemicals increases the corrosion rate in a sour environment in an additive form [47-49]. So we can say that the total corrosion rate is the sum of the contribution of the chloride and the hydrogen sulfide together:

$$CR = CR \text{ (chloride)} + CR \text{ (hydrogen sulfide)}$$

In other words,

$$I_{p,Total} = I_p^{[Cl^-]} + I_p^{[H_2S]}$$

The general form of the additive total corrosion rate can have different forms depending on the fixed temperature or the temperature and concentration of the corrosion species:

$$I_p(t) = I_p([Cl]) + I_p([H_2S])$$

$$I_p(t) = \{A \exp ( B \times \log ([Cl]) ) \} + \{ C \exp ( D \times [H_2S] ) \}$$

or,

$$I_p(t) = \{A \exp ( B (24.5 + 1.1 T) \log ([Cl]) ) \exp [(-3.92 E) T] + \\ C \exp\{D ( -5.73895 + 0.00665 T [K] + 0..174 [H_2S] )\}$$

### Bayesian parameter estimation

An actual failed pipeline from the field, at the Ruwais Refinery in Abu Dhabi, UAE, was investigated, and the following conditions were gathered:

- Pipeline Material: Carbon Steel
- Medium Flow: Heavy Vacuum Gas Oil
- Operating Temperature (T): 443 K
- Operating Pressure ( $\sigma$ ): 1.547 MPa
- Loading Frequency ( $\nu$ ):  $4.76 \times 10^{-7}$  Hz
- Wall thickness ( $a_f$ ): 0.00635 meters
- Service Life (N): 375.2784 cycles
- A & B Weibull distribution parameters are given in Equation 17.

The updated model was utilized to run the simulation and obtain the crack size “a<sub>i</sub>” values, which were then fitted to Weibull, as shown in Figure 9.

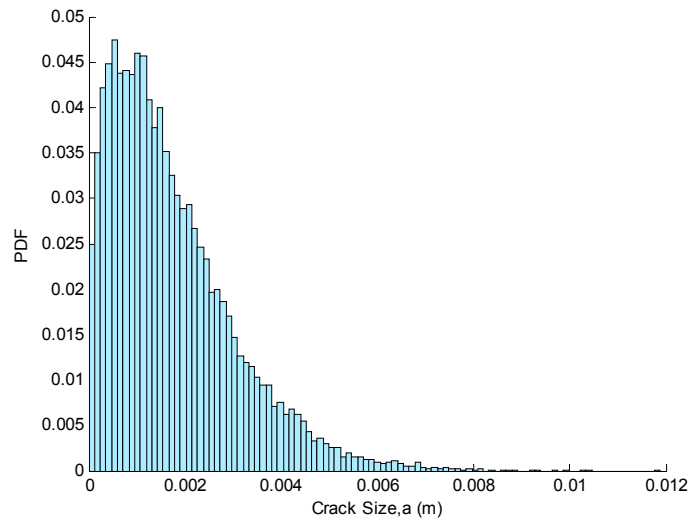


**Figure 9. The pdf of crack size “a”**

- Parameters for “a” Weibull distribution:  $\alpha= 0.00189$  ;  $\beta=1.3337$
- The CDF value for a crack size of 0.00635 m is 0.99348

From the outcomes one can see that the probability of a crack reaching the surface of the pipeline for complete fracture is 0.652%. This very low probability was expected, given that such type of pipeline failures happens very rarely. However, the corrosion fatigue phenomenon occurs over long period of time, and eventually, if the crack goes undetected, it will cause a complete crack through. Over the past 25 years there have been rare occasions of such incidents; and our model outcome is consistent with the industry’s historical experience. This model’s findings should support the introduction of new inspection cycles, which we believe will enhance the maintenance program.

### **Model Validation**

The main focus at this stage of the project was to construct the methodology to validate the proposed empirical model structure. However, this activity must take place in parallel with data collection to accomplish this task appropriately. The available field data are not sufficient but have been considered in the validation process. The experimental data would ultimately determine the probabilistic validity of the empirical model. Bayesian analysis is being employed with the help of a computer program to facilitate the probabilistic validation of the empirical model structure.

The Cortest corrosion-fatigue testing equipment was received and installed at UM.

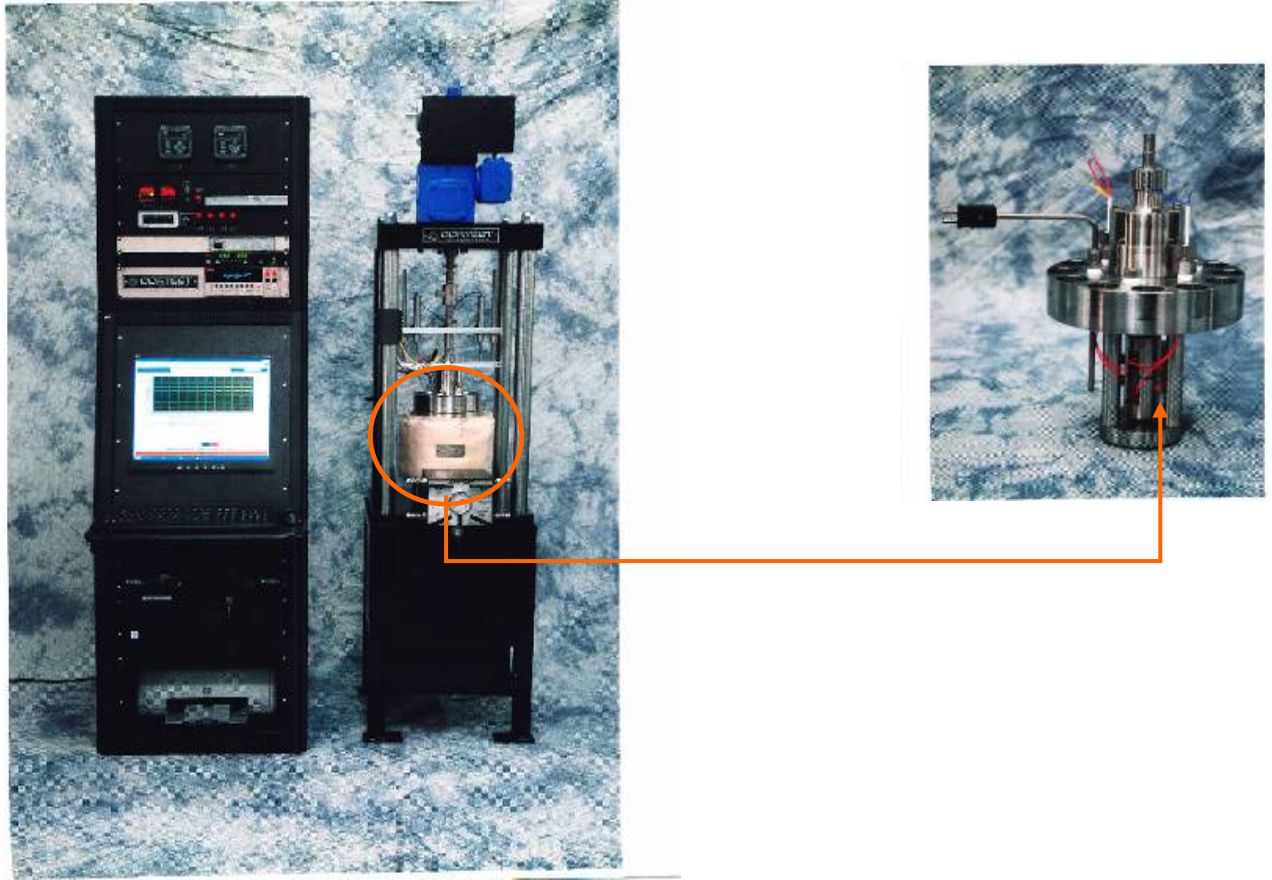


**Figure 10. Corrosion-fatigue testing equipment received from Cortest Corp.**

## 5. Recommendations for future work

- The assumption for making the  $n_c$  and  $n_r$ , fatigue exponent and corrosion fatigue exponent respectively, could be eased by considering them as random variables. This would add quite a cumbersome step in the computational analysis, but would bring the proposed empirical model closer to the realistic domain.
- The crack growth in the proposed empirical model assumed a constant shape factor of the crack to avoid the expenses of challenging analysis and computer programming. Nevertheless, adopting a varying crack shape factor would enhance the outcomes of the empirical model.
- The proposed empirical model did not consider two critical processes: pit nucleation and pit-to-crack transition. These two processes are still under wide investigation, and a solid acceptable modeling for them is yet to be determined. To include these two processes in the proposed empirical model means building almost a complete empirical model that could be further developed to a physical model.
- The empirical model has been mainly developed using generic data of high strength carbon steel that is widely common in the oil and gas industry fields. In addition, the on-going tests are mainly applied for the same material due to various limiting criteria. Hence, testing the empirical model application against other ferrous and non-ferrous

- material used in the oil and gas industry would claim the global application of the proposed empirical model.
- The widely acceptable superposition model of Wei had been employed as a bench model in the development of the empirical model. The corrosion fatigue part assumed the fracture mechanics simplest fatigue crack model, the Paris model. The following effects could be considered in future attempts:
    - Stress ratio
    - Plasticity at crack tip
    - Thickness effect
    - Limitation for small cracks
    - Sequence effects
    - Crack closure
  - The corrosion current in the proposed empirical model represents the corrosion effect of two major species: Chloride and Sulphur. The selection of these two species was based on the vast acceptance in the industry of their widespread affect in many failing pipelines. However, other degrading corrosive species could be considered, such as Napthanic acid, oxygen, caustic, and sulphate reducing bacteria (SRB). Though these species tend to be related to very specific applications, the resulting damages are quite intense. Hence, developing empirical model tailored specifically to account for these species would help avoid failures in critical applications of oil and gas industry.
  - The rotating equipment in the oil and gas industry plays a major role in sustaining the plants operation. Thus, considering the dynamics of this equipment in the modeling process would attract the end-user's attention to a powerful life assessment tool.
  - The experiments are underway at this point and are being conducted using seawater. More appropriate chemicals such as H<sub>2</sub>S should be tested, but this requires control and well ventilated lab facilities currently being built at PI.

## 6. Conclusion

The piping used in power plants and in chemical and petroleum industries have a history of experiencing degradation processes that result in economic losses due to interrupted operation, diminished production, and increased maintenance and inspection costs. A significant contributor of such degradation process is the corrosion-fatigue phenomenon. Recent research results from several research activities have shown to be promising in modeling the corrosion-fatigue mechanism. The research proposes a simple empirical corrosion-fatigue model consisting of only two parameters to be determined from field and experimental data. The process of pitting corrosion leading to initial crack forms the first term of the empirical model, while the second term accounts for the dominating degradation process of fatigue crack growth. The physical parameters in the proposed model reflect the actual pipeline conditions. The generic data collected from the open literature helped in the model development; however the field and experimental data need to supplement this data. An actual application of the model for field collected data has shown that this model is useful and reasonable. Additional field data and experimental data will be needed to conclusively validate the proposed model. This is part of the ongoing research and the outcomes of the tests will be reported in the dissertation of this project's GRA.

## 7. Key References

- [1] Harlow, D. G., and Wei, R. P. (1993). "A Mechanistically Based Approach to Probability Modeling for Corrosion Fatigue Crack Growth." *Engineering Fracture Mechanics*, 45, 1, 79-88.
- [2] Wei, R. P., and Harlow, D. G. (2005). "Mechanistically Based Probability Modeling, Life Prediction and Reliability Assessment," *Modeling Simulation Material Science Engineering*, 13, R33-R51.
- [3] Harlow, D. G., and Wei, R. P. (2001). "Probability Modeling and Statistical Analysis of Damage in the Lower Wing Skins of Two Retired B-707 Aircraft," *Fatigue Fractur Engineering Material Structure*, 24, 523-535.
- [4] Wei, R. P., Masser, D., Liu, H., and Harlow, D. G. (1994). "Probabilistic Considerations of Creep Crack Growth," *Material Science and Engineering*, A189, 69-76.
- [5] Wei, R. P. (2001). "A Model for Particle Induced Pit Growth in Aluminum Alloys," *Scripta Materialia*, 44, 2647-2652.
- [6] Dolley, E. J., Lee, B., and Wei, R. P. (2000). "The Effect of Pitting Corrosion on Fatigue Life," *Fatigue Fracture Engineering Material Structure*, 23, 555-560.
- [7] Wei, R. P. (2002). "Environmental Considerations for Fatigue Cracking. *Fatigue & Fracture of Engineering Materials & Structures*," 25, 8/9, 845-854.
- [8] Trethewey, K. R., and Chamberlain, J. (1995). *Corrosion for Science and Engineering*. Longman, England.
- [9] Harlow, D. G., and Wei, R. P. (1994). "Probability Approach for Prediction of Corrosion and Corrosion Fatigue Life," *AIAA Journal*, 32, 10, 2073-2079.
- [10] Kondo, Y. (1989). "Prediction of Fatigue Crack Initiation Life Based on Pit Growth," *Corrosion*, 45, 7-11.
- [11] Atkins, P. W. (1994). *Physical Chemistry*. W. H. Freeman and Company, NY.
- [12] Dowling, N. E. (1993). *Mechanical Behavior of Materials*. Prentice Hall, NJ.
- [13] Wei, R. P., and Gao, M. (1983). "Reconsideration of the Superposition Model for Environmentally Assisted Fatigue Crack Growth," *Scripta Metallurgica*, 17, 959-962.
- [14] State Structures Research Laboratory, and State Materials Office – Corrosion Research Laboratory (2002). "Galvanic Testing of Stressed Strands Inside Carbon Steel Pipe – Final Report," Florida Department of Transportation.
- [15] Chen, H.N., Chen, L.S., Lin, Q.H., and Long, X. (1999). *Corrosion* 55, p. 626.
- [16] Pardo, A., Otero, E., Merino, M.C., López, M.D., Utrilla, M.V., and Moreno, F. (2000). *Corrosion* 56, p. 411.
- [17] Romero, M., Duque, Z., Rincón, O., Pérez, O., Araujo, I. and Martinez, A. (2000). *Corrosion*, 56, p. 867.
- [18] Singh, I.B. (2001). *Corrosion*, 57, p. 483.
- [19] Laitinen, T. (2000). *Corros. Sci.*, 42, p. 421.
- [20] Gabetta, G. (1997). *Corrosion*, 53, p. 516.
- [21] Yamakawa, K., and Nishimura, R. (1999). *Corrosion*, 55, p. 24.
- [22] Sierra, R.C., Sosa, E., Oropeza, M.T., and González, I. (2002). *Electrochim. Acta*, 47, p. 2149.
- [23] Carneiro, R.A., Ratnapuli, R.C., and Lins, V.F.C. (2003). *Mater. Sci. Eng., A* 357, p. 104.
- [24] Omweg, G.M., Frankel, G.S., Bruce, W.A., Ramirez, J.E., and Koch, G. (2003). *Corrosion*, 59, p. 640.
- [25] Moraes, F.D., Bastina, F.L., and Ponciano, J.A. (*Corros. Sci.* 47 (2005), p. 1325.
- [26] Ren, C., Liu, D., Bai, Z., and Li, T. (2005). *Mater. Chem. Phys.*, 93, p. 305.
- [27] Kuzyukov, A.N., Nikhayenko, Y.Y., Levchenko, V.A., Borisenko, V.A., and Moisa, V.G. (2005). *Int. J. Hydrogen Energy*, 27, p. 813.
- [28] Chen, Y.Y., Liou, Y.M., and Shih., H.C. (2005). "Stress corrosion cracking of type 321 stainless steels in simulated electrochemical process environments containing hydrogen sulfide and chloride," *Materials Science and Engineering*, A 407, pp.114–126.

- [29] Gutzeit, J. et al. Corrosion in Petroleum Refining and Petrochemical Operations. *Metals Handbook*, 9th Ed., **13**, Corrosion Metals Park, Ohio 44073.
- [30] Gutzeit, J. (2000). "Effect of Organic Chloride Contamination of Crude Oil on Refinery Corrosion," *Corrosion*, Paper No. 00694.
- [31] [www.nace.org/nacestore/assets/ConferencePapers/2000/00694.pdf](http://www.nace.org/nacestore/assets/ConferencePapers/2000/00694.pdf)
- [32] Lin, C. J., et.al. "Scanning Microelectrode Studies of Early Pitting Corrosion of 18/8 Stainless Steel," *Corrosion*, Vol 54, No.4, pp.265-270.
- [33] Chapter 9. Pitting Corrosion, KAIST, <http://corrosion.kaist.ac.kr>
- [34] Andijani, I., et.al. (1999). "Studies on corrosion of carbon steel in deaerated saline solutions in presence of scale inhibitor," Presented at the WSTA IV Golf Conference, Bahrain.
- [35] Petek, A., et.al. (2007). "Localized Dissolution Kinetics of Low Carbon Steel," *Acta Chim Slov.* 54, pp 725-729.
- [36] Huisert, M. "Electrochemical Characterisation of Filiform Corrosion on Aluminium Rolled Products," [www.iospress.nl/html/9789040722363.php](http://www.iospress.nl/html/9789040722363.php)
- [37] Joseph, C., Farmer, et.al. (1997). "Crevice Corrosion & pitting of High-Level Waste Containers: Integration of Deterministic & Probabilistic Models," UCRL\_JC\_127980 Part 1.
- [38] Sardisco, J. B., et.al. (1965). "Corrosion of iron in an H<sub>2</sub>S-CO<sub>2</sub>-H<sub>2</sub>O system composition and protectiveness of the sulfide film as a function of pH," *Corrosion*, Vol 21, pp 350-354.
- [39] Brossia, C. S., and Cragolino, G. A. (2000). "Effect of Environmental Variables on localized Corrosion of Carbon Steel," *Corrosion*, Vol 56, No 5, pp 505-514.
- [40] Mack, L. P., et.al. (1984). "Effect of Bromide Ions on the Electrochemical Behavior of Iron," *Corrosion*, Vol 40, No 5.
- [41] Sorell, G., and Hoyt, W. B., (1956). "Collection and Correlation of High Temperature Hydrogen Sulfide Corrosion Data," The 12<sup>th</sup> Annual NACE Conference. The M. W. Kellogg Co., New York, N. Y.
- [42] Corrosion Doctors (2008). Corrosion Rate Conversion. <http://corrosiondoctors.org/Principles/Conversion.htm>
- [43] Shannon, D. W., and Boggs, J. E. (1958). "Factors Affecting the Corrosion of Steel By Oil-Brine-Hydrogen Sulfide Mixtures," *NACE*, Vol. 15, pp. 299t-302t.
- [44] Shannon, D. W., and Boggs, J. E. (1958). "An Analytical Procedure for Testing the Effectiveness of Hydrogen Sulfide Corrosion Inhibitors," *NACE*, Vol. 15, pp. 303t.
- [45] Carroll, J. J. (1998). "Software for Phase Equilibria in Natural Gas-Water Systems, A Discussion of the Effect of pH on the Solubility of Hydrogen Sulfide," *AQUALibrium*. <http://www.telusplanet.net/public/jcarroll/ION.HTM>.
- [46] Backnesto, E. B., Drew, R. E., and Stapleford, C. C. (1956). "High Temperature Hydrogen Sulfide Corrosion," *Corrosion*, Vol. 12, No. 1, pp. 22-31.
- [47] Ma, H.Y., Cheng, X.L., Chen, S.H., Li, Chen, G.Q., X., Lei, S.B., and Yang, H.Q. (1998). "Theoretical Interpretation on Impedance Spectra for Anodic Iron Dissolution in Acidic Solutions Containing Hydrogen Sulfide," *CORROSION*-Vol. 54, No. 8.
- [48] Lauvstad, G. Ø. (2007). "Breakdown in Passivity of Austenitic Stainless Steels in Cl<sup>-</sup> and H<sub>2</sub>S – Modeling and Characterization of the Pit Initiation Process," *NACE Corrosion*. Paper No.07660.
- [49] Wei, S., and Nescic S. (2007). "A Mechanistic Model of H<sub>2</sub>S Corrosion of Mild Steel," *NACE Corrosion*. Paper No. 07655.

## 9. Publications

- I. Chookah, M., Modarres, M. and Nuhi, M., "Development of a Probabilistic Model for Mechanistic Evaluation of Reliability of Oil Pipelines Subject to Corrosion-Fatigue Cracking," ASME DAC 2008 conference proceedings, New York, NY, 3-6 Aug 2008. (paper presented and published in the conference proceedings)

- II. Chookah, M., Modarres, M. and Nuhi, M., "Structuring a Probabilistic Model for Reliability Evaluation of Piping Subject to Corrosion-Fatigue Degradation" Probabilistic Safety Assessment & Analysis (PSA) 2008 conference proceedings, Knoxville, Tennessee, 7-11 Sep 2008. (presented and published in the conference proceedings)
- III. Chookah, M., Modarres, M. and Nuhi, M., Poster presentation, "PHM-International Conference on Prognostics and Health Management" (affiliated with the IEEE Reliability Society), Denver, CO, October 2008.
- VI. Chookah, M., Modarres, M. and Nuhi, M., Poster presentation, "Second International Energy 2030 Conference" held in Abu Dhabi, UAE, 4-5 November 2008.

## 10. Visits

1. 1st Trip: Mohamed Chookah visited Ruwais & Abu Dhabi Refineries of Takreer to collect data in Oct 2007. Along also, PI was visited to meet Dr. Seibi to discuss the data collection process.
2. 2nd Trip: Dr. Modarres and M. Chookah participated in the first Energy Education and Research Collaboration (EERC) Workshop held at the PI in Abu Dhabi from 4-5 January, 2008.
3. Dr. Seibi was hosted in Nov 2007 to attend M. Chookah's PhD thesis proposal and discuss the project's different aspects.
4. Dr. Ali Al-Mansoori was hosted by Dr. Modarres to explore new project regimes of common interest.
5. Dr. Seibi visited UMD in Sept 2008 to discuss the latest progress in the project and finalize the testing equipment shipment destination to UMD.

## 10. GRAs (names, degrees, graduation)

- Mohamed Chookah is the project graduate research assistant and currently a PhD candidate. He is expected to defend his PhD in May 2009.
- Mohamad Nuhi, is a faculty research assistant and currently a PhD candidate. He performs experimental tests, test planning, and lab management.

## **Appendices**

## Appendix A

### Second EERC PI-UMD Workshop The Petroleum Institute, Abu Dhabi, UAE November 2-3, 2008

#### Agenda

##### Sunday, November 2

8:00-8:15 Registration and Refreshments

8:15-8:30 Opening Remarks: University of Maryland and PI- Partners in Higher Education 89  
Prof. M. Ohadi, Provost and Interim President of PI.

8:30-9:00 EERC: Present and Future  
Prof. A. Bar-Cohen(UM)

9:00-9:30 Discussion

9:30-10:00 First Research Thrust:  
Energy Recovery and Conversion  
Prof. A. Gupta(UM)

10:00-10:30 Discussion

10:30-10:45 Coffee Break

10:45-11:15 Second Research Thrust:  
Energy Efficient Transport Processes  
Prof. R. Radermacher(UM)

11:15-11:45 Discussion

11:45-12:00 Title: ADNOC Scholars at UM  
Mr. E. Al-Hajri (Ph. D. Candidate, UM )

12:00-12:30 Third Research Thrust:  
Energy System Management  
Prof. S. Azarm(UM)

12:30-13:00 Discussion

13:00-14:30 Lunch

Emerging Research Topics:

14:30 -14:50 1: Reservoir Simulation  
Dr. A. Riaz(UM)

14:50-15:00 2: Robotics at PI  
Dr. H. Karki (PI)

15:00-15:30 Education And Transfer of Best Practices  
Dr. A. Nazeri (UM)

15:30-16:00 Discussion

16:00-16:30 Presentations by PI Undergraduate Interns at UM

- Mohamad, Tamer Chaklab-

- Amro El Hag

- Mahmoud Mohamed Adi

- Mohamed Al Hebsi

- Bakeer Bakeer

16:30 Adjournment (Sign-up for Monday's Working-Group Meetings)

##### Monday, November 3

Working-Group Meetings on individual Research Topics (parallel Sessions)

9:00-11:00 Individual meetings between PI and UMD researchers to be scheduled at the request of either

party. (sign-up the previous evening)

11:00-13:00 Individual Working-Group meetings on three Thrust areas. (2 hrs each in parallel).

Working-Group Meetings on individual Educational Topics (parallel Sessions)

9:00 Dr. Nazeri meet with Director of Arzana campus Dr. Al Hasani and female faculty, graduate and undergraduate students to discuss Women in Engineering (§3.2.4).

9:45 Dr. Bar-Cohen meet with Dr. Seibi and select members of PI to discuss Civil infrastructure program (§3.2.9).

10:30 Dr. Nazeri meet with Drs. Mooney, Karkoub and select members of PI to discuss Accreditation related issues (§3.2.3)

11:15 Dr. Nazeri meet with Janet Olearsky and select members of the Student Council on Student Exchange, Internship and other Exchange programs

13:00 Lunch

15:00-17:00 Debriefing session between UMD team and Provost and Director of Research to discuss the findings from this visit and finalize the path forward.

17:00 Adjournment

## Appendix B:

### Second EERC PI-UMD Workshop Attendees

#### **UMD:**

Avram Bar-Cohen  
Joseph Schork  
Reinhard Radermacker  
Grag Jackson  
Shapour Azarm  
Ashwani Gupta  
PK. Kannan  
Azar Nazeri  
Ebrahim Al Hajri

#### **PI/ADNOC:**

Mike Ohadi (Provost & Acting President)  
Karl Berteussen (Acting Director of Research)  
Shahin Negahban ( ADCO, Division Manager)

#### **Mechanical Engineering**

Tahar Nabil Tarfa  
Ebru G. Canbaz  
Isoroku Kubo  
Petros Voulgaris  
Abdenmour Seibi  
Hamad Karki  
Peter Rodgers  
Dennis Siniger  
Lyes Khezzar

#### **Chemical Engineering**

Bruce Palmer  
K. Nandakumar  
S. Alhashimi  
A. Almansoori  
Ghada bassioni  
Ahmed Addala  
Ahmed Al Shoaibi

#### **Electrical Engineering**

Abdurrahim Elkeib  
Yousef Abdel-Majid  
Lisa Lamont  
Lana Chaar

#### **Petroleum Geosciences**

Sandra Vega

#### **Arts & Sciences**

Albert Wijeweera  
Mirella Elkadi  
Addellatif Bouchalkka  
Curtis Bradley  
Nabil Al Nahari  
Celal Hakar Canbaz  
S. Morad  
S. Berrouk